Gerhard Schweitzer
Eric H. Maslen
Editors

Hannes Bleuler
Matthew Cole
Patrick Keogh
René Larsonneur
Eric Maslen
Rainer Nordmann
Yohji Okada
Gerhard Schweitzer
Alfons Traxler
Contributors

Magnetic Bearings

Theory, Design, and Application to Rotating Machinery



Springer

Magnetic Bearings

Gerhard Schweitzer · Eric H. Maslen
Editors

Magnetic Bearings

Theory, Design, and Application to Rotating Machinery

Contributors
Hannes Bleuler
Matthew Cole
Patrick Keogh
René Larsonneur
Eric Maslen
Rainer Nordmann
Yohji Okada
Gerhard Schweitzer
Alfons Traxler

Springer

Editors
Prof. Gerhard Schweitzer
Mechatronics Consulting
Lindenbergstr. 18A
8700 Kuesnacht
Switzerland
g.schweitzer@ggaweb.ch

Prof. Eric H. Maslen
University of Virginia
Dept. Mechanical &
Aerospace Engineering
122 Engineer's Way
Charlottesville VA 22904-4746
USA
ehm7s@virginia.edu

ISBN 978-3-642-00496-4 e-ISBN 978-3-642-00497-1
DOI 10.1007/978-3-642-00497-1
Springer Dordrecht Heidelberg London New York

Library of Congress Control Number: 2009922148

© Springer-Verlag Berlin Heidelberg 2009
This work is subject to copyright. All rights are reserved, whether the whole or part of the material is concerned, specifically the rights of translation, reprinting, reuse of illustrations, recitation, broadcasting, reproduction on microfilm or in any other way, and storage in data banks. Duplication of this publication or parts thereof is permitted only under the provisions of the German Copyright Law of September 9, 1965, in its current version, and permission for use must always be obtained from Springer. Violations are liable to prosecution under the German Copyright Law.
The use of general descriptive names, registered names, trademarks, etc. in this publication does not imply, even in the absence of a specific statement, that such names are exempt from the relevant protective laws and regulations and therefore free for general use.

Cover design: eStudio Calamar S.L.

Printed on acid-free paper

Springer is a part of Springer Science+Business Media (www. springer.com)

Preface

Active magnetic bearings generate forces through magnetic fields. There is no contact between bearing and rotor, and this permits operation with no lubrication and no mechanical wear. A special advantage of these unique bearings is that the rotordynamics can be controlled actively through the bearings. As a consequence, these properties allow novel designs, high speeds with the possibility of active vibration control, high power density, operation with no mechanical wear, less maintenance and therefore lower costs. Examples for actual *application areas* for magnetic bearings are

- vacuum techniques
- turbo machinery
- machine tools, electric drives, and energy storing flywheels
- instruments in space and physics
- non-contacting suspensions for micro-techniques
- identification and testing equipment in rotor dynamics
- vibration isolation

The main application area, actually, is *turbo machinery*. Applications range from small turbo-molecular pumps, blowers for CO_2 lasers in machine tools, compressors and expanders for air conditioning and natural gas, to large turbo-generators in the Megawatt range for decentralized power plants. The temperature range goes from very low temperatures close to -270 degree C up to 550 degree C. The number of industrial AMB applications is growing steadily.

Magnetic Bearings are a typical *mechatronic product*. The hardware is composed of mechanical components combined with electronic elements such as sensors and power amplifiers, and an information processing part, usually in the form of a microprocessor. In addition, an increasingly important part is *software*. The inherent ability for sensing, information processing and actuation give the magnetic bearing the potential to become a key element in *smart and intelligent machines*.

The *objectives of this book* are to convey principal knowledge about design and components of a magnetic bearing system, to build up the ability to assess a magnetic bearing for its use in an industrial application, in designing new machinery, or in rotordynamics, and to deal with it competently during operation. Therefore, the book equally addresses engineers and physicists in research, development, and in practice, who want to use magnetic bearings expertly or develop new applications.

The book has several authors, and this for a good reason. Three of the authors published a book on Active Magnetic Bearings (AMB) more than a decade ago. This book, published first in German by Springer-Verlag, then in English and Chinese, is out of print. A new edition alone would not have met the needs of this demanding area, and it is not possible for any single person to represent the whole area. Therefore, initiated by Gerhard Schweitzer at Tsinghua University in Beijing and encouraged by the research group of Prof. Yu Suyuan of the Institute of Nuclear and Novel Energy Technology, an other way of presenting the advanced knowledge in this field was realized. A group of authors agreed to contribute to the book, each of them an expert in his field, and the coordination and editing of the contributions has been done by two of them. The contributions emerged from many years of experience of the authors in research, development, and industrial application.

Research on AMB is being done worldwide. The control of magnetic bearings has become a reference example in many control labs, due to its inherent complexity, the opportunity to try out novel ideas and the practical relevance of the research. The progress in mechatronics technology, the availability of power electronics and computational hardware, and eventually the ability to make extensive use of advanced software within the AMB will continue to stimulate AMB research and application.

The contents of the book are arranged according to the requirements of advanced lectures and courses for continued education on magnetic bearings. The emphasis lies on explanation of the theoretical background and its relation to practical application. Some chapters focus on explaining the state-of-the-art in AMB design, others give a more conceptual outlook on areas still under development. Each chapter closes with an extensive literature reference.

The book would not have appeared without the on-going stimulation of our students, our colleagues, and our customers. We are very grateful for their comments and their support. The manuscript has been carefully and critically reviewed by Philipp Buehler (Mecos Traxler AG) and Larry Hawkins (Calnetix), and the authors are indebted to them for their many valuable suggestions. Finally, we thank Springer-Verlag for their obliging and informal acceptance of our suggestions and their fast implementation.

Zürich/Florianópolis and Charlottesville *Gerhard Schweitzer*
January 2009 *Eric Maslen*

Contents

1 Introduction and Survey
Gerhard Schweitzer 1

2 Principle of Active Magnetic Suspension
René Larsonneur 27

3 Hardware Components
Alfons Traxler and Eric Maslen 69

4 Actuators
Alfons Traxler and Eric Maslen 111

5 Losses in Magnetic Bearings
Alfons Traxler 135

6 Design Criteria and Limiting Characteristics
Gerhard Schweitzer 151

7 Dynamics of the Rigid Rotor
Gerhard Schweitzer 167

8 Control of the Rigid Rotor in AMBs
René Larsonneur 191

9 Digital Control
René Larsonneur 229

10 Dynamics of Flexible Rotors
Rainer Nordmann 251

11 Identification
Rainer Nordmann 299

12 Control of Flexible Rotors
Eric Maslen 319

13 Touch-down Bearings
Gerhard Schweitzer and Rainer Nordmann 389

14 Dynamics and Control Issues for Fault Tolerance
Patrick S. Keogh and Matthew O.T. Cole 407

15 Self–Sensing Magnetic Bearings
Eric Maslen 435

16 Self–Bearing Motors
Yohji Okada 461

17 Micro Magnetic Bearings
Hannes Bleuler 487

18 Safety and Reliability Aspects
Gerhard Schweitzer 505

Index 523

List of Contributors

Prof. Dr. Hannes Bleuler
Department de Microtechnique
EPFL
Lausanne - Ecublens 1015
Switzerland
Tel.: +41 - 21 - 693 59 27
Fax: +41 - 21 - 693 38 66
h.bleuler@ieee.org
people.epfl.ch/hannes.bleuler

Dr. Matthew O. T. Cole
Dept, of Mechanical Engineering,
Chiangmai University
Chiangmai 50200
Thailand
Tel.: +66 (0) 53 944146
Fax: +66 (0) 53 944145
motcole@chiangmai.ac.th
dome.eng.cmu.ac.th/~matt

Dr. Patrick Keogh
Centre for Power Transmission and Motion Control
Dept. of Mechanical Engineering
University of Bath
Bath BA2 7AY
UK
Tel.: +44 (0)1225 385958
P.S.Keogh@bath.ac.uk

Dr. René Larsonneur
MECOS Traxler AG
Industriestrasse 26
8404 Winterthur
Switzerland
Tel.: +41 - 52 - 235 14 11
Fax: +41 - 52 - 235 14 25
rene.larsonneur@mecos.com
www.mecos.com

Prof. Dr. Eric H. Maslen
Dept. of Mechanical and Aerospace Engineering
University of Virginia
Charlottesville, VA 22904-4746
USA
Tel.: +1 - 434 - 924 6227
Fax: +1 - 434 - 982 2037
ehm7s@virginia.edu
people.virginia.edu/~ehm7s/

Prof. Dr. Rainer Nordmann
Mechatronische Systeme, FB 16
Univ. of Technology Darmstadt
64287 Darmstadt
Germany
Tel.: +49 - 6151 - 16 21 74
Fax: +49 - 6151 - 16 53 32
nordmann@mim.tu-darmstadt.de
www.mim.maschinenbau.tu-darmstadt.de/Seiten/Mitarbeiter/nordmann.html

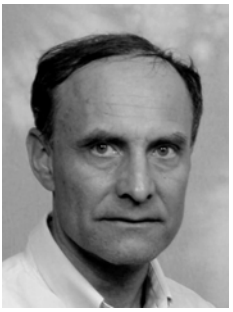
Prof. Dr. Yohji Okada
Ibaraki University
Dept. of Mechanical Engineering
4-12-1 Nakanarusawa
Hitachi, Ibaraki 316-8511
Japan
Tel.: +81 - 294 - 38 50 25
Fax: +81 - 294 - 38 50 47
okada@mx.ibaraki.ac.jp
www.mech.ibaraki.ac.jp/~okada

Dr. Alfons Traxler
MECOS Traxler AG
Industriestrasse 26
8404 Winterthur
Switzerland
Tel.: +41 - 52 - 235 14 10
Fax: +41 - 52 - 235 14 20
alfons.traxler@mecos.com
www.mecos.com

Prof. Dr. Gerhard Schweitzer
Lindenbergstr. 18A
8700 Küsnacht
Switzerland
Tel.: +41 - 44 - 910 94 59
g.schweitzer@ggaweb.ch
www.mcgs.ch

The Authors

Hannes Bleuler



Professor Bleuler earned his Master of Science from the ETH Zürich in Electrical Engineering in 1978. From 1979 through 1984, he was a teaching assistant at the ETH, Institute of Mechanics while he pursued his doctorate under the supervision of Professor Dr. Gerhard Schweitzer. He was awarded his Ph.D. in mechatronics with a specialization in magnetic bearings in 1984. From 1985 through 1987, he was a research engineer at Hitachi Ltd., Japan, in the Mechanical Engineering Research Laboratory. From 1988 to 1991, he served as a lecturer and senior assistant at ETH Zürich. During this time, he was co-founder of MECOS Traxler AG. From 1991 through 1995, Professor Bleuler held the Toshiba Chair of "Intelligent Mechatronics" at the Institute of Industrial Science of the University of Tokyo, where he then became a regular associate professor. From 1995 to the present, he has been a full professor at EPFL Lausanne in microrobotics and biomedical robotics. In 2000, he was a co-founder of xitact SA, Morges, who develop robotic surgery instrumentation and simulators. Since 2006, he has been member of the Swiss Academy of Technical Sciences (SATW).

Matthew Cole



Matthew Cole received his B.A. degree in Natural Sciences from the University of Cambridge, UK in 1994. He then spent nine years at the University of Bath completing both M.Sc. and Ph.D. degrees and then continuing as a researcher to develop his work on magnetic bearing control systems. In 2003, he moved to Thailand to take up a post teaching at Chiangmai University. He currently divides his time between Thailand and the UK and is active in research, teaching and consultancy on magnetic bearing control systems, rotor dynamics and active vibration control. He has chaired sessions on magnetic bearings at ISMB, MOVIC and ASME/IGTI Turbo Expo conferences. Recently his research has focused on the use of Lyapunov-based methods for optimization of rotordynamic system design and active control.

Patrick Keogh



Patrick Keogh received his B.Sc. degree from the University of Nottingham in 1979 and his Ph.D. degree from the University of Manchester in 1983. He then spent eight years working in the Engineering Research Centre of GEC Alsthom (now Alstom) as a Research Technologist before joining the Department of Mechanical Engineering at the University of Bath, UK in 1990. He now holds the position of Reader and is Head of the Machine Systems Group. His research interests include rotor dynamics, magnetic bearing systems, active vibration control, modern optimal control for multivariable systems, contact dynamics and associated thermal behavior of auxiliary bearings. He has been a member of the ISO TC108/SC2/WG7 committee for magnetic bearing standards since 1998. He is also a Point Contact for the rotor dynamics and magnetic bearings sessions at the ASME/IGTI Turbo Expo conferences. He recently became a Fellow of the Institution of Mechanical Engineers in the UK.

René Larsonneur



After graduation from the ETH Zürich in 1983 René Larsonneur worked as a teaching and research assistant at the Institute of Mechanics and later at the Institute of Robotics under the direction of Professor Dr. Gerhard Schweitzer. During this time he was involved in various research projects on active magnetic bearings (AMB) and specialized in the fields of control and rotordynamics for high speed rotation. In 1989 he joined the newly founded spin-off company MECOS Traxler AG, shortly before he was granted his ETH doctoral degree in 1990. Since that time, only interrupted by a one-year postdoctoral research fellowship on micro robotics in Japan in 1992, he has been a staff member of MECOS, focusing on rotordynamics and new control concepts for industrial AMB systems. In 2002, he joined the ISO TC108/SC2/WG7 technical committee for the development of a new magnetic bearing standard, and in 2006, he became a member of the IFToMM rotordynamics committee. Today, Dr. Larsonneur can look back to 25 years of involvement into the technology which still hasn't lost any of its original fascination to him. As a result of this long experience he is often called into the field as a chief commissioning engineer for challenging AMB systems, tasks he still counts among his main hobbyhorses. Dr. Larsonneur lives with his wife and his three children in Winterthur, Switzerland.

Eric Maslen



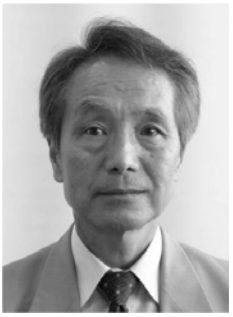
Eric Maslen earned his Bachelor of Science in mechanical engineering from Cornell University in 1980. Subsequently, he worked for five years for the Koppers Company as a research and development engineer with time off for a stint in the United States Peace Corps. He was awarded his doctorate in mechanical and aerospace engineering from the University of Virginia in 1990 and immediately joined the faculty at the same university. He was promoted to Professor in 2003. His research focus since his doctoral studies has been in controls, magnetics, and rotating machine dynamics with special application to magnetic bearings. Professor Maslen has been a member of the ISO TC108/SC2/WG7 committee for magnetic bearing standards since 1998. He has been a visiting professor at the Technical University of Vienna (1995), the Technical University of Darmstadt (2001), the University of California at Berkeley (2002), and Shandong University (2007 and 2008).

Rainer Nordmann



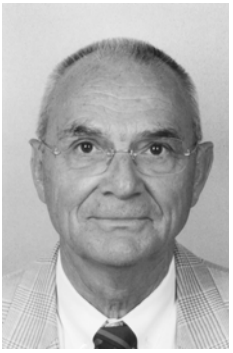
Rainer Nordmann became Professor of Machine Dynamics at the University of Kaiserslautern in 1980, where he was working in education and research until 1995. He then joined the Technical University of Darmstadt as a Professor of Mechatronics in Mechanical Engineering. His research interests include the dynamics of rotating machinery, identification and modal testing, machine diagnostics and mechatronic systems with special applications to active components in rotating machines like active magnetic bearings and piezoactuators. Between 1991 and 2007, he chaired several SIRM Rotordynamics conferences and in 1998 the 5th International IFToMM Rotordynamics Conference in Darmstadt. In addition, he is the chairman of the IFToMM Technical Committee on Rotordynamics. He was a visiting professor at the Universities of Tokyo and Kobe in 1991 invited by the Japan Society for the Promotion of Sciences (JSPS) and received the first Jorgen Lund Memorial Medal at the IFToMM Conference in Sydney 2002.

Yohji Okada



Dr. Okada was born in Iwaki, Japan in 1942. He received the B.S., M.S., and Ph.D. degrees in Mechanical Engineering, from Tokyo Metropolitan University, Tokyo, Japan, in 1965, 1967, and 1973, respectively. From 1971 to 1989, he was an Assistant/Associate Professor of Mechanical Engineering at Ibaraki University, Hitachi, Japan. He was then a Professor of Mechanical Engineering at Ibaraki University until March 31, 2007. He is currently a Professor Emeritus and an Industrial Cooperative Researcher in Ibaraki University. His research interests include magnetic bearings and application, self-bearing motors, artificial heart pumps, active/regenerative vibration control, servo control systems, and electromagnetic engine valve drives. Dr. Okada is a member of the Japan Society of Mechanical Engineers, and a member of the Japan Society of Applied Electromagnetics and Mechanics.

Gerhard Schweitzer



Gerhard Schweitzer worked for several research institutes and universities (DLR Oberpfaffenhofen, University of Stuttgart, TU Munich, NASA Marshall Space Flight Center, Huntsville) for 16 years before joining, in 1978, the ETH Zürich (Swiss Federal Institute of Technology) as a Professor of Mechanics. In 1989 he became Head of the Institute of Robotics and founded the International Center for Magnetic Bearings at the ETH. In 1988 he chaired the First International Symposium on Magnetic Bearings. He was a founding member of the Mechatronics Group, of the Neuro-Informatics Group, and of the Nano-Robotics Project at the ETH. He was a visiting professor at Stanford University, USA, at Campinas and at Florianopolis, Brazil, and at the ZiF of the University Bielefeld, Germany. His research interests include the dynamics of controlled mechanical systems, especially interactive robots, magnetic bearings and mechatronics. He is a member of the Swiss Academy of Technical Sciences. Since retiring from official duties at the ETH in 2002, he is a private Mechatronics Consultant. During 2003/04 he was appointed chair professor at Tsinghua University, Beijing, at the Institute of Novel and Nuclear Energy Technology. He lives in Brazil and Switzerland.

Alfons Traxler



Alfons Traxler had been working several years as an engineer in the air defense industry when he started his masters study at the ETH Zürich (Swiss Federal Institute of Technology). After graduation from the ETH in 1978, he joined the newly established research group of Prof. Dr. Gerhard Schweitzer. In addition to his research work, he was responsible for the AMB lab and for the design of several AMB systems built for other universities and research institutes. His doctoral thesis on properties and design of Active Magnetic Bearings was completed in 1985. To transfer the experience, the expertise and the practical know-how from the research projects in Active Magnetic Bearings into industrial products, he established MECOS Traxler AG in 1988 as a spin-off company to design, produce and market industrial AMB systems. He is the president of MECOS which has become one of the leading suppliers of Active Magnetic Bearings with many thousands of industrial AMB systems out in the field.

1

Introduction and Survey

Gerhard Schweitzer

In the first part of this introduction the basic function of the actively controlled electromagnetic bearing will be shown. It offers a novel way of solving classical problems of rotor dynamics by suspending a spinning rotor with no contact, wear and lubrication, and controlling its dynamic behavior. In a general sense such an *Active Magnetic Bearing - AMB* is a typical mechatronics product, and definitions of *mechatronics* will point to the knowledge base for successfully dealing with AMB. The history of AMB is briefly addressed: first applications of the electromagnetic suspension principle have been in experimental physics, and suggestions to use this principle for suspending transportation vehicles for high-speed trains go back to 1937. There are various ways of designing magnetic suspensions for a contact free support - the AMB is just one of them. A classification of the various methods is shown as a survey. The main characteristics of AMB, their advantages and drawbacks are listed, and finally, some examples of the application of AMB in research and industry are given.

1.1 Principles of Magnetic Bearing Function

Generating contact free magnetic field forces by actively controlling the dynamics of an electromagnet is the principle which is actually used most often among the magnetic suspensions. The Figures 1.1 and 1.2 present the main components and explain the function of a simple bearing for suspending a rotor just in one direction:

> A sensor measures the displacement of the rotor from its reference position, a microprocessor as a controller derives a control signal from the measurement, a power amplifier transforms this control signal into a control current, and the control current generates a magnetic field in the actuating magnets, resulting in magnetic forces in such a way that the rotor remains in its hovering position.

G. Schweitzer, E.H. Maslen (eds.), *Magnetic Bearings*,
DOI 10.1007/978-3-642-00497-1_1, © Springer-Verlag Berlin Heidelberg 2009

The control law of the feedback is responsible for the stability of the hovering state as well as the stiffness and the damping of such a suspension. Stiffness and damping can be varied widely within physical limits, and can be adjusted to technical requirements. They can also be changed during operation. Figure 1.3 shows a demonstration model for a vertical, one degree of freedom suspension. In this case the displacement of the small pencil-sharpener in the shape of a globe is measured optically by a simple photo transistor.

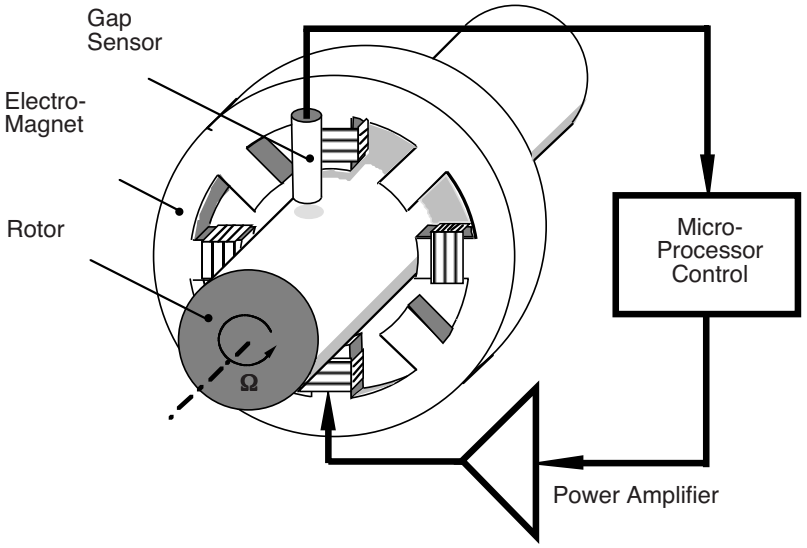


Fig. 1.1. Function principle of an active electromagnetic bearing, suspension of a rotor in vertical direction

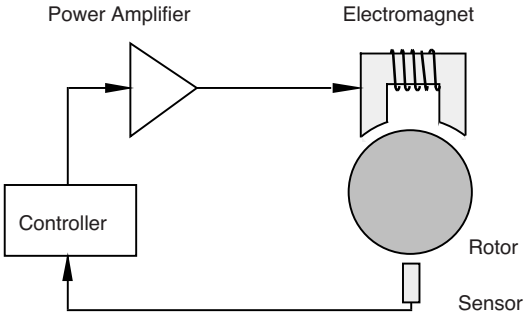


Fig. 1.2. Schematic of the function principle of the active electromagnetic suspension

A real rotor of course needs several magnets, which in the example of Fig. 1.4 are connected to one another by a multivariable controller.

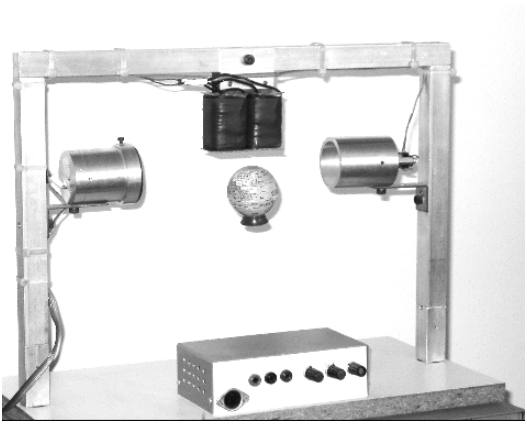


Fig. 1.3. Demonstration bearing

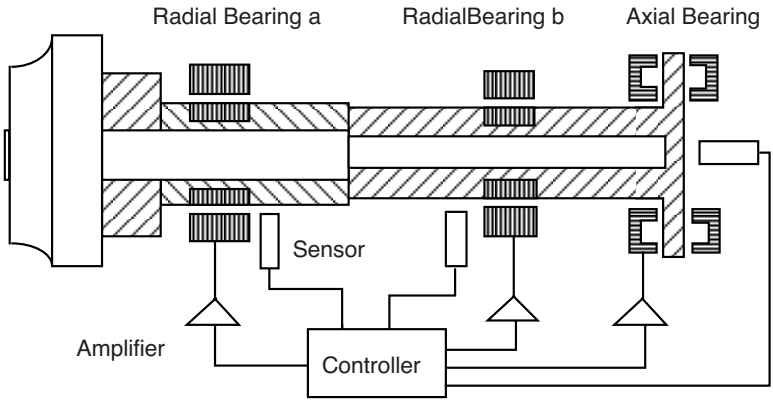


Fig. 1.4. Schematic for the suspension of a rotor in one plane

The corresponding hardware is shown in the classical demonstration model [46] of Fig. 1.5. The rotor has a length of about 0.8 m and a weight of 12 kg. The displacement measurement is done optically through a CCD-array, which directly produces digital signals for the microprocessor controller. The air gap for this demonstration rotor was 10 mm, which is quite large.

The electromagnetic rotor bearing belongs to a group of products which basically all have a similar structure and can be investigated with similar

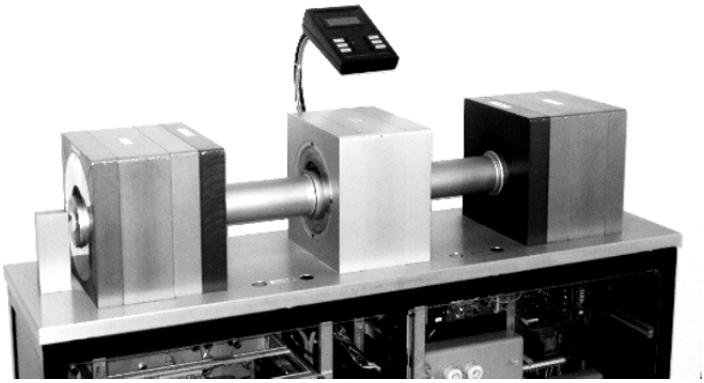


Fig. 1.5. Rotor in magnetic bearings, right and left, with motor drive in the middle, for the Zürich Exhibition Phænomena (1984) [46]

methods. They can be characterised by the keyword *mechatronic product*. Their common properties will be discussed in the next section.

1.2 The Magnetic Bearing as a Mechatronic Product

Mechatronics is an interdisciplinary area of engineering sciences based on the classical fields of mechanical and electrical engineering and on computer science. A typical mechatronic system picks up signals, processes them and puts out signals to produce, for example, forces and motions. The main issue is that of extending and completing mechanical systems by sensors and microcomputers. The fact that such a system senses changes in its environment and reacts to these changes according to a suitable method of information processing makes it different from conventional machines. The schematic of Fig. 1.6 demonstrates the interconnections of elements from mechanical and electrical engineering and from computer science, forming a mechatronic product. There are a number of other definitions of mechatronics, edited by various scientific organizations or for emphasizing local preferences, but the differences are not decisive. Examples for mechatronic systems are robots, digitally controlled combustion engines, self-adjusting machine tools, or automated guided vehicles. Typical for such a product is the high extent of system knowledge and software which is necessary for its design, construction, and operation. The software is built into the product itself, representing an integral part of it. In such a case it is absolutely justified to denominate *software as a machine element*.

With its interconnection of mechanical and electronic components and with a large amount of software being part of the system, the electromagnetic bearing represents a typical product of mechatronics. Therefore the magnetic

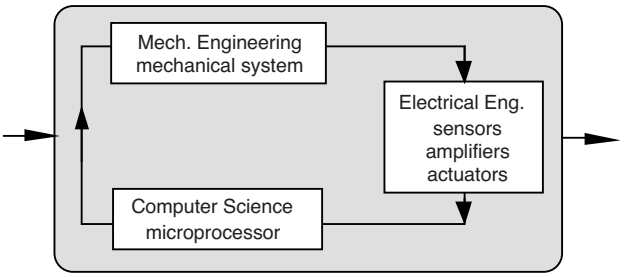


Fig. 1.6. Mechatronic System: The system picks up signals from its environment, processes them in an intelligent way and reacts, for example, with forces or motions. Methods for connecting the various areas of knowledge - mechanical, electrical engineering and computer science - are provided by the basic engineering sciences, system theory, control techniques and information processing

bearing is a good example for demonstrating and teaching the structure and design of mechatronic products. Methods for modeling the dynamics of the mechanical plant and designing the controller will be demonstrated and explained in the subsequent chapters. Important components such as sensors and microprocessors will be introduced, and their properties and applications will be discussed in the context of magnetic suspension of rotors. Before doing that, however, the next section will briefly outline historic developments, the actual technical situation, and applications in research and industry.

1.3 The Magnetic Bearing in Transportation, Physics and Mechanical Engineering

The idea of letting a body hover without any contact by using magnetic forces is an old dream of mankind. It is, however, not simple to fulfill. As early as 1842, Earnshaw stated that it is impossible to stably levitate any static array of magnets by any arrangement of fixed magnets and gravity [17]. Earnshaw's theorem can be viewed as a consequence of the Maxwell equations, which do not allow the magnitude of a magnetic field in a free space to possess a maximum, as required for stable equilibrium. In 1939, when there was already real interest in technical applications of magnetic bearings, Braunbek [14] independently gave further physical insights.

However, recent results reveal a tendency to overextend the validity of Earnshaw's law. The *Levitron* is a gyro top, which demonstrates that a spinning body under certain conditions can hover freely within an array of permanent magnets, and which for this reason has become a famous physical toy. The gyroscopic action must do more than prevent the top from flipping. It must act to continuously align the top's precession axis to the local magnetic field directions. A theoretical derivation of the behavior is given in [43, 9]. A

more technical explanation, in terms of classical rotor dynamics, is given in [20, 35]: A particle in space, with three degrees of freedom, may be constrained by three restoring forces, characterized by three stiffness coefficients. The spinning body, however, has six degrees of freedom, and it needs a 6×6 stiffness matrix to characterize the stiffness properties. Indeed, it is the joint effect of gyroscopic forces and the coupling terms for translation and inclination in the stiffness matrix that leads to a limit-stable range for the spin velocity with lower and upper boundaries. For permanent magnet arrangements the field distribution and its optimization has been calculated in [34].

Still another way to allow stable hovering in a permanent magnetic field is to use *diamagnetic materials*, which respond to magnetic fields with mild repulsion. Diamagnets are known to flout Earnshaw's theorem, as their negative susceptibility results in the requirement of a minimum rather than a maximum in the field's magnitude [21]. Thus, stable levitation of a magnet can be achieved using the feeble diamagnetism of materials that are normally perceived as being non-magnetic: even human fingers can keep a magnet hovering in midair without touching it. Up to now, however, the diamagnetically produced magnetic forces have been too small to be of technical interest.

It is the use of *ferromagnetic material* that allows generation of the high magnetic forces by industrial bearing applications. To make use of the large forces achievable by ferromagnets for a stable free hovering, the magnetic field has to be adjusted continuously in response to the hovering state of the body. This can be done with controlled electromagnets. In 1937, suggestions toward this aim were published for two very different areas: transportation and physics. These suggestions, and the consequences which have developed in the course of time, will be presented briefly, leading into the main body of the chapter, where the electromagnetic suspension of rotors, especially in the area of mechanical engineering, will be examined.

Kemper, in 1937, applied for a patent [28] for a hovering suspension, a possibility for a *new means of transportation*. In [29] he described an experiment in which an electromagnet with a pole area of 30 by 15 cm with 0.25 Tesla flux density and with a power of 250 W carried a load of 210 kg over an air gap of 15 mm. For the control, he used inductive or capacitive sensors and valve amplifiers. This experiment was the predecessor of the later magnetically levitated vehicles. These vehicles were built in the sixties in various designs, mainly in England, Japan, and Germany. The magnetically levitated vehicle KOMET of the company Messerschmitt-Bölkow-Blohm, for example, achieved a speed of 360 km/h in as early as 1977 on a special experimental track in Germany.

The magnetically levitated vehicle, *MAGLEV*, which uses the electromagnetic principle, is suspended without any contact by several magnets from the iron track, as shown in Fig. 1.7. An important element of the MAGLEV characterising the load-carrying properties of a supporting magnet is the *magnetic wheel*. Figures 1.8, 1.9, and 1.10, taken from the papers of Gottzein [23, 22], show the mechanical arrangement of the magnetic wheel, and its

control structure. Each of these electro-magnets was controlled separately. The block-diagram of Fig. 1.10 shows that the air gap s, the acceleration $\ddot{z}$ of the vertical motion of the magnet, and the magnet current I are measured for each magnet. The control input is the magnet voltage U. The design of the control is documented by extensive literature.

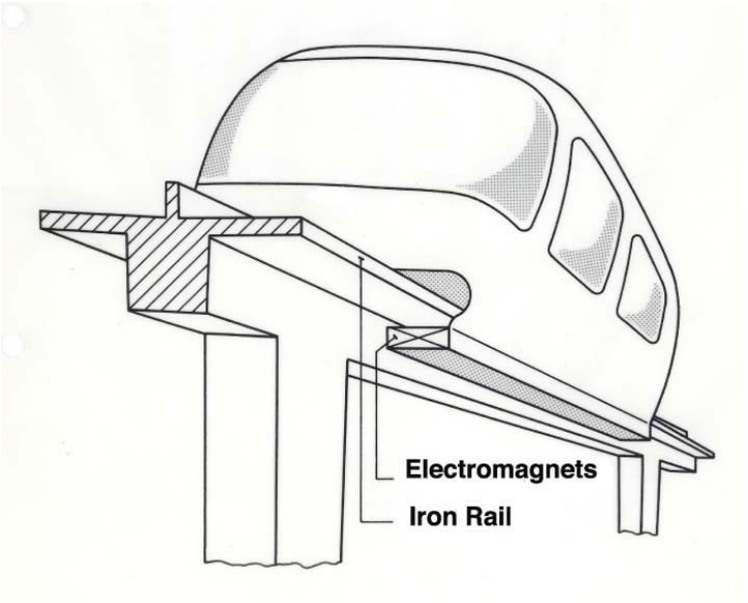


Fig. 1.7. Scheme of a MAGLEV on an elevated guideway

MAGLEVs are regularly discussed at international conferences, and magnetic components are often presented in the *IEEE-Transactions on Magnetics*. Recently, a short route between the Center of Shanghai and the Pudong Airport has been put into regular operation. Route extensions and construction of new routes are now being discussed in various countries [31].

The construction of *physical apparatuses* is another most interesting application of electromagnets. It was given an essential impulse in 1937 by Beams and Holmes at the University of Virginia [7, 27]. They suspended small mm-sized steel balls in a hovering state, and they brought them to very high rotation speeds for testing their material strength. They reached a spectacular rotation speed of about 18 million rpm (300 kHZ) which caused the steel balls to burst from centrifugal forces [8].

An area which gave some incentive to the design of AMB and provided some interesting magnetic bearing construction is *aerospace*. One of the very early investigations aimed at magnetically suspending a rate gyro for deriving the angular rate directly from the control signals of the magnetic bearing

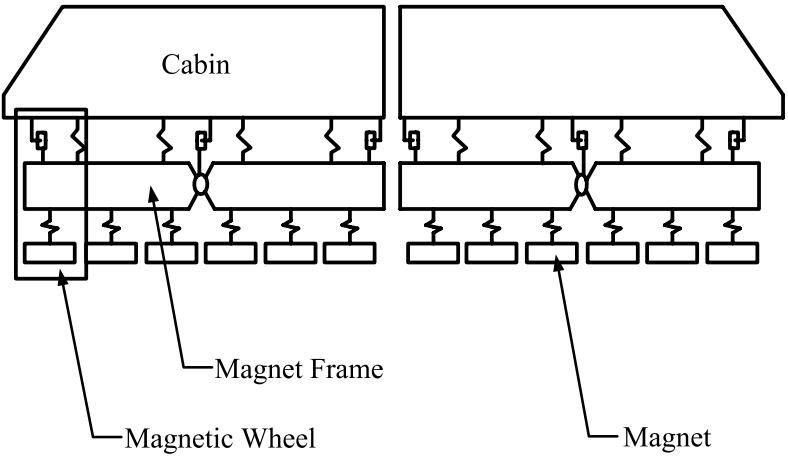


Fig. 1.8. Schematic diagram of a vehicle with modular support and guidance systems. The numerical specifications for the prototype experimental vehicle Transrapid 06 are as follows. Year of construction: 1982, weight: 122 t, speed: 400 km/h, motoring system: synchronous linear motor, iron casing, power: approx. 12 MW; elevated guideway: 25 m field-length, steel reinforced concrete twin supports, 5 m high

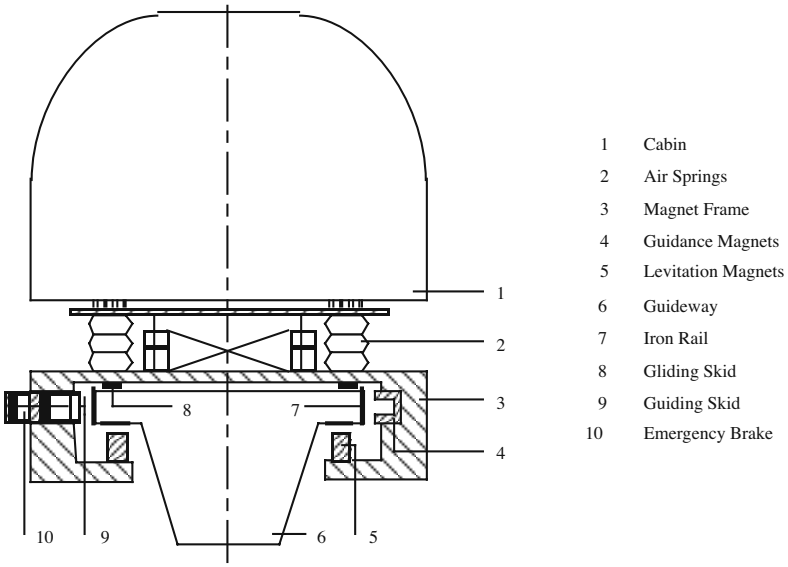


Fig. 1.9. Schematic figure for the mechanical structure of the *magnetic wheels* with secondary suspension and mechanical support

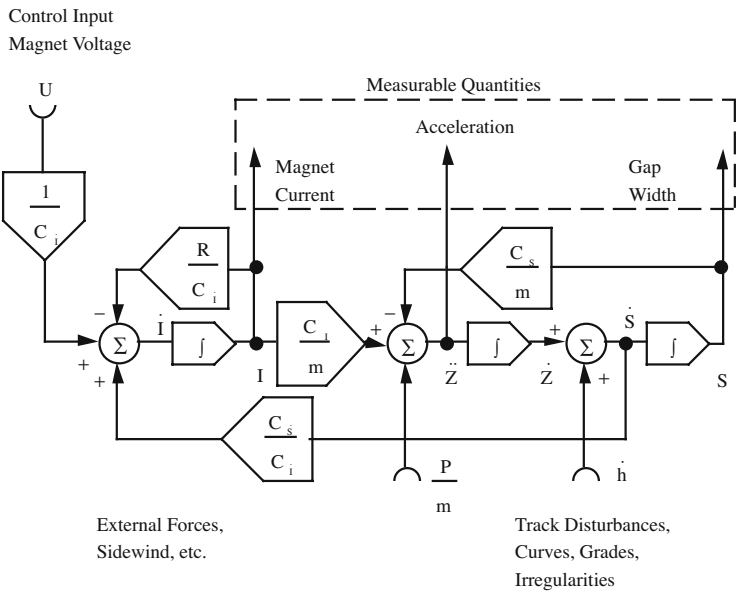


Fig. 1.10. Structure of the controller for a single *magnetic wheel*

was performed by [30]. Another early research focus was on magnetically suspended momentum-wheels for the attitude control of satellites [44]. These investigations have been continued intensively in various countries. For the vibration-free suspension of sensitive components, for example for optical devices in satellites or for microgravity experiments, magnetic suspensions have also been suggested.

The technology on the magnetic suspension of *rotors for technical purposes* has been developing greatly in the past decades. There are several reasons for this. One is the availability of components for *power electronics* and *information processing*. Another reason is the theoretical progress in *control design* and in *modelling the dynamics of the rotor*. Thus, as early as in 1975, there were theoretical and experimental solutions for active damping of self-excited vibrations of centrifuges [41]. Essential contributions for the introduction of magnetic bearings to industrial applications have come from *Habermann* and the company *Société de Mécanique Magnétique (S2M)* [24]. The company S2M, founded in 1976, was a spin-off of the French Société Européenne de Propulsion (SEP). In the meantime there are several companies which specialise in the engineering and the manufacturing of magnetic bearings. Thorough surveys on the state of the art are given by the *International Symposia on Magnetic Bearings (ISMB)*, and in its proceedings. The first three ones took place in Switzerland [42], Japan [25], and the United States [6], and the symposia have been continued biannually in these countries. A recent survey on research and industrial activities on AMB is presented on a website of the

University of Vienna [19]. The widening industrial application initiated first efforts to standardize AMB vocabulary, and performance [1, 2, 3, 4].

1.4 Classification of Magnetic Bearings

In addition to the active electromagnetic bearing which will be dealt with in detail in this book, there are numerous other design variations to generate field forces to support or to suspend a body without any contact. Even when a body cannot hover in a stable and free way, at least the hovering can be achieved in some of the degrees of freedom. Figure 1.11 presents a survey on a possible classification of the magnetic forces and the magnetic hovering [12].

This classification systematically covers the known types of magnetic bearings. Two main groups can be distinguished by the way in which magnetic forces can be calculated and represented, distinguishing between *reluctance force* and *Lorentz force*. Of course, the basic physical principle, the cause of the magnetic effect in moving electric charges, is the same for both groups.

In the first case of the *reluctance force*, when not concerned with atomic or subatomic scale, engineering practice has found a nice way around dealing with quantum physics by describing the media with the *magnetization constant* $\mu = \mu_r \mu_0$, with the *relative permeability* μ_r depending on the material. Such materials are subject to a magnetic force called a reluctance force, as opposed to the Lorentz force obtained in the second case. The reluctance force is derived from the energy stored in the magnetic field which can be converted to mechanical energy. Thus the reluctance force $\underline{\mathbf{f}}$ is obtained from the *principle of virtual work*:

$$\underline{\mathbf{f}} = \partial W / \partial \underline{\mathbf{s}} \tag{1.1}$$

with the field energy W and the virtual displacement $\partial \mathbf{s}$ of the hovering body. A magnetic force of this type always arises at the surface of media of different relative permeability μ_r, e.g. iron and air. The force direction is perpendicular to the surface of the different materials. The greater the difference in the permeability, the greater the force f. For ferromagnetic materials with $\mu_r \gg 1$ the forces can become very large, thus fulfilling an essential prerequisite for a technical use. In the literature on electrical machines, the magnetic resistance of an arrangement is called reluctance. It is inversely proportional to the permeability μ_r. The force is acting in such a way that it tends to decrease the reluctance of the mechanical arrangement. Electrical drives making use of this property are called reluctance motors.

A further prerequisite for real hovering is that the magnetic forces acting on the body actually keep the body in a stable state of levitation. Usually, in industrial applications, it is necessary to have active means, a control loop, to continuously adapt the magnetic field to the motion of the body. This requirement leads to the category of active magnetic bearings. In Fig. 1.11

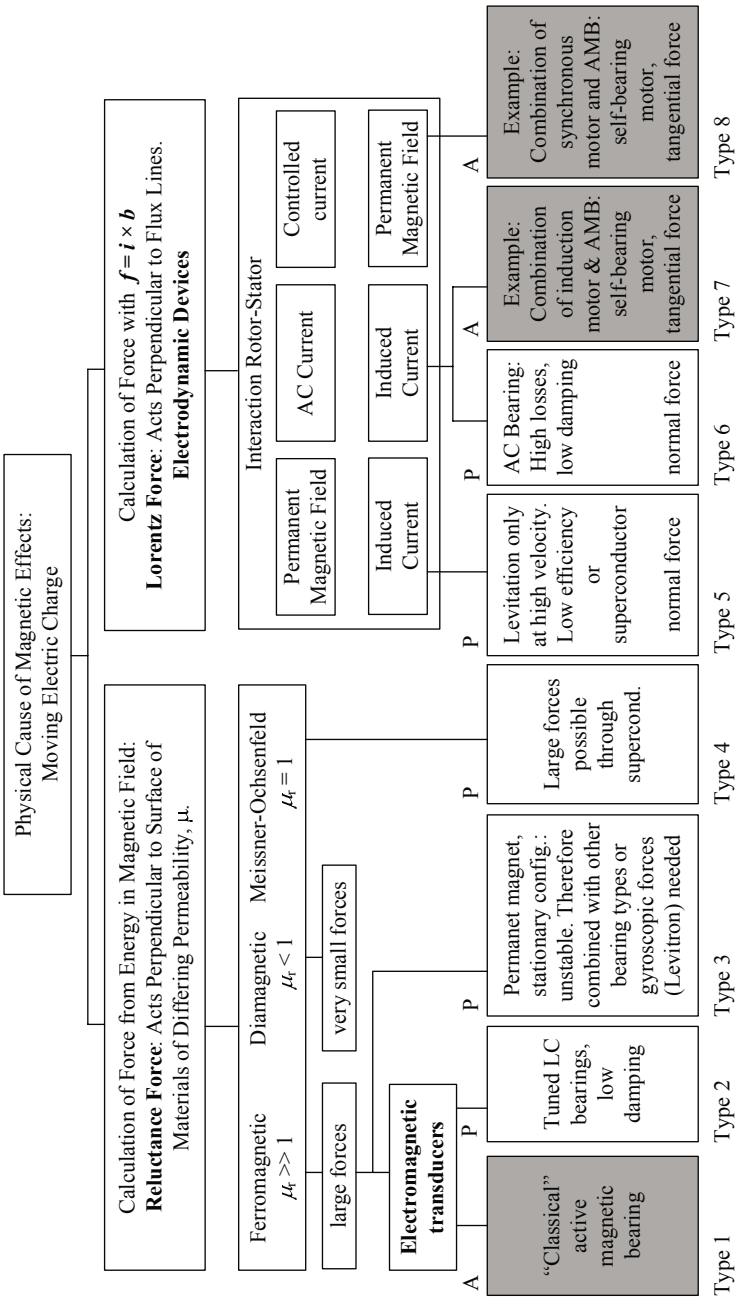


Fig. 1.11. Classification of magnetic bearings and levitation (from [12]). A: stable only with active control, P: passively stable with no control. Lorentz force bearings: *normal* or *tangential* refers to the force direction with respect to the air gap.

they are designated with an "A". With no control, in a purely passive way, designated in Fig. 1.11 by a "P", in general, the feasibility to stabilize a suspension in all degrees of freedom simultaneously, is limited and requires very specific approaches.

Active reluctance-force bearings fall into the group of magnetic bearings of *type 1*. Even within this group various other forms can be distinguished, for example by the way in which the active control has been realised. There are forms where the magnetic field, the magnetic flux, the distance between stator and rotor, or, in the case of the self-sensing bearing, the inductance is controlled. This will be detailed in subsequent chapters.

The *tuned LCR circuit bearing* (*type 2*) achieves a stable stiffness characteristic in an LC circuit excited slightly off resonance. The LC circuit is formed with the inductance of the electromagnetic bearing coil and a capacitor. The mechanical displacement of the rotor changes the inductance of the electromagnet. The LC circuit is operated near resonance and tuned in such a way that it approaches resonance as the rotor moves away from the electromagnet. This results in an increased current from the AC-voltage source and thus pulls the rotor back to its nominal position. The forces and stiffnesses are not very large but sufficient for certain instrumentation applications. Since it is stable without a control loop it is called "passive". The power supply consists of an AC source operating at a constant frequency. The main drawback is that there is no damping, i.e. without additional measures such as mechanical damping or active bearings such systems tend to go unstable. They have been used for gyroscopes [39], but now that powerful controllers can be realized at relatively low costs their simple design does not balance their inherent drawbacks. Thus today they are in some sense "outsiders", although they are still being investigated [26].

Permanent magnets ($\mu_r \gg 1$, *type 3*) in a stationary configuration are not able to stabilize a levitated body's position. As discussed previously, such suspensions require the addition of gyroscopic forces as in the case of the Levitron, or diamagnetic material ($\mu_r < 1$) to obtain stable hovering with small forces involved, or superconductors ($\mu_r = 0$). Nevertheless, it can be quite useful to apply permanent magnets to support a body or reduce its load on a conventional bearing in just one direction. Permanent magnets have been widely applied, e.g. for domestic electric energy meters. Some other applications are in combination with active electromagnetic bearings, e.g. turbomolecular pumps for very high vaccuum, leading to so-called hybrid bearings. In such applications, the disadvantage of relatively low damping of the passive bearings versus the active ones becomes apparent. Therefore, this kind of hybrid bearing has been limited to special cases where it has lead to very attractive solutions [18, 13]. Even the use of a mechanical displacement control for adjusting the position of the permanent magnet has been suggested for MAGLEV-vehicles [5], and later on for other applications, too.

Devices of *type 4* rely on the very special material property $\mu_r = 0$. Only this property of so-called *superconducting material* (Meissner-Ochsenfeld ef-

fect) leads to strong forces and meets a wide technical interest. Although still in the laboratory stage, industrial applications might develop in the not too distant future. The key characteristic of superconductivity is that, at very low temperatures, the electric resistance vanishes. A current in a superconducting coil will continue to flow even when there is no longer any driving voltage. All of the magnetic field will be squeezed out of the superconductor by the so-called Meissner-Ochsenfeld effect, thus allowing a stable hovering by means of permanent magnets. The recent *high-temperature superconducting (HTS) materials* exhibit this valuable behaviour at the temperature of liquid nitrogen already, and some more exotic materials at even higher temperatures. There are actually increasingly many application-oriented experiments taking place. Moon [36] describes experiments using high-temperature super-conductors to support a rotor which can rotate at 120000 rpm, and actually lab versions of flywheels for energy storage have been built in various countries [32, 47]. Research on HTS-motors and generators is being done internationally. Recently, a test rig for a passive bearing designed for a 4 MVA HTS synchronous generator (bearing capacity 500 kg, maximum speed 4500 rpm, Fig. 1.22) has been realized by SIEMENS and NEXAN SuperConductors [33]. In the temperature range below 60 K the bearing capacity remains almost constant. The bearing, initially cooled down to 28K, can be operated for about 2 hours without additional cooling. It can be expected that, in future, the damping of the rotor motion can be achieved by an additional AMB outside of the cooled area. Any further mechanical auxiliary bearings can be very simple and will only be needed for maintenance purposes.

The so-called *Lorentz force* is the characterizing term for the second large group in the classification of magnetic bearings. The force $\underline{\mathbf{f}}$ acting on an electric charge Q results from the basic law

$$\underline{\mathbf{f}} = Q(\underline{\mathbf{E}} + \underline{\mathbf{v}} \times \underline{\mathbf{B}}) \tag{1.2}$$

with the electric field $\underline{\mathbf{E}}$, and Q moving at the velocity $\underline{\mathbf{v}}$ in a magnetic flux density $\underline{\mathbf{B}}$. The energy density of feasible electrical fields $\underline{\mathbf{E}}$ in macroscopic technical arrangements is usually a factor of about 100 smaller than the energy density of feasible magnetic fields. Therefore, the electrostatic term in (1.2) is not considered further here, although it can become important at the micro scale. In (1.2) the product of charge and velocity ($Q\underline{\mathbf{v}}$) is replaced by the current $\underline{\mathbf{i}}$, leading to the well-known cross-product

$$\underline{\mathbf{f}} = \underline{\mathbf{i}} \times \underline{\mathbf{B}} \tag{1.3}$$

In this case, the force is orthogonal to the flux lines, independent of the air gap and linearly dependent on the current, assuming that the flux does not also depend on that current. There are four basic Lorentz force magnetic levitation types. They are grouped according to the source of the macroscopic current $\underline{\mathbf{i}}$. This current can be either induced or actively controlled. For the induction there are two possible mechanisms: either there is an interaction between a permanent magnetic field and a moving conductor, or the interaction

occurs - without relative motion - between a conductor and an AC powered electromagnet. On the other hand, the current can be controlled actively and interact with a magnetic field. There are again two possibilities: either the magnetic field is produced by a permanent magnet, or there is an interaction between the controlled current and an induced current. These four types 5 to 8 are described subsequently in some more detail.

Electro-dynamic levitation occurs without active control (*type 5*) when high eddy currents are induced through a sufficiently fast relative motion between the stator and the moving body. The repulsive forces generated by high-speed motions are large enough to carry the moving body. Such bearings have been thoroughly studied for high-speed vehicles and occasionally for rotor bearings, and they are described extensively in the literature, i.e. [45]. In order to generate the high flux densities necessary for a technical application, superconductors have been used on the vehicle. This method, however, is not yet economically realizable, and therefore, the electromagnetic suspension of type 1 is actually preferred for such MAGLEV applications. From early works on magnetic suspensions the two types 1 and 5 are best known. This seems to be the reason why it is often assumed that electromagnetic bearings are active while electrodynamic bearings have to be passive. This simplifying notion is not true, as seen among the variety of solutions in Fig. 1.11.

The *type 6* bearing depends on the interaction of AC and induced current, leading to a passive levitation as in the case of type 5. Now, however, the relative motion is replaced by an alternating flux. Again, with normal conduction the levitating force produced by eddy currents is relatively weak, considering the power losses. At the same time, such bearings, sometimes called *AC bearings*, have poor damping properties [38].

The interaction between an AC current and the induced current can also be achieved by an active system, leading to the two following types 7 and 8 of magnetic bearings using Lorentz forces. *Type 7*, is in some way similar to an induction motor. However, in the motor version, the forces act in the circumferential direction to generate the driving torque, whereas in the bearing type, the forces act in the radial direction to support the rotor. In this case the stator, for example, has two different types of windings. The first one corresponds to the windings of an asynchronous drive, and it produces a couple for driving the rotor. The current through the second winding produces a force component in radial direction, and by suitably controlling the current, using air gap sensors for the feedback and synchronous with the rotating flux field, the levitation of the rotor can be stabilized. Thus, a combination of drive and magnetic suspension has been achieved [16], and in literature this combination is known as a *self-bearing motor* (see Chap. 16). Even considering the complexity of the control, this combination will allow some interesting design solutions, for example for resonance dampers or for especially short magnetic bearing/drive arrangements.

The bearing of *type 8*, finally, is similar to the previous one except for the fact that the rotor with its induced current is replaced by a permanently mag-

netized rotor. Such a Lorentz-force active magnetic bearing has been realized by Bichsel [10, 11] with a synchronous motor/active bearing combination.

The electrodynamic principle, where a force is acting upon a current-leading conductor in a magnetic field, is equally valid, of course, for arrangements containing no iron. Although the forces obtained are small, the principle is often used in cases where disturbing effects in ferromagnetic material, such as remanence or hysteresis, have to be avoided, as in loudspeakers. The constant magnetic field is produced by permanent magnets, and the current through a coil, which is placed within the air gap, is controlled in such a way that Lorentz forces suitable for levitating the coil are generated. Such arrangements have been used for the suspension of momentum wheels in satellites [44], or for the practically vibration-free suspension of a micro-g platform for research purposes in a space craft.

1.5 Characteristics of Active Magnetic Rotor Bearings

In the following chapters, the most widely used bearing types: the active electromagnetic bearing AMB (*type 1*), and to some extent the self-bearing motor (*type 7, 8*), will be presented in more detail. First, at this introductory level, some specific properties, which render the AMB particularly useful for some applications, and may also open up new applications, will be summarized:

- The property of being *free of contact*, and the *absence of lubrication and contaminating wear* allow the use of such bearings in vacuum systems, in clean and sterile rooms, or for the transport of aggressive or very pure media, and at high temperatures.
- The *gap between rotor and bearing* amounts typically to a few tenths of a millimeter, but for specific applications it can be as large as 20 mm. In that case, of course, the bearing becomes much larger.
- The rotor can be allowed to rotate at *high speeds*. The high circumferential speed in the bearing – only limited by the strength of material of the rotor – offers the possibilities of designing new machines with higher power concentration and of realizing novel constructions. Actually, about 350 m/s are achievable, for example by using amorphous metals which can sustain high stresses and at the same time have very good soft-magnetic properties, or by binding the rotor laminations with carbon fibers. Design advantages result from the absence of lubrication seals and from the possibility of having a higher shaft diameter at the bearing site. This makes the shaft stiffer and less sensitive to vibrations.
- The *low bearing losses*, which at high operating speeds are 5 to 20 times less than in conventional ball or journal bearings, result in lower operating costs.
- The *specific load capacity* of the bearing depends on the type of ferromagnetic material and the design of the bearing magnet. It will be about 20

N/cm^2 and can be as high as 40 N/cm^2. The reference area is the cross sectional area of the bearing. Thus the maximum bearing load is mainly a function of the bearing size.

- The *dynamics* of the contact-free hovering depends mainly on the implemented control law. The control is implemented by a microprocessor, which makes the design very versatile. Thus, it is possible to adapt the stiffness and the damping, within physical limits, to the bearing task and even to the actual state of operation and the rotor speed. The terms *stiffness* and *damping* include the conventional static parts, known as spring and damping constants, and the frequency dependent part, the *dynamic stiffness*. This renders it possible, for example, to use the bearings for vibration isolation, to pass critical speeds with no large increase in vibration amplitude, or to stabilize the rotor when it is excited by nonconservative disturbances.
- *Retainer bearings* are additional ball or journal bearings, which in normal operation are not in contact with the rotor. In case of overload or malfunction of the AMB they have to operate for a very short time: they keep the spinning rotor from touching the housing until the rotor comes to rest or until the AMB regains control of the rotor. The design of such retainer bearings depends on the specific application and despite a variety of good solutions still needs special attention.
- The *unbalance compensation and the force-free rotation* are control features where the vibrations due to residual unbalance are measured and identified by the AMB. The signal is used to either generate counteracting and compensating bearing forces or to shift the rotor axis in such away that the rotor is rotating force-free.
- The *precision* with which the state of the rotor can be controlled, for example the precise rotation about a given axis, is mainly determined by the quality of the measurement signal within the control loop. Conventional inductive sensors, for example, have a measurement resolution of about 1/100 to 1/1000 of a millimeter.
- *Diagnostics* are readily performed, as the states of the rotor are measured for the operation of the AMB anyway, and this information can be used to check operating conditions and performance. Even active diagnostics are feasible, by using the AMB as actuators for generating well defined test signals simultaneously with their bearing function.
- The AMB has the potential to be a key element in a *smart machine*. The AMB can make use of its measured state information in order to optimize the operation of the whole machine. It contributes to the overall process control, and supports the safety and reliability management.
- The *lower maintenance costs and higher life time* of an AMB have been demonstrated under severe conditions. Essentially, they are due to the lack of mechanical wear. Currently, this is the main reason for the increasing number of applications in turbomachinery. The maintenance and

reliability properties can be even further improved by making use of the smart machine concept.
– The *cost structure of an AMB* is that of a typical mechatronics product. The costs for developing a prototype, mainly because of the demanding software, can be rather high. On the other side, a series production will lower the costs considerably because of the portability of that software.
– The *design of an AMB* for a specific application requires knowledge in mechatronics, ie. in mechanical and electrical engineering, and in information processing, in addition to knowledge about the specific application area. Therefore a close cooperation between AMB producer and the manufacturer of application machinery (OEM) is necessary.

Subsequently, some typical applications of magnetic bearings in research and industry have been compiled, demonstrating the broad potential for a variety of applications.

1.6 Examples from Research and Industry

The various advantages of the magnetic bearing have led to applications mainly in the five following areas:

- *Vacuum and cleanroom systems*: The bearings will not suffer from any mechanical wear or give rise to any related contamination, and if necessary, the bearings can even be arranged outside the vacuum container with field forces acting through the container walls. The absence of aerodynamic drag losses and the low energy consumption of the bearings is a welcome feature for flywheels for energy storage.
- *Machine tools*: A main advantage is the high precision that can be attained and the high rotational speed with relatively high load capacity. This is useful for heavy-duty high speed milling of aluminum. The high speed is an essential requirement in the precision grinding of small parts.
- *Medical devices*: A specific application is the use of magnetic bearings in an artificial heart pump, or more precisely, in a left ventricular assist device intended to assist an ailing heart in keeping the pumped blood at a desired rate, which is needed to provide the circulatory requirements.
- *Turbo-machinery*: Actually, the main application area of AMB is turbomachinery. The area covers small turbo-molecular pumps up to turbogenerators and compressors in the Megawatt range. Turbo-generators in the 300 MW range are in an early planning stage already. An advantage is the possibility of controlling and damping vibrations, and obtaining a well-defined dynamic behaviour. Furthermore, it is possible to simplify machine construction, as there are no bearing fluids, usually oil, that have to be kept away from the process fluid by seals. Other important features that have been corroborated by practical experience are the inherent means for self control and diagnosis, the very low maintenance costs, and the low energy

consumption. With the availability of very high efficiency power electronics, the need for turbo-generators running at a low 50/60 Hz speed or the necessity of coupling a high speed gas turbo engine to a reduction gear for driving a generator has decreased, and for high-speed machinery with high power density, the AMB is the bearing of choice. Even for aero engines, generating just thrust and electric energy for the all electric airplane of the future, research on AMB applications is going on.

- *Superconducting bearings*: The advances of superconducting bearings with their inherent passive stability promise a future alternative to active magnetic bearings, see Sect. 1.4 and Fig. 1.22. However, in order to achieve damping properties in a superconductive suspension for rotating machinery the use of additional active dampers by AMBs may still be necessary.

The examples, shown in the Figs. 1.12 through 1.22 demonstrate recent products and developments, and an outlook on ongoing research projects.

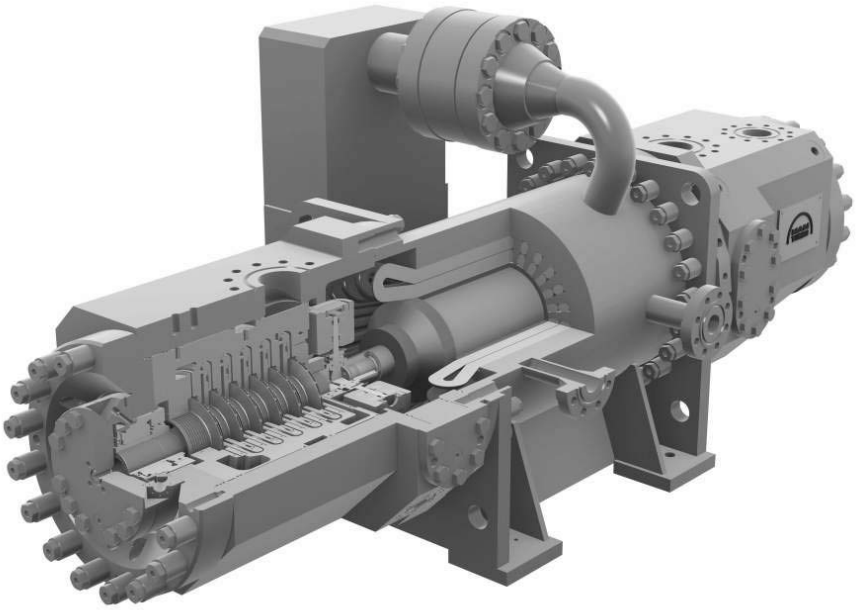


Fig. 1.12. Pipeline compressor HOFIM from MANTurbo/S2M, 6 MW, 9000 rpm, integration of direct drive and magnetic bearing in the turbomachine. The first version, MOPICO, is described in [40] (image courtesy MANTurbo)



Fig. 1.13. Turbo-molecular pump suspended in active magnetic bearings. HiMag 2400®, delivery 2100 l/sec, speed 29400 rpm (photo courtesy Pfeiffer Vacuum-Mecos)



Fig. 1.14. Cooling gas compressor for power laser, speed 54000 rpm, motor power 12 kW (photo courtesy TRUMPF/Mecos)



Fig. 1.15. Turboexpander-generator with magnetic bearings for energy recovery from natural gas, 450 kW, 32000 rpm, rotor mass 112 kg, rotor length 1100 mm, bearing diameter 110 mm, high-speed motor with carbon fiber reinforcement, [15]

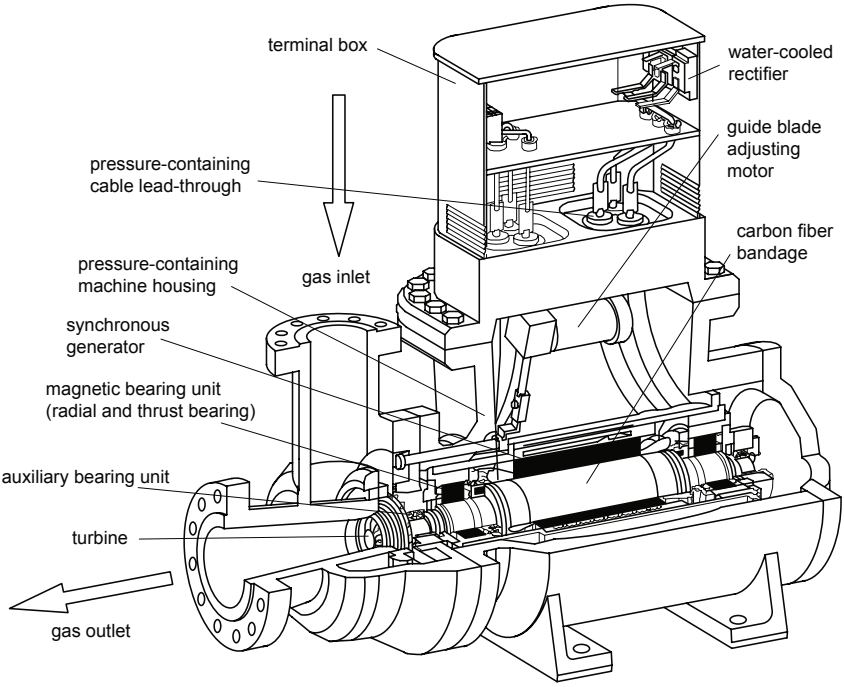


Fig. 1.16. Schematic of turbo-expander of Fig. 1.15

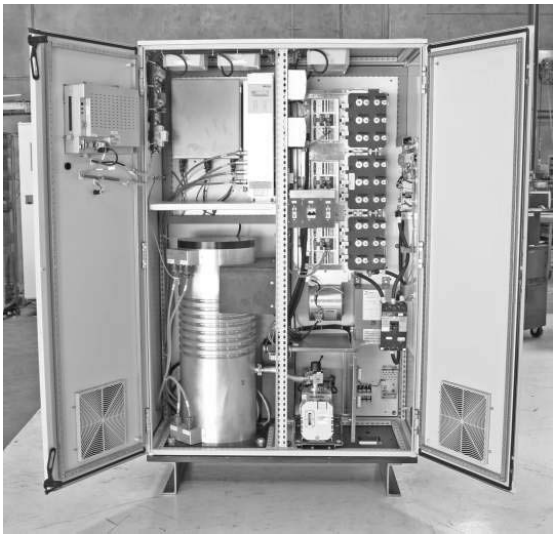


Fig. 1.17. 125 kW energy storage flywheel in cabinet for UPS application and ride-through service. The flywheel is on the lower left, magnetic bearing controller is at upper middle, motor/generator and system controller on upper left, and motor/generator power electronics on the right (photo courtesy CALNETIX, [37])

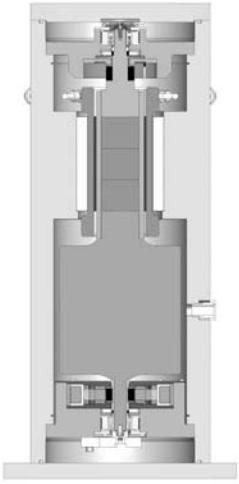


Fig. 1.18. Cross-section of the energy storage flywheel of Fig. 1.17. The flywheel has a steel hub, a 2-pole brushless DC motor/generator, and permanent magnet biased magnetic bearings. The lower magnetic bearing is a three-axis combination radial and thrust bearing. The upper magnetic bearing is a two axis radial bearing, with the bias flux returning through an axial face, providing passive support for approximately half of the rotor weight (image courtesy CALNETIX)

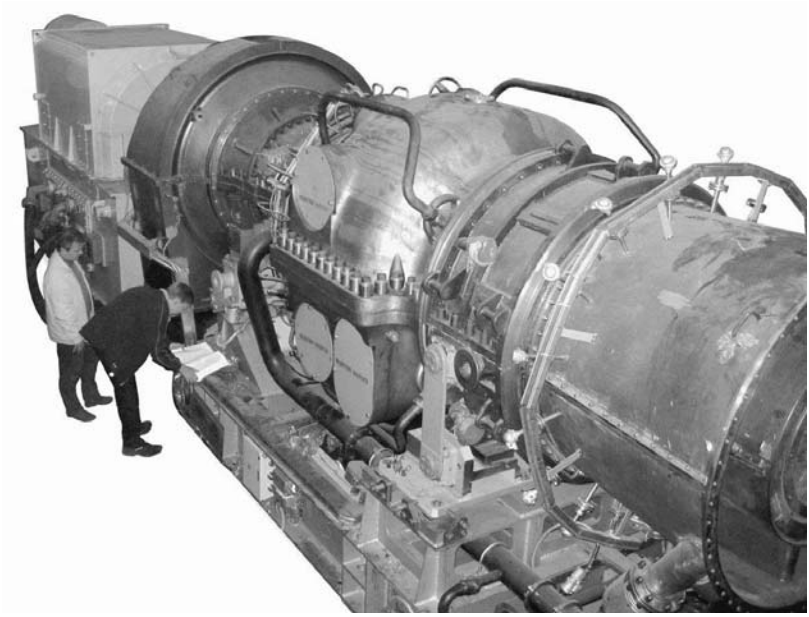


Fig. 1.19. Gas turbine-generator with 4 radial bearings and 1 thrust bearing for power generation, 6010 rpm, 9000 kW, bearing diameter 400 mm (photo courtesy S2M)

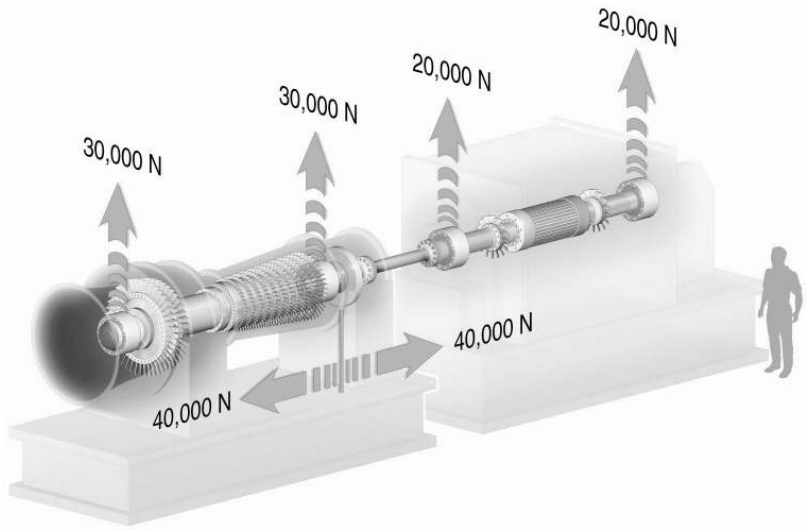


Fig. 1.20. Schematic of the gas turbine-generator of Fig. 1.19 (image courtesy S2M)



Fig. 1.21. Schematic cross-section of a turbo-generator for a nuclear power plant, the first pebble-bed high temperature gas-cooled test reactor with the gas turbine in the direct cycle (HTR-10GT, under construction), 6 MW, 15000 rpm, vertical rotor axis, 4 radial bearings, 2 axial bearings, length of turbine 3.5 m, mass of turbine 1000 kg, Chinese government key project (image courtesy Institute of Nuclear and Novel Energy Technology INET, Tsinghua University, Beijing, [48])

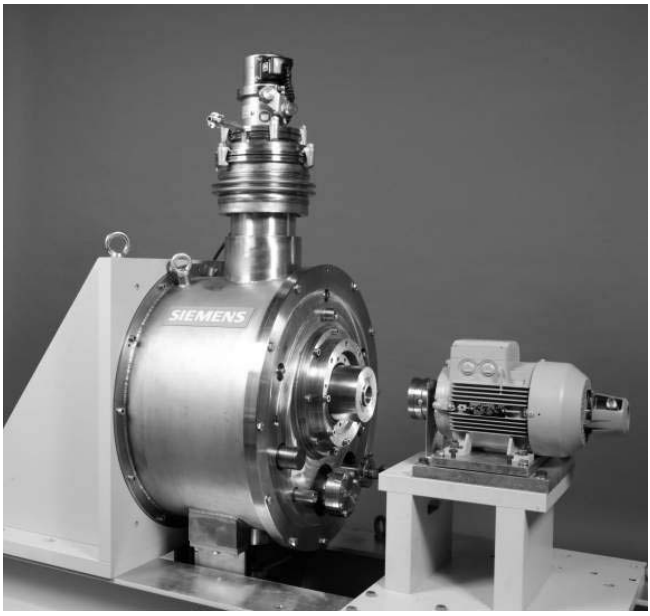


Fig. 1.22. Test rig for a superconductive bearing designed for a 4 MVA HTS synchronous generator, bearing capacity 500 kg, maximum speed 4500 rpm. In the temperature range below 60 K the bearing capacity remains almost constant. The bearing, initially cooled down to 28K, can be operated for 2 hours without additional cooling (photo courtesy SIEMENS, [33])

References

1. ISO Standard 14839-1. Mechanical vibration - Vibrations of rotating machinery equipped with active magnetic bearings - Part 1: Vocabulary, 05 2002.
2. ISO Standard 14839-2. Mechanical vibration - Vibrations of rotating machinery equipped with active magnetic bearings - Part 2: Eval. of vibration, 05 2004.
3. ISO Standard 14839-3. Mechanical vibration - Vibrations of rotating machinery equipped with active magnetic bearings - Part 3: Evaluation of stability margin, 01 2005.
4. ISO Standard 14839-4. Mechanical vibration - Vibrations of rotating machinery equipped with active magnetic bearings - Part 4: Technical guidelines, system design (Draft), 09 2006.
5. M. Abe. A study on fundamentals of mechanically controlled permanent magnet levitation system for maglev transportation vehicle. 11th intl. conf. on magnetically levitated vehicles and linear drives. In *Magnetic Bearings. First Internat. Symposium on Magnetic Bearings*. Springer-Verlag, Berlin, 1988.
6. P. Allaire, editor. *Magnetic Bearings. Proc. Third. Internat. Symp. on Magnetic Bearings*, Washington, 1992.
7. J.W. Beams. High rotation speeds. *J. Applied Physics*, 8:795–806, 1937.
8. J.W. Beams, J.L. Young, and J.W. Moore. The production of high centrifugal fields. *J. Applied Physics*, pages 886–890, 1946.

9. M.V. Berry. The Levitron: an adiabatic trap for spins. *Proc. Roy. Soc. Serie A 452*, pages 1207–1220, 1996.
10. J. Bichsel. *Beiträge zum lagerlosen Elektromotor.* PhD thesis, ETH Zurich, Nr. 9303, 1990.
11. J. Bichsel. The bearingless electrical machine. In *Proc. Internat. Symp. on Magn. Susp. Technol.* NASA Langley Research Ctr., Hampton, USA, Aug. 1991.
12. H. Bleuler. A survey of magnetic levitation and magnetic bearing types. *JSME Internat. Journal Series III*, 35(3), Sept. 1992.
13. K. Boden. Wide-gap, electro-permanentmagnetic bearing system with radial transmission of radial and axial forces. In *Magnetic Bearings. First Internat. Symposium on Magnetic Bearings.* Springer-Verlag, Berlin, 1988.
14. W. Braunbek. Frei schwebende Körper im elektrischen und magnetischen Feld. *Z. Phys.*, 112:753–763, 1939.
15. W. Canders, N. Ueffing, U. Schrader-Hausmann, and R. Larsonneur. MTG400: A magnetically levitated 400 KW turbo generator system for natural gas expansion. In G. Schweitzer, R. Siegwart, and R. Herzog, editors, *Proc. 4th Internat. Symp. on Magnetic Bearings*, pages 435–440, Aug. 1994.
16. A. Chiba. Radial forces in a bearingless reluctance motor. *IEEE Trans. on Magnetics*, 27(2):786–791, 1991.
17. S. Earnshaw. On the nature of the molecular forces which regulate the constitution of the lumiferous ether. *Trans. Camb. Phil. Soc.*, 7, Part I:97–112, 1842.
18. J.K. Fremerey. Radial shear force permanent magnetic bearing system with zero-power axial control and passive radial damping. In *Magnetic Bearings. First Int. Symp. on Magnetic Bearings*, pp. 25–32. Springer-Verlag, Berlin, 1988.
19. Inst. fuer Mechanik und Mechatronik der TU Wien. Active Magnetic Bearing homepage http://www.mdmt.tuwien.ac.at/forschung/magnetlager/, 2004.
20. R. Gasch and M. Lang. Levitron - ein Beispiel für die rein permanentmagnetische Lagerung eines Rotors. *ZAMM*, 80(2):137–144, 2000.
21. A.K. Geim, M.D. Simon, M.I. Boamfa, and L.O. Heflinger. Magnet levitation at your fingertips. *Nature*, 400:323–324, July 1999.
22. E. Gottzein. *Das "Magnetische Rad" als autonome Funktionseinheit modularer Trag- und Führssysteme für Magnetbahnen* . Fortschr.-Ber., Reihe 8, Nr. 68. VDI-Verlag, Düsseldorf, 1984.
23. E. Gottzein, L. Miller, and R. Meisinger. Magnetic suspension control system for high speed ground transportation vehicles. In *World Electrotechn. Congr.*, volume Section 7, Paper 07, Moscow, June 1977.
24. H. Habermann and G. Liard. Le palier magnétique active: un principe révolutionaire. *SKF Rev. Roulements Nr. 192*, 1977.
25. T. Higuchi, editor. *Magnetic Bearings. Proc. Sec. Internat. Symp. on Magnetic Bearings.* Tokyo University, 1990.
26. T. Higuchi. Realization of non-contact ac magnetic suspension. In *Proc. 34th Jap. Joint Automatic Conf. (SICE and IEEE AC Tokyo)*, Keio Univ. Tokyo, Nov. 1991.
27. F.T. Holmes. Axial magnetic suspension. *Rev. Sci. Inst.*, 8:444–447, 1937.
28. H. Kemper. Overhead suspension railway with wheel-less vehicles employing magnetic suspension from iron rails. Germ. Pat. Nos. 643316 and 644302, 1937.
29. H. Kemper. Schwebende Aufhängung durch elektromagnetische Kraft; eine Möglichkeit für eine grundsätzlich neue Fortbewegungsart. *Elektrotechn. Z.*, 59:391–395, 1938.

30. W. Klimek. A contribution to the measurement technique using electromagnetic suspension. Forschungsbericht 72-30, DLR, 1972.
31. R. Koehler. Transrapid - development and application status. In *Proc. 8th Int. Symp. on Magn. Susp. Technol. (ISMST)*, pages 23–28, Dreden, Sept. 2005.
32. N. Koshizuka and F. Ishikawa et al. Progress of superconducting bearing technologies for flywheel energy storage systems. *Physica*, C 386(444-450), 2003.
33. P. Kummeth, W. Nick, and HW. Neumüller. Development of superconducting bearings for industrial application. In H. Bleuler and G. Genta, editors, *Proc. 10th Internat. Symp. on Magnetic Bearings*, page Keynote, Martigny, Switzerland, Aug. 2006.
34. M. Lang. *Berechnung und Optimierung von passiven permanentmagnetischen Lagern für rotierende Maschinen*. PhD thesis, TU Berlin, 2003.
35. M. Lang. Levitron - an example of gyroscopic stabilization of a rotor. In *Proc. 8th Int. Symp. on Magn. Susp. Tech. (ISMST)*, pp. 177–181, Dresden, Sept. 05.
36. F.C. Moon and P.Z. Chang. High-speed rotation of magnets on high-Tc superconducting bearings. *J. Applied Physics*, 56:397–399, 1990.
37. P. Mc Mullen, V. Vuong, and L. Hawkins. Flywheel energy storage system with active magnetic bearings and hybrid backup bearings. In H. Bleuler and G. Genta, editors, *Proc. 10th Internat. Symp. on Magnetic Bearings*, Martigny, Switzerland, Aug. 2006.
38. J.L. Nicolajsen. Experimental investigation of an eddy-current bearing. In *Magnetic Bearings. First Internat. Symposium on Magnetic Bearings*. Springer-Verlag, Berlin, 1988.
39. R.B. Parente. Stability of a magnetic suspension device. *IEEE Trans. on Aerospace and Electronic Systems*, pages 474–485, May 1969.
40. J. Schmied. Experience with magnetic bearings supporting a pipeline compressor. In T. Higuchi, editor, *Magnetic Bearings. Proc. Sec. Internat. Symp. on Magnetic Bearings*. Tokyo Univ., July 1990.
41. G. Schweitzer. Stabilization of self-excited rotor vibrations by an active damper. In F.I. Niordson, editor, *Proc. IUTAM Symp. on Dynamics of Rotors*, Lyngby, August 1974. Springer-Verlag, Berlin.
42. G. Schweitzer, editor. *Magnetic Bearings. Proc. First Internat. Symposium on Magnetic Bearings*. ETH Zurich, Springer-Verlag, Berlin, 1988.
43. M. Simon and al. Spin stabilized magnetic levitation. *Am. J. Phys.*, 65, April 1997.
44. R. Sindlinger. Magnetic bearing momentum wheels with vernier gimballing capability for 3-axis active attitude control and energy storage. In *Proc. VII IFAC Symp. on Auto. Control in Space*, Rottach-Egern, Germany, May 1976.
45. P.K. Sinha. *Electromagnetic suspension, dynamics and control*. IEE Control Engin. Series Nr. 30. Peregrinus Ltd, London, 1987.
46. A. Traxler. *Eigenschaften und Auslegung von berührungsfreien elektromagnetischen Lagern*. PhD thesis, ETH Zurich No 7851, 1985.
47. F.W. Werfel and U. Floegel-Delor et al. Flywheel energy storage system with hts magnetic bearings. In *Proc. 8th Internat. Symp. on Magn. Susp. Technol. (ISMST)*, pages 256–260, Dresden, Sept. 2005.
48. Suyuan YU, Guojun YANG, Lei SHI, and Yang XU. Application and research of the active magnetic bearing in the nuclear power plant of high temperature reactor. In H. Bleuler and G. Genta, editors, *Proc. 10th Internat. Symp. on Magnetic Bearings*, keynote, Martigny, Switzerland, Aug. 2006.

2

Principle of Active Magnetic Suspension

René Larsonneur

2.1 The Magnetic Bearing as a Controlled Suspension

Magnetic bearings can be basically categorized into two groups depending on the physical cause of the magnetic effect involved. The first group are referred to as *reluctance force* bearings while the second group is made up by the *Lorentz force* bearings. Whereas the latter bearing type has lately gained an increasing importance mainly in the field of the *self-bearing motor*, it is still the case that the bulk of industrial magnetic bearing applications employ reluctance force bearings.

This chapter, therefore, only considers reluctance force bearings (the self-bearing motor is treated in detail in Chap. 16). Moreover, within this group, the focus is entirely put on *active* magnetic bearings since they constitute the technically most important group member. *Passive* and *superconducting* magnetic bearings as additional classes of either reluctance or Lorentz force bearings are not treated here with the exception of a short comparison between active and passive magnetic bearings presented in the following section.

2.1.1 Active and Passive Magnetic Bearings

After more than thirty years of industrial utilization of magnetic bearings it has become evident that active magnetic bearings (AMBs) are clearly favored over passive ones (PMBs). The term *active* implies that bearing forces are actively controlled by means of electromagnets, a suitable feedback control loop and other elements such as sensors and power amplifiers. In contrast to this

G. Schweitzer, E.H. Maslen (eds.), *Magnetic Bearings*,
DOI 10.1007/978-3-642-00497-1_2, © Springer-Verlag Berlin Heidelberg 2009

architecture, a purely *passive*[1] suspension produces bearing forces generated by *permanent magnets*[2] acting alone.

The reason for this preference of active magnetic bearings over their passive counterparts immediately becomes clear when the advantages and disadvantages in terms of bearing properties are compared. As a main advantage, active magnetic bearings feature capabilities that are freely (within the physical limitations, though) adjustable by the control, whereas passive magnetic bearings have a fixed set of properties given by their size and mechanical design. Typical examples of adjustable bearing parameters and additional capabilities of active magnetic bearings are static and dynamic stiffness, damping, load-independent static positioning, unbalance force attenuation in rotating systems, excitation force generation and monitoring, to name only a few (see Sect. 2.2.2).

It is also important to mention here that a purely passive suspension, i.e. a suspension of a rigid body in all of its six degrees of freedom by using permanent magnets only, is physically impossible since there is always at least one unstable degree of freedom (Earnshaw's theorem [11]). Consequently, unstable degrees of freedom in a passive magnetic bearing arrangement have to be stabilized by a force of different physical origin, e.g. by a mechanical bearing, an active electromagnet, superconductor-to-magnet or diamagnetic-to-magnet interactions. Earnshaw's theorem, however, only applies to "static", i.e. to non-rotating, systems. Hence, spin or "gyroscopic" stabilization of an otherwise purely passive suspension is feasible.

A further disadvantage of passive magnetic bearings is their typically very low damping. Therefore, their industrial utilization is either limited to applications where another source of damping is available, e.g. a fluid in which the levitated body is submerged. Otherwise, additional mechanical or electromagnetic damping elements become necessary in order to provide a suitable external damping force needed in nearly every technical system. Another possibility to introduce damping into a permanent magnet suspension is by

[1] The terms *passive magnetic bearing*, *passive magnetic suspension* or *passive mechanical system* used in this contribution just refer to the use of *permanent magnets* or refer to mechanical *spring-damper* type systems. These terms are not to be confused with others such as *passive control* or *passive system* used in modern control theory to address dynamic systems that fulfill certain structural properties important for the assessment of feedback control stability.

[2] A further source of confusion about *active* and *passive* magnetic bearings might be the term "permanent magnet". As a passive magnetic bearing we consider bearings that are *only* made up of permanent magnets and ferromagnetic material for flux guidance. Hence, passive magnetic bearings do not feature any additional active components such as copper coils. On the other hand, permanent magnets can also be integrated into an active magnetic bearing e.g. for providing a *bias flux* for the linearization of the bearing characteristics without any power consumption. These *PM biased* magnetic bearings still provide copper windings for flux control and, therefore, belong to the group of *active* magnetic bearings.

providing electrically conductive materials, in which eddy currents can be generated by the motion of the suspended body, in the stationary frame of the passive bearing assembly.

Nevertheless, some systems incorporating passive magnetic bearing elements have been built in the past. One important industrial example are referred to as *hybrid turbomolecular pumps* (TMPs) which feature a combination of active and passive magnetic bearings and eventually also mechanical damping elements. In spite of the complexity of this setup this approach was justifiable by the comparably high costs of a full five axes active suspension at the time. To date, however, the costs of a fully active system have been cut to a most competitive level and, consequently, hybrid turbomolecular pumps are being replaced by fully active TMPs.

Another example of a successful utilization of PMBs in combination with an AMB are the lately developed *blood pumps* or *artificial hearts* [10, 15]. Here, the lack of damping of these bearings is less important since enough damping is provided by the blood itself which completely surrounds the levitated rotor. Moreover, the fully encapsulated design of these pumps asks for suitably high bearing forces despite the comparably large air gaps, one of the few requirements which PMBs can better fulfill than AMBs, especially when the bearing volume is limited.

2.1.2 Elements of the Control Loop

Figure 2.1 depicts a most simple example of a magnetic bearing control loop though comprising all the necessary components of a "standard" active magnetic bearing system. In the following, these elements and functionalities are briefly described.

A rotor ("flotor" for non-rotating objects) is to be levitated freely at a prescribed distance x_0 from the bearing electromagnet. A contact-less position sensor (most often an eddy current or inductive type sensor) steadily measures the deviation between desired position x_0 and actual rotor position x and feeds this information into a controller (nowadays most often a *digital* controller). The primary goal of the controller is to maintain the rotor position at its desired value. For this not only an equilibrium of the involved forces – here just the magnet force f_m and the rotor weight mg – must be established but also, as a most important quality of the control, a *stabilization* of the control loop must be achieved (see further below in this section what renders the open-loop system unstable). Finally, the controller sends out a positioning command signal to a power amplifier which transforms this signal into an electric current in the coil of the bearing electromagnet and a magnetic field in the iron of the magnet, thus generating the desired magnet force f_m.

The power amplifier and bearing electromagnet are tightly interdependent elements. Important overall properties of the magnetic bearing such as e.g. the force dynamics strongly depend on both power amplifier and electromagnet design, i.e. on amplifier voltage and current, bearing geometry and number

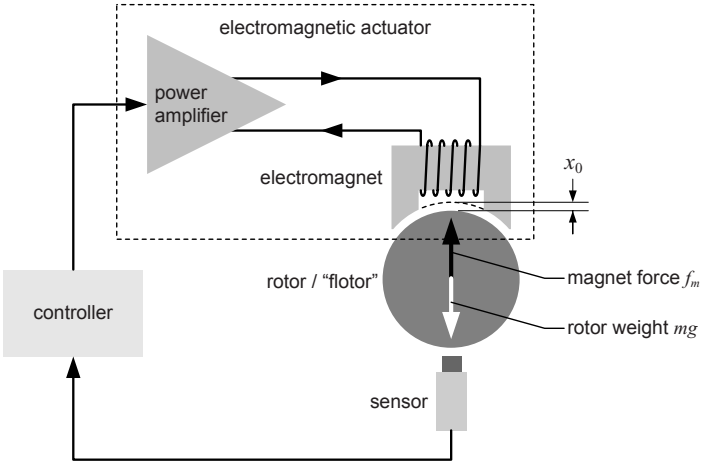


Fig. 2.1. The basic magnetic bearing control loop and its elements

of turns and inductance of the bearing coil. Therefore, the combination of power amplifier and bearing electromagnet is also called the *electromagnetic actuator* in the literature.

The setup of Fig. 2.1 describes a one degree of freedom, i.e. single-channel, rigid body suspension and, thus, corresponds to a strong simplification of a "real" magnetic bearing: Rotations and transverse motions of the rotor cannot be controlled by a single electromagnet and require a more complex arrangement of several magnets and a multi-channel control. Nevertheless, the basic properties of a magnetic bearing control loop can be easily investigated using this simple bearing example, for which a mathematical model is derived in the following section.

2.1.3 Basic Magnetic Bearing Model

To derive a suitably simple model, at first, any dynamics of the sensor and power amplifier electronics are neglected. In practice, this simplification leads to fairly good results if the resulting eigenfrequencies of the closed-loop system are not too high, i.e. if the realized bearing stiffness is in a physically "reasonable" range.

A second simplification is that the bearing force characteristic, i.e. its dependency on coil current, rotor position and other physical quantities, is not derived in detail here. A detailed derivation can be found in Chap. 4.

Finally, the basic magnetic bearing model is derived along with the accompanying example of a mechanical spring system. This is to emphasize the fundamental differences between a magnetic bearing and such a mechanical system, mainly in terms of open-loop stability, and should facilitate the basic understanding. By doing this it is, however, in no way the author's intention

to give the impression that the goal of AMB design is to simply emulate the behavior of a mechanical bearing. On the contrary, a real AMB design by making use of all their advantages will achieve system properties beyond the reach of mechanical bearings (see Sect. 2.2.2).

As can be seen in Fig. 2.2 the magnetic force f_m behaves in an opposite way to the mechanical spring force f_s: Whereas the latter *decreases* and even changes its sign with the distance x', thus producing a repelling effect which stabilizes the rotor motion around the equilibrium point (x_0, s_0), the magnetic force *increases* dramatically with decreasing air gap s (constant bias current i_0 assumed), which results in an unstable behavior. This basic instability property is well known to everybody who, maybe as a child, has experienced playing with permanent magnets or electromagnets.

The mechanical stiffness of the suspension is equal to the negative derivative of the suspension force with respect to displacement: $k = -df/dx$. Mathematically, the sign of the mechanical stiffness at the operating point (x_0, i_0, mg) determines the stability of this equilibrium position. For an open-loop magnetic bearing, this mechanical stiffness is *negative*.

Figure 2.2 also illustrates the quality of the dependency of the magnet force f_m on the air gap s and the coil current i'. Basically, the magnet force is proportional to the inverse of the square of the air gap on the one hand and proportional to the square of the coil current on the other hand. For small air gaps or large coil currents respectively the magnetic flux in the iron path becomes saturated, which, in addition to the basic characteristics, constitutes a further nonlinearity of the magnet force. Finally, the displacement x' will, of course, be limited geometrically to the size of the air gap.

Despite these strong nonlinearities a magnetic bearing system can usually be well controlled by a linear control scheme. For this, the force/displacement and the force/current dependencies of the magnet force f_m have to be linearized at the operating point (x_0, i_0, mg) which, as stated before, denotes the desired equilibrium position, i.e. $f_m(x_0, i_0) = mg$. Figure 2.3 describes this situation.

In order to eliminate all operating point quantities from the resulting equations it makes sense to introduce new variables for force f, current i and displacement x as follows:

$$f = f_m - mg \tag{2.1a}$$

$$i = i' - i_0 \tag{2.1b}$$

$$x = x' - x_0 \tag{2.1c}$$

This yields the following linearized force/current and force/displacement relationship (2.2) at the operating point (equilibrium position):

$$f(x, i) = -k_s x + k_i i \tag{2.2}$$

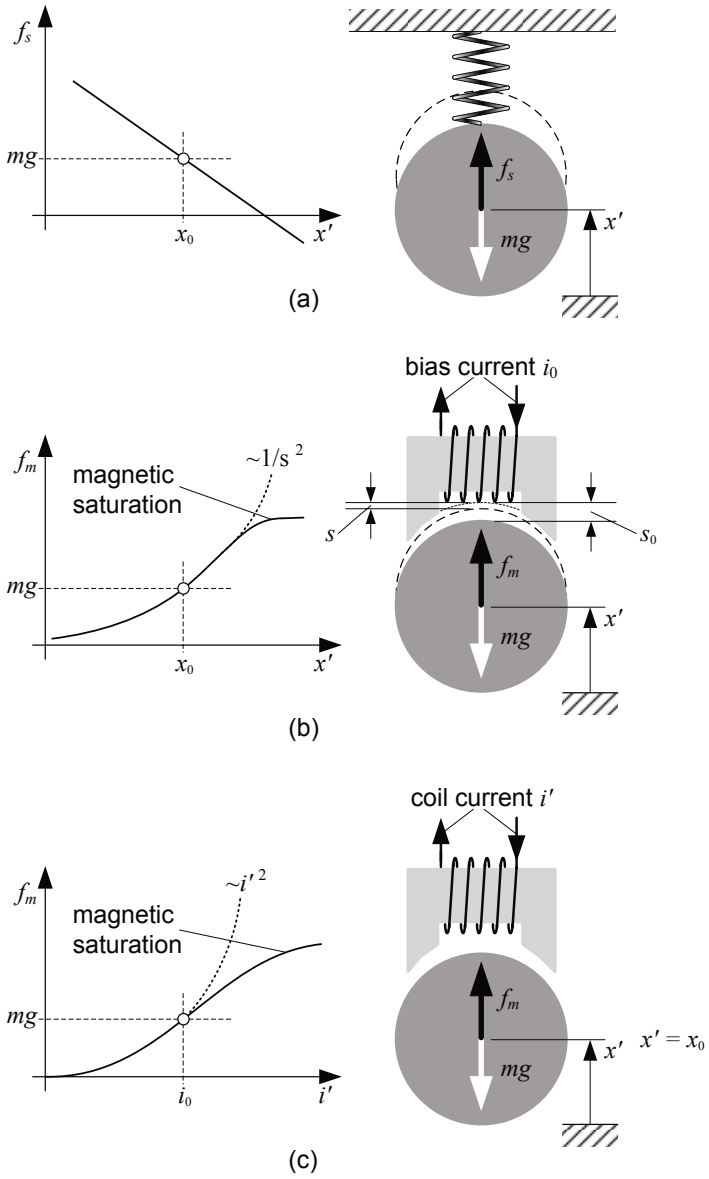


Fig. 2.2. Comparison of forces: (**a**) mechanical spring; (**b**) electromagnet (constant bias current $i' = i_0$); (**c**) electromagnet (constant air gap $x' = x_0$)

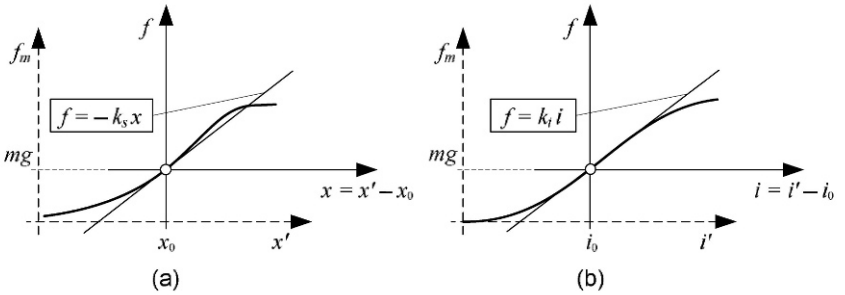


Fig. 2.3. Linearization at the operating point: (**a**) force/displacement relationship (slope is positive so $k_s < 0$); (**b**) force/current relationship (slope is positive so $k_i > 0$)

Equation (2.2) can be considered the *fundamental* description of the behavior of an active magnetic actuator under current control. Although this equation is only a linear approximation of the true relationship and, therefore, only accurate in the proximity of the operating point, it has proved through many years of practical experience to work extraordinarily well for a wide range of applications. Only when it comes to limit cases such as rotor-stator contact, flux saturation, very low bias currents, etc., does it become necessary to use more detailed and typically nonlinear models.

The constants k_s (N/m) and k_i (N/A) in (2.2) are commonly called the *force/displacement factor* (in the literature also equivalently defined as the *negative bearing stiffness*) and the *force/current factor* [23]. Both constants play an important role in any current controlled active magnetic bearing control design process. The next section describes how such a design process can be carried out for the simple example of Fig. 2.1.

2.2 Closing the Control Loop of a Magnetic Bearing

As we have seen in Sect. 2.1.3 an open-loop active magnetic bearing is an unstable dynamic system, a fact which will also be mathematically proved in terms of *open-loop system eigenvalues* in the next section. The task of stabilizing this unstable system by a suitable controller essentially comes down to finding an appropriate current command signal i, as shown in Fig. 2.4.

The following sections describe some basic linear approaches to this problem. Reference to more elaborate modern control design techniques is done e.g. in Chap. 12.

2.2.1 Design of a Simple Active Magnetic Bearing Control System

The first goal of the magnetic bearing control loop must obviously be the stabilization of the otherwise unstable rotor motion in the equilibrium point.

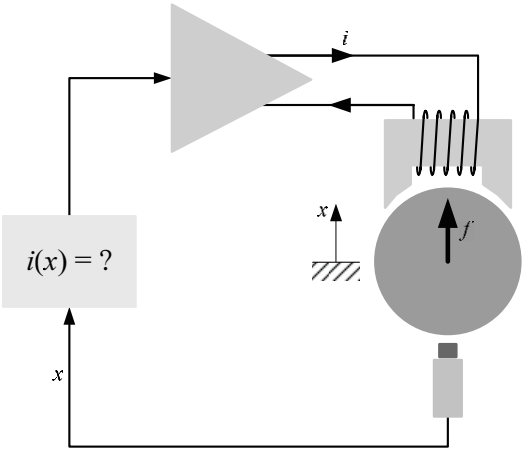


Fig. 2.4. Closing the magnetic bearing control loop by finding an appropriate control current i

Hence, the control must provide a restoring force, e.g. similar to that of the mechanical spring. In addition, the control force must provide a damping component in order to attenuate oscillations around the operating point.

As a most simple approach one might set up the desired control force f in such a way that the closed-loop behavior becomes similar to that of a mechanical spring-damper system. This results in an expression for the bearing force f with linear coefficients for stiffness k and damping d:

$$f = -kx - d\dot{x} \tag{2.3}$$

The equivalence of expressions (2.2) and (2.3) makes it possible to express the control current i as a function of the rotor displacement x and its time derivative[3] (velocity) $\dot{x}$:

$$i(x) = -\frac{(k - k_s)x + d\dot{x}}{k_i} \tag{2.4}$$

As mentioned in Sect. 2.1.3 no sensor, amplifier or other dynamics are included in (2.4).

In any control design process, the main interest is to achieve an acceptable closed-loop behavior of the controlled system. Suitable criteria for the assessment of the control loop quality are the closed-loop eigenvalues, static and dynamic stiffness (frequency response, see Sect. 2.4) and the robustness

[3] Note that this feedback law makes use of the time derivative $\dot{x}$ of the rotor displacement x. In a practical application, this simple kind of control cannot be implemented since the velocity is most often not available as a direct measurement signal but has to be *estimated* instead. Nevertheless, the velocity signal is introduced here only for its conceptual value.

of the system. Here, we just want to analyze its closed-loop eigenvalues. The starting point for this analysis is Newton's law:

$$m\ddot{x} = f \tag{2.5}$$

As a shortcut we could now directly insert expression (2.3) for the desired force f into (2.5) and easily obtain the system eigenvalues. However, we take the approach of inserting (2.2) into (2.5) in order to verify the system's basic property – its open-loop instability – also mathematically. Hence, we obtain the following expression to start with:

$$m\ddot{x} = -k_s x + k_i i \tag{2.6}$$

In the open-loop case the control current i is zero. It is important, however, to keep in mind that the system has been linearized at the operating point, hence, the coil current in the electromagnet is not zero but corresponds to the bias current i_0 (a bias current is needed in most active magnetic bearing systems to achieve acceptable system dynamics). We know from our experience that an electromagnet with a constant current will attract any ferromagnetic target once near enough so that it will stick to the electromagnet's surface. This unstable behavior is also visible in (2.6) by setting i to zero and by inserting the exponential function $x(t) = \mathrm{e}^{\lambda t}$ to obtain the solution of (2.6) in the open-loop case. This yields the following characteristic polynomial:

$$m\lambda^2 + k_s = 0 \tag{2.7}$$

Since k_s is a negative number the solution of (2.7) becomes obviously $\lambda_1 = +\sqrt{|k_s|/m}$ and $\lambda_2 = -\sqrt{|k_s|/m}$. Both eigenvalues λ_1 and λ_2 of the open-loop system are real, and λ_1 is located in the right half of the complex plane which proves that the system is open-loop unstable. This situation is plotted in Fig. 2.5.

The closed-loop system differential equation can be obtained when inserting (2.3) into (2.5):

$$m\ddot{x} + d\dot{x} + kx = 0 \tag{2.8}$$

The characteristic polynomial corresponding to (2.8) is

$$m\lambda^2 + d\lambda + k = 0 \tag{2.9}$$

with the following solution for the now conjugate complex eigenvalues λ_1 and λ_2:

$$\lambda_1 = -\sigma + j\,\omega \tag{2.10a}$$

$$\lambda_2 = -\sigma - j\,\omega \tag{2.10b}$$

$$\sigma = \frac{d}{2m} \tag{2.10c}$$

$$\omega = \sqrt{\frac{k}{m} - \frac{d^2}{4m^2}} \tag{2.10d}$$

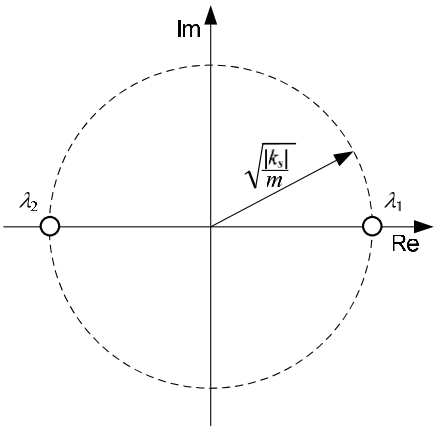


Fig. 2.5. Eigenvalues of the open-loop system

Figure 2.6 shows the plot of the closed-loop eigenvalues in the complex plane. The stiffness k mainly influences the frequency ω, i.e. the imaginary part of the eigenvalues $\lambda_{1,2}$. The damping d, on the other hand, moves both eigenvalues into the left half of the complex plane, thus stabilizing the system (without damping the closed-loop system is not asymptotically but only limit-stable). The larger the damping coefficient d the smaller the frequency ω, though leaving the magnitude of the eigenvalues constant ($|\lambda_{1,2}| = \omega_0 = \sqrt{k/m}$). As can be seen in (2.10d), however, large damping yields real eigenvalues again (critical or overcritical damping respectively), thus removing the oscillation capability of the closed-loop system. In this case both eigenvalues are still in the left half of the complex plane, but one approaches zero with the consequence of not yielding a satisfactory system performance any more, see Sect. 2.2.3).

The time domain solution of the linear and homogeneous differential equation (2.8) for a not too large, i.e. an *undercritical*, damping is an oscillation of the following form:

$$x(t) = \mathrm{e}^{-\sigma t}\big(A\cos(\omega t) + B\sin(\omega t)\big) \tag{2.11}$$

As the differential equation (2.8) is of second order, there are two eigenvalues $\lambda_{1,2}$ and, consequently, two constants A and B in the time domain solution. These constants have to be determined by the initial condition $x(t = 0)$ and $\dot{x}(t = 0)$ of the motion.

A more common but mathematically identical formulation of the solution (2.11) can be given by (2.12) with coefficient C and φ for the *amplitude* and *phase angle* respectively:

$$x(t) = C\mathrm{e}^{-\sigma t}\cos(\omega t - \varphi) \tag{2.12}$$

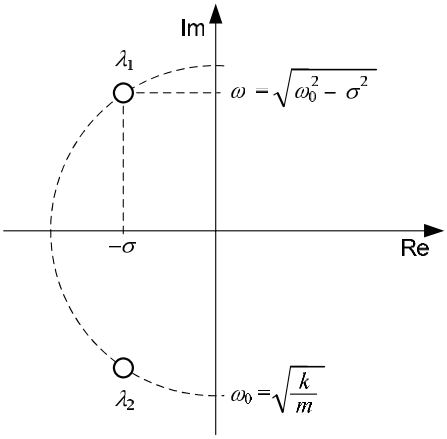


Fig. 2.6. Eigenvalues of the closed-loop system ($d < 2\sqrt{mk}$)

Equation (2.12) describes an oscillatory motion with an exponentially decaying amplitude. Hence, this motion cannot be considered harmonic or even periodic in the mathematically strict sense (for vanishing damping, though, the solution would be purely harmonic). Nevertheless, there is a periodic component in this damped oscillation which becomes clear when examining the time between two consecutive zero-crossing points, as shown in Fig. 2.7.

As can be seen from Fig. 2.7 the time T between the zero-crossing points is constant, even if the oscillation amplitude becomes smaller. It is important to mention, however, that this does not hold for the time between two relative amplitude maxima. The time T can, therefore, only be called the "pseudo period" of the damped system, and, correspondingly, ω can be called the "pseudo angular frequency". Despite this fact one speaks, in practice, most often of the *eigenfrequency* ω and of the *eigendamping* σ of the system.

2.2.2 Differences between Active and Passive Magnetic Bearings

In (2.3) we have set up the desired control force of a magnetic bearing system in accordance to a simple mechanical spring-damper system. As stated before this approach of designing a control law is only one possible out of many. Modern control design techniques such as $\mathcal{H}_\infty$ or $\mu-$synthesis can produce control laws that differ strongly from such a simple approach and also yield a superior closed-loop performance. But even when realizing a spring-damper type control law the active magnetic bearing provides a number of important advantages over a conventional solution or over a solution with passive magnetic bearings:

- Magnetic bearings work without any mechanical contact. Therefore, the bearings feature low bearing losses and have a long life cycle with a strongly reduced need for maintenance.

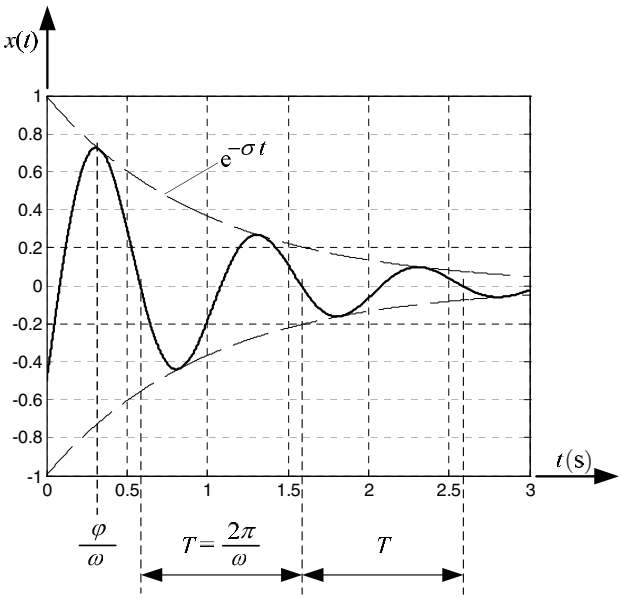


Fig. 2.7. Transient response according to (2.12) with "pseudo frequency" ω and decay rate σ ($C = 1$, $\sigma = 1$, $\omega = 2\pi/\text{s}$, $\varphi = 2\pi/3$)

- Since no lubrication is required, processes will not be contaminated, which constitutes another important advantage over conventional bearing technologies.
- AMB systems can also work in harsh environments or in a vacuum.
- The reduced need for maintenance and the possibility of omitting the complete lubrication system lead to considerable cost reductions.
- The rotational speed is only limited by the strength of the rotor material (centrifugal forces). Peripheral speeds of 300 m/s are a standard in state-of-the-art AMB applications, a value not reachable by most other bearings.
- The electromagnetic bearing is an active element which enables accurate shaft positioning and which makes its integration into process control very easy. The vibrations of a rotor can be actively damped, which becomes especially important when passing through bending critical speeds.
- It is also possible to let the rotor rotate about its principal axis of inertia to cancel the dynamic forces caused by the unbalance. Thus, no vibration forces are transmitted to the machine founding in spite of the presence of unbalances. Very often, rotors in AMBs do not have to be balanced at all.
- In the case of active magnetic bearings important properties such as stiffness and damping can be changed and, thus, adapted to the momentary needs without further system modification. State-of-the-art digital control systems usually provide possibilities for on-line tuning and adaptation.

- The operating position of a rotor in AMBs can be controlled independently of the stiffness and the external load (see Sect. 2.2.3).
- Due to their built-in sensors and actuators, i.e. their built-in instrumentation, active magnetic bearings as a typical "mechatronic" system are perfectly suited for not only positioning and levitation of a rotor but also for serving additional purposes such as monitoring, preventive maintenance or system identification (see Sect. 2.4.3). These important features are possible without the need for any additional instrumentation.

It is the sum of all these features and advantages that render active magnetic bearings so attractive for many demanding industrial applications.

2.2.3 PD and PID Control

In Sect. 2.2.1 a possible control law (2.4) for the current command signal as a function of the displacement x and its time derivative $\dot{x}$ was developed as:

$$i(x) = -\frac{(k - k_s)x + d\dot{x}}{k_i}$$

This control essentially contains two feedback parts, a *proportional* feedback with control parameter P and a *differential* feedback with control parameter D, as denoted by (2.13). Such a control law is well-known under the name *PD control*.

$$P = \frac{k - k_s}{k_i} \tag{2.13a}$$

$$D = \frac{d}{k_i} \tag{2.13b}$$

PD Control: Selection of Stiffness and Damping

The parameters P and D of the above control law are determined by choosing appropriate values for stiffness k and damping d of the closed-loop system. Along with the maximum force (load capacity) of a magnetic bearing the bearing stiffness is one of the most basic bearing parameters and should already be defined in the early stages of a magnetic bearing project, since the design of important system components such as the bearing size and the amplifier power rating depend on this selection.

Evidently, the choice of the closed-loop stiffness underlies the specifications of a particular application. Typically, high force or high precision applications, such as a machine tool spindles or fluid pumps, will require a high stiffness, whereas applications with no or only low external loads, such as turbomolecular pumps, flywheels, blowers and some types of turbo compressors and expanders, will not require such a high bearing stiffness, since the AMB

must only provide the ability for a contact-free, low vibration and high-speed rotation.

The following sections provide a short guideline for a suitable selection of the control parameters P and D.

Very Low Stiffness

In the case of very low stiffness values k the proportional gain P, as resulting from (2.13), just compensates for the negative bearing stiffness k_s and merely stabilizes the system. This is reflected by the location of the closed-loop eigenvalues very near to zero, as shown in Fig. 2.8.

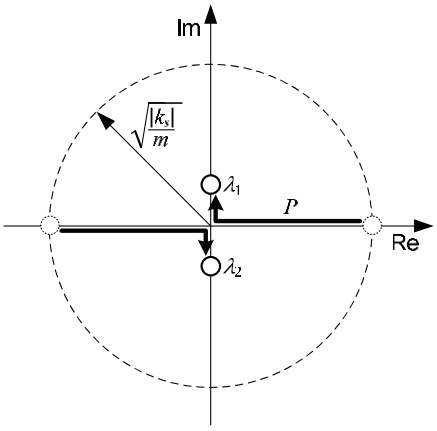


Fig. 2.8. Closed-Loop eigenvalues for very low stiffness values k ($P \approx -k_s/k_i$)

It should be emphasized that the value of k_s is nearly always subject to significant uncertainty. It is controlled by the length of the magnet gap, s_0, and by the current operating point, i_0. The magnet gap is, in turn, usually uncertain due to manufacturing processes and is further altered by differential thermal growth between the rotor and stator and by centrifugal growth of the rotor. Since k_s depends on s_0^3, even relatively small changes in s_0 produce relatively large changes in k_s. Further, the current operating point, i_0, depends on the static load carried by the bearing: small changes in static load can lead to significant changes in k_s. Taken together, these considerations lead to a typical assumption for design purposes that a well characterized value of k_s still carries with it an uncertainty on the order of 20%.

One consequence of this is that small stiffness values $k \ll |k_s|$ are rather delicate to realize in a real application and require a very exact knowledge of the system parameters, namely of the negative bearing stiffness k_s. The reason for this is the fact that the location of the closed-loop eigenvalues $\lambda_{1,2}$ given by

(2.10a, 2.10b) becomes very sensitive[4] to changes of k_s. If the negative bearing stiffness is not known properly or if it changes during operation then the closed-loop system might even become unstable. If, for some reason, very low stiffness values are important, then k_s must be kept small either by designing a small magnetic bearing or by selecting a low bias current so that k and k_s have comparable (small) magnitudes. An alternative approach is to avoid using current control for the bearing, as discussed in Sect. 4.5.3.

Very High Stiffness

The determination of the upper limit of the closed-loop stiffness k is more difficult. There are a number of effects that arise when choosing high proportional feedback gains P.

First of all the closed-loop eigenvalues $\lambda_{1,2}$ tend to have large imaginary parts ω. This means that the *rigid body eigenfrequencies* are high, as shown in Fig. 2.9. High closed-loop eigenfrequencies, however, always require an appropriately high bandwidth of the controller, the sensor and, above all, the power amplifier which must not get into *dynamic saturation*. If the necessary bandwidth of a system component cannot be achieved, the high stiffness cannot be realized and the closed-loop system will be unstable, mostly with a clearly audible *chattering* of the rotor. Due to the nonlinearities in the system it is even possible that, despite a marginal closed-loop stability achieved and the rotor levitating, the system may suddenly exhibit uncontrollable chattering after an external disturbance such as a force impact.

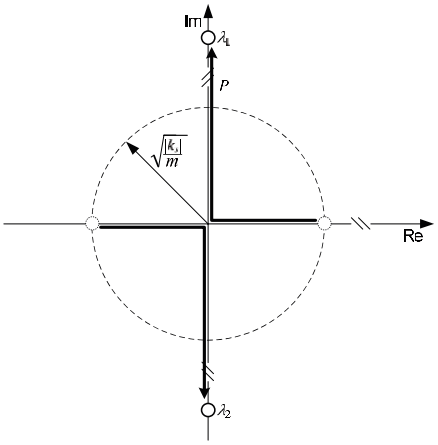


Fig. 2.9. Closed-Loop eigenvalues for very large stiffness values k ($P \gg -k_s/k_i$)

[4] A high sensitivity of the eigenvalues with respect to k_s means that the eigenfrequency ω and the eigendamping σ can vary greatly in the presence of only small changes of k_s.

Other problems associated with a high proportional feedback gain P are the magnetic flux saturation already occurring at small rotor displacements x and, above all, the high tendency to noise generation since any noise in the feedback path, namely in the sensor and power amplifier, will be strongly amplified. Hence, an indispensable prerequisite for the implementation of a high bearing stiffness are sensors featuring a very low noise level, which can be difficult to realize in an industrial machine environment.

If the design specification that leads to a high feedback gain P is primarily the need for a high *static* stiffness in order to produce only small position deviations in the presence of static external loads, a *PID* control with an integrating feedback component will be the better choice (see below).

"Natural" Stiffness

Technically easiest to achieve is, of course, an "intermediate" or "natural" stiffness value. It is called "natural" since it is based on the design and size of the magnetic bearing itself. Such a net stiffness k will always be of the same order of magnitude as the negative bearing stiffness k_s, typically $1 \ldots 3 \times |k_s|$.

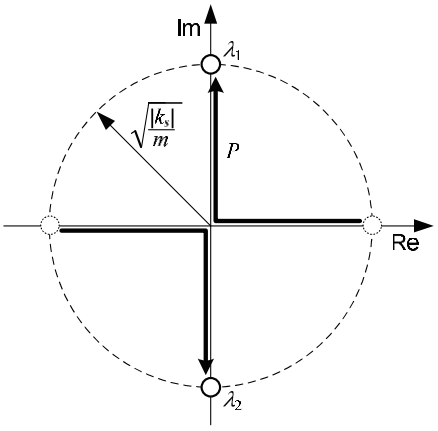


Fig. 2.10. Closed-Loop eigenvalues for a "natural" stiffness k ($P \approx -2k_s/k_i$)

For the special case of $k = |k_s|$ ($P = -2k_s/k_i$) the absolute value of the open-loop and closed-loop eigenvalues will be equal ($\omega_0 = \sqrt{-k_s/m}$), according to the "rule of thumb" that the time constants of the open-loop system should be preserved by the control. This is shown in Fig. 2.10.

A similar result will be obtained when attempting to apply modern robust control design techniques to a magnetic bearing system: In the presence of uncertainties of the negative bearing stiffness k_s the design process will always come up with a control law that provides a closed-loop stiffness value in the range of k_s.

Damping

The choice of the amount of damping d or velocity feedback D respectively depends on the stiffness. The higher the stiffness the higher the damping coefficient must be chosen in order to achieve satisfactory results. However, high damping feedback gains will lead to a high noise level, since the velocity signal $\dot{x}$ usually contains more signal noise than the corresponding displacement signal x.

The *critical* damping often constitutes an upper limit for useful levels of velocity feedback. Critical damping is reached when the damped oscillation $x(t)$ degenerates to a creeping towards zero, i.e. when $\omega = 0$. This is the case for a damping coefficient $d = 2\sqrt{mk}$. Practical experience shows that, for a mechanical system with active magnetic bearings, critical or even higher damping can be achieved for the *rigid body modes* if the system provides low noise position (and velocity) signals. For higher frequency modes, i.e. for the *bending* or *flexible* modes, obtaining high or even critical damping is nearly impossible.

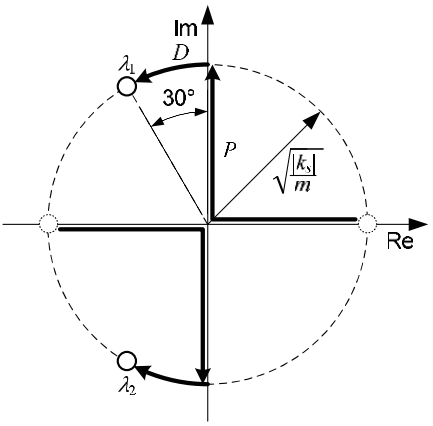


Fig. 2.11. Closed-Loop eigenvalues for "natural" stiffness $k = |k_s|$ and damping $d = \sqrt{m|k_s|}$

"Natural" damping is achieved for values $0 < d < 2\sqrt{mk}$. Very small damping values do not provide enough oscillation attenuation and might, in addition, lead to an unstable closed-loop behavior in the presence of system nonlinearities. In practice a value $d = \sqrt{mk}$, which corresponds to a damping ratio of 50%, i.e. $\sigma = \omega_0/2$ ($\omega_0 = \sqrt{k/m}$), is a good choice (see Fig. 2.11). For the damping of flexible modes, e.g. bending modes, a damping ratio of 10%, i.e. $\sigma/\omega_0 \approx 0.1$, is usually appropriate. More detailed information concerning the control of flexible modes is given in Chap. 12.

PD Control: Position Reference Command Input

For an active magnetic bearing with PD control an external static load Δf_e will always result in a change of the steady position x. The magnitude Δx of this position change depends on the implemented stiffness k and is, therefore, given by $\Delta x = \Delta f_e / k$, identically to a body suspended by a mechanical spring (see also Fig. 2.14).

Such a position change in the presence of external loads is mostly undesired in a technical application, and an active magnetic bearing can easily compensate for it by means of a position reference command input signal r, as shown in the signal flow chart displayed in Fig. 2.12. Clearly, this is only possible within the physical limits given by the load capacity and the air gap of the magnetic bearing.

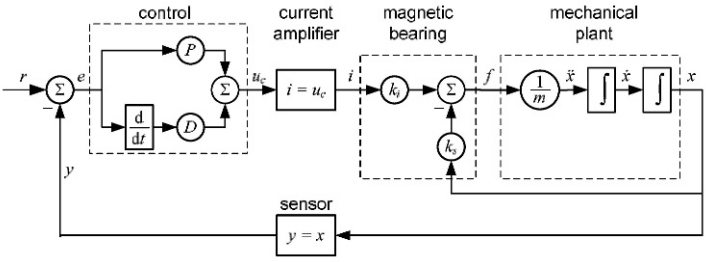


Fig. 2.12. Active magnetic bearing PD control loop with linearized mechanical plant model, sensor, reference command input, current amplifier and linearized actuator force according to (2.2)

The error signal e, i.e. the difference between the reference command input signal r and the measured position signal y, is fed into the controller. The output of the controller u_c (u_c according to the desired current i in (2.4)) is considered a command signal for the power amplifier, which has to transform this signal into the physical current i flowing through the electromagnet's coil. In this case the power amplifier is configured as a *current amplifier* or *transconductance amplifier*, a control scheme which is the most widely implemented in industrial active magnetic bearing systems (see Sect. 2.2.4).

In this simple example, it is assumed that the sensor and amplifier dynamics are ideal, hence $y = x$ and $i = u_c$. The P and D control parameters are set to achieve a net stiffness k and a damping d, as given by (2.13). Moreover, only the steady state response in the presence of Δf_e and r is considered, hence $\dot{x} = \ddot{x} = f \equiv 0$. From this the following condition for the steady state position and current deviations Δx and Δi respectively can be formulated:

$$f = 0 \rightarrow -k_s \Delta x + k_i \Delta i + \Delta f_e = 0 \tag{2.14}$$

In case of a pure PD control, it is important to see how the steady state position deviation Δx depends on the external force Δf_e and the command

reference input signal r. By expressing the control current Δi by the error signal e and by simultaneously applying the control law (2.4), the following dependency can be obtained for the static case:

$$\Delta i = \frac{k - k_s}{k_i} e = \frac{k - k_s}{k_i}(r - \Delta x) \tag{2.15}$$

By inserting (2.15) into (2.14), one obtains the following static relationship between the steady state position deviation Δx, the command reference input signal r and the external force Δf_e:

$$(k - k_s)r - k\Delta x + \Delta f_e = 0 \tag{2.16}$$

From (2.16) we can, e.g., determine the operating point change Δx for a vanishing external load Δf_e and for a given reference command input signal r:

$$\Delta x = \frac{k - k_s}{k} r \tag{2.17}$$

We see that, in case of the PD control, the position deviation Δx does *not* follow the reference command r exactly, and it even becomes larger than the command reference r since $k_s < 0$. For a small stiffness value k this error can become quite substantial, as can be concluded from (2.17).

In the presence of a non-zero external disturbance force Δf_e, the position deviation Δx also becomes non-zero if the reference command r vanishes. In order to compensate for this undesired effect a reference command input signal r can be applied such that $\Delta x = 0$:

$$r = -\frac{\Delta f_e}{k - k_s} \tag{2.18}$$

According to (2.18) we have to know the magnitude of the external force Δf_e in order to determine the correct reference command input r for the compensation of the disturbance. Moreover, uncertainties in the negative bearing stiffness k_s will also deteriorate the quality of the compensation. Finally, the steady state current Δi given in (2.15) will change the operating point of the force/current relationship and therefore the force/current factor k_i, as visible in Fig. 2.3b, which constitutes another source of error in the compensation of the external disturbance.

Integrating Feedback (PID Control)

In order to overcome both problems mentioned in the previous section a *PID* control scheme with integrating feedback can be implemented. In AMB practice, this is virtually always the case. Figure 2.13 shows such a PID control scheme.

In the steady state, all signals within the control loop are constant, hence, the error signal e must be identically zero so that the integrator state remains

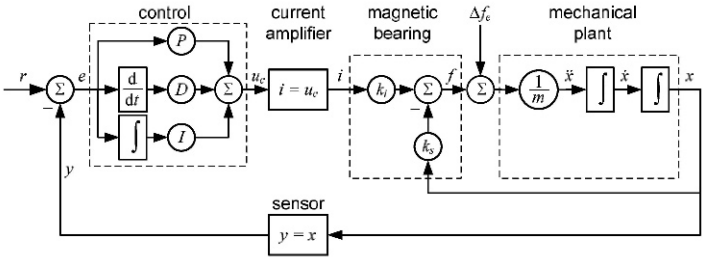


Fig. 2.13. Active magnetic bearing PID control loop with linearized mechanical plant model, sensor, reference command input, current amplifier, linearized actuator force according to (2.2) and external load

unchanged. Consequently, the position measurement signal y exactly follows the position reference command input signal r, *independently* of the external load Δf_e as long as this load is constant. It is important to keep in mind, however, that this is only true for the steady state: dynamically, the error signal e will not be zero but will depend on the various time constants in the loop (see Fig. 2.14 which shows a simulated response to a step change in Δf_e). At this point, the concept of the *dynamic stiffness* becomes important (see Sect. 2.4). The data for the simulation presented in Fig. 2.14 are summarized in Table 2.1.

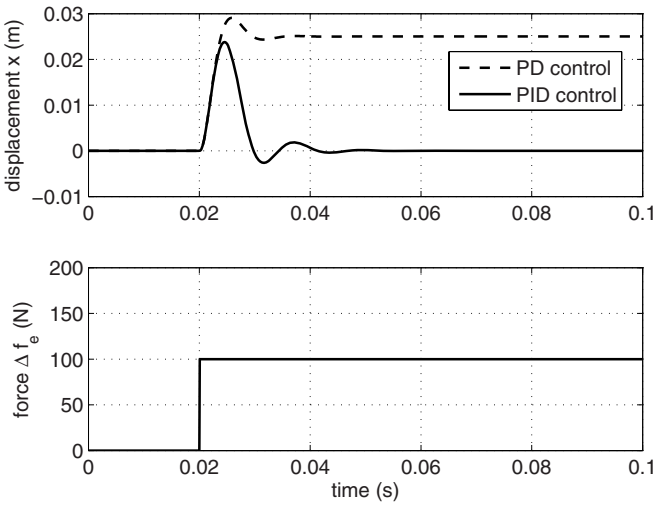


Fig. 2.14. Step response of the rotor position to an external disturbance force with PD and PID control

Table 2.1. Data for the PD and PID control simulation in Fig. 2.14

symbol	value	units
m	0.1	kg
k_s	-10^4	N/m
k_i	10	N/A
P	5×10^3	A/m
I	8×10^5	A/m s
D	6.32	A s/m
Δf_e	100	N
r	0	m

The property of maintaining the desired position independently of the external load can be considered an *infinite static stiffness* of the bearing. This property is unique to *active* magnetic bearings and of great importance for high precision or high force applications. The limitations of this property are in a first place the load capacity of the bearing, i.e. the maximum force that the bearing can produce, the rigidity of the rotor itself and the accuracy of the position measurement. Moreover, the integrating feedback gain I must not be chosen too large in order to preserve good performance of the closed-loop system (the integrating feedback produces a controller phase lag that counteracts the phase lead of the velocity feedback). The magnetic bearing's load capacity itself might, in addition, be limited by the bearing coil current which, depending on system design, might only be maintained over a specific time period in order to prevent the power amplifier and the bearing coils from overheating. This, however, is a thermal management issue and is not further discussed here.

A consequence of the limited load capacity with PID control is the behavior of an AMB when the external force becomes too large: Up to the load capacity or the maximum allowed integrator state value respectively, the rotor position is kept constant ($y = x = r$). If the external force exceeds this limit the rotor displacement will suddenly become large, eventually as large as the air gap, and then contact between the rotor and the bearing occurs. To prevent damage to the rotor–bearing system various schemes, such as retainer bearings and touch-down recovery control, have been developed (see Chap. 13 on retainer bearings, Chap. 14 on dynamics and control for fault tolerance and Chap. 18 on safety and reliability aspects). Thus, one can say that the magnetic bearing does *not* provide any *overload capability*, which is fundamentally different from conventional ball or fluid film bearings. Consequently, a magnetic bearing has to be designed such that the load capacity is well above the maximum expected external disturbance force.

2.2.4 Current vs. Voltage Command

Up to this point it has been a tacit assumption that the magnetic bearing current i (power amplifier output) instantly follows the command signal u_c (power amplifier input), as shown in Figs. 2.12 and 2.13. This assumption has been motivated by the fundamental law of the linearized bearing force (2.2) which expresses the force as a function of the current. However, the *inductance* of the magnetic bearing coil will resist any sudden change in current and, hence, fast current changes can only be achieved by a suitably high internal amplifier *voltage*. In other words, the coil current i is a *system state* and contributes to the overall system dynamics. Therefore, the basic magnetic bearing model derived in Sect. 2.1.3 must be expanded by taking into account the electrical properties of the bearing magnet and the power amplifier, i.e. the coil inductance L and its resistance R as well as the amplifier voltage u.

The inductance (or "self-inductance") L varies with the rotor position x. For a linearized description, however, L is defined for an assumed constant position (see Chap. 4) and its value is considered in the operating point $x = 0$. The rotor motion in the magnetic field of the bearing magnet also generates a voltage across the bearing coil, similar to the case of a motor. This induced voltage is proportional to the velocity $\dot{x}$ of the rotor. Hence, the total voltage of the power amplifier is used for overcoming the coil inductance and resistance and the motion induced voltage (coefficient k_u):

$$u = Ri + L\frac{d}{dt}i + k_u\frac{d}{dt}x \tag{2.19}$$

A detailed discussion of (2.19) is found in [27]. Based on the theory of electromechanical energy conversion, it can be shown that the coefficient k_u is theoretically equal to the force/current factor k_i. Moreover, it can be shown that the magnetic bearing constants k_i and k_s and the coil inductance L are interdependent quantities ($L = k_i^2/|k_s|$). The reason for this is the fact that the magnetic bearing is a device that can transform electrical into mechanical energy back and forth, similar to electric motors and generators. In reality, this energy transformation is not conservative, since losses occur from eddy currents, flux leakage, magnetic hysteresis and other nonlinear sources, all of which compromise this ideal equivalence of k_u and k_i [19, 26, 28].

Following from the important statement about the coil winding voltage u being the "true" system input variable rather than the coil current i, the complete set of basic linearized model equations additionally comprises the AMB's voltage-current dynamics (2.19), together with the force/current relation (2.2) and the equation of motion (2.5) of the mechanical system part. Consequently, the power amplifier can no more be considered a voltage-to-current amplifier (refer to Figs. 2.12 and 2.13 where, in fact, the command signal u_c physically represents an electrical voltage). More precisely, we have to speak of a voltage-to-voltage amplifier when addressing the AMB system's power amplifier. The new control scheme is called "voltage control" rather

than "current control" as suggested before. In Fig. 2.15 the closed-loop block diagram of a linearized voltage controlled AMB system is shown.

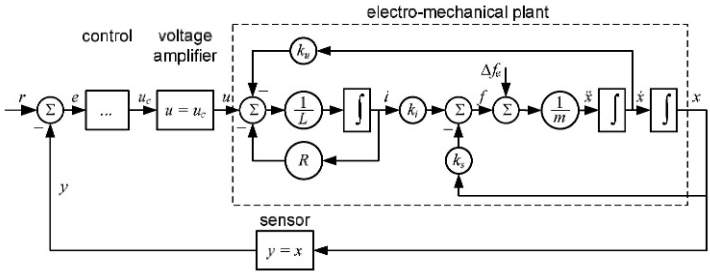


Fig. 2.15. Voltage controlled linearized magnetic bearing system with voltage command signal u_c coil inductance L, coil resistance R and induced voltage $k_u\dot{x}$

The consequence of this input variable shift from current to voltage is an augmentation of the number of system states by one, represented by the additional integrator in Fig. 2.15 as a part of the magnetic actuator.

A most important difference between current and voltage controlled AMB systems is the location of the open-loop system eigenvalues. Current control yields $\lambda_{1,2} = \pm\sqrt{-k_s/m}$ for the open-loop eigenvalues and, therefore, results in an unstable open-loop system having one eigenvalue in the right half of the complex plane. On the other hand, for $R = 0$ and $k_u = k_i$, it can be shown that voltage control yields an open-loop eigenvalue triple located at zero ($\lambda_{1,2,3} = 0$), which, of course, also represents an unstable open-loop system [27].

The reason why, up to the present, most industrial AMB systems for rotating machinery[5] have been realized on the basis of current control can be explained from exactly this location of the open-loop system poles: Whereas a current controlled AMB system can be stabilized by a rather simple "conventional" PID type control scheme, more complex control algorithms have to be used with voltage control. Moreover, in the case of voltage control, the control parameters can no more be readily interpreted by analogy to a mechanical spring-damper system as in the case of current control. These drawbacks of voltage control mainly explain the motivation for generally implementing the more "practical" current control in industrial AMB systems, even though current amplifiers have a more complex architecture, since they have to realize an underlying current control loop for the additional system dynamics introduced by the coil inductance L, as described by (2.19). Usually, this underlying current control loop is realized in hardware and is designed to be much faster than the remaining system dynamics, so that the one system

[5] Differing from rotating machinery, industrial MAGLEV transportation systems feature voltage control as a standard.

eigenvalue corresponding to the coil inductance dynamics is located in the far left of the complex plane.

However, apart from the need of a more complex control topology, voltage control features a couple of other advantages over current control:

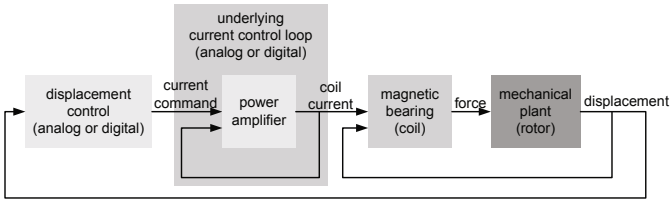
- Higher overall system robustness since the plant model is more accurate (especially in the presence of dynamics limitations e.g. due to a low DC bus voltage or due to power amplifier bandwidth limitations)
- Weaker open-loop instability (no eigenvalue in right half of the complex plane)
- Very low stiffness values easier to implement
- Simpler power amplifier architecture (no underlying current control loop)
- Possibility to benefit from the "two-way" property of electromechanical transducers ("self-sensing bearing" [27])

Lately, a certain trend back from current to voltage control is perceivable in AMB technology, which, as a matter of fact, is already state-of-the-art in modern motor control, a technology rather similar to that of AMB systems.[6] This trend absolutely makes sense in the case of digital control where there is no longer any real motivation to establish one part of the system control in software (PID or other current control based control schemes) and another part in hardware (underlying current control loop), as shown in Fig. 16(a).

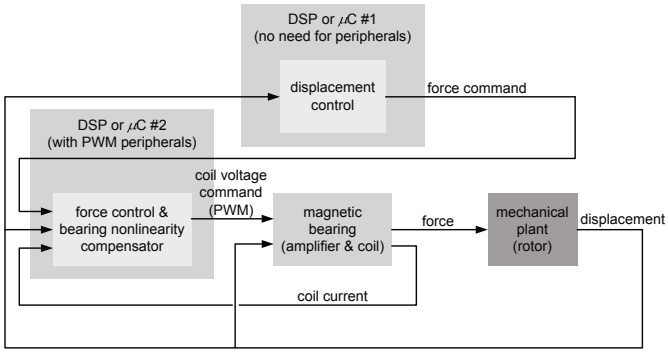
The present trend in AMB technology is also facilitated by modern digital signal processors (DSPs) which provide all the peripherals necessary to directly generate the appropriate pulse width modulated (PWM) output voltage command signals for control of the bearing currents or bearing forces respectively. However, PWM modulation techniques and appropriate power electronics topologies have been known for a long time, mainly in the field of motor control [25, 24], and have only started lately to make their appearance also in AMB technology.

Voltage control with digitally generated PWM command signals also allows for implementing rather complex control topologies in order to reach a much more linear bearing behavior compared to conventional current control, even in the presence of large rotor displacements and large forces or bearing currents respectively. Such an approach constitutes a very valuable alternative to earlier methods of improving the bearing linearity such as *flux control* [4]. Based on modern DSP and FPGA technology [6, 12, 16] highly integrated AMB control architectures are feasible that feature several processors for individual tasks such as an overlying displacement control and an underlying bearing force control with built-in force linearization that transforms the force command signal from the displacement control into a suitable PWM command signal for the coil voltage in order to provide the appropriate bearing current, even in the presence of the bearing nonlinearities. In addition

[6] Motor and AMB control can be considered different applications within the technology of *motion control*.



(a) Conventional underlying current control in hardware or software



(b) Voltage control based on modern DSPs or microcontrollers (μC) with an overlying displacement control and an underlying force control featuring nonlinearity compensation and direct PWM output signal generation

Fig. 2.16. AMB system control topologies

to a state-of-the-art current control scheme, though, the coil current must be available as a measured quantity to be fed into the underlying force control. Similar control and linearization topologies with direct PWM generation by microprocessors or DSPs are well known from motor control [5, 20, 14, 18], and implementations for AMB systems have been made [7] but have not yet become an industrial standard. A block diagram of such a control architecture for an AMB system is shown in Fig. 16(b).

2.3 Feedback Control Design

2.3.1 State Space Description

A rigid body has six degrees of freedom of motion (DOF). When elasticity is considered as well, the number of DOFs becomes even larger. Theoretically, any continuum features an *infinite* number of DOFs.

It is rather often the case in AMB technology that a simple single-input-single-output (SISO) control strategy, as treated up to now, will not do an adequate job. It can even happen, however, that no adequately stabilizing SISO

control can be found. In this case a more complex multiple-input-multiple-output (MIMO) control scheme must be implemented. The state space description will be very useful when analyzing such MIMO control structures. Moreover, in order to include non-mechanical system quantities such as the coil voltage, flux, and current introduced in (2.19) into the system analysis, the state space description becomes mandatory. Finally, non-measured system states such as the rotor velocity can only be addressed when treating the system in the state space. The state space description, together with the frequency response treated in Sect. 2.4, is also a prerequisite for the application of modern control design methodologies such as $\mathcal{H}_\infty$ or $\mu-$synthesis.

For each dynamic system, the definition of system states can be done differently, hence, different state space descriptions can exist yet yielding the same dynamic properties. For linear systems, any linear combination of system states can again be used as a system state. Generally, a system state corresponds to a "storage unit" for energy or information. The content of such a storage unit is associated with a *state variable*. The rate of change of each state is described by a first-order differential equation for the corresponding state variable, which in general also depends on all the other states (*coupled* system). Usually, the state variables of a dynamic system are combined into a *state vector* $\mathbf{x}$. This yields the following first-order vector differential equation:

$$\dot{\mathbf{x}} = \mathbf{f}(\mathbf{x}(t), \mathbf{u}(t), t) \tag{2.20a}$$

$$\mathbf{x}(t = 0) = \mathbf{x}_0 \tag{2.20b}$$

In (2.20a) the state vector $\mathbf{x}$ and the generally nonlinear vector function $\mathbf{f}$ are of nth order, corresponding to the number of system states n. The length of the input vector $\mathbf{u}$ depends on the number of input signals to the system. The vector $\mathbf{x}_0$ contains the *initial conditions*, i.e. the values of all state variables of the system at the time $t = t_0$. The initial conditions represent the necessary and sufficient information which, together with the knowledge of $\mathbf{f}$ and $\mathbf{u}$, uniquely determines the behavior of the system for times $t \geq t_0$.

When treating mechanical systems in the state space there is a simple relationship between the state space system order n and the number of mechanical degrees of freedom n_{DOF}. As a mechanical system features two "storage units" for each DOF, i.e. *kinetic* and *potential* energy, two state variables, mostly position and velocity, must be attributed to each DOF. This yields for the state space system order n:

$$n = 2n_{\mathrm{DOF}} \tag{2.21}$$

State Space Description of an AMB System with Current Control

The simple one DOF active magnetic bearing system of Sect. 2.2.1 has been introduced based on the tacit assumption of current control. Its state space description can be obtained if the two state variables for position x and velocity

$v = \dot{x}$ are combined in the state vector $\mathbf{x}$:

$$\mathbf{x} = \begin{bmatrix} x \\ v \end{bmatrix} \tag{2.22}$$

By introducing the time derivative of the velocity $\dot{v}$ the linearized second-order differential equation of motion (2.6) can be rewritten as a first-order differential equation:

$$\dot{v} = \frac{-k_s}{m} x + \frac{k_i}{m} i \tag{2.23}$$

The combination of (2.22) and (2.23) into matrix form yields the well-known state space description:

$$\dot{\mathbf{x}} = \mathbf{A}\mathbf{x} + \mathbf{B}\mathbf{u} \tag{2.24}$$
$$\mathbf{A} = \begin{bmatrix} 0 & 1 \\ \frac{-k_s}{m} & 0 \end{bmatrix}, \mathbf{B} = \begin{bmatrix} 0 \\ \frac{k_i}{m} \end{bmatrix}, \mathbf{u} = \begin{bmatrix} i \end{bmatrix}$$

Equation (2.24) is the linear equivalent to the general nonlinear state space description (2.20a). Note that the coil current $i(t)$ is the only element of input vector $\mathbf{u}$.

The two eigenvalues of matrix $\mathbf{A}$ are, as can be easily shown, $\lambda_{1,2} = \pm\sqrt{-k_s/m}$, hence the same result as obtained from (2.7) as the solution of the homogeneous part of second-order differential equation of motion (2.6). This is a consequence of the fact that the eigenvalues of a linear dynamic system are always independent of its mathematical description.

State Space Description of an AMB System with Voltage Control

A more precise model than obtained in the previous section will account for an additional "storage unit" of energy, i.e. the energy of the magnetic field of the bearing. This is achieved by introducing the more precise *voltage control* model description with the coil current i being no longer an input signal but a state variable. The "true" input signal to the system is the coil voltage u, as introduced in (2.19).

As mentioned above, different but equivalent choices of state variables are possible here again. For simplicity the following state vector $\mathbf{x}$ containing the state variables for position x, velocity $v = \dot{x}$ and coil current i is chosen:

$$\mathbf{x} = \begin{bmatrix} x \\ v \\ i \end{bmatrix} \tag{2.25}$$

As shown in the previous section the equation of motion (2.6) and the description (2.19) of the electromechanical part of the system can be transformed into the following first-order state space description with the coil voltage u as input signal (assumption $k_u = k_i$):

$$\dot{\mathbf{x}} = \mathbf{A}\mathbf{x} + \mathbf{B}\mathbf{u} \tag{2.26}$$

$$\mathbf{A} = \begin{bmatrix} 0 & 1 & 0 \\ -k_s/m & 0 & k_i/m \\ 0 & -k_i/L & -R/L \end{bmatrix}, \quad \mathbf{B} = \begin{bmatrix} 0 \\ 0 \\ 1/L \end{bmatrix}, \quad \mathbf{u} = \begin{bmatrix} u \end{bmatrix}$$

A more detailed description of modeling more complex AMB systems with voltage control can be found in [28].

2.3.2 State and Output Feedback Control Design

Linear control theory offers various control design methods for systems described in the form $\dot{\mathbf{x}} = \mathbf{A}\mathbf{x} + \mathbf{B}\mathbf{u}$, whatever the number of state variables or the system order n respectively might be [8, 13].

Among the most well-known state feedback control design concepts are the *full order state feedback* approaches such as *LQ-control* and *pole-placement* (see Table 2.2). These approaches imply that all system states can be measured and fed back to the system input. This, however, constitutes a very strong idealization. In a real AMB system, e.g., only a restricted number of position signals – mostly five – are measured and the *velocities* as most important further system states are not measured but have to be estimated from the available position signals. Moreover, higher order states corresponding to flexible system modes are hardly ever directly measurable.

Therefore, the concept of the full order state feedback has to be abandoned in favor of the *output feedback* concept. To do this, the state space description (2.24) has to be augmented as shown in Fig. 2.17.

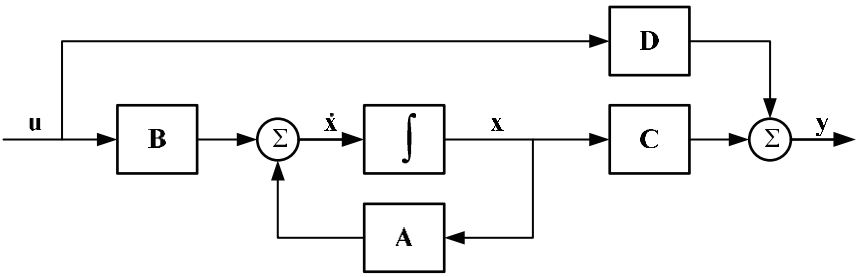


Fig. 2.17. Linear state space description with output matrix C and feed-through matrix D

The mathematical description of the linear state space system corresponding to Fig. 2.17 can be expressed as follows:

$$\dot{\mathbf{x}} = \mathbf{A}\mathbf{x} + \mathbf{B}\mathbf{u} \tag{2.27a}$$

$$\mathbf{y} = \mathbf{C}\mathbf{x} + \mathbf{D}\mathbf{u} \tag{2.27b}$$

The newly introduced matrices $\mathbf{C}$ (*output* matrix) and $\mathbf{D}$ (*feed-through* matrix) expand the description handled so far by the vector $\mathbf{y}$, which is generally a linear combination of measurable system state variables and input signals. Equation (2.27) constitutes the *fundamental* description of any linear dynamic plant for which a suitable control has to be designed. Most modern linear control design techniques use this description.

It is not the target of this chapter to discuss the different state-of-the-art control design methodologies in detail, since this is the subject of other contributions to this book (e.g. Chap. 12). Instead, a short overview over some well-known and over the presently most important control design methods for AMB systems together with a short validation of their practical applicability is given in the following Tables.

Table 2.2 gives an overview of control design methods that are well-known but no longer widely used for AMB systems, most often for the reason of a certain lack of practicability in industrial systems. Table 2.3 summarizes the actually most frequently used state-of-the-art control design approaches in AMB technology.

2.4 Forced Vibration and Frequency Response

Up to this point, the analysis of the dynamic behavior of an AMB system has only been discussed in the time domain, mainly in terms of *eigenvalues* and *eigenmodes* (see Sect. 2.2). However, in technical systems, the reaction to external forces is of crucial interest. Among the various types of external excitation mechanisms the class of *periodic* and *harmonic* disturbances plays the most important role. This is not surprising for the field of rotating machinery since most excitation mechanisms, e.g. unbalance excitation, are directly linked to the rotation of the machine itself and, therefore, contain the synchronous frequency component and often also its harmonics. If the system is linear its response to a general periodic excitation can be set-up as the superposition of the system responses to each single harmonic component of the excitation force ("Fourier" decomposition).

2.4.1 Harmonic Excitation Response

In order to analyze the effect of a harmonic external excitation along with the simple AMB system of Sect. 2.2, the model description has to be augmented, i.e. the right hand side of the homogeneous differential equation (2.8) will

Table 2.2. Well-known but rarely applied control design methods for AMB systems ("•": specific property, "+": strength, "−": shortcoming)

method	short description & validation	ref.
pole-placement	• full order state feedback • direct prescription of closed-loop system dynamics − requires all system states to be measurable − sensible choice of closed-loop system poles requires high skillfulness − bandwidth limitations and sensor noise difficult to address	[2]
LQ-control	• full order state feedback • "L" → *linear*, "Q" → *quadratic* • minimization of a quadratic cost function − requires all system states to be measurable − requires skill and experience for proper choice of weighting matrices + bandwidth limitations (e.g. in power amplifier) manageable by weighting matrices	[2]
LQG-control	• output feedback (not all states must be measurable) • "L" → *linear*, "Q" → *quadratic* "G" → *Gaussian* • minimization of a quadratic cost function + estimation of non-measurable system states by *linear full order state observer* scheme − requires skill and experience for proper choice of weighting matrices − requires exact knowledge of plant dynamics (high sensitivity to *plant model uncertainties* (→ low *robustness*)	[13, 8]
structure predefined control	• output feedback (not all states must be measurable) • allows to apply LQ-control design methodology without necessity for implementing a full order observer + arbitrary controller structure predefinable − requires skill and experience for proper choice of weighting matrices − low robustness to plant uncertainties	[17]

Table 2.3. Most important state-of-the-art control design methods for AMB systems ("•": specific property, "+": strength, "−": shortcoming)

method	short description & validation	ref.
passive control	• output feedback (not all states must be measurable) • uses "passivity" property of plant and controller + preservation of closed-loop stability in the presence of modelling errors (e.g. by avoiding "spill-over" effects) − passivity property difficult to preserve in the presence of non-ideal dynamics (sensor, amplifier), plant nonlinearities and digital control	[22]
$\mathcal{H}_\infty$, $\mu-$*synthesis*	• output feedback (not all states must be measurable) • controller design by frequency domain weighting functions + practical choice of weighting functions based on engineering specifications + high robustness to plant and other uncertainties + highly suited for complex plants and MIMO control problems − high controller order requires large computational resources (digital control) + currently still rarely used but of a high technical potential for industrial applications	[21, 9, 3]
"PID + filter"	• output feedback (not all states must be measurable) + high level of practicability due to intuitive and physically motivated design process + easily extendable by "hand-made" structural enhancements (e.g. "parallel/conical" decomposition) + well suited for SISO (e.g. *decentralized*) control schemes + well applicable for and achieving an absolutely satisfying closed-loop system in a large number of industrial applications − requires physical insight into the system dynamics and profound knowledge of classical frequency domain control theory and can be considered an art performed only by experienced control engineers − might become less important in the future as the theoretical and practical burdens of modern robust control design techniques become lower and as industrial AMB systems become more complex	

no longer be zero but will describe the time dependence of the disturbance force (see also Chap. 7 on the dynamics of the rigid rotor). This results in the following *inhomogeneous* differential equation:

$$m\ddot{x} + d\dot{x} + kx = f\cos(\omega t) \tag{2.28}$$

It can be shown that, asymptotic system stability presumed (all eigenvalues in the left half of the complex plane), any transient system response will die out after some time, leaving the system response to the external excitation as the sole signal component, which can be described by the *particular* solution $x_p(t)$ of (2.28). As can be shown for this class of linear differential equations, $x_p(t)$ can always be expressed as a generalized form of the excitation signal itself, such as:

$$x_p(t) = C_p\cos(\omega t + \phi_p) \quad (C_p > 0) \tag{2.29}$$

Hence, $x_p(t)$ is a harmonic oscillation with the same frequency ω as the excitation, but with different amplitude C_p and with a phase shift ϕ_p relative to the excitation signal.

By inserting (2.29) into (2.28) and by some mathematical transformations (comparison of coefficients, goniometric correlations, etc.) the unknown oscillation amplitude C_p and phase shift ϕ_p can be expressed by the properties of the dynamic system (mass, stiffness, damping) and by the amplitude and frequency of the external force. An even simpler description can be obtained if the expressions for the undamped and damped eigenvalues of (2.28), given by (2.10), are used. This yields:

$$C_p = \frac{1}{m\sqrt{({\omega_0}^2 - \omega^2)^2 + (2\sigma\omega)^2}}\, f \tag{2.30a}$$

$$\tan(\phi_p) = -\frac{2\sigma\omega}{{\omega_0}^2 - \omega^2} \quad ({\omega_0}^2 = \frac{k}{m},\ \sigma = \frac{d}{2m}) \tag{2.30b}$$

For graphical visualization of (2.30) it is useful to introduce the dimensionless frequency $\kappa = \omega/\omega_0$ and damping coefficient $\varepsilon = 2\sigma/\omega_0$ and to introduce the *amplification* $g = C_p/f$ as the ratio between the displacement amplitude C_p and the excitation force f:

$$g = \frac{C_p}{f} = \frac{1}{m{\omega_0}^2}\frac{1}{\sqrt{(1-\kappa^2)^2 + (\varepsilon\kappa)^2}} \tag{2.31a}$$

$$\tan(\phi_p) = -\frac{\varepsilon\kappa}{1-\kappa^2} \tag{2.31b}$$

In Fig. 2.18, the phase shift ϕ_p between the displacement $x_p(t)$ and the external force $f(t)$ is plotted as a function of the dimensionless frequency κ for varying dimensionless damping coefficients ε. Generally for this kind of dynamic system, the phase shift becomes negative and falls with the excitation frequency as a result of the system inertia, the slope of decay depending on damping. At low frequencies, nevertheless, there is little phase shift, force and

vibration response are nearly in phase, whereas at very high frequencies the phase shift is $-180°$, hence, the oscillation of the mass m is in counter phase to the excitation force.

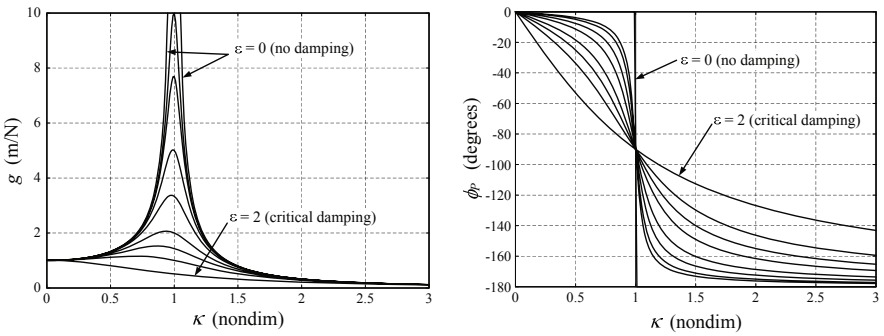


Fig. 2.18. Phase shift ϕ_p and amplification g as a function of the dimensionless frequency κ for varying damping coefficients ε

Most interesting is the system behavior for $\kappa = 1$, i.e. if the excitation frequency ω is equal to the eigenfrequency ω_0 of the *undamped* system. This case is called "resonance"[7] and is one of the most important phenomena of oscillatory systems of any kind (mechanical, electrical, optical, etc.). The best known and also most feared effect resulting from a resonance is the large amplification of the system response. For small damping coefficients, a large system response can occur even if the excitation force is small. Despite the fact that the system is asymptotically stable, resonance can lead to system destruction due to an excessively high vibration amplitude.

2.4.2 Generalization of the Frequency Response

In the previous section we have derived the phase shift ϕ_p and the amplification g of the system response $x_p(t)$ for the simple one degree of freedom oscillatory system described by (2.28). This important finding can be generalized for any linear dynamic system by a transition from the time domain to the frequency domain description, i.e. by applying the *Laplace transform* to the differential equation (2.28):

$$\begin{aligned} &\mathcal{L}\{m\ddot{x}(t) + d\dot{x}(t) + kx(t) = f\cos(\omega t)\} \\ \rightarrow\ &ms^2X(s) + dsX(s) + kX(s) = F(s) \end{aligned} \tag{2.32}$$

[7] The definition of resonance is not made based on the maximum response amplitude (amplification), as is often wrongly assumed, but on the phase shift ϕ_p. By definition, resonance occurs if $\phi_p = -90°$.

The *transfer function* $G(s)$ is defined as the quotient between the transformed displacement $X(s)$ and force $F(s)$, hence:

$$G(s) = \frac{X(s)}{F(s)} = \frac{1}{ms^2 + ds + k} = \frac{1}{m(s^2 + 2\sigma s + \omega_0^2)} \tag{2.33}$$

The *frequency response* is obtained by evaluating the transfer function $G(s)$ along the imaginary axis, hence for $s = j\omega$:

$$G(j\omega) = \frac{1}{m(-\omega^2 + j2\sigma\omega + \omega_0^2)} \tag{2.34}$$

Usually, the complex frequency response is analyzed by examining its absolute value and its argument. In this case one speaks of the *amplitude* and *phase* response of the system:

$$|G(j\omega)| = \frac{1}{m\sqrt{(\omega_0^2 - \omega^2)^2 + (2\sigma\omega)^2}} \tag{2.35a}$$

$$\angle G(j\omega) = \arctan\left(\frac{\mathfrak{Im}(G(j\omega))}{\mathfrak{Re}(G(j\omega))}\right) = \arctan\left(\frac{-2\sigma\omega}{\omega_0^2 - \omega^2}\right) \tag{2.35b}$$

By comparison of (2.35) with (2.30, 2.31) it is easily recognized that the absolute value of the frequency response $|G(j\omega)|$ exactly corresponds to the amplification g and that its argument $\angle G(j\omega)$ is equal to the phase shift ϕ_p:

$$g = |G(j\omega)| \tag{2.36a}$$

$$\phi_p = \angle G(j\omega) \tag{2.36b}$$

This finding constitutes a very important and general fact for any linear dynamic system: Instead of explicitly deriving the phase shift and the amplification of the frequency response based on the time domain solution - a rather cumbersome approach for more complex systems - one can simply obtain the same quantities directly from the complex transfer function, a much more elegant and fast approach, which is even feasible for the general state space description of a linear dynamic system as represented by (2.27). By the following Laplace transform,

$$\mathcal{L}\{\dot{\mathbf{x}}(t) = \mathbf{A}\mathbf{x}(t) + \mathbf{B}\mathbf{u}(t)\} \rightarrow s\mathbf{X}(s) = \mathbf{A}\mathbf{X}(s) + \mathbf{B}\mathbf{U}(s) \tag{2.37a}$$

$$\mathcal{L}\{\mathbf{y}(t) = \mathbf{C}\mathbf{x}(t) + \mathbf{D}\mathbf{u}(t)\} \rightarrow \quad \mathbf{Y}(s) = \mathbf{C}\mathbf{X}(s) + \mathbf{D}\mathbf{U}(s) \tag{2.37b}$$

one directly obtains the transfer function response *matrix* $\mathbf{G}(s)$:

$$\begin{aligned} \mathbf{Y}(s) &= \mathbf{G}(s)\mathbf{U}(s) \\ \mathbf{G}(s) &= \mathbf{C}[s\mathbf{I} - \mathbf{A}]^{-1}\mathbf{B} + \mathbf{D} \end{aligned} \tag{2.38}$$

Note that, despite matrices are involved in (2.38), the transfer function can be a scalar (SISO case) or a matrix (MIMO case) with a size depending on the number of input and output signals. However, even in the scalar case, the transfer function cannot be built up by a direct division of terms as in (2.33) since the mathematical rules for matrix inversion have to be followed.

2.4.3 The Frequency Response as a Powerful Tool

If an analytic description of a dynamic system, such as given by (2.27), is available then the transfer function (2.38) does not contain any additional information and is, in fact, mathematically equivalent to the time domain description. This can, e.g., be illustrated by the system eigenvalues that are usually determined from a formulation of the eigenvalue problem for (2.27) and from solving the resulting characteristic polynomial. As can be seen in (2.38) the transfer function involves the inversion of the matrix $[s\mathbf{I}-\mathbf{A}]$, and a matrix inversion always involves its determinant $\det(s\mathbf{I}-\mathbf{A})$ in the denominator of each transfer function element. By a comparison of the expression for the determinant with the eigenvalue problem it can be easily seen that the *roots* of the transfer function (2.38) are equal to the eigenvalues of (2.27).

Despite the fact that $\mathbf{G}(s)$ does not contain more information than the time domain description, the frequency response, i.e. the evaluation of $\mathbf{G}(s)$ along the imaginary axis ($s = j\omega$), still constitutes a very elegant tool for quickly determining the amplitude and phase of the system response to a harmonic disturbance force.

This, however, is by far not the only benefit of the frequency response. Even if there is *no analytic description* of a dynamic system available, the frequency response function can still be *measured directly* by building the *Fourier* transform of measured input and output signals, e.g. by numerical means such as the *Fast Fourier Transform* (FFT), and by subsequently building the quotients of these transformed signals. The resulting complex numbers – one number for each frequency sample ω – are then equivalent to the numerical evaluation of (2.38) for $s = j\omega$. By a series of suitable elements this can even be done in the MIMO case with the result of obtaining the numerical values of the complex *elements* of the frequency response matrix. Such a directly measured frequency response will show many important properties and characteristics of the dynamic plant, such as resonances, zeroes, phase shifts, and so forth. Hence, it will exactly correspond to the analytically obtained graph shown in Fig. 2.18. Moreover, in a closed-loop system – asymptotic stability is required as a prerequisite – the *performance* of the control can be determined based on the measured responses by e.g. assessing the resonance peaks to check for an appropriate damping or by assessing the static and dynamic response amplitude to check for a suitable system stiffness, all *without* having an analytic system description. Hence, this approach can help to *identify* the unknown system model on the basis of the measured frequency response (see Chap. 11 on identification).

Finally, but most importantly, there is a huge benefit from the concept of transfer functions or frequency responses, respectively, in the field of modern *robust control design* techniques such as $\mathcal{H}_\infty$ and $\mu-$synthesis. These methods generally use frequency domain functions for addressing system uncertainties, and they can predict the system robustness, i.e. the performance of the closed-loop control in the presence of those system uncertainties, just

on the basis of transfer functions, whether available analytically or measured only. This finding has a huge impact on system quality evaluation by means of frequency response measurements: If the *sensitivity function* is measured (see Chap. 8 and Chap. 12), then the system *robustness* can be directly determined just by examining its *peaks*[8] (note that the system *performance* is determined by other types of frequency response measurement). This important concept has already been followed in the lately emerged ISO standard for AMB applications [1] and will drastically improve the quality of such systems.

Figure 2.19 displays a general block diagram of a magnetic bearing control system together with the necessary excitation nodes for frequency response measurement according to the ISO standard. Table 2.4 lists the most common types of frequency response measurements along with a short description of their typical use in practical applications. Finally, Fig. 2.20 displays typical shapes of frequency responses, generated on the basis of the simple example from Sect. 2.2.

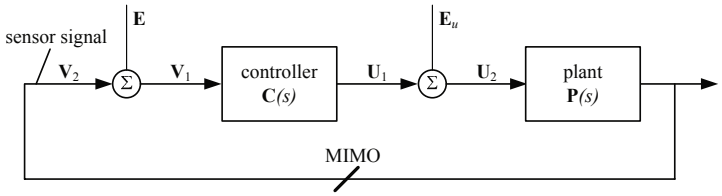


Fig. 2.19. Signals and excitation nodes for frequency response measurement according to the ISO standard [1]

It is of utmost importance to notice at this point that the transfer function measurements indicated in Fig. 2.19 and listed in Table 2.4 have to be carried out while the plant is *levitating*. This is specially important for the open-loop plant measurement $\mathbf{P}(s)$ itself in order to obtain results that are not falsified by a potential rotor-stator contact. It might appear unfamiliar that an *open-loop* measurement can be carried out within a *closed-loop*, however, if one considers the signals in Fig. 2.19, it is easily recognizable that a measurement from the plant input $\mathbf{U}_2$ to the plant output $\mathbf{V}_2$ is possible while the loop is maintained closed and while exciting the system at $\mathbf{E}$ or $\mathbf{E}_u$.

A short discussion of the various frequency response shapes follows below.

Plant Transfer Function

Plant transfer functions, as shown in Fig. 2.20a, are typically used for plant identification and control design purposes. The information content includes

[8] The phase of the sensitivity function is usually not addressed and contains no information of practical interest.

Table 2.4. Types of transfer functions or frequency responses, respectively, and their information content in AMB systems

transfer type	exc. @	name	$\mathbf{G}(s)$ $(s = j\omega)$	system properties validated
$\mathbf{U}_2 \rightarrow \mathbf{V}_2$	$\mathbf{E}_u$	*open-loop plant*	$\mathbf{P}(s)$	identification of (unknown) plant dynamics
$\mathbf{V}_1 \rightarrow \mathbf{U}_1$	$\mathbf{E}$	*controller*	$\mathbf{C}(s)$	controller performance
$\mathbf{E} \rightarrow \mathbf{V}_1$	$\mathbf{E}$	*input sensitivity*	$[\mathbf{I} - \mathbf{P}(s)\mathbf{C}(s)]^{-1}$	robustness to uncertainties (mainly in plant)
$\mathbf{E}_u \rightarrow \mathbf{V}_2$	$\mathbf{E}_u$	*dynamic compliance, complementary sensitivity*	$[\mathbf{I}-\mathbf{P}(s)\mathbf{C}(s)]^{-1}\mathbf{P}(s)$	attenuation (damping), resonances, transmission zeroes
$\mathbf{V}_2 \rightarrow \mathbf{E}_u$	$\mathbf{E}_u$	*dynamic stiffness*	$\mathbf{P}^{-1} - \mathbf{C}$	static and dynamic stiffness (inverse of dynamic compliance, $\mathbf{P}^{-1}$ must exist)
$\mathbf{E}_u \rightarrow \mathbf{U}_2$	$\mathbf{E}_u$	*output sensitivity*	$[\mathbf{I} - \mathbf{C}(s)\mathbf{P}(s)]^{-1}$	identical to input sensitivity only in SISO case
$\mathbf{V}_1 \rightarrow \mathbf{V}_2$	$\mathbf{E}$	*Nyquist, open-loop system*	$\mathbf{P}(s)\mathbf{C}(s)$	used for Nyquist diagram (mostly used only for SISO case)

Table 2.5. Model data for frequency response plots in Fig. 2.20 (model equal to Sect. 2.2 but with an additional "flexible mode" in the mechanical plant and with a low pass filter $G_{\text{filt}}(s) = (n_2 s^2 + n_1 s + n_0)/(d_3 s^3 + d_2 s^2 + d_1 s + d_0)$ in series to the controller)

symbol	value	units
m_{total}	0.1	kg
k_s	-10^4	N/m
k_i	10	N/A
P	5×10^3	A/m
I	1×10^5	A/m s
D	6.32	A s/m
ω_{flexible}	500	Hz
n_2	1.6×10^{-1}	(-)
n_1	5.0265×10^3	(-)
n_0	3.9478×10^7	(-)
d_3	3.1831×10^{-4}	(-)
d_2	2.6×10^0	(-)
d_1	1.7593×10^4	(-)
d_0	3.9478×10^7	(-)

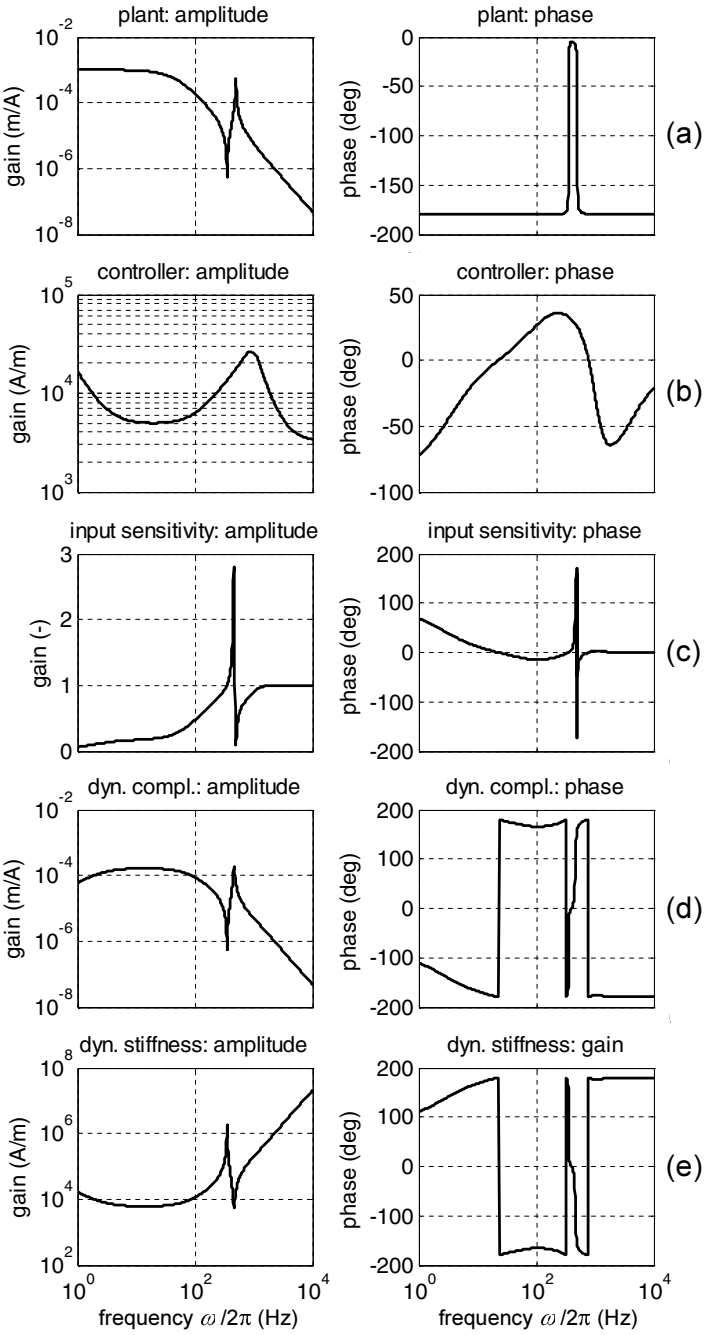


Fig. 2.20. Typical shapes of most frequently used AMB transfer functions according to Table 2.4 (numerical values from Table 2.5): (**a**) plant; (**b**) controller; (**c**) input sensitivity; (**d**) dynamic compliance; (**e**) dynamic stiffness

mechanical resonances and anti-resonances (transmission zeroes) characterized primarily by their frequencies. They are also characterized by their phase lags which are mostly due to non-mechanical plant elements as well as noise perturbation levels of the measurement, especially at higher frequencies.

As the plant is mainly of a mechanical nature the transfer function most commonly exhibits a low pass characteristic. However, since sensor and power amplifier dynamics are also included in the plant measurement, high pass or band pass characteristics might result from these additional components, constituting most undesired effects that have to be considered in the controller design.

Plant transfer functions can be measured in a SISO or MIMO configuration. However, since a general AMB rotor plant inherently exhibits a MIMO open-loop structure (two radial DOFs are always coupled by the inertia properties of the system, and all four can become coupled by the gyroscopic system properties), a "correct" open-loop plant measurement can only be obtained by a corresponding MIMO plant measurement, even if the control structure itself is SISO (refer to [1] and Chap. 7). In the case of a SISO plant measurement, also called "1-cut" transfer function measurement instead of "N-cut" [1], substantially wrong results e.g. with respect to the identified resonance frequencies, the "free-free" eigenfrequencies of the plant, might be generated. The physical reason for this is the fact that stiffness and damping from the uncut control signal paths always penetrate the 1-cut measurement through the plant couplings. Hence, it is highly recommendable to carry out MIMO open-loop plant measurements as a general rule in order to obtain good identification results.

Controller Transfer Function

The controller transfer function measurement (see Fig. 2.20b) can be carried out in a SISO or MIMO procedure depending on the implemented control structure itself. It is most commonly needed for stability assessment purposes and simulations of the controlled system. Typically, the so-called SISO "open-loop" control design methods such as the "PID + filter" method listed in Table 2.3 make use of the controller transfer function's gain and phase information for determining the closed-loop system's gain and phase margin.

Usually, the controller transfer function is *a priori* known, especially in the case of digital control. Consequently, it does not need to be measured. However, a frequency response measurement of its implementation on a microcontroller can be of high practical interest for control firmware debugging purposes.

Input Sensitivity Function

The sensitivity function measurement (see Fig. 2.20c) is one of the most important closed-loop transfer function measurements to be carried out on an AMB system and should be implemented as a mandatory procedure prior

to long-term operation, as regulated by the corresponding ISO standard for AMB systems [1].

The interpretation of the sensitivity function is based on modern robust control theory and, despite its high expressiveness, is fairly simple: The overall peak of the sensitivity function is a measure for robustness of the control system to parameter changes, e.g. due to temperature drifts or component aging. The lower the sensitivity function peak becomes, the more robust to such changes the system performs. Usually, a peak value of 3 or less is desirable for a newly commissioned system.

Based on the current ISO standard, interpretation of the sensitivity function only makes use of the gain information contained in the diagonal elements of the MIMO sensitivity function matrix, hence, a SISO measurement scheme turns out to be sufficient. The phase information is not of practical interest.

Dynamic Compliance

In contrast to the sensitivity function measurement with the sole purpose of system robustness assessment, the dynamic compliance transfer function measurement (see Fig. 2.20d) constitutes a means for assessing the controlled system's *performance*, most notably in terms of stiffness, damping of resonances and suppression of high frequency noise. The lower the gain of the dynamic compliance can be established, the lower the amplification of an external excitation at a particular frequency becomes and, therefore, the higher the dynamic stiffness of the system at this frequency turns out.

Most commonly, one is interested at determining the system's response (signal $\mathbf{V}_2$ or a scalar component of it, see Fig. 2.19) solely to a single excitation signal, i.e. to a scalar signal component of the vectors $\mathbf{E}$ or $\mathbf{E}_u$ respectively, a SISO or reduced MIMO measurement is usually suitable to do the job. Here, the system's response to an excitation at input $\mathbf{E}_u$ corresponds to that of a real external force applied at the bearing locations.

It is evident that the phase information of the dynamic compliance transfer function contains information about the phase shift between excitation signal and plant response. However, the phase information can also be used to assess closed-loop resonance frequencies of modes that are highly damped and, therefore, not well visible as resonances, as e.g. in the case of rigid body modes. Here, the resonance frequency to be identified can be obtained from the frequency point where a ninety degree phase shift of the frequency response is found (see Fig. 2.18). This approach, nevertheless, only produces useful results in the case of a weakly coupled system.

Dynamic Stiffness

As mentioned in earlier sections of this chapter, the stiffness of a system levitated by AMBs is not a scalar number but depends on the *frequency* of the corresponding excitation. Therefore, it makes sense to use the term *dynamic*

stiffness. The dynamic stiffness is determined by the plant and controller characteristics in the frequency range of interest. In contrast to this, the *static* stiffness of an AMB system, i.e. the stiffness at *zero* frequency, is solely determined by the *load capacity* of the magnetic bearings, provided that an *integrating feedback* is implemented (see Sects. 2.1.1, 2.2.2 and 2.1.1).

Dynamic stiffness and dynamic compliance are closely linked, i.e. the dynamic stiffness is the *inverse* of the dynamic compliance, as can also be seen in Table 2.4. Therefore, the typical shape of the dynamic stiffness transfer function exhibits a high level at very low frequencies due to the integrating feedback, comparably low levels in an intermediate frequency range and again a very high level at high frequencies, which is a consequence of the inertia of the plant (see Fig. 2.20e). This high stiffness at high frequencies is, for example, utilized in AMB applications such as machine tool spindles where high frequency cutting forces as a result of high speed rotation do not strongly affect spindle displacements, a fact resulting in a good surface quality obtained by a high speed milling or grinding process.

References

1. ISO 14839-3. *Mechanical vibration - Vibration of rotating machinery equipped with active magnetic bearings - Part 3: Evaluation of stability margin*. International Organization for Standardization ISO, 2006.
2. J. Ackermann. *Sampled Data Control Systems*. Springer-Verlag, Berlin, 1985.
3. G. J. Balas, J. C. Doyle, K. Glover, A. K. Packard, and R. Smith. *μ Analysis and Synthesis Toolbox User's Guide*. The MathWorks, Natick, MA, 1995.
4. H. Bleuler, et al. New concepts for cost effective magnetic bearing control. *AUTOMATICA*, 30:5, 1994.
5. S. R. Bowes and M. J. Mount. Microprocessor control of PWM inverters. *IEEE Transactions on Industry Applications*, 128(6):293–305, 1981.
6. S. Brown and J. Rose. Architecture of FPGAs and CPLDs: A tutorial. *IEEE Design and Test of Computers*, 13(2):42–57, 1996.
7. Ph. Bühler. *Hochintegrierte Magnetlagersysteme*. PhD thesis, No. 11287, Federal Institute of Technology (ETH), Zürich, Switzerland, 1995.
8. J. C. Doyle, B. A. Francis, and A. R. Tannenbaum. *Feedback Control Theory*. MacMillan, New York, 1992.
9. J. C. Doyle and G. Stein. Multivariable feedback design: Concepts for a classical/modern synthesis. *IEEE Transactions on Automatic Control*, 26(1):4–16, 1981.
10. B. W. Duncan. Pediatric mechanical circulatory support: A new golden era? *Artificial Organs (Blackwell Publishing Ltd.)*, 29(12):925–926, December 2005.
11. S. Earnshaw. On the nature of the molecular forces, which regulate the constitution of the luminiferous ether. *Transactions of Cambridge Philosophical Society*, 7:97–112, 1842.
12. P. Ekas. FPGAs rapidly replacing high-performance DSP capability. *DSP Engineering Magazine (DSP-FPGA.com)*, February 2007.
13. H. P. Geering. *Mess- und Regelungstechnik*. Springer-Verlag, Berlin, second edition, 1990.

14. J. Holtz. Pulsewidth modulation – a survey. *IEEE Transactions of Industrial Electronics*, 39(5):410–420, December 1992.
15. H. Hoshi, T. Shinshi, and S. Takatani. Third-generation blood pumps with mechanical noncontact magnetic bearings. *Artificial Organs (Blackwell Publishing Ltd.)*, 30(5):324–338, May 2006.
16. R. Jastrzebski, R. Pöllännen, O. Pyrhönen, A. Kärkkäinen, and J. Sopanen. Modeling and implementation of active magnetic bearing rotor system for FPGA-based control. In *Proceedings of the Tenth International Symposium on Magnetic Bearings*, Martigny, Switzerland, August 2006.
17. R. Larsonneur. *Design and Control of Active Magnetic Bearing Systems for High Speed Rotation*. PhD thesis, No. 9140, Federal Institute of Technology (ETH), Zürich, Switzerland, 1990.
18. H. Le-Huy. Microprocessors and digital ICs for motion control. *Proceedings of the IEEE*, 82(8):1140–1163, 1994.
19. A. Lenk. *Elektromechanische Systeme*. VEB Technik, Berlin, GDR, third edition, 1971.
20. S. Meshkat and I. Ahmed. Using DSPs in AC induction motor drives. *Control Engineering Practice*, 35(2):54–56, February 1988.
21. K. Nonami, H. E. Weidong, and H. Nishimura. Robust control of magnetic levitation systems by means of H_∞ control/$\mu-$synthesis. *JSME International Journal*, 37(3):513–520, 1994.
22. J. Salm. *Eine aktive magnetische Lagerung eines elastischen Rotors als Beispiel ordnungsreduzierter Regelung grosser alastischer Systeme*. PhD thesis, Fortschrittberichte VDI, Reihe 1, Nr. 162, Düsseldorf, Germany, 1988, ISBN 3-18-14-6201-2.
23. G. Schweitzer and R. Lange. Characteristics of a magnetic rotor bearing for active vibration control. In *Proceedings of the International Conference on Vibrations in Rotating Machinery*, Churchill College, Cambridge, U.K., 1976.
24. H. Stemmler. Inverter circuit for supplying current to polyphase motors. US Patent 3 346 794, 1967.
25. H. Stemmler and A. Schönung. Frequenzumformung. Brown Bovery Mitteilungen, Nr. 8/9, Baden, Switzerland, 1964.
26. J. Thoma. *Simulation by Bondgraphs*. Springer-Verlag, Berlin, 1990.
27. D. Vischer. *Sensorlose und spannungsgesteuerte Magnetlager*. PhD thesis, No. 8665, Federal Institute of Technology (ETH), Zürich, Switzerland, 1988.
28. D. Vischer and H. Bleuler. A new approach to sensorless and voltage controlled AMBs based on network theory concepts. In *Proceedings of the Second International Symposium on Magnetic Bearings*, University of Tokyo, Japan, July 1990.

3

Hardware Components

Alfons Traxler and Eric Maslen

As illustrated in Fig. 3.1, active magnetic bearings are created by combining electromagnets, power amplifiers, non-contact position sensors, and an electrical control system. The control system uses signals from the position sensors to determine what commands (signals) to send to the amplifiers. The amplifiers, in turn, drive current through the electromagnet coils to produce forces which act on the suspended rotor. This relationship between components is described in detail in Chap. 2.

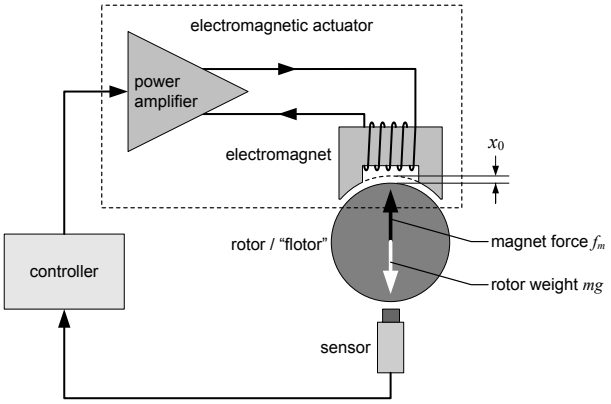


Fig. 3.1. The most basic AMB, showing the primary components

This chapter describes the structure, underlying function, and general design or selection criteria for these electromagnets, amplifiers, and sensors. The behavior of the combination of the electromagnets and amplifiers, which together constitute the *actuators* is described in Chap. 4. The controller, presumed to be digital in nearly all modern active magnetic bearing systems, is

G. Schweitzer, E.H. Maslen (eds.), *Magnetic Bearings*,
DOI 10.1007/978-3-642-00497-1_3, © Springer-Verlag Berlin Heidelberg 2009

described in Chap. 9. Modeling of the rotor as a flexible rotating component is detailed in Chap. 10.

3.1 Bearing Electromagnets

Magnetic bearings exert forces on the rotor without direct physical contact by using electromagnets. The electromagnets attract the ferromagnetic rotor, generating forces. The strength of these forces can then be regulated by controlling the currents in the electromagnet coils.

3.1.1 Magnetism

A brief introduction or review of magnetism will establish the basic ideas and nomenclature exploited in the remainder of this discussion of electromagnets.

Effects of the Magnetic Field

The magnetic field in a space is specified by mechanical forces and electrical induction. Both effects can be used to define a measure of the intensity of the magnetic field. In a stationary magnetic field the *Lorentz force* acts perpendicular to the velocity of a charge Q. The magnetic field vector $\underline{\mathbf{B}}$ (magnetic induction or flux density) is perpendicular to the force $\underline{\mathbf{f}}$ and speed $\underline{\mathbf{v}}$:

$$\underline{\mathbf{f}} = Q(\underline{\mathbf{v}} \times \underline{\mathbf{B}}) \tag{3.1}$$

This vector product means that the force is determined only by the component $\underline{\mathbf{B}}_w$ of $\underline{\mathbf{B}}$ which is perpendicular to the velocity $\underline{\mathbf{v}}$ (Fig. 3.2). Equation (3.1) leads to the measuring unit of magnetic flux density $\underline{\mathbf{B}}$:

$$\mathrm{N} = \mathrm{Coul}\frac{\mathrm{m}}{\mathrm{sec}} \times (\mathrm{B\ units}) = \mathrm{A\ sec}\frac{\mathrm{m}}{\mathrm{sec}} \times (\mathrm{B\ units})$$

$$\Rightarrow (\mathrm{B\ units}) = \frac{\mathrm{N}}{\mathrm{A\ m}} \equiv \mathrm{Tesla}$$

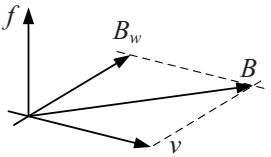


Fig. 3.2. Lorentz force

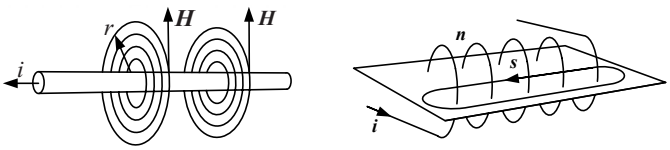
One Tesla (SI unit) may be defined as the flux density of a magnetic field where a force of 1 N acts on a conductor with a current of 1 A and a length

of 1 m. The conductor is perpendicular to the flux. The magnetic flux can be visualized by magnetic field lines. The density of these lines represents the flux density modulus, and the direction of the lines indicates the direction of the field vector of the flux density. Each field line is always closed. The total magnetic flux Φ passing through a surface A is the integral of flux density $\underline{\mathbf{B}}$ over the surface:

$$\Phi = \iint_A \underline{\mathbf{B}} \cdot d\underline{\mathbf{A}} \tag{3.2}$$

A Magnetic Field Generated by an Electric Current

Magnetic fields can be generated by moving charges (current), alternating electric fields, and permanent magnets (molecular circular currents and electron spin). A rotation-symmetrical magnetic field is generated around a straight conductor with a constant current $\underline{\mathbf{i}}$. The magnetic field $\underline{\mathbf{H}}$ is inversely proportional to the distance r from the conductor, and its direction is tangential to concentric circles around the conductor (Fig. 3.3).



(a) Conductor with magnetic field (b) Air coil

Fig. 3.3. Magnetic fields around conductors

Here, the magnetic field intensity is determined by the current density independently of the medium. A contour integral has either a fixed value or else it vanishes, depending on whether the path leads around the conductor or not.

$$\oint \underline{\mathbf{H}} \cdot d\underline{\mathbf{s}} = i \tag{3.3}$$

The magnitude of the magnetic field vector in the case of Fig. 3.3 is therefore

$$H = |\underline{\mathbf{H}}| = \frac{i}{2\pi r} \tag{3.4}$$

If the integration path encompasses several current loops, as is the case with the air coil in Fig. 3.3b, then the integral of the current *density* $\underline{\mathbf{J}}$ through the surface a enclosed by the integration path yields I_{en}, the enclosed current,

$$\oint \underline{\mathbf{H}} \cdot d\underline{\mathbf{s}} = \iint_A \underline{\mathbf{J}} \cdot d\underline{\mathbf{a}} = ni \equiv I_{en} \tag{3.5}$$

The formulation (3.5) is called the Ampère's circuital law [11]. The magnetic field **H** and the magnetic induction (flux density) **B** are linked by the *constitutive law*

$$B = \mu_0 \mu_r H \tag{3.6}$$

Here, $\mu_0 = 4\pi \times 10^{-7}$ Vs/Am stands for the *magnetic permeability* of a vacuum. The *relative permeability* μ_r depends on the medium upon which the magnetic field acts. For a vacuum, μ_r equals 1 and is also approximately unity in air. The SI unit of the magnetic field **H** is A/m.

Electromagnetic Inductance

Electromagnetic inductance is in fact the inversion of the dynamic effect of magnetic fields, as referred to at the beginning of this chapter. When a conductor is moved in a magnetic field, all of its charged particles are moved, too. According to equation (3.1), a Lorentz force acts on these particles, and they move perpendicularly to the field and the direction of the conductor. The motion of the charged particles in the conductor corresponds to the electric current.

A current is always caused by an electric field. The electric field generating the induction current is produced by a change in the magnetic flux which passes through the surface surrounded by a conductor as in Fig. 3.4. The

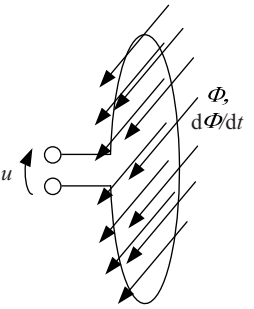


Fig. 3.4. Time variation of flux induces a voltage around a conductor loop, $n = 1$

resulting potential difference is called an induction voltage. This flux change may be due to either a movement of the conductor or a change in the magnetic field. The voltage u induced in a coil with n windings equals the product of the winding number and the derivative of the flux with respect to time t (induction law):

$$u = n\frac{d\Phi}{dt} \tag{3.7}$$

3.1.2 Properties of Ferromagnetic Material

When a magnetic field with a density $\underline{\mathbf{H}}$ acts on a material, the magnetic flux density $\underline{\mathbf{B}}$ generated will be either higher or lower than the flux density $\mu_0\underline{\mathbf{H}}$ generated in the vacuum, depending on material properties. The part of $\underline{\mathbf{B}}$ originating from the material itself is called magnetic polarization $\underline{\mathbf{M}}$:

$$\underline{\mathbf{B}} = \mu_0\underline{\mathbf{H}} + \underline{\mathbf{M}} \tag{3.8}$$

Comparing (3.8) with $\underline{\mathbf{B}} = \mu_0\mu_r\underline{\mathbf{H}}$ yields

$$\underline{\mathbf{M}} = (\mu_r - 1)\mu_0\underline{\mathbf{H}} = \chi_m\mu_0\underline{\mathbf{H}} \tag{3.9}$$

in which $\chi_m = \mu_r - 1$ is called the *magnetic susceptibility*. This describes the relationship between the magnetic polarization and the flux density of the vacuum.

Materials with $\chi_m < 0 \;\; (\mu_r < 1)$ are called *diamagnetic*. They reduce flux density. Materials where $\chi_m > 0 \;\; (\mu_r > 1)$ are called *paramagnetic*. In some paramagnetic materials, coupling of the resulting atomic magnetic moments can occur. When they are parallel, the material is called ferromagnetic. In this kind of material μ_r is generally $\gg 1$ and depends both on the size of the magnetic field and the magnetic "history" of the material.

In general, the parallel arrangement of the atomic magnetic dipoles applies only to a limited space, referred to as *Weiss' domains*. The transition zones between these domains, where the atomic moments change from one privileged direction to another, are called *Bloch walls*.

The behavior of magnetic material is usually visualized in a B-H diagram (Fig. 3.5). Thus, when an unmagnetized ferromagnetic sample is placed within a homogeneous magnetic field with a value H (scalar) of increasing intensity, the magnitude of flux density B increases rapidly along the new curve in the first quadrant, due to Bloch wall shifts. Meanwhile, the domains having their privileged direction parallel to the field direction expand - at the expense of the others.

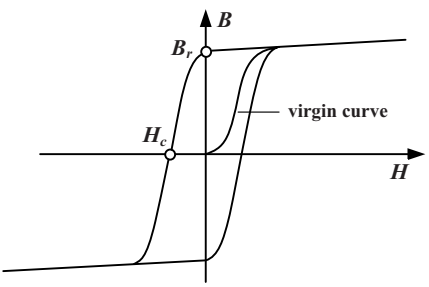


Fig. 3.5. B-H diagram, hysteresis loop

If H keeps increasing, flux density increases, but slowly. Now, the so-called turning processes take place, where the dipoles of the Weiss' domains that are left after the wall shifts change from their privileged direction in the field direction. Once all magnetic dipoles are parallel to the outer magnetic field, saturation is achieved, and B only increases with slope μ_0.

When the outer field is reduced to $H = 0$ flux density does not run reversibly along the original curve, but irreversibly along a *hysteresis loop*. Before reaching value $H = 0$, only part of the turning processes are reversed. The remaining flux density is referred to as remanence B_r. If H is increased in the opposite direction, further turning processes will take place first. Then, remagnetization through wall shifts occurs, and B drops. The field intensity necessary to attain $B = 0$ is called coercive field intensity H_c. With increasing intensity of the counter field the sample is magnetized until saturation in the opposite direction is achieved. By resetting the field to zero and by increasing it subsequently in the original direction, saturation is achieved again, and the hysteresis loop has thus been run through once [7].

3.1.3 Magnetic Circuit

In the magnetic bearing technology, electromagnets or permanent magnets cause the flux to circulate in a magnetic loop. When analyzing such magnetic loops, an exact theoretical computation of the field is rarely possible and seldom required. One usually works with analytic methods of approximation, based on the simplifying assumption that the flux, except for in the air gap, runs entirely through the iron (no leakage flux). Since the permeability $\mu = \mu_0\mu_r$ of iron is considerably larger than that of air, the magnetic field lines leave the iron almost perpendicularly to its surface. Both for constant and alternating fields the computational methods used for static fields are applied, which is admissible as long as the alternating fields have a very large wavelength, compared with the geometry of the field. Since software for field computation in PCs is available, the numerical approach, as opposed to the analytic one, is usually more rewarding for all but the very simplest geometries.

For the computation of flux density B, the following simplifying assumptions are made: Flux Φ runs entirely within the magnetic loop with iron cross section A_{fe} which is assumed to be constant along the entire loop and equal to cross-section A_a in the air gap. From

$$\Phi = B_{fe}A_{fe} = B_aA_a \tag{3.10}$$

and

$$A_{fe} = A_a \tag{3.11}$$

follows

$$B_{fe} = B_a = B \tag{3.12}$$

The field within the magnetic loop is assumed to be homogeneous both in the iron and in the air gap. Therefore, we base our calculation on a mean length ℓ_{fe} of the magnetic path and an air gap length of $2s$.

Flux Density Assuming Constant Permeability in the Iron

For the magnetic circuit in Fig. 3.6 follows from (3.5)

$$\oint \underline{\mathbf{H}} \cdot d\underline{\mathbf{s}} = \ell_{fe} H_{fe} + 2sH_a = ni \tag{3.13}$$

The term ni in (3.5) and (3.13) is often called the magnetomotive force (mmf)

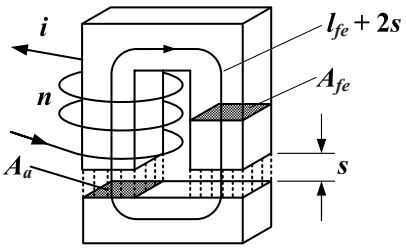


Fig. 3.6. Magnetic circuit

that "forces" flux through a magnetic circuit [11]. In the ensuing discussion, we will use NI with capital letters as a symbol for the magnetomotive force.

Since according to (3.12), the flux density B in the iron and in the air gap is identical, field intensities H_{fe} and H_a from (3.13) can be replaced by (3.6):

$$\ell_{fe} \frac{B}{\mu_0 \mu_r} + 2s \frac{B}{\mu_0} = ni = NI \tag{3.14}$$

Solving (3.14) for B yields

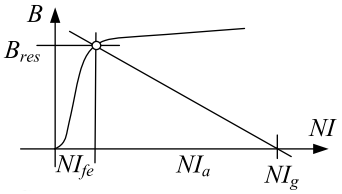
$$B = \mu_0 \frac{NI}{\left(\frac{\ell_{fe}}{\mu_r} + 2s\right)} \tag{3.15}$$

In the iron, $\mu_r >> 1$, so the magnetization of the iron is often neglected. In this case, (3.15) may be simplified:

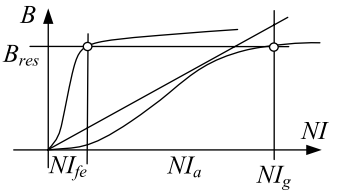
$$B = \mu_0 \frac{NI}{2s} \tag{3.16}$$

Determining the Flux Density with the B-H Diagram of the Iron

Equation (3.15) is a good approximation as long as the iron is kept far below the saturation flux density, since relative permeability has but little effect on the steep rise of the magnetization curve. However, if the iron is kept close to saturation with high flux densities, we must consider the characteristics of the magnetization curve, and the flux density B can no longer be calculated directly from the enclosed current I_{en}.



(a) Graphical determination of flux density B for a given mmf NIg



(b) Magnetization curve for the magnetic circuit with airgap

Fig. 3.7. Graphical determination of magnetization.

In the simple case of a magnetic circuit with a constant cross section, the flux can be determined graphically using the magnetization curve. To do this, the first step is to scale the H axis of the B-H diagram using the relation $H_{fe}l_{fe} = NI$ so that the graph shows the flux density as a function of the magnetomotive force NI. In the next step, intersect the magnetization curve of the iron with the air gap curve (straight line with slope $-\mu_0/2s$) drawn from the given mmf NI_g to the left (Fig. 3.7). The intersection point shows the resulting flux density B_{res}. Figure 3.7a shows two portions of the given mmf, a portion NI_{fe} needed to "force" flux in the iron and a portion NI_a needed to "force" flux in the airgap. With flux density B_{res} a magnetization curve for the magnetic circuit with airgap can be drawn (Fig. 3.7b).

Inductance L in the Magnetic Circuit

Inductance L is the ratio of the so-called winding flux Φ_w generated by one single turn in the coil to the generating current i. For a coil with N turns the inductance seen at the coil terminal ends is

$$L = \frac{N\Phi}{i} \tag{3.17}$$

in which Φ is the *total* flux generated by the N turns.

If the iron is neglected, the flux density B from (3.16) and the cross section of the air gap A_a can be inserted in (3.17), and the inductance L of a magnetic circuit can thus be calculated approximately:

$$L = \frac{\mu_0 N^2 A_a}{2s} \tag{3.18}$$

This approximation of L generally overestimates the actual value because it neglects iron reluctance, flux leakage, and the geometric size of the coil. Since the relationships between B and H, and between Φ and i, are non-linear, L will also depend on the operating point of the B-H diagram. Therefore, we can also define a differential inductance $L_d = n\ d\Phi/di$ which corresponds to the gradient in a "Φ-i diagram".

The inductance of a bearing magnet is also of importance to the design of the power amplifier. According to the law of inductance, the induced voltage u in a coil with N turns equals

$$u = N\frac{d\Phi}{dt} = L_d\frac{di}{dt} \tag{3.19}$$

If the copper resistance of the coil and the reaction of the moving rotor on the bearing magnet are neglected, then the output voltage of the power amplifier generates a current slope in the coil according to (3.19). Obviously, the smaller the inductance L_d is, the faster the current rises.

3.1.4 Magnetic Force

Magnetic Forces, Neglecting the Iron

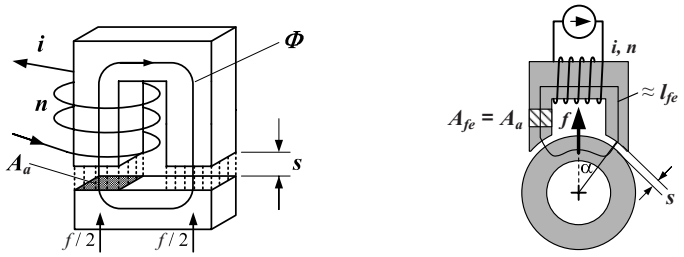
In contrast to the forces acting on conductors in a magnetic field (Lorentz force), the attraction force of magnets is generated at the boundaries between differing permeability μ (also refer to the list in Fig. 1.11). The calculation of these forces is based on the field energy.

We consider the energy W_a stored in the volume of the air gap, $V_a = 2sA_a$. In the case of the homogeneous field in the air gap of the magnetic loop, as represented in Fig. 3.8a, the stored energy W_a obeys

$$W_a = \frac{1}{2}B_a H_a V_a = \frac{1}{2}B_a H_a A_a (2s) \tag{3.20}$$

The force acting on the ferromagnetic body ($\mu_r \gg 1$) is generated by a change of the field energy in the air gap, as a function of the body displacement. For small displacements ds the magnetic flux $B_a A_a$ remains constant.

When the air gap s increases by ds, the volume $V_a = 2sA_a$ increases, and the energy W_a in the field increases by dW_a. This energy has to be provided mechanically, i.e. an attractive force has to be overcome. Thus, force f equals



(a) Force (b) Geometry

Fig. 3.8. Force and geometry of a radial magnet

the partial derivative of the field energy W_a with respect to the air gap s (principle of virtual displacement):

$$f = -\frac{\partial W_a}{\partial s} = B_a H_a A_a = \frac{B_a^2 A_a}{\mu_0} \tag{3.21}$$

In the case of a closed system, the force f can be derived from the principle of virtual displacement. For electromagnets (Fig. 3.8), electric energy is introduced into the system through the coil terminals to set up the magnetic field. In order for (3.21) to remain valid, the differentiation has to be carried out as if there is no electric energy exchange between the coil and its power supply, i.e. when flux density B remains constant. To derive force f as a function of coil current and the air gap, $B(i, s)$ is inserted into (3.21) after differentiating. In the simplest of cases where the iron is neglected, B_l is replaced by (3.16). The resulting force f will be

$$f = \mu_0 A_a \left(\frac{ni}{2s}\right)^2 = \frac{1}{4}\mu_0 n^2 A_a \frac{i^2}{s^2} = k\frac{i^2}{s^2} \tag{3.22}$$

in which the area A_a is assumed to be the *projected* area of the pole face, rather than the curved surface area.

Equation (3.22) shows the quadratic dependence of the force on the current and the inversely quadratic dependence on the airgap, as illustrated in Figures 2.2 and 2.3. In the case of a real radial bearing magnet, the forces of both magnetic poles affect the rotor with an angle α (Fig. 3.8b), as opposed to the model of the U-shaped magnet shown in Fig. 3.8a. In the case of a radial bearing with four pole pairs (Fig. 3.12a) α equals, for instance, 22.5°. Considering α produces

$$f = \frac{1}{4}\mu_0 n^2 A_a \frac{i^2}{s^2}\cos\alpha = k\frac{i^2}{s^2}\cos\alpha \tag{3.23}$$

Magnetic Forces, Assuming Constant Permeability in the Iron

To include the effect of iron with a constant, finite permeability μ_r, equation (3.15) will replace B_a in equation (3.21). The force resulting in this case, again considering α, will be

$$f = \mu_0 \left(\frac{ni}{\ell_{fe}/\mu_r + 2s} \right)^2 A_a \cos\alpha \tag{3.24}$$

Determining the Force from the B-H Diagram of the Iron

Section 3.1.3 described a graphical procedure to determine B with the B-H diagram. The flux density thus obtained can be used in (3.21), and the force can be calculated accordingly. Also, the procedure may easily be written in a computer program (refer to Section 3.1.5).

Force-Current Relation of Bearing Magnets

With magnets, the relationship between force and current in equation (3.22) is quadratic, i.e. non-linear. In control theory, linear relations are preferred for computation. Non-linear functions are often approximated by linearizing at the operating point. The operating point is generally the expected equilibrium condition of the system. For an AMB, the operating point is defined by the set of currents required to support the static load, including the effect of the bias currents. In some cases, the effect of the static load is neglected (because it is often small) and the operating point is defined solely by the bias currents. See, in particular, Sec. 2.1.3.

Force-Current Factor k_i and Force-Displacement Factor k_s

The force of a magnet at an operating point can be written in the linearized form

$$f_x(x, i) = k_i i_x - k_s x$$

Here, force f_x is given by a tangent (slope k_i) to a parabola at the operating point. This operating point is given by the bias current i_0 and the nominal air gap s_0 (Fig. 3.9 a). Furthermore, k_s is the slope of the curve $1/s^2$ at the operating point (Fig. 3.9 b).

Linearization of the Force-Current Relation

Usually, two counteracting magnets are operated in a bearing magnet (see the geometry in Fig. 3.10). This configuration makes it possible to generate both positive and negative forces. In the case of the so-called differential driving mode, one magnet is driven with the sum of bias current i_0 and control current

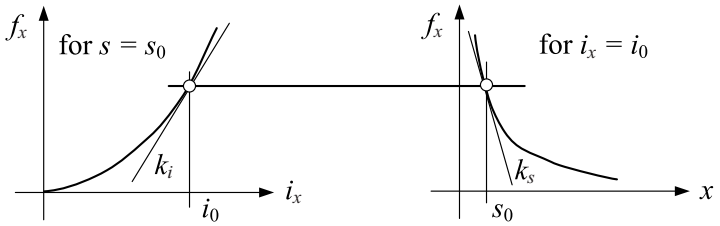


Fig. 3.9. Left: Force-current factor k_i right: Force-displacement factor k_s

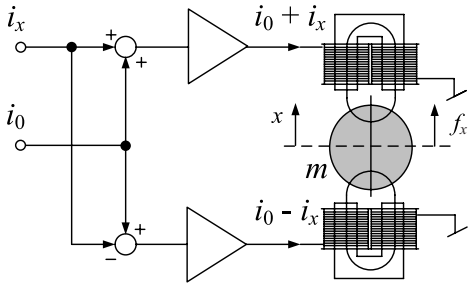


Fig. 3.10. Differential driving mode of the bearing magnets

i_x, and the other one with the difference $(i_0 - i_x)$. Consequently, if the magnetization of the iron is neglected, this scheme produces a linear force-current relation [18] as discussed below.

Force f_x in Fig. 3.10 represents the difference of forces between both magnets. Both forces are obtained by inserting the sum $(i_0 + i_x)$ and the difference $(i_0 - i_x)$ for current i in (3.23). For the air gaps, $(s_0 + x)$ and $(s_0 - x)$ are inserted:

$$f_x = f_+ - f_- = k \left(\frac{(i_0 + i_x)^2}{(s_0 - x)^2} - \frac{(i_0 - i_x)^2}{(s_0 + x)^2} \right) \cos\alpha \tag{3.25}$$

with

$$k = \frac{1}{4} \mu_0 n^2 A_a \tag{3.26}$$

If we simplify (3.25) and linearize it with respect to $x \ll s_0$, we obtain the relation

$$f_x = \frac{4ki_0}{s_0^2} (\cos\alpha) i_x + \frac{4ki_0^2}{s_0^3} (\cos\alpha) x = k_i i_x - k_s x \tag{3.27}$$

in which

$$k_i \equiv \frac{4ki_0}{s_0^2} (\cos\alpha) \tag{3.28}$$

and

$$k_s \equiv -\frac{4ki_0^2}{s_0^3} (\cos\alpha) \tag{3.29}$$

Figure 3.11 shows the measured force-current characteristics of a bearing magnet linearized with differential driving mode. The deviation of the measured curve from the calculated linear relation occurs at high driving levels of the control current, and is due to the saturation of the iron.

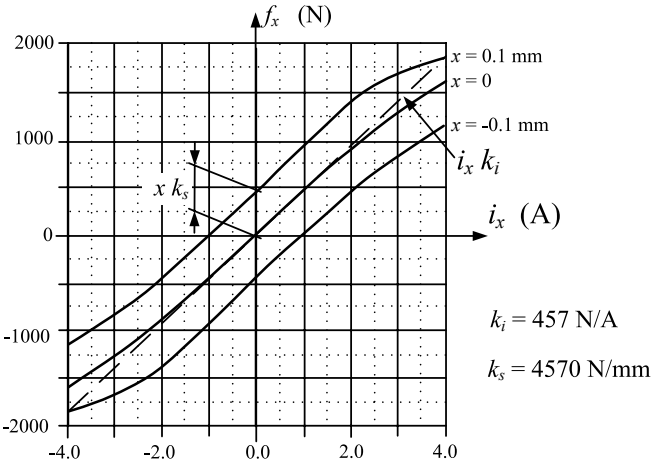


Fig. 3.11. Measured force-current characteristic of a radial bearing with $d = 90$ mm, $b = 70$ mm, $s_0 = 0.4$ mm

3.1.5 Design of Bearing Magnets

Load Capacity, Magnetic Flux

The load capacity of a magnetic bearing is the force obtained with the maximum admissible magnetomotive force $NI_{\max}$.

The achievable magnetomotive force $NI_{\max}$, i.e. the product of the maximum current $i_{\max}$ and winding number n, depends on the available winding cross section, the mean winding length, and the achievable heat dissipation. The maximum heat dissipation depends on the kind and amount of cooling. For an effective computation of the load capacity it is therefore essential to first calculate the relevant cooling capability. In the bearing magnet both the iron of the magnetic loop and the copper of the winding require space.

In order to optimize the bearing geometry, we distribute the space available in the bearing magnet optimally between iron and copper for maximum load capacity. Optimization can already be achieved with a simple model of the magnetic loop, as shown in Section 3.3. However, this model can still be refined by considering, for instance, the stray flux effect, as long as it can be easily modeled, or by admitting different cross sections in the iron and the air gap,

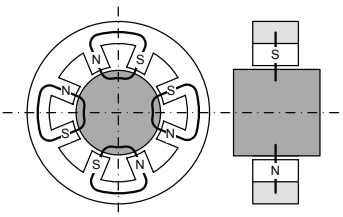
as they occur with magnets with pole shoes. Finally, the load capacity of the optimized bearing geometry can be checked by finite element modeling.

Whether the magnetic flux is generated with high current and a low number of windings or else with low current and a great number of windings is irrelevant for the optimization of the bearing geometry. Variations in the coil design allow matching the magnetic bearing with the power amplifier.

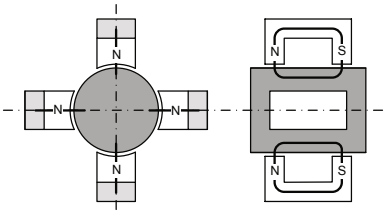
Structural Configurations of Radial Electromagnets

Basically, there are two primary structural configurations for radial electromagnets and the distinction is made on the basis of the magnetic polarities seen by the rotor as it rotates. If all of the magnetic flux is confined to a plane perpendicular to the axis of rotor rotation, as shown in Fig. 3.12a, then the magnetic poles will alternate in polarity around the rotor. Alternatively, if at least some portion of the magnetic flux can pass axially along the rotor and/or stator, as shown in Fig. 3.12b, then it is possible for all of the poles in a given plane to have the same polarity: alternation of polarity occurs instead in the axial direction. No matter what the configuration is, the total magnetic flux passing through the rotor surface must be zero so there must always be polarity alternation in some direction.

Bearings with the polarity configuration shown in Fig. 3.12a are called *heteropolar* and can be manufactured in a manner similar to that for electric motors. In order to keep the eddy current loss as low as possible, the rotor must be laminated, i.e.: the magnetically active part of the rotor must be built from a stack of disk shaped layers of ferromagnetic sheets which are electrically insulated one from the next.



(a) *Heteropolar*: polarities of the stator poles in a given rotational plane vary. Here, the sequence is N-S-S-N-N-S-S-N.



(b) *Homopolar*: in any given rotational plane stator poles have the same polarities (N in the left plane and S in the right plane)

Fig. 3.12. Structural configurations of radial bearings. See Figs. 3.18 and 3.22 for more realistic depictions of the physical layouts.

With an arrangement similar to that of Fig. 3.12 b, all of the poles in a given rotational plane can have the same magnetic polarity and such a magnet

structure is called *homopolar*. The result is much less field variation around the circumference of the rotor so that the eddy current loss due to rotor rotation is substantially reduced. Homopolar configurations are most commonly used in conjunction with permanent magnets (PM), as discussed in Sec. 3.2.

A clear comparison of the relative merits of heteropolar *versus* homopolar structures is difficult and usually very dependent on the particular target application. However, it may be useful to outline some of the key differences between the two bearing types and their implications to system performance:

1. The most common implementation of a heteropolar magnet structure, which uses only one stator lamination stack, is usually the simplest, lowest-cost solution. Homopolar structures are generally more complicated and more expensive.
2. Homopolar magnet structures produce much lower rotational losses since the rotor experiences less field variation when spinning, and consequently has lower induced eddy currents (see Chap. 5). This is particularly important in vacuum applications because any heat generated on the rotor must be removed by radiation transfer to the housing (rather than by convection as in non-vacuum AMB systems or conduction as in rolling element bearing systems): there is a high premium on rotor losses.
3. Using permanent magnets to produce bias flux (Sec. 3.2) in homopolar magnet structures offers both advantages and disadvantages [3]. These include:
   a) Modern rare-earth permanent magnet materials such as NdFeB or SmCo make the actuator stack more compact because they permit a smaller coil, working in conjunction with the PM, to produce the same total field. This mitigates part of the axial length advantage of heteropolar bearings and also reduces total coil heat losses significantly.
   b) PM-biased radial magnetic bearings have a lower force-displacement factor, k_s, than do current-biased bearings and variation in k_s with changes in rotor position is also smaller.
   c) PMs make the bearing more complicated and expensive. This cost increase is partially offset by the lower power consumption and the fact that fewer actuator wires and fewer feed-thru connectors are needed.
   d) The magnetic field and associated forces from the PM are always present, making the assembly of the machines more difficult and requiring more assembly tooling.

These considerations will all play significant roles in selecting which magnet structure to use in a given application. In some applications, the choice between homopolar and heterpolar approaches will be clear; in many others, it may be necessary to examine both types of design in detail to establish their actual relative merits.

In the ensuing material, except for Sec. 3.2, we focus on the characteristics of heteropolar bearings. However, most of the discussion can readily be adapted to homopolar bearings.

The advantage of eight-pole radial bearings, as illustrated in Fig. 3.12a, is the fact that two pole pairs each can be assigned to the Cartesian coordinates x and y which are often used in mechanics. Simulation of the mechanical system, control design, and measurement of the rotor motion are usually based on these coordinates, simplifying bearing control.

In order to be able to generate forces independently in two orthogonal radial directions, a minimum of three poles is sufficient. However, the coil drive operation becomes more difficult because the magnet configuration is inherently highly coupled and conventional linearization is no longer possible [15]. Other pole configurations can generally be linearized in a manner similar to that presented in (3.25), although the math is more complex [12]. In the case of large bearings, it is typically best to increase the number of poles above eight in order to keep the outer diameter low with respect to the inner diameter; small bearings often favor stator designs with fewer than eight poles.

Since the saturation effect of the iron ought to be especially considered when optimizing the geometry of magnetic bearings, the magnetic force can only be determined using the B-H diagram (Fig. 3.7). This diagram can easily be implemented in software. For a given air gap, a function table of $B_{fe}(H)$ of the iron is used to calculate a new table $\Phi(NI)$ of the magnetization curve of the magnetic circuit with airgap as follows:

$$\Phi = B_{fe} A_{fe} \tag{3.30}$$

$$NI(B_{fe}, H) = H\ell_{fe} + \frac{B_{fe} A_{fe}}{\mu_0 A_a} 2s \tag{3.31}$$

In this manner, the flux Φ for a given magnetic magnetomotive force NI can be interpolated from the tabulated virgin magnetization curve.

When the magnet, as usual, is composed from single insulated sheets in order to avoid eddy currents, the iron cross section A_{fe} has to be multiplied with a bulk factor K_{st}. Doing this, one respects the fact that the insulating layers are not magnetically conducting. The bulk factor K_{st} usually lies between 0.94 and 0.97.

Cooling Capacity

Assumptions: Heat loss in the bearing magnet is composed of two parts: copper and iron losses. Considerable iron loss mainly results when using switching amplifiers. But even in this case iron loss is negligible, compared with copper loss - provided that adequate material was chosen for the iron, and proper sheeting was done.

The current load in the winding of a bearing magnet can vary during operation, depending on size and direction of the force generated. Provided that a heat exchange takes place in the bearing, only the overall heat dissipation in the bearing will be examined in the following.

In the first step, the power dissipation is calculated from the admissible temperatures in the bearing magnet and from the cooling capacity provided by the geometrical dimensions. Then, the admissible magnetomotive force $NI_{\max}$ can be calculated with the admissible power dissipation, which is equal to the cooling capacity, and other geometric values.

When there is no load on a bearing magnet, the bias current runs through all of its windings. In the following, the maximum bearing temperature is estimated for the worst case, i.e.: when there is maximum-level driving in both the $x-$ and $y-$ directions. In designing a bearing magnet for a specific application, the thermal design should accomodate the standard (expected average) load plus a small amount of reserve to handle brief peak loads. With differential control (see Fig. 3.10), the current will be zero in one magnet and maximum in the opposite magnet. The copper losses will be twice as high as when there is a load on all windings with a premagnetization $NI_{\max}/2$.

According to Fig. 3.12a, axis x of a bearing has four windings, each with a winding number $n/2$. Each winding has a copper resistance $R_{cu}/2$. So, with maximum current, copper dissipation P_x for axis x will be

$$P_x = R_{cu} i_{\max}^2 \tag{3.32}$$

Thermal network: There is a formal equivalence between thermal flow and electric current. Therefore, thermal flow can be split up into different one-dimensional thermal flows, analogous to an electric resistor network. Analogous to Ohm's law in electrical engineering, we obtain, for a homogeneous thermal conductor with a length l, cross section A and a temperature difference $\Delta\vartheta$,

$$\Delta\vartheta = R_w P = \frac{1}{\Lambda} P \tag{3.33}$$

with a thermal resistance R_w, the copper dissipation P and a coefficient of thermal conduction Λ,

$$\Lambda = \frac{A}{l}\lambda \tag{3.34}$$

with a thermal conductivity λ of the heat conducting material (eg. λ of the isolation paper used between coil and iron core: 0.16 W/mK).

To obtain the heat transfer from a surface to a cooling medium like air or water, a coefficient of thermal conduction Λ_s is calculated from body surface O and heat transfer coefficient α , such that

$$\Lambda_s = O\alpha \tag{3.35}$$

(eg.: α from the coil surface to air: 0.15 W/m^{2}K).

Figure 3.13 illustrates an example of a thermal network for a magnetic bearing. The bearing is air cooled with a temperature ϑ_0. Each pair of coils is regarded as a heat source. Each heat source is represented with the mean surface temperature ϑ_{cu}. Due to heat transfer, the thermal flow travels from the coil heads into the cooling medium, and due to heat conduction, through

the insulation between the coil and the iron core. Finally, due to heat transfer, thermal flow travels from the iron core to the air.

The heat resistance of the iron core is much lower than that of the electrical insulation between coil and iron core, and is therefore neglected.

We now want to determine the thermal conductivity coefficients. For insulation with a thickness e_i, we obtain

$$\Lambda_i = \frac{2O_i}{e_i}\lambda_i \tag{3.36}$$

The surface area O_i of the insulation corresponds to the inner surface of the iron core slot. For the transfer from the iron core to the air we obtain

$$\Lambda_{fe} = O_{fe}\alpha \tag{3.37}$$

We consider the areas at the outer circumference of the bearing, as well as the end areas, as the iron surface O_{fe}, as long as they are not covered by the coil heads. In the case of a heat flow via a housing, the contact areas of the bearing ought to be considered separately, and the thermal network must be modified accordingly.

For the coil heads,

$$\Lambda_{cu} = O_{cu}\alpha \tag{3.38}$$

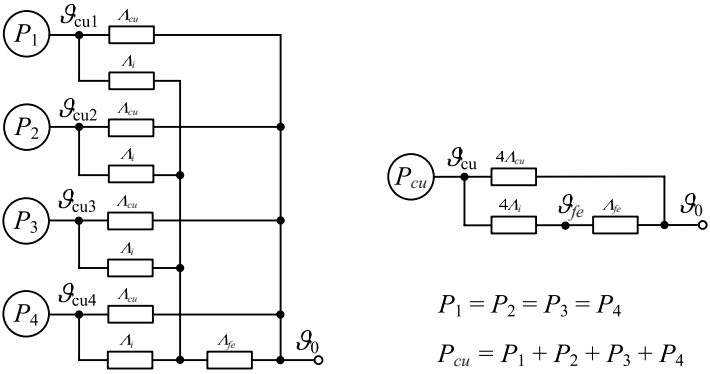
holds. The copper surface O_{cu} of the coil heads can be approximated or estimated with a simplified geometry.

With equal load on all four coils, as is the case where there is no driving, but only bias current, the thermal network can be simplified according to Fig. 3.13b.

When calculating the thermal network, one obtains only the mean surface temperatures of the bodies. The temperature distribution and the maximum temperatures inside the bodies must therefore be determined separately. A calculation of the maximum temperature in the coil is found in [21]. For more complete thermal analysis targeted at identifying hot spots in coils, a finite element thermal analysis may be required [16]. In addition, if the coils are to be cooled using external convection, then a fluid mechanics analysis may be required in order to evaluate the complex flow and effective convection mechanisms [20].

Admissible Magnetomotive Force

The admissible maximum temperature in the coil, depending on the insulation class, is known. Thus, using the difference between the winding temperature and that of the cooling medium, we obtain the maximum admissible power dissipation by using the thermal network method. For the differential driving mode the power dissipation P_x of an axis, with maximum-level driving, is calculated according to (3.32). The power dissipation of copper P_{cu} from both axes for the bearing magnet is twice as high, i.e.:



(a) detailed (b) simplified

Fig. 3.13. Thermal network for a radial bearing magnet

$$P_{cu} = 2P_x = 2R_{cu}i^2_{\max} \tag{3.39}$$

The copper resistance R_{cu} of the winding can be calculated using the wire cross section A_d, the mean length of turns l_m, and the specific resistance ρ as follows

$$R_{cu} = \frac{\rho n l_m}{A_d} \tag{3.40}$$

Considering the bulk factor K_{st}, the slot cross section A_n equals the product of wire cross section A_d and the number of turns n:

$$A_n K_n = A_d n \tag{3.41}$$

If we now solve (3.41) for wire cross section A_d and insert it into (3.40), and if we insert (3.40) in (3.39), we obtain

$$P_{cu} = \frac{2\,\rho\,l_m n^2}{A_n\,K_{st}} i^2_{\max} \tag{3.42}$$

The admissible maximum magnetomotive force

$$NI_{\max} = ni_{\max} \tag{3.43}$$

is now inserted into (3.42) and solved for $NI_{\max}$:

$$NI_{\max} = \sqrt{P_{cu}\frac{A_n K_{st}}{2\,\rho\,l_m}} \tag{3.44}$$

Model Refinements

In Section 3.1.4, the magnetic force was calculated with a model of a simplified magnetic loop. The deviations between the model and real magnet will be listed below once more:

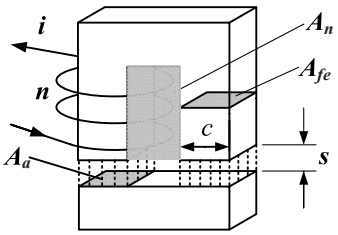


Fig. 3.14. Very simple bearing geometry

- The flux does not merely run within the iron and the air-gap cross section. Unavoidable leakage flux between the pole limbs does not contribute to the generation of force, and consequently reduces it.
- Due to the leakage, the flux in the air gap is not limited to the width of the pole shoes, which increases the size of the air gap cross section and thus also reduces the force.
- The iron cross section A_{fe} is not uniform.

Comparing the results of the model computation with those of a numerical computation, the model can be checked and refined accordingly [21]. In the case of ordinary bearing geometries with small air gaps, as are found in industrial applications, the error in predicted force will remain within a range of 5 to 10%.

Optimizing the Bearing Geometry

When optimizing the bearing geometry, the leg width c (see Fig. 3.18) of the magnet poles can be varied. With a larger leg width, the slot cross section A_n is reduced, as well as the admissible magnetomotive force $NI_{\max}$. Both an increase in leg width (increase of the iron cross section) and a reduction of $NI_{\max}$ reduce the flux density in the iron. The maximum flux density in the iron can therefore be varied with the leg width.

The maximum carrying force $f_{\max}$ may now be evaluated as a function of the air gap s_0 for different leg widths c to obtain a family of curves as shown in Fig. 3.15. Obviously, one of the curves will yield a maximum load capacity for a certain air gap, i.e. the corresponding leg width c will be optimal. The envelope curve from Fig. 3.15 demonstrates the optimum carrying force f_{opt} as a function of the air gap.

Coil Design

The admissible coil temperature: The admissible coil temperature is determined by the choice of the insulation type (i.e. 155°C for NEMA class F insulation). The admissible magnetomotive force follows from the admissible

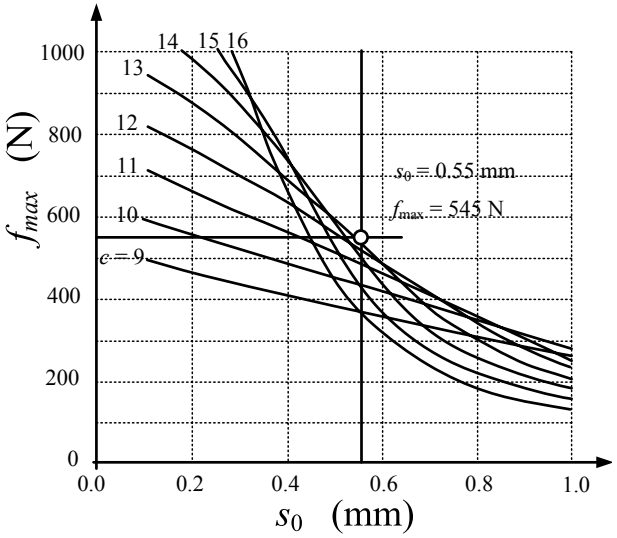


Fig. 3.15. Maximum force $f_{\max}$ as a function of the air gap for different values of leg width c. d=80 mm, d_a=140 mm, b=40 mm, $\Delta\vartheta = 80°\mathrm{K}$

coil temperature. This calculation usually holds for a stable thermal equilibrium, i.e. for control current in both axes. The admissible coil temperature is usually not achieved during standard operation, since a bearing magnet has to be designed in order to continually maintain a reserve for dynamic loads, in addition to the static load.

The bearing magnet can also be designed for medium loads so that its admissible coil temperature can be achieved at normal operation. In this case, however, the coil temperature has to be monitored by thermal sensors, since prolonged maximum control currents may occur in the case of brief excessive dynamic loads.

Selection of the number of turns: By selecting the number of turns appropriately, the bearing magnet can be adapted to the power amplifier. The number of turns n is selected in order to achieve the admissible magnetomotive force $NI_{\max}$ at a maximum output current $i_{\max}$ of the power amplifier. Once n is determined, the wire cross section A_d and subsequently the wire diameter can be calculated using (3.41).

Winding scheme: The winding scheme defines how the coils of the poles are to be wound, and the connection scheme shows how the single coils are connected to each other. Both schemes depend on the type of magnetic bearing and the driving mode chosen. The winding is arranged so as to keep remagnetization of the rotor as low as possible upon rotation. Figure 3.16 shows an example of

both a winding and a connection scheme for a radial bearing with differential driving mode.

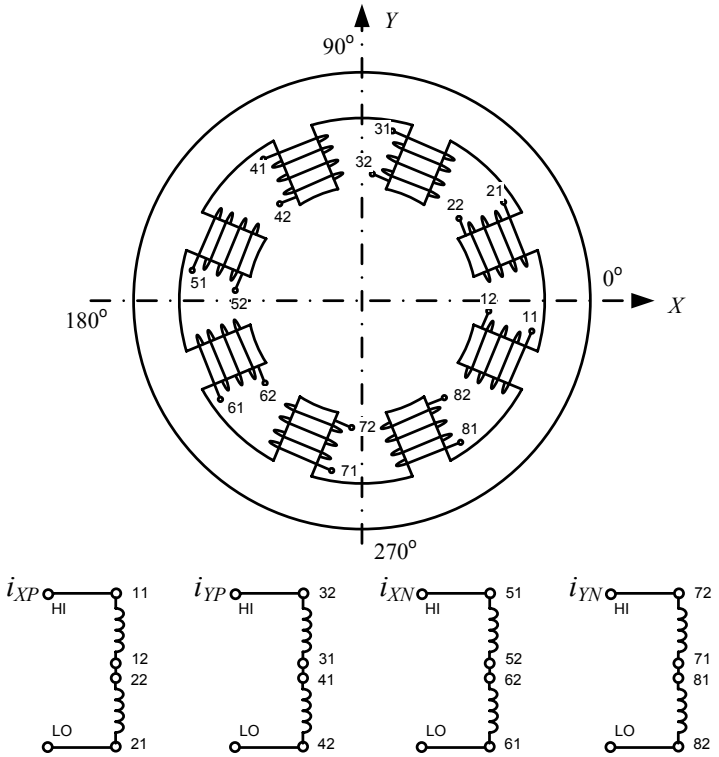


Fig. 3.16. Winding scheme of an eight pole radial bearing for differential driving mode

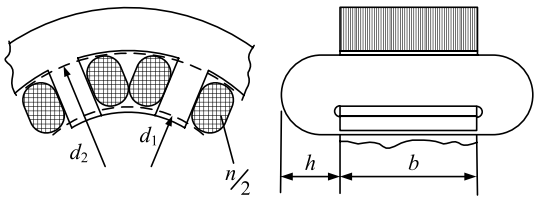


Fig. 3.17. Coil geometry

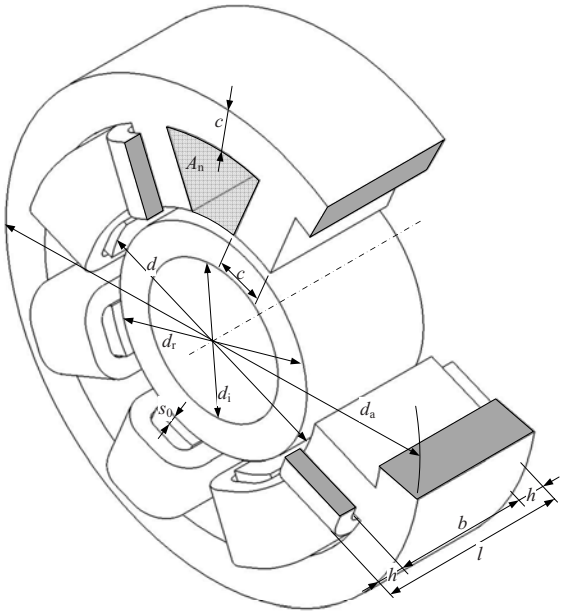
The *height of the coil head* h from Fig. 3.17 can be estimated as

$$h = (d_1 + d_2)\frac{\pi}{16} \tag{3.45}$$

$$n = NI_{\max}/i_{\max} \tag{3.46}$$

This value can be used to calculate the admissible power dissipation, and as a guide value for the space required. The exact space requirement should be determined with a prototype. The height of the coil head h also depends on the facilities of the company producing the winding. If the aim is to keep h as low as possible, man hours and costs will usually rise.

3.1.6 Geometry



d	Inner diameter (bearing diameter)	d_a	Outer diameter
c	Leg width	d_i	Shaft diameter
h	Winding head height	b	Bearing width (magnetically active)
A_n	Slot cross section (winding space)	l	Bearing length
d_r	Rotor diameter	s_0	Nominal air gap

Fig. 3.18. Typical geometry of the radial bearing magnet

Figure 3.18 shows the geometrical parameters of typical radial bearing magnets. The air gap length, s_0 is exaggerated to make it visible. The diagram

illustrates a geometry in which the radial thickness of the back-iron is the same as the width of the legs, c. If the coils are connected so that the pole polarization sequence is N-S-N-S-N-S-N-S, then the back-iron need only be as thick as half the leg width. If the coils are instead connected so that the pole polarization sequence is N-S-S-N-N-S-S-N, then the back-iron must be as thick as the leg width. Ultimately, the geometry should be checked using Finite Element Analysis to establish that the back-iron is thick enough to avoid premature magnetic saturation. The same observations apply to the radial thickness of the journal sleeve: $(d_r - d_i)/2$.

3.1.7 Assessment of the Load Capacity: Radial Bearings

The following derivation approximates the achievable specific load capacity of an evenly spaced, eight pole radial magnetic bearing (Fig. 3.18) for a simple assessment of the maximum achievable load capacity. The static load capacity $f_{\max}$ of a radial magnetic bearing represents the maximum static force acting towards one of the four U-shaped magnets of the bearing. Two perpendicular magnets achieve a maximum force increased by a factor 1.41 over that of one magnet. This can be used in the case of heavy static loads where the mounting of the bearings should be chosen accordingly.

The specific load capacity can be related to the projection of bearing area db. Let us assume that the pole shoe width p equals the leg width c. On the bearing diameter d we have one eighth of the circumference per pole at our disposal. Using 50% of that for the pole shoe width p, the pole shoe surface is given by

$$A_a = \frac{d\pi}{8} 0.50 b \tag{3.47}$$

With current Si-alloyed transformer sheets, which are used for bearing magnets, a maximum flux density $B_{\max}$ of 1.6 Tesla is recommended. Inserting this value for B_a in equation (3.21), and considering that the forces of both poles do not act perpendicularly, but at an angle of $\pi/8$, we obtain with A_a from (3.47) and (3.21) the specific load capacity

$$\frac{f_{\max}}{db} = \frac{B_{\max}^2 \pi}{\mu_0 8} 0.50 \cos\frac{\pi}{8} = \frac{1.6^2 \pi}{\mu_0 8} 0.50 \cos 22.5^\circ = 0.37 \text{ MPa} \tag{3.48}$$

This relationship is illustrated in Fig. 3.19.

Using (expensive) cobalt-alloys with a saturation flux density as high as 2.4 Tesla, the magnets can be designed for a flux density on the order of 1.9 Tesla from which a specific load capacity of up to 0.65 MPa can be produced. However, it is important to note that these assessments do not provide any information about the required flux or the space required for the coil windings and therefore do not indicate anything about the outer diameter. Often, the entire space requirement of the bearing has to be optimized when designing

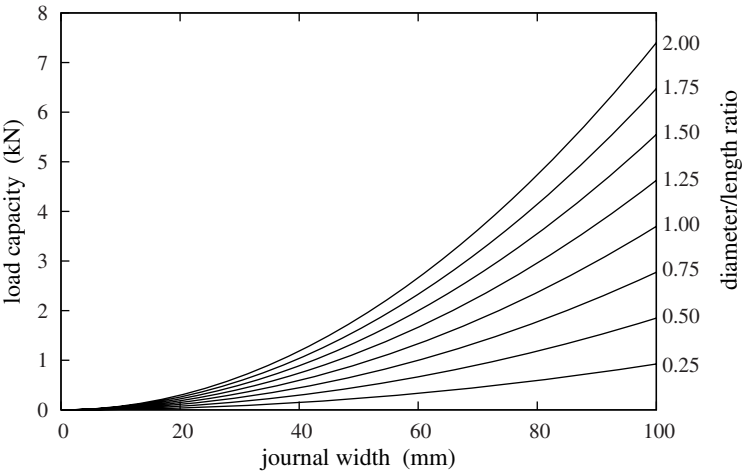


Fig. 3.19. Load capacity of radial bearings having width b and diameter d at a specific load capacity of 0.37 MPa. Pole faces cover 50% of the journal.

the bearing magnets, and in many cases the above-mentioned values cannot be achieved because of limited space, insufficient cooling, or extremely wide air gaps.

3.1.8 Design of Thrust Magnetic Bearings

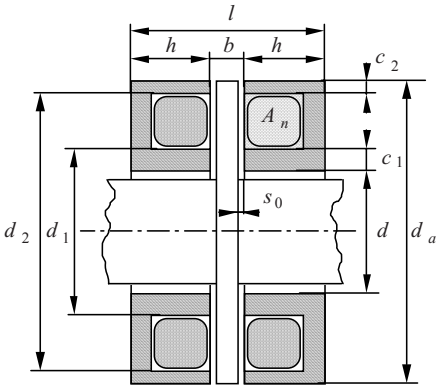
Figure 3.20 illustrates the geometry of a typical thrust magnetic bearing. An important design consideration for thrust bearing magnets is to balance the radial thicknesses of the inner and outer legs so that they both saturate at approximately the same coil current.

First, define the pole area for the inner pole:

$$A_p = \frac{\pi(d_1^2 - d^2)}{4} \tag{3.49}$$

Neglecting flux leakage and other non-idealities, the balanced pole area condition is achieved when

$$\frac{\pi(d_a^2 - d_2^2)}{4} = A_p \tag{3.50}$$



d	Inner diameter (or bearing diameter)	d_a	Outer diameter
c_1	Inner leg width	d_1	Inner winding space diameter
d_2	Outer winding space diameter	A_n	Slot cross section (winding space)
h	Pot magnet height		
s_0	Nominal air gap	c_2	Outer leg width
l	Bearing length	h_n	Slot depth

Fig. 3.20. Geometry of a typical thrust bearing magnet

Further, the radial component of the stator needs to have a minimum area matching that of the pole faces:

$$\frac{\pi d_1(l-b-2h_n)}{2} = A_p \tag{3.51}$$

as does the thrust disk:

$$\frac{\pi d_1(b-2s_0)}{2} = \frac{\pi(d_1^2-d^2)}{4} \tag{3.52}$$

If these design constraints are met, then the load capacity of the thrust bearing magnet depends on the pole area and the magnetic saturation density of the stator or the thrust disk. In general, strength limitations dictate that the thrust disk is composed of a higher strength material than is the stator: a general trend in magnetic materials is that increasing yield strength corresponds to decreasing saturation flux density. Often, good design of thrust bearings exploits a compromise between these two limitations in which the thrust disk is substantially saturated at maximum load capacity while the thrust stator is much less saturated in order to avoid excessive coil currents.

In any case, once the useful saturation density, B_{sat}, is selected, the load capacity of the thrust bearing magnet is readily approximated as

$$f_{\max} = \frac{B_{\text{sat}}^2 A_p}{\mu_0} \tag{3.53}$$

3.2 Permanent Magnet Biased Magnetic Bearings

As discussed in Sects. 2.1.3 and 3.1.3, it is most common to operate the magnets of an active magnetic bearing at a *bias* point. While this biasing tends to linearize the actuator, the bias field itself *does no work*. Consequently, it is possible to provide the bias field using a permanent magnet rather than an electromagnet. Bearings which use permanent magnets to generate the bias field and electromagnets to redistribute this field to produce net forces are called *permanent magnet biased* bearings [22, 13, 17]. The primary advantage of such a scheme is that the electrical power losses associated with generating the bias field are eliminated, so there is less heat to remove from the bearing and it consumes less electrical power.

The magnetic circuit depicted in Fig. 3.21 illustrates the essential concept. The objective of the circuit is to produce a net force in the vertical direction.

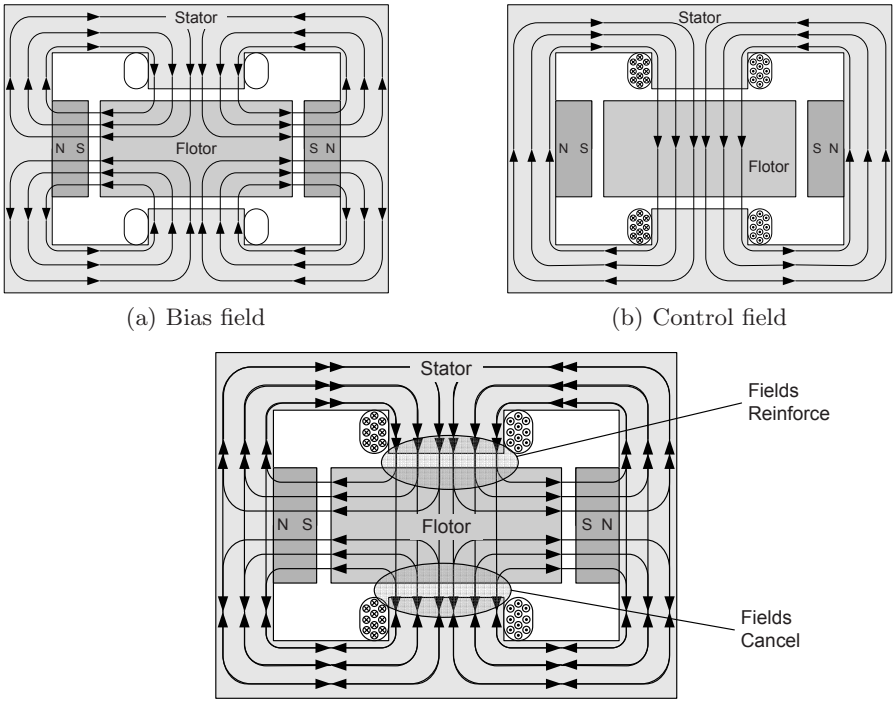


Fig. 3.21. Schematic of a very simple PM biased electromagnet.

In Fig. 3.21a, the control coils are not energized and the permanent magnets produce a bias flux distribution which is directed toward the center of the

flotor[1] in the vertical direction and away from the center in the horizontal direction. In Fig. 3.21b, the flux due to the permanent magnets is not shown, but the control coils are now energized to produce a flux that passes vertically through the flotor. Very little of the flux generated by the coil passes through the permanent magnets because the relative permeability of permanent magnet material is very low, on the order of 1.1. This low permeability means that the permanent magnets look like air gaps to the coil so the reluctance of the horizontal flux paths is very high.

Figure 3.21c shows the superposition of the control and bias fields. The fields reinforce one another in the upper gap but tend to cancel one another in the lower gap. The result is that the net flux in the upper gap is larger than that in the lower gap, leading to a net vertical force on the flotor. Note that, if the flotor is centered horizontally and the permanent magnets are matched, then there is no net horizontal force acting on the flotor.

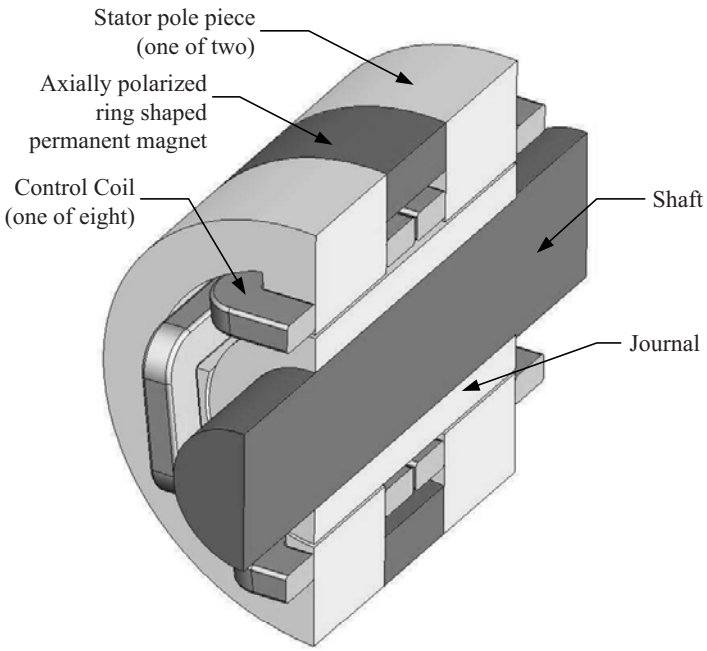


Fig. 3.22. Cross-section sketch of a realistic PM biased radial AMB magnet set.

A common structure for a permanent magnet biased radial AMB magnet set is sketched in Fig. 3.22. This structure has two stator pieces, each with

[1] The use of the term "flotor" here is meant to distinguish the magnetically suspended component (the *floating* component) from a rotor: in this diagram, the flotor is rectangular and does not rotate so it is not a "rotor."

four radial poles in a homopolar arrangement [5] (see Sec. 3.1.5). While it is topologically easiest to use permanent magnet biasing in a homopolar configuration, it is also possible to construct heteropolar bearings with permanent magnet biasing [3]. The two stators are separated by an axially polarized ring magnet, which supplies the bias field. Opposing coils are wired in series and also in series with the corresponding coils on the adjacent stator so that only two power amplifiers are needed to control the full set of coils while achieving independent control of the force in the two orthogonal radial directions. Note that it is not necessary to wind both stators: the function of the bearing does not depend on this and significant space savings may be realized by winding only one. In this case, the unwound stator also need not have pole slots or laminations and can, instead, be a simple disk.

3.3 Power Amplifiers

The power amplifiers convert the control signals to control currents. Apart from the bearing magnets the power amplifiers contribute most to the losses occurring in a magnetic bearing system. For economical and technical reasons these losses must be kept as low as possible. In industrial applications, switching amplifiers are used almost exclusively because their losses are considerably lower than those of analog amplifiers. Admittedly, the switching may cause electromagnetic disturbances.

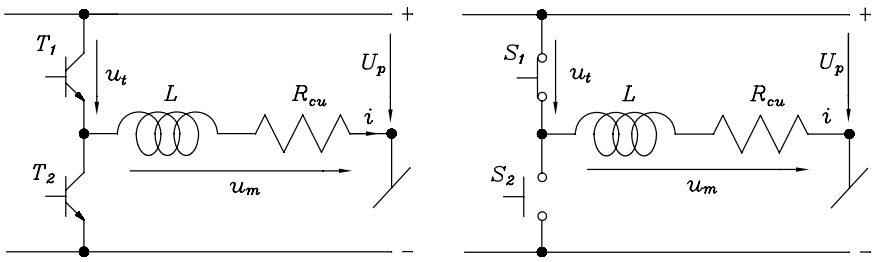
Because of their simple structure, analog amplifiers are usually used for sensitive applications where switching disturbances would be a problem or for applications requiring only very low power.

3.3.1 Principle of the Analog Amplifier

With the analog amplifier (Fig. 3.23a), the desired output voltage u_m is generated by driving transistor T1 (T2) for positive (negative) voltage to the point where voltage u_t over the transistor is the difference between supply voltage U_p and output voltage u_m. The other transistor is usually non-conducting. In the conducting transistor, the power $P = iu_t$ is converted to heat. As an example, in an amplifier with an input voltage U_p of 150 V, a maximum output current of 6 A, and a winding resistance R_{cu} of 2Ω, a power dissipation of 828 W in the conducting transistor will occur.

3.3.2 Principle of the Switching Amplifier

With the switching amplifier (Fig. 3.23b), the positive and the negative voltage U_p are alternately switched among the winding of the bearing with a given frequency (50 kHz, for example). In this so-called pulse-width modulation, current i alternately increases and decreases. When, within the period



(a) analog amplifier (b) switching amplifier

Fig. 3.23. Amplifier principles

of 20 μs, the positive voltage is switched on longer than the negative one, i.e. longer than 10 μs, a positive mean voltage of u_m will result, and current i will rise over several switching periods (Fig. 3.25). To reduce the current, the negative voltage must be switched on longer. Since only the low forward voltage u_t lies on the conducting transistor, the losses $P = u_t i$ are kept considerably lower than with analog amplifiers.

With the above example, the losses are of approximately 20 W. If one current direction is enough, as it is often the case, one switch may be replaced by a diode, and the minimum of one switch will suffice. Most commonly, only a positive voltage is available and an H-bridge arrangement with two switches and two diodes is used, as indicated in Fig. 3.24.

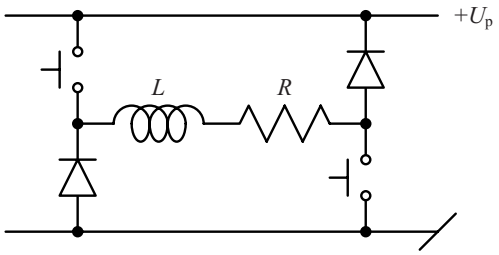


Fig. 3.24. Semi-passive H-bridge arrangement permits bipolar coil excitation but only unipolar coil current.

The disadvantage of the switching amplifiers is in the oscillations in of the current which cause remagnetization loss in the magnetic bearing. However, the shorter the switching period T, the weaker the oscillations in the current.

Instead of using the pulse-width modulation, switching amplifiers can also be made with a switching controller. In addition, the control value and true value for the current can be compared at a given frequency, in order to guarantee a minimum switching time that is needed for the transistor.

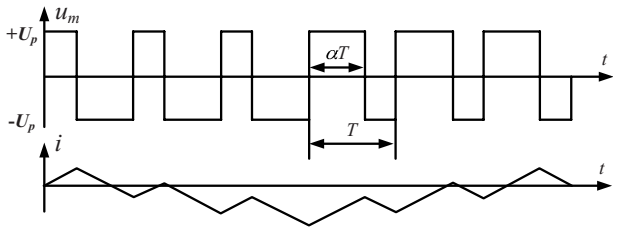


Fig. 3.25. Current at pulse-width modulated voltage (purely inductive load).

3.4 Sensors

An important part of the performance of a magnetic bearing depends on the characteristics of the displacement sensors used. In order to measure the position of a moving rotor, contact-free sensors must be used which, moreover, must be able to measure on a rotating surface. Consequently, the geometry of the rotor, i.e. its surface quality, and the homogeneity of the material at the sensor will also influence the measuring results. A bad surface will thus produce noise disturbances, and geometry errors may cause disturbances with the rotational frequency or with multiples thereof.

In addition, depending on the application, speeds, currents, flux densities and temperatures are to be measured in magnetic bearing systems. In the following section, the most important measuring principles and their areas of application will be presented.

3.4.1 Terms

Measuring range: The output signal of a sensor changes according to a physical effect as a function of the measured quantity (Fig. 3.26). The range in which the output signal can be used often corresponds to that range having an approximately linear correlation between measured quantity and output signal. This linear measuring range can be considerably smaller than the physical one.

Linearity: The linearity is usually represented as a percentage of the maximum measuring range. It shows to what extent the measured quantity deviates from a linear relationship between measured quantity and output signal.

Sensitivity: The sensitivity indicates the ratio of the output signal over the quantity to be measured; for a displacement sensor, for instance, it is indicated in mV/μm. The sensitivity can be enhanced by electronic amplification of the output signal. This ability to amplify seems to imply that sensitivity is arbitrary: however, amplification boosts noise along with signal. Consequently, the signal-to-noise ratio (SNR) of the sensor establishes a maximum bound on sensitivity.

Resolution: In addition to the useful signal, each sensor system produces noise disturbances in the output signal. The value of the useful signal which can be distinguished from the noise disturbance (mostly peak-to-peak value of the noise disturbance) is called *resolution.*

The resolution is usually indicated in absolute values - for instance in m or μm for a displacement sensor. It cannot be improved by amplification, but it largely depends on the physical effect used and on the electronic parts. The resolution, however, can often be improved by low-pass filters - at the expense of the frequency range. External disturbances may considerably reduce the resolution.

Frequency range: A linear frequency response, i.e. a sensitivity independent of the frequency, is desirable in magnetic bearing applications, especially for the displacement sensors. The frequency with a sensitivity reduced by 3 dB is usually called *cut-off frequency.* One must consider here that the output signal at the cut-off frequency, depending on the sensor, may already show an significant phase lag.

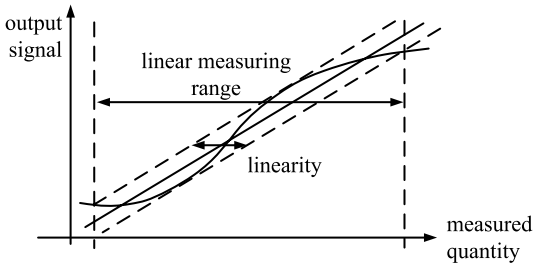


Fig. 3.26. Useful measuring range and linearity.

3.4.2 Displacement Measurement

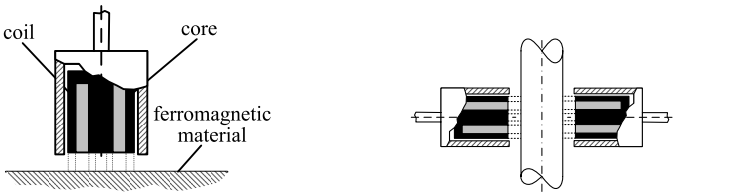
When selecting the displacement sensors, depending on the application of the magnetic bearing, measuring range, linearity, sensitivity, resolution, and frequency range are to be taken into account as well as:

- Temperature range, temperature drift of the zero point and sensitivity.
- Noise immunity against other sensors, magnetic alternating fields of the electromagnets, electromagnetic disturbances from switched amplifiers.
- Environmental factors such as dust, aggressive media, vacuum, or radiation.
- Mechanical factors such as shock and vibration.
- Electrical factors such as grounding issues associated with capacitive sensors.

Inductive Displacement Sensors

An inductor coil on a ferromagnetic core is driven by an oscillator (Fig. 3.27 a). When a ferromagnetic object, whose position is to be measured, approaches the coil the inductance changes. This change in the inductance is sensed by electronics and converted to a sensor output voltage proportional to the displacement.

Two sensors opposing each other are frequently arranged on a rotor (Fig. 3.27 b). They are operated differentially in a bridge circuit with a constant bridge frequency, producing a nearly linear signal. Inductive sensors are operated with modulation frequencies from approximately 5 kHz up to 100 kHz. The cut-off frequency of the output signal lies in a range between one tenth and one fifth of the modulation frequency. Normally, inductive sensors are not overly sensitive to external magnetic fields near bearing magnets as long as the fields are not sufficient to modulate the permeability of the sensor core material. However, massive disturbances may occur when the magnetic bearings are driven by switched power amplifiers and the switching frequency of the amplifiers is close to the modulation frequency.



(a) Sensor head (b) Differentially measuring sensors

Fig. 3.27. Inductive displacement sensor

Eddy Current Sensors

High-frequency alternating current runs through the air-coil embedded in a housing. The electromagnetic coil section induces eddy currents in the conductive object whose position is to be measured, thus absorbing energy from the oscillating circuit. Depending on the clearance, the inductance of the coil varies, and external electronic circuitry converts this variations into an output signal. The usual modulation frequencies lie in a range of 1 - 2 MHz, resulting in a useful measuring frequency ranges of 0 Hz up to approximately 20 kHz.

Inhomogeneities in the material of the moving rotor cause noise-like disturbances and reduce the resolution accordingly: see Fig. 3.28. Manufacturers usually indicate the sensitivity used on aluminium. When measuring steel, the sensitivity is smaller. Shielded sensors must be used for applications near bearing magnets where high frequency magnetic fields occur. However, the

shielded sensors are not supplied by all manufacturers, and disturbance sensitivity may therefore have to be determined by trial and error.

Sensors may also cause mutual interference. Therefore, the minimum clearance between sensors is mostly defined in the mounting guide. A minimum clearance must also be respected with regard to the surrounding conducting material. The minimum clearance with shielded sensors is smaller. When operating several sensors in the same system, the modulation frequencies should be synchronised. However, synchronization may not be possible with all sensor systems.

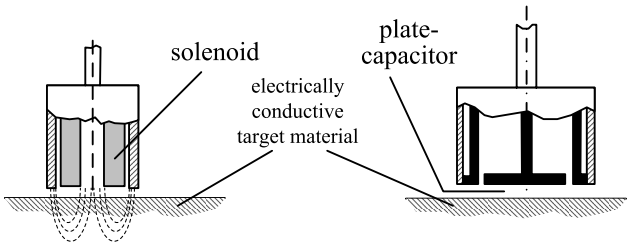


Fig. 3.28. Left: eddy-current displacement sensor Right: capacitive sensor

Eddy Current Radial Displacement Sensor on a PCB (Transverse Flux Sensor)

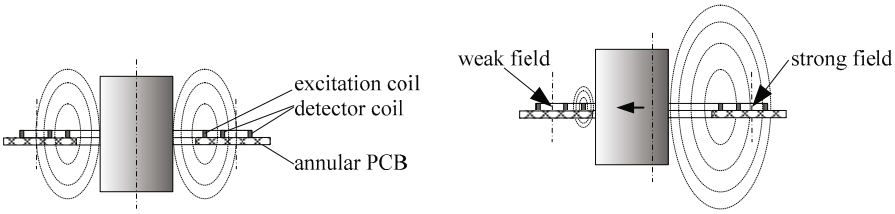
In order to minimize space requirement and to save production cost of the sensor it would be desirable to place the eddy current sensor coils directly on a printed circuit board (PCB) which is placed around the rotor. Such a design is known as Transverse Flux Sensor (TFS) [4, 9].

The magnetic field of the coil of an eddy current displacement sensor is directed towards the rotor, i.e. the axis of a radial sensor coil is perpendicular to the rotation axis of the rotor (Fig. 3.29). This arrangement provides a suitably high sensitivity to target displacements only in a direction perpendicular to the coil surface, whereas sensitivity to displacements in any lateral direction is poor. This behavior is due to the fact that magnetic field strength is highest in the coil's center and that the maximum field gradient component is perpendicular to its surface.

This is especially the case when using flat coils, hence, when PCB coils come into consideration. A PCB coil arranged with a surface normal vector parallel to the axis of rotation shows almost zero sensitivity to lateral rotor displacements and is, therefore, not useful as a lateral position sensor.

The basic idea for achieving a PCB coil arrangement featuring a high lateral sensitivity for measuring the radial x and y position of a rotor while still keeping all the necessary coils arranged in a very thin annular PCB board

placed around the rotor is to use a combination of one excitation coil concentric to the rotor and four detector coils. The strength of the electro-magnetic field of the excitation coil is strongly dependent on the position of the rotor within the excitation coil. Measuring this field strength with the detection coils gives high lateral sensitivity in x and y direction (Fig. 3.29).



(a) rotor concentric within the sensor (b) with rotor displacement

Fig. 3.29. Transverse Flux Sensor (TFS)

Capacitive Displacement Sensors

The capacity of a plate capacitor varies with its clearance. Using the capacitive measuring method, the sensor and the opposing object to be measured form one electrode of a plate capacitor each (Fig. 3.28). Within the measuring system, an alternating current with a constant frequency runs through the sensor. The voltage amplitude at the sensor is proportional to the clearance between the sensor electrode and the object to be measured, and it is demodulated and amplified by a special circuit. Commercially available capacitive displacement measuring systems are expensive, but they typically have extraordinary resolution (for instance 0.02 μm at a measuring range of 0.5 mm). The bandwidth of the output signal ranges between approximately 5 kHz and 100 kHz.

The electrostatic charging of the contactless rotor may cause interferences too. The sensors are sensitive to dirt which modifies the dielectric constant in the air gap.

Magnetic Displacement Sensors

When current i is kept constant in a magnetic loop with an air gap, flux density B can be used to measure the size of the air gap. In the arrangement shown in Fig. 3.30, a well linearized displacement signal results from the difference between the measured flux density $U_{Bp} - U_{Bn}$. Flux density B may be measured with Hall sensors or with field plates (see Sec. 3.4.3). Magnetic displacement sensors are sensitive to interference by external magnetic fields.

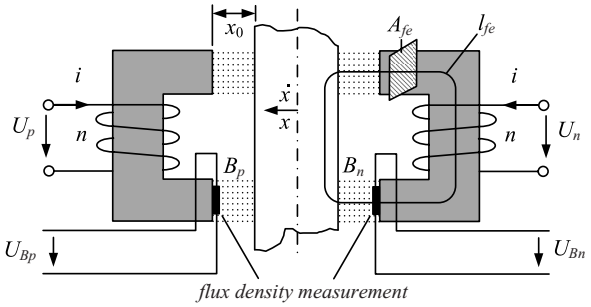


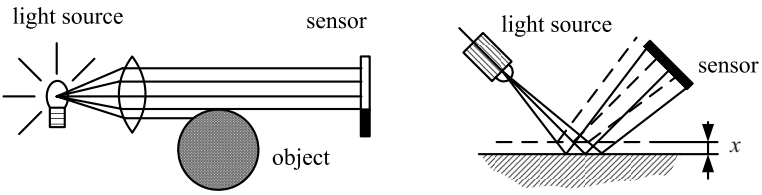
Fig. 3.30. Combined displacement-velocity sensor

Velocity Measurement

If the current i is kept constant in a magnetic circuit, the flux Φ varies with the air gap. Voltage U is proportional to the derivative $d\Phi/dt$ and the velocity dx/dt. With an arrangement as shown in Fig. 3.30, the difference between the voltages $U_p - U_n$ yields a nearly linear velocity signal. This kind of sensor is also appropriate for measuring displacement and velocity. Furthermore, permanent magnets can be used instead of electric excitement.

Optical Displacement Sensors

The most simple principle of an optical displacement sensor consists of covering a light source opposite to a light-sensitive sensor by the object to be measured (Fig. 3.31 a). The resulting difference in light intensity is converted into an electric signal and serves as a measurement for the position of the object. By selecting appropriate light sources, light sensors, and suitable apertures, we obtain a nearly linear displacement signal.



(a) Light barrier principle (b) Reflection principle

Fig. 3.31. Optical sensing methods.

A similar approach consists of reflecting light by the object to be measured. The fraction of light received by the sensor changes according to the motion

of the object (Fig. 3.31 b). For this kind of system photo diodes, photo transistors, photo resistors, and photo-electric cells can be used as sensors. The wavelength of the light source should be matched to the peak sensitivity of the sensor. Such systems can be made almost completely insensitive to the influence of extraneous light by modulating the light of the light source (a LED for instance), and by demodulating the signal.

Another possibility is the application of an image sensor. Take, for example, a line array camera (CCD sensor) in a magnetic bearing system (Fig. 3.32). The rotor image is reflected both for the $x-$ and the $y-$ direction over a mirror on a CCD sensor. The picture of the rotor, tinted black in front of a lit-up background, is converted into a video signal. By counting the pixels (light-sensitive dots) until the light-dark boundary is reached one obtains a digital displacement signal.

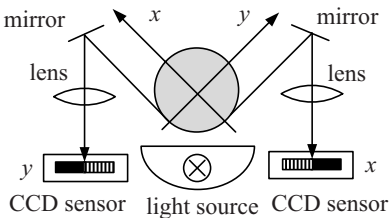


Fig. 3.32. Optical displacement sensor using CCD technology.

However, optical displacement measuring systems are not appropriate for many application fields, since they are very sensitive to dirt, and the resolution is limited due to diffraction effects.

3.4.3 Flux and Current Measurement

Hall Effect

When a current travels along a thin, band-shaped conductor, and when this conductor lies in a magnetic field perpendicular to the band plane, forces act perpendicularly to the band on the electrons which move at a drifting speed v along the conductor (Fig. 3.33). This leads to an accumulation of positive and negative charges on both longitudinal sides of the band, and consequently to an electric voltage U_b. This Hall voltage is proportional to flux density B and current i [6].

$$U_b = k_h B i \tag{3.54}$$

The proportionality factor k_h depends on the geometry of the conductor and its material. When measuring the flux density, the Hall sensors are driven by a constant-current source. Commercially available Hall sensors have been

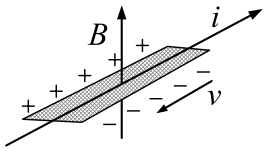


Fig. 3.33. Hall effect.

optimized regarding the size of k_h and the temperature drift of the zero point. The thickness of the smallest sensors is about 0.25 mm. Hall sensors with integrated constant-current source and integrated amplifier are also available.

Field Plate

Field plates are resistors that vary with the flux density. The thinnest field plates available have a thickness of approximately 0.5 mm. The basic resistance R_0 and the ratio of the relative resistance change R_b/R_0 at a certain flux density can be found in data sheets; for instance $R_0 = 250\Omega$, $R_b/R_0 = 15$ at a flux density B of 1 Tesla.

Coil and Integrator

According to the induction law (3.7), the voltage u across a coil with n turns is

$$u = n\frac{d\Phi}{dt}$$

If a measurement coil is mounted on a magnet and if the resulting voltage is fed to an electronic integrator, the integrator output signal will be proportional to the flux through the measurement coil (Fig. 3.34). This procedure, however, has the disadvantage that only the alternating components of the flux can be measured.

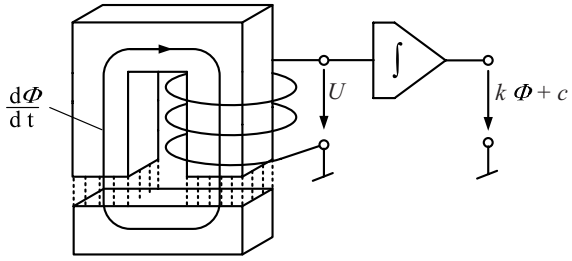


Fig. 3.34. Flux measurement with coil and integrator

Current Measurement with a Hall Sensor

A common method of measuring currents with isolation uses a Hall sensor in a magnetic loop excited by one or several turns of the current i to be measured. The flux density measured by the Hall sensor is equilibrated with a controller, a power amplifier and an auxiliary coil (Fig. 3.35). The zero balance is reached when the flux from the current in the auxiliary winding with n turns is opposite to the flux generated by current i to be measured. The input signal U_i of the power amplifier is therefore a direct measure of the current i.

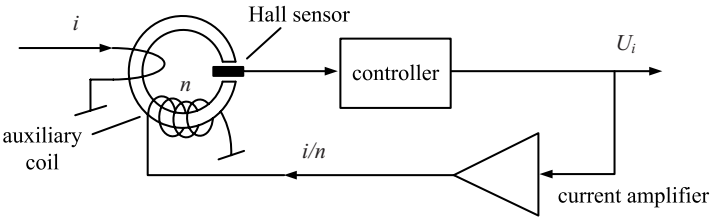


Fig. 3.35. Current measurement with a Hall sensor

3.5 Concluding Remarks

This chapter has explored some of the more central themes of component selection and design for magnetic bearings, covering the range of sensors, magnet sets, and power amplifiers. Treatment of the combined action of the electromagnets and the power amplifiers, called the *actuator* is provided in Chap. 4, reflecting the system nature of this combination. In some AMB systems, it may be appropriate to consolidate the sensing and actuation functions into a single device, called a *self-sensing* bearing: see Chap. 15 for a detailed discussion of this notion.

All of these areas are active focii of current AMB research. In sensing, there is a continual interest in better integration of sensing into the overall AMB structure, in reducing cost, and in reducing noise coupling between the magnet coils and the sensing head. In high precision applications like grinding or milling, the premium on sensor performance is very high. Research in power amplifiers generally seeks to reduce hardware complexity, realize better integration with the controller, improve the composite behavior of the actuator (electromagnet/amplifier combination), reduce emitted acoustic and/or electromagnetic noise from the actuator or electrical noise back into the power supply, and of course to reduce cost. Work on the electromagnet set is variously aimed at reducing cost, increasing the unit load capacity, reducing both

rotating and stator losses, reducing wire count / complexity, increasing fault tolerance, and enabling operation in extreme environments: primarily, low and high temperatures.

References

1. Boden, K., "Permanentmagnetic Bearing System with Radial Transmission of Radial and Axial Forces." Proceedings of the *First International Symposium on Magnetic Bearings*, ETH Zürich, May 1988. Springer Verlag, Berlin, 1988.
2. Earnshaw, S., "On the Nature of the Molecular Forces." Trans. Cambridge Phil. Soc. 7, 97-112, 1842.
3. Ehmann, C., Sielaff, T, and Nordmann R., "Comparison of Active Magnetic Bearings with and Without Permanent Magnet Bias," Proceedings of the *Ninth International Symposium on Magnetic Bearings*, Lexington, KY, USA, Aug. 2004.
4. European Patent No. EP 1 422 492.
5. Filatov, A., McMullen, P., Hawkins L., and Blumber E., "Magnetic Bearing Actuator Design for a Gas Expander Generator," Proceedings of the *Ninth International Symposium on Magnetic Bearings*, Lexington, KY, USA, Aug. 2004.
6. Hall, E. H., "On a New Action of the Magnet on Electric Currents," *American Journal of Mathematics*, Vol. 2, No. 3 (Sep., 1879), pp. 287-292.
7. Heck, C.,"Magnetische Werkstoffe und ihre technische Anwendung." Dr. A. Hütling Verlag, 1975.
8. Krupp WIDIA GmbH, "Dauermagnetische Werkstoffe und Bauteile." Firmenschrift, Essen, 1989.
9. Larsonneur, R. and Bühler, P., "New Radial Sensor for Active Magnetic Bearings," Proceedings of the *Ninth International Symposium on Magnetic Bearings*, Lexington KY, USA, August 3-6, 2004.
10. Marinescu, M., "Dauermagnetische Radiallager." Firmenschrift, Marinescu Ing.-Büro für Magnettechnik, Frankfurt, 1982.
11. Marshall, S.V. and Skitek, G.G., *Electromagnetic Concepts & Applications*. Second edition, Prentice-Hall International, London, 1987.
12. Maslen, E. H., and Meeker, D. C., "Fault Tolerance of Magnetic Bearings by Generalized Bias Current Linearization," IEEE *Transactions on Magnetics*, Vol. 31, No. 3, May 1995, pp. 2304–2314.
13. Maslen, E. H., Allaire, P. E., Noh, M., and Sortore, C. K., "Magnetic Bearing Design for Reduced Power Consumption," ASME *Journal of Tribology,* Vol. 118, No. 4, October 1996, pp. 839–846.
14. McMullen, P., Huynh, C., Hayes, R., "Combination Radial-Axial Magnetic Bearing," Proceedings of the *Seventh International Symposium on Magnetic Bearings*, Zurich, August 2000.
15. Meeker, D., and Maslen, E., "Analysis and Control of a Three Pole Radial Magnetic Bearing," Proceedings of the *Tenth International Symposium on Magnetic Bearings*, Martigny, Switzerland, August 21–23, 2006.
16. Minkowycz, W. J, Sparrow, E. M., and Murthy, J. Y., *Handbook of Numerical Heat Transfer*, John Wiley and Sons, 2006.

17. Pichot, Mark A. and Driga, Mircea D., "Magnetic Circuit Analysis of Homopolar Magnetic Bearing Actuators," Proceedings of the *Ninth International Symposium on Magnetic Bearings,* Lexington, KY, August 3-6, 2004.
18. Schweitzer, G. and Lange, R., "Characteristics of a Magnetic Rotor Bearing for Active Vibration Control." Proceedings of the *Conference on Vibrations in Rotating Machinery*, Instn. of Mech. Engrs., Cambridge, Sept. 1976, C239/76.
19. Sobotka, G. and Hübner, K.D., "Dauermagnetische Radiallager und Axiallager: Entwicklungsstand und Tendenz." Maschinenmarkt 87 (1981) Heft 5 und 10, Vogel-Verlag, Würzburg.
20. Tannenhill, J. C., Anderson, D. A., and Pletcher, R. H., *Computational Fluid Mechanics and Heat Transfer*, Taylor and Frances, 1997.
21. Traxler, A., "Eigenschaften und Auslegung von berührungsfreien elektromagnetischen Lagern." Diss ETH Zürich Nr. 7851, 1985.
22. Wilson, M. and Studer, P. A., "Linear Magnetic Bearings," *Fifth International Workshop on Rare Earth–Cobalt Permanent Magnets and their Applications*, Roanoke, Va, 7-10 June 1981.

4

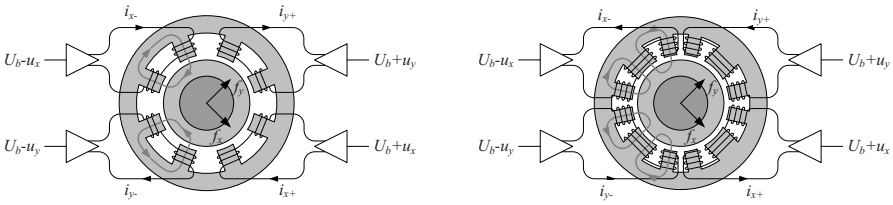
Actuators

Alfons Traxler and Eric Maslen

Perhaps the defining element of an active magnetic bearing is its actuator. This is the combined system of amplifiers and electromagnets which, together, convert electrical signals from the controller (force commands) into actual forces applied to the rotor. The objective of this chapter is to detail the interaction of these components in order to understand the design and modeling of the combination.

4.1 Structure

In general, the actuator for an AMB system may be composed of an arbitrary array of electromagnets connected to some array of amplifiers. For simplicity, the present discussion will focus on the most commonly applied structures which include radial actuators and thrust actuators. Fig. 4.1 details the two most common arrangements for a radial actuator while Fig. 4.2 describes the most common arrangement for a thrust actuator. All of these schemes involve magnets acting in opposition: each magnet can only pull toward its faces so generating forces of either sign requires this opposition.



(a) eight pole (b) "E"-core

Fig. 4.1. Conventional radial actuator arrangements

G. Schweitzer, E.H. Maslen (eds.), *Magnetic Bearings*,
DOI 10.1007/978-3-642-00497-1_4, © Springer-Verlag Berlin Heidelberg 2009

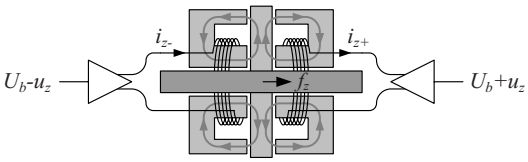


Fig. 4.2. Conventional thrust actuator arrangement

Clearly, all of these actuators contain the same types of elements: power amplifiers, electromagnet stators with coil windings, and the moving part of the electromagnet which is attached to the rotor. Models for the amplifiers and for the electromagnets are required in order to understand and describe the functioning of this combination.

4.2 Amplifiers

Although it is common to consider each amplifier to be a bandwidth limited transconductance device: $i_{\mathrm{mag},i} = T_{\mathrm{amp},i}u_i$, the present discussion will use a bit more sophisticated model which incorporates the effect of rotor motion. This model looks at the internal feedback of the amplifier:

$$u_{\mathrm{amp},i} = G_{\mathrm{amp},a,i}u_i - G_{\mathrm{amp},b,i}R_f i_{\mathrm{mag},i} \tag{4.1}$$

That is, the output voltage of the amplifier is produced by a feedforward term from the controller command u_i and feedback of the measured current $i_{\mathrm{mag},i}$: this structure is indicated in Fig. 4.3. The term R_f represents the current sensor gain and has units of volts/amp, or Ohms.

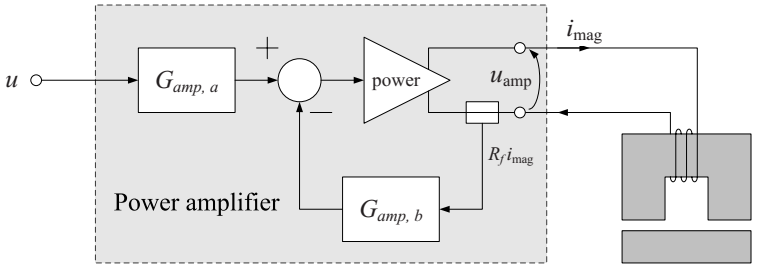


Fig. 4.3. Typical power amplifier scheme.

Note that not all amplifiers will implement all elements of this schematic: in some cases, for instance, there may be no feedback of measured current. The objective of this model structure is to cover the range of possible amplifier construction where it is assumed that the amplifier is essentially linear and

maps available signals (a reference input u and, potentially, measured output current i_{mag}) to its output voltage.

The electromagnet itself will react to this applied voltage $u_{\ amp,i}$ with the result that a current $i_{\text{mag},i}$ will be induced. Thus, while it is conventional to model the coil current as measured internally to the amplifier, it is actually an *output* of the electromagnet: a response to $u_{\text{amp},i}$ and the rotor position.

In general, manufacturers will not supply such an internal model. In this case, how can this internal model be deduced from available information? Assume that the amplifier is tested when connected to a load $Ls + R$ and found to have a closed loop transconductance $T_{\text{amp},i}(s)$:

$$u_{\text{amp},i} = G_{\text{amp},a,i}u_i - G_{\text{amp},b,i}R_f i_{\text{mag},i}\ , \quad (Ls+R)i_{\text{mag},i}(s) = u_{\text{amp},i}$$

$$\Rightarrow\ i_{\text{mag},i}(s) = \frac{G_{\text{amp},a,i}}{Ls + R + G_{\text{amp},b,i}R_f}u_i(s) = T_{\text{amp},i}(s)u_i(s)$$

If it may be assumed that $G_{\text{amp},a,i} = G_{\text{amp},b,i}$, then this last equation may be solved for $G_{\text{amp},1,i}$:

$$G_{\text{amp},a,i} \equiv G_{\text{amp},b,i} \quad \Rightarrow \quad G_{\text{amp},a,i} = \frac{(Ls+R)T_{\text{amp},i}}{1 - T_{\text{amp},i}R_f} \tag{4.2}$$

As an example, suppose that $L = 20\text{mH}$, $R = 0.5\Omega$, $R_f = 1\Omega$, and

$$T_{\text{amp},i} = \frac{1}{2\times 10^{-8}s^2 + 2\times 10^{-4}s + 1}$$

In this case, the amplifier transfer functions are readily computed as

$$G_{\text{amp},a,i}(s) = 1.14\times 10^6 \frac{s+25}{s(s+12000)}$$

which represents bandwidth limited PI feedback control.

Some AMB amplifier schemes may use $G_{\text{amp},b,i} \neq G_{\text{amp},a,i}$. In this case, it is not possible to independently ascertain both $G_{\text{amp},a,i}$ and $G_{\text{amp},b,i}$ from measured $T_{\text{amp},i}$ and one must resort to other measurements or obtain this information from the amplifier supplier. One approach is to measure the amplifier loop gains T_1 and T_2 when driving two different load impedances Z_1 and Z_2. In this case,

$$G_{\text{amp},b,i}(s) = \frac{Z_1T_{\text{amp},1} - Z_2T_{\text{amp},2}}{R_f\left(T_{\text{amp},2} - T_{\text{amp},1}\right)}$$

$$G_{\text{amp},a,i}(s) = T_{\text{amp},1}\left(Z_1 + G_{\text{amp},b,i}R_f\right)$$

To produce a state space form of this amplifier model, assume that $G_{\text{amp},a,i}$ is represented by the *monic rational polynomial*

$$G_{\text{amp},a,i} = \frac{\sum_{j=0}^{n-1}\beta_j s^j}{s^n + \sum_{i=0}^{n-1}\alpha_i s^i} \tag{4.3}$$

If so, then a state space representation of $G_{\mathrm{amp},a,i}$ is

$$\frac{d}{dt}\mathbf{x}_{\mathrm{amp},a,i} = \begin{bmatrix} 0 & 1 & 0 & \cdots & 0 \\ 0 & 0 & 1 & & 0 \\ \vdots & & & \ddots & \vdots \\ 0 & 0 & \cdots & 0 & 1 \\ -\alpha_0 & -\alpha_1 & -\alpha_2 & \cdots & -\alpha_{n-1} \end{bmatrix} \mathbf{x}_{\mathrm{amp},a,i} + \begin{bmatrix} 0 \\ 0 \\ \vdots \\ 0 \\ 1 \end{bmatrix} u_i \tag{4.4a}$$

$$u_{\mathrm{amp},a,i} = \begin{bmatrix} \beta_0 & \beta_1 & \cdots & \beta_{n-1} \end{bmatrix} \mathbf{x}_{\mathrm{amp},a,i} \tag{4.4b}$$

or,

$$\frac{d}{dt}\mathbf{x}_{\mathrm{amp},a,i} = \mathbf{A}_{\mathrm{amp},a,i}\mathbf{x}_{\mathrm{amp},a,i} + \mathbf{B}_{\mathrm{amp},a,i}u_i \tag{4.5a}$$

$$u_{\mathrm{amp},a,i} = \mathbf{C}_{\mathrm{amp},a,i}\mathbf{x}_{\mathrm{amp},a,i} \tag{4.5b}$$

In the same manner, the transfer function $G_{\mathrm{amp},b,i}R_f$ is represented by

$$\frac{d}{dt}\mathbf{x}_{\mathrm{amp},b,i} = \mathbf{A}_{\mathrm{amp},b,i}\mathbf{x}_{\mathrm{amp},b,i} + \mathbf{B}_{\mathrm{amp},b,i}i_{\mathrm{mag},i} \tag{4.6a}$$

$$u_{\mathrm{amp},b,i} = \mathbf{C}_{\mathrm{amp},b,i}\mathbf{x}_{\mathrm{amp},b,i} \tag{4.6b}$$

The total amplifier output voltage is $u_{\mathrm{amp},i} = u_{\mathrm{amp},a,i} - u_{\mathrm{amp},b,i}$ and this is constructed by combining the previous two state space models:

$$\begin{aligned} \frac{d}{dt}\begin{bmatrix} \mathbf{x}_{\mathrm{amp},a,i} \\ \mathbf{x}_{\mathrm{amp},b,i} \end{bmatrix} &= \begin{bmatrix} \mathbf{A}_{\mathrm{amp},a,i} & 0 \\ 0 & \mathbf{A}_{\mathrm{amp},b,i} \end{bmatrix} \begin{bmatrix} \mathbf{x}_{\mathrm{amp},a,i} \\ \mathbf{x}_{\mathrm{amp},b,i} \end{bmatrix} + \begin{bmatrix} \mathbf{B}_{\mathrm{amp},a,i} \\ 0 \end{bmatrix} u_i \\ &\quad + \begin{bmatrix} 0 \\ \mathbf{B}_{\mathrm{amp},b,i} \end{bmatrix} i_{\mathrm{mag},i} \\ &= \mathbf{A}_{\mathrm{amp},i}\mathbf{x}_{\mathrm{amp},i} + \mathbf{B}_{\mathrm{amp},1,i}u_i + \mathbf{B}_{\mathrm{amp},2,i}i_{\mathrm{mag},i} \end{aligned} \tag{4.7a}$$

$$\begin{aligned} u_{\mathrm{amp},i} &= \begin{bmatrix} \mathbf{C}_{\mathrm{amp},a,i} & -\mathbf{C}_{\mathrm{amp},b,i} \end{bmatrix} \begin{bmatrix} \mathbf{x}_{\mathrm{amp},a,i} \\ \mathbf{x}_{\mathrm{amp},b,i} \end{bmatrix} \\ &= \mathbf{C}_{\mathrm{amp},2,i}\mathbf{x}_{\mathrm{amp},i} \end{aligned} \tag{4.7b}$$

Monitoring the performance of the amplifier requires knowledge of the amplifier input voltage, which is limited to some fixed range like ±10 volts, and the output voltage, which is limited by the DC link voltage: perhaps ±160 volts. The two signals are readily obtained:

$$\begin{aligned} \begin{bmatrix} u_{\mathrm{amp},i} \\ u_i \end{bmatrix} &= \begin{bmatrix} \mathbf{C}_{\mathrm{amp},a,i} & -\mathbf{C}_{\mathrm{amp},b,i} \\ 0 & 0 \end{bmatrix} \begin{bmatrix} \mathbf{x}_{\mathrm{amp},a,i} \\ \mathbf{x}_{\mathrm{amp},b,i} \end{bmatrix} + \begin{bmatrix} 0 \\ I \end{bmatrix} u_i \\ &= \mathbf{C}_{\mathrm{amp},1,i}\mathbf{x}_{\mathrm{amp},i} + \mathbf{D}_{\mathrm{amp},i}u_i \end{aligned} \tag{4.8}$$

Finally, combine (4.7) and (4.8) to form the amplifier model

$$\frac{d}{dt}\mathbf{x}_{\mathrm{amp},i} = \mathbf{A}_{\mathrm{amp},i}\mathbf{x}_{\mathrm{amp},i} + \mathbf{B}_{\mathrm{amp},1,i}u_i + \mathbf{B}_{\mathrm{amp},2,i}i_{\mathrm{mag},i} \tag{4.9a}$$

$$\begin{bmatrix} u_{\mathrm{amp},i} \\ u_i \end{bmatrix} = \mathbf{C}_{\mathrm{amp},1,i}\mathbf{x}_{\mathrm{amp},i} + \mathbf{D}_{\mathrm{amp},i}u_i \tag{4.9b}$$

$$u_{\mathrm{amp},i} = \mathbf{C}_{\mathrm{amp},2,i}\mathbf{x}_{\mathrm{amp},i} \tag{4.9c}$$

4.3 Electromagnets

The conventional linearized model of the electromagnet set is that it is a static gain from applied current and rotor motion to a net force applied to the rotor:

$$f_i = k_i i_i - k_s y_{\text{mag}}$$

in which i_i is the deviation of magnet currents from the *bias* point and y_{mag} is the displacement of the actuator journal. However, consistent with the modified model of the amplifier discussed above, a somewhat more physical view of the magnet set is adopted here which reflects the fact that an electromagnet stores magnetic energy and therefore has its own dynamics which interact with the amplifiers in a specific manner.

To establish this model, consider an opposed pair of electromagnets, as indicated in Fig. 4.4. These magnets each have a pole area A and a nominal

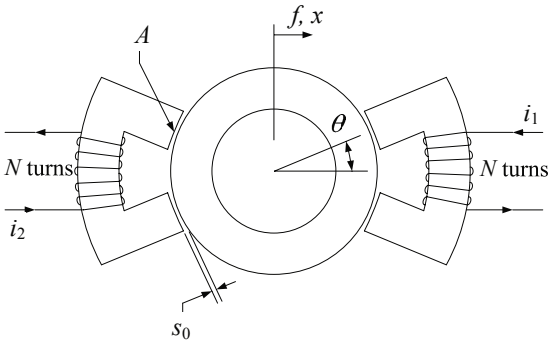


Fig. 4.4. Simple AMB using opposed electromagnets.

air gap length s_0. The angle of each pole relative to the centerline between the poles is θ. Each is wound with N turns of wire to produce a coil with resistance R.

Ignoring the reluctance of the stator and rotor iron, the flux densities in the two magnets may be related to the respective coil currents using Ampère's loop law by

$$B_1 = \frac{\mu_0 N i_1}{2(s_0 - y\cos\theta)} \quad \Rightarrow \quad i_1 = \frac{2(s_0 - y\cos\theta)}{\mu_0 N} B_1 \tag{4.10a}$$

$$B_2 = \frac{\mu_0 N i_2}{2(s_0 + y\cos\theta)} \quad \Rightarrow \quad i_2 = \frac{2(s_0 + y\cos\theta)}{\mu_0 N} B_2 \tag{4.10b}$$

while the evolution of gap flux in each magnet is controlled (via Faraday's and Ohm's laws) by coil voltages, v_1 and v_2 through

$$NA\frac{dB_1}{dt} = v_1 - i_1 R = v_1 - \frac{2(s_0 - y\cos\theta)R}{\mu_0 N^2 A} NAB_1 \tag{4.11a}$$

$$NA\frac{dB_2}{dt} = v_2 - \frac{2(s_0 + y\cos\theta)R}{\mu_0 N^2 A} NAB_2 \tag{4.11b}$$

Each electromagnet exhibits a nominal inductance (when $y = 0$) of

$$L = N\frac{d\Phi}{di} = NA\frac{dB}{di} = \frac{\mu_0 N^2 A}{2s_0} \tag{4.12}$$

and the pair of magnets produces a net force on the rotor of

$$f_{\text{mag}} = \frac{A\cos\theta}{\mu_0}\left(B_1^2 - B_2^2\right) = \frac{A\cos\theta}{\mu_0}(B_1 - B_2)(B_1 + B_2) \tag{4.13}$$

For convenience in the ensuing development, the following definitions are introduced to transform from top/bottom coordinates to sum and difference coordinates:

$$x_a \equiv \frac{s_0}{\mu_0 N}(B_1 - B_2) \qquad x_b \equiv \frac{s_0}{\mu_0 N}(B_1 + B_2) \tag{4.14a}$$

$$v_a \equiv (v_1 - v_2)/2 \qquad v_b \equiv (v_1 + v_2)/2 \tag{4.14b}$$

$$i_a \equiv (i_1 - i_2)/2 \qquad i_b \equiv (i_1 + i_2)/2 \tag{4.14c}$$

so that the dynamic model of the magnet pair becomes

$$\frac{d}{dt}x_a = -\frac{R}{L}x_a + \frac{R}{L}\frac{\cos\theta}{s_0}yx_b + \frac{1}{L}v_a \tag{4.15a}$$

$$\frac{d}{dt}x_b = -\frac{R}{L}x_b + \frac{R}{L}\frac{\cos\theta}{s_0}yx_a + \frac{1}{L}v_b \tag{4.15b}$$

$$i_a = x_a - \frac{\cos\theta}{s_0}yx_b \tag{4.15c}$$

$$i_b = x_b - \frac{\cos\theta}{s_0}yx_a \tag{4.15d}$$

$$f_{\text{mag}} = \frac{\mu_0 N^2 A\cos\theta}{s_0^2}x_b x_a \tag{4.15e}$$

This model is obviously nonlinear: the output force is proportional to the product of the two states x_a and x_b. Consistent with the usual approach to this problem, linearize (4.15) about the *biasing* point

$$x_a = 0,\ x_b = X_b$$

and discard remaining terms that contain products of states to obtain the linear model

$$\frac{d}{dt}x_a = -\frac{R}{L}x_a + \frac{R}{L}\frac{X_b\cos\theta}{s_0}y + \frac{1}{L}v_a \tag{4.16a}$$

$$\frac{d}{dt}x_b = -\frac{R}{L}x_b + \frac{1}{L}v_b \tag{4.16b}$$

$$i_a = x_a - \frac{X_b\cos\theta}{s_0}y \tag{4.16c}$$

$$i_b = x_b \tag{4.16d}$$

$$f_{\text{mag}} = \frac{\mu_0 N^2 A X_b\cos\theta}{s_0^2}x_a \tag{4.16e}$$

Now, define the actuator gain K_i and the actuator nominal stiffness K_s by

$$K_i \equiv \frac{\mu_0 N^2 A\cos\theta i_b}{s_0^2} \quad \text{and} \quad K_s \equiv -K_i\frac{i_b}{s_0}\cos\theta$$

so that

$$\frac{d}{dt}x_a = -\frac{R}{L}x_a - \frac{R}{L}\frac{K_s}{K_i}y + \frac{1}{L}v_a \tag{4.17a}$$

$$\frac{d}{dt}x_b = -\frac{R}{L}x_b + \frac{1}{L}v_b \tag{4.17b}$$

$$i_a = x_a + \frac{K_s}{K_i}y \tag{4.17c}$$

$$i_b = x_b \tag{4.17d}$$

$$f_{\text{mag}} = K_i x_a \tag{4.17e}$$

Equation (4.17) is a completely general model form for a bias linearized electromagnet set and may be developed in a similar manner for more complicated magnet topologies.

4.4 Actuator assembly

Consistent with Sec. 4.2, suppose that the two coils are driven by power amplifiers according to

$$v_1 = G_{\text{amp},a,1}u_1 - G_{\text{amp},b,1}i_1 \quad \text{and} \quad v_2 = G_{\text{amp},a,1}u_2 - G_{\text{amp}_b,2}i_2$$

and assume that $G_{\text{amp},a,1} = G_{\text{amp},a,2}$ and that $G_{\text{amp},b,1} = G_{\text{amp},b,2}$. This allows us to compute the difference and sum coil voltages,

$$v_a = G_{\text{amp}_a}u_a - G_{\text{amp}_b}i_a \quad \text{and} \quad v_b = G_{\text{amp}_a}u_b - G_{\text{amp}_b}i_b$$

The usual convention for bias linearization with a control signal u and a bias signal U_b is

$$u_1 = U_b + u \quad \text{and} \quad u_2 = U_b - u$$

so that the difference and sum commands become

$$u_a = u \quad \text{and} \quad u_b = U_b$$

With this, assume that U_b is suitably chosen to produce $x_b = X_b$. In this case, it is only necessary to model the control dynamics:

$$v_a = G_{\text{amp}_a}(s)u - G_{\text{amp}_b}(s)i_a \tag{4.18a}$$

$$\frac{d}{dt}x_a = -\frac{R}{L}x_a + \frac{1}{L}v_a - \frac{R}{L}\frac{K_s}{K_i}y \tag{4.18b}$$

$$i_a = x_a + \frac{K_s}{K_i}y \tag{4.18c}$$

$$f_{\text{mag}} = K_i x_a \tag{4.18d}$$

It is worth noting that, while (4.18) seems to be inconsistent with the usual simpler model $f_{\text{mag}} = K_i i - K_s y$, its output equation (4.18d) may be rewritten in terms of the control current $i_{\text{mag},i}$ rather than the magnet state $x_{\text{mag},i}$ by solving (4.18c) for the state in terms of current and displacement. The result is the familiar $f_{\text{mag},i} = K_i i_{\text{mag},i} - K_s y_{\text{mag},i}$. The difference, and the value added by this model, is that the magnet current now depends not only on the amplifier command signal u_i but also on the rotor displacement $y_{\text{mag},i}$. Consequently, the destabilizing effect of K_s turns out to have a bandwidth limit similar to that which is conventionally applied to K_i[1].

In addition, it will prove useful to have the model report the control flux density since this needs to be compared to its limit values (saturation density - bias density) in performance assessment:

$$b \equiv (B_1 - B_2)/2 = \frac{\mu_0 N}{2s_0}x_a$$

Equation (4.18) is written as a mixture of state space and transfer function models. To be consistent with the notation from Sec. 4.2, convert the transfer functions to state space form and introduce standard notation for the electromagnet properties:

$$\frac{d}{dt}\mathbf{x}_{\text{amp},i} = \mathbf{A}_{\text{amp},i}\mathbf{x}_{\text{amp},i} + \mathbf{B}_{\text{amp},1,i}u_i + \mathbf{B}_{\text{amp},2,i}i_{\text{mag},i} \tag{4.19a}$$

$$\begin{bmatrix} u_{\text{amp},i} \\ u_i \end{bmatrix} = \mathbf{C}_{\text{amp},1,i}\mathbf{x}_{\text{amp},i} + \mathbf{D}_{\text{amp},i}u_i \tag{4.19b}$$

$$u_{\text{amp},i} = \mathbf{C}_{\text{amp},2,i}\mathbf{x}_{\text{amp},i} \tag{4.19c}$$

[1] If $G_{\text{amp},a} = G_{\text{amp}_b}$, then both K_i and K_s have the same bandwidth as the nominal amplifier transconductance. However, some AMB amplifier designs select G_2 to have a much lower bandwidth than G_1 with the result that the bandwidth of the K_s term is quite low relative to that of the K_i term. This arrangement can present significant advantages in terms of system stability.

$$\frac{d}{dt}x_{\mathrm{mag},i} = A_{\mathrm{mag},i}x_{\mathrm{mag},i} + B_{\mathrm{mag},1,i}u_{\mathrm{amp},i} + B_{\mathrm{mag},2,i}y_{\mathrm{mag},i} \quad (4.19d)$$

$$i_{\mathrm{mag},i} = C_{\mathrm{mag},1,i}x_{\mathrm{mag},i} + D_{\mathrm{mag},i}y_{\mathrm{mag},i} \quad (4.19e)$$

$$b_{\mathrm{mag},i} = C_{\mathrm{mag},2,i}x_{\mathrm{mag},i} \quad (4.19f)$$

$$f_{\mathrm{mag},i} = C_{\mathrm{mag},3,i}x_{\mathrm{mag},i} \quad (4.19g)$$

in which

$$A_{\mathrm{mag},i} = -\frac{R}{L} \quad B_{\mathrm{mag},1,i} = \frac{1}{L} \quad B_{\mathrm{mag},2,i} = -\frac{RK_s}{LK_i}$$

$$C_{\mathrm{mag},1,i} = 1 \quad C_{\mathrm{mag},2,i} = \frac{\mu_0 N}{2s_0} \quad C_{\mathrm{mag},3,i} = K_i \quad D_{\mathrm{mag},i} = \frac{K_s}{K_i}$$

Using this, the composite electromagnet set/amplifier model may be properly formulated by constructing a state vector which concatenates the amplifier and magnet states and then exploiting the internal connections of (4.19):

$$\frac{d}{dt}\begin{bmatrix}\mathbf{x}_{\mathrm{amp},i}\\ x_{\mathrm{mag},i}\end{bmatrix} = \begin{bmatrix}\mathbf{A}_{\mathrm{amp},i} & \mathbf{B}_{\mathrm{amp},2,i}C_{\mathrm{mag},1,i}\\ B_{\mathrm{mag},1,i}\mathbf{C}_{\mathrm{amp},2,i} & A_{\mathrm{mag},i}\end{bmatrix}\begin{bmatrix}\mathbf{x}_{\mathrm{amp},i}\\ x_{\mathrm{mag},i}\end{bmatrix} + \begin{bmatrix}\mathbf{B}_{\mathrm{amp},1,i}\\ 0\end{bmatrix}u_i + \begin{bmatrix}\mathbf{B}_{\mathrm{amp},2,i}D_{\mathrm{mag},i}\\ B_{\mathrm{mag},2,i}\end{bmatrix}y_{\mathrm{mag},i} \quad (4.20a)$$

$$\begin{bmatrix}u_{\mathrm{amp},i}\\ u_i\\ i_{\mathrm{mag},i}\\ b_{\mathrm{mag},i}\end{bmatrix} = \begin{bmatrix}\mathbf{C}_{\mathrm{amp},1,i} & 0\\ 0 & C_{\mathrm{mag},1,i}\\ 0 & C_{\mathrm{mag},2,i}\end{bmatrix}\begin{bmatrix}\mathbf{x}_{\mathrm{amp},i}\\ x_{\mathrm{mag},i}\end{bmatrix} + \begin{bmatrix}0\\ D_{\mathrm{mag},i}\\ 0\end{bmatrix}y_{\mathrm{mag},i} + \begin{bmatrix}\mathbf{D}_{\mathrm{amp},i}\\ 0\\ 0\end{bmatrix}u_i \quad (4.20b)$$

$$f_{\mathrm{mag},i} = \begin{bmatrix}0\ C_{\mathrm{mag},3,i}\end{bmatrix}\begin{bmatrix}\mathbf{x}_{\mathrm{amp},i}\\ x_{\mathrm{mag},i}\end{bmatrix} \quad (4.20c)$$

Now, for compactness of notation, denote

$$\mathbf{x}_{\mathrm{act},i} \equiv \begin{bmatrix}\mathbf{x}_{\mathrm{amp},i}\\ x_{\mathrm{mag},i}\end{bmatrix} \quad \mathbf{A}_{\mathrm{act},i} \equiv \begin{bmatrix}\mathbf{A}_{\mathrm{amp},i} & \mathbf{B}_{\mathrm{amp},2,i}C_{\mathrm{mag},1,i}\\ B_{\mathrm{mag},1,i}\mathbf{C}_{\mathrm{amp},2,i} & A_{\mathrm{mag},i}\end{bmatrix}$$

$$\mathbf{B}_{\mathrm{act},1,i} \equiv \begin{bmatrix}\mathbf{B}_{\mathrm{amp},1,i}\\ 0\end{bmatrix} \qquad \mathbf{B}_{\mathrm{act},2,i} \equiv \begin{bmatrix}\mathbf{B}_{\mathrm{amp},2,i}D_{\mathrm{mag},i}\\ B_{\mathrm{mag},2,i}\end{bmatrix}$$

$$\mathbf{C}_{\mathrm{act},1,i} \equiv \begin{bmatrix}\mathbf{C}_{\mathrm{amp},1,i} & 0\\ 0 & C_{\mathrm{mag},1,i}\\ 0 & C_{\mathrm{mag},2,i}\end{bmatrix} \quad \mathbf{C}_{\mathrm{act},2,i} \equiv \begin{bmatrix}0\ C_{\mathrm{mag},3,i}\end{bmatrix}$$

$$\mathbf{z}_{\mathrm{act},i} \equiv \begin{bmatrix}u_{\mathrm{amp},i}\\ u_i\\ i_{\mathrm{mag},i}\\ b_{\mathrm{mag},i}\end{bmatrix} \quad \mathbf{D}_{\mathrm{act},1,i} \equiv \begin{bmatrix}\mathbf{D}_{\mathrm{amp},i}\\ 0\\ 0\end{bmatrix} \quad \mathbf{D}_{\mathrm{act},2,i} \equiv \begin{bmatrix}0\\ D_{\mathrm{mag},i}\\ 0\end{bmatrix}$$

so that (4.20) may be written as

$$\frac{d}{dt}\mathbf{x}_{\mathrm{act},i} = \mathbf{A}_{\mathrm{act},i}\mathbf{x}_{\mathrm{act},i} + \mathbf{B}_{\mathrm{act},1,i}u_i + \mathbf{B}_{\mathrm{act},2,i}y_{\mathrm{mag},i} \tag{4.21a}$$

$$\mathbf{z}_{\mathrm{act},i} = \mathbf{C}_{\mathrm{act},1,i}\mathbf{x}_{\mathrm{act},i} + \mathbf{D}_{\mathrm{act},1,i}u_i + \mathbf{D}_{\mathrm{act},2,i}y_{\mathrm{mag},i} \tag{4.21b}$$

$$f_{\mathrm{mag},i} = \mathbf{C}_{\mathrm{act},2,i}\mathbf{x}_{\mathrm{act},i} \tag{4.21c}$$

In this manner, the entire collection of amplifiers and electromagnets may be represented by

$$\frac{d}{dt}\mathbf{x}_{\mathrm{act}} = \mathbf{A}_{\mathrm{act}}\mathbf{x}_{\mathrm{act}} + \mathbf{B}_{\mathrm{act},1}\mathbf{u} + \mathbf{B}_{\mathrm{act},2}\mathbf{y}_{\mathrm{mag}} \tag{4.22a}$$

$$\mathbf{z}_{\mathrm{act}} = \mathbf{C}_{\mathrm{act},1}\mathbf{x}_{\mathrm{act}} + \mathbf{D}_{\mathrm{act},1}\mathbf{u} + \mathbf{D}_{\mathrm{act},2}\mathbf{y}_{\mathrm{mag}} \tag{4.22b}$$

$$\mathbf{f}_{\mathrm{mag}} = \mathbf{C}_{\mathrm{act},2}\mathbf{x}_{\mathrm{act}} \tag{4.22c}$$

The reason for retaining the outputs $\mathbf{u}_{\mathrm{amp}}$, $\mathbf{u}$, $\mathbf{i}_{\mathrm{mag}}$, and $\mathbf{b}_{\mathrm{mag}}$ (the elements of $\mathbf{z}_{\mathrm{act}}$) is that later, when evaluating the performance of the system, it will make sense to look at these signals to ensure that they don't exceed acceptable limits. Thus, these signals become *performance measures*. In particular, the amplifier voltages should not exceed the power supply limits, the magnet currents should not exceed amplifier capacities or coil ratings, and the magnet flux densities should not exceed the magnetic saturation limits.

4.5 Examples

To understand the nature of this model, two examples are developed here. Both examples use the simple two horseshoe electromagnet set depicted in Fig. 4.4. In the first example, the amplifier is assumed to have the same transfer function to voltage as current: $G_{\mathrm{amp},a} = G_{\mathrm{amp},b}$ with a nominal closed loop transfer function T having a bandwidth of 800 Hz. In the second example, the two transfer functions are altered so that the amplifier has, effectively, a transpermeance behavior: the magnet flux tracks the amplifier input signal u.

4.5.1 Electromagnet model

The parameters of the electromagnet are listed in Table 4.1. Each opposed magnet saturates at a current of

$$i_{\mathrm{sat}} = \frac{2s_0 B_{\mathrm{sat}}}{\mu_0 N} = 9.5\,\mathrm{A}$$

and has the potential to produce a saturation force of

$$f_{\mathrm{sat}} = \frac{B_{\mathrm{sat}}^2 A\cos\theta}{\mu_0} = 1059\ \mathrm{N}$$

Table 4.1. Model parameters of the electromagnet set for the example

parameter	value
A, pole area	1000 mm^2
N, coil turns	100
s_0, nominal air gap	0.5 mm
θ, pole angle	22.5°
R, coil resistance	0.5 Ω
$i_b = X_b$, bias current	3.82 A
B_{sat}, saturate flux density	1.2 Tesla
L_0, nominal inductance	12.6 mH

The linearized coefficients of the magnet set are

$$K_i = 177.4\,\text{N/A} \quad K_s = -1.252\,\text{kN/mm}$$

Assuming that the coil currents are limited to be always non-negative, the linearization is valid at least until the control current matches the bias current:

$$f_{\text{linear}} = K_i i_b = 677.6\,\text{N}$$

which is slightly more than half of the saturation capacity[2]. If the currents *are* permitted to go negative, then the peak force is reached when the sum of the control current and the bias current equal the saturation current:

$$f_{\max} = K_i(i_{\text{sat}} - i_b) = 1016\,\text{N}$$

which is only four percent lower than the saturation force.

Following the development of Sect. 4.3, the model of this electromagnet set becomes

$$\frac{d}{dt}x_{\text{mag}} = -39.8x_{\text{mag}} + 79.8u_{\text{amp}} + 2.8 \times 10^5 y_{\text{mag}} \tag{4.23a}$$

$$i_{\text{mag}} = x_{\text{mag}} - 7058y_{\text{mag}} \tag{4.23b}$$

$$b_{\text{mag}} = 0.126x_{\text{mag}} \tag{4.23c}$$

$$f_{\text{mag}} = 177.4x_{\text{mag}} \tag{4.23d}$$

4.5.2 Transconductance Amplifier

First, consider use of a conventional transconductance amplifier, designed to produce one ampere of output for one volt applied. Assuming a bandwidth of

[2] The useful linear range of the actuator is probably actually higher than this because saturation effects in the stator iron will mitigate the apparent quadratic rise in actuator force beyond this point: a careful finite element analysis or experimental assessment is needed to accurately determine the useful linear range of the actuator

800 Hz and reasonably well tuned damping, the closed loop transconductance when driving the resistance and nominal inductance of the electromagnets described above is

$$T(s) = \frac{2.53 \times 10^7}{s^2 + 7108s + 2.53 \times 10^7}$$

and, using the nominal inductance and resistance reported in Table 4.1, the transfer functions from signal and current to output voltage are

$$G_{\mathrm{amp},a} = G_{\mathrm{amp},b} = \frac{3.18 \times 10^5 s + 1.26 \times 10^7}{s^2 + 7108s}$$

The full model may be assembled as outlined in Sect. 4.4. The resulting model is inconvenient to report in state space form, but the transfer functions from reference signal to force and from journal displacement to force are:

$$\begin{aligned} f_{\mathrm{act}}(s) = &\frac{4.48 \times 10^9}{(s^2 + 7108s + 2.53 \times 10^7)} u(s) \\ &+ \frac{4.98 \times 10^7 (s + 6.42 \times 10^5)(s + 39.35)}{(s + 39.79)(s^2 + 7108s + 2.53 \times 10^7)} y_{\mathrm{mag}}(s) \end{aligned}$$

For comparison purposes, it is useful to nondimensionalize these two transfer functions. Rescale y_{mag} by dividing by the natural displacement scale of the rotor: the nominal air gap: $\hat{y}_{\mathrm{mag}} = y_{\mathrm{mag}}/s_0$. Rescale $u(s)$ by the natural current request scale of the electromagnets. In this case, since one volt requests one amp and the natural current scale is the bias current, use this to rescale u: $\hat{u} = u/i_b$. Finally, nondimensionalize the output force by the "linear limit" computed previously: $\hat{f}_{\mathrm{act}} = f_{\mathrm{act}}/f_{\mathrm{linear}}$. The resulting Bode plots are shown in Fig. 4.5.

The main things to notice in Fig. 4.5 are that:

1. the nondimensionalized DC gains are both 1.0
2. the bandwidth of both effects is about 800 Hz (the amplifier's nominal bandwidth)

4.5.3 Transpermeance Amplifier

Rather than constructing an amplifier which attempts to make the output current track a reference signal, it seems to make better sense to consider making the output *flux density* track a reference signal. Since the force – flux relationship is not sensitive to the rotor position, this might reduce the destabilizing effect of K_s.

However, without actually installing flux sensors on the magnet faces, this behavior can only be approximated. One way to do this, is to note that the flux can be computed in two ways:

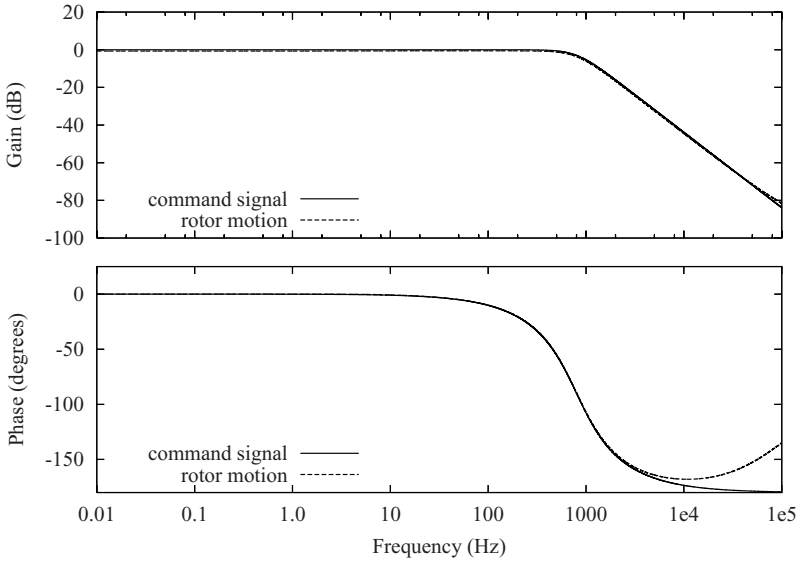


Fig. 4.5. Bode plot of actuator gain from command signal and rotor diplacement to force, transconductance amplifier.

1. by measuring the current:

$$B = \frac{\mu_0 N}{2(s_0 \pm x)} i$$

2. by integrating the coil voltage:

$$B = \int \frac{1}{NA}(u - iR)dt$$

The first estimate is only as good as knowledge of the actual gap while the second estimate has problems at very low frequencies, where the integral is difficult to compute. Assuming that the rotor motion at very low frequencies is negligible (use of an integrator in the feedback controller will help ensure this), a reasonable estimate of flux at low frequencies is:

$$B_{\text{low}} = \frac{\mu_0 N}{2s_0} i$$

while at high frequencies[3]:

[3] This model neglects the effects of eddy currents in the stator iron. It is possible to include these as well, but we have omitted this effect for clarity of presentation. For a well-laminated stator, it is reasonable to neglect the eddy currents for frequencies as high as perhaps 800 Hz.

$$B_{\text{high}} = \frac{1}{sNA}(u - Ri)$$

Combine these two by the simple rule

$$B = \frac{a}{s+a}B_{\text{low}} + \frac{s}{s+a}B_{\text{high}}$$

Thus, the estimate is

$$\begin{aligned} B &\approx \frac{\mu_0 Na}{2s_0(s+a)}i + \frac{1}{NA(s+a)}(u - Ri) \\ &= \left(\frac{\mu_0 Na}{2s_0(s+a)} - \frac{R}{NA(s+a)}\right)i + \frac{1}{NA(s+a)}u \\ &= \frac{\mu_0 N^2 Aa - 2s_0 R}{2s_0 NA(s+a)}i + \frac{1}{NA(s+a)}u \end{aligned}$$

That is, the amplifier should compare the reference signal to a combination of measured coil current and output voltage.

Using this strategy, the following pair of amplifier transfer transfer functions was derived:

$$G_a = \frac{318000(s+39.62)(s+0.6283)}{(s+40.06)(s^2+7069s+2.5\times 10^7)} \qquad G_b = -\frac{39.16}{s+0.6283}_a$$

Notice that the current feedback gain is negative now, so the system is effectively using *positive* current feedback if $a < L/R$. In the special case that $a = L/R$, the scheme becomes *pure voltage control*.

The resulting performance is illustrated in Fig. 4.6 which uses the same nondimensionalization as in the previous example. The key difference is that the gain on rotor motion, which is destabilizing, rolls off very early (a frequency of 0.1 Hz was selected for a above) and is about 40 dB lower from 10 Hz to 1 kHz than with the transconductance amplifier. Thus, the effect is very significant.

4.6 Driving Modes and Linearization

In Sec. 3.1.4 and also in Sec. 4.3 it was shown how the force-current characteristics can be linearized by differential drive. In a radial bearing, two pole pairs are driven independently by two power amplifiers, as shown in Fig. 3.10.

4.6.1 Differential Winding

The same effect can be achieved through differential coils, as indicated in Fig. 4.7. Here, each pole pair is equipped with a premagnetization coil and a control coil. The premagnetization coil of all pole pairs are connected in series,

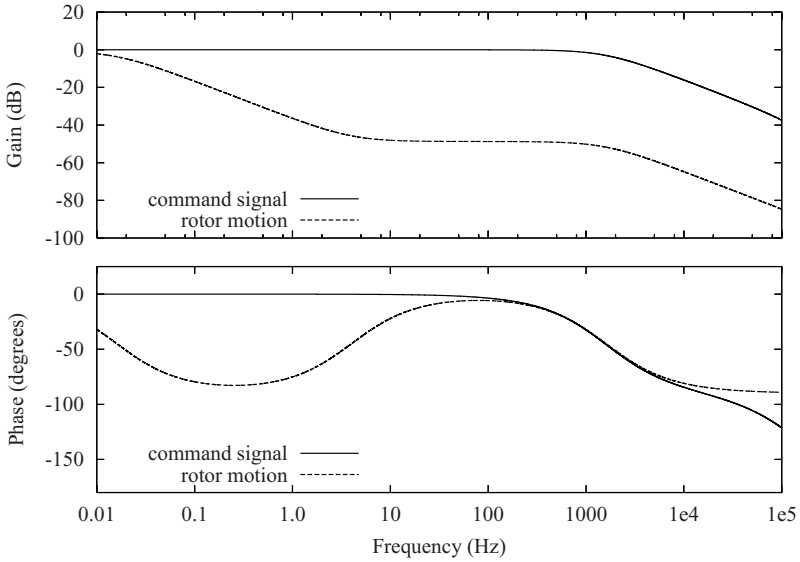


Fig. 4.6. Bode plot of actuator gain from command signal and rotor diplacement to force: transpermeance amplifier.

and supplied by a constant bias current. The control coil of two opposing pole pairs are connected in series in such a way that the flux generated by the bias and the control current add in one pole pair and substract in the other. With this drive mode only two power amplifiers and one (generally less expensive) constant current source per radial bearing are necessary.

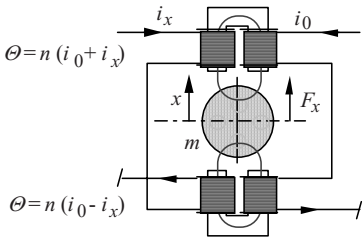


Fig. 4.7. Differential coils for linearization of the force-current characteristics

However, the copper losses in the coils are higher than with differential drive. This becomes particularly obvious at maximum input, where the maximum force is generated. In one magnet, the flux of the premagnetization coil and the control coil are added. In the opposing magnet the flux vanishes,

although the premagnetization and control coil have the maximum current (and copper losses).

A similar objective is accomplished by permanent magnet biasing, as described in Sect. 3.2. The advantage to permanent magnet biasing is that the copper loss penalty is eliminated.

4.6.2 External Linearization

The nonlinear relation between current and force can also be compensated by an electronic circuit. The desired current signal is fed through a compensation circuit, and the power amplifiers are driven by the corrected desired value of the current. When the polarity changes, the control system must switch from one pole pair to the opposite one.

In Fig. 4.8, the quadratic relationship between the current and the force from equation (4.13) is compensated by a root-forming circuit and the relationship between the displacement and the force is compensated using a multiplier circuit.

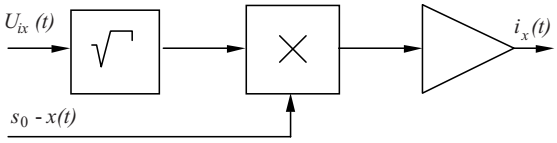


Fig. 4.8. External linearization by root and multiplier circuits

When a microprocessor is used for control, it can linearize with a (measured) table, i.e. it replaces each output value by the corresponding table value before being sent to the DA converter. The advantage of external linearization is that only those magnets in the direction of which a force shall be generated carry a current. From this, the smallest possible losses in the bearing magnet result. However, one considerable disadvantage is that, near the zero point of the force-current characteristic - and due to the horizontal tangent at the zero point - a significant current increase is necessary to obtain only a modest force increase. Since the slope of the current is limited by the available voltage, bad dynamic behavior occurs near the zero point. Therefore, external linearization should only be applied where heavy static loads push the operating point of the bearing far beyond the zero point. Considerable research has been done on this problem: see especially [4, 7].

4.6.3 Amplifier Modes

The most common amplifier mode described in the AMB literature and underlying most models is *transconductance* in which the output voltage is chosen

to attempt to drive the magnet coil currents to track a reference signal: this is the mode described in the example of Sect. 4.5.2. However, as that example illustrated, transconductance mode emphasizes the destabilizing properties of the actuator. Indeed, it can be shown that saturation nonlinearities and eddy current effects are also emphasized by this wide bandwidth feedback of output current.

Section 4.5.3 illustrated the improvement in actuator performance that can be achieved by changing amplifier mode from transconductance to *transpermeance*: even better performance can be realized by actually feeding back measured magnet flux instead of estimating the flux. These observations lead to an interest in avoiding transconductance mode and using a more general approach to combined control of the actuator and the overall system. Such an approach is generally referred to as a *voltage* mode because output current is not fedback through a dedicated loop in the amplifier but is, instead, made available to the AMB controller as one of many signals used in making control decisions. Such approaches have received substantial attention in the literature: see, for example, [1, 2, 3, 8].

4.7 Response Limitations of the Magnetic Actuator

The linear model presented by (4.22) assumes that the amplifier output voltage is linearly related to input signals and that the electromagnets are not saturated: that iron permeability is very high compared to that of air. Of course, this model is only valid over some limited range: the output voltage of the power amplifier cannot exceed the power supply bus (DC link) potential, the current is usually limited to protect the amplifier's output devices, and the electromagnet iron will certainly saturate at a very finite flux density. These limits lead to an amplitude limitation on the forces generated by the actuator.

Current / Flux Limitation

The current provided by the amplifiers is limited to $i_{\max}$. The premagnetization (bias) current i_0 is selected to be some fraction γ of the maximum output current $i_{\max}$. For practical purposes, $0.2 < \gamma \leq 0.5$. Hence, a control range of $\pm(1-\gamma)i_{\max}$ for the control current i_x results. The gain of the bias linearized actuator scales in proportion to γ so the force range limitation due to this biasing choice scales roughly as $\gamma(1-\gamma)$. The peak value of this product is attained for $\gamma = 0.5$ where $\gamma(1-\gamma) = 0.25$. However, thermal considerations may dictate operation at lower values of γ. At a bias ratio of $\gamma = 0.3$, this product diminishes to $\gamma(1-\gamma) = 0.21$.

In a properly matched amplifier–electromagnet combination, this maximum output current results in a saturated electromagnet. That is,

$$B(i_{\max}) = B_{\text{sat}}$$

where this saturation is attained with the journal in its worst case position: usually displaced as far from the electromagnet as possible. Of course, the magnet flux density also depends on the air gap distribution in the actuator so this condition is, ideally, met for the worst case air gap distribution, which means that the magnets may saturate at a lower current when the gap distribution is other than this worst case condition.

In any case, it is common to design this pair to essentially match $i_{\max}$ to B_{sat} on the premise that an undersaturated magnet wastes iron while an undersaturated amplifier wastes capacity. Hence, the two limitations are considered to be the same for the present discussion.

Voltage Limitation

Faraday's induction law dictates that limitations in the output voltage of the amplifier to $\pm U_p$ limit the achievable current rate di_x/dt. When the magnetic circuits of an electromagnet array do not interact as in Fig. 4.4, each electromagnet winding may be simplified as an R-L series connection:

$$u_{\text{amp}} = L\frac{di_{\text{mag}}}{dt} + Ri_{\text{mag}}$$

For a sinusoidal voltage with frequency ω, the current response will also be sinusoidal:

$$|u_{\text{amp}}| = \sqrt{L^2\omega^2 + R^2}\,|i_{\text{mag}}| \le U_p$$

Thus, at $\omega = 0$, it would appear that U_p should be chosen as $U_p = Ri_{\max}$: any larger voltage would *apparently* represent excess capacity. However, this would severely limit the dynamic performance of the actuator because it would result in much lower maximum current swings at higher frequencies:

$$|i_{\text{mag}}| \le \frac{1}{\sqrt{L^2\omega^2 + R^2}}U_p$$

Consequently, U_p is generally much larger than $Ri_{\max}$.

Define the frequency

$$\omega_{\text{sat}} \equiv \sqrt{\frac{\left(\frac{U_p}{(1-\gamma)i_{\max}}\right)^2 - R^2}{L^2}} \tag{4.24}$$

and the coil current is subject to the *pair* of limitations:

$$|i_{\text{mag}}| \le \begin{cases} (1-\gamma)i_{\max} : 0 \le \omega_{\text{sat}} \\ \frac{U_p}{\sqrt{L^2\omega^2+R^2}} \quad : \omega > \omega_{\text{sat}} \end{cases}$$

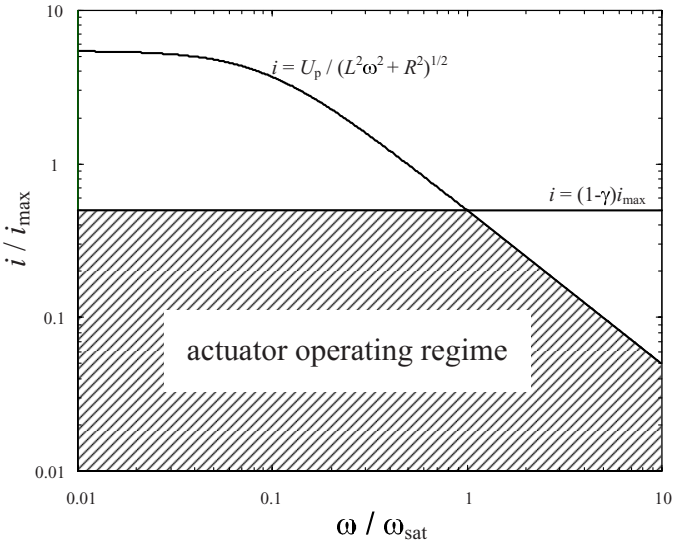


Fig. 4.9. Operating range of a magnetic bearing actuator (power amplifier with bearing magnet)

This limitation is presented in Fig. 4.9. The characteristic frequency for this limitation, ω_{sat} is sometimes referred to as the *knee frequency* or *power bandwidth*.

At frequencies beyond ω_{sat}, the output voltage of the amplifier enters saturation if the current is pushed beyond the curve indicated in Fig. 4.9, and the dynamic behavior of the amplifier becomes nonlinear. This limitation can be mitigated by increasing the amplifier power. To see this, recognize that

$$i_{\max} \propto \frac{1}{N} \quad \Rightarrow \quad i_{\max} = \frac{i_{\max,N}}{N}$$

where N is the number of coil terms while, at the same time,

$$R = R_N N \quad \text{and} \quad L = L_N N^2$$

in which $i_{\max,N}$, R_N, and L_N may be considered properties of the electromagnet which are essentially independent of the number of winding turns. With this, (4.24) becomes

$$\omega_{\text{sat}} \equiv \frac{i_{\max}}{i_{\max,N}} \sqrt{\frac{\left(\frac{U_p}{(1-\gamma)i_{\max,N}}\right)^2 - R_N^2}{L_N^2}} \tag{4.25}$$

As stated previously, $U_p \gg (1-\gamma) i_{\max} R$ so that

$$\omega_{\text{sat}} \approx i_{\max} U_p \frac{1}{(1-\gamma) i_{\max,N}^2 L_N} \tag{4.26}$$

The *power capacity* of the amplifier is the product of maximum voltage and maximum current: $P_{\text{amp}} = U_p i_{\max}$ so, for a given magnet design and biasing level, the power bandwidth of the actuator is simply proportional to the power capacity of the amplifier.

Finally, noting that if the rotor is not moving, then the actuator force may be accurately approximated as

$$f = K_i i_{\text{mag}}$$

then the maximum rate of change of the actuator force is

$$\left|\frac{df}{dt}\right| = K_i \left|\frac{di_{\text{mag}}}{dt}\right| = K_i \left|\frac{u_{\text{amp}} - Ri_{\text{mag}}}{L}\right| < \frac{U_p K_i}{L}$$

For a simple pair of opposed horseshoes as depicted in Fig. 4.4,

$$L = \frac{\mu_0 A N^2}{2s_0} \quad \text{and} \quad K_i = \frac{\mu_0 A \cos\theta N^2 \gamma i_{\max}}{s_0^2} \quad \Rightarrow \quad \frac{K_i}{L} = \frac{2\cos\theta\gamma i_{\max}}{s_0}$$

so that the actuator maximum force slew rate is

$$\left|\frac{df}{dt}\right| < i_{\max} U_p \frac{2\gamma\cos\theta}{s_0} \tag{4.27}$$

Again, the amplifier power product controls the maximum rate of change of actuator force. Here, note that this maximum slew rate is also dependent upon the biasing ratio γ: increasing the biasing ratio increases the available slew rate up to the useful limit of $\gamma \leq 0.5$. Further, the slew rate is inversely related to the nominal air gap length: reducing the nominal gap will increase the available slew rate.

Note that, for this geometry, (4.26) may be further interpreted by using the relationship

$$f_{\max} = K_i(1-\gamma) i_{\max}$$

so that

$$\omega_{\text{sat}} \approx i_{\max} U_p \frac{2\gamma\cos\theta}{s_0 f_{\max}} \tag{4.28}$$

Eddy current issues

The assumptions in developing the linear magnet model (4.17) also hold for alternating fields with frequencies of up to approximately 2 kHz, if the eddy currents in the stator and in the rotor can be reduced sufficiently (lamination). In experiments reported in [6] with a radial bearing constructed from sheets of a thickness 0.35 mm, a constant force-current factor k_i was measured up to a frequency of 1.4 kHz.

If, for any reason, solid (non-laminated) iron is used, k_i is reduced when the frequency increases, since the eddy-currents reduce the generating magnetic

field. Additionally, the penetration depth of the field, and consequently the available iron cross section, are reduced. This is particularly true for thrust bearings where lamination of the stator is difficult and lamination of the rotor is generally not feasible. In such cases, the dynamic model of the electromagnet may be extended to approximately include the effect of these eddy currents, as outlined for instance in [9].

4.8 Measuring System Characteristics

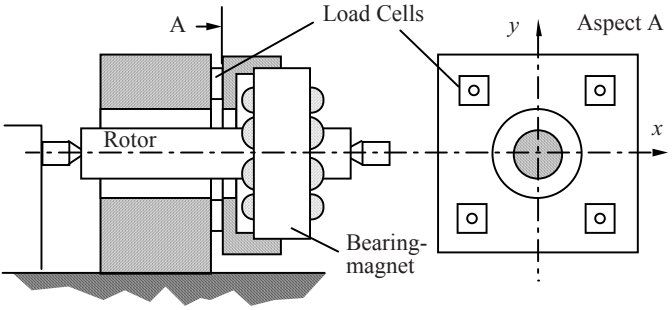


Fig. 4.10. Cross-section of a dynamometer.

Calculated characteristics of magnetic bearings have to be validated by measurements. Of primary interest when current control is used (the conventional approach) are the relationships between control current and bearing force for various displacements of the rotor from its rest position. To determine hysteresis loss, one has to consider the braking (drag) torques.

The Force of Bearing Magnets as a Function of Control Current

Measurement of the static force-current characteristics of a bearing is best done using a dynamometer. Figure 4.10 shows a setup allowing the measurement of forces in $x-$ and $y-$ directions. With this arrangement, the stator can be mounted on the table base of a lathe and the rotor fixed between mandrels, which allows easy adjustment of the radial rotor displacement. Note, of course, that it is critical in such an experimental setup that the mechanical stiffness of the test fixture must be larger than the magnitude of k_s.

If a full control loop is available, the rotor has only one or two radial bearings, and there is access to the rotor when levitated, then an alternative method of characterizing the bearing magnets uses the full system. In this case, the rotor is levitated with a controller that includes the integral of the rotor position so that the rotor position will stay fixed independent of static

load. Various static loads are applied to the rotor and the bearing currents are noted. For modest static loads, the currents should vary in proportion to the load:

$$f_{external} = k_i i \quad \Leftrightarrow \quad k_i = \frac{\delta f_{external}}{\delta i} \tag{4.29}$$

Note that it is usually necessary to consider the location of load application relative to the bearing locations to determine that portion of the applied load that is actually seen by each bearing.

Once the actuator gain is measured using this approach, the magnetic stiffness, k_s, can be assessed in a simple manner. With no external loads applied, introduce a position offset so that the rotor position moves by a distance δx. Most digital control systems provide a reference position offset which permits such a shift. As the rotor position changes, the currents must also change because the applied load does not. Consequently for two different positions x_1 and x_2:

$$k_i i_1 - k_s x_1 = k_i i_2 - k_s x_2 \quad \Leftrightarrow \quad k_s = k_i \frac{i_1 - i_2}{x_1 - x_2} \tag{4.30}$$

Because k_s is actually dependent on the equilibrium position of the rotor, this test should be conducted for a number of different positions x_2 and a polynomial regression performed on i as a function x: finally, $k_s = k_i di/dx$.

Measuring Dynamic Bearing Forces

It is difficult to measure dynamic forces, since the force signals provided by the measurement cell practically always include inertia forces. These are caused by the motion of the object to be measured and the measuring equipment.

If the dynamometer provides sufficient stiffness the inertia forces can be compensated by taking into account the signals from one or several acceleration sensors on the mounting plate.

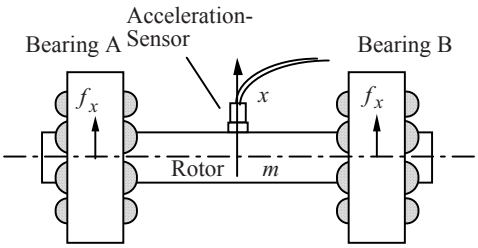


Fig. 4.11. Determination of the dynamic bearing forces by measuring rotor acceleration.

Instead of using the signal of an acceleration sensor to compensate inertia forces, the dynamic bearing force can also be determined directly from the

measured acceleration of the magnetically born rotor [5]. To do this, the signal for the desired rotor position can be modulated with a test signal while measuring the acceleration of the suspended rotor simultaneously. White noise can be used as a test signal. With a stiff rotor having a mass m, the bearing force acting on the rotor is easily linked to the measured acceleration signals in the $x-$ direction by the equation

$$m\ddot{x} = 2f_x \quad \text{with } f_x = k_i i_x - k_s x \tag{4.31}$$

The frequency spectrum of the acceleration measured thus directly shows the frequency spectrum of the bearing forces $2f_x$.

To determine the behavior of the force-current factor k_i within a certain frequency range, the spectrum of the current must also be measured. The force-current spectrum ratio leads to the spectrum of k_i corresponding to a transfer function between the current and force.

Since the bearing force f_x includes a term $k_s x$, and since the rotor moves during measurement, this part of the force must be compensated with the displacement spectrum measured. To do this, one has to measure the transfer function between the displacement and current (Fig. 4.12b). The sum of the transfer functions force/current (Fig. 4.12a), and that of displacement/current yields the spectrum of k_i shown in Fig. 4.12c.

References

1. Bleuler, H., Vischer, D., Schweitzer, G., Traxler, A. and Zlatnik, D. New concepts for cost-effective magnetic bearing control. *Automatica*, Vol. 30, No. 5, May 1994, pp. 871–6.
2. Lichuan Li, Shinshi, T., and Shimokohbe, A., "Asymptotically exact linearizations for active magnetic bearing actuators in voltage control configuration," *IEEE Transactions on Control Systems Technology*, Vol. 11, No. 2, March 2003, pp. 185–95.
3. Lindlau, J.D. and Knospe, C.R., "Feedback linearization of an active magnetic bearing with voltage control," *IEEE Transactions on Control Systems Technology*, Vol. 10, No. 1, Jan. 2002, pp. 21–31.
4. Sivrioglu, S., Nonami, K. and Saigo, M., "Low power consumption nonlinear control with $\mathcal{H}_\infty$ compensator for a zero-bias flywheel AMB system," *Journal of Vibration and Control*, Vol. 10, No. 8, Aug. 2004, pp. 1151–66.
5. Traxler, A. and Schweitzer, G. "Measurement of the Force Characteristics of a Contactless Electromagnetic Rotor Bearing." 4th Symposium of the IMEKO TC on Measurement Theory, Bressanone, Italy, May 1984.
6. Traxler, A., "Eigenschaften und Auslegung von berührungsfreien elektromagnetischen Lagern." Diss ETH Zürich Nr. 7851, 1985
7. Tsiotras, Panagiotis and Wilson, Brian C., "Zero- and low-bias control designs for active magnetic bearings," *IEEE Transactions on Control Systems Technology*, Vol. 11, No. 6, November 2003, pp. 889–904.

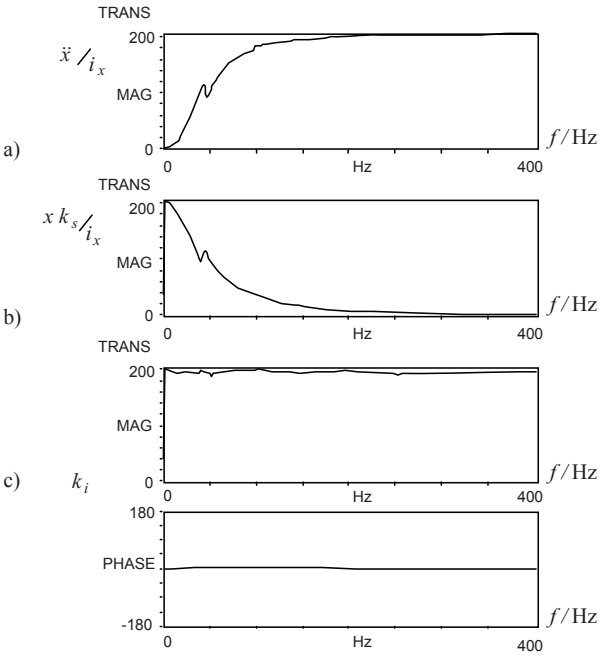


Fig. 4.12. Transfer functions: a) Acceleration/current, b) Displacement/current, and c) Force/current measured with a Fourier signal analyzer and noise exitation.

8. Vischer, D., Bleuler, H., "A new Approach to Sensorless and Voltage Controlled AMBs Based on Network Theory Concepts". 2nd Internat. Symp. on Magnetic Bearings, July 12-14, 1990, Tokyo, Japan.
9. Zhu, L., Knospe, C. R., and Maslen, E. H., "An Analytic Model for a Non–laminated Cylindrical Magnetic Actuator Including Eddy Currents," IEEE *Transactions on Magnetics.* Vol. 41, No. 4, April 2005, pp 1248–1258.

5

Losses in Magnetic Bearings

Alfons Traxler

5.1 Overview

Active magnetic bearings generally have much lower losses than roller bearings or fluid film bearings. However, since AMBs are complex mechatronic systems, there are many potential power loss mechanisms. Consequently, the minimizing of losses is the sum of various measures and depends very much on the requirements of the application. Whereas for turbomachinery, minimizing of the overall losses to increase the efficiency is most important, in vacuum applications like turbomolecular pumps, the focus lies on minimizing the losses in the rotor to avoid heating of the rotor since cooling is not effective. Figure 5.1 shows the flow of energy necessary to cover the losses from the sources (drive-electronics and AMB-electronics) to the power loss mechanisms.

With contact-free rotors there is no conventional mechanical friction in the magnetic bearings. However, aerodynamic or windage losses continue to act on the rotor and the magnetic fields introduce a new loss mechanism: iron losses. A braking torque resulting from iron loss occurs in the ferromagnetic bearing bushes, or journals, of the rotor. These losses, which heat up the rotor, have to be compensated by the drive power of the motor. A large portion of iron losses comes from eddy currents induced in the (non-laminated) target of axial bearings when compensating for dynamic axial loads.

Section 5.2 focuses on iron losses, covering magnetic hysteresis in Sect. 5.2.1 and eddy current losses in Sect. 5.2.2. Section 5.3 then provides a summary of windage losses. The chapter concludes with a discussion of experimental measurement of rotor losses in Sect. 5.4 and hints on measures to reduce losses in Sect. 5.5.

5.1.1 Rotor Losses

Aerodynamic Loss (Windage Loss, Gas Friction Loss)

Aerodynamic losses are dominant in high speed applications especially in compressors and expanders where the gas is under high pressure but obviously

G. Schweitzer, E.H. Maslen (eds.), *Magnetic Bearings*,
DOI 10.1007/978-3-642-00497-1_5, © Springer-Verlag Berlin Heidelberg 2009

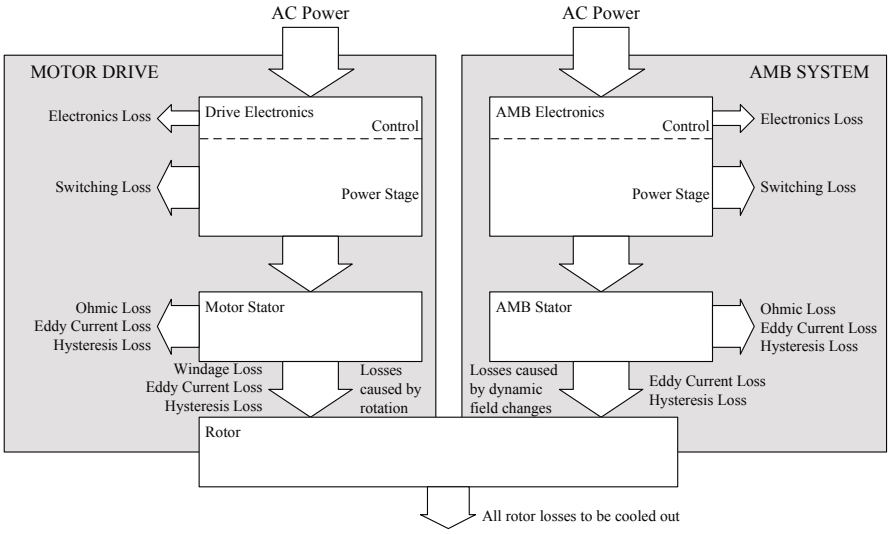


Fig. 5.1. Flow of energy covering losses in a motor driven AMB system.

not in vacuum applications. The dominant part of these losses is caused independently of the bearings, in the motor, in sealings etc.. Often the thrust bearing disc with its high circumferential speed is the most critical bearing part with respect to windage losses.

As a rule of thumb, the air losses basically are proportional to the cube of circumferential speed. The calculation of a good approximation of air loss is difficult. Results of various analytical methods differ very much and are valid only for a small range of specific cases. They may have to be validated experimentally for a specific case. The method described in Sect. 5.3 is based on experimental results for small machines.

Iron Loss (Magnetic Loss)

Magnetic losses on the rotor are caused by the variation of the magnetic flux density B in the iron parts. For high speed applications, the *eddy current* losses are most important. Changes of flux density induce eddy currents in the iron. These eddy currents generate losses via the electrical resistance in the iron. The flux density and polarity varies when the iron of the rotating rotor moves along the poles of the bearing magnets with opposite polarity. The eddy current losses are basically proportional to the square of the frequency of the variation and therefore proportional to the square of the rotor speed and proportional to the square of the amplitude of the flux density. The eddy current losses can be reduced by increasing the electrical resistance of the iron and by lamination of the iron (see Sect. 5.2.2). Since the magnetic field distribution around the rotor is rather far from being sinusoidal, its Fourier series

representation will include many harmonics of the rotational angle. Especially higher order harmonics will be expelled from the laminations due to the skin effect. A detailed analysis of rotating losses can be found in [8].

The hysteresis losses are caused by the hysteresis in the magnetization of ferromagnetic material (see Sect. 3.1.2 on *Properties of Ferromagnetic Materials*) [1]. The hysteresis losses are basically proportional to rotor speed and are therefore not as critical in high speed applications as the eddy current losses. They also depend on the flux density B and are proportional to $B^{1.6}$. A detailed treatment of the hysteresis losses can be found in [9].

The iron losses can be influenced by the design of magnetic bearings, via homopolar vs. heteropolar design (see Sect. 5.2.2), the volume of the iron, the lamination of iron, the use of iron with small hysteresis-loop of the *B-H*-diagram and high Ohmic resistance, etc.

5.1.2 Losses in the Bearing Magnets (Stator)

Copper Loss (Ohmic Loss)

The copper losses, caused by the control current in the resistance of the coils are usually dominant in the bearing magnets. The thermal balance between copper losses and cooling capacity is the most important design criterion of the bearings. The copper losses can be influenced in the design process by balancing the amount of volumes for copper and for iron within the total available volume for the bearing. The copper losses can be reduced by using a larger cross section of the copper wires, obviously leading to more volume for the copper (see. Sect. 3.1.5 on *Design of Bearing Magnets*) [7].

Iron Loss

The description of the iron losses in Sect. 5.1.1 is valid also for the losses in the bearing magnets. But the variation of the flux density in the bearing magnets is caused by the variation of the control current. On one hand it is caused by the variations of flux to vary the bearing force and on the other hand variations (ripple) are caused by the pulse width modulation (PWM) of the power amplifiers (Sect. 3.3 on Power Amplifiers, Fig. 3.25).

5.1.3 Losses in the Power Amplifier

The power amplifier supplies to the bearing magnet primarily reactive power and secondarily the power to cover the copper losses and the magnetic losses in the stator as well as copper losses in the cables. The losses in the control electronics and the power supply are usually negligible compared to losses in the power stage.

There are two basic designs of power amplifiers: Analog amplifier and switched amplifier (see. Sect. 3.3 on *Power Amplifiers*). Because switched

power amplifiers are by far more efficient than analog amplifiers, analog amplifiers are used only for special applications (i.e. if noise is crucial).

In switched amplifiers, switching losses are dominant. The switching losses are about proportional to the switching frequency and depend on the design of the electronic switches and the properties of the specific switching transistors employed. Usually, the switching frequency is not lower than 20 kHz to avoid noise in the audible frequency range. High switching frequency reduces the ripple on the control current and as a consequence reduces the iron losses in the bearing magnets.

5.1.4 Losses in Cables

In applications where long cables (> 20m) are used, the Ohmic losses in the cables may present a substantial part of the total losses. The losses in the cables depend on the length and the cross section of the cable wires. The losses in the cables have to be covered by the power amplifiers.

5.2 Iron Losses in the Rotor

The iron loss P_{fe} depends on the rotor speed, the material used for the bearing bushes, and the distribution of flux density B over the circumference of the bushes. The braking torque caused by the iron losses consists of a constant component of hysteresis loss and a component of eddy-current losses which increase with the rotational speed (see also Fig. 5.11).

5.2.1 Hysteresis Losses P_h

At remagnetization, the iron in the B-H-diagram travels along a hysteresis loop (Fig. 3.5). At each loop, the energy diminishes by $W_h = V_{fe} A_{BH}$. Here, A_{BH} stands for the area of the hysteresis loop, and V_{fe} for the volume of the iron. Consequently, the hysteresis losses are proportional to the frequency of remagnetization f_r. The area of the hysteresis loop depends on the material of the magnet and on the amplitude B_m of the flux density. For iron and flux densities between 0.2 and 1.5 Tesla, the relationship

$$P_h = k_h f_r B_m^{1.6} V_{fe} \tag{5.1}$$

holds [6], where the material constant k_h has to be derived from loss measurements and from the area of the hysteresis loop respectively. Equation (5.1) and the loss indications used in electric engineering hold for one-dimensional alternating fields. Hysteresis losses caused by rotating fields may increase by the double. They can be converted with experimentally determined curves [2]. Since the magnetic field distribution around the rotor is rather far from

being sinusoidal, its Fourier series representation will include many harmonics of the rotational angle. The skin effect will significantly change the field distribution inside the iron when the rotor spins. For a detailed analysis of hysteresis losses, higher order harmonics must be considered.

5.2.2 Eddy-Current Losses P_e

When the flux density within the iron core changes, eddy currents are generated. A solid magnetic core (Fig. 5.2a) acts like a short circuit winding and generates large eddy currents. The eddy-current losses can be reduced by dividing the iron core in insulated sheets (Fig. 5.2b), or in particles (sintered cores).

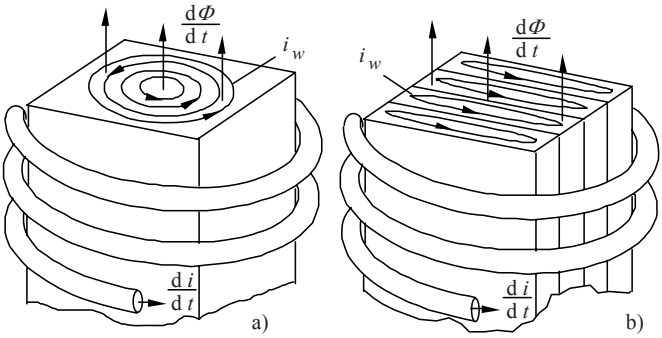


Fig. 5.2. Reducing the eddy current losses by dividing the iron core into sheets

The smaller these divisions are made, the smaller the eddy-current losses become. Losses in laminated iron can be calculated approximately, if the flux in the sheets is sinusoidal and distributed evenly [1]:

$$P_e = \frac{1}{6\rho}\pi^2 e^2 f_r^2 B_m^2 V_{fe} \tag{5.2}$$

Here, ρ is the specific electric resistance of the iron, e stands for thickness of the sheets, f_r for remagnetization frequency, and B_m for the maximum flux density or the amplitude of the flux density respectively.

In electrical engineering, iron loss is mostly referred to in a standard way, i.e. for a frequency of 50 Hz or 60 Hz, and expressed in W/kg for flux densities of 0.5 Tesla, 1 Tesla or 1.5 Tesla. When calculating the losses at other frequencies and flux densities, the overall losses have to be divided into hysteresis losses and eddy-current losses [7], before both parts can be converted with (5.1) and (5.2).

The flux density on the rotor surface, and the inherent hysteresis loss, depends on the structural shape of the bearing. In the bearing design indicated

in Fig. 5.3a, the iron is remagnetized twice upon one revolution [4]. Eddy-current losses can be kept low here since the rotor can be laminated easily, i.e. built as a stack of punched circular lamination sheets. Figure 5.3a shows a magnetic polarity sequence of NSSNNSSN. In this design, the remagnetization frequency is twice the rotation frequency. If a magnetic polarity sequence of NSNSNSNS is chosen, the remagnetization frequency is four times the rotation frequency. A comparison of the two designs can be found in [4].

The magnetic polarity sequence of NSNSNSNS has the advantage that the flux of each pole splits on the rotor into two halves to both adjacent poles. The result is that the total journal volume can be half for this sequence, allowing for a higher inner diameter of the journal, leading to higher rotor stiffness.

If, on the contrary, the bearing has the design indicated in Fig. 5.3b, the iron passes below poles with equal polarity, which keeps the iron losses smaller than with format a. However, it is almost impossible to laminate rotor b. Design b is is often used for bearings with permanent magnet bias.

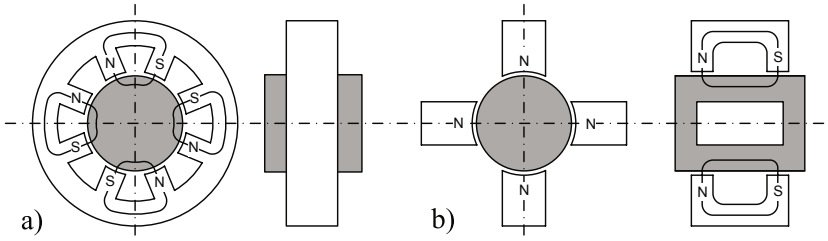


Fig. 5.3. Designs of radial bearings: a) Field lines perpendicular to the rotor axis b) Field lines parallel to the rotor axis

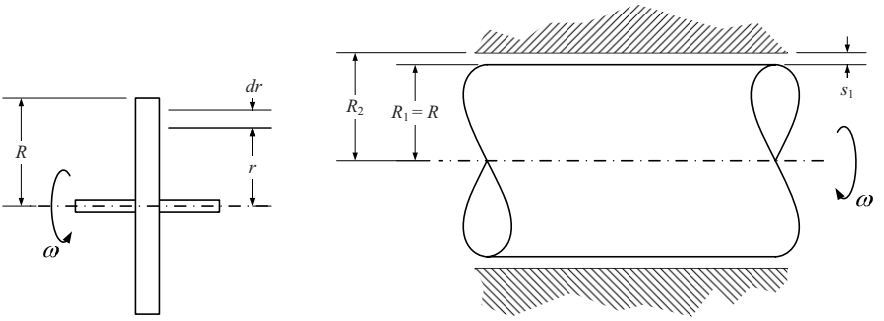
5.3 Aerodynamic Losses, Windage Losses

This section is based on the experimental results of research on small rotors done by Mack [3]. Mack has measured rotors with length up to 200 mm and diameters up to 75 mm. His publication has the advantage of experimentally verified results which are otherwise hard to find in the literature.

5.3.1 Basics

The viscous drag of a body moved in gas or liquid is usually described by a dimensionless drag coefficient c. For bodies with geometric form similar to a cylinder or a disc (Fig. 5.4) , c is dependent only on the *Reynolds number*, Re:

$$Re = \frac{R_2 \omega}{\nu} \tag{5.3}$$



(a) disk (b) cylinder

Fig. 5.4. Geometry of disc and cylinder.

The value of the kinematic viscosity ν depends on the medium and its temperature. Tables of values can be found in literature, e.g. in [5]. For calculations on magnetic bearings, two basic geometries are the most important: A rotating disk with negligible thickness and a cylinder which is very long compared to its diameter (Fig. 5.4)

a. Disk
The braking torque for the disc can be calculated as

$$M_s = \pi c_s \rho \omega^2 R^5 \tag{5.4}$$

where ρ is the density of the gas surrounding the disk and c_s is the drag coefficient for the disc.

b. Cylinder
The braking torque for the cylinder can be calculated as

$$M_z = \pi c_z \rho \omega^2 R^4 L \tag{5.5}$$

where L is the length and c_z is the drag coefficient of the very long cylinder.

c. Cylindrical rotor: a combination of disk and cylinder
A rotor used in a technical application is most often a combination of cylinder and disc. For rotors with a ratio L/R in the range of 0.5 to 6 it is not permissible to use c_z for the cylindrical part and c_s for its ends because the disturbances of the flow at the edges between cylindrical part and the ends become more and more important with decreasing ratio L/R. For such cases Mack [3] has defined a drag coefficient c_w which depends on the ratio L/R. The braking torque for a cylindrical rotor with L/R in the range of 0.5 to 5 can be calculated as

$$M_w = \pi c_w \rho \omega^2 R^5 (1 + L/R) \tag{5.6}$$

5.3.2 Drag coefficient of a free cylindrical rotor

Mack has experimentally determined c_w for rotors with ratio $0.1 < L/R < 6$. The surface of the rotors had a finish which is usual for machine parts. Mack has analyzed c_w for very low Re. The measured results in Fig. 5.5 show that, in the domain of $Re < 4000$, the results for the various L/R fall together and c_w becomes independent of the ratio L/R:

a. for $Re < 170$, $c_w \approx 8Re^{-1}$

b. for $170 < Re < 4000$, $c_w \approx 0.616Re^{-0.5}$

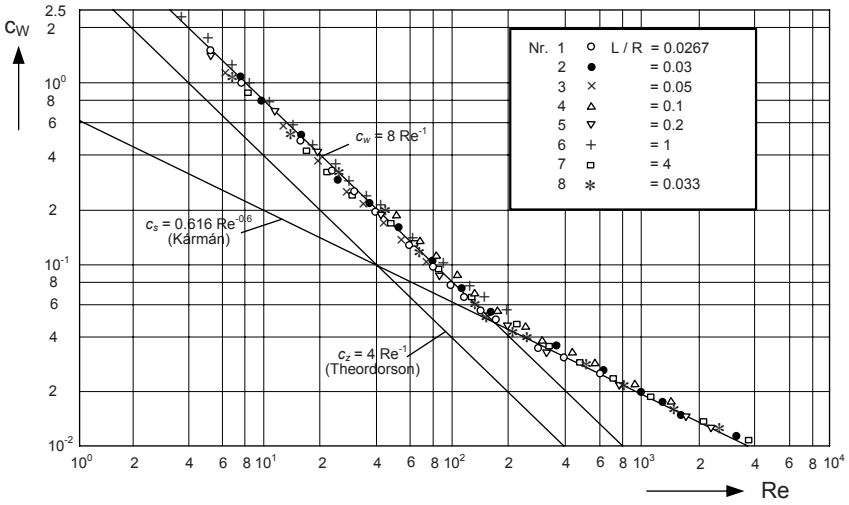


Fig. 5.5. Measured drag coefficients of rotating free cylindrical rotors [3].

The measured results in Fig. 5.6 show that, in the domain with turbulent flow ($Re > 4000$), the results for the various L/R lie between the calculated results for $L/R = 0$ (disc) and $L/R = \infty$ (very long cylinder). For rotors with $L/R > 6$, the drag coefficient c_z of the very long cylinder is a very good approximation and can be applied in many technical applications where $L/R > 6$ is fulfilled.

c. for $Re > 4000$ and $L/R > 6$: $c_w = 6.3 \times 10^{-2} Re^{-0.225}$

These results are summarized in Table 5.1.

5.3.3 Drag coefficient of a shrouded cylindrical rotor with grooves in the stator

The case of the shrouded cylindrical rotors where the ratio of air gap s to radius R is small, is important in technical applications. The drag coefficients

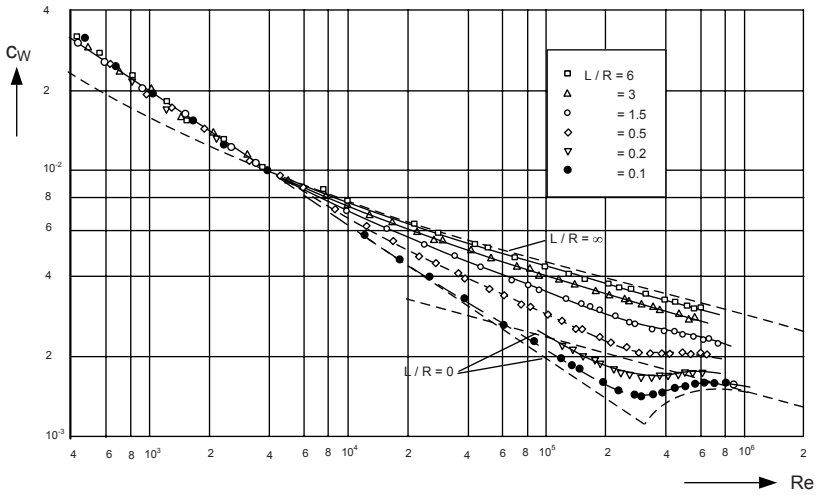


Fig. 5.6. Measured drag coefficients of rotating free cylindrical rotors [3].

Table 5.1. Cylindrical drag coefficients, from [3]

flow regime	drag coefficient
$Re < 170$	$c_w = 8Re^{-1}$
$170 < Re < 4000$	$c_w = 0.616Re^{-0.5}$
$Re > 4000$ and $L/R > 6$	$c_w = 6.3 \times 10^{-2} Re^{-0.225}$

of a shrouded cylinder depend on the ratio s/R. In this case, a *Taylor number*, which depends on the airgap s, is used in addition to the Renolds number:

$$Ta = \frac{R_1 \omega s_1}{\nu} \sqrt{\frac{s_1}{R_1}} \tag{5.7}$$

where $41.3 < Ta < 400$ characterizes the transition from laminar to turbulent flow. In motors as well as in magnetic bearings, the stator surrounding the rotor is most often grooved. Mack has analyzed the case of such cylindrical bores with grooves.

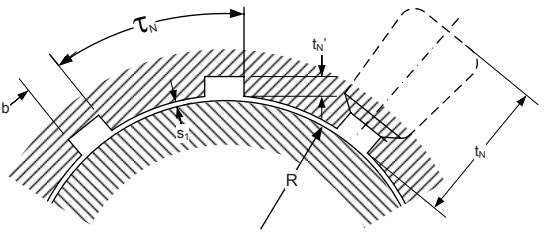


Fig. 5.7. Shrouded cylinder with grooves in the stator

Based on his experimental results, Mack distinguishes three categories for the drag coefficient c_{z2}:

a. For $Re < 170$ and $s/R > 0.25$, the shroud and the grooves have no influence and the equation of the free rotor can be applied:

$$c_{z2} = 8Re^{-1} \tag{5.8}$$

b. Figure 5.8 shows that for $Ta < 41.3$,

$$c_{z2} = \frac{1.8}{Re}\left(\frac{s_1}{R}\right)^{-0.25}\frac{R_2^2}{R_2^2 - R_1^2} \tag{5.9}$$

c. Figure 5.8 shows that for $Ta > 41.3$ and $s/R < 0.0125$,

$$c_{z2} = \text{constant} = c_{z2}(Ta = 41.3) \tag{5.10}$$

The measured drag coefficients in Fig. 5.8 also show that c_{z2} is almost independent of the grooves.

5.3.4 Other methods

Other calculation methods can be found in [10] and [11]. The results of calculations have to be verified by experiments because the results of different methods are very sensitive on geometrical variations and the results can differ enormously. Figure 5.9 shows the comparison of aerodynamic losses calculated for the example of a thrust disc for a range of diameters. The results for the airgap of 0.5 mm differ by a factor of 20. The method of Sigloch is not applicable for very small air gaps. In [12], the Mayle algorithm for the numerical calculation of airloss and pressure in axial airgaps of disks can be found.

5.3.5 Calculation of brake torque of air loss

To calculate the air losses of a rotor we have to split the rotor into sections with similar air- friction conditions. Thus, a simple cylindrical rotor is divided, for instance, into

– cylinders without shroud, including front side
– disk areas within the axial bearing
– shrouded cylinders within the bearing and the motor
– shrouded cylinder within the sensors
– shrouded cylinders within the touch-down bearings

The various braking torques have to be calculated and then added. The method of Mack allows for an efficient rough calculation of the air loss with a satisfying accuracy. For higher accuracy much more complex and costly FE calculations have to be done. Figure 5.11 shows a concrete example where calculated and measured braking torques are compared.

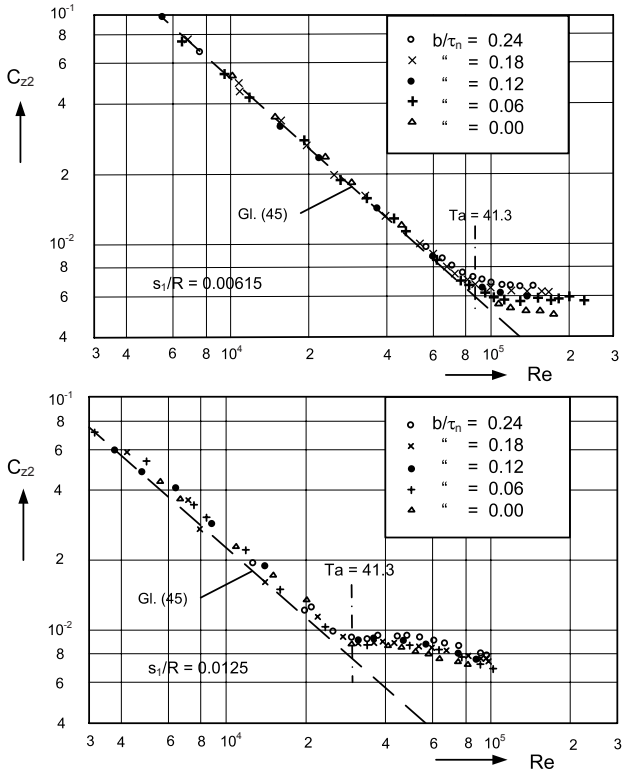


Fig. 5.8. Measured drag coefficients c_{z2} of rotating shrouded cylindrical rotors [3] with $s_1/R = 0.0125$ and 0.00615, for various grooves in the borehole.

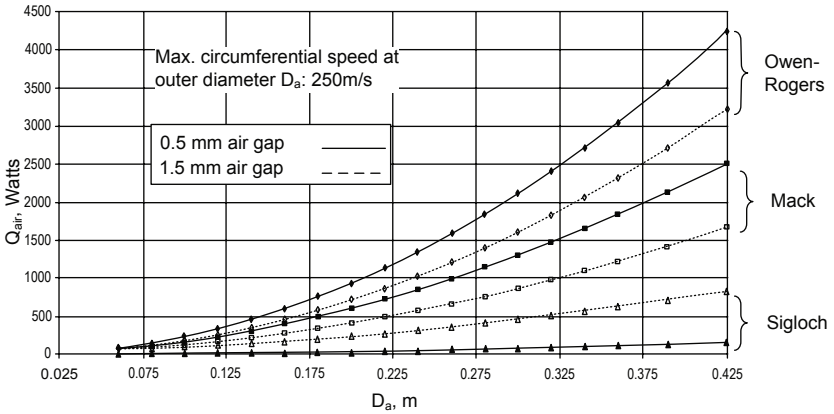


Fig. 5.9. Comparison of calculated aerodynamic losses of a thrust disk.

5.4 Determining Rotor Losses

Since the braking torques of magnetic bearings are very small, they are not easy to measure. A simple and frequently used approach in the manufacturing of electrical drives is the spin-down test. Here, a change in the rotational speed is proportional to the braking torque. Therefore, by differentiating the spin-down curve with respect to time, the braking torque can be determined quite accurately.

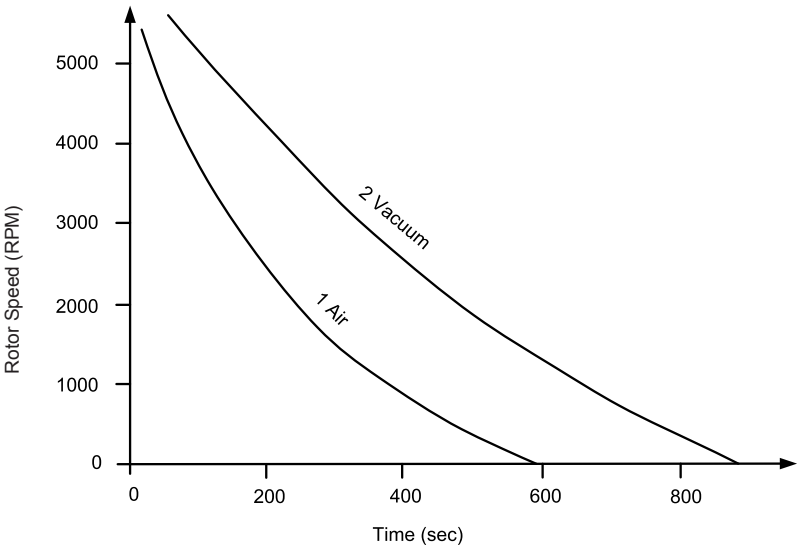


Fig. 5.10. Measured spin–down curves (1 under normal pressure, 2 under a vacuum).

The spin-down curves of a rotor with a diameter 80 mm and a length 500 mm, as shown in Fig. 5.10, were measured and evaluated. The inertia moment of the rotor was measured with the rotating-pendulum method (0.0115 kg m^2), and subsequently the braking torque was calculated from the change in rotational speed. Figure 5.11 shows the calculated torques of a spin-down trial under normal pressure and under vacuum. The measurement under a vacuum was used to determine the pure iron losses.

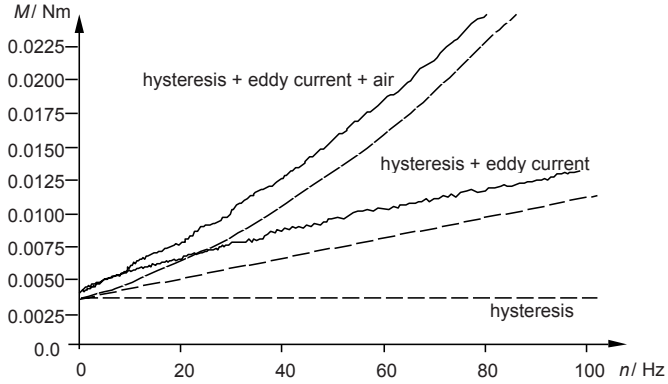


Fig. 5.11. Braking torques determined from spin-down tests (solid lines) compared to the calculated values (dashed lines).

5.5 Measures to Reduce Losses

5.5.1 Rotor Losses

Reduction of Aerodynamic Losses

To reduce aerodynamic losses the reduction of the pressure in the machine is most effective. This needs seals between high pressure part (i.e. impeller housing) and machine housing (motor and bearings). Obviously, the seals (e.g. labyrinth seals) will also cause some aerodynamic losses. Optimizing the surface of rotor and stator in the airgap might also be effective. Because the influence of the surface texture and roughness is not well known an optimization needs experimental testing. The thrust disk has often the maximum diameter of the rotor and its size has to be minimized. The thrust disk often acts as a primitive compressor. It may be worth to make sure that the air can flow through the airgaps in the thrust disc, thus reducing the pressure and improving the cooling.

Reduction of Iron Losses

Hysteresis and eddy current loss can be reduced, using optimized (costly) iron. The eddy current can be reduced using smaller sheet thickness of the lamination except for the axial bearings, where the target is practically impossible to laminate.

Iron losses can be reduced by minimizing and dynamic handling of the bias current. A reduction of the bias current leads to lower force dynamics. Therefore the bias current may be kept low for standard operating conditions and increased only for specific operation conditions (i.e. for the run up /

run down, crossing critical speeds, etc.) where high dynamics of the force is needed.

Homopolar bearings reduce the iron loss caused by the rotor speed most efficiently as long as the radial bearings have no static load as is the case if the rotation axis is vertical. When the rotor is not vertical, homopolar bearings will also exhibit significant circumferential field variation in order to provide force to counter gravity load. This circumferential field variation reduces the advantage of homopolar bearings and dictates that the rotor must be laminated. Section 3.1.5 provides a detailed discussion of the relative merits of homopolar and heteropolar bearings.

5.5.2 Losses in the Bearing Magnets (Stator)

In the bearing magnets, copper losses can be reduced by using permanent magnets to generate a bias flux instead by a bias current. The electrical power losses associated with generating the bias field are eliminated but the design of the bearing is more complicated and often more costly.

5.5.3 Losses in the Power Amplifier

In switched amplifiers, switching losses are dominant and the switching losses are about proportional to the switching frequency. Therefore minimizing of the switching frequency is helpful. But lower switching frequency increases the control current ripple. Especially in applications that need high dynamic forces, a trade-off between current ripple and switching losses in the power amplifier has to be found. Filtering of the control current to improve the electromagnetic compatibility (EMC) is often necessary. In this case the filters have to be optimized for minimum losses and maximum effect. The use of power transistors with low "on resistance"[1] and topologies with small switching losses further reduce the losses.

5.5.4 Losses in Long Cables

To lower the current density and therefore the copper losses, the cross section of the wires in the cable may be increased. This increases also the cost of the cable and therefore leads to a trade-off between losses and cost of the cables.

5.6 Losses in Various Applications

Depending on the application, the goal of loss reduction can be different. Improving the performance of the bearing system may be more important than

[1] The "on resistance" of a switching transistor is the ratio of effective voltage drop to conduction current when the transistor is saturated in its conduction mode.

the minimizing of the losses. Instead of reducing losses, measures to improve the cooling may be more important, allowing higher losses and improving the performance of the bearing (i.e. the reduction of the size of the bearing may improve the rotor dynamics but increase the Ohmic losses).

Compressors

Due to high pressure, windage losses are dominant in compressors. Most critical is the thrust bearing disc with relatively high diameter and surface speed. To reduce windage loss, the pressure is often reduced inside the machine by means of sealings which separate the high pressure in the impeller housing from the reduced pressure in the machine housing. Compressors are often used in harsh environment where the AMB electronics is placed in a protected control room. In such a case, a remarkable part of losses can arise in long cables. These losses as well as the cost for long cables can be reduced if the AMB electronics is placed close to the compressor in housing adequate to harsh environment.

Vacuum Applications

Magnetic bearings are perfectly suited for the operation in a vacuum because they do not need lubrication. In most vacuum applications, minimization of the rotor losses is more important than minimization of the overall losses. This is because the rotor is cooled almost solely by radiation which is relatively ineffective: management of rotor temperature requires careful attention to losses incurred in the rotor volume. This desire to minimize rotor losses suggests the use of homopolar bearings to take advantage of their potential loss advantages. However, probably the most common commercial vacuum application of AMBs is to turbomolecular pumps: the orientation of these pumps is dictated by the equipment to which they are applied and they commonly are not oriented with the rotor vertical. Consequently, the advantages of homopolar bearings in turbomolecular pumps are less clear than for flywheels and most commercial implementations of turbomolecular pumps have favored heteropolar bearings.

Flywheels

Especially in flywheels for long time storage of energy, high efficiency is most important and the minimization of the overall losses is a must. The rotor axis of flywheels is usually vertical which provides a clear advantage to the use of homopolar bearings. With permanent magnet bias or with dynamic management of bias current, the Ohmic losses will be reduced. Whereas the permanent magnet bias reduces the copper loss in the bearing magnets, the dynamic management of bias current allows for a reduction of rotor losses

because the flux density in the rotor can be minimized as long as no dynamic forces are needed. This is often the case over long time in the energy storage. To reduce aerodynamic losses flywheels are operated in a vacuum and all statements concerning vacuum applications also apply to flywheels.

References

1. Heck, C., Magnetische Werkstoffe und ihre technische Anwendung. Dr. A. Hütling Verlag, 1975
2. Kornetzki, M. and Lucas, I., "Zur Theorie der Hystereseverluste im magnetischen Drehfeld." Zeitschrift für Physik, Bd. 142, 1955, pp. 70–82.
3. Mack, M., "Luftreibungsverluste bei elektrischen Maschinen kleiner Baugröße." Diss. TH Stuttgart, 1967.
4. Matsumura, K. and Hakate, K., "Relation between Pole Arrangement and Magnetic Loss in Magnetic Bearings." 2nd Internat. Symp. on Magnetic Bearings, July 12-14, 1990, Tokyo, Japan.
5. Schlichting, H., *Grenzschichttheorie*. G. Braun Verlag, Karlsruhe, 1965.
6. Steinmetz, C., "Note on the Law of Hysteresis". Electrician, 26, Jan. 1891, pp. 261–262.
7. Traxler, A., "Eigenschaften und Auslegung von berührungsfreien elektromagnetischen Lagern." Diss. ETH Zürich, Nr. 7851, 1985.
8. Meeker D. C. and Maslen E. H., "Prediction of rotating losses in heteropolar radial magnetic bearings," ASME *Journal of Tribology*, vol. 120, no. 3, pp. 629–635, 1998.
9. Meeker D.C., Filatov A.V., and Maslen E.H., "Effect of Magnetic Hysteresis on Rotational Losses in Heteropolar Magnetic Bearings," IEEE *Transactions on Magnetics*, vol. 40, No. 5., Sept. 2004.
10. Sigloch, H., *Technische Fluidmechanik*. Springer, 6. Aufl., 2007, ISBN: 978-3-540-44633-0.
11. Owen, J.M. and Rogers R.H., *Flow & Heat Transfer in Rotating-Disc Systems, Volume 1 Rotor-Stator Systems*, Research Studies Press, Wiley, 1989.
12. Mayle, R.E., Hess, S., Hirsch, C., and Van Wolfersdorf, J., "Rotor-Stator Gap Flow Analysis and Experiments," IEEE *Transactions on Energy Conversion*, No. 13, 2, June 1998.

6

Design Criteria and Limiting Characteristics

Gerhard Schweitzer

Initially, three decades ago, active magnetic bearings (AMB) have been designed to overcome the deficiencies of conventional journal or ball bearings. Mostly in research labs, they showed their ability to work in vacuum with no lubrication and no contamination, or to run at high speed, and to shape novel rotor dynamics. Today, magnetic bearings have been introduced into the industrial world as a very valuable machine element with quite a number of novel features, and with a vast range of diverse applications. Now, there are questions coming up about the actual potential of these bearings: what experiences have been made as to the performance, what is the state of the art, what are the physical limits, what can be expected? In particular, there are features such as *load, size, stiffness, temperature, precision, speed, losses and dynamics*. Even such complex issues as *reliability/safety* and *smartness* of the bearing can be seen as features, with increasing importance and growing maturity. In this chapter the most essential design criteria and their limitations will be briefly discussed and summarized, with references to other chapters where more detailed derivations will be shown. A survey is given in the conclusion, Sect. 6.9.

6.1 Load Capacity

The term *load* touches upon basic properties of magnetic bearings. The load capacity depends on the arrangement and geometry of the electromagnets, the magnetic properties of the material, of the power electronics, and of the control laws. Furthermore, carrying a load is not just a static behavior, usually it has strong dynamic requirements. Subsequently a survey on characteristic limitations is given, the theoretical background and details are derived in Chap. 3 on the *Hardware Components* and in Chap. 4 on *Actuators*.

In magnetic bearing technology electromagnets or permanent magnets cause the *magnetic flux* to circulate in a magnetic loop. The magnetic flux Φ can be visualized by magnetic field lines. Each field line is always closed

G. Schweitzer, E.H. Maslen (eds.), *Magnetic Bearings*,
DOI 10.1007/978-3-642-00497-1_6, © Springer-Verlag Berlin Heidelberg 2009

in a loop. The density of these lines represents the flux density B. By using *ferromagnetic material* the magnetic loop can be concentrated in that core material. The behavior of ferromagnetic material is usually visualized in a $B - H$ diagram, Fig. 3.5 in Chap. 3, showing the well-known phenomena of *hysteresis* and *saturation*. Saturation means, as a consequence, that the flux density B does not increase much more beyond B_{sat} even when the magnetic field H and the generating current i is further increased.

The *force* generated by the magnetic field increases with the maximum admissible "magnetomotive force" ni_{max}, i.e. the product of the maximum current i_{max} and the number of windings n in the coils of the electromagnets. This value is subject to design limitations. As a consequence, the maximum value for the force depends on the winding cross section, the mean winding length and the possible *heat dissipation*, or the available amount of cooling, respectively. Therefore, one limitation for a high static load is the adequate dissipation of the heat generated by the coil current due to the Ohm resistance of the windings. This "soft" limitation can be overcome by a suitable high temperature design, see Sect. 6.5.

Assuming that this problem has been adequately considered, then the current i_{max} will eventually reach a value where the flux generated will cause saturation, and then the carrying force has reached its maximal value f_{max}. Any overload beyond that physically motivated "hard" limitation of the carrying force f_{max} will cause the rotor to break away from its centre position and touch down on its touch–down bearings.

In order to compare the carrying performance of different bearing sizes, the carrying force is related to the size of the bearing, or more precisely, to the cross sectional area of the bearing, leading to the *specific load capacity*. With actually available Si-alloyed transformer sheets, which are used for bearing magnets, a maximum flux density $B_{max} \approx 1.6$ Tesla $< B_{sat}$ is recommended. The resulting specific load capacity of 37 N/cm^2 (or 0.37 MPa) is considerably lower than that for oil lubricated bearings, which is about four times as high. Using (expensive) cobalt-alloys with a saturation flux density B_{sat} of up to 2.4 Tesla, the magnets can be designed for a specific load capacity of up to 65 N/cm^2. For details see Sec. 3.1.7.

Examples on high loads, which have been actually realized, include a rotor with a mass of 50 tons (hydropower, axial bearing, built by the company S2M). The support of rotors for turbo-machinery in the gas- and petro-industry with masses in the range of tons is state of the art.

6.2 Controller and Actuator

A key feature of the AMB is the hardware and software for *information processing*. The *controller* is part of the information processing system, usually consisting of a Digital Signal Processor (DSP), or possibly a Field Programmable Gate Array (FPGA). The controller is responsible for the *dynamic*

behavior of the rotor motion in the AMB suspension. The input to the controller are measured signals on the state of the rotor motion, the output is fed to the amplifiers generating the voltage or current for the coils of the electromagnets, i.e. generating the bearing force. There is an actual trend: by making use of additional software, the DSP is taking over additional tasks, such as the control of the motor drive, the interface to the basic process control of the total machine, and the safety and maintenance management (see Sect. 6.8).

The dynamic behavior of the rotor motion usually is characterized by the terms *stiffness* and *damping*. The stiffness of a bearing characterizes its spring-like behavior, i.e. the ratio of the supported load with respect to the resulting displacement of that load. The term is based on the understanding that a bearing is a mechanical element. In classical bearings the stiffness stems for example from the elasticity of the oil film or the deformation of balls and inner ring of a ball bearing. In an AMB the force is generated by a control current, which can be adjusted to the needs and opens a novel way of shaping the stiffness and even the overall dynamic behavior, and thus the term "stiffness" may not be the best way to describe the performance of an AMB, but it is still used for comparison reasons with classical bearings.

The term *dynamic stiffness* characterizes the fact that in an AMB the force depends on the control current, and it is frequency dependent, as well as the displacement. There are limitations on the frequency range which will be explained subsequently. The current is generated in a power amplifier, and it makes sense to look at the electromagnet and power amplifier as a unit, the whole unit being termed *magnetic actuator*. For high power requirements switched amplifiers are used. The output voltage of the power amplifier is limited to a value $\pm U_p$, which is given by the design of the amplifier. The voltage is used to drive a current through the coils of the electromagnets, and to overcome their resistance and inductivity. In order to be able to generate rapidly changing bearing forces the current through the coils has to change rapidly as well. As the inductance of the coils increases with high frequencies the current will drop down. The highest frequency where the actuator can still operate with its maximal current is called *power bandwidth* ω_{pbw}. The bandwidth can be enhanced by increasing the power of the amplifier.

The required power bandwidth is determined by the frequencies the AMB is supposed to control. If a critical vibration of the rotor at a frequency of ω_{crit} has to be controlled with maximum force then the power bandwidth ω_{pbw} should be sufficiently higher. The theoretical background and details are derived in Chap. 3 on *Hardware Components*, and in Chap. 4 on *Actuators*.

As an example, a force of 1000 N can be generated over an air gap of 0.3 mm with a 1 kVA amplifier up to a frequency of about 500 Hz. Most of that power is used for the *dynamic forces*, which can be seen as an inductive load, and not for carrying a static load, i.e. the weight of the rotor. The actual energy loss is much less.

Shaping the dynamics of the system requires a careful design of the mechanical properties of the rotor and the supporting structure, and the control laws. Software for design and operation plays an ever increasing role.

6.3 Speed

The features characterizing a *high-speed rotor* can be looked at under various aspects. The term "high-speed" can refer to the rotational speed, the circumferential speed of the rotor in a bearing, the circumferential speed of the rotor at its largest diameter, or the fact that a rotor is running well above its first critical bending frequency. The requirements on the AMB and its design limitations can be very different.

Rotational Speed

A record from about 50 years ago are the 300 kHz (!) rotation speed that have been realized in physical experiments for testing the material strength of small steel balls (about 0.7 mm in diameter) under centrifugal load [4]. In today's industrial applications, rotational speeds that have been realized are in the range of about 3 kHz for a grinding spindle, or about 5 kHz for small turbo-machinery. Problems arise from eddy current and hysteresis losses in the magnetic material, air losses, and the related requirements for power generation for the motor drive, and adequate heat dissipation if the rotor runs in vacuum.

Circumferential Speed

The circumferential speed is a measure for the centrifugal load and leads to specific requirements on design and material [13, 23]. The centrifugal load, Fig. 6.1, causes *tangential and radial stresses* in the rotor, given by

$$\begin{aligned} \sigma_t &= \tfrac{1}{8}\rho\Omega^2\left[(3+\nu)(r_i^2+r_a^2)+(3+\nu)\tfrac{r_i^2 r_a^2}{r^2}-(1+3\nu)r^2\right] \\ \sigma_r &= \tfrac{1}{8}(3+\nu)\rho\Omega^2\left[r_i^2+r_a^2-\tfrac{r_i^2 r_a^2}{r^2}-r^2\right] \end{aligned} \tag{6.1}$$

where r_i and r_a are the inner and outer radius of the rotor, respectively, and $\nu = 0.3$ is the Poisson number.

The tangential stress, as the most critical one, is shown in Fig. 6.2. Highest stress values occur at the inner boundaries of a rotor disc. As the rotor partially consists of laminated soft iron sheets, which usually have to be shrink-fit to the rotor shaft, the tangential stress at the inner rim is still further increased. Numerous lab experiments have been performed. Rotor speeds of up to 340 m/s in the bearing area can be reached with iron sheets from amorphous metal (metallic glass), having good magnetic and mechanical properties

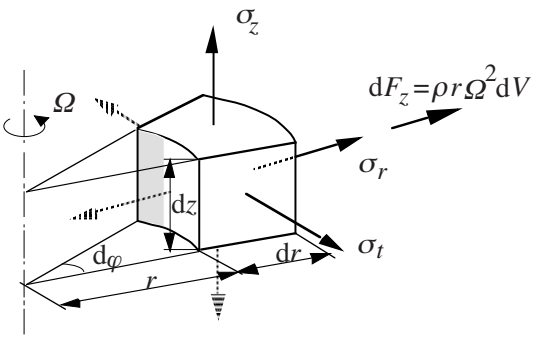


Fig. 6.1. Centrifugal loads acting on the volume element of a rotor

[13]. The theoretical value for the achievable speed v_{max} lies much higher. It can be derived from (6.2), where σ_S is the yield strength, ρ is the density of the material, and the according values for some materials are given in Table 6.1.

$$v_{max} = (r_a \Omega)_{max} = \sqrt{\frac{8\sigma_S}{(3+\nu)\rho}} \tag{6.2}$$

Table 6.1. Achievable circumferential speeds for a full disc

Material	v_{max}/ [m/sec]
Steel	576
Bronze	434
Aluminum	593
Titanium	695
soft ferromagnetic sheets	565
amorphous metal	826

In industrial applications, the speed usually is limited not by the bearings themselves, but by the mechanical design of the rotor, especially when a motor is included. Figure 6.3 shows an example of a motor rotor which has failed due to centrifugal loading. Figure 6.4 gives a survey on various AMB applications that have been realized conventionally [24]. For high speeds permanent magnet synchronous drives are used where the rotor is wound with carbon fibres, allowing speeds of about 300 m/s.

Supercritical speed

A rotor may well have to pass one or more *critical bending speeds* in order to reach its operational rotation speed. In classical rotor dynamics this task is

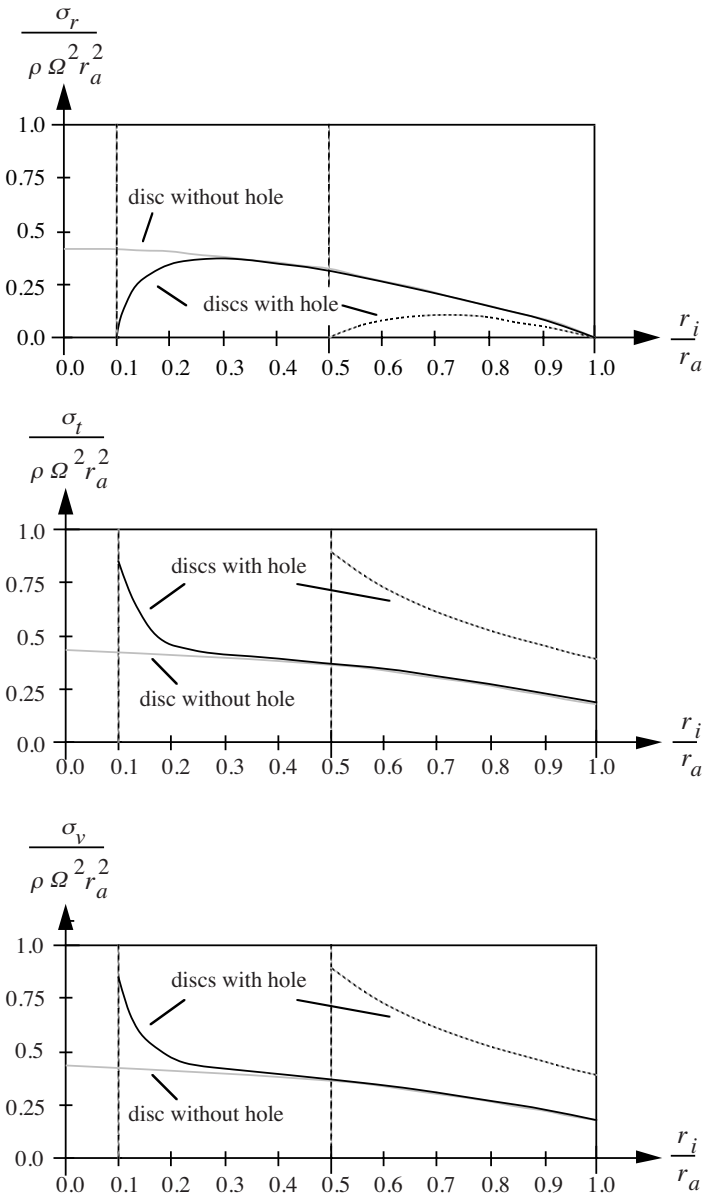


Fig. 6.2. Radial, tangential and average stress distribution for a disc with and without hole in the center



Fig. 6.3. Rotor ring, broken under centrifugal load

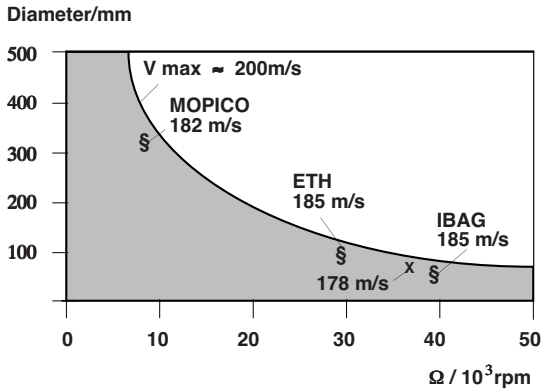


Fig. 6.4. Examples for the maximal diameter of the (asynchronous) motor drive in function of the rotor speed. The (x) indicates the rotor of Fig. 6.3 broken at 178 m/s

difficult to achieve. In AMB technology it is the controller that has to be designed carefully to enable a stable and well-damped rotor behavior, as well as sufficiently small displacements at the relevant rotor locations. Passing just the first critical elastic speed is state of the art and can be very well done with AMB. This has been shown even with an automated controller design, based on self-identification and subsequent self-tuning with the H_∞-method [14]. In many lab experiments two critical speeds have been passed, too, using various design methods, for example [13]. Three elastic modes have been dealt with in [9], using additional notch filters and a zero-pole canceling filter. Further research in developing methods for the design of robust controllers

for highly elastic systems, including the elasticity of supporting structure and foundation, is necessary (see Chap. 12 on the Control of Flexible Rotors).

6.4 Size

In principle, there appears to be no upper limit for the bearing size, it can be adapted to any load. Problems arising with assembling *large bearings* lead to special design variations, where the bearing is separated in two halves, or the single magnets are even treated individually.

Small bearings are of special interest to micro-techniques. Potential applications are video heads, medical instruments, hard disk drives, and optical scanners. The challenge lies in simplifying the design and in the manufacturing process. Chap. 17 on *Micro-Bearings* is showing the state of the art and details.

6.5 High Temperature

The application of active magnetic bearings (AMBs) for gas-turbines and aircraft engines would open large potentials for novel design. In order to utilize the full advantages of active magnetic bearings, an operation in gas-turbine and aircraft engines requires that the magnetic bearing should work properly at high temperatures. Challenges in designing such bearings consist in *material evaluation, manufacturing process* and *high temperature displacement sensor development*. High temperature active magnetic bearings (HT AMBs) are under development in various places [12, 17, 21, 25, 26], Fig. 6.5. Operating temperatures of up to 800 °C have been realized [5]. Even rotor speeds of 50000 rpm at 600 °C have been reached [17]. Such a performance cannot be obtained by any other kind of bearing. The soft magnetic materials for stator and rotor are cobalt based alloys [12], such as Hiperco 50 and Hiperco 50-HS, the electrical connections are made of silver wire, the windings of ceramic coated copper with high temperature potting materials. Research on feasibility, temperature distribution within the bearing, high temperature sensors, materials and insulations have been an objective of the European research project MAGFLY [6, 7]. Functional tests were quite successful, but the *long-term exposure to high temperature* needs further research, as the actually available materials do not yet allow a sufficient life time at temperatures above 400 °C. Problems arise from structural changes of the material, micro migration of alloys, and creep. In addition, heat dissipation of the internally generated losses under heavy bearing loads will need special attention.

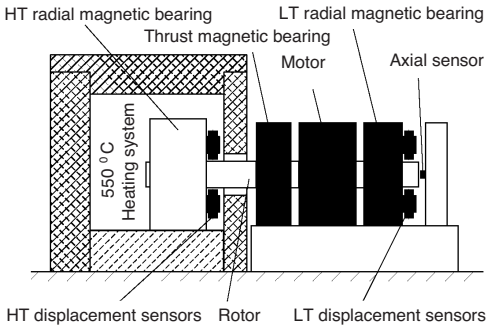


Fig. 6.5. Test rig for a high temperature active magnetic bearing [25], operating in a containment heated up to 550 °C, and running at 30.000 rpm

6.6 Losses

Magnetic bearings work with no contact, and consequently there is no mechanical friction. Therefore, the operation of a spinning rotor in active magnetic bearings causes much less losses than the use of conventional ball or journal bearings. But, nevertheless, the remaining losses have to be taken into account, and sometimes they lead to limitations. The theoretical background and details are given in Chap. 5 on *Losses in AMB*. Losses can be grouped into losses arising in the stationary parts and in the rotor [2, 3, 15, 16, 19], and losses related to the design of the control [8, 18, 27].

Losses in the stationary parts of the bearing arise mainly from copper losses in the windings of the stator and from losses in the amplifiers. The copper losses are a heat source, and, if no sufficient cooling is provided, they represent a limit to the control current and hence the maximal achievable load capacity, as described in Sect. 6.1.

Losses in the rotor part are more complex and lead to more severe limitations. The losses heat up the rotor, cause a braking torque on the rotor, and have to be compensated by the driving power of the motor. The rotor losses, comprising iron losses caused by hysteresis and eddy currents, and air drag losses, are summarized subsequently.

- The iron losses depend on the rotor speed, the material used for the bearing journal, and the distribution of the flux density B over the circumference of the journal. The braking torque caused by the iron losses consists of a constant component of hysteresis losses and a component of eddy-current losses, which grow proportionally to the rotational speed. The iron losses in the rotor can limit operations, as, in particular in vacuum applications, it can be difficult to dissipate the generated heat.
- The hysteresis losses arise if at re-magnetization the $B - H$-curve in the diagram of Fig. 3.5 in Chap. 3 travels along a hysteresis loop. At each

loop the energy diminishes by an amount proportional to the area covered by the loop. Consequently, the hysteresis losses are proportional to the frequency of re-magnetization. The area of the hysteresis loop depends on the material of the magnet and on the amplitude of the flux density variation. It is obvious that soft magnetic material with a very small loop area will reduce these losses. Experimentally derived data are presented in [3]. The use of iron free magnetic bearings and drives with no hysteresis effects at all, based on Lorentz forces, has been investigated mainly for precision bearings, where the influence of hysteresis would be detrimental to precision control. This approach will be dealt with in the next Sect. 6.7 on *Precision*.

- The eddy-current losses arise when the flux density within the iron core changes. The eddy-current losses can be reduced by dividing the iron core into insulated, laminated sheets, or using sintered cores. The thinner these sheets or divisions, the smaller are the eddy-current losses. The flux density on the rotor surface, and the inherent losses, depend on the structural shape of the bearing, i.e. whether the field lines of the flux are orthogonal to the rotor axis (heteropolar) or parallel to the rotor axis (homopolar). The use of a vertically oriented rotor and homopolar bearings is recommended when the rotor is massive and can not be laminated, for example in ultra high vacuum applications.
- The air losses can be predominant at high rotation speeds, and for special applications, such as flywheels for energy storage. Very small air gaps increase the air drag. The air losses can be calculated or rather estimated by dividing the rotor into sections with similar air-friction conditions, in order to take into account different rotor geometries. Thus, a simple cylindrical rotor is divided, for instance, into cylinders without sheathing, including frontal areas/cylinder front areas within the axial bearing/cylinders within the bearing and the motor/cylinders within the retainer bearing. The braking torque elements have now to be calculated and then added. Information on how to calculate the braking torques can be found in [15].

The concept of "zero power" control [8, 18, 27] is another way of reducing the losses by *reducing the control current* itself as much as possible. The static magnetic field, for compensating the static load or for pre-magnetization, is supplied by permanent magnets. The control current is only used for stabilizing the rotor hovering. The rotor is expected to rotate about its main axis of inertia, thus performing a so-called *permanent, force-free rotation*. The control required for that kind of operation needs information about the periodic parts of the disturbances acting on the rotor, which have to filtered out or compensated for in the sensor signals. The approach is very useful in cases where the energy losses have to be kept minimal, for example for energy flywheels, and where the residual vibratory motions of the geometric rotor axis can be tolerated.

6.7 Precision

Precision in rotating machinery means most often the question: how precise can the position of the rotor axis be guaranteed? This has consequences for machine tool spindles, i.e. for the dimensional and surface quality of parts that are being machined by grinding, milling or turning, or for the efficiency in turbo-machines, where the gap between rotor and housing should be kept small. In addition, the question of how precise can magnetic bearings become in principle, is of interest for applications in optical devices, such as an optical scanner, wafer stepper, or in lithography. These machines and processes are key elements for semiconductor industry. Active magnetic bearings levitate an object, rotating or not, with feedback control of measured displacement sensor signals. The performance of AMB systems is therefore directly affected by the *quality of the sensor signals*. Precision control is facilitated by the absence of hysteresis and of deformation-prone heat sources, which depends on material and design aspects.

The *displacement sensors* used in AMB systems can be very sensitive to the surface quality of a rotor and this sensitivity becomes exaggerated when the sensing tip is small. Thus, small-tipped sensors may require additional algorithms to detect and compensate for the unnecessary signal contents induced by the geometric errors of a rotor, such as surface roughness, roundness, unbalance run-out, misalignment. Accordingly, on-line control with the probe type sensors becomes more cumbersome and more complicated as soon as high precision is aimed at. Algorithms for smoothing out higher order harmonics of geometric rotor errors in the sensor signal, particularly suited for *capacitive sensors*, have been investigated, for example in [11]. Orbits with displacement errors of the rotation axis of 10 to 20 μm have been obtained in industrial applications.

A *very high precision level* in keeping a hovering position for non-rotating objects has been demonstrated, for example, for a long-range scanning stage, being used for positioning samples beneath a scanning-tunneling microscope [10, 20]. Iron-free drives, capacitance probe sensors and heterodyne laser interferometers contribute to a positioning resolution of 0.1 nm, positioning repeatability of 1 nm, and a positioning accuracy of 10 nm.

6.8 Smart Machine Concept

The *smart machine technology* is an actual topic for mechatronics products, signaling the growing importance and capability of the *software within the product*. AMBs are typical mechatronic devices, and one of the most attractive features of such devices is their ability of internal information processing. The machine is termed smart if it uses its internally measured signals to optimize its state [22]. Such a smart machine makes use of the built-in active control to incorporate additional or higher performance functions. Thus, the

machine may acquire higher precision and the ability for self-diagnosis, it can calibrate itself, it can give a prognosis about its future ability to function in a satisfactory way, or about its remaining lifetime, and possibly, it can suggest a correction measure, a therapy, or even induce it itself. It is the mechatronic structure of the machine, the built-in control, its sensors, processors, actuators, and above all, its software which enable these novel features. This is a way to design machines and products with higher performance, less maintenance costs, longer lifetime, and an enhanced customer attraction. In this respect, AMBs already show promising features, but they have by no means reached their full potential. The main contribution of the smart machine technology is seen in managing safety, reliability and maintenance issues and thus in reducing costs. A more detailed outlook on the concept and structure of such a smart machine is given in Chap. 18 on *Safety and Reliability Aspects*.

6.9 Conclusions

Limitations in Active Magnetic Bearings arise from two reasons: the state of the actual technology in design and material, and from basic physical relations. This chapter has given a survey on such limitations, with a brief theoretical background and references to other chapters where details are derived. It has shown examples and pointed to actual data. They may help to make preliminary design decisions. The various issues are summarized subsequently:

- The maximal load capacity depends on design.
- The specific load capacity depends on the available ferromagnetic material and its saturation properties, and is therefore limited to 32 to 60 N/cm^2.
- The frequency and the amplitude of disturbances acting on the rotor, such as unbalance forces, that can be adequately controlled, depend mainly on the design of the power amplifier (power and bandwidth).
- The maximal rotation speed that has been achieved is about 300 kHz in physical experiments. For industrial applications values of about 6 kHz have been realized.
- Circumferential speeds, causing centrifugal loads, are limited by the strength of material. Values of about 250 to 300 m/s have been realized up to now.
- Supercritical speed means that one or more critical speeds can be passed by the elastic rotor. It appears to be difficult to pass more than two or three, but research is going on. The consideration of the elastic properties of the supporting structure and foundation is a research topic as well.
- The size of the bearing depends on design and manufacturability. There are large bearings with dimensions and loads in meters and tons. The smallest bearings actually built have dimensions in the range of a few mm, with a thickness being as small as 150 μm.
- High temperature bearings have been realized, operating in experiments at a temperature of 800 °C (1100 °F). For temperatures above about 400 °C

lifetime is still a limiting factor. For ferromagnetic material the Curie temperature would be a physical limit.
- The losses of magnetic bearings at operating speed are much smaller than that of classical bearings. Eddy current losses will limit the rotation frequency of massive rotors (heating up, driving power), the air drag will be crucial at high circumferential speeds (driving power).
- A high precision of the position of the rotor axis (in the range of μm) requires high resolution sensors and adequate signal processing to separate disturbance signals from the desired ones.
- A very high precision, aimed at for non rotating suspension and position servoing of optical devices (in the range of nm), requires iron free magnetic paths to avoid hysteresis effects, and adequate sensing.
- The information processing within the AMB system can be used to make the rotating machinery smart. Actual limits have not yet been determined.

Some remarks on the state of the art and an outlook on future trends in design aspects conclude this chapter:

- A first approach to a systematic comparison of AMB performance with that of classical ball and journal bearings is given in [1].
- The joint operation of a magnetic bearing with a roller bearing under emergency situations, in load sharing or in touch down contacts, needs further experiments and design efforts. *Touch–down Bearings* are dealt with in Chap. 13, *Fault Tolerant Control* in Chap. 14.
- The operation at supercritical speeds, passing many elastic rotor and structure frequencies needs more research on the control design.
- The advanced information processing within the bearing system, extending the smartness of the rotating machinery, will be a promising research area.
- The potential of high temperature super-conductors, as an extension or an alternative to AMBs, is promising but has not yet reached an industrial application level (see Chap. 1, *Introduction and Survey*).

References

1. ISO Standard 14839-4. Mechanical vibration - Vibrations of rotating machinery equipped with active magnetic bearings - Part 4: Technical guidelines, system design (Draft), 09 2006.
2. M. Ahrens and L. Kucera. Analytical calculation of fields, forces and losses of a radial magnetic bearing with rotating rotor considering eddy currents. In *Proc. 5th Internat. Symp. on Magnetic Bearings*, pages 253–258, Kanazawa, August 1996.
3. P.E. Allaire, M.E.F. Kasarda, and L.K. Fujita. Rotor power losses in planar radial magnetic bearings – effects of number of stator poles, air gap thickness, and magnetic flux density. In *Proc. 6th Internat. Symp. on Magnetic Bearings*, pages 383–391. MIT Cambridge, August 1998.

4. J.W. Beams, J.L. Young, and J.W. Moore. The production of high centrifugal fields. *J. Applied Physics*, pages 886–890, 1946.
5. L. Burdet. *Active magnetic bearing design and characterization for high temperature applications*. PhD thesis, EPF Lausanne, 2006.
6. L. Burdet, R. Siegwart, and B. Aeschlimann. Thermal model for a high temperature AMB. In *Proc. 9th Internat. Symp. on Magnetic Bearings*, pages 21–26. Univ. of Kentucky, Lexington, August 2004.
7. D. Ewins and R. Nordmann et al. Magnetic bearings for smart aero-engines (MAGFLY). Final Report EC GROWTH Research Project G4RD-CT-2001-00625, European Community, Oct. 2006.
8. J.K. Fremerey. Radial shear force permanent magnet bearing system with zero-power axial control and passive radial damping. In *Proc. 1st Internat. Symp. on Magnetic Bearings*, pages 25–32. ETH Zurich, Springer-Verlag, 1988.
9. H. Fujiwara, O. Matsushita, and H. Okubo. Stability evaluation of high frequency eigen modes for active magnetic bearing rotors. In *Proc. 7th Internat. Symp. on Magnetic Bearings*, pages 83–88. ETH Zurich, Aug. 2000.
10. M. Holmes, R.J. Hocken, and D.L. Trumper. The long-range scanning stage: a novel platform for scanned-probe microscopy. In *Precision Engineering* Vol. 24, No. 3, July, 2000.
11. S. Jeon, H.J. Ahn, and D.C. Han. New design of cylindrical capacitive sensor for on-line precision control of amb spindle. In *Proc. 7th Internat. Symp. on Magnetic Bearings*, pages 495–500. ETH Zurich, August 2000.
12. A.S. Kondoleon and W.P. Kelleher. Soft magnetic alloys for high temperature radial magnetic bearings. In *Proc. 7th Internat. Symp. on Magnetic Bearings*, pages 111–116. ETH Zurich, August 2000.
13. R. Larsonneur. *Design and control of active magnetic bearing systems for high speed rotation*. PhD thesis, ETH Zurich, No 9140, 1990.
14. F. Loesch. *Identification and automated controller design for active magnetic bearing systems*. PhD thesis, ETH Zurich No 14474, 2002.
15. M. Mack. *Luftreibungsverluste bei elektrischen Maschinen kleiner Baugrössen*. PhD thesis, TH Stuttgart, 1967.
16. D. Meeker, E. Maslen, and M. Kasarda. Influence of actuator geometry on rotating losses in heteropolar magnetic bearings. In *Proc. 6th Internat. Symp. on Magnetic Bearings*, pages 392–401. MIT Cambridge, August 1998.
17. M. Mekhiche, S. Nichols, J. Oleksy, J. Young, J. Kiley, and D. Havenhill D. 50 krpm, 1,100 °F magnetic bearings for jet turbine engines. In *Proc. 7th Internat. Symp. on Magnetic Bearings*, pages 123–128. ETH Zurich, August 2000.
18. T. Mizuno. A unified transfer function approach to control design for virtually zero power magnetic suspension. In *Proc. 7th Internat. Symp. on Magnetic Bearings*, pages 117– 123. ETH Zurich, August 2000.
19. T. Mizuno and T. Higuchi. Experimental measurement of rotational losses in magnetic bearings. In *Proc. 4th Internat. Symp. on Magnetic Bearings*, pages 591–595. ETH Zurich, August 1994.
20. A. Molenaar, E.H. Zaaijer, and H.F. van Beek. A novel low dissipation long stroke planar magnetic suspension and propulsion stage. In *Proc. 6th Internat. Symp. on Magnetic Bearings*, pages 650–659. MIT Cambridge, August 1998.
21. M. Ohsawa, K. Yoshida, H. Ninomiya, T. Furuya, and E. Marui. High temperature blower for molten carbonate fuel cell supported by magnetic bearings. In *Proc. 6th Internat. Symposium on Magnetic Bearings*, pages 32–41. MIT Cambridge, August 1998.

22. G. Schweitzer. Magnetic bearings as a component of smart rotating machinery. In *Proc. 5th Internat. IFToMM Conf. on Rotor Dynamics, Darmstadt*, pages 3–15, Sept. 1998.
23. S.P. Timoshenko and J.N. Goodier. *Theory of elasticity.* McGraw-Hill, 3 edition, 1970.
24. F. Viggiano. *Aktive magnetische Lagerung und Rotorkonstruktion elektrischer Hochgeschwindigkeitsantriebe.* PhD thesis, ETH Zurich, Nr. 9746, 1992.
25. L. Xu, L. Wang, and G. Schweitzer. Development for magnetic bearings for high temperature suspension. In *Proc. 7th Internat. Symp. on Magnetic Bearings*, pages 117–123. ETH Zurich, August 2000.
26. L. Xu and J. Zhang. A study on high temperature displacement sensor. *IEEE Trans. on Instrumentation and Measurement*, 2000.
27. K. Yakushi, T. Koseki, and S. Sone. Three degree-of-freedom zero power magnetic levitation control by a 4-pole type electromagnet. In *Proc. Internat. Power Electronics Conference IPEC*, Tokyo, 2000.

7

Dynamics of the Rigid Rotor

Gerhard Schweitzer

7.1 Introduction

This chapter on the dynamics of the rigid rotor regards the basic properties of the mechanical plant within the active magnetic bearing loop. It presents methods for its mathematical investigation, and points to characteristics and physical limitations in its behavior. Rotordynamics is a challenging part of machine dynamics. On one hand it refers to classical results of vibration theory and gyro mechanics, and from this point of view it explains terms such as *natural vibrations*, *forward and backward whirl*, *critical speeds*, or *nutation* and *precession*. On the other hand, in practical rotordynamics there are always questions connected to phenomena which often decisively influence the operation of technical rotors. Such phenomena include process forces in machine tools, for example in milling and grinding machines, electromagnetic forces in electrical drives, interactions of fluid forces with a turbo-rotor, or non-conservative forces in seals and gaps. In these cases AMB can counteract detrimental influences on the rotor dynamics or control them. In addition, AMB with their inherent capability of measuring and influencing rotor states can make a contribution to investigate, explain and identify such phenomena, which are still areas of actual research.

7.2 Inertia Properties

The objectives of this section are to describe the *inertia properties of a rigid body* in the context of rotational motions in rotordynamics. Basic information can be found, for example, in textbooks on mechanics [7, 20], or for more advanced issues in Magnus [12] or Kane/Levinson [9]. A more direct reference to rotordynamics is given in Gasch et al. [6] or [4, 11].

The inertia properties of a rigid body for rotational motions are characterized by six mass moments of second order, the so-called inertia scalars. They can be expressed in the coordinates of a body-fixed reference system P-xyz

G. Schweitzer, E.H. Maslen (eds.), *Magnetic Bearings*,
DOI 10.1007/978-3-642-00497-1_7, © Springer-Verlag Berlin Heidelberg 2009

(Fig. 7.1), and they are grouped into the *moments of inertia* and the *products*

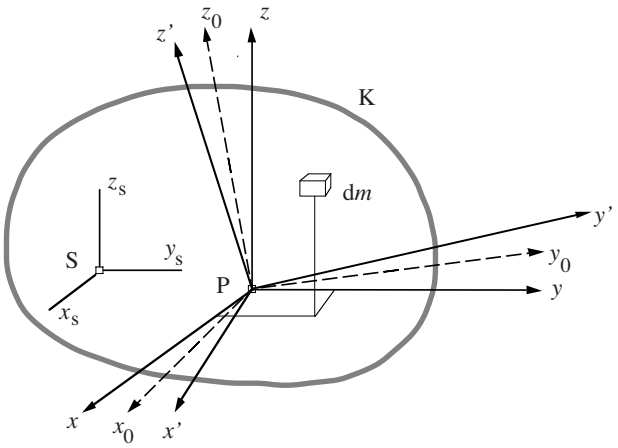


Fig. 7.1. Definition of moments and products of inertia

of inertia

$$\begin{aligned} I_x &= \int (y^2+z^2)\mathrm{d}m, \qquad & I_{yz} &= \int yz\mathrm{d}m, \\ I_y &= \int (z^2+x^2)\mathrm{d}m, \qquad & I_{zx} &= \int zx\mathrm{d}m, \\ I_z &= \int (x^2+y^2)\mathrm{d}m, \qquad & I_{xy} &= \int xy\mathrm{d}m \end{aligned} \tag{7.1}$$

The following inequalities are derived directly from (7.1), and are similar to the inequalities between the lengths of the sides of a triangle (triangle inequalities):

$$I_x + I_y \geq I_z, \qquad I_y + I_z \geq I_x, \qquad I_z + I_x \geq I_y$$

These relations can be quite useful when checking the consistency of experimental or numerical data on inertias. For a thin disc with equally distributed mass – the z-axis for example being the rotation axis – equality holds such that $I_x + I_y = I_z$.

The moments and products of inertia are the elements of a symmetric tensor, and can be represented in the well-known matrix form

$$\mathbf{I}_\mathrm{P} = \begin{bmatrix} I_x & -I_{xy} & -I_{zx} \\ \dots & I_y & -I_{yz} \\ \mathrm{sym} & \dots & I_z \end{bmatrix} \tag{7.2}$$

When changing the reference point P or changing the direction of the reference system in the body, the inertia tensor will also change. Shifting the reference system in a parallel manner by (a, b, c) from the center of mass S to P leads to

$$\begin{aligned} I_x &= I_{\mathrm{S}x} + m(b^2 + c^2)\ , & I_{yz} &= I_{\mathrm{S}yz} + mbc, \\ I_y &= I_{\mathrm{S}y} + m(c^2 + a^2)\ , & I_{zx} &= I_{\mathrm{S}zx} + mca, \\ I_z &= I_{\mathrm{S}z} + m(a^2 + b^2)\ , & I_{xy} &= I_{\mathrm{S}xy} + mab \end{aligned} \tag{7.3}$$

When changing the direction of the reference system P-xyz into the new direction P-$x'y'z'$, characterized by the transformation matrix $\mathbf{T}$, see [15, 25] or [9], the new inertia matrix is

$$\mathbf{I}_{\mathrm{P}}{}' = \mathbf{T}\mathbf{I}_{\mathrm{P}}\mathbf{T}^{\mathrm{T}} \qquad \text{with} \qquad [x, y, z]^{\mathrm{T}} = \mathbf{T}[x', y', z']^{\mathrm{T}} \tag{7.4}$$

There are well-defined directions P-$x_0y_0z_0$ for a reference system where the inertia matrix takes on a diagonal form

$$\mathbf{I}_{\mathrm{P}0} = \begin{bmatrix} I_{x0} & 0 & 0 \\ 0 & I_{y0} & 0 \\ 0 & 0 & I_{z0} \end{bmatrix} \tag{7.5}$$

These special coordinate axes are called *principal axes of inertia*, the corresponding moments of inertia are the *principal moments of inertia*. When a homogeneous body has geometrical symmetries, then the axes of symmetry are principal axes of inertia. (Fig. 7.2).

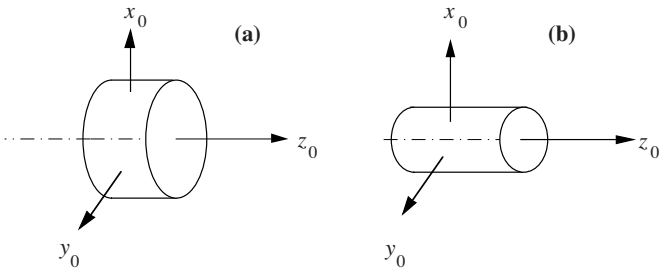


Fig. 7.2. Symmetrical rotors
(**a**) disk-like with $I_{x0} = I_{y0} < I_{z0}$, (**b**) elongated with $I_{x0} = I_{y0} > I_{z0}$

Subsequently, these relations will be illustrated using a *technical example*. The circumference of an otherwise symmetrical centrifuge drum, i.e. the rotor, with mass m carries a small additional mass Δm, an unbalance influence on the inertia (Fig. 7.3). As a consequence, the center of mass shifts by the *eccentricity* **e**. The principal axis of inertia, up to now corresponding with the geometric axis of symmetry, is now inclined by the angle ϵ. These two parameters, **e** and ϵ, characterize a *static* and a *dynamic unbalance* of the rotor (see Sect.7.5). When the rotor is rotating about the z-axis these unbalances will generate vibrating forces and torques in the bearings. Subsequently, at first, the effects of this additional mass on the mass distribution are determined. Starting from the undisturbed case the center of mass of the rotor with mass

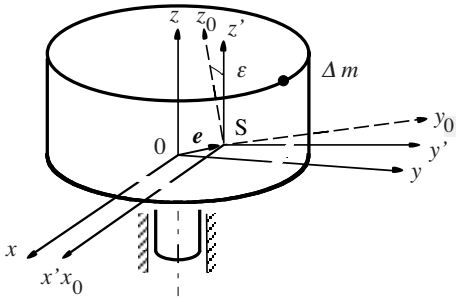


Fig. 7.3. Centrifuge cylinder with a small unbalance

m lies in 0, the inertia matrix with respect to the 0-xyz coordinate system for the symmetric rotor ($I_{x0} = I_{y0}$) is

$$\mathbf{I}_{\mathrm{O}} = \begin{bmatrix} I_x & 0 & 0 \\ 0 & I_x & 0 \\ 0 & 0 & I_z \end{bmatrix} \tag{7.6}$$

Now, the additional mass Δm with $\Delta m \ll m$ is attached at the location $(0, b, c)$, and leads to a small displacement $\mathbf{e}$ of the center of mass from O to S

$$\mathbf{e} = [e_x, e_y, e_z]^{\mathrm{T}} = [x_{\mathrm{S}}, y_{\mathrm{S}}, z_{\mathrm{S}}]^{\mathrm{T}} = [0, \frac{\Delta m}{m} b, \frac{\Delta m}{m} c]^{\mathrm{T}} \tag{7.7}$$

The inertia matrix of the disturbed rotor in the O-xyz system now is, following (7.3),

$$\mathbf{I}_{\mathrm{O}} + \Delta\mathbf{I} = \begin{bmatrix} I_x & 0 & 0 \\ 0 & I_x & 0 \\ 0 & 0 & I_z \end{bmatrix} + \begin{bmatrix} b^2 + c^2 & 0 & 0 \\ 0 & c^2 & -bc \\ 0 & -bc & b^2 \end{bmatrix} \Delta m \tag{7.8}$$

It is useful to parallel shift the coordinate system from O to the new center of mass S, as for this special point of reference the equations of motion are derived more easily (see Sect. 7.6). Then the inertia matrix in the S-$x'y'z'$ system becomes

$$\mathbf{I}_{\mathrm{S}} = \begin{bmatrix} I_{\mathrm{S}x} & 0 & 0 \\ 0 & I_{\mathrm{S}y} & -I_{\mathrm{S}yz} \\ 0 & -I_{\mathrm{S}yz} & I_{\mathrm{S}z} \end{bmatrix} \tag{7.9}$$

with

$$I_{\mathrm{S}x} = (I_x + \Delta m(b^2 + c^2)) - (m + \Delta m)(y_{\mathrm{S}}^2 + z_{\mathrm{S}}^2) \approx I_x$$

$$I_{\mathrm{S}y} \approx I_x, \qquad I_{\mathrm{S}z} \approx I_z \tag{7.10}$$

$$I_{\mathrm{S}yz} = \Delta mbc - (m + \Delta m) y_{\mathrm{S}}^2 z_{\mathrm{S}}^2 \approx \Delta mbc = I_{yz}$$

If the unbalances are sufficiently small ($\Delta m \ll m, I_{yz} << I_x$), the inertia matrix simplifies to

$$\mathbf{I}_{\mathrm{S}} \approx \begin{bmatrix} I_x & 0 & 0 \\ 0 & I_y & -I_{yz} \\ 0 & -I_{yz} & I_z \end{bmatrix} \tag{7.11}$$

The rotational axis z, and the axis z' parallel to it, are now, because $I_{yz} \neq 0$, no longer axes of inertia. The new principal axis z_0 is inclined by the angle ϵ , where

$$\tan 2\epsilon = \frac{2I_{yz}}{I_z - I_x} \tag{7.12}$$

From the above relation immediately a useful consequence for practical applications can be derived. The inclination of the principal axis with respect to the rotation axis, i.e. the sensitivity with respect to dynamic unbalances, becomes especially large, if the moments of inertia about the rotational axis and the axis orthogonal to it are equal ($I_x = I_z$). It means that such a design has to be avoided, if a smooth operation with low-level vibrations is desired.

7.3 Natural Vibrations of a Rotor on Elastic Supports

Any elastically supported body can undergo vibrations. The vibrations are described by the equations of motion of the body, which in our case is the spinning, rigid rotor. The vibrations are called *natural vibrations* if they are caused by some initial condition with no further exciting forces, and they are called forced vibrations if they are caused by some external time-varying forces. Natural vibrations characterize the dynamic behavior of the vibrating structure, i.e., its *eigenfrequencies*, its *natural modes*, and the *stability of motion*.

7.3.1 Model and Equations of Motion

The rotor of Fig. 7.4 is supported radially in two bearings. Under certain assumptions the axial suspension can be treated separately and independently from the radial one, and it, therefore, will not be considered here. To begin with, the radial bearing forces $\mathbf{f}$ are represented in a general way by four control forces, which act within the bearing planes in the x_{I}- and y_{I}-directions

$$\mathbf{f} = [f_{ax}, f_{bx}, f_{ay}, f_{by}]^{\mathrm{T}} \tag{7.13}$$

The assumptions underlying the equations of motion are the following:

- The rotor is *symmetric* and *rigid*.
- In the nominal reference position of the rotor, when it is at rest, its center of mass S coincides with the origin of the inertially fixed coordinate system I-$x_{\mathrm{I}}y_{\mathrm{I}}z_{\mathrm{I}}$.

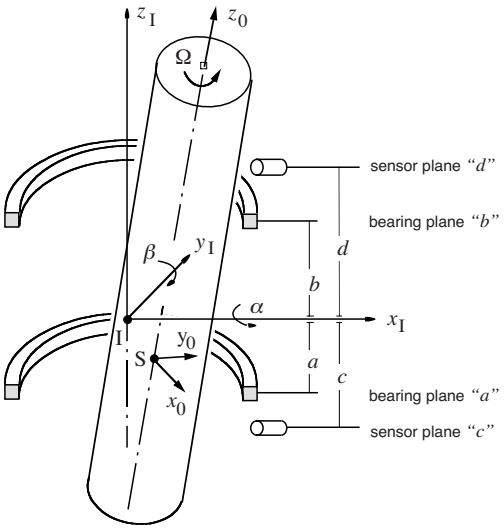


Fig. 7.4. Rigid rotor in two radial bearings. The bearing distances are considered to be negative, if they correspond to negative coordinate directions

- Deviations from the reference position are small compared to the rotor dimensions. This allows a *linearization* of the equations of motion and a decoupling of the radial motion from the axial one.
- The position of the rotor, which includes its translational and angular displacements, is characterized by the position of the rotor-fixed system of principal axes S-$x_0y_0z_0$ with respect to the inertially fixed coordinate system I-$x_\mathrm{I}y_\mathrm{I}z_\mathrm{I}$.
- The angular velocity Ω of the rotor about its longitudinal axis z_0 is assumed to be constant.

The small motions of the rotor are described by the displacements $x_\mathrm{S}, y_\mathrm{S}$ of its center of mass S with respect to the inertial reference I-$x_\mathrm{I}y_\mathrm{I}z_\mathrm{I}$ and by its inclinations. These inclinations and the angular motion around the rotor spin axis are described by the three so-called Cardan angles α, β, γ [9, 12, 20, 23]. The spin velocity $\dot{\gamma} = \Omega$ is assumed to be constant. Linearization leads to characterizing the angles α, β as inclinations about the x_I- and y_I-axis. The equations of motion for the variables

$$\mathbf{z} = [\beta, x_\mathrm{S}, -\alpha, y_\mathrm{S}]^\mathrm{T} = [z_1, z_2, z_3, z_4]^\mathrm{T} \tag{7.14}$$

follow, for example, from Lagrange's equations

$$\frac{\mathrm{d}}{\mathrm{d}t}\left(\frac{\partial T}{\partial \dot{z}_i}\right) - \frac{\partial T}{\partial z_i} = Z_i \tag{7.15}$$

with the kinetic energy T and the generalized forces Z_i.

The kinetic energy T is

$$T = \frac{1}{2}m(\dot{x}_S^2 + \dot{y}_S^2 + \dot{z}_S^2) + \frac{1}{2}(I_{x0}\omega_{x0}^2 + I_{y0}\omega_{y0}^2 + I_{z0}\omega_{z0}^2), \tag{7.16}$$

where the angular velocities are expressed in the rotor-fixed system S-$x_0y_0z_0$

$$\omega = \begin{bmatrix} \omega_{x0} \\ \omega_{y0} \\ \omega_{z0} \end{bmatrix} = \begin{bmatrix} \dot{\alpha}\cos\Omega t & +\dot{\beta}\sin\Omega t & +((\ldots)) \\ -\dot{\alpha}\sin\Omega t & +\dot{\beta}\cos\Omega t & +((\ldots)) \\ \Omega & & \end{bmatrix} \tag{7.17}$$

In (7.17), as a consequence of linearization, only the two first order terms have been retained while terms which are second order or higher and assumed to be small are omitted. The generalized forces Z_i depend on the bearing forces $\mathbf{f}$ of (7.13)

$$\begin{bmatrix} Z_1 \\ Z_2 \\ Z_3 \\ Z_4 \end{bmatrix} = \mathbf{Z} = \mathbf{B}\mathbf{f} \qquad \text{with} \qquad \mathbf{B} = \begin{bmatrix} a & b & 0 & 0 \\ 1 & 1 & 0 & 0 \\ 0 & 0 & a & b \\ 0 & 0 & 1 & 1 \end{bmatrix} \tag{7.18}$$

Hence the *equations of motion* follow in the form

$$\mathbf{M}\ddot{\mathbf{z}} + \mathbf{G}\dot{\mathbf{z}} = \mathbf{Z}$$

$$\mathbf{M} = \mathrm{diag}(I_{x0}, m, I_{x0}, m), \qquad \mathbf{G} = \begin{bmatrix} 0 & 0 & 1 & 0 \\ 0 & 0 & 0 & 0 \\ -1 & 0 & 0 & 0 \\ 0 & 0 & 0 & 0 \end{bmatrix} I_{z0}\Omega \tag{7.19}$$

The *gyroscopic effects* are typically characterized by a skew-symmetric matrix, the gyrocopic matrix $\mathbf{G} = -\mathbf{G}^{\mathrm{T}}$, which contains the rotor speed Ω as a linear factor.

In the equations of motion (7.19) the character of the *bearing forces* $\mathbf{Z}$, see (7.18), is not yet specified. Before considering them as "active" forces, i.e. controlled magnetic forces, – as will be done in Chap. 8 on the Control of the Rigid Rotor – let us investigate how the rotor would behave in classical elastic bearings. The elastic behavior may be represented by conventional linear mechanical springs. This will help us to introduce and define technical terms which characterize the dynamics of a vibrating rotor and to establish a comparison basis. Therefore, we subsequently assume that the bearing forces $\mathbf{f}$ are proportional to the displacements at the bearing sites (x_a, y_a, x_b, y_b).

The *bearing stiffness* k, for the sake of simplicity, is equal at all bearing positions and thus the following relations for the bearing forces hold:

$$\mathbf{f} = -k \begin{bmatrix} x_a \\ y_a \\ x_b \\ y_b \end{bmatrix} = -k \begin{bmatrix} a & 1 & 0 & 0 \\ b & 1 & 0 & 0 \\ 0 & 0 & a & 1 \\ 0 & 0 & b & 1 \end{bmatrix} \mathbf{z}$$

$$\mathbf{Z} = \mathbf{B}\mathbf{f} = -k \begin{bmatrix} a^2+b^2 & a+b & 0 & 0 \\ a+b & 2 & 0 & 0 \\ 0 & 0 & a^2+b^2 & a+b \\ 0 & 0 & a+b & 2 \end{bmatrix} \mathbf{z} = -\mathbf{K}\mathbf{z} \tag{7.20}$$

This, finally, leads to the following form for the equations of motion:

$$\mathbf{M}\ddot{\mathbf{z}} + \mathbf{G}\dot{\mathbf{z}} + \mathbf{K}\mathbf{z} = \mathbf{0} \qquad \text{with} \qquad \mathbf{z} = [\beta, x_\mathrm{S}, -\alpha, y_\mathrm{S}]^\mathrm{T} \tag{7.21}$$

In general, the translatory motions $x_\mathrm{S}, y_\mathrm{S}$ and the angular motions α, β will be *coupled*. In addition to that, the motions in the $x_\mathrm{I}z_\mathrm{I}$-plane will be coupled with the motions in the $y_\mathrm{I}z_\mathrm{I}$-plane, if the rotor speed $\Omega \neq 0$.

7.3.2 Stability of Motion

Equations of motion of the form (7.21) have been extensively treated in the literature, especially with regard to the stability of their solutions. In order to investigate stability, it is not even necessary to derive the solutions $\mathbf{z}(t)$ explicitly; it is already sufficient [12, 13] to look somewhat closer at the *structural matrices* in (7.21). These structural matrices characterize the mass and stiffness distributions within the mechanical system, and they have well-defined symmetry and definiteness properties [15, 25]. The mass matrix is symmetric and positive definite, $\mathbf{M} = \mathbf{M}^\mathrm{T} > 0$; the gyroscopic matrix is skew symmetric, $\mathbf{G} = -\mathbf{G}^\mathrm{T}$; and the stiffness matrix is symmetric, $\mathbf{K} = \mathbf{K}^\mathrm{T}$. The system (7.21) is conservative, i.e., it does not show any energy dissipation, and thus it is limit-stable if for the stiffness matrix $\mathbf{K} > 0$ holds: in other words, if it is statically stable. Such a system can not be destabilized by gyroscopic forces, and therefore it will remain stable at any rotor speed Ω.

A usual model for the vibrational motions of a rotor system with no excitations acting on it, and somewhat extended with respect to (7.21), is the homogeneous, linear system of equations

$$\mathbf{M}\ddot{\mathbf{z}} + (\mathbf{G}+\mathbf{D})\dot{\mathbf{z}} + (\mathbf{K}+\mathbf{N})\mathbf{z} = \mathbf{0} \tag{7.22}$$

A new term is the damping matrix $\mathbf{D} = \mathbf{D}^\mathrm{T} \geq 0$, and the matrix of the *nonconservative bearing forces* $\mathbf{N} = -\mathbf{N}^\mathrm{T}$. For $\mathbf{N} \equiv \mathbf{0}$ the solution is asymptotically stable or at least limit-stable, if the system is statically stable, independent of how large the damping is. On the other hand, the nonconservative bearing

forces can have stabilizing as well as destabilizing effects (see also Sect. 7.4.4). In this case, an investigation of stability has to be supported by an explicit analysis of the eigenvalues.

7.3.3 Natural Vibrations

The solutions of the system (7.21) of linear, homogeneous differential equations for an undamped mechanical vibration system will be harmonic vibrations with amplitudes depending on initial conditions [14, 19, 22]. The system under consideration here is of 8th order and its solution is characterized by 4 natural vibrations, with properties – the natural frequencies and the natural modes – which follow from the eigenvalues. But even for this still technically simple example, the eigenvalues cannot be determined analytically any longer. However, meaningful limit cases which can be easily explained can be obtained for the free rotor, with the bearing stiffness $k \equiv 0$, and for the non-rotating rotor with $\Omega \equiv 0$.

For the *free rotor* ($k \equiv 0$), rotation and translation are decoupled, and hence the eigenfrequencies follow as

$$\omega_1, \omega_2, \omega_3 = 0, \qquad \omega_4 = \omega_{\text{N}} = \Omega I_{z0}/I_{x0} \tag{7.23}$$

The three "zero" natural frequencies stand for the so-called rigid-body-modes, where two of them are translational motions and one is an angular motion. The fourth natural frequency ω_{N} belongs to the natural vibration called nutation. This nutation frequency will be equal to the rotor frequency Ω, if $I_{x0} = I_{z0}$. Obviously such a coincidence between a natural frequency and the rotor frequency, which is a potential disturbance frequency, is highly undesirable, as it could be a source of a *permanent resonance* (see (7.12) as well). Resonances will be dealt with in more detail in Sect. 7.6 on Rotor Excitations and Critical Speeds. It should be mentioned that, for a disc-like rotor, because $I_{z0} > I_{x0}$, it is always true that $\omega_{\text{N}} > \Omega$, and therefore no resonance with a nutation frequency will ever occur in this case.

For the *non-rotating rotor* ($\Omega \equiv 0$) the system of equations (7.21) splits up into two independent, equal parts, i.e., the natural vibrations in the xz- and in the yz-plane are equal and decoupled. If, additionally, both of the bearings are arranged symmetrically ($a = -b$), then the natural vibrations in each plane degenerate to pure translational vibrations in the x_{I}- and y_{I}-direction, respectively, with the frequency

$$\omega_{\text{T}} = \sqrt{2k/m} \tag{7.24}$$

and to pure angular vibrations about the angles β and α, respectively, with the frequency

$$\omega_{\text{D}} = \sqrt{2ka^2/I_{x0}} \tag{7.25}$$

For a special set of parameters, the eigenvalues as well as the shapes of the corresponding natural modes are displayed with their dependance on the rotor

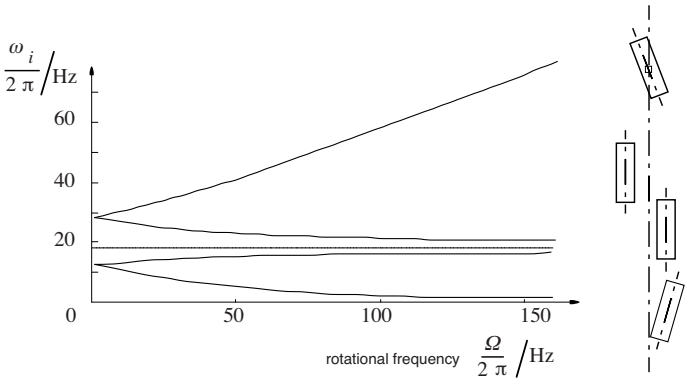


Fig. 7.5. Eigenvalues depending on the rotor speed for an elastically supported, rigid rotor. On the right side the typical shapes of the corresponding natural modes are outlined. ($m = 10$ kg, $I_{x0} = 1$ kgm^2, $I_{z0} = 0.1$ kgm^2, $a = 0.33$ m, $b = 0.15$ m, $k = 200$ N/mm)

speed Ω in Fig. 7.5. The influence of the rotor speed shows in a typical way, and this will be demonstrated in more detail in the next section.

7.4 Influence of Rotor Speed and Gyroscopic Effects

The basic differences between the dynamic behavior of a non-rotating body and a rotating one are caused by gyroscopic properties [12, 19]. When the inertia I_{z0} of the spinning rotor about its axis of rotation z is large with respect to the inertia about a transversal axis, i.e. when the rotor is sufficiently disc-like ($I_{z0} > I_{x0}$), or when the rotor is rotating very fast ($\Omega \gg 1$), then the gyroscopic term $\mathbf{G}$ in (7.19), which is proportional to $I_{z0}\Omega$, can not be neglected. This gyroscopic term contributes in characteristic ways to the dynamics of the rotor vibrations.

7.4.1 Gyrodynamics

The differences in the dynamics of a spinning and a non-spinning rotor can be easily seen by looking at the behavior of a free rotor (imagine that it is spinning in space in a gravity-free environment) when it is disturbed by an impulse. We distinguish between a *force* impact and a *torque* impact.

When a *force* impact $\underline{\mathbf{F}}$ is acting on the center of mass S of such a free rotor with mass m, then its *momentum* $\underline{\mathbf{p}}$ during that very short time of impact changes by the value $\Delta\underline{\mathbf{p}} = \int \underline{\mathbf{F}} \mathrm{d}t$, and hence, following Newton's Law, the center of mass moves in the direction of the applied force with the velocity $\Delta\underline{\mathbf{p}}/m$, assuming that the rotor center of mass has been initially at rest. This means that, due to this disturbance, the displacement of the rotor with

respect to an inertially fixed reference position will increase linearly with time, independent of whether the rotor is rotating or not.

The *torque* impact $\underline{\mathbf{M}}$, however, generated for example by the force couple $(\underline{\mathbf{F}}, \underline{-\mathbf{F}})$ of Fig. 7.6 during a short period of time resulting in $\underline{\mathbf{M}} = \underline{\mathbf{d}} \times \underline{\mathbf{F}}$, corresponds to the change of the *moment of momentum* $\Delta\underline{\mathbf{L}} = \int \underline{\mathbf{M}} \mathrm{d}t$. The original moment of momentum of the rotor is $\underline{\mathbf{L_0}} = I_{z0}\underline{\mathbf{\Omega}}$, if the rotor is rotating with angular speed $\underline{\mathbf{\Omega}}$ about its principal axis z_0. Thus this original moment of momentum $\underline{\mathbf{L_0}}$ changes its size and its direction and due to the torque impact becomes $\underline{\mathbf{L_1}}$. The small change of its size means that the rotor speed Ω has changed by only a small amount. The change of direction, however, is more relevant. The outcome is shown in Fig. 7.6, and is explained in more detail subsequently. Initially, the rotor may rotate about the inertially fixed axis z_I, and its body-fixed principal axis z_0 coincides with this inertially fixed axis. This is the case of a *permanent rotation*: principal axis, rotation axis, and the axis of the moment of momentum coincide. The torque impact, then, generates a step-like change of the vector of the moment of momentum from $\underline{\mathbf{L_0}}$ to $\underline{\mathbf{L_1}}$. The axis of rotation, however, does not change its direction during the short duration of the impact, and thus, after the impact, the axis of rotation and the axis of the moment of momentum have different directions.

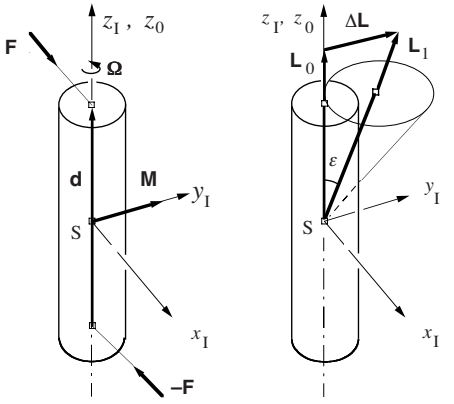


Fig. 7.6. A torque impact on the rotor, caused for example by the couple $(\underline{\mathbf{F}}, \underline{-\mathbf{F}})$, acting during a very short time period, is leading to a change in direction for the axis of the moment of momentum and to a nutational motion of the rotor axis

This leads to a visible motion of the rotor axis, a *nutation*, where the rotor axis whirls around the inertially fixed, new direction of the axis of the moment of momentum. The motion, in the case of the symmetric rotor, is

a conical one, the cone angle following from $\tan\epsilon = \Delta L/L_1$. In the average, therefore, the axis of the spinning rotor is inclined by the angle ϵ. This angular displacement becomes smaller and smaller the faster the rotor is spinning. By its spin the rotor becomes "stiff" with respect to disturbing torques.

The above mentioned conical motion is represented in (7.21) in such a way, that the angular motions α, β of the rotor are coupled through the gyroscopic matrix $\mathbf{G}$. As soon as the rotor is spinning ($\Omega \neq 0$), the angles $\alpha(t)$ and $\beta(t)$ will not be independent from one another any more. The resulting "whirl" will be discussed in the following section.

7.4.2 Forward and Backward Whirl

In Sect. 7.3, the natural vibrations of a mechanical system according to (7.21) have been considered in a general way. Now, the next step will be to relate these natural vibrations to the spinning of the rotor.

Typical natural vibrations of a spinning rotor manifest themselves as a "whirling" of the rotor axis, which whirls in the same sense as the rotor spin Ω, i.e. in a *forward whirl*, or opposite to it in a *backward whirl*. A distinction between forward and backward whirl is important as any operating rotor is exposed to harmonic excitations caused by unbalances (see Sect. 7.6). As the unbalances rotate with the rotor spin they can only excite natural vibrations whirling in the same sense as the rotor, i.e. forward whirls, leading actually to the well-known classical "resonances". Of course, if the rotor system is not symmetric or if there are other kinds of excitations (see Sect. 7.6) then both forward and backward whirls can lead to resonances.

7.4.3 Behavior at High Rotor Speeds

In order to come to know the dynamics of the rotor at high speeds Ω, the asymptotic behavior of the eigenvalues as a function of Ω will be considered. By doing this, it will be possible to distinguish *nutation* and *precession* frequencies, which vary with the rotor speed, and frequencies for *pendulous vibrations* which are largely independent of the rotor speed. General investigations of this kind concerning the behavior of rotor systems are described in more detail in [12, 14, 18].

For a discussion of their asymptotic behavior at very high rotor speed Ω the eigenvalues are arranged in four groups. The positive constants m, g, k in (7.26–7.29) characterize values for the inertia, the gyroscopic effects and the stiffness, each of the constants related to the natural vibration under consideration. The constants lie within the range of values of the structural matrices $\mathbf{M}, \mathbf{G}, \mathbf{K}$, respectively, and their specific values can be estimated by Rayleigh-quotients [14, 18]. Thus, the following equations demonstrate the behavior of the natural frequencies at high rotor speed Ω for the four typical groups of natural vibrations.

In the simple example of Fig. 7.5, these four groups just correspond to the four natural frequencies at high rotor speed:

Nutations are always forward whirls and have frequencies which increase with Ω :

$$\omega_{\mathrm{N}} = \Omega \mathrm{g_N}/\mathrm{m_N} \tag{7.26}$$

In the case of the example of Sect. 7.3 there is only one nutation frequency, and, following (7.23), it tends to the value $\omega_{\mathrm{N}} = \Omega I_{z0}/I_{x0}$. Here, the constant $\mathrm{g_N}$, characterizing the inertia properties, is equal to the ratio of the two moments of inertia I_{z0}/I_{x0}.

Precessions are backward whirls and their frequencies decrease with Ω

$$\omega_{\mathrm{P}} = \frac{\sqrt{\mathrm{k_P}/\mathrm{m_P}}}{\Omega \mathrm{g_P}} \qquad \text{and} \qquad \lim_{\Omega \to \infty} \omega_{\mathrm{P}} = 0 \tag{7.27}$$

Forward whirling pendulous vibrations have frequencies which are largely independent of Ω. They occur if the gyroscopic effects do not pervade all degrees of freedom

$$\omega_{\mathrm{FW}} = \sqrt{\mathrm{k_{FW}}/\mathrm{m_{FW}}} \tag{7.28}$$

Backward whirling pendulous vibrations, too, have frequencies which are largely independent of Ω

$$\omega_{\mathrm{BW}} = \sqrt{\mathrm{k_{BW}}/\mathrm{m_{BW}}} \tag{7.29}$$

When the bearing forces will not be passively generated by springs, but actively by magnetic bearings, it is these four natural vibrations which have to be taken care of by a suitable control. For example, it is obvious that it will be very difficult to control the nutations because, from physical reasons, they are high frequency vibrations. The considerations above can be extended to systems with damping. It can be shown that the *natural damping* of a precessional vibration decreases with the rotor speed, and this means that the *active damping control* of a precessional motion, may become – again for physical reasons – a difficult task as well.

7.4.4 Nonconservative Forces

Special attention has to be given to the *destabilizing properties of nonconservative or circulatory forces*, arising for example from internal damping, steam whirl in turbines, seal effects, or process forces in grinding, which all can lead to a self-excitation in technical rotors (see also Sect. 7.3.2 on the Stability of Motion). These nonconservative forces **Nz** in (7.22) usually depend directly on the rotor speed, or for their existence they at least require a vibrating, spinning rotor. There is special literature on the modeling of these effects [4, 11, 17].

In practical rotordynamics it quite often is not simple at all to clearly recognize such phenomena and to identify them. Therefore, once again there are issues in the physical and mathematical modeling of phenomena which can often decisively influence the operation of technical rotors. These include the nonconservative interaction of fluid forces with the elastic rotor of a turbine or the effects of fluid forces in clearances, leakages and seals, the process forces in machine tools for milling and grinding, or electromagnetic forces within an electric drive. These phenomena are areas of active research, where magnetic bearings can contribute to clarify such phenomena and to control them.

In these cases, magnetic bearings can be useful in two ways. On one side, they allow the building of test rigs where these nonconservative forces can be measured in a well-defined way and separately from other influences of the bearing. On the other side, magnetic bearings may be used to generate bearing forces, first in order to control the effects of nonconservative disturbances and second to simultaneously superimpose test forces acting on the spinning rotor. Such test forces allow identification of the dynamics of a rotor (see Chap. 11 on Identification), to experimentally determine unknown parameters such as damping, unbalances, process forces, or the nonconservative characteristics of a classical oil-film bearing.

7.5 Static and Dynamic Unbalance

It is appropriate to add some remarks to this important term *unbalance*, extending the explanations on the inertia of a rotor in Sect. 7.2. In the technical example of Fig. 7.3, the eccentricity e and the inclination ϵ of the principal axis of inertia PA characterize a *static unbalance* and a *dynamic unbalance* of the rigid rotor. Both of them are shown as distinctly separate unbalances in Figs. 7.7 and 7.8.

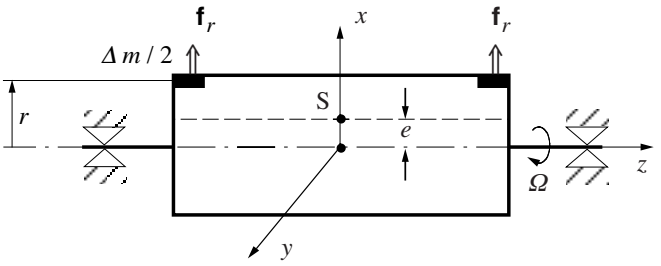


Fig. 7.7. Static unbalance

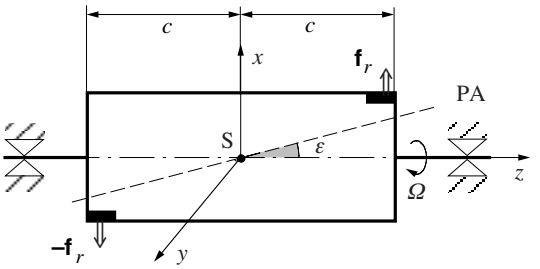


Fig. 7.8. Dynamic unbalance

When the rotor is rotating with the speed Ω the resulting centrifugal force $\underline{\mathbf{f}}_r$, acting on one of the additional masses $\Delta m/2$ and rotating together with the rotor, is

$$\mathbf{f}_r = \left[\frac{\Delta m}{2} r\Omega^2, 0, 0\right]^{\mathrm{T}} \tag{7.30}$$

For a *static unbalance*, the centrifugal forces acting upon the two small additional masses of Fig. 7.7 can be combined into a resulting force through the center of mass S. For the *dynamic unbalance* of Fig. 7.8, however, the centrifugal forces acting on the two additional masses have a distance of $2c$ and opposite directions, i.e.: there is a couple due to these inertia forces about the y-axis, resulting in a torque $\underline{\mathbf{M}}$. With (7.30) and $I_{zx} = 2cr\Delta m/2$, this leads to

$$\mathbf{M} = [0, M_y, 0]^{\mathrm{T}}, \qquad \text{with} \qquad M_y = 2cf_r = rc\Delta m\Omega^2 = I_{zx}\Omega^2 \tag{7.31}$$

Seen from an inertially fixed observer, the rotor, of course, does not exert a constant force or a constant torque but vibrating forces, which finally act through the bearings onto the housing. If the bearings are suspended elastically the rotor has the possibility to move, and it will vibrate. These vibrations in the bearings can be measured, and from the phase angles and the amplitudes of the vibrations with respect to the rotation angle of the rotor, the unbalances can be determined: a static unbalance leads to equally phased vibrations in the left and in the right bearing, a dynamic unbalance to vibrations with opposite phase. Then the unbalances can be eliminated by *balancing*, by adding or by removing suitable masses, or even by shifting counter-masses along the circumference of the rotor [1], in predetermined correction planes.

The *required balance quality grade* and the *permissible residual unbalance* depend on the application area to which the rotor belongs, and on the rotor speed. A measure for the quality of balancing is the velocity with which the center of mass circles the rotation axis, this circular speed $e\Omega$ being measured in mm/s. A classification of various applications and the corresponding balance quality grades are detailed in the ISO Standard 1940 [8], or the VDI-Richtlinie 2060. Table 7.5 shows a part of this classification. Further literature

Table 7.1. Various groups of unbalance quality grades for representative rigid rotors, following ISO Standard 1940

Balance quality grade	$\frac{e}{\mathrm{mm/s}}$	Rotor types - General examples
...	...	...
G 6.3	6.3	centrifuge drums, fans, flywheels, pump impellers, normal electrical armatures
G 2.5	2.5	gas and steam turbines, rigid turbo-generator rotors, turbo-compressors, machine-tool drives, medium and large electrical armatures, turbine-driven pumps
G 1	1	grinding machine drives, tape recorder drives, small electrical armatures with special requirements
...	...	...

about this large field of balancing rigid and elastic rotors may be found in [5, 6, 10, 16].

Using magnetic bearings can contribute to solving the problem of "balancing". For example, it is possible to design a control that lets the rotor spin about its principal axis of inertia within the air gap and without touching the housing. Thus, the rotor is suspended in such a way that no unbalance forces are acting on it any more. This procedure is well known in AMB-applications, and indeed, such a compensation of unbalance signals by a suitable feed-forward control is a very useful feature of AMB-technology. Some of the known concepts on the "force-free" spinning of a rotor and the unbalance compensation will be dealt with in Chap. 8 on the Control of the Rigid Rotor.

7.6 Rotor Excitations and Critical Speeds

Various sources of excitation of the rotor system can lead to *resonance phenomena*, to critical speeds and to critical loads. The resonances occur at certain speeds of the rotor, the "critical speeds", usually when the frequency of some excitation source corresponds to or is in a special relation to a natural frequency of the rotor-bearing system. Excitation sources can be the rotor itself with its unbalances; the whole suspension system can be excited when the rotor is mounted on a moving base; the industrial process, where a rotor is used, can cause excitations as in a milling machine tool; and the rotor system itself can be particularly sensitive to certain excitations due to internal structural properties such as rotating asymmetries. The technically most important source for exciting vibrations in a rotor system are unbalances. As

technical rotors almost always have small residual unbalances and as they are the most frequent source of disturbances, these "classical" critical speeds due to unbalance excitation will be dealt with somewhat more extensively in the following section.

7.6.1 Critical Speeds by Rotor Unbalances

Rotor unbalances have been discussed in the previous section. In order to investigate the effects of such unbalances on the state of motion of the rotor, in a first step, the unbalance excitation has to be included into the equations of motion (7.21). The unbalance is represented by a small *eccentricity* $\underline{\mathbf{e}}$, i.e. a deviation of the center of mass S from the geometric center C of the rotor, and by *products of inertia* (see example of Fig. 7.3). The equations of motion will be formulated using the center of mass S as point of reference (Fig. 7.9), and as in Sect. 7.3.1 the kinetic energy will be the starting point:

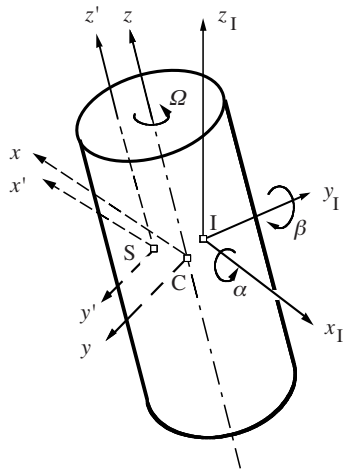


Fig. 7.9. Coordinates and variables for the rotor with unbalance

$$T = \frac{1}{2}m(\dot{x}_\mathrm{S}^2 + \dot{y}_\mathrm{S}^2 + \dot{z}_\mathrm{S}^2) + \frac{1}{2}\omega^\mathrm{T}\mathbf{I}_\mathrm{S}\omega \tag{7.32}$$

Here, $\dot{x}_\mathrm{S}, \dot{y}_\mathrm{S}, \dot{z}_\mathrm{S}$ are the velocities of the center of mass S with respect to the inertially fixed coordinate system I-$x_\mathrm{I}y_\mathrm{I}z_\mathrm{I}$. The angular velocity ω of the rotor, i.e. of the rotor-fixed S-$x_0y_0z_0$-system with respect to the fixed one is the same as that of the rotor-fixed C-xyz-system, and therefore ω can be taken over from (7.17). The inertia matrix $\mathbf{I}_\mathrm{S}$ with respect to S-$x_0y_0z_0$ now contains products of inertia as well, because of unbalances.

Considering Sect. 7.2, the inertia matrix becomes

$$\mathbf{I}_{\mathrm{S}} = \begin{bmatrix} I_x & -I_{xy} & -I_{zx} \\ \dots & I_y & -I_{yz} \\ \mathrm{sym} & \dots & I_z \end{bmatrix} \tag{7.33}$$

When deriving the equations of motion according to Lagrange, linearization will lead to considerable simplifications. In addition to the variables and their derivatives, the unbalances, too, will be treated as small quantities. With the generalized variables

$$\mathbf{z}_{\mathrm{S}} = [z_{\mathrm{S}1}, z_{\mathrm{S}2}, z_{\mathrm{S}3}, z_{\mathrm{S}4}]^{\mathrm{T}} = [\beta, x_{\mathrm{S}}, -\alpha, y_{\mathrm{S}}]^{\mathrm{T}} \tag{7.34}$$

using, for example, the Lagrange's equations

$$\frac{\mathrm{d}}{\mathrm{d}t}\left(\frac{\partial T}{\partial \dot{z}_{\mathrm{S}i}}\right) - \frac{\partial T}{\partial z_{\mathrm{S}i}} = Z_{\mathrm{S}i} \tag{7.35}$$

the equations of motion can be obtained. However, in the end, there is more interest in describing the motion $\mathbf{z}$ of the geometric center C of the rotor

$$\mathbf{z} = [z_1, z_2, z_3, z_4]^{\mathrm{T}} = [\beta, x_{\mathrm{C}}, -\alpha, y_{\mathrm{C}}]^{\mathrm{T}} \tag{7.36}$$

than in the motion $\mathbf{z}_{\mathrm{S}}$ of the center of mass. The motion $\mathbf{z}$ of this geometric rotor center C is amenable to measurements with suitable displacement sensors. The position of the center of mass S, however, is usually not even precisely known and not accessible to simple measurements. Therefore, the eccentricity $\underline{\mathbf{e}}$, i.e., the distance between C and S

$$\mathbf{e} = [e_x, e_y, e_z]^{\mathrm{T}} \qquad \text{with} \qquad |e| \ll 1$$

has to be considered in order to change the variables from $\mathbf{z}_{\mathrm{S}}$ to $\mathbf{z}$:

$$\mathbf{z}_{\mathrm{S}} = \begin{bmatrix} \beta \\ x_{\mathrm{S}} \\ -\alpha \\ y_{\mathrm{S}} \end{bmatrix} = \mathbf{z} + \begin{bmatrix} 0 \\ e_x \cos \Omega t - e_y \sin \Omega t \\ 0 \\ e_x \sin \Omega t + e_y \cos \Omega t \end{bmatrix} \tag{7.37}$$

The generalized forces acting on the geometric rotor center C are approximated by

$$\mathbf{Z} \approx \mathbf{Z}_{\mathrm{S}} \tag{7.38}$$

Then the equation of motion (7.19) takes on the form

$$\mathbf{M}\ddot{\mathbf{z}} + \mathbf{G}\dot{\mathbf{z}} = \mathbf{Z} + \mathbf{U}\mathbf{s} \tag{7.39}$$

with

$$\mathbf{U} = \Omega^2 \begin{bmatrix} I_{yz} & I_{zx} \\ -me_y & me_x \\ I_{zx} & I_{yz} \\ me_x & me_y \end{bmatrix}, \qquad \text{and with} \qquad \mathbf{s} = \begin{bmatrix} \sin \Omega t \\ \cos \Omega t \end{bmatrix} \tag{7.40}$$

Considering the bearing forces contained in $\mathbf{Z}$ as elastic forces, together with (7.20), finally the following equations of motion are obtained

$$\mathbf{M}\ddot{\mathbf{z}} + \mathbf{G}\dot{\mathbf{z}} + \mathbf{K}\mathbf{z} = \mathbf{U}\mathbf{s} \tag{7.41}$$

The right-hand side represents a harmonic excitation. The response to harmonic excitations is a harmonic vibration, too, with the same frequency, but with an amplitude and phase which depend on the excitation frequency. The response is characterized by the so-called *frequency response* [6, 22]. A peculiarity of the unbalance excitation, i.e. of the structure of $\mathbf{Us}$ is, that it can only excite natural vibrations which whirl in the same sense as the direction of the rotor spin (*forward whirl*, see Sect. 7.4.2). Thus the *resonance curves* or the *amplitude frequency responses* show that a system with n different natural frequencies has only $n/2$ resonance peaks, and that therefore there can only be $n/2$ critical speeds due to unbalance for this iso-elastically suspended rotor.

A *simple example* may explain the behavior of the rotor center C and the mass center S during an unbalance excitation. We assume that the rotor system is symmetric, and therefore the translational motions are decoupled from the angular ones. Then, the static unbalance of Fig. 7.10 leads to a simplification, too, of (7.41) for the motion $x_\mathrm{C}, y_\mathrm{C}$ of the rotor center C:

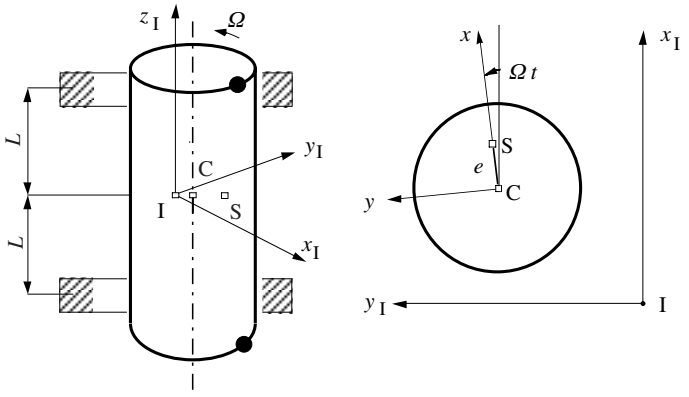


Fig. 7.10. Symmetrically supported rotor excited by a static unbalance

$$\begin{bmatrix} \ddot{x}_C \\ \ddot{y}_C \end{bmatrix} + \begin{bmatrix} \omega^2 & 0 \\ 0 & \omega^2 \end{bmatrix} \begin{bmatrix} x_C \\ y_C \end{bmatrix} = \begin{bmatrix} e\Omega^2 \cos \Omega t \\ e\Omega^2 \sin \Omega t \end{bmatrix}, \qquad \omega^2 = k/m \tag{7.42}$$

For this simple example, the solution can be determined analytically. The assumed solution

$$x_\mathrm{C}(t) = c(\Omega) \cos \Omega t, \qquad y_\mathrm{C}(t) = s(\Omega) \sin \Omega t \tag{7.43}$$

is introduced into (7.42), resulting in a solution for the vibration amplitudes

$$c(\Omega) = s(\Omega) = e\frac{\Omega^2/\omega^2}{1-\Omega^2/\omega^2} \tag{7.44}$$

The rotor center C moves in a forward whirl on a circular trajectory with the radius

$$r_{\mathrm{C}}(\Omega) = \sqrt{{x_{\mathrm{C}}}^2 + {y_{\mathrm{C}}}^2} = e\frac{\Omega^2/\omega^2}{1-\Omega^2/\omega^2} \tag{7.45}$$

The mass center S, too, moves on a circle with the radius

$$\begin{aligned} r_{\mathrm{S}}(\Omega) = \quad & \sqrt{{x_{\mathrm{S}}}^2 + {y_{\mathrm{S}}}^2} \quad = \frac{e}{1-\Omega^2/\omega^2}, \qquad \text{with} \\ x_{\mathrm{S}}(t) \; &= x_{\mathrm{C}}(t) + e\cos\Omega t = \frac{e}{1-\Omega^2/\omega^2} \quad \cos\Omega t \\ y_{\mathrm{S}}(t) \; &= y_{\mathrm{C}}(t) + e\sin\Omega t = \frac{e}{1-\Omega^2/\omega^2} \quad \sin\Omega t \end{aligned} \tag{7.46}$$

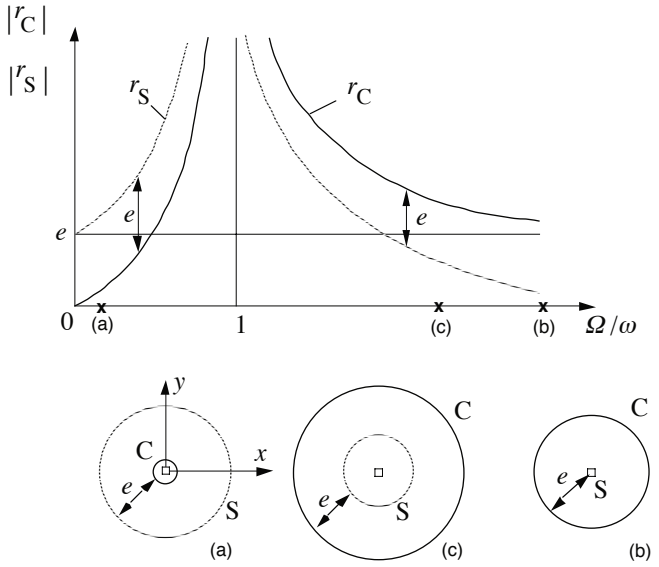


Fig. 7.11. Resonance curves and trajectories for the geometric center C and the center of mass S

Figure 7.11 shows the resonance curves and additionally the trajectories for C and S. They illustrate the "switching" from a sub-critical to a super-critical range of the rotor frequency Ω. For low rotor frequencies (location (a) on the frequency-axis), S whirls on the outer trajectory, and at high rotor speed, higher than (c), the rotor tends towards spinning about an axis through S, thus

centering itself. The phase jump occurs at the critical speed. This principle of "self-centering" explains, too, that it is important to balance the rotor, i.e. to make C and S coincide, if in all ranges of the rotor speed a smooth operation is desired.

7.6.2 Other Harmonic Excitations

The *backward whirls*, which are not excited by unbalances, can definitely also lead to resonances if there are other differently structured excitations. They arise, for example, if the foundation vibrates horizontally with $x_{\mathrm{I}e}(t) = h \sin \Omega_e t$ in x_{I}-direction (Fig. 7.12 left), or if a tool at the tip of the rotor experiences an oscillatory force $f_{\mathrm{I}x} = f_0 \sin \Omega_e t$ in x_{I}-direction (Fig. 7.12 right), or if the rotor is exposed to varying forces due to the magnetic pull of an electric drive.

For example, the oscillatory excitation of the rotor tip (Fig. 7.12 right) is described by a right-hand side of (7.39) in the form

$$\mathbf{Us} = f_0 \begin{bmatrix} c \\ 1 \\ 0 \\ 0 \end{bmatrix} \sin \Omega_e t \tag{7.47}$$

The resonance curves resulting from this kind of excitation show that the trajectories of a point on the rotor axis are not circles any more but ellipses.

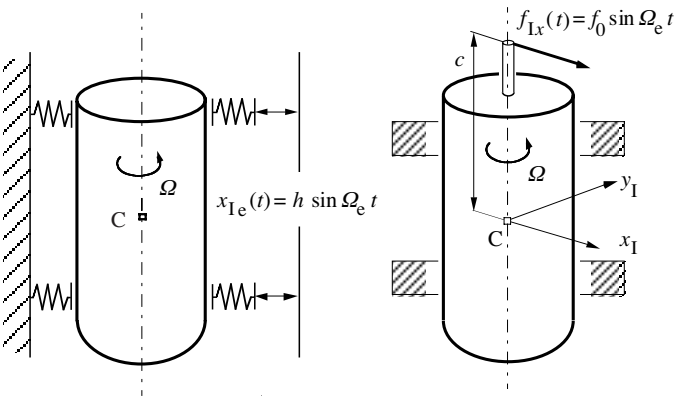


Fig. 7.12. Excitation of the rotor by vibrations of the foundation (left), or by oscillatory forces on a tool at the tip of the rotor (right)

7.6.3 Excitation by Mechanical Sensor and Actuator Offsets

Up to this point, there has been a tacit assumption: that the points of attack for the bearing forces lie on the geometric axis of symmetry of the rotor. This

actually does not have to be the case, for example, if the rotor is bent. For a magnetic bearing there may be the additional effect that the "magnetic axis" of the rotor, through which the resulting magnetic bearing force passes, may deviate from the geometric axis. The same effect can happen to the "sensor axis" as well. This is the axis, the motion of which is measured by the sensors, and consequently the result of the measurements depends on the correct mounting of the sensors, too. These deviations from an ideal state can all lead to an excitation of vibrations of the rotor, or to displacements of the rotor axis. However, modeling for this kind of excitations still is not yet generally available for magnetic bearings.

7.6.4 Parametric Excitations by Unsymmetries

So far, the equations of motion have been described as linear differential equations with constant coefficients. In some technical rotor applications this is not sufficient any more, even when only considering small displacements. If there are *asymmetries in the distribution of mass or stiffness in a rotating system*, in general, these asymmetry parameters will lead to linear differential equations with periodically time-varying coefficients [14]. As a consequence of this so-called *parameter-excitation*, the rotor motion in many ranges of the rotor frequency will be unstable or weakly damped. For example, a turbo-generator with two poles will have a radially asymmetric cross-section, and therefore the moments of inertia as well as the stiffness will be different about the two lateral axes. For centrifuge-like rotors, such effects have been investigated even with respect to a magnetic suspension [2]. Similar, and even more complex parameter-excitations, can occur in liquid-filled rotors, as have been dealt with, for example, by Brommundt [3].

7.6.5 Non-Periodic Excitations

Of special interest are transitional motions of the rotor, i.e. a non-stationary behavior as a consequence of a variety of disturbances, which can lead to critical rotor states, too. Technical reasons for such disturbances, for example, are the sudden loss of a blade in a turbo-machine [24], the breakage of the tool of a milling-spindle, or a sudden pressure increase by a leakage in a turbo-molecular pump. The contact of a spinning rotor with the housing is a highly nonlinear impact/rubbing phenomenon, which can lead to chaotic vibrations as shown already in [21]. Because of its relevance for AMB operation under emergency conditions, it will be dealt with later in a special chapter on Touch-down Bearings (Chap. 13). Non-periodic excitations can as well be used as an intentional test signal – they could even be generated with the magnetic bearing itself – as a deliberate vibration input for identification purposes (Chap. 11).

References

1. K. Adler, Ch. Schalk, R. Nordmann, and B. Aeschlimann. Active balancing of a supercritical rotor on active magnetic bearings. In H. Bleuler and G. Genta, editors, *Proc. 10th Internat. Symp. on Magnetic Bearings*, pages 49–54, Martigny, Aug. 2006.
2. E. Anton. *Stabilitätsverhalten und Regelung von parametererregten Rotorsystemen.* Fortschr.-Ber., Reihe 8, Nr. 67. VDI-Verlag, Düsseldorf, 1984.
3. E. Brommundt and G.P. Ostermeyer. Zur Stabilität eines flüssigkeits-gefüllten Rotors mit anisotrop elastischer Lagerung. *ZAMM*, 66, 1986.
4. D. Childs. *Turbomachinery Rotordynamics: Phenomena, Modeling, and Analysis.* John Wiley and Sons, 1993.
5. M.S. Darlow. *Balancing of High-Speed Machinery.* Springer-Verlag, 1989.
6. R. Gasch, R. Nordmann, and H. Pfützner. *Rotordynamik.* Springer-Verlag, 2001.
7. R.C. Hibbeler. *Engineering Mechanics and Dynamics.* Pearson Prentice Hall, 9 edition, 2000.
8. ISO Standard 1940. Balance quality of rotating rigid bodies, 1973.
9. T.R. Kane and Levinson D.A. *Dynamics: Theory and Applications.* MacGraw-Hill Comp., 1985.
10. W. Kellenberger. *Elastisches Wuchten.* Springer-Verlag, Berlin, 1987.
11. E. Krämer. *Dynamics of Rotors and Foundations.* Springer-Verlag, 1993.
12. K. Magnus. *Kreisel, Theorie und Anwendungen.* Springer-Verlag, 1971.
13. P.C. Müller. *Stabilität und Matrizen.* Springer-Verlag, 1977.
14. P.C. Müller. Allgemeine lineare Theorie für Rotorsysteme ohne oder mit kleinen Unsymmetrien. *Ing. Archiv*, 51:61–74, 1981.
15. D. Poole. *Linear Algebra: A Modern Introduction.* Brooks Cole, 2002.
16. H. Schneider. *Auswuchttechnik, mit DIN ISO 1940-1 und DIN ISO 11342.* VDI-Verlag, Düsseldorf, 2003.
17. G. Schweitzer. Stabilization of self-excited rotor vibrations by an active damper. In F.I. Niordson, editor, *Proc. IUTAM Symp. on Dynamics of Rotors*, Lyngby, Aug. 1974. Springer-Verlag, Berlin.
18. G. Schweitzer. *Critical Speeds of Gyroscopes.* Centre Internat. des Sciences Mécaniques (CISM), Course Nr. 55. Springer-Verlag, Wien, 1972.
19. A.A. Shabana. *Vibration of discrete and continuous systems (Mechanical Engineering Series).* Springer-Verlag, 1996.
20. A.A.. Shabana. *Dynamics of multibody systems.* Cambridge University Press, 2005.
21. W. Szczygielski and G. Schweitzer. Dynamics of a high speed rotor touching a boundary. In *Proc. IUTAM/IFToMM Symposium on Dynamics of Multibody Systems*, Udine, 1987. Springer-Verlag, Berlin.
22. B.H. Tongue. *Principles of vibration.* Oxford University Press, 2001.
23. B.H. Tongue and S.D. Sheppard. *Dynamics: Analysis and design of systems in motion.* J. Wiley, 2004.
24. F. Viggiano and G. Schweitzer. Blade loss dynamics of a magnetically supported rotor. In *Proc. Third Internat. Symp. on Transport Phen. and Dynamics of Rotating Machinery (ISROMAC)*, Honolulu, USA, April 1990.
25. R. Zurmühl and S. Falk. *Matrizen und ihre Anwendungen, Teil 1, Grundlagen.* Springer-Verlag, 1996.

8

Control of the Rigid Rotor in AMBs

René Larsonneur

In Chap. 7, the model of the rotating rigid rotor was derived and its properties, including *gyroscopic* effects, were discussed. This chapter is intended to combine the rigid rotor model with the model of the AMBs and with their control, extending the control approaches of Chap. 2. Different control structures and their individual properties are discussed. In Chap. 12 the rigid rotor AMB model as well as the control will be extended to flexible rotors.

8.1 The Rotor–Bearing Model

Figure 8.1 displays a rigid rotor together with the bearing magnets and the position sensors. This setup basically corresponds to a practical and most straightforward implementation of such a system. For simplicity the axial rotor motion as well as any axial bearing components are omitted, since this degree of freedom (DOF) is – within a linearized approach – completely decoupled from the radial motion and can be treated as shown in detail for the simple one DOF AMB system discussed in Chap. 2.

The derivation of the linearized equations of motion for the setup of Fig. 8.1 becomes most simple if the (small) center of mass displacements x and y as well as the *Euler* angles α and β, all combined into the vector $\mathbf{q}$, are used, as already lined out in Chap. 7. Differently from the one DOF system its output signals, i.e. the measured rotor displacements x_{seA} and x_{seB}, are comprised in the output vector $\mathbf{y}$, yielding the following expressions:

$$\mathbf{M}\,\ddot{\mathbf{q}} + \mathbf{G}\,\dot{\mathbf{q}} = \mathbf{B}\,\mathbf{u}_f \tag{8.1a}$$

$$\mathbf{y} = \mathbf{C}\,\mathbf{q} \tag{8.1b}$$

$$\mathbf{M} = \begin{bmatrix} I_y & 0 & 0 & 0 \\ 0 & m & 0 & 0 \\ 0 & 0 & I_x & 0 \\ 0 & 0 & 0 & m \end{bmatrix},\ \mathbf{G} = \begin{bmatrix} 0 & 0 & I_z\Omega & 0 \\ 0 & 0 & 0 & 0 \\ -I_z\Omega & 0 & 0 & 0 \\ 0 & 0 & 0 & 0 \end{bmatrix},\ \mathbf{B} = \begin{bmatrix} a & b & 0 & 0 \\ 1 & 1 & 0 & 0 \\ 0 & 0 & a & b \\ 0 & 0 & 1 & 1 \end{bmatrix} \tag{8.1c}$$

G. Schweitzer, E.H. Maslen (eds.), *Magnetic Bearings*,
DOI 10.1007/978-3-642-00497-1_8, © Springer-Verlag Berlin Heidelberg 2009

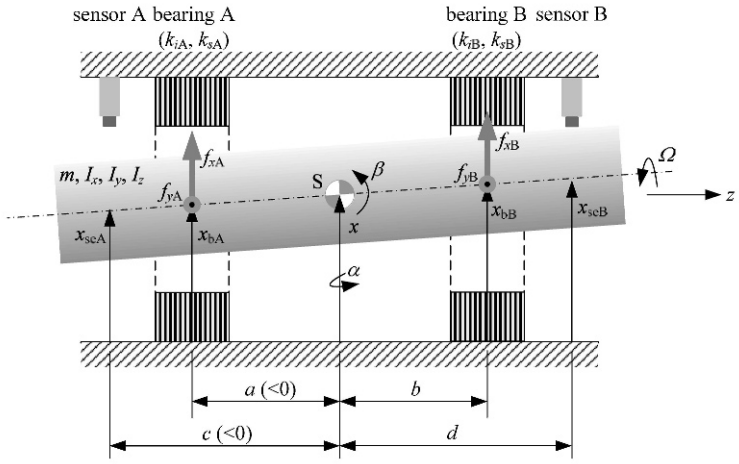


Fig. 8.1. The rigid rotor equipped with bearing magnets and sensors

$$\mathbf{q} = (\beta, x, -\alpha, y)^{\mathrm{T}},\ \mathbf{u}_f = (f_{x\mathrm{A}}, f_{x\mathrm{B}}, f_{y\mathrm{A}}, f_{y\mathrm{B}})^{\mathrm{T}} \tag{8.1d}$$

$$\mathbf{C} = \begin{bmatrix} c & 1 & 0 & 0 \\ d & 1 & 0 & 0 \\ 0 & 0 & c & 1 \\ 0 & 0 & d & 1 \end{bmatrix},\ \mathbf{y} = (x_{\mathrm{seA}}, x_{\mathrm{seB}}, y_{\mathrm{seA}}, y_{\mathrm{seB}})^{\mathrm{T}} \tag{8.1e}$$

In Chap. 2 we have seen that, by closing the control loop, the magnetic bearing force $\mathbf{u}_f$ can be described as a linearized function of the rotor displacements in the bearing and the coil currents, involving the *force/current* factor k_i and the *force/displacement* factor k_s.[1] In general, these constants are not equal in each bearing, however, they are equal in both x and y directions, since the bearing is usually symmetric. Hence, the following relationship results for the force vector $\mathbf{u}_f$ used in (8.1):

$$\begin{aligned} \mathbf{u}_f = \begin{bmatrix} f_{x\mathrm{A}} \\ f_{x\mathrm{B}} \\ f_{y\mathrm{A}} \\ f_{y\mathrm{B}} \end{bmatrix} &= - \begin{bmatrix} k_{s\mathrm{A}} & 0 & 0 & 0 \\ 0 & k_{s\mathrm{B}} & 0 & 0 \\ 0 & 0 & k_{s\mathrm{A}} & 0 \\ 0 & 0 & 0 & k_{s\mathrm{B}} \end{bmatrix} \begin{bmatrix} x_{\mathrm{bA}} \\ x_{\mathrm{bB}} \\ y_{\mathrm{bA}} \\ y_{\mathrm{bB}} \end{bmatrix} + \begin{bmatrix} k_{i\mathrm{A}} & 0 & 0 & 0 \\ 0 & k_{i\mathrm{B}} & 0 & 0 \\ 0 & 0 & k_{i\mathrm{A}} & 0 \\ 0 & 0 & 0 & k_{i\mathrm{B}} \end{bmatrix} \begin{bmatrix} i_{x\mathrm{A}} \\ i_{x\mathrm{B}} \\ i_{y\mathrm{A}} \\ i_{y\mathrm{B}} \end{bmatrix} \\ &= -\mathbf{K}_s \mathbf{q}_{\mathrm{b}} + \mathbf{K}_i \mathbf{i} \end{aligned} \tag{8.2}$$

The vector $\mathbf{q}_{\mathrm{b}} = (x_{\mathrm{bA}}, x_{\mathrm{bB}}, y_{\mathrm{bA}}, y_{\mathrm{bB}})^{\mathrm{T}}$ introduced in (8.2) comprises the rotor displacements within the magnetic bearings, whereas the vector

[1] The constants k_i and k_s are generally defined based on the assumption that the power amplifier is operated as a *current amplifier* or *transconductance amplifier*. For simplicity, amplifier and other electronic component dynamics, e.g. from sensor filters, are not considered here.

$\mathbf{i} = (i_{x\mathrm{A}}, i_{x\mathrm{B}}, i_{y\mathrm{A}}, i_{y\mathrm{B}})^{\mathrm{T}}$ contains the individual coil control currents of all four bearing magnets.

By combining the rotor model (8.1) and the linearized bearing force description (8.2) we obtain the following basic matrix differential equation of motion for the rigid rotor to be levitated by AMBs:

$$\mathbf{M}\,\ddot{\mathbf{q}} + \mathbf{G}\,\dot{\mathbf{q}} = \mathbf{B}\,(-\mathbf{K}_s\,\mathbf{q}_{\mathrm{b}} + \mathbf{K}_i\,\mathbf{i}) \tag{8.3a}$$

$$\mathbf{y} = \mathbf{C}\,\mathbf{q} \tag{8.3b}$$

8.2 Feedback Control Design

With (8.3) we are basically ready for closing the feedback loop, i.e. for expressing the coil current vector $\mathbf{i}$ by a suitable control law (remember that the open-loop AMB system is unstable due to the negative "spring constant" or "bearing stiffness", respectively, in each bearing represented by the force/displacement matrix $\mathbf{K}_s$).

Before we can actually design a control law for (8.3) we encounter a problem associated with the chosen set of coordinates: For the motion description the *center of mass* or *center of gravity* (COG) coordinates, combined in the vector $\mathbf{q}$, have been used, with a good reason since this description yields the most simple mathematical structure of the resulting differential equations. The bearing force, however, involves the rotor position in the bearings and, therefore, the use of the *bearing coordinates* $\mathbf{q}_{\mathrm{b}}$ for the representation of the negative bearings stiffness with matrix $\mathbf{K}_s$, as shown in detail in Chap. 7 on the dynamics of the rigid rotor. There is even a third set of coordinates, the *sensor coordinates* comprised in the output vector $\mathbf{y}$.

In order to discuss the properties of the resulting closed-loop system it is essential to involve only *one* set of coordinates for the motion description. This can be easily achieved by transforming the bearing coordinates $\mathbf{q}_{\mathrm{b}}$ into the center of mass or COG coordinates $\mathbf{q}$ respectively by means of a linear transformation matrix ${}_{\mathrm{b}}\mathbf{T}_{\mathrm{S}}$ involving the geometrical quantities a and b introduced in Fig. 8.1.

$$\mathbf{q}_{\mathrm{b}} = \begin{bmatrix} x_{\mathrm{bA}} \\ x_{\mathrm{bB}} \\ y_{\mathrm{bA}} \\ y_{\mathrm{bB}} \end{bmatrix} = \begin{bmatrix} a & 1 & 0 & 0 \\ b & 1 & 0 & 0 \\ 0 & 0 & a & 1 \\ 0 & 0 & b & 1 \end{bmatrix} \begin{bmatrix} \beta \\ x \\ -\alpha \\ y \end{bmatrix} \tag{8.4a}$$

$$\mathbf{q}_{\mathrm{b}} = {}_{\mathrm{b}}\mathbf{T}_{\mathrm{S}}\,\mathbf{q} \tag{8.4b}$$

When comparing expressions (8.1) and (8.4) we can easily recognize that the transformation matrix is just the transpose of the input matrix, i.e. ${}_{\mathrm{b}}\mathbf{T}_{\mathrm{S}} = \mathbf{B}^{\mathrm{T}}$. This property is generally fulfilled in a magnetic bearing system, whether rigid or flexible.

Hence, by insertion of (8.4) into (8.3), one obtains the following differential matrix equation in COG coordinates $\mathbf{q}$ solely:

$$\mathbf{M}\,\ddot{\mathbf{q}} + \mathbf{G}\,\dot{\mathbf{q}} = \underbrace{-\mathbf{B}\,\mathbf{K}_s\,\mathbf{B}^{\mathrm{T}}}_{-\mathbf{K}_{s\mathrm{S}}}\mathbf{q} + \mathbf{B}\,\mathbf{K}_i\,\mathbf{i} \tag{8.5}$$

Equation (8.5) involves the negative bearing stiffness matrix $\mathbf{K}_{s\mathrm{S}}$ transformed into COG coordinates. As any displacement proportional term the negative stiffness term can be brought to the left side of (8.5) so that only the control current term remains on the right hand side, which results in:

$$\mathbf{M}\,\ddot{\mathbf{q}} + \mathbf{G}\,\dot{\mathbf{q}} + \mathbf{K}_{s\mathrm{S}}\,\mathbf{q} = \mathbf{B}\,\mathbf{K}_i\,\mathbf{i} \tag{8.6}$$

It is essential to realize here that all matrices on the left hand side of (8.6) have their dedicated symmetry properties. Based on such properties immediate statements on the stability of motion can be made (see Chap. 7). As can be seen from (8.1) the mass matrix $\mathbf{M}$ is symmetric, and the gyroscopic matrix $\mathbf{G}$ is skew-symmetric. The symmetry property of the transformed negative bearing stiffness matrix $\mathbf{K}_{s\mathrm{S}}$ is also immediately recognizable from (8.5) together with the fact that $\mathbf{K}_s$ is diagonal.

$$\mathbf{K}_{s\mathrm{S}}{}^{\mathrm{T}} = (\mathbf{B}\,\mathbf{K}_s\,\mathbf{B}^{\mathrm{T}})^{\mathrm{T}} = \mathbf{B}\,\mathbf{K}_s{}^{\mathrm{T}}\,\mathbf{B}^{\mathrm{T}} = \mathbf{K}_{s\mathrm{S}} \tag{8.7a}$$

$$\mathbf{K}_{s\mathrm{S}} = \begin{bmatrix} k_{s\mathrm{A}}a^2 + k_{s\mathrm{B}}b^2 & k_{s\mathrm{A}}a + k_{s\mathrm{B}}b & 0 & 0 \\ k_{s\mathrm{A}}a + k_{s\mathrm{B}}b & k_{s\mathrm{A}} + k_{s\mathrm{B}} & 0 & 0 \\ 0 & 0 & k_{s\mathrm{A}}a^2 + k_{s\mathrm{B}}b^2 & k_{s\mathrm{A}}a + k_{s\mathrm{B}}b \\ 0 & 0 & k_{s\mathrm{A}}a + k_{s\mathrm{B}}b & k_{s\mathrm{A}} + k_{s\mathrm{B}} \end{bmatrix} \tag{8.7b}$$

8.2.1 Decentralized Control

The most straightforward and intuitive approach for designing a control law for the rigid rotor in AMBs described by (8.6) is by implementing a PID control scheme such as done in Chap. 2, however *locally* for each bearing unit and *separately* for each bearing axis, as shown in Fig. 8.2. This, however, means to ignore the fact that the bearings and sensors are *non-collocated*, i.e. that their axes differ by a certain distance (see Fig. 8.1). This non-collocation, though, is a property of a large majority of industrial magnetic bearing systems, since the sensors (mostly of eddy current or inductive type) can usually not be integrated into the bearing.[2] Since it is common practice in industrial AMB systems to control a *rigid* rotor with such a decentralized control scheme, it is essential to discuss this approach and its specific properties here in a first place. As we will see in Chap. 12 the control of *flexible* rotor systems, however, will generally require a more elaborate control design approach.

[2] Exceptions are the *self-sensing* bearing approach and some special (and often expensive) bearing–sensor arrangements.

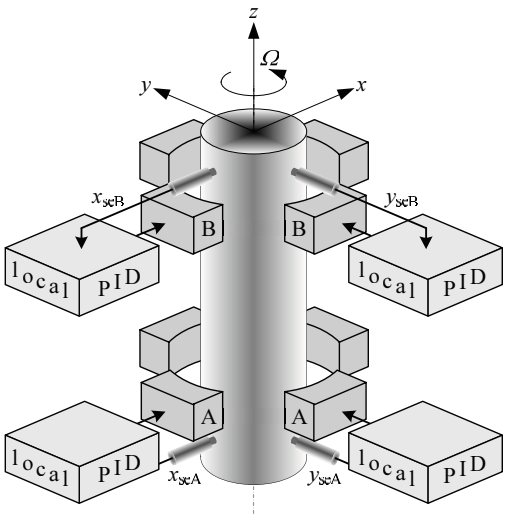


Fig. 8.2. Decentralized control structure with PID control (also called "side-by-side" or "local" control)

The local control shown in Fig. 8.2 feeds each local sensor signal back to the corresponding bearing control current using the feedback gains $P_{\mathrm{A,B}}$ and $D_{\mathrm{A,B}}$ respectively (for simplicity the integral feedback part is omitted in the following considerations):

$$i_{x\mathrm{A}} = -P_{\mathrm{A}}\, x_{\mathrm{seA}} - D_{\mathrm{A}}\, \dot{x}_{\mathrm{seA}} \tag{8.8a}$$
$$i_{x\mathrm{B}} = -P_{\mathrm{B}}\, x_{\mathrm{seB}} - D_{\mathrm{B}}\, \dot{x}_{\mathrm{seB}} \tag{8.8b}$$
$$i_{y\mathrm{A}} = -P_{\mathrm{A}}\, y_{\mathrm{seA}} - D_{\mathrm{A}}\, \dot{y}_{\mathrm{seA}} \tag{8.8c}$$
$$i_{y\mathrm{B}} = -P_{\mathrm{B}}\, y_{\mathrm{seB}} - D_{\mathrm{B}}\, \dot{y}_{\mathrm{seB}} \tag{8.8d}$$

Equation (8.8) can be brought to matrix description by combining the four output signals in the output vector $\mathbf{y}$ introduced in (8.1e)[3]:

$$\mathbf{i} = -(\mathbf{P}\,\mathbf{y} + \mathbf{D}\,\dot{\mathbf{y}}) \tag{8.9a}$$
$$\mathbf{P} = \mathrm{diag}(P_{\mathrm{A}}, P_{\mathrm{B}}, P_{\mathrm{A}}, P_{\mathrm{B}}),\ \mathbf{D} = \mathrm{diag}(D_{\mathrm{A}}, D_{\mathrm{B}}, D_{\mathrm{A}}, D_{\mathrm{B}}) \tag{8.9b}$$

The combination of (8.9) with differential equation (8.6) and with the output signal relationship given by (8.1) yields

[3] As done in Chap. 2 it is, for simplicity, assumed that the velocity signals $\dot{x}_{\mathrm{seA,B}}$, $\dot{y}_{\mathrm{seA,B}}$ are directly measurable and that the bearing parameters in each bearing are equal in both x and y directions.

$$\mathbf{M}\,\ddot{\mathbf{q}} + \mathbf{G}\,\dot{\mathbf{q}} + \mathbf{K}_{s\mathrm{S}}\,\mathbf{q} = -\mathbf{B}\,\mathbf{K}_i\,(\mathbf{P}\mathbf{C}\,\mathbf{q} + \mathbf{D}\mathbf{C}\,\dot{\mathbf{q}})\,, \tag{8.10}$$

from which the following homogenous matrix differential equation, solely involving the COG coordinates $\mathbf{q}$, can be obtained by arranging all terms on the left hand side:

$$\mathbf{M}\,\ddot{\mathbf{q}} + \mathbf{G}\,\dot{\mathbf{q}} + \mathbf{K}_{s\mathrm{S}}\,\mathbf{q} + \underbrace{\mathbf{B}\,\mathbf{K}_i\,\mathbf{P}\mathbf{C}}_{\mathbf{K}_c}\,\mathbf{q} + \underbrace{\mathbf{B}\,\mathbf{K}_i\,\mathbf{D}\mathbf{C}}_{\mathbf{D}_c}\,\dot{\mathbf{q}} = \mathbf{0} \tag{8.11}$$

The newly introduced matrices $\mathbf{K}_c$ and $\mathbf{D}_c$ are the *stiffness* and *damping* matrices provided by the local PD feedback control. As shown in Chap. 2 for the simple one DOF system the stiffness matrix has to compensate for the negative bearing stiffness $\mathbf{K}_{s\mathrm{S}}$ in order to yield closed-loop eigenvalues located on the imaginary axis, and the damping matrix is necessary to achieve asymptotic system stability, i.e. to achieve closed-loop eigenvalues entirely located in the left half of the complex plane.

The closed-loop system eigenvalues λ of (8.11) can be calculated if the second-order matrix differential equation is transformed into a state space description, as shown in Chap. 2. This yields the following state space matrix $\mathbf{A}$ and the characteristic equation for its eigenvalues λ:

$$\mathbf{A} = \begin{bmatrix} \mathbf{0} & \mathbf{I} \\ -\mathbf{M}^{-1}(\mathbf{K}_{s\mathrm{S}} + \mathbf{K}_c) & -\mathbf{M}^{-1}(\mathbf{G} + \mathbf{D}_c) \end{bmatrix} \tag{8.12a}$$

$$\det(\lambda\mathbf{I} - \mathbf{A}) = 0 \tag{8.12b}$$

Note that the gyroscopic matrix $\mathbf{G}$ defined in (8.1c) is speed dependent and that, therefore, different eigenvalues λ will result for each rotational speed Ω.

In Fig. 8.3 an eigenvalue trajectory or root locus plot of the eigenvalues resulting from (8.12) is shown as a function of the rotor speed (the corresponding model parameters are summarized in Table 8.1). Although there are totally eight eigenvalues at each speed – corresponding to the size of the $\mathbf{A}$ matrix – only four eigenvalues are plotted. The other four eigenvalues are equal to the first four due to the symmetry with respect to the rotation axis. The dashed circles in Fig. 8.3 are only shown in order to underline that a finding made in Chap. 2 concerning a specific selection of feedback control parameters also partially applies to the more general four DOF rigid body AMB system: In case of a "natural" stiffness and damping the open-loop and closed-loop eigenvalues are located on a circle with center in the origin of the complex plane. As can be seen in Fig. 8.3, this finding exactly applies to one pair of eigenvalues and approximately also applies to the second one.

The eigenvalue plot shown in Fig. 8.3 underlines the well-tempered behavior of the rigid rotor AMB system with decentralized PD control: The system shows "natural" closed-loop eigenfrequencies in the same range as the magnitude of its open-loop poles, the damping is good and the rotation speed does not substantially deteriorate system performance. As shown by the *sensitivity*

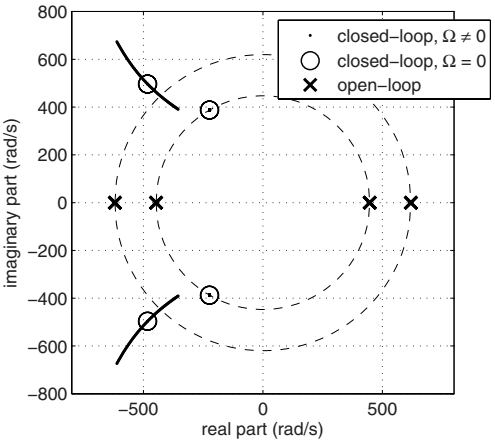


Fig. 8.3. Eigenvalue trajectory plot according to (8.12) as a function of the rotational speed Ω for local PD control of a symmetric rigid rotor AMB system ($\Omega/2\pi = 0 \ldots 500$ Hz)

Table 8.1. Model data for eigenvalue trajectory plot of Fig. 8.3 with "natural" stiffness and damping, as shown for the simple one DOF system in Chap. 2

symbol	value	units
m	100	kg
$I_x = I_y$	8.3333	$\mathrm{kg\,m^2}$
I_z	0.75	$\mathrm{kg\,m^2}$
$b = -a$	0.4	m
$d = -c$	0.45	m
$k_{s\mathrm{A}} = k_{s\mathrm{B}}$	-1×10^7	N/m
$k_{i\mathrm{A}} = k_{i\mathrm{B}}$	250	N/A
$P_\mathrm{A} = P_\mathrm{B} = \frac{-2k_{s\mathrm{A}}}{k_{i\mathrm{A}}}$	8×10^4	A/m
$D_\mathrm{A} = D_\mathrm{B} = \frac{\sqrt{\frac{-mk_{s\mathrm{A}}}{2}}}{k_{i\mathrm{A}}}$	89.4427	A s/m
$\Omega/2\pi$	$0 \ldots 500$	Hz

function plot in Fig. 8.4 according to the latest ISO standard for the assessment of AMB system robustness [3], the sensitivity function peak values are well below 3 and, therefore, the system with decentralized control can also be considered a "Zone A" system which is optimally robust to changes in the plant such as e.g. changes in the sensor output gains due to temperature drift or system aging.

The chosen AMB rotor system has, apart from its rotation axis symmetry, a further symmetry property (see Table 8.1): The center of gravity is located exactly mid span between the magnetic bearings, and the bearing and control

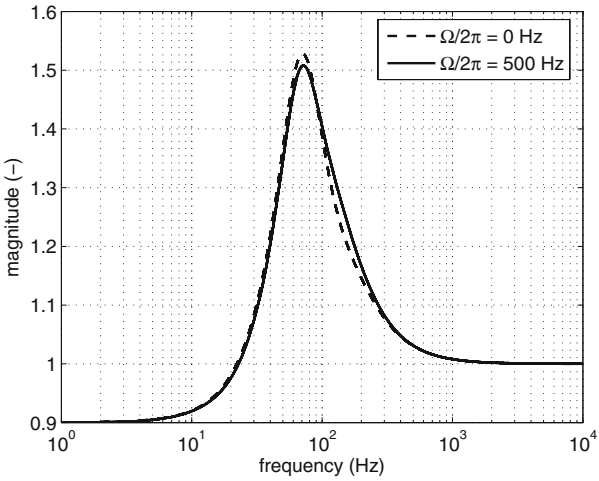


Fig. 8.4. Sensitivity function according to ISO robustness requirements for local PD control of the symmetric rigid rotor AMB system defined by Table 8.1 ($\Omega/2\pi = 0$ Hz and $\Omega/2\pi = 500$ Hz)

feedback parameters are equal on each side. It is interesting to see that this symmetry property is also visible in Fig. 8.3 in terms of the dependence of the closed-loop eigenvalues on the rotor speed: One pair of eigenvalues is changing its real and imaginary values with speed, whereas the other pair shows absolutely no speed dependency. This behavior can be physically explained: The symmetric AMB system and feedback control setup automatically provides a closed-loop eigenmode decomposition into the *parallel* and *conical* modes. In the parallel mode only the center of gravity of the rotor moves in x and/or y direction without any tilting of the rotation axis and, consequently, without any change of the angular momentum of the rotor. Accordingly, this mode is *not affected* by any gyroscopic effect and its eigenvalues are independent of the rotational speed. The tilting motion, however, is strongly influenced by the rotational speed Ω since the tilting angles α and β become coupled by the gyroscopic matrix $\mathbf{G}$ and, thus, describe a *conical* motion of the rotor axis without any associated displacement of the center of gravity. There are generally two conical modes, commonly referred to as the *nutation* and *precession* modes. They differ, in the first place, in the direction of rotation of the eigenmode with respect to the sense of the rotation itself: The nutation is commonly referred to as a *forward* mode, whereas the precession is a *backward* mode. Moreover, the two conical modes differ in the behavior of their eigenvalues: The nutation mode features eigenvalues with eigenfrequencies, i.e. imaginary parts, that rise with the rotational speed. Contrarily to this the precession mode eigenfrequencies drop with increasing rotational speed. This effect of rising and dropping imaginary parts of the eigenvalues is also well visible in Fig. 8.3. A more detailed description of this important property of

rotordynamic systems is given in Chap. 7 of this book and is widely discussed in the literature, for instance [15].

We will see further below (Sect. 8.2.3) how the decomposition into parallel and conical modes can be utilized for an enhanced rigid body control scheme in the presence of any general and non-symmetric AMB rotor system.

8.2.2 Limitations of Decentralized Control

The approach of setting up a *decentralized* or *local* feedback control scheme for a rigid body AMB system, as shown in the previous section, is physically well justifiable and features, as one of its most important advantages, control parameters that can be designed solely based on physical considerations by selecting appropriate stiffness and damping values. Despite the fact that this approach utilizes the magnetic bearings in the same way as mechanical springs and dampers without taking further advantage of their numerous capabilities, it has been shown that decentralized control is well applicable to a large number of AMB systems without major deficiencies [11]. Moreover, in most of these cases the closed-loop AMB system will feature acceptable performance and robustness properties fulfilling the requirements of the latest ISO standard [2, 3] for magnetic bearings.

However, local PD or PID control can also lead to substantial problems when the AMB rotor system exhibits specific (and common) properties, as will be shown in the following two sections.

Destabilization by Rotor Speed in the Presence of Non-Collocation

The fact that the magnetic bearing actuator and the neighboring sensors are usually *not collocated* in a standard AMB system (see Fig. 8.1) may, for some specific plant configurations in conjunction with local PD control, lead to instability of the closed-loop AMB system at certain rotor speeds. This effect is illustrated in Fig. 8.5 by a corresponding eigenvalue trajectory plot (the model parameters for this example are different from those used in Fig. 8.3, namely the rotor is non-symmetric and the bearing parameters are different):

As can be seen in Fig. 8.5a there is a speed region – the calculation shows that this region of $\Omega/2\pi$ is located between roughly 45 and 460 Hz – in which some closed-loop eigenvalues show a positive real part for the non-collocated system, whereas this effect does not occur at all in case of perfect collocation of sensors and actuators.

The only speed dependent term in the state space matrix $\mathbf{A}$ given by (8.12) is coming from the gyroscopic matrix $\mathbf{G}$. This suggests that the gyroscopic effects are the actual physical reason for the instability. As a matter of fact, however, this is not entirely true since the sole presence of the gyroscopic matrix $\mathbf{G}$ cannot yet lead to instability [15, 38, 45].

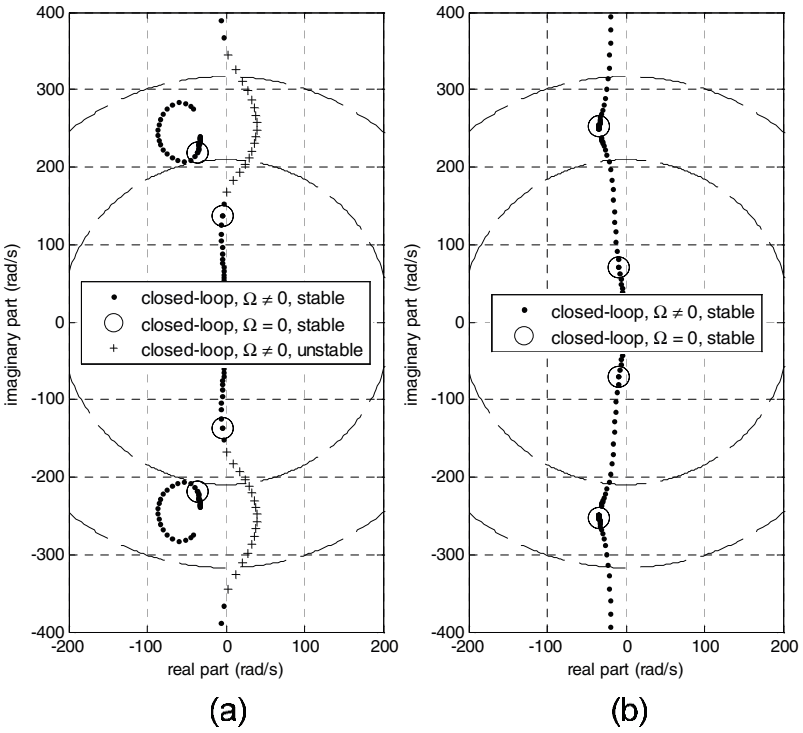


Fig. 8.5. Eigenvalue trajectory plot according to (8.12) as a function of the rotational speed Ω for local PD control of a rigid rotor AMB system ($\Omega/2\pi = 0 \ldots 500$ Hz): (**a**) non-collocated system, (**b**) collocated system

The true physical reason for the instability is the speed dependent change of the eigenmodes due to gyroscopic effects *in conjunction* with the property of non-collocation and the magnitude of the associated feedback gains and phase angles. For a gyroscopic rigid rotor the eigenmodes always become coupled motions between the x-z and y-z planes. The geometry, inertia and control feedback properties for the example of Fig. 8.5a (see Table 8.2) are in fact chosen such that this eigenmode coupling causes a substantial *phase lag* between the sensor plane and bearing plane orbits at least for one closed-loop eigenmode, as shown in Figs. 8.6a and 8.6b. The consequence of this phase lag due to non-collocation is that the total controller phase angle γ_{contr}, i.e. the angle between the control force f and the corresponding (negative) bearing orbit vector, can become *positive*. In this case, the control force no longer provides negative velocity feedback and, therefore, proper damping but in fact features a destabilizing component in the direction of the eigenmode velocity, as shown in Fig. 8.6b. If both controller phase angles γ_{contrA} and γ_{contrB} are positive (and smaller than 180 degrees), a sufficient condition for system instability is met, however, instability can even occur if only one controller

Table 8.2. Model data for eigenvalue trajectory plot of Fig. 8.5

symbol	value (non-collocated)	value (collocated)	units
m	10	10	kg
$I_x = I_y$	0.2083	0.2083	$\mathrm{kg\,m^2}$
I_z	0.0258	0.0258	$\mathrm{kg\,m^2}$
a	-0.2	-0.2	m
b	0.04	0.04	m
c	-0.25	-0.2	m
d	-0.01	0.04	m
$k_{s\mathrm{A}}$	-2×10^5	-2×10^5	N/m
$k_{s\mathrm{B}}$	-8×10^5	-8×10^5	N/m
$k_{i\mathrm{A}}$	10	10	N/A
$k_{i\mathrm{B}}$	20	20	N/A
P_{A}	2.2×10^4	2.2×10^4	A/m
P_{B}	7×10^4	7×10^4	A/m
D_{A}	7	7	A s/m
D_{B}	30	30	A s/m
$\Omega/2\pi$	$0 \ldots 500$	$0 \ldots 500$	Hz

phase angle has the wrong sign, as shown in Fig. 8.6c. A necessary and sufficient condition for closed-loop instability is the sign of the total mechanical power applied to the system by the control forces f_{A} and f_{B}, as shown in Fig. 8.6d: If the total power is positive the system is unstable.

It is important to mention at this point that this potential for instability of the closed-loop AMB system (8.11) can already be seen when examining the *structure* of the matrix differential equation, namely the *symmetry properties* of its matrices, without necessity for the exact calculation of the system eigenvalues. It can be shown that, if the property of *positive definiteness*[4] is fulfilled for the symmetric mass, damping and stiffness matrices, the system *cannot* be destabilized by the gyroscopic matrix solely, whereas a destabilization is actually possible if the system also contains a *skew-symmetric stiffness matrix* [15, 38, 45].

The corresponding situation can be easily verified for the present example: As a matter of fact the feedback matrices $\mathbf{D}_c$ and $\mathbf{K}_c$ in (8.11) are neither symmetric nor skew-symmetric:

$$\mathbf{D}_c \neq \mathbf{D}_c^{\mathrm{T}} \,,\; \mathbf{K}_c \neq \mathbf{K}_c^{\mathrm{T}} \tag{8.13}$$

[4] Mathematically, the condition for positive definiteness of a general matrix $\mathbf{A}$ can be formulated as follows: $\mathbf{A} > \mathbf{0} \Longleftrightarrow \mathbf{x}^{\mathrm{T}}\mathbf{A}\mathbf{x} > 0$ for all $\mathbf{x} \neq \mathbf{0}$. For a symmetric and real matrix $\mathbf{A} = \mathbf{A}^{\mathrm{T}} \in \mathbb{R}^{n\times n}$, positive definiteness can be decided directly based on its always real eigenvalues: $\mathbf{A} > \mathbf{0} \Longleftrightarrow \mathrm{eig}(\mathbf{A}) > 0$.

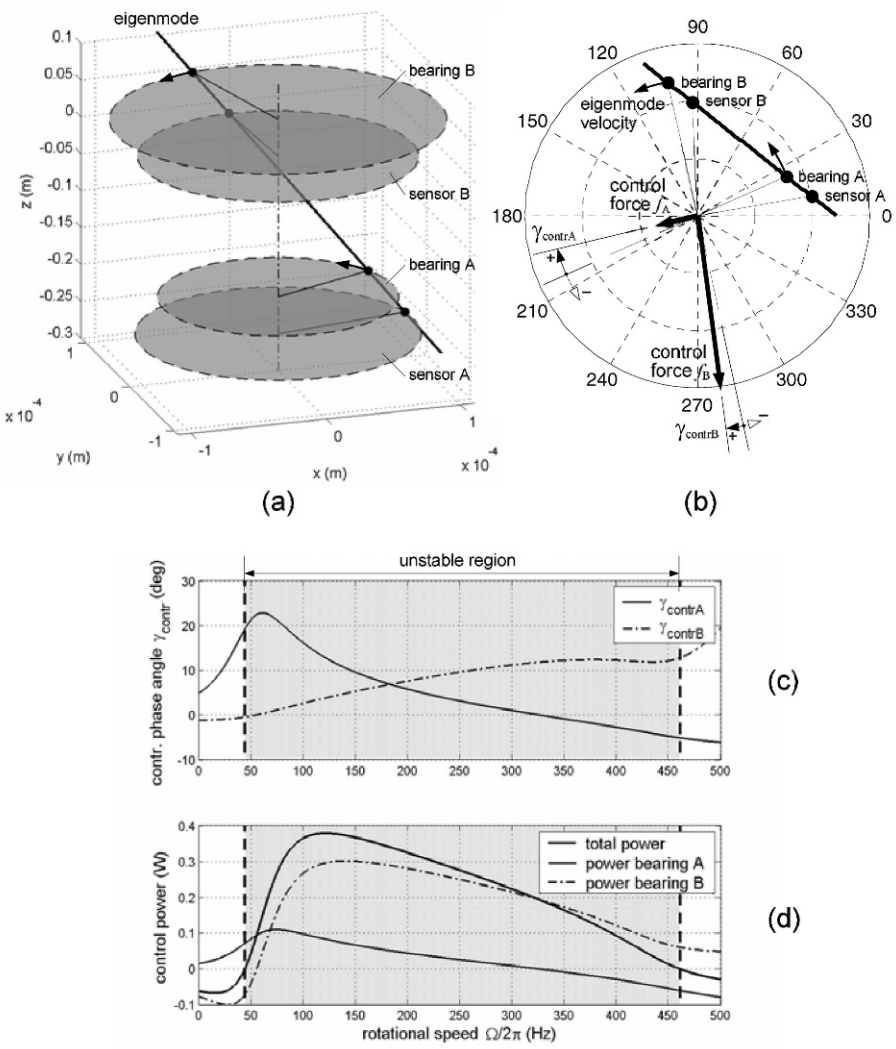


Fig. 8.6. Destabilization mechanism due to non-collocated local PD control for a gyroscopic rigid rotor AMB system: (**a**) 3D view of the x-y coupled forward eigenvector motion at $\Omega/2\pi = 144$ Hz, (**b**) top view of the eigenvector motion at $\Omega/2\pi = 144$ Hz with direction of the control forces f_{A} and f_{B} and with controller phase angles γ_{contrA} and γ_{contrB}, (**c**) controller phase angle in both bearings as a function of speed ($\Omega/2\pi = 0 \ldots 500$ Hz), (**d**) mechanical power applied to the rotor motion by control forces in both bearings as a function of speed ($\Omega/2\pi = 0 \ldots 500$ Hz)

Like any quadratic matrix, however, these feedback matrices can be split up into their symmetric and skew-symmetric parts,

$$\mathbf{D}_{c_{\mathrm{symm}}} = \frac{1}{2}(\mathbf{D}_c + \mathbf{D}_c^{\mathrm{T}})\,,\ \mathbf{D}_{c_{\mathrm{skew}}} = \frac{1}{2}(\mathbf{D}_c - \mathbf{D}_c^{\mathrm{T}}) \tag{8.14a}$$

$$\mathbf{K}_{c_{\mathrm{symm}}} = \frac{1}{2}(\mathbf{K}_c + \mathbf{K}_c^{\mathrm{T}})\,,\ \mathbf{K}_{c_{\mathrm{skew}}} = \frac{1}{2}(\mathbf{K}_c - \mathbf{K}_c^{\mathrm{T}}) \tag{8.14b}$$

and by using expressions (8.1) through (8.11) together with the numerical values from Table 8.2 one can show that all the symmetric matrices in (8.11), i.e. the mass, total damping and total stiffness matrices, are indeed positive definite (the skew-symmetric part $\mathbf{D}_{c_{\mathrm{skew}}}$ of $\mathbf{D}_c$ can be considered an additional "gyroscopic" term):

$$\mathbf{M} = \mathbf{M}^{\mathrm{T}} > \mathbf{0} \tag{8.15a}$$

$$\mathbf{D}_{c_{\mathrm{symm}}} = \mathbf{D}_{c_{\mathrm{symm}}}^{\mathrm{T}} > \mathbf{0} \tag{8.15b}$$

$$\mathbf{K}_{c_{\mathrm{symm}}} + \mathbf{K}_{s\mathrm{S}} = (\mathbf{K}_{c_{\mathrm{symm}}} + \mathbf{K}_{s\mathrm{S}})^{\mathrm{T}} > \mathbf{0} \tag{8.15c}$$

Hence, following the above mentioned general stability criteria, the only destabilizing term in (8.11) is the skew-symmetric part $\mathbf{K}_{c_{\mathrm{skew}}}$ of the feedback matrix $\mathbf{K}_c$, which has the following form:

$$\mathbf{K}_{c_{\mathrm{skew}}} = \mathbf{N} = \begin{bmatrix} 0 & n_{12} & 0 & 0 \\ -n_{12} & 0 & 0 & 0 \\ 0 & 0 & 0 & n_{12} \\ 0 & 0 & -n_{12} & 0 \end{bmatrix} = -\mathbf{N}^{\mathrm{T}} \tag{8.16a}$$

$$n_{12} = \frac{k_{i\mathrm{A}} P_{\mathrm{A}}(a-c) + k_{i\mathrm{B}} P_{\mathrm{B}}(b-d)}{2} \tag{8.16b}$$

The skew-symmetric stiffness matrix $\mathbf{K}_{c_{\mathrm{skew}}}$ is also called the matrix $\mathbf{N}$ of the *non-conservative bearing forces*, as pointed out in Chap. 7. As can be easily derived from (8.16), $\mathbf{N}$ will be zero for a collocated system, i.e. for $a = c$ and $b = d$, or for very specific values of a, b, c and d. Hence, the sole potential source of destabilization of the closed-loop system (8.11) will vanish for $\mathbf{N} \equiv \mathbf{0}$, i.e. in the case of collocation of sensors and actuators.

The example discussed in this sub section might seem somewhat academic, mainly in view of its special parameter set summarized in Table 8.2. However, the intention of examining this example in detail is to show that a potential stability problem of decentralized control in conjunction with non-collocation *does exist*. Moreover, there are also other physical sources of destabilization by non-conservative forces, such as inner damping in flexible rotors or cross-stiffness and cross-damping in fluid seals, all of them leading to the existence of a matrix $\mathbf{N}$, which can be even speed dependent. Consequently, the AMB

control engineer *must* be aware of the problem associated with its occurrence. As a rule of thumb, additional external damping or a change of bearing stiffness will shift the problem out of the operating speed range in many practical cases, but a general elimination of the problem just by decentralized control is not possible. A more advanced control design approach, such as MIMO control in general (MIMO = "multiple-input-multiple-output"), can take care of such problems (see also Sect. 8.2.3).

Large Difference between Eigenfrequencies

Another problem associated with decentralized (local) feedback control for a rigid rotor AMB system is the effect of a large difference between the resulting closed-loop eigenfrequencies. This problem can become particularly aggravated in case of symmetric rotor systems, even for collocated ones, if specific system properties accumulate unluckily, as shown in Fig. 8.7.

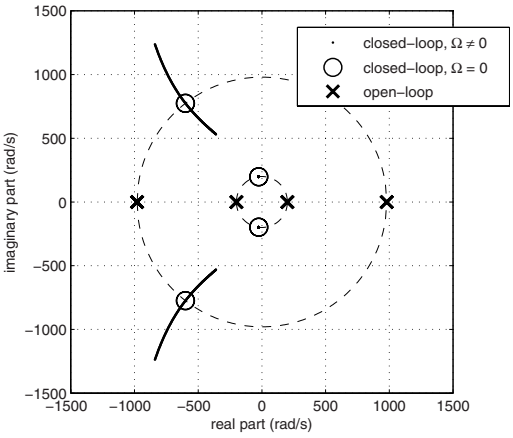


Fig. 8.7. Eigenvalue trajectory plot according to (8.12) as a function of the rotational speed Ω for local PD control of a symmetric and collocated rigid rotor AMB system featuring a large difference between the closed-loop eigenfrequencies ($\Omega/2\pi = 0 \ldots 500$ Hz)

As can be seen in Fig. 8.7 the closed-loop eigenfrequencies are widely separated, one of it is just below 200 rad/s, whereas the other one is roughly 775 rad/s, hence about four times higher. Instead, in the example of Fig. 8.3, this relation was close to one. The gap between the eigenfrequencies becomes even larger when the system is rotating, since the gyroscopic effects raise the eigenfrequency of the forward conical eigenmode to almost 1250 rad/s, whereas the parallel mode eigenfrequencies below 200 rad/s remain unchanged.

The actual physical reason for this – as will be shown problematic – situation is the large difference of the *open-loop* eigenvalues caused by the special inertia properties of the system on the one hand and by its symmetry on the other hand. It can be shown that the ratio r_λ of the absolute values of the open-loop eigenvalues at standstill depends, for this symmetric case, in a very simple manner solely on the inertia and geometry properties of the system:

Table 8.3. Model data for eigenvalue trajectory plot of Fig. 8.7

symbol	value	units
m	100	kg
$I_x = I_y$	0.6667	$\mathrm{kg\,m^2}$
I_z	0.15	$\mathrm{kg\,m^2}$
$b = d = -a = -c$	0.4	m
$k_{s\mathrm{A}} = k_{s\mathrm{B}}$	-2×10^6	N/m
$k_{i\mathrm{A}} = k_{i\mathrm{B}}$	100	N/A
$P_\mathrm{A} = P_\mathrm{B}$	4×10^4	A/m
$D_\mathrm{A} = D_\mathrm{B}$	25	A s/m
$\Omega/2\pi$	$0 \ldots 500$	Hz

$$r_\lambda = \frac{|\lambda_\mathrm{open}|_\mathrm{max}}{|\lambda_\mathrm{open}|_\mathrm{min}} = \sqrt{\frac{ma^2}{I_x}} \tag{8.17}$$

In the present example r_λ has a value of 4.899, whereas it was only 1.3856 in the example of Fig. 8.3 (see Table 8.1), which constituted a much more "manageable" situation. From (8.17) we can conclude that either a large rotor mass m in conjunction with a long distance a between the magnetic bearings or a very small transverse moment of inertia I_x lead to large values of r_λ and, consequently, to substantial problems in practical applications, the most important of which are briefly lined out in the following paragraphs.

First of all the bandwidth of the decentralized PD control must be high enough to adequately stabilize the closed-loop eigenmode corresponding to the high eigenfrequency. When trying to practically implement such a high bandwidth control in a "real" AMB system a number of very undesired effects are the consequence: The high control bandwidth will tend to generate high frequency noise, possibly also dynamic amplifier saturation, and, last but not least, the *bending modes* of the rotor (see Chap. 12), which are always present in reality, will most probably be destabilized by the local PD control. In practice, a *roll off* of the control gain between the rigid body and bending modes has to be implemented as a standard feature in order to avoid these undesired effects. This is achieved by utilizing suitable low pass filters in series with the PD control. However, the high rigid body eigenfrequencies in systems similar to this example will constitute a lower limit for the roll off frequency of

such low pass filters, which leads to a low frequency separation between rigid body and bending modes, so that noise as well as bending mode vibration attenuation will be unsatisfactory.

A second very typical and not less critical problem of local PD control for systems similar to the present example is the very unequal distribution of the damping over the two rigid body eigenmodes: The conical modes feature a very adequate real part of their eigenvalues already at standstill, whereas the parallel modes remain only very weakly damped, as can be seen in Fig. 8.7. This situation cannot be resolved by simply increasing the amount of velocity proportional feedback in the PD control, which is the first most straightforward idea for a solution of the problem. In fact, only the conical modes excessively profit from an increase of damping and even tend to be overcritically damped, as illustrated by Fig. 8.8.

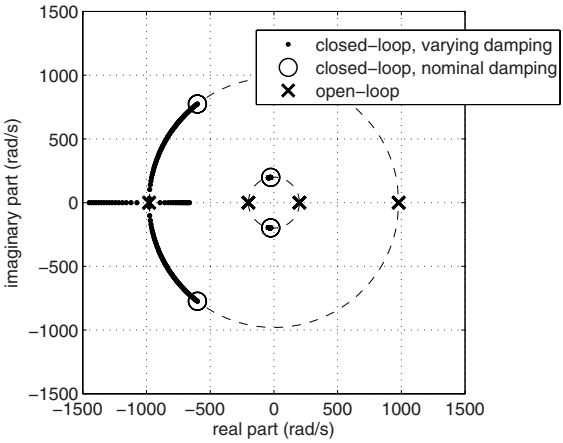


Fig. 8.8. Eigenvalue trajectory plot ($\Omega/2\pi = 0$ Hz) according to (8.12) as a function of the damping feedback gain for local PD control of a symmetric and collocated rigid rotor AMB system featuring a large difference between closed-loop eigenfrequencies (system parameters as given by Table 8.3, but with varying damping feedback gains $D_\mathrm{A} = D_\mathrm{B} = 25 \ldots 44$)

Finally, for the example system under discussion, there is even a third undesired property resulting from local PD control. As shown in Chap. 7 all rotors feature specific common properties with respect to rigid body eigenfrequencies in the presence of gyroscopic effects. The most important among these properties is the fact that, at high rotational speeds, the eigenfrequency ω_nut of the forward conical mode, i.e. of the *nutation* mode, always asymptotically tends to a value $\omega_{\mathrm{nut}_\infty}$ solely determined by the ratio of the polar and transverse moments of inertia I_z and I_x respectively:

$$\omega_{\mathrm{nut}_\infty} = \frac{I_z}{I_x}\Omega \tag{8.18}$$

This asymptotic behavior, which can also be considered the open-loop behavior of the plant, can be shown along with the *Campbell* diagram, which constitutes a plot of the rigid body eigenfrequencies as a function of the rotational speed Ω. In Fig. 8.9 the Campbell diagram for the present example is shown (numerical values from Table 8.3).

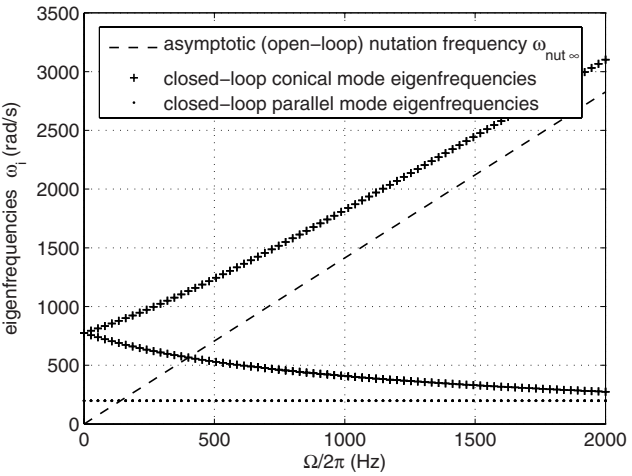


Fig. 8.9. Campbell diagram (rigid body closed-loop eigenfrequencies as a function of speed) for local PD control (system parameters as given by Table 8.3, but with rotation speed $\Omega/2\pi$ up to 2 kHz)

The Campbell diagram shows that, for a rotational speed $\Omega/2\pi$ up to 500 Hz – the maximum speed for this example – the effective nutation mode eigenfrequency is far, i.e. almost by a factor of two, above the theoretical value given by the asymptotic or open-loop behavior. This is entirely caused by the *structure* of local PD control which forces the conical mode eigenfrequencies to be high already at standstill. The consequence is that, at higher speeds, the control effort or control forces respectively become very high due to the velocity proportional feedback that must be introduced to provide damping for the nutation mode. For most practical systems, however, it is not adequate or it is even impossible to "counteract" the natural behavior of the nutation mode that strongly, i.e. to raise its eigenfrequency that high compared to the open-loop behavior. Hence, local PD control cannot be considered an adequate solution for applications with properties similar to this example.

8.2.3 Decoupled Control of Parallel and Conical Modes

The example discussed in the previous section has shown that, for – often symmetric – AMB systems featuring inertia and geometry properties that yield a large difference or ratio r_λ respectively between the open-loop eigenvalues, decentralized PD control turns out to have fundamental *structural deficiencies* which lead to a very unsatisfactory closed-loop system performance, even if the control parameters are chosen in accordance with the recommendations for "natural" stiffness and damping values as made for the simple one DOF system in Chap. 2. Moreover, it can be shown that implementing different stiffness and damping values in each of the two magnetic bearings even aggravates the problem in case of symmetric rotor systems. Finally, a gain reduction in order to yield a lower maximum closed-loop eigenfrequency will not fix the problem either, since the second rigid body eigenfrequency will be unpractically low in this case. In other words: Decentralized control cannot solve the problem so that closer eigenvalues, i.e. a value of r_λ closer to 1, are achieved.

Unlike the destabilization problem due to non-collocation in conjunction with local PD control the "r_λ problem" occurs rather often in practical applications and, therefore, it is important to come up with a solution to it.

In fact, by restraining oneself to decentralized control, one looses an important design freedom. If looked at the rigid body AMB system in only one motion plane, there are two system inputs – the magnetic bearing forces – and two system outputs – the sensor signals. Hence, we basically deal with a 2×2 MIMO plant (MIMO = "multiple-input-multiple-output"), but only the diagonal terms of the total 2×2 feedback matrices $\mathbf{P}$ and $\mathbf{D}$ in (8.9) are addressed by decentralized control, whereas the off-diagonal terms, i.e. the most essential coupling between the bearings A and B in one motion plane, are not implemented.

As will be shown in Chap. 12, which deals with flexible AMB rotor systems, "pure" MIMO control requires more elaborate and more "abstract" control design techniques as it is no more possible to "interpret" the feedback coefficients as direct physical properties of the system. Being able to do so in decentralized control, namely to interpret those feedback coefficients directly as stiffness and damping of a virtual mechanical suspension, was in fact the main underlying motivation for implementing local feedback.

Therefore, an enhanced control structure is introduced here which, on the one hand, solves both shortcomings of decentralized control shown above and, on the other hand, implements MIMO control while *keeping* the possibility for interpreting feedback parameters as physical quantities in a SISO like way (SISO = "single-input-single-output"), similarly to local feedback. This control structure makes use of the physical effect that the *parallel* and *conical* modes of the rigid body plant are *decoupled*, as can be seen in (8.1). There is just a coupling between the x and y motion of the conical modes by the gyroscopic effects, represented by the matrix $\mathbf{G}$. Hence, by transforming the controller input signals in such a way that the parallel and conical modes can

be detected separately, these modes can also be controlled separately. The control output signals, physically corresponding to the moment of force with respect to the rotor's center of gravity S and to the concentrated force in S, must then only be transformed into suitable forces in the bearing planes A and B. In this way, essentially "modal" PID control of the rigid body modes is achieved. Figure 8.10 shows the corresponding control architecture.

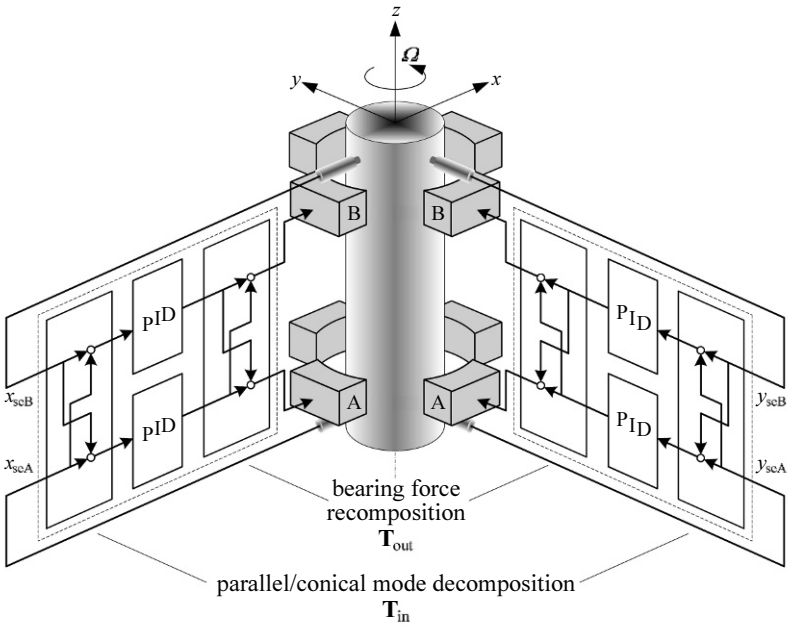


Fig. 8.10. Feedback structure for decoupled control of parallel and conical modes

Mathematically, this approach can be formulated as follows: Starting from (8.6), which basically describes the plant with its bearing force inputs, we can, similarly to (8.9), formulate a PD type feedback law which utilizes the center of gravity displacements rather than the sensor coordinates by involving the transformation matrix $\mathbf{T}_{\text{in}}$. At the output side the transformation matrix $\mathbf{T}_{\text{out}}$ has to be applied for the recomposition of the bearing forces or currents respectively:

$$\mathbf{M}\,\ddot{\mathbf{q}} + \mathbf{G}\,\dot{\mathbf{q}} + \mathbf{K}_{s\text{S}}\,\mathbf{q} = \mathbf{B}\,\mathbf{K}_i\,\mathbf{i} \tag{8.19a}$$

$$\mathbf{i} = -\mathbf{T}_{\text{out}}\,\mathbf{P}\,\mathbf{T}_{\text{in}}\,\mathbf{q}_{\text{se}} - \mathbf{T}_{\text{out}}\,\mathbf{D}\,\mathbf{T}_{\text{in}}\,\dot{\mathbf{q}}_{\text{se}} \tag{8.19b}$$

$$\mathbf{q}_{\text{se}} = (x_{\text{seA}}, x_{\text{seB}}, y_{\text{seA}}, y_{\text{seB}})^{\text{T}} \tag{8.19c}$$

$$\mathbf{P} = \text{diag}(P_{\text{con}}, P_{\text{par}}, P_{\text{con}}, P_{\text{par}}) \tag{8.19d}$$

$$\mathbf{D} = \text{diag}(D_{\text{con}}, D_{\text{par}}, D_{\text{con}}, D_{\text{par}}) \tag{8.19e}$$

The transformed sensor signals must represent the parallel and conical modes respectively, hence, the input transformation matrix $\mathbf{T}_{\text{in}}$ is identical to the inverse of the system output matrix $\mathbf{C}$ introduced in (8.1):

$$\mathbf{q} = \mathbf{T}_{\text{in}}\,\mathbf{q}_{\text{se}} = \mathbf{C}^{-1}\,\mathbf{q}_{\text{se}} \tag{8.20a}$$

$$\mathbf{T}_{\text{in}} = \begin{bmatrix} c\,1\,0\,0 \\ d\,1\,0\,0 \\ 0\,0\,c\,1 \\ 0\,0\,d\,1 \end{bmatrix}^{-1} = \frac{1}{d-c}\begin{bmatrix} -1 & 1 & 0 & 0 \\ d & -c & 0 & 0 \\ 0 & 0 & -1 & 1 \\ 0 & 0 & d & -c \end{bmatrix} \tag{8.20b}$$

At the controller output side things are a bit more complex. The transformation matrix $\mathbf{T}_{\text{out}}$ for the decomposition of the control signals into the bearing forces must, together with the force distribution matrix $\mathbf{B}$ in (8.6) or (8.19a), respectively, and with the diagonal force/current matrix $\mathbf{K}_i$, generate a pure moment of force with respect to the center of gravity S out of the first "modal" control coordinate of each motion plane. Similarly, a concentrated force has to be generated out of the second "modal" coordinate of each plane. Mathematically speaking, the total output path $\mathbf{B}\,\mathbf{K}_i\,\mathbf{T}_{\text{out}}$ must be *diagonal*. Since there is an infinite number of solutions fulfilling this diagonalization requirement, a unique solution for $\mathbf{T}_{\text{out}}$ is found by postulating that the total output path is described by the *identity matrix* $\mathbf{I}$:

$$\mathbf{B}\,\mathbf{K}_i\,\mathbf{T}_{\text{out}} = \mathbf{I} \tag{8.21a}$$

$$\Longrightarrow \mathbf{T}_{\text{out}} = {\mathbf{K}_i}^{-1}\,\mathbf{B}^{-1} = \frac{1}{k_{i\text{A}}(b-a)}\begin{bmatrix} -1 & b & 0 & 0 \\ \frac{k_{i\text{A}}}{k_{i\text{B}}} & -\frac{k_{i\text{A}}}{k_{i\text{B}}}a & 0 & 0 \\ 0 & 0 & -1 & b \\ 0 & 0 & \frac{k_{i\text{A}}}{k_{i\text{B}}} & -\frac{k_{i\text{A}}}{k_{i\text{B}}}a \end{bmatrix} \tag{8.21b}$$

With (8.21) the total closed-loop matrix differential equation for the rigid rotor in AMBs with this "COG coordinate" control scheme (COG = "center of gravity") can be written as follows:

$$\begin{aligned} &\mathbf{M}\,\ddot{\mathbf{q}} + \mathbf{G}\,\dot{\mathbf{q}} + \mathbf{K}_{s\text{S}}\,\mathbf{q} + \\ &\underbrace{\mathbf{B}\,\mathbf{K}_i\,\mathbf{T}_{\text{out}}}_{\mathbf{I}}\,\mathbf{P}\,\underbrace{\mathbf{T}_{\text{in}}\,\mathbf{q}_{\text{se}}}_{\mathbf{q}} + \underbrace{\mathbf{B}\,\mathbf{K}_i\,\mathbf{T}_{\text{out}}}_{\mathbf{I}}\,\mathbf{D}\,\underbrace{\mathbf{T}_{\text{in}}\,\dot{\mathbf{q}}_{\text{se}}}_{\dot{\mathbf{q}}} = \mathbf{0} \end{aligned} \tag{8.22a}$$

$$\Longleftrightarrow \mathbf{M}\,\ddot{\mathbf{q}} + \mathbf{G}\,\dot{\mathbf{q}} + \mathbf{K}_{s\text{S}}\,\mathbf{q} + \underbrace{\mathbf{P}}_{\mathbf{K}_c}\,\mathbf{q} + \underbrace{\mathbf{D}}_{\mathbf{D}_c}\,\dot{\mathbf{q}} = \mathbf{0} \tag{8.22b}$$

$$\mathbf{P} = \text{diag}(P_{\text{con}}, P_{\text{par}}, P_{\text{con}}, P_{\text{par}}) \tag{8.22c}$$

$$\mathbf{D} = \text{diag}(D_{\text{con}}, D_{\text{par}}, D_{\text{con}}, D_{\text{par}}) \tag{8.22d}$$

In contrast to the differential equation (8.11) for decentralized control the resulting stiffness and damping matrices in (8.22b), $\mathbf{K}_c$ and $\mathbf{D}_c$ respectively,

are diagonal, as postulated. Hence, the dynamic properties of the parallel and conical modes can be defined *independently* from each other by the corresponding feedback gains in $\mathbf{P}$ and $\mathbf{D}$. As further expected, the gyroscopic effects taken into account by the skew-symmetric matrix $\mathbf{G}$ only affect the conical modes, whereas for general AMB systems with decentralized control *both* rigid body eigenmodes are affected by the gyroscopic effects due to the coupling terms in the feedback matrices. In fact, this is the most important advantage of COG coordinate control over decentralized control, since only *one* control channel has to cope with the gyroscopics and, therefore, requires a controller transfer function featuring a suitably high bandwidth, while the speed independent parallel modes can be stabilized by a simpler and lower bandwidth controller.

However, in practice it is often forgotten that the introduction of the transformation matrices $\mathbf{T}_{\text{in}}$ and $\mathbf{T}_{\text{out}}$ does *not yet* lead to a fully decoupled control of parallel and conical modes, which constitutes a small but often non-negligible flaw of the approach represented by (8.22). As can be seen in (8.22b) the generally *non-diagonal* matrix $\mathbf{K}_{s\text{S}}$, introduced by the negative stiffness of each magnetic bearing, destroys the decoupling. Only in case of a fully *symmetric* AMB system with identical bearings on each side the negative stiffness matrix $\mathbf{K}_{s\text{S}}$, described by (8.7b), will also be diagonal, and an ideally decoupled system will result. This coupling effect can also be physically explained: If it is assumed that a general non-symmetric rotor instantaneously performs a pure translational motion in one plane, different negative stiffness forces will result in both bearings, despite the "modal" control, and will, also due to the different levers, exert a non-zero moment of force with respect to the center of gravity S, which will on its part start excitation of the conical mode. Hence, the parallel and conical modes become coupled.

There is no other way out of this situation than the introduction of a *negative stiffness compensation* scheme, which must be implemented *in parallel* to the COG coordinate control described by (8.19). Hence, the control law for the bearing currents comprised in $\mathbf{i}$ must be *augmented* by a compensation term as follows:

$$\mathbf{i} = \underbrace{-\mathbf{T}_{\text{out}}\,\mathbf{P}\,\mathbf{T}_{\text{in}}\,\mathbf{q}_{\text{se}} - \mathbf{T}_{\text{out}}\,\mathbf{D}\,\mathbf{T}_{\text{in}}\,\dot{\mathbf{q}}_{\text{se}}}_{\text{parallel/conical mode control}} \quad \underbrace{-\mathbf{K}_{s\text{S}_{\text{comp}}}\,\mathbf{q}_{\text{se}}}_{k_s\text{ compensation term}} \tag{8.23a}$$

$$\mathbf{K}_{s\text{S}}\,\mathbf{q} = -\mathbf{B}\,\mathbf{K}_i\,\mathbf{K}_{s\text{S}_{\text{comp}}}\,\mathbf{q}_{\text{se}} \tag{8.23b}$$

By introducing the relationship (8.20a) between the two different coordinate vectors $\mathbf{q}$ and $\mathbf{q}_{\text{se}}$ into (8.23b) and by considering (8.21b) one obtains

$$\begin{aligned}\mathbf{K}_{s\text{S}_{\text{comp}}} &= -\mathbf{K}_i^{-1}\,\mathbf{B}^{-1}\,\mathbf{K}_{s\text{S}}\,\mathbf{C}^{-1}\\ &= -\mathbf{T}_{\text{out}}\,\mathbf{K}_{s\text{S}}\,\mathbf{T}_{\text{in}},\end{aligned} \tag{8.24}$$

and by additionally considering expressions (8.1c), (8.2), (8.7b) and (8.20b) the following final result for the negative stiffness compensation matrix $\mathbf{K}_{s\mathrm{S}_{\mathrm{comp}}}$ is obtained:

$$\mathbf{K}_{s\mathrm{S}_{\mathrm{comp}}} = \frac{-1}{d-c} \begin{bmatrix} \frac{k_{s\mathrm{A}}}{k_{i\mathrm{A}}}(d-a) & \frac{k_{s\mathrm{A}}}{k_{i\mathrm{A}}}(a-c) & 0 & 0 \\ \frac{k_{s\mathrm{B}}}{k_{i\mathrm{B}}}(d-b) & \frac{k_{s\mathrm{B}}}{k_{i\mathrm{B}}}(b-c) & 0 & 0 \\ 0 & 0 & \frac{k_{s\mathrm{A}}}{k_{i\mathrm{A}}}(d-a) & \frac{k_{s\mathrm{A}}}{k_{i\mathrm{A}}}(a-c) \\ 0 & 0 & \frac{k_{s\mathrm{B}}}{k_{i\mathrm{B}}}(d-b) & \frac{k_{s\mathrm{B}}}{k_{i\mathrm{B}}}(b-c) \end{bmatrix} \tag{8.25}$$

Only with this additional compensation term a *fully* decoupled control of parallel and conical modes becomes possible, as summarized by the following set of equations for the closed-loop differential equation and for the feedback law:

$$\mathbf{i} = -(\mathbf{T}_{\mathrm{out}}\,\mathbf{P}\,\mathbf{T}_{\mathrm{in}} + \mathbf{K}_{s\mathrm{S}_{\mathrm{comp}}})\,\mathbf{q}_{\mathrm{se}} - \mathbf{T}_{\mathrm{out}}\,\mathbf{D}\,\mathbf{T}_{\mathrm{in}}\,\dot{\mathbf{q}}_{\mathrm{se}} \tag{8.26a}$$

$$\mathbf{P} = \mathrm{diag}(P_{\mathrm{con}}, P_{\mathrm{par}}, P_{\mathrm{con}}, P_{\mathrm{par}}) \tag{8.26b}$$

$$\mathbf{D} = \mathrm{diag}(D_{\mathrm{con}}, D_{\mathrm{par}}, D_{\mathrm{con}}, D_{\mathrm{par}}) \tag{8.26c}$$

$$\underbrace{\mathbf{K}_{s\mathrm{S}_{\mathrm{comp}}} = -\mathbf{T}_{\mathrm{out}}\,\mathbf{K}_{s\mathrm{S}}\,\mathbf{T}_{\mathrm{in}}}_{} \tag{8.26d}$$

$$\underbrace{\mathbf{M}\,\ddot{\mathbf{q}} + \mathbf{G}\,\dot{\mathbf{q}} + \mathbf{K}_{s\mathrm{S}}\,\mathbf{q} = \mathbf{B}\,\mathbf{K}_i\,\mathbf{i}}_{(8.6)} \;\longrightarrow\; \mathbf{M}\,\ddot{\mathbf{q}} + \mathbf{G}\,\dot{\mathbf{q}} + \mathbf{P}\,\mathbf{q} + \mathbf{D}\,\dot{\mathbf{q}} = \mathbf{0} \tag{8.26e}$$

The superiority of the "COG coordinate" control scheme over decentralized feedback can be verified along with the symmetric rotor example from Sect. 8.2.2, which was not well manageable using local feedback (see Figs. 8.7 and 8.8). In Fig. 8.11 the corresponding eigenvalue trajectory plot is shown.

As a clear difference and major improvement compared to local feedback both rigid body closed-loop eigenfrequencies can be *individually* set to "reasonable" values well below 100 Hz, hence, the large gap between the closed-loop eigenfrequencies has vanished. Moreover, a suitable amount of damping can now also be attributed to the parallel mode. As a further benefit from COG coordinate control the maximum rigid body eigenfrequency coming from the nutation mode at full speed is now at approximately 140 Hz, which is only about 25% above the theoretical value for the open-loop nutation frequency given by (8.18). This corresponds to a physically much more reasonable control effort than with decentralized control (see Campbell diagram in Fig. 8.9).

To summarize: Decoupled parallel and conical mode control or "COG coordinate" control respectively, described by the set of equations (8.26), can be considered the *most important* and in practice *universally applicable* PD type feedback control law for a rigid rotor in AMBs. The deficiencies of decentralized (local) feedback described in Sect. 8.2.2 can be fully overcome by this approach which, however, only performs correctly also in the case of general non-symmetric rotor systems if the "k_s compensation term" given by (8.23a) and (8.26d) is implemented as well. A gain scheduling of the control

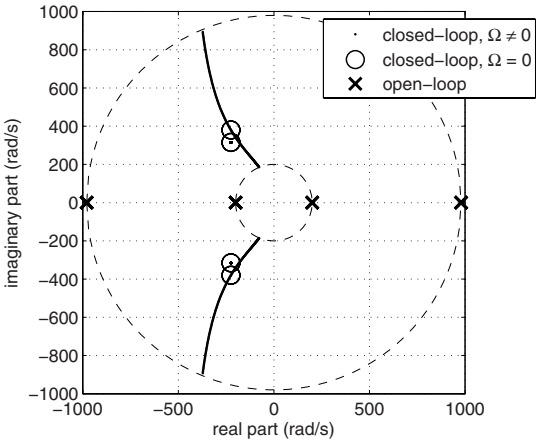


Fig. 8.11. Eigenvalue trajectory plot according to (8.12) as a function of the rotational speed Ω for a symmetric and collocated rigid rotor AMB system with decoupled parallel and conical mode control ("COG coordinate" control) according to (8.26) (model data summarized in Table 8.4, $\Omega/2\pi = 0 \ldots 500$ Hz)

Table 8.4. Model data for eigenvalue trajectory plot of Fig. 8.11

symbol	value	units
m	100	kg
$I_x = I_y$	0.6667	$\mathrm{kg\,m^2}$
I_z	0.15	$\mathrm{kg\,m^2}$
$b = d = -a = -c$	0.4	m
$k_{s\mathrm{A}} = k_{s\mathrm{B}}$	-2×10^6	N/m
$k_{i\mathrm{A}} = k_{i\mathrm{B}}$	100	N/A
P_{con}	1.3×10^5	N m
P_{par}	1.5×10^7	N/m
D_{con}	300	N s m
D_{par}	4.5×10^4	N s/m
$\Omega/2\pi$	$0 \ldots 500$	Hz

parameters with the rotational speed is not necessary for the huge majority of applications.

It is evident that this approach can also be extended without any shortcomings to an *integrating* feedback component, i.e. to PID control, as shown for the simple one DOF AMB system discussed in Chap. 2. In this case, however, a closed-loop system description in the "**MDGKN**" second-order matrix differential equation form, i.e. with mass, stiffness, damping, gyroscopic and non-conservative force matrices as given by (8.26), is not possible anymore, hence, a state space differential equation with a system matrix $\mathbf{A}$ similar to

(8.12a) must be set up in order to account for the additional integrator states, resulting in the following general state space description for an AMB system including its control part as well as its input and output signal paths:

$$\dot{\mathbf{x}} = \mathbf{A}\mathbf{x} + \mathbf{B}\mathbf{u} \tag{8.27a}$$

$$\mathbf{y} = \mathbf{C}\mathbf{x} + \mathbf{D}\mathbf{u} \tag{8.27b}$$

8.2.4 Other Feedback Control Concepts

As an alternative to decentralized or decoupled parallel and conical mode control, the *state feedback* control techniques can be considered. As the full system state including the *velocities* is usually not directly measured in a standard rigid body AMB system, the only choice will be an *observer* or *state estimator* based control design approach such as LQG-control (LQG = "linear-quadratic-gaussian"). Consequently, other full order state feedback techniques such as "pole-placement" or LQ-control (LQ = "linear-quadratic") are not applicable [6, 16].

There is a huge number of textbooks in control theory that cover LQ- and LQG-control. In the case of a rigid body AMB system it can be shown, however, that these methods do not feature appreciable advantages over decentralized [11] and particularly not over COG coordinate control.

Apart from potential robustness problems due to uncertainties in the dynamics of the state estimator LQG-control even features a potential for destabilization of the closed-loop AMB system with the rotational speed. If LQG-control is designed for the system at *stand-still* and implemented *separately* and *identically* for both x-z and y-z motion planes (see Fig. 8.1), the control will most probably also be stable a higher speeds. However, if the LQG-control design is made for the *rotating* system, there is a very high chance that stiffness couplings between the two motion planes are introduced as a result of the coupled plant dynamics. The closed-loop system will behave nicely at the design speed, but most probably it will become unstable at other speeds. This stability problem is associated with the matrix $\mathbf{N}$ (see Sect. 8.2.2) of the non-conservative forces introduced by the control itself. In this case the LQG-control must be gain scheduled over the rotational speed range, which constitutes a major drawback compared to the less abstract and more physically motivated approach of parallel/conical mode control. This is also the main reason why these methods have not succeeded in industrial practice of rigid body AMB control.

Other than the above mentioned estimator based state feedback control techniques the modern $\mathcal{H}_\infty$ or $\mu-$synthesis control design concepts [7] are much more promising for the use in AMB applications, in particular for elastic rotors. Many results from industrial implementations are not yet available, though, mostly due the relative freshness of these approaches. For pure rigid body control it is, furthermore, not to be expected that these methods will lead to far better results than those obtained by decoupled parallel/conical mode

control, since the structure of the feedback matrices obtained with $\mathcal{H}_\infty$ or $\mu-$synthesis control will not be fundamentally different from what is achievable with COG coordinate control, potentially combined with suitable low pass filters.

These modern and more elaborate control design techniques will fully prove their abilities and, hence, become very important in the case of *flexible* AMB rotor systems. They will be dealt with in Chap. 12.

8.3 Unbalance Control

Vibrations caused by mass unbalance are a common and well-known problem in rotating machinery (see Chap. 7). Perfect balancing, i.e. the achievement of a precise alignment of the rotor's axis of geometry with its principal axis of inertia, is very costly and sometimes even impossible without additional arrangements, if the unbalance distribution changes during operation. Thus, a certain amount of residual unbalance will always occur. In the case of conventional bearing arrangements this will inevitably lead to residual vibrations transmitted to the machine founding, with tolerable vibration levels defined by standards such as ISO 1940 or API 617 [4, 5].

8.3.1 Strategies of Unbalance Control with AMBs

As one of their most important and unique features, active magnetic bearings (AMBs) provide possibilities for actively controlling the system's response due to unbalances, a concept not possible with conventional ball, air or fluid film bearings. This additional control facility allows the rotor to either spin around its inertial axis – provided that the air gap between rotor and magnetic bearing is sufficiently large, which is, in practice, most often the case – or to compensate for the residual unbalance force so that the rotor is forced to rotate around its axis of geometry. Moreover, there are also further unbalance control schemes that are used to facilitate the passing of bending critical speeds.

Existing standards addressing machine vibration, such as ISO 1940 or API 617, do not account for the specific capabilities of AMBs in conjunction with the treatment of unbalance. For example, ISO 1940 defines balancing grades that depend on the rotation speed: The faster a system with a given unbalance distribution rotates, the worse its balancing grade becomes. While such a definition is sensible for conventional ball or oil bearing systems, where bearing reaction forces due to unbalance quadratically rise with the rotation speed, it fails to work with active magnetic bearing equipped machines which, in fact, are suitable for unlimited, reliable and safe operation even in the presence of "large" residual unbalance levels by allowing the rotor shaft to rotate about its principal axis independently of the rotor speed and by thus eliminating unbalance induced bearing reaction forces. For this reason, the laborious and expensive process of establishing and verifying residual unbalance levels, as

extensively described in API 617 and ISO 1940, becomes unnecessary and "obsolete" for magnetic bearings. Annex 4F of API 617, which is specific to magnetic bearing equipped machines, does address this issue by defining a much simpler criterion as an alternative to the residual unbalance level requirement, and it further clarifies that "... this criterion supersedes all other vibration acceptance criteria as described for oil bearing machines ..." [5].

Unbalance control with active magnetic bearings has a long history. First attempts to use AMBs for synchronous unbalance vibration attenuation were done by Burrows and his colleagues in the early 1980's [12, 13]. Today, there exist a variety of different control strategies and proprietary implementations, yet *all* resulting in the *same physical effect*: The suppression of unbalance induced vibration forces or displacements. An early comparison of unbalance control strategies can be found in [50]. An extensive overview of the currently existing unbalance control strategies with both research and industrial background can be found in Table 8.5 together with an assessment of technical properties, merits and shortcomings of the various approaches.

8.3.2 A Generalized View of Unbalance Control

All of the methods listed in Table 8.5, whether for the attenuation of forces (group A) or vibrations (group B) or for the generation of synchronous damping forces (group C), have in common that *very narrow band* and *rotation speed synchronous* signals are *injected* into the control loop. The methods only differ in *where* these signals are injected into the control loop, *how* they are generated and *what* adaptation process is used to adapt the signals to the unknown rotor unbalance. In Fig. 8.12 such a *generalized view* of an unbalance control is shown.

It can be seen in Fig. 8.12 that *all* the different unbalance control strategies belonging to a specific group - whether implemented as linear or nonlinear, time varying or time-invariant control schemes - feature the *same physical input-output behavior* when looked at them as "black boxes". Therefore, all these methods can be *understood* and also *mathematically treated* as "generalized notch filters" [18], since they all feature a very narrow band transfer characteristic $\mathbf{N}(s)$ in order to generate the appropriate rotation synchronous injection signals $\mathbf{I}_1$ or alternatively $\mathbf{I}_2$ out of the available broad band sensor signal $\mathbf{V}_2$ of the AMB system.

The term "generalized notch filter" is motivated by the fact that, differing from a "classical" notch filter, the open-loop pole location p of such a filter $N(s)$ as described by (8.28a) can be *allocated freely*, which enables stabilization of the resulting closed-loop system, including unbalance control, over virtually the entire speed range, hence also within the rigid body critical speeds.

As can be seen in Table 8.5 also *misleading* terms have been used in the past in conjunction with unbalance control, such as "automatic balancing", "feedforward" or "open-loop" control. In fact, *none* of the specific unbalance control methods addressed here yield at physically balancing a rotor, i.e. at

Table 8.5. Existing strategies of unbalance control with AMBs together with their properties ("•"), strengths ("+") and shortcomings ("−")

unbalance control strategy	control system term used in literature	control system properties
Group A: cancellation/ rejection of synchronous bearing reaction force	• Automatic Balancing System (ABS) • Automatic Balancing Control [19, 34] • Feedforward Compensation (FFC) [31, 32] • Rotating Reference Control [14] • Inertial Autocentering Control [57, 36] • Adaptive Feedforward Compensation [33, 32, 54] • Adaptive Unbalance Control [27, 59] • Adaptive Vibration Control (AVC) [10, 29, 9] • Adaptive Forced Balancing (AFB) [8, 53] • Automatic Vibration Rejection (AVR) [55, 56] • Open-Loop Control [26] • Periodic Learning Control (PLC) [21, 20] • Disturbance Estimation Control [44] • Unbalance Compensation Control [18, 42, 35] • Unbalance Force Rejection Control (UFRC) (generic term defined by ISO standard [1])	+ elimination of synchronous bearing reaction forces + reduction of housing vibrations + reduction of machine noise emissions + avoidance of dynamic power amplifier saturation + reduction of power consumption (reactive power) + cost reduction (lower installed power) + can be applied for rigid body modes depending on implementation – cannot be applied when passing bending critical speeds

Table 8.5. (cont'd)

unbalance control strategy	control system term used in literature	control system properties
Group B: cancellation/ reduction of unbalance vibration	• Compensation for Unbalance [19, 34, 49, 52, 59, 39] • Periodic Learning Control (PLC) [21] • Real Time Balancing [24] • Open-Loop Control [26] • Rotating Reference Control [14] • Adaptive Open-Loop Control [33, 28, 25, 30, 23, 46, 54] • Adaptive Vibration Control (AVC) [37, 22, 58] • Synchronous Vibration Control [13, 51] • Synchronous Feedback Control [50]	+ attenuation of unbalance induced vibrations by suitable compensation forces generated in the magnetic bearings + suitable for high precision positioning applications – needs high bearing forces and high amplifier power when used at high rotor speeds
Group C: passing of bending critical speeds	• Optimum Damping Control (ODC) [17] • Cross Stiffness Control [43, 48] • Synchronous Vibration Control [13, 40] • Unbalance Vibration Reduction [41] • Feedforward Control to Unbalance Force Cancellation [47]	+ vibration reduction when passing through bending critical speeds – needs high bearing forces and high amplifier power in the presence of large residual rotor unbalance

adding or removing suitable balancing weights. Moreover, pure "open-loop" or "feedforward" unbalance compensation is *generally not possible* if the unbalance distribution is *unknown*, which is the case in the vast majority of applications. Therefore, other terms such as "adaptive feedforward" or "adaptive open-loop" control have been found to be more appropriate, since they reflect the fact that the control output of these schemes has to be *adapted* to the unknown rotor unbalance. This also makes clear why *any* unbalance control scheme must provide specific constraints to its system parameters in order to achieve *closed-loop stability* of the adaptation process.

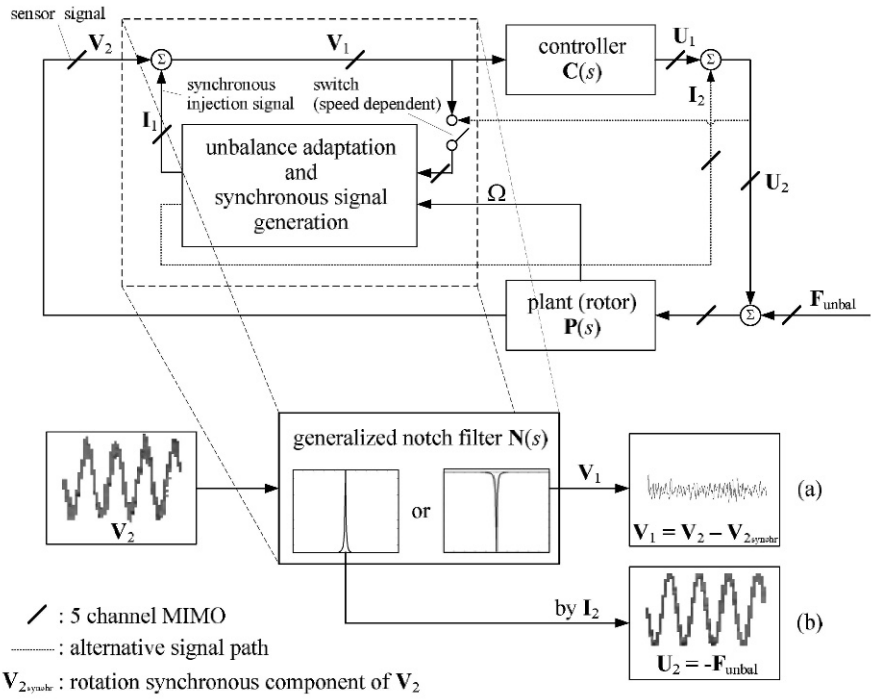


Fig. 8.12. Schematic diagram of a generalized multi-channel unbalance control scheme for AMBs: (**a**) cancellation/rejection of synchronous bearing reaction force (group A); (**b**) cancelation of unbalance vibration (group B)

In the SISO case a typical representation of a generalized notch filter can be obtained by the following transfer function [18],

$$N(s) = \frac{s^2 + \Omega^2}{(s-p)(s-\bar{p})} \tag{8.28a}$$

$$p = j\Omega + re^{j\Phi} \quad (r, \Phi \text{ must yield closed loop stability}) \tag{8.28b}$$

and in the MIMO case the entire transfer function matrix $\mathbf{N}(s)$ can be obtained by setting up the following block diagonal form:

$$\mathbf{N}(s) = \mathrm{diag}(N_1(s) \ldots N_5(s)) \tag{8.29}$$

It must be emphasized here again that the actual *physical implementation* of an unbalance control scheme does *not at all* need to be of the form given by (8.29). As a matter of fact the transfer function representation may even be an inappropriate topology if very narrow band width characteristics are aimed at. However, as mentioned before, (8.29) constitutes a "prototype" model for

the representation of the system dynamics of a very large number of state-of-the-art unbalance control schemes.

Although control of the axial magnetic bearing is not considered in this chapter, it must be mentioned here that a block diagonal implementation of an unbalance compensation scheme according to (8.29) makes it possible to address rotation synchronous signal components even in the axial control channel, a feature which can be very useful in practice. Therefore, the MIMO unbalance control scheme shown in Fig. 8.12 is typically of size 5x5 (four radial plus one axial channel).

The injection point for the rotation synchronous compensation signal can be either at the controller input ($\mathbf{I}_1$) or at its output ($\mathbf{I}_2$), without loss of generality. For the group A of synchronous bearing reaction force rejection schemes (UFRC) [1], which are the most often applied in industrial AMB systems, signal injection at the controller input ($\mathbf{I}_1$) can have advantages, especially in the case of digital control with fixed-point microprocessors (see Chap. 9), since the control input $\mathbf{V}_1$ is completely freed from the harmonic and rotation synchronous signal components contained in the original sensor signal $\mathbf{V}_2$ (see Fig. 8.12a), which leads to a better numerical conditioning of the digital control algorithm represented by $\mathbf{C}(s)$ mainly due to the absence of numerical saturation effects. In the case of a group B implementation for unbalance vibration reduction, harmonic signal injection usually takes place at the controller output (see Fig. 8.12b).

8.3.3 An Example of Unbalance Control: UFRC

Most often unbalance control with UFRC (group A in Table 8.5) is activated when the rotor system has reached a certain speed. This speed is generally much lower than the expected normal operating speed range of the machine, however, for a number of known unbalance control schemes, it must be above the rigid body critical speeds in order to achieve a stable unbalance compensation algorithm. If a control scheme is implemented that corresponds to the generalized notch filter topology introduced by (8.28/8.29) stable unbalance control can also be achieved at lower speeds and even down to standstill.

In Fig. 8.13 a typical transient response of a rotor system's displacement and magnetic bearing current signals is shown at the time of activation of the unbalance control scheme. All system properties are modeled according to (8.26), and the unbalance force excitation is modeled according to Chap. 7.

Figure 8.13 impressively shows that unbalance control achieves a complete cancelation, i.e. a reduction to zero, of the rotation synchronous bearing current components in both bearings within only very few rotor revolutions, hence, the chosen unbalance control performance can be considered suitably stable. UFRC also reduces the synchronous displacement orbits at the sensor locations, which constitutes a well-known property of unbalance control: Whether displacement orbits are reduced or become larger when unbalance

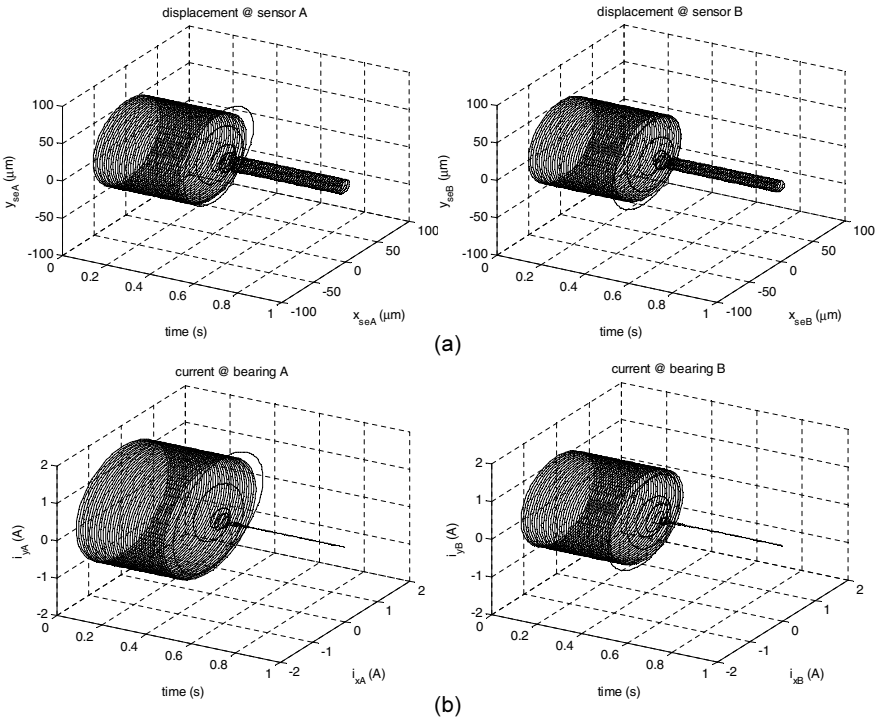


Fig. 8.13. Unbalance induced rotor orbits at the time of activation of unbalance force rejection control (UFRC) according to (8.28/8.29) (system parameters summarized by Table 8.6, $\Omega/2\pi = 100$ Hz): (**a**) sensor displacement orbits; (**b**) magnetic bearing current orbits

control is switched on depends on the rotational speed as well as on the plant and feedback control characteristics.

It is important to notice at this point that the chosen topology of unbalance control does not need any prior knowledge of the unbalance distribution on the rotor. Consequently UFRC usually also suppresses synchronous control forces in the presence of a changing unbalance distribution e.g. due to temperature effects.

In Fig. 8.14 the effect of UFRC on the displacement and bearing current orbit amplitudes over the entire speed range is displayed. As can be seen, UFRC is already switched on and can be stably operated at a speed of 50 Hz, which is well below the rigid body critical speeds. Above this speed, the displacement orbit amplitudes with UFRC are considerably smaller than without unbalance control. Although this behavior does not seem intuitive at a first glance – why does the cancelation of the synchronous bearing force lead to a smaller orbit amplitude at the same time? – it can be shown that this is in perfect accordance with theory. The main reason for the effect is the rigid

Table 8.6. Model data for UFRC activation response plot of Fig. 8.13

symbol	value	units	remarks
m	100	kg	
$I_x = I_y$	0.6667	$\mathrm{kg\,m^2}$	
I_z	0.15	$\mathrm{kg\,m^2}$	
$b = d = -a = -c$	0.4	m	
$k_{s\mathrm{A}} = k_{s\mathrm{B}}$	-2×10^6	N/m	
$k_{i\mathrm{A}} = k_{i\mathrm{B}}$	100	N/A	
P_{con}	1.3×10^5	N m	
P_{par}	1.5×10^7	N/m	
D_{con}	150	N s m	
D_{par}	2.25×10^4	N s/m	
r	10	rad/s	according to (8.28b)
Φ	160	deg	according to (8.28b)
$\Delta m e_{\mathrm{A}}$	1×10^{-4}	kg m	mass unbalance sensor plane A
$\Delta m e_{\mathrm{B}}$	0	kg m	mass unbalance sensor plane B
$\Omega/2\pi$	100	Hz	

body resonance which vanishes with UFRC, since the system behaves as if there was no external stiffness that otherwise leads to the resonance.

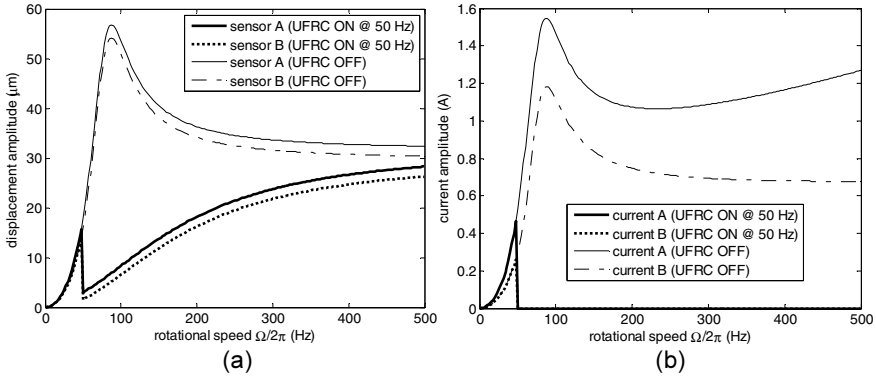


Fig. 8.14. Unbalance induced rotor response as a function of the rotational speed Ω with and without UFRC (system parameters summarized by Table 8.6, generalized notch filter parameters r and Φ scheduled with Ω according to [18], $\Omega/2\pi = 0 \ldots 500$ Hz): (**a**) sensor displacement orbit amplitude $\sqrt{x^2_{\mathrm{seA,B}} + y^2_{\mathrm{seA,B}}}$; (**b**) magnetic bearing current orbit amplitude $\sqrt{i^2_{x\mathrm{A,B}} + i^2_{y\mathrm{A,B}}}$

Apart from the displacement orbit reduction the most important benefit and actual target of UFRC is the reduction of the synchronous magnetic

bearing reaction force. This reduction also helps to avoid power amplifier saturation effects at high rotational speeds that would otherwise be present in any practical AMB system.

However, although UFRC is implemented in this way in the majority of industrial AMB systems, it can be shown that the main target – the *complete* suppression of the synchronous bearing reaction force yielding a rotation about the rotor's axis of inertia – *cannot* be correctly achieved by this topology. This becomes immediately clear when looking at the displacement orbit amplitudes in Fig. 8.14a: If there was truly no synchronous external bearing reaction force the rotor would rotate about its principal axis of inertia, which remains identical for all rotational speeds. Obviously, this is not the case here, at least not at low speeds. The reason is simple: Although the synchronous control *current* component is canceled by UFRC there still exists a synchronous *force* component resulting from the *negative bearing stiffness* in conjunction with the non-zero unbalance induced rotor displacement, an effect which has also been described in [36]. In fact, it can be shown that the displacement orbit amplitude shown in 8.14a is identical to the unbalance induced frequency response of the unstable open-loop plant *including* the negative bearing stiffness, as given by (8.6).

Similarly to what was shown in Sect. 8.2.3 it also turns out here that a special treatment of the negative bearing stiffness becomes necessary again in order to achieve a "true" UFRC, i.e. force-free, operation: The k_s compensation must be *left out* of the UFRC scheme, i.e. the k_s compensation matrix $\mathbf{K}_{s\mathrm{S}_{\mathrm{comp}}}$ used in (8.26) *must not* be affected by any synchronous component cancelation scheme.

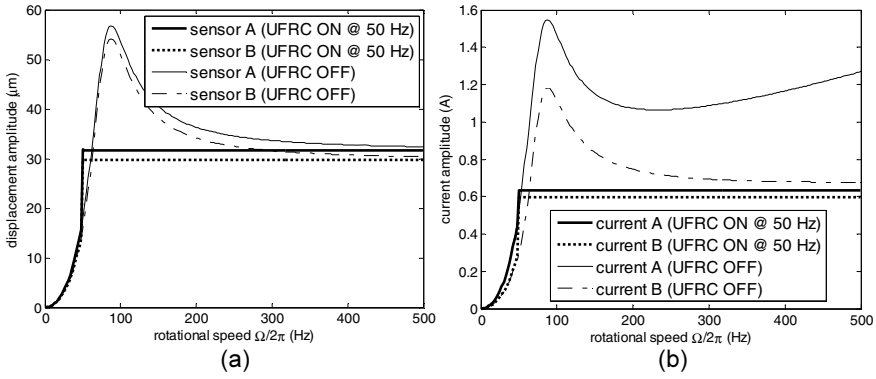


Fig. 8.15. Unbalance induced rotor displacement amplitude as a function of the rotational speed Ω with a modified UFRC scheme leaving out the k_s compensation term (system and generalized notch filter parameters identical to Fig. 8.14, $\Omega/2\pi = 0 \ldots 500$ Hz): (**a**) sensor displacement orbit amplitude $\sqrt{x^2_{\mathrm{seA,B}} + y^2_{\mathrm{seA,B}}}$; (**b**) magnetic bearing current orbit amplitude $\sqrt{i^2_{x\mathrm{A,B}} + i^2_{y\mathrm{A,B}}}$

In Fig. 8.15 the response of a correspondingly modified UFRC scheme is shown. As expected the bearing *current* orbit amplitudes become non-zero and constant over the rotation speed, the resulting synchronous bearing *forces*, however, are completely rejected so that the rotor starts to rotate in a true force-free manner about its principal axis of inertia as soon as unbalance control is activated.

All considerations in this chapter were made for AMB systems using a bearing force linearization scheme with a constant bias current (*current control*). As mentioned before, this scheme is the most widely used and state-of-the-art control topology in industrial AMB systems. However, some disadvantages are inherently linked to this approach. The two "adverse" effects of current control shown in this chapter – the negative bearing stiffness firstly not allowing for an ideal decoupled control of parallel and conical modes and secondly leading to only partial synchronous bearing force rejection – can only be overcome if a corresponding compensation term is separately implemented and left out of any unbalance force cancelation scheme. Although not further discussed in this chapter these effects do not exist if, for example, a *voltage control* scheme is implemented (see also Chap. 2 and the example in Sect. 4.5.3). If voltage control is used, UFRC can be directly applied to the AMB coil voltage. Hence, any synchronous component will be removed from the coil voltage, and consequently the synchronous coil flux component which directly determines the magnetic bearing force will be zero. As mentioned in Chap. 2 such more appropriate AMB control topologies will presumably be implemented in the future in conjunction with digitally generated pulse width modulation (PWM) command signals, allowing for a further improved AMB control technology.

References

1. ISO 14839-1. *Mechanical vibration - Vibration of rotating machinery equipped with active magnetic bearings - Part 1: Vocabulary.* International Organization for Standardization ISO, 2002.
2. ISO 14839-2. *Mechanical vibration - Vibration of rotating machinery equipped with active magnetic bearings - Part 2: Evaluation of vibration.* International Organization for Standardization ISO, 2004.
3. ISO 14839-3. *Mechanical vibration - Vibration of rotating machinery equipped with active magnetic bearings - Part 3: Evaluation of stability margin.* International Organization for Standardization ISO, 2006.
4. ISO Standard 1940. *Balance quality of rotating rigid bodies.* International Organization for Standardization ISO, 1973.
5. API 617. *Axial and centrifugal compressors and turboexpanders for petroleum, chemical and gas industry services.* American Petroleum Institute API, Washington D.C., seventh edition, 2002.
6. J. Ackermann. *Sampled Data Control Systems.* Springer-Verlag, Berlin, 1985.
7. G. J. Balas, J. C. Doyle, K. Glover, A. K. Packard, and R. Smith. *μ Analysis and Synthesis Toolbox User's Guide.* The MathWorks, Natick, MA, 1995.

8. S. Beale, B. Shafai, P. LaRocca, and E. Cusson. Adaptive forced balancing for magnetic bearing systems. In *Proceedings of the Third International Symposium on Magnetic Bearings*, University of Virginia, USA, July 1992.
9. F. Betschon and C. Knospe. Gain scheduled adaptive vibration control. In *Proceedings of the Seventh International Symposium on Magnetic Bearings*, ETH Zürich, Switzerland, August 2000.
10. F. Betschon and R. Schöb. On-line-adapted vibration control. In *Proceedings of the Sixth International Symposium on Magnetic Bearings*, Massachussetts Institute of Technology (MIT), Cambridge MA, USA, August 1998.
11. H. Bleuler. *Decentralized Control of Magnetic Rotor Bearing Systems.* PhD thesis, No. 7573, Federal Institute of Technology (ETH), Zürich, Switzerland, 1984.
12. C. R. Burrows and M. N. Sahinkaya. Vibration control of multi-mode rotor-bearing systems. In *Proceedings of the Royal Society of London (Series A)*, volume 386, 1983.
13. C. R. Burrows, N. Sahinkaya, A. Traxler, and G. Schweitzer. Design and application of a magnetic bearing for vibration control and stabilization of a flexible rotor. In *Proceedings of the First International Symposium on Magnetic Bearings*, ETH Zürich, Switzerland, June 1988.
14. J. De Miras and A. Charara. Unbalance cancellation with rotating reference control for a horizontal shaft. In *Proceedings of the Sixth International Symposium on Magnetic Bearings*, Massachussetts Institute of Technology (MIT), Cambridge MA, USA, August 1998.
15. R. Gasch, H. Pfützner, and R. Nordmann. *Rotordynamik.* Springer-Verlag, Berlin, second edition, 2002.
16. H. P. Geering. *Mess- und Regelungstechnik.* Springer-Verlag, Berlin, second edition, 1990.
17. H. Habermann and M. Brunet. The active magnetic bearing enables optimum damping of flexible rotors. In *Proceedings of the ASME International Gas Turbine Conference*, Amsterdam, Netherlands, 1994.
18. H. Herzog, Ph. Bühler, C. Gähler, and R. Larsonneur. Unbalance compensation using generalized notch filters in the multivariable feedback of magnetic bearings. *IEEE Transactions on Control Systems Technology*, 4(5):580–586, September 1996.
19. T. Higuchi, T. Mizuno, and M. Tsukamoto. Digital control system for magnetic bearings with automatic balancing. In *Proceedings of the Second International Symposium on Magnetic Bearings*, University of Tokyo, Japan, July 1990.
20. T. Higuchi, M. Otsuka, and T. Mizuno. Identification of rotor unbalance and reduction of housing vibration by periodic learning control in magnetic bearings. In *Proceedings of the Third International Symposium on Magnetic Bearings*, University of Virginia, USA, July 1992.
21. T. Higuchi, M. Otsuka, T. Mizuno, and T. Ide. Application of periodic learning control with inverse transfer function compensation in totally active magnetic bearings. In *Proceedings of the Second International Symposium on Magnetic Bearings*, University of Tokyo, Japan, July 1990.
22. M. Hirschmanner and H. Springer. Adaptive vibration and unbalance control of a rotor supported by active magnetic bearings. In *Proceedings of the Eighth International Symposium on Magnetic Bearings*, Mito, Japan, August 2002.

23. M. Hisatani and T. Koizumi. Adaptive filtering for unbalance vibration suppression. In *Proceedings of the Fourth International Symposium on Magnetic Bearings*, ETH Zürich, Switzerland, August 1994.
24. Y. Kanemitsu, M. Ohsawa, and K. Watanabe. Real time balancing of a flexible rotor supported by magnetic bearings. In *Proceedings of the Second International Symposium on Magnetic Bearings*, University of Tokyo, Japan, July 1990.
25. C. Knospe, S. Tamir, and S. Fedigan. Design of robust adaptive unbalance response controllers for rotors with magnetic bearings. In *Proceedings of the 3rd International Symposium on Magnetic Suspension Technology*, Tallahassee, USA, 1995.
26. C. R. Knospe. Robustness of unbalance response controllers. In *Proceedings of the Third International Symposium on Magnetic Bearings*, University of Virginia, USA, July 1992.
27. C. R. Knospe, R. W. Hope, S. J. Fedigan, and R. D. Williams. Adaptive online rotor balancing using digital control. In *Proceedings of the "MAG '93" Conference and Exhibition for Magnetic Bearings, Magnetic Drives and Dry Gas Seals*, University of Virginia, USA, July 1993.
28. C. R. Knospe, R. W. Hope, S. J. Fedigan, and R. D. Williams. New results in the control of rotor synchronous vibration. In *Proceedings of the Fourth International Symposium on Magnetic Bearings*, ETH Zürich, Switzerland, August 1994.
29. C. R. Knospe, J. D. Lindlau, and R. W. Hope. Synthesis techniques for robust adaptive vibration control. In *Proceedings of the Sixth International Symposium on Magnetic Bearings*, Massachussetts Institute of Technology (MIT), Cambridge MA, USA, August 1998.
30. C. R. Knospe and S. M. Tamer. Experiments in robust unbalance response control. In *Proceedings of the Fifth International Symposium on Magnetic Bearings*, Kanazawa, Japan, August 1996.
31. R. Larsonneur. A high speed rotor in active magnetic bearings. In *Proceedings of the 3rd International Conference on Rotordynamics (IFToMM)*, CNRS Lyon, France, September 1990.
32. R. Larsonneur and R. J. P. Herzog. Feedforward compensation of unbalance: New results and application experiences. In *Proceedings of the IUTAM Symposium "The Active Control of Vibration"*, University of Bath, U.K., September 1994.
33. R. Larsonneur, R. Siegwart, and A. Traxler. Active magnetic bearing control strategies for solving vibration problems in industrial rotor systems. In *Proceedings of the Institution of Mechanical Engineers IMechE Symposium "Vibrations in Rotating Machinery"*, University of Bath, U.K., September 1992.
34. J. Lee, A. M. Mohamed, and F. Matsumura. Q-parameterization control of magnetic bearing systems with imbalance. In *Proceedings of the Fifth International Symposium on Magnetic Bearings*, Kanazawa, Japan, August 1996.
35. W.-L. Lee, W. Schumacher, and W.-R. Canders. Unbalance compensation on AMB system without a rotational sensor. In *Proceedings of the Eighth International Symposium on Magnetic Bearings*, Mito, Japan, August 2002.
36. L. Li, T. Shinshi, X. Zhang, and A. Shimokohbe. A simple method for rotation about the inertial axis of a rigid AMB rotor. In *Proceedings of the Eighth International Symposium on Magnetic Bearings*, Mito, Japan, August 2002.

37. Z. Liu and K. Nonami. Adaptive non-stationary vibration control for magnetic bearing system from startup-up to operational speed. In *Proceedings of the Seventh International Symposium on Magnetic Bearings*, ETH Zürich, Switzerland, August 2000.
38. K. Magnus. *Kreisel, Theorie und Anwendungen*. Springer-Verlag, Berlin, 1971.
39. R. Markert, N. Skricka, and X. Zhang. Unbalance compensation on flexible rotors by magnetic bearings using transfer functions. In *Proceedings of the Eighth International Symposium on Magnetic Bearings*, Mito, Japan, August 2002.
40. T. Matsubara, K. Tanaka, and S. Murakami. Development of hybrid magnetic spindle – synchronous control with rotation –. In *Proceedings of the Fifth International Symposium on Magnetic Bearings*, Kanazawa, Japan, August 1996.
41. F. Matsumura, M. Fujita, and C. Oida. A design of robust servo controllers for an unbalance vibration in magnetic bearing systems. In *Proceedings of the First International Symposium on Magnetic Bearings*, ETH Zürich, Switzerland, June 1988.
42. F. Matsumura, M. Fujita, and K. Okawa. Modeling and control of magnetic bearing systems achieving a rotation around the axis of inertia. In *Proceedings of the Second International Symposium on Magnetic Bearings*, University of Tokyo, Japan, July 1990.
43. O. Matsushita, M. Takagi, M. Yoneyama, T. Yoshida, and I. Saitoh. Control of rotor vibration due to cross stiffness effect of active magnetic bearing. In *Proceedings of the 3rd International Conference on Rotordynamics (IFToMM)*, CNRS Lyon, France, September 1990.
44. T. Mizuno and T. Higuchi. Design of magnetic bearing controllers based on disturbance estimation. In *Proceedings of the Second International Symposium on Magnetic Bearings*, University of Tokyo, Japan, July 1990.
45. P. C. Müller. *Stabilität und Matrizen*. Springer-Verlag, Berlin, 1977.
46. K. Nonami, Q. Fan, and H. Ueyama. Unbalance vibration control of magnetic bearing systems using adaptive algorithm with disturbance frequency estimation. In *Proceedings of the Sixth International Symposium on Magnetic Bearings*, Massachussetts Institute of Technology (MIT), Cambridge MA, USA, August 1998.
47. K. Nonami and S. Kawamata. Feedforward control to unbalance force cancellation for flexible rotor systems. In *Proceedings of the International Symposium on Advanced Computers for Dynamics and Design ("ACD & D '89")*, Tsuchiura, Japan, September 1989.
48. Y. Okada et. al. Cross-feedback stabilization of the digitally controlled magnetic bearing. *ASME Journal of Vibration and Acoustics*, 144:54–59, 1992.
49. M. Paul, W. Hofmann, and H. F. Steffani. Compensation for unbalances with aid of neural networks. In *Proceedings of the Sixth International Symposium on Magnetic Bearings*, Massachussetts Institute of Technology (MIT), Cambridge MA, USA, August 1998.
50. N. K. Rutland, P. S. Keogh, and C. R. Burrows. Comparison of controller designs for attenuation of vibration in a rotor-bearing system under synchronous and transient conditions. In *Proceedings of the Fourth International Symposium on Magnetic Bearings*, ETH Zürich, Switzerland, August 1994.
51. M. N. Sahinkaya, M. O. T. Cole, and C. R. Burrows. On the use of Schroeder phased harmonic sequences in multi-frequency vibration control of flexible ro-

tor/magnetic bearing systems. In *Proceedings of the Eighth International Symposium on Magnetic Bearings*, Mito, Japan, August 2002.
52. J. D. Setiawan, R. Mukherjee, and E. Maslen. Variable magnetic stiffness approach for simultaneous sensor runout and mass unbalance compensation in active magnetic bearings. In *Proceedings of the Seventh International Symposium on Magnetic Bearings*, ETH Zürich, Switzerland, August 2000.
53. B. Shafai, S. Beale, P. LaRocca, and E. Cusson. Magnetic bearing control systems and adaptive forced balancing. *IEEE Control Systems Technology*, pages 4–12, April 1994.
54. J. Shi, R. Zmood, and L. Qin. The indirect adaptive feed-forward control in magnetic bearing systems for minimizing selected vibration performance measures. In *Proceedings of the Eighth International Symposium on Magnetic Bearings*, Mito, Japan, August 2002.
55. V. Tamisier, F. Carrère, and S. Font. Synchronous unbalance cancellation across critical speed using a closed-loop method. In *Proceedings of the Eighth International Symposium on Magnetic Bearings*, Mito, Japan, August 2002.
56. V. Tamisier and S. Font. Optimal vibration control of a milling electrospindle. In *Proceedings of the Ninth International Symposium on Magnetic Bearings*, Lexington, Kentucky, USA, August 2004.
57. J. v. Löwis and J. Rudolph. Adaptive inertial autocentering of a rigid rotor with unknown imbalance supported by active magnetic bearings. In *Proceedings of the Seventh International Symposium on Magnetic Bearings*, ETH Zürich, Switzerland, August 2000.
58. R. Yunheng and K. Nonami. Novel robust and adaptive vibration control for active magnetic bearing system. In *Proceedings of the Tenth International Symposium on Magnetic Bearings*, Martigny, Switzerland, August 2006.
59. H. Zhao, L. Zhao, and W. Jiang. Simulation and experimental research on unbalance vibration control of AMB system. In *Proceedings of the Seventh International Symposium on Magnetic Bearings*, ETH Zürich, Switzerland, August 2000.

9

Digital Control

René Larsonneur

The main focus of this chapter is to give a general overview of the special properties and various features of a digitally controlled AMB system, while keeping mathematical derivations at a minimum wherever possible. This information can be found in the textbooks about sampled data control systems.

9.1 Digital vs. Analog Control

While early industrial AMB control implementations in the 1970's and 1980's were realized in analog electronics, digital control has taken over for the majority of applications since the early 1990's. This transition from analog to digital control was mainly made possible by the fast progress in microprocessor and peripheral device technology such as the appearance of fast signal processors, analog-to-digital (A/D) and digital-to-analog (D/A) converter as well as pulse width modulation (PWM) units.

Due to its high flexibility digital control offers a number of advantages over the traditional analog control:

- Easy control parameter tuning enabling rapid prototyping
- No control parameter drifting due to aging and temperature changes
- Possibility for complex control algorithms, including nonlinear or adaptive control techniques, gain scheduling or speed dependent control as well as special start-up and shut-down procedures
- Realization of important additional tasks, such as
  - Unbalance control
  - Set-point adjustment depending on machine process state
  - Monitoring of forces, vibration levels and other operating conditions
  - On-line system identification
  - Machine state diagnosis and preventive maintenance
  - Sophisticated communication with higher machine control or remote control units

G. Schweitzer, E.H. Maslen (eds.), *Magnetic Bearings*,
DOI 10.1007/978-3-642-00497-1_9, © Springer-Verlag Berlin Heidelberg 2009

In the beginning of the transition process from analog to digital control it was the AMB system manufacturer who profited most from the enhanced flexibility and added capabilities of digital control. Today, however, the benefit is clearly on the user side: Thanks to its inherently built-in instrumentation in conjunction with digital control, an AMB equipped machine can, apart from the actual contact-free levitation, offer a host of insights into machine internal quantities, such as process forces or balancing quality, which would not be as readily accessible with other bearing technologies. Moreover, thanks to the various interfacing capabilities of a modern digital AMB control system, the end-user can easily integrate it into an overall machine control system.

9.2 Digital Control Hardware and Timing Issues

Basically, the hardware of a digital AMB control system comprises at least one microprocessor or digital signal processor (DSP), analog-to-digital (A/D) and digital-to-analog (D/A) converters, filters, memory, peripherals and other interfacing components. A system can be set up with only one single microprocessor at its core, which must be powerful enough to accomplish all the needed tasks. Alternative implementations can be based on a multi-processor architecture featuring several processors, each one dedicated to a special sub-task. Such a topology can, e.g., comprise a processor for pure levitation control, another one for generating the pulse-width-modulation (PWM) signal patterns needed by the power amplifier to drive the AMB coil currents, and further processors for monitoring tasks or even for an integrated motor control.

Today, many commercially available microprocessors and DSPs, especially those with a *fixed-point* structure (16 or 32 bit), feature on-chip A/D and D/A converters as well as peripherals such as PWM generators. This trend in hardware development has been substantially driven by the requirements of digital motor control, which are very similar to those of AMB control. However, in many cases, there are only one or two parallel A/D conversion channels available, with the consequence that a multiplexer topology has to be used to read in all the needed signals from the sensors of an AMB system. This consecutive sampling instead of a "one-shot" parallel sampling causes, on the one hand, time delays that vary between the individual control channels, and, on the other hand, it can lead to the undesired *inter-sample skew* effect if sampling of the various A/D channels is not properly synchronized using *sample-and-hold* amplifiers. Today, most processors for real-time dynamic system control feature built-in sample-and-hold amplifiers and, thus, help to avoid inter-sample skew.

Variable time delays between the individual control channels are most undesired if MIMO control is applied (MIMO = "multiple-input-multiple-output"), since they deteriorate control performance. Here, the only way out is to implement either enough parallel conversion channels or very fast A/D converters. In the case of SISO control (SISO = "single-input-single-output"),

variable time delays are more acceptable, specially if the AMB system can be considered only weakly coupled (slender rotor shaft, weak gyroscopic effects). Here, a control structure can be implemented where each control channel, including corresponding A/D and D/A conversions, is worked through sequentially, keeping time delays and inter-sample skew at a minimum.

From the control theoretical point of view it is most essential to generally keep the time delay between data input (A/D conversion) and data output (D/A conversion) at a minimum, yielding best performance and best accordance with the mathematical representation of a discrete-time dynamic system given by (9.2). However, this requires very short A/D and D/A conversion times and a high computation power of the microprocessor, especially in the case of MIMO control involving high controller orders as resulting from modern robust control design techniques. A way out from this is to *distribute* the various steps of the control algorithm computation along the entire control loop, as shown in Fig. 9.1a. This approach takes advantage from the fact that the bulk of the entire computation, i.e. the controller state update represented by (9.2a), can be carried out after delivery of the latest control output signals. If suitably fast A/D converters are not available or if the computation power is limited longer time delays must be accepted and adequately considered in the control design process. In this case, a control loop structure as shown in Fig. 9.1b will result with computation delays that are usually longer than one sampling period but shorter than two.

It is often assumed that digital control performance is inherently boosted if a powerful processor is used allowing for a very high sampling rate. This is not entirely true because the overall control performance very much also depends on the processor peripherals. Namely, it does not make sense to sample at very high rates while, at the same time, coping with comparably low A/D or D/A converter resolutions. In this case, it is more appropriate to utilize the processor performance for implementing an *over-sampling* of the A/D conversion channels in conjunction with a subsequent digital filtering of the input signals. This allows for artificially raising the A/D conversion resolution and, thus, for substantially reducing signal quantization noise, while keeping the actual control sampling rate comparably low so that it matches the requirements of the signal output architecture (D/A converters or PWM units). Moreover, digital over-sampling reduces the hardware expense for the *anti-aliasing* filters, which can be built simpler since most of the high quality signal treatment is accomplished digitally.

While, nowadays, nobody would truly doubt the superiority of digital over analog control – even the cost level of digital hardware can compete with its analog counterpart unless a real mass production system reaching several hundred thousand units a year is considered – there is a new trend away from firmware based back to hardware based systems. Differently from the former analog hardware architecture, however, this new trend involves *FPGA* technology (FPGA = "Field Programmable Gate Array") [7], which replaces software running on microprocessors by a purely digital programmable and

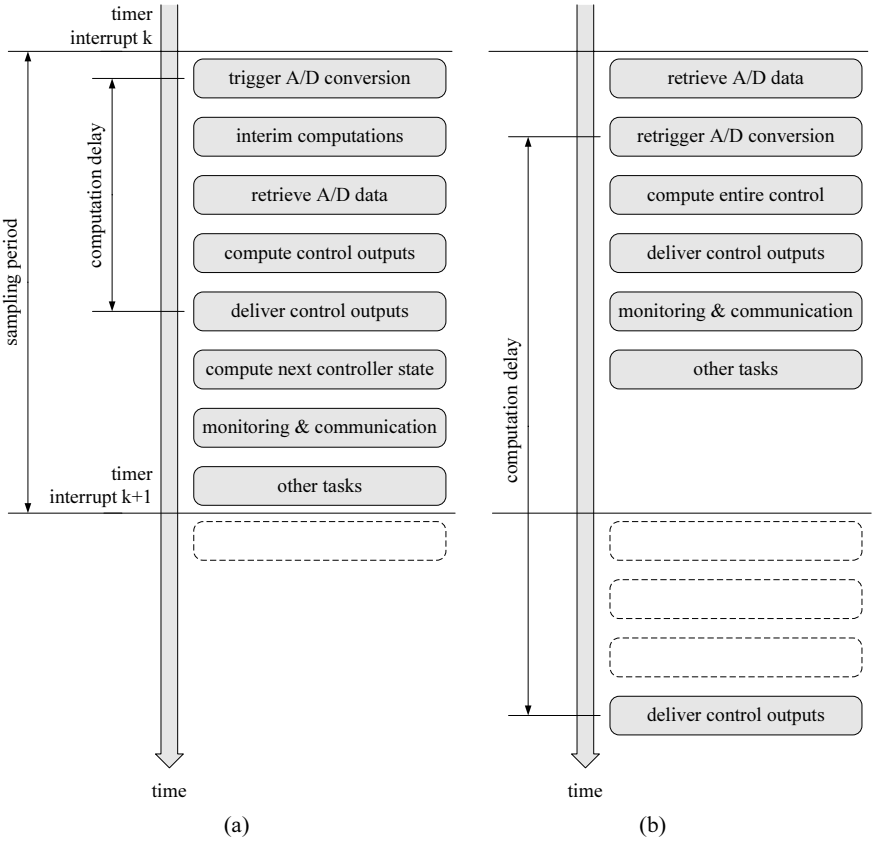


Fig. 9.1. Examples of timing diagrams of the core control loop (*timer interrupt*): (**a**) distributed minimum time delay computation structure; (**b**) non-distributed computation structure

configurable hardware. It is to be expected that, in the near future, this trend is even intensified so that FPGA technology will eventually replace more traditional microprocessor and DSP based control topologies for AMB systems [10, 18].

9.3 Basics of Discrete-Time Control

9.3.1 From Differential to Difference Equations

In Chap. 2 and Chap. 8, the general state space description for the dynamic behavior of an AMB system was derived (refer to expressions (2.27) and (8.27) respectively):

$$\dot{\mathbf{x}}_c = \mathbf{A}_c\mathbf{x}_c + \mathbf{B}_c\mathbf{u}_c \tag{9.1a}$$
$$\mathbf{y}_c = \mathbf{C}_c\mathbf{x}_c + \mathbf{D}_c\mathbf{u}_c \tag{9.1b}$$

The subscript "c" in (9.1) stands for *continuous-time*, while "d" will, as we will see further below, stand for *discrete-time*.

Differently from analog control, where the entire system dynamics can be described by the continuous-time first-order linear matrix differential equation (9.1), digital control requires a different description of the system dynamics, since system states are only sampled at *discrete moments* and since control outputs usually *remain constant* between these sampling instants, involving *zero-order hold* (ZOH) elements.

It is important to notice that digital control, in general, involves two discretization steps:

- Discretization in time
- Discretization in value (*quantization*)

The quantization effect mainly originates from the finite resolution of the A/D and D/A converters. In addition to that, quantization is also aggravated by the fixed data length given by the microprocessor architecture (e.g. 16 or 32 bit data resolution).

The mathematical treatment of the input and output quantization is done by considering signal quantization as noise at the level of signal resolution. It is common practice, however, to neglect this effect for control design and analysis of discrete-time dynamic systems, a simplification which usually does not lead to substantial limitations.

However, the discretization in time must always be accounted for. The mathematical treatment is simple, though, and is described in detail in many textbooks about sampled data control systems [4, 17, 13, 20]. The main modeling idea is that, in between the discrete sampling points, the dynamic system behaves *autonomously*, hence, the development of the system state only depends on the state condition at the previous sampling point "k" and, due to the ZOH element, on the constant input signal between this and the next sampling instant "$k+1$". Based on this understanding a linear description of the discrete-time system dynamics can be developed. Instead of a matrix differential equation as given by (9.1) a *matrix difference* equation results, which describes the *state transition* between two consecutive sampling instants:

$$\mathbf{x}_{k+1} = \mathbf{A}_d\mathbf{x}_k + \mathbf{B}_d\mathbf{u}_k \tag{9.2a}$$
$$\mathbf{y}_k = \mathbf{C}_d\mathbf{x}_k + \mathbf{D}_d\mathbf{u}_k \tag{9.2b}$$

In order to illustrate the relationship given by (9.2) a block diagram of a multi-variable discrete-time control system, as typically used for AMB control, is shown in Fig. 9.2. The continuous-time plant, representable by (9.1), is sampled at a constant sampling rate, i.e. with sampling period t_s, involving

sample-and hold elements as well as A/D converters. The sampled measurable plant output signals, comprised in the vector $\mathbf{y}_k$, serve as an input for the discrete-time controller. The zero-order hold (ZOH) elements, which keep the controller's output signals, comprised in the vector $\mathbf{u}_k$, constant during a sampling period, are usually attributed to the plant, as well as the A/D and D/A converters. In order to distinguish between plant and controller in Fig. 9.2, prescripts "p" (plant) and "c" (controller) are used.

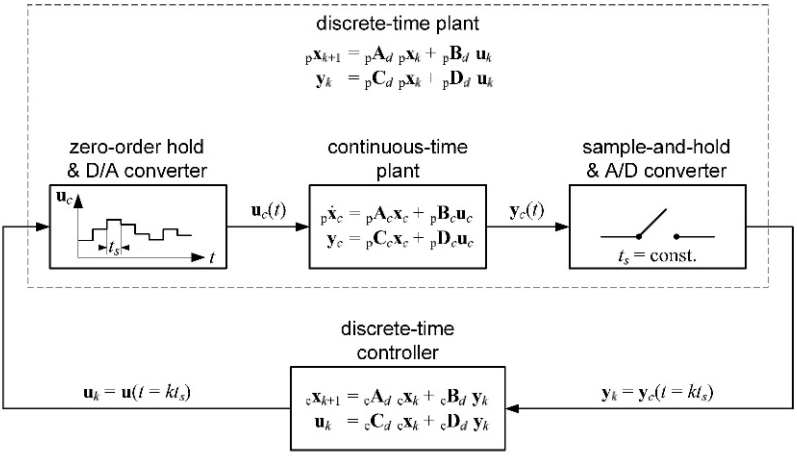


Fig. 9.2. Multi-variable discrete-time control system setup with a continuous-time plant, sample-and-hold and zero-order hold (ZOH) elements, A/D and D/A converters as well as with a discrete-time controller

9.3.2 Properties of Sampled Continuous-Time Systems

It is essential to mention at this point that there is a distinct interrelationship between the matrices $\mathbf{A}_c$, $\mathbf{B}_c$, $\mathbf{C}_c$, $\mathbf{D}_c$ of a continuous-time system and the corresponding matrices $\mathbf{A}_d$, $\mathbf{B}_d$, $\mathbf{C}_d$, $\mathbf{D}_d$ of its equivalent discrete-time representation. Basically, the matrix differential equation of the continuous-time plant (9.1) has to be integrated over one sampling period to obtain the transition from sampling instant k to instant $k+1$, with the state vector $\mathbf{x}_k = \mathbf{x}_c(t = kt_s)$ as initial condition and under the assumption that the control input $\mathbf{u}_c(t)$ remains constant during one sampling period. This piecewise integration process yields the following correspondences between continuous-time and discrete-time representations of a given dynamic system (an explicit mathematical derivation can be found in the literature):

$$\mathbf{A}_d = \mathrm{e}^{\mathbf{A}_c t_s} = \mathbf{I} + \frac{1}{1!}\mathbf{A}_c t_s + \frac{1}{2!}(\mathbf{A}_c t_s)^2 + \ldots \tag{9.3a}$$

$$\mathbf{B}_d = \int_0^{t_s} \mathrm{e}^{\mathbf{A}_c(t_s-\tau)}\mathbf{B}_c \,\mathrm{d}\tau \tag{9.3b}$$

$$\mathbf{C}_d = \mathbf{C}_c \tag{9.3c}$$

$$\mathbf{D}_d = \mathbf{D}_c \tag{9.3d}$$

In (9.3) the state space matrix $\mathbf{A}_d$ is also called the *state transition matrix* of the dynamic system, because it describes the state transition between consecutive sampling instants. It is also important to notice that (9.3) is an *exact* description of the the discrete-time system dynamics without any approximation.

In practice, numerical solutions of the Taylor series or integral expressions in (9.3) do not have to be calculated manually. In fact, most commercially available software packages for control design and system analysis, such as the well-known MATLAB® software [1], provide a set of functions which are specifically dedicated to the conversions between continuous-time and discrete-time system dynamics.

There are further substantial correspondences between a continuous-time system description and its discrete-time counterpart, which are shortly listed here, again without mathematical derivation. One of them is the relationship between the system eigenvalues, which are the most important descriptors of the system dynamics:

$$\begin{aligned} \lambda_i \;&=\; \mathrm{eig}(\mathbf{A}_c)\;; z_i = \mathrm{eig}(\mathbf{A}_d) \quad (\mathbf{A}_c, \mathbf{A}_d \in \mathbb{R}^{n\times n}) \\ &\Longrightarrow\; z_i = \mathrm{e}^{\lambda_i t_s} \quad i = 1 \ldots n \end{aligned} \tag{9.4}$$

From (9.4) one can easily see that continuous-time eigenvalues λ_i located in the left half of the complex plane are mapped to discrete-time eigenvalues z_i located in the area limited by the unit circle. Hence, *asymptotic stability* of a discrete-time dynamic system is equivalent to postulating that all of its eigenvalues are located within the unit circle, hence, have magnitude less than 1.

It is interesting that stability is actually easier to interpret in the discrete form than in the continuous form. While it takes a bit of math to see that we need the continuous-time eigenvalues to be in the left half plane, needing the discrete eigenvalues to have magnitude less than 1 simply means that, lacking an input, a sequence of states starting from any initial state must continually get smaller.

Finally, there is also a correspondence between the transfer functions of continuous-time and discrete-time dynamic systems. In Chap. 2 we have seen that the continuous-time transfer function $\mathbf{G}_c(s)$ is obtained by a Laplace transform of (9.1), yielding

$$\mathbf{G}_c(s) = \mathbf{C}_c[s\mathbf{I} - \mathbf{A}_c]^{-1}\mathbf{B}_c + \mathbf{D}_c \tag{9.5}$$

The discrete-time transfer function $\mathbf{G}_d(z)$ is obtained by a $\mathcal{Z}$ transform of (9.2) into the $z-$domain which, instead of s, introduces the discrete-time complex frequency variable z:

$$\mathbf{G}_d(z) = \mathbf{C}_d[z\mathbf{I} - \mathbf{A}_d]^{-1}\mathbf{B}_d + \mathbf{D}_d \tag{9.6}$$

The correspondence between the complex frequency variables s and z in (9.6) follows the same mapping rule as given by (9.4) for the eigenvalues,

$$z = \mathrm{e}^{st_s} \tag{9.7}$$

hence, in order to obtain the frequency response of the discrete-time system, i.e. the system response to harmonic input signals with frequency ω, the transfer function (9.6) must be evaluated for $z = \mathrm{e}^{j\omega t_s}$, i.e. along the unit circle. The correspondence (9.7) is only invertible if the frequency ω is limited to the range $[-\pi/t_s; \pi/t_s]$, where π/t_s denotes the *Nyquist* frequency ω_{Ny}. For frequencies outside this range *aliasing* effects will occur, which mirror these frequencies back into the range limited by ω_{Ny}. Commonly, the Nyquist frequency is defined as a function of the sampling frequency f_s and is indicated in Hz rather than in rad/s:

$$f_{\mathrm{Ny}} = \frac{\omega_{\mathrm{Ny}}}{2\pi} = \frac{1}{2t_s} = \frac{f_s}{2} \tag{9.8}$$

From (9.8) it can be concluded that discrete-time frequency responses are only uniquely defined up to a frequency which corresponds to half the sampling rate, a finding exactly corresponding to the *Shannon theorem*, which basically postulates that harmonic signals cannot be reconstructed properly if sampled at a rate lower than twice the signal frequency. For the discrete-time control of a continuous-time system it is, therefore, necessary to filter out signal components above f_{Ny} by means of analog hardware, i.e. by anti-aliasing filters. Of course, it is not precisely possible to filter out all signal components above f_{Ny} and, indeed, if the system is linear, failure to do so has no stability consequences. The important consequence of poor anti-aliasing filtering is one of performance: The aliased signals are mapped into the frequency spectrum below f_{Ny} as noise, and the mechanical plant will react to that noise mainly in the low frequency range. Therefore, it is common to see higher low frequency output from a digitally controlled system than would seem to be predicted from an analysis of sensor noise, because the discrete output from the D/A converters excites system response above f_{Ny} which is then automatically aliased to the entire spectrum below the Nyquist frequency. So even a completely noise free sensor would result in this broad spectrum response, which could only be eliminated through perfect anti-aliasing requiring very high filter orders. In practice, one often compromises on aliasing induced noise and uses low order anti-aliasing filters, typically of first or second order. This has the important advantage of reducing the phase lag introduced by the anti-aliasing filter itself.

9.3.3 A Simple Discrete-Time PD Control Example

For the illustration of the above mentioned properties of a sampled continuous-time dynamic system let us consider a very simple example: A unit mass ($m = 1\,\mathrm{kg}$) shall be actively controlled by means of a discrete-time PD control. Hence, the resulting system dynamics should correspond to a spring-mass-damper system. For simplicity, we do not involve dedicated actuators and sensors, thus, the scalar plant input signal u_c shall directly represent the force f acting on the mass, while the scalar plant output signal y_c shall directly correspond to the position of the mass.

As shown in Sect. 2.3.1, the state space description of this system according to (9.1) can be easily derived (subscript p for the plant):

$$ {}_{\mathrm{p}}\dot{\mathbf{x}} = {}_{\mathrm{p}}\mathbf{A}_c \; {}_{\mathrm{p}}\mathbf{x} + {}_{\mathrm{p}}\mathbf{B}_c \mathbf{u}_c \tag{9.9a} $$

$$ \mathbf{y}_c = {}_{\mathrm{p}}\mathbf{C}_c \; {}_{\mathrm{p}}\mathbf{x} + {}_{\mathrm{p}}\mathbf{D}_c \mathbf{u}_c \tag{9.9b} $$

$$ {}_{\mathrm{p}}\mathbf{A}_c = \begin{bmatrix} 0 & 1 \\ 0 & 0 \end{bmatrix}, \; {}_{\mathrm{p}}\mathbf{B}_c = \begin{bmatrix} 0 \\ 1 \end{bmatrix}, \; {}_{\mathrm{p}}\mathbf{C}_c = \begin{bmatrix} 1 & 0 \end{bmatrix}, \; {}_{\mathrm{p}}\mathbf{D}_c = \begin{bmatrix} 0 \end{bmatrix} \tag{9.9c} $$

Let us further assume that the digital control involves a sampling frequency $f_s = 1/t_s$ of 10 Hz (a rather low value, but suitable for this textbook example). This yields, together with the analytic solution of (9.3) applied to the matrices of (9.9), the following discrete-time description of the sampled plant:

$$ {}_{\mathrm{p}}\mathbf{x}_{k+1} = {}_{\mathrm{p}}\mathbf{A}_d \; {}_{\mathrm{p}}\mathbf{x}_k + {}_{\mathrm{p}}\mathbf{B}_d \; \mathbf{u}_k \tag{9.10a} $$

$$ \mathbf{y}_k = {}_{\mathrm{p}}\mathbf{C}_d \; {}_{\mathrm{p}}\mathbf{x}_k + {}_{\mathrm{p}}\mathbf{D}_d \; \mathbf{u}_k \tag{9.10b} $$

$$ {}_{\mathrm{p}}\mathbf{A}_d = \begin{bmatrix} 1 & t_s \\ 0 & 1 \end{bmatrix}, \; {}_{\mathrm{p}}\mathbf{B}_d = \begin{bmatrix} \frac{t_s^2}{2} \\ t_s \end{bmatrix}, \; {}_{\mathrm{p}}\mathbf{C}_d = \begin{bmatrix} 1 & 0 \end{bmatrix}, \; {}_{\mathrm{p}}\mathbf{D}_d = \begin{bmatrix} 0 \end{bmatrix} \tag{9.10c} $$

As can be easily seen both open-loop eigenvalues $z_{1,2}$ of ${}_{\mathrm{p}}\mathbf{A}_d$ are 1 (matrix ${}_{\mathrm{p}}\mathbf{A}_d$ is Jacobian and, therefore, its eigenvalues are equivalent to its diagonal elements). This also perfectly corresponds to the result which we would obtain from (9.4), since both eigenvalues of the continuous-time system are zero.

In Fig. 9.3 the open-loop frequency response of the simple mass system according to (9.6) is shown. As expected the frequency response of the sampled system is only defined up to the Nyquist frequency which, in this case, is 5 Hz. However, the plots in Fig. 9.3 also reveal a surprising effect, namely, that the frequency responses for the continuous-time system and its sampled counterpart *are not equal* as one might have expected. Although they are very similar at frequencies much lower than the sampling rate, the differences become substantial as the frequency approaches f_{Ny}. It is especially the *phase* of the frequency response of the sampled plant that differs most and, in fact, features substantial lag at higher frequencies. As we know from continuous-time control, the phase of the open-loop plant is most important for the controller

design. Consequently, we can expect that discrete-time control will be somewhat more demanding than continuous-time control due to the reduced phase margin.

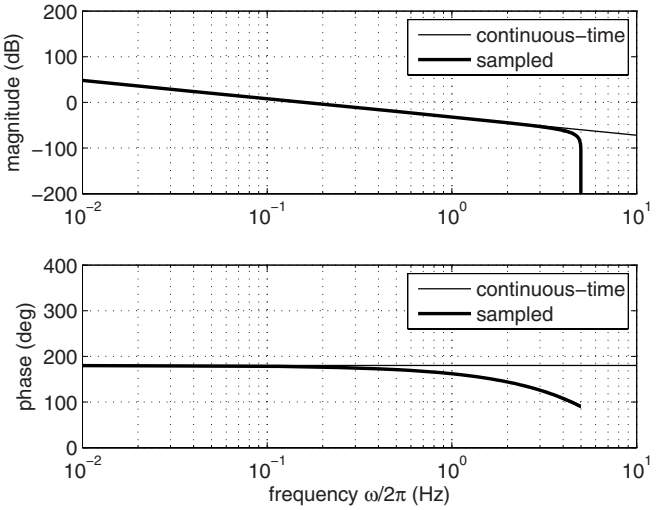


Fig. 9.3. Open-loop plant frequency response according to (9.5), (9.6) and (9.7) of the continuous-time simple mass system and its sampled, i.e. discrete-time, representation

In fact, the noticed plant phase lag is common to *all* sampled continuous-time systems: It is caused by the *sampling delay* which is inherently introduced by the zero-order hold (ZOH) element at the plant input, as shown in Fig. 9.2. The sampling delay phase lag φ_{ZOH} can be described by the following expression (without explicit derivation):

$$\varphi_{\mathrm{ZOH}} = -\frac{\omega t_s}{2} \tag{9.11}$$

According to (9.11) the sampling delay phase lag rises *linearly* with the frequency ω and becomes $-\pi/2$ when the excitation frequency reaches the Nyquist frequency ($\omega = \omega_{\mathrm{Ny}} = \pi/t_s$). This finding corresponds well with the phase plot of the sampled system shown in Fig. 9.3, which drops from 180 to 90 degrees whereas the phase of the continuous-time plant constantly remains at 180 degrees.

Note that the term *sampling delay*, as used in the context of this chapter, is a pure consequence of the ZOH element and does not address any additional time delays within the digital control algorithm, e.g. due to A/D conversion or computation *dead times*. These additional dead times in the digital control will even further deteriorate the phase margin of the system.

A plausible explanation for the source of the phase lag effect due to sampling delay is given in Fig. 9.4: The piecewise constant values of $u_{\#}(t)$, as they are generated by a discrete-time controller, follow the sampled continuous-time signal $u(t)$ with an average time lag of $t_s/2$, as indicated by the dashed signal $u_{\mathrm{sd}}(t)$. This average time lag causes the phase lag φ_{ZOH} as given by (9.11). A more theoretical explanation can be found in a typical digital control textbook such as [20].

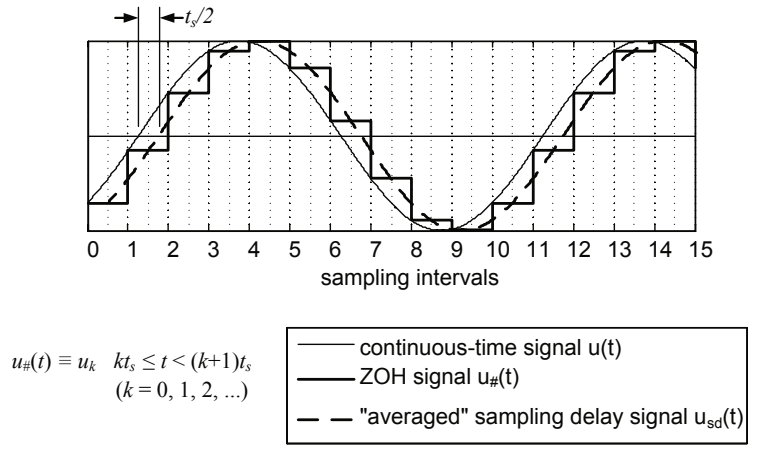


Fig. 9.4. Plausibility explanation for the sampling delay due to a zero-order hold (ZOH) element: Harmonic continuous-time signal $u(t)$ sampled 10 times per period, piecewise constant signal $u_{\#}(t)$ and "averaged" sampling delay signal $u_{\mathrm{sd}}(t)$

Now, we close the loop by implementing a discrete-time PD controller with proportional and differential feedback constants P and D. Since the velocity of the plant is not an available measurement signal we have to approximate it by setting up a first order *secant* algorithm (also called *backward difference* algorithm). In a first step no additional low pass filtering to avoid high frequency noise due to the differentiating characteristics of the control is considered. This yields the following expression for the control output sequence $\mathbf{u}_k$ as a function of the sampled position signal sequence $\mathbf{y}_k$:

$$\mathbf{u}_k = -\big(P\,\mathbf{y}_k + \frac{D}{t_s}\,(\mathbf{y}_k - \mathbf{y}_{k-1})\big) \tag{9.12}$$

The control law (9.12) involves a signal $\mathbf{y}_{k-1}$ which lies one sampling period in the past. Therefore, the control algorithm is of first order and, hence, the associated matrices and state vectors according to (9.2) all become scalars:

$${}_{\mathrm{c}}\mathbf{x}_{k+1} = {}_{\mathrm{c}}\mathbf{A}_d\ {}_{\mathrm{c}}\mathbf{x}_k + {}_{\mathrm{c}}\mathbf{B}_d\ \mathbf{y}_k \tag{9.13a}$$

$$\mathbf{u}_k = {}_{\mathrm{c}}\mathbf{C}_d \; {}_{\mathrm{c}}\mathbf{x}_k + {}_{\mathrm{c}}\mathbf{D}_d \; \mathbf{y}_k \tag{9.13b}$$

$${}_{\mathrm{c}}\mathbf{A}_d = \left[\,0\,\right],\; {}_{\mathrm{c}}\mathbf{B}_d = \left[\,\tfrac{D}{t_s}\,\right],\; {}_{\mathrm{c}}\mathbf{C}_d = \left[\,1\,\right],\; {}_{\mathrm{c}}\mathbf{D}_d = \left[\,-(P + \tfrac{D}{t_s})\,\right] \tag{9.13c}$$

In Fig. 9.5 the closed-loop step response of the sampled plant (9.10) with the discrete-time PD control (9.13) is shown and compared with the corresponding continuous-time control. As can be seen the system is adequately damped for both types of control, although the performance of the continuous-time control is slightly superior, a fact which must be attributed to the inherent sampling delay of discrete-time systems. Nicely visible is also the piecewise constant behavior of the controller output signal, i.e. the force acting on the mass, in the discrete-time case.

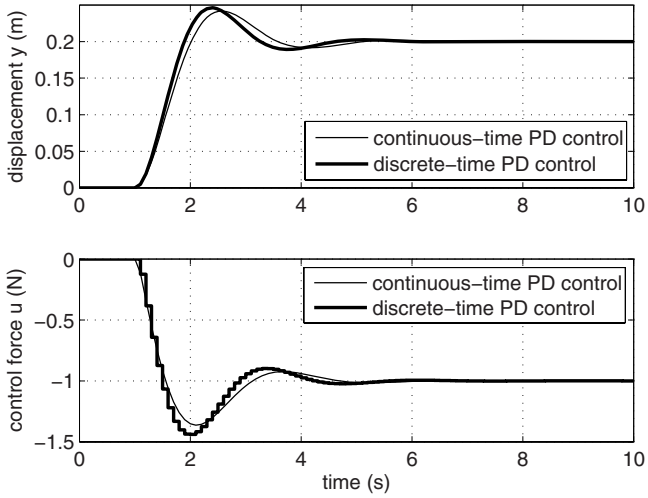


Fig. 9.5. Closed-loop system response to unit force step for the simple mass system with continuous-time and discrete-time PD control ($m = 1\,\mathrm{kg}$, $t_s = 0.1\,\mathrm{s}$, $P = 5\,\mathrm{N/m}$, $D = 2\,\mathrm{N\,s/m}$)

The closed-loop eigenvalues λ_i and z_i of the continuous-time and discrete-time systems as well as the *equivalent* continuous-time eigenvalues ${}_{\#}\lambda_i$ obtained by the inversion of (9.4) are given by the following expressions. Note that, apart from the controller pole (subscript 3), the equivalent continuous-time eigenvalues of the sampled system are very similar to those of the genuine continuous-time control. This shows that it is good practice to transform discrete-time eigenvalues back to the continuous-time domain by applying the inversion of (9.4) in order to obtain values that are closer to engineering experience and to provide a better physical understanding of the system.

$$\text{continuous-time:} \quad \lambda_{1,2} = -0.9995 \pm j\,2.0028 \tag{9.14a}$$

$$\lambda_3 = -998.0010 \tag{9.14b}$$

$$\text{discrete-time:} \quad z_{1,2} = 0.8756 \pm j\,0.2039 \tag{9.14c}$$

$$z_3 = 0.1237 \tag{9.14d}$$

$$\text{equiv. cont.-time:} \quad {}_{\#}\lambda_{1,2} = \frac{\ln(z_{1,2})}{t_s} = -1.0638 \pm j\,2.2883 \tag{9.14e}$$

$${}_{\#}\lambda_3 = \frac{\ln(z_3)}{t_s} = -20.8982 \tag{9.14f}$$

As can be seen in Fig. 9.5 the sampling delay effect is almost negligible for the present example. However, in practice there are most often sampled plants that feature higher eigenfrequencies, e.g. due to flexible modes. In these cases the sampling delay can cause serious problems and, most often, leads to an instability of the associated high frequency modes. As the sampling delay is an unescapable fact these problems can only be avoided by suitable filtering algorithms or by a more elaborate and higher order control which accounts for all the dynamics of the sampled plant.

Low Pass Filtering

In practice any discrete-time control for AMB systems will incorporate a low pass filter characteristic in order to reduce high frequency noise and to avoid destabilization of higher frequency system modes. Most often, the low pass filter characteristic will be a direct result of the control design process itself, specially in the case of the modern MIMO robust control design approaches.

In the case of SISO control a common and simple approach is to add a low pass filter in series to the control algorithm itself. For the present PD control example a simple second order low pass filter can be defined by the following discrete-time transfer function (sampling period $t_s = 0.1\,\mathrm{s}$):

$$\mathbf{G}_{d_{\mathrm{filter}}}(z) = \frac{0.3567z^2 + 0.5107z + 0.2805}{z^2 - 0.5332z + 0.6811} \tag{9.15}$$

By applying the inversion of (9.4) to the poles and zeroes of (9.15) one can easily see that the discrete-time filter contains a lightly damped conjugate complex pole pair at about 2 Hz and a transmission zero near 4 Hz. This behavior is also visible in the frequency response plot (bode plot) shown in Fig. 9.6.

As can be seen from the bode plot in Fig. 9.6 the magnitude of the controller transfer function compared to the pure PD control is decreased by approximately 20 dB at high frequencies by the added filter. The downside of this gain reduction at high frequencies, however, is the always occurring controller phase reduction at lower frequencies. Hence, the filter poles and zeroes have to be chosen such that the entire system's closed-loop behavior remains acceptable. One can show for this example that the step response,

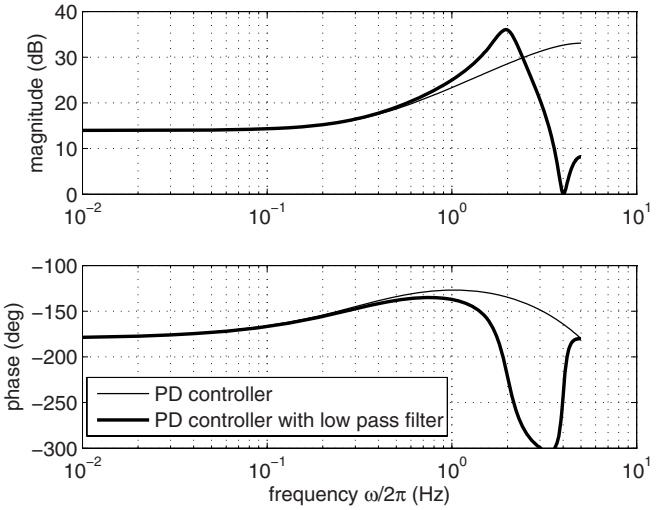


Fig. 9.6. Frequency response of the discrete-time PD controller represented by (9.13) ("secant" respectively "backward difference" algorithm) with and without additional low pass filter (9.15) (numerical values as specified for Fig. 9.5)

as shown in Fig. 9.5, is only very marginally affected by the chosen low pass filter, which can, therefore, be considered suitable.

9.4 Control Design for Discrete-Time Systems

Control of rotors in active magnetic bearings can be very challenging, specially in the presence of high frequency flexible modes and strong gyroscopic effects. Therefore, textbook style control design concepts as described in the literature [4, 17, 13, 20] are sometimes not sufficient and must be accompanied by a good deal of pragmatic approaches and good engineering intuition based on an appropriate amount of experience.

The chapters about the control of rigid and flexible AMB rotor systems provided by this book show that there exist a number of different control design methods. Some of them, such as PID control, are strongly motivated by a physical approach and thus reveal useful insights of the rotor-bearing systems, however, the control parameter selection can be time consuming. Some other more modern MIMO control design concepts, such as $\mathcal{H}_\infty$ and $\mu-$synthesis [21, 9, 5, 6], originate from a mathematically more abstract level and target automatic generation of optimal control parameters.

These modern robust control design concepts are a very promising approach to standardize AMB control and to definitely take it out of the "wizard's kitchen" which, today, seems to be accessible only by the experienced

engineer. However, although there are discrete-time equivalents to continuous-time control design concepts such as LQ-control, pole-placement and PID control (see Sect. 9.3.3), there is still a lack of such discrete-time counterparts to the MIMO control design concepts of robust control.

The present way out of this is that the entire digital control design is carried out in the continuous-time domain. There are two prerequisites for doing this: On the one hand, a continuous-time system description of the plant, on which the controller design is based, must be found which is equivalent to the sampled plant in the sense that it correctly represents the sampling delay introduced by the zero-order hold (ZOH) element. On the other hand, the controller obtained by the continuous-time design process must be converted back to a discrete-time representation in order to be implemented in digital control hardware. Unfortunately, there is *no exact* mathematical conversion for either of the two steps so *approximation* methods have to be used.

A well-known approximation method for both conversion directions is a bilinear transformation called *Tustin* or *central difference* approximation. While the background of the method is not discussed here, the result, which can e.g. be computed by means of specially dedicated MATLAB® functions [1], is briefly outlined along with the example of Sect. 9.3.3.

At first, the bilinear approximation is applied to the conversion of the sampled plant (9.10). The behavior of the resulting continuous-time equivalent is shown in Fig. 9.7 in terms of an open-loop frequency response plot.

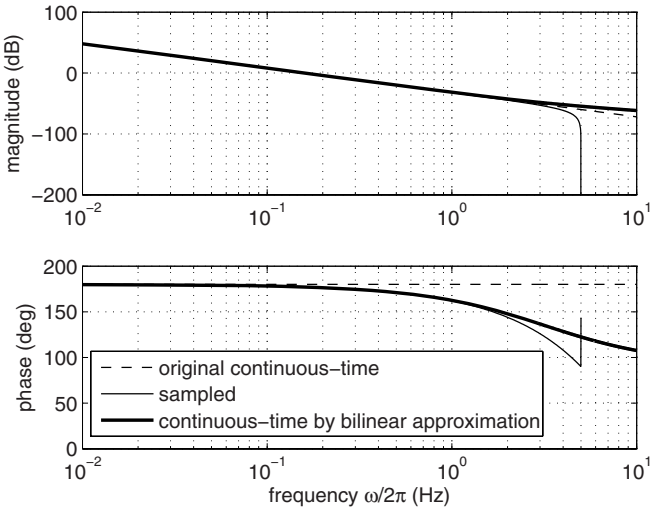


Fig. 9.7. Open-loop frequency response of the original continuous-time plant, its discrete-time representation as well as of the continuous-time equivalent to the sampled system obtained by a conversion with bilinear approximation (numerical values according to the example of Sect. 9.3.3)

As can be seen the bilinear approximation method is capable of adequately representing the phase lag due to the sampling delay of the discrete-time plant in a frequency range up to about a fifth of the sampling frequency. In this range also the magnitude of the frequency response shows a good correspondence to its sampled equivalent. Consequently, the sampling rate of the digital control algorithm should be chosen high enough to contain all major plant dynamics in the frequency range well represented by the bilinear approximation method.

Figure 9.8 shows the result of the bilinear approximation method being carried out into the other direction, i.e. being applied to the conversion of the continuous-time PD controller into a discrete-time representation. For this conversion process a ZOH element does *not* have to be taken into account as was necessary for the plant, since the states of a discrete-time controller do not change in between two sampling instants.

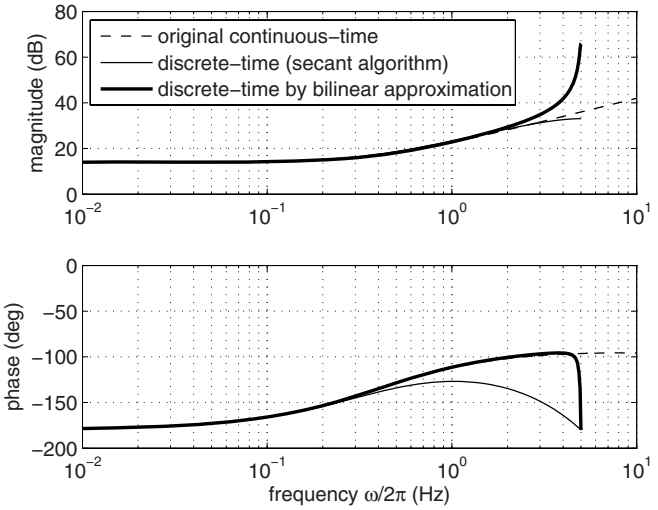


Fig. 9.8. Frequency response of the continuous-time PD controller and its discrete-time representations obtained by the "secant" algorithm (9.13) and by a conversion with bilinear approximation (numerical values according to the example of Sect. 9.3.3)

Figure 9.8 also impressively documents the superiority of the discrete-time controller obtained by a conversion of the continuous-time PD controller using the bilinear approximation method: The phase lead, especially at high frequencies, is considerably better than realized by the "secant" algorithm introduced in Sect. 9.3.3, despite the fact that both discrete-time representations feature the same system order one. Moreover, this phase lead is not realized at the cost of a substantially higher controller gain. This allows for even implementing a much higher system stiffness, i.e. a considerably higher

closed-loop eigenfrequency, together with a satisfying amount of damping, thus, system properties not achievable by the "secant" algorithm PD control.

This simple example shows that a continuous-time control design process for a sampled system is feasible using bilinear approximation for both necessary conversion directions, paving the way for the application of modern MIMO robust control design methods for discrete-time control implementations. As will be shown in Chap. 12, computation delays in addition to the ZOH sampling delay, as also shown in Fig. 9.1b, can be addressed by including further finite order dynamic system elements in the overall system model. The most widely made approach to approximate additional computation delay is based on using the *Padé approximation*.

9.5 Implementation Aspects of Digital Control

Implementation of digital control very much depends on the available control hardware. In a first place, the complexity of the control algorithm and the achievable sampling rate are determined by the computational power and the type of arithmetics – integer or floating point – of the chosen microprocessor or digital signal processor (DSP) system. Theoretically, by following the Shannon theorem, the sampling rate must at least be twice as high as the highest frequency in the system to be controlled. In practice, however, the sampling rate must be chosen substantially higher, e.g. five to ten times the highest frequency to be reproduced by the controller. This is also underlined by the example in the previous section which shows that discrete-time controllers obtained by a bilinear approximation method show good correspondence to the continuous-time original up to about a fifth of the sampling frequency.

Sampling rates must not be chosen too high either, though. High sampling frequencies in conjunction with signal noise and a comparably low A/D conversion resolution can cause important numerical conditioning problems and tend to amplify signal noise. This is especially the case if a hardware with integer arithmetics is used. In practice, if there is surplus computation power of the control hardware, it is better to invest into a high quality digital input signal filtering rather than implementing the entire control algorithm at a high sampling rate.

In order to avoid aliasing effects, suitable analog filters must be provided that match with the chosen sampling rate. In practice, second order low pass filters are found to be sufficient for this task. Here, it is essential to determine which dynamics of the plant have to be controlled and which part of them should be filtered out. For a standard magnetic bearing system sampling rates usually range between 5 and 10 kHz, in some cases 20 kHz might be necessary.

As pointed out in Sect. 9.2, time delays, i.e. delays between the A/D conversion of the controller input signals and the D/A conversion to the corresponding output signals, must be kept at an absolute minimum, since they

drastically deteriorate controller performance. Note here again that computational time delays and sampling delay caused by the ZOH element are not the same. Computational time delays become especially important in the case of MIMO control in conjunction with sequential A/D conversion based on a multiplexer architecture. Here, it is usually necessary to strongly invest into the optimization of the controller firmware structure, i.e. into the type of implementation of the discrete-time control algorithm, in order to keep time delays at a minimum.

Usually, a straightforward implementation of the controller state space description as represented by (9.13) is not advisable since the number of control parameters and necessary MAC operations (MAC = "multiply-accumulate") will be excessively high, requiring large amounts of memory and computational power or leading to unacceptably low sampling rates. In fact, a state space description contains a substantial amount of numerical redundancy, so that numerical structuring methods – not to be confounded with controller order reduction techniques – can be applied to reduce control algorithm complexity. Among these numerical structuring methods, the *bi-quad* implementation features a very good compromise between numerical conditioning and number of necessary MAC operations. Basically, a bi-quad representation transforms the controller state space matrix into a block diagonal form where each 2×2 block comprises the dynamics associated to one conjugate complex eigenvalue pair. In case of integer arithmetics the bi-quad implementation also strongly accommodates for an optimum numerical scaling of the control parameters and system states.

The memory storage, computational time and MAC operation advantage of such a restructuring of the control model is that most of the $\mathbf{A}$ matrix is zero and the location of the non-zero part is precisely known. Hence, it is not necessary to compute products of zero, which saves a tremendous number of computations. As an example, for a general radial controller with 4 inputs, 4 outputs and 20 controller states, a full state space realization including $\mathbf{D}$ matrix will require 576 MAC operations. By contrast, a bi-quad representation of the same controller, hence consisting of ten 2×2 blocks in the $\mathbf{A}$ matrix, will require only 216 MAC operations.[1] As the order n of the controller increases (see especially the developments in Chap. 12), this comparison rapidly favors the bi-quad form.

9.6 Diagnostic Capabilities of Digitally Controlled AMBs

Compared to conventional ball, oil or air bearings active magnetic bearing systems provide the unique feature of an inherently *built-in instrumentation*: In

[1] The mathematical expression for the number of MAC operations for a system with n states is $4n/2 + 4n + 4n + 4^2 = 10n + 4^2$ for a bi-quad representation and $n^2 + 4n + 4n + 4^2 = (n + 4)^2$ for a full state space representation.

addition to pure levitation, the bearings can also serve as actuators that transform signals additionally injected into the control-loop into superimposed excitation forces, allowing for generating deliberate vibrations of the suspended rotor. Similarly, the position sensor signals will measure the rotor response to this external excitation, in addition to the position measurement needed for feedback stabilization.

Although the utilization of the magnetic bearing as an actuator–sensor unit has been practiced for many years [16], the built-in instrumentation concept has, to date, not obtained adequate attention to the full extent of its capabilities [15]. Namely, it can be extended to include the *replacement* of external signal generator and Fourier analyzer units [14], used as today's standard instrumentation to assess AMB system stability and performance, by *pure software* within the *existing* magnetic bearing controller, i.e. implemented directly on the microprocessor or DSP used for levitation control. Thus, signal injection, FFT computation (FFT = "Fast Fourier Transform"), frequency response measurement, and other functions usually performed by external devices such as digital storage oscilloscopes can all be added to the digital AMB control, making external instrumentation *virtually superfluous*. Thus, a laptop computer used on-site or connected remotely, equipped with a suitable signal analysis software [1], is sufficient to carry out all the needed measurements for plant identification (see Chap. 11), control design, performance assessment and parameter tuning. Such an approach can drastically reduce commissioning times, to the benefit of both AMB system manufacturer and user. Moreover, it strongly helps to implement the procedures for stability and robustness assessment required by the lately emerged ISO standards for AMB systems [2, 3]. Consequently, the user additionally profits from a standardized reference for specification, acceptance and long-term monitoring of his machine.

Finally, a built-in excitation and measurement system can be extremely helpful to carry out MIMO measurements on an AMB system, such as for the exact identification of the eigenfrequencies of a strongly gyroscopic rotating shaft necessary for a proper MIMO robust control design, since measurement and excitation channels do not have to be sequentially switched in order to determine all elements of a multi-variable transfer function matrix, a laborious and time-consuming process if carried out utilizing a standard external two-channel frequency analyzer.

An integrated excitation and measurement environment for a digital AMB control system, as e.g. described in [14, 22, 8, 12], offers the following capabilities:

- Multi-variable signal injection with freely selectable frequency, amplitude, phase, and injection point
- Measurement of arbitrary SISO and MIMO open-loop and closed-loop transfer functions at any rotor speed

- Identification of gyroscopic effects and automatic generation of Campbell diagrams
- Virtual real-time multi-channel oscilloscope with built-in trigger, step response measurement and FFT computation functionalities
- Continuous monitoring and analysis of system states, such as displacements, temperatures, balancing conditions or even bending mode eigenfrequencies
- On-line rotor balancing
- Versatile control parameter design and simple download of complex parameter structures if embedded in a control design software package such as MATLAB® [1]
- Field bus communication interface to a higher level machine control and monitoring system

Hence, a digital AMB control system with integrated measurement and communication capabilities has the flexibility to accomplish tasks that are otherwise complex and time-consuming. For example, it is possible to continuously monitor bending mode eigenfrequencies as part of a preventive maintenance program and detect undesirable changes already at an early stage [11, 19]. Another example is the fully automatic generation of Campbell diagrams as a result of autonomously carried out MIMO transfer function measurements at different rotor speeds, as shown in Fig. 9.9.

An integrated measurement and communication environment follows today's industrial trend to more autonomous, communicative and *intelligent* systems and should, therefore, be incorporated into any state-of-the-art digital AMB control architecture. This just requires additional software for real-time signal generation and data analysis to be implemented together with the levitation control software on the microprocessor or DSP in use, so that there is no need for any additional instrumentation hardware. This concept paves the way to take full advantage of the diagnostic capabilities of an active magnetic bearing system in conjunction with digital control.

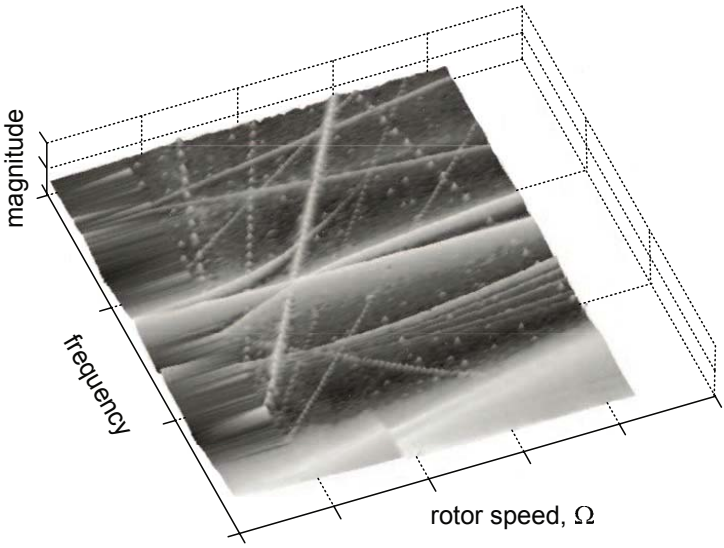


Fig. 9.9. "Rotordynamic footprint" of a magnetically levitated turbomolecular pump in the form of a Campbell "waterfall" diagram for the synoptic visualization of rigid body, bending and turbine blade eigenfrequencies as well as of rotation synchronous signal components as a function of the rotor speed Ω (diagram automatically generated using a built-in MIMO excitation and frequency response measurement system as described in [22, 12])

References

1. MATLAB® – *The Language of Technical Computing*. The MathWorks, Inc., www.mathworks.com.
2. ISO 14839-2. *Mechanical vibration - Vibration of rotating machinery equipped with active magnetic bearings - Part 2: Evaluation of vibration*. International Organization for Standardization ISO, 2004.
3. ISO 14839-3. *Mechanical vibration - Vibration of rotating machinery equipped with active magnetic bearings - Part 3: Evaluation of stability margin*. International Organization for Standardization ISO, 2006.
4. J. Ackermann. *Sampled Data Control Systems*. Springer-Verlag, Berlin, 1985.
5. G. J. Balas, J. C. Doyle, K. Glover, A. K. Packard, and R. Smith. *μ Analysis and Synthesis Toolbox User's Guide*. The MathWorks, Natick, MA, 1995.
6. S. P. Boyd and C. H. Barratt. *Linear Controller Design – Limits of Performance*. Prentice Hall, New Jersey, 1991.
7. S. Brown and J. Rose. Architecture of FPGAs and CPLDs: A tutorial. *IEEE Design and Test of Computers*, 13(2):42–57, 1996.
8. W. R. Canders, Ueffing N., U. Schrader-Hausmann, and R. Larsonneur. MTG400: A magnetically levitated 400 kW turbo generator system for natural gas expansion. In *Proceedings of the Fourth International Symposium on Magnetic Bearings*, ETH Zürich, Switzerland, August 1994.

9. J. C. Doyle and G. Stein. Multivariable feedback design: Concepts for a classical/modern synthesis. *IEEE Transactions on Automatic Control*, 26(1):4–16, 1981.
10. P. Ekas. FPGAs rapidly replacing high-performance DSP capability. *DSP Engineering Magazine (DSP-FPGA.com)*, February 2007.
11. C. Gähler, M. Mohler, and R. Herzog. Multivariable identification of active magnetic bearing systems. In *Proceedings of the Fifth International Symposium on Magnetic Bearings*, Kanazawa, Japan, August 1996.
12. C. Gähler, M. Mohler, and R. Herzog. Multivariable identification of active magnetic bearing systems. *JSME International Journal–Special Section on Magnetic Bearings*, 40(4):584–592, 1997.
13. H. P. Geering. *Mess- und Regelungstechnik*. Springer-Verlag, Berlin, second edition, 1990.
14. R. Herzog and R. Siegwart. High performance data acquisition, identification and monitoring for active magnetic bearings. In *Proceedings of the 2nd International Symposium on Magnetic Suspension Technology*, Seattle, USA, August 1993.
15. R. W. Hope, G. W. Smith, T. A. Harris, and B. J. Drain. Design of an industrial single-DSP magnetic bearing controller. In *Proceedings of the "MAG '95" Conference & Exhibition for Magnetic Bearings, Magnetic Drives and Dry Gas Seals*, University of Virginia, USA, August 1995.
16. R. R. Humphris. A device for generating diagnostic information for rotating machinery using magnetic bearings. In *Proceedings of the "MAG '92" Conference & Exhibition for Magnetic Bearings, Magnetic Drives and Dry Gas Seals*, University of Virginia, USA, July 1992.
17. R. Isermann. *Digitale Regelsysteme*. Springer-Verlag, Berlin, second edition, 1988.
18. R. Jastrzebski, R. Pöllännen, O. Pyrhönen, A. Kärkkäinen, and J. Sopanen. Modeling and implementation of active magnetic bearing rotor system for FPGA-based control. In *Proceedings of the Tenth International Symposium on Magnetic Bearings*, Martigny, Switzerland, August 2006.
19. M. E. Kasarda, D. Inman, R. G. Kirk, D. Quinn, G. Mani, and T. Bash. A magnetic bearing actuator for detection of shaft cracks in rotating machinery supported in conventional bearings. In *Proceedings of the Tenth International Symposium on Magnetic Bearings*, Martigny, Switzerland, August 2006.
20. B. C. Kuo. *Digital Control Systems*. Saunders College Publishing, USA, 1992.
21. K. Nonami, H. E. Weidong, and H. Nishimura. Robust control of magnetic levitation systems by means of H_∞ control/$\mu-$synthesis. *JSME International Journal*, 37(3):513–520, 1994.
22. R. Y. Siegwart, R. J. P. Herzog, and R. Larsonneur. Identification and monitoring of turbo rotors in active magnetic bearings. In *Proceedings of the ASME International Gas Turbine and Aeroengine Congress and Exposition*, The Hague, Netherlands, June 1994.

10

Dynamics of Flexible Rotors

Rainer Nordmann

10.1 Introduction

A good knowledge of the dynamic behaviour of flexible rotors is very important, especially when they are running in active magnetic bearings. Particularly for the design of the controller, a good model for such mechanical systems is necessary.

Elastic rotors usually have a continuous mass- and stiffness distribution, varying in the axial direction. To be precise, they must be considered as continua, described by partial differential equations with derivatives with respect to time and space. It is difficult to find exact solutions for such systems. However, continua can also be modeled by discretization. This can either be done with *lumped* parameters (mass, stiffness and damping elements) by an intuitive engineering discretization or by a mathematical discretization, particularly by means of the Finite Element method. Discretization leads to ordinary differential equations. Linear differential equations can be used when the considered physical effects show a linear behavior, particularly when the vibrations are small.

In this chapter, two different types of elastic rotor models will be considered. The simplest elastic rotor with lumped parameters is commonly referred to as the *Jeffcott rotor* – also called the *Laval shaft* – consisting of an elastic shaft with a rigid disk in the center. The basic vibrational behavior will be shown for this simple model, including results corresponding to those from Chap. 7, on *Dynamics of the Rigid Rotor*.

More advanced modeling is concerned with real elastic rotors, like rotors in turbo machinery, aero engines, pumps, machine spindles, motors and generators. They have a continuous mass- and stiffness distribution with changing masses and stiffnesses along the shaft. They are mostly modeled by means of the Finite Element method, which is the most powerful discretization method today.

For the two elastic rotor types, it will be shown how the physical laws have to be applied in order to obtain the equations of motion as a base for

G. Schweitzer, E.H. Maslen (eds.), *Magnetic Bearings*,
DOI 10.1007/978-3-642-00497-1_10, © Springer-Verlag Berlin Heidelberg 2009

solutions for the rotor dynamic behavior. Such solutions describe the motions (displacements, velocities, accelerations) of defined rotor points, which are the lateral vibrations of the rotor. They can be subdivided into natural vibrations, without any external excitation, and forced vibrations. Natural vibrations are characterized by natural frequencies, the damping ratios and the mode shapes (eigenvectors) of the rotor system. Forced vibrations are excited by time dependent forces or moments and/or displacements (e.g. excitation via the foundation). The most important excitation in rotating machinery is due to unbalance forces. Other excitation forces are process forces, such as cutting forces in machine tool systems or fluid forces in turbo machinery.

A very powerful solution procedure to determine forced vibrations is based on modal analysis. By this method, the originally coupled system of equations of motion can be decoupled. This leads to generalized single degree of freedom equations of motion, which can be solved easily. The decoupling of the equation system is possible by means of the mode shapes (eigenvectors) of the elastic rotor system.

The dynamic behavior of elastic rotor systems is dependent not only on the shaft bending stiffness and the mass distribution along the shaft. Stiffness and damping in bearings, gyroscopic effects in case of large moments of inertia and high speeds and self excitation forces in seals or due to cutting forces also have an important influence on the rotor dynamic behavior.

This chapter shows how flexible rotor systems can be modeled based on physical laws and how the equations of motion can be solved analytically or numerically. The rotor dynamic behavior, as a result of the solutions, will be discussed, subdivided into natural vibrations and forced vibrations. Besides analytical and numerical solutions, quite often experimental investigations are necessary. Combined numerical and experimental procedures are also applied, where partly experimental results are used to find the overall solution. In Chap. 11, *Identification*, it will be shown how physical and/or modal parameters of flexible rotors can be determined by means of measurements. As an example, the experimental modal analysis is a very powerful tool in order determine experimentally the natural frequencies, the damping ratios and the mode shapes (eigenvectors) of a flexible rotor. The modal parameters can either be used to update the model for the numerical solution or the measured values (e.g. the damping ratios) can directly be used to calculate the forced vibrations. Finally, the equations of motion are formulated in a way that can be used for designing a controller of the interconnected AMB-system (see Chap. 12, *Control of Flexible Rotors*).

10.2 Jeffcott Rotor – a Simple Flexible Rotor

10.2.1 Mechanical Model of the Jeffcott Rotor

A very simple model of a flexible rotor is the so called Jeffcott rotor, sometimes also called Laval rotor. This rotor system has historical meaning due to the

fact that Jeffcott published the theory about this system in 1918, while Laval investigated experimentally the self centering effect of the rotor already in 1883. At this time, the type of this rotor system was used as a one-disk steam turbine. Today, the Jeffcott rotor is often used in order to explain the basic dynamic behavior of a flexible shaft with a mass located in the shaft center [3, 6, 14, 13].

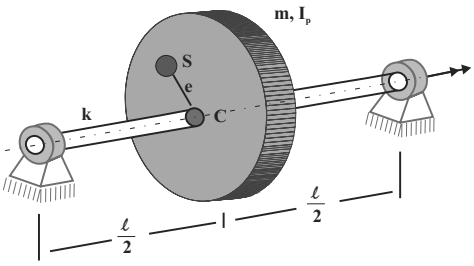


Fig. 10.1. Model of the Jeffcott rotor

Figure 10.1 shows the model of the Jeffcott rotor. It consists of an elastic shaft with a stiffness $k = 48EJ/l^3$ (EJ is the elastic stiffness product, l is the length of the shaft) and a rigid disk. The rigid disk with mass m and polar moment of inertia $I_\mathrm{p} = mi_\mathrm{p}^2$ (i_p is the polar inertia radius) is located at the shaft center between the two bearings. Due to some imperfections (manufacturing, inhomogeneous material, etc.), the geometric center of the disk C does not coincide with the center of gravity S. The distance between the two points is the mass eccentricity e. The shaft is running in two bearings with angular velocity Ω. The bearings are considered to be rigid as a first approximation. Damping is also neglected in this preliminary model.

In order to describe the motion of the disk, we introduce a coordinate system (Fig. 10.2). Its origin is at the shaft center between the two bearings when the shaft is unloaded (static and dynamic forces are equal zero). In a displaced position, when the rotor system vibrates, the disk center has the displacements x, y and the center of gravity the displacements x_S, y_S. The direction line C — S has an angle γ relative to the axis x. The distance between C and S is e. Figure 10.3 illustrates how the displacements are related.

$$x_\mathrm{S} = x + e\,\cos\gamma \tag{10.1a}$$

$$y_\mathrm{S} = y + e\,\sin\gamma \tag{10.1b}$$

The mechanical system has three degrees of freedom, e.g. x, y and γ, if we allow radial movements for the disk only. The tilting motion is not considered in this simple model. The following equations express the accelerations of the center of gravity S. They are needed for the derivation of the equations of motion for the disk.

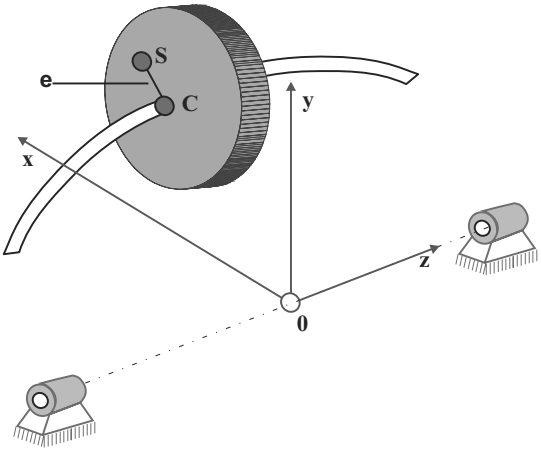


Fig. 10.2. Coordinate system and displacements of the disk center

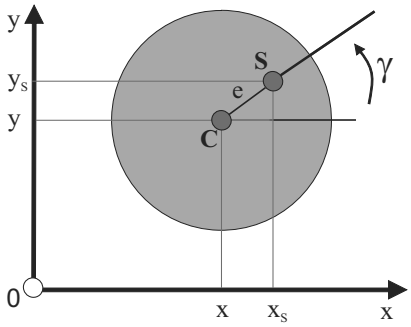


Fig. 10.3. Relations between displacements and angle

$$\ddot{x}_S = \ddot{x} - e\,\dot{\gamma}^2\,\cos\,\gamma\, - e\,\ddot{\gamma}\,\sin\,\gamma \tag{10.2a}$$

$$\ddot{y}_S = \ddot{y} - e\,\dot{\gamma}^2\,\sin\,\gamma\, + e\,\ddot{\gamma}\,\cos\,\gamma \tag{10.2b}$$

The terms $-e\dot{\gamma}^2\cos\gamma$, $-e\dot{\gamma}^2\sin\gamma$ are centrifugal accelerations, while $-e\ddot{\gamma}\sin\gamma$, $e\,\ddot{\gamma}\,\cos\,\gamma$ are tangential accelerations.

10.2.2 Equations of Motion for the Disk

The equations of motion for the disk can be derived using Newton's second law. With the forces and moments, shown in Fig. 10.4, the following equations can be found:

$$m\ddot{x}_S = -kx \tag{10.3a}$$

$$m\ddot{y}_S = -ky - f_g \tag{10.3b}$$

$$I_p\ddot{\gamma} = M + ke(y\,\cos\gamma - x\,\sin\gamma) \tag{10.3c}$$

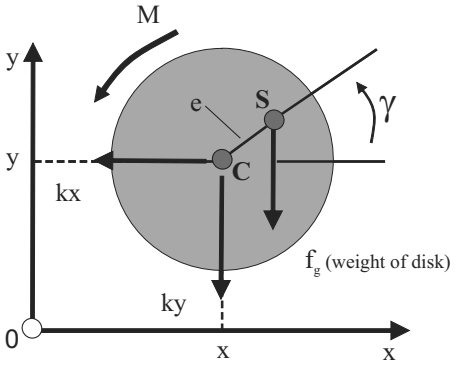


Fig. 10.4. Forces and moments acting on the disk

Introduction of equations (10.2a) and (10.2b) into the equations of motion (10.3a), (10.3b), (10.3c) leads to the new equations:

$$m\,\ddot{x} \;+\; kx = me\,\dot{\gamma}^2\,\cos\,\gamma + me\,\ddot{\gamma}\sin\,\gamma \tag{10.4a}$$

$$m\,\ddot{y} \;+\; ky = me\,\dot{\gamma}^2\,\sin\,\gamma - me\,\ddot{\gamma}\cos\,\gamma - f_{\mathrm{g}} \tag{10.4b}$$

$$mi_{\mathrm{p}}^2\,\ddot{\gamma} = M \;+\; ke\,(y\,\cos\,\gamma \;-\; x\,\sin\,\gamma) \tag{10.4c}$$

For the special case $M = 0$, which is the case of steady state operation (drive moment = moment of losses), the expression

$$\ddot{\gamma} = \frac{k}{m}\,\frac{e}{i_{\mathrm{p}}}\,\frac{y\,\cos\,\gamma \;-\; x\,\sin\,\gamma}{i_{\mathrm{p}}} \tag{10.5}$$

is very small, due to the fact $e << i_{\mathrm{p}}$ and $x, y << i_{\mathrm{p}}$. If $\ddot{\gamma} = 0$, it follows that the angular velocity $\dot{\gamma} = \Omega$ is constant and the angle γ is proportional to time t:

$$\ddot{\gamma} = 0 \tag{10.6a}$$

$$\dot{\gamma} = \Omega \;=\; \text{constant} \tag{10.6b}$$

$$\gamma = \Omega t \;+\; \gamma_0 \tag{10.6c}$$

The following two equations remain:

$$m\ddot{x} \;+\; kx = me\,\Omega^2\,\cos\,(\Omega t + \gamma_0) \tag{10.7a}$$

$$m\ddot{y} \;+\; ky = me\,\Omega^2\,\sin\,(\Omega t + \gamma_0) - f_{\mathrm{g}} \tag{10.7b}$$

Equations (10.7a) and (10.7b) are independent from each other. Each equation describes the vibration behavior of a single degree of freedom system with a force excitation, depending on the unbalance quantity me and the squared angular velocity Ω^2. Equation (10.7b) has also a static part due to the weight f_{g} of the disk. The differential equations are linear, inhomogeneous and have constant coefficients.

10.2.3 Natural Vibrations and Natural Frequency

The equations (10.7a), (10.7b) can be solved independently of each other. Each equation has two solution parts, the solution for the homogeneous equation (without right hand side) and the solution for the inhomogeneous equation (with right hand side). From the following homogeneous equations:

$$m\ddot{x} + kx = 0 \tag{10.8a}$$

$$m\ddot{y} + ky = 0 \tag{10.8b}$$

it follows for the natural vibrations

$$x(t) = A_{\mathrm{x}} \cos \omega t + B_{\mathrm{x}} \sin \omega t \tag{10.9a}$$

$$y(t) = A_{\mathrm{y}} \cos \omega t + B_{\mathrm{y}} \sin \omega t \tag{10.9b}$$

where

$$\omega = \sqrt{\frac{k}{m}} \tag{10.10}$$

is the circular natural frequency of the Jeffcott rotor. $A_{\mathrm{x}}, B_{\mathrm{x}}, A_{\mathrm{y}}, B_{\mathrm{y}}$ depend on the initial conditions.

Equations (10.9a), (10.9b) do not show any decay of x and y due to the fact that damping was neglected. In reality, the damping will lead to a decrease of the natural vibrations with time.

10.2.4 Forced Unbalance Vibrations

If we now consider the complete inhomogeneous equations (10.7a), (10.7b), it can be shown that the overall solutions for $x(t)$ and $y(t)$ consist of different parts

$$x(t) = A_{\mathrm{x}} \cos \omega t + B_{\mathrm{x}} \sin \omega t + e \frac{(\Omega/\omega)^2}{1-(\Omega/\omega)^2} \cos(\Omega t + \gamma_0) \tag{10.11a}$$

$$y(t) = \underbrace{A_{\mathrm{y}} \cos \omega t + B_{\mathrm{y}} \sin \omega t}_{\text{Natural vibrations with circular natural frequency } \omega. \text{ With damping, this solution decays with time.}} + \underbrace{e \frac{(\Omega/\omega)^2}{1-(\Omega/\omega)^2} \sin(\Omega t + \gamma_0)}_{\text{Forced unbalance vibration with circular frequency } \Omega\text{: see also (7.45).}} - \underbrace{\frac{f_{\mathrm{g}}}{k}}_{\text{Static solution due to weight.}} \tag{10.11b}$$

In practice, there is always damping in the system, which leads to a decrease of the natural vibrations. After this part of the overall response decays, only the forced unbalance vibrations of the disk center C remain:

$$x_{\mathrm{e}}(t) = \hat{x}_{\mathrm{e}} \cos(\Omega t + \gamma_0) \tag{10.12a}$$

$$y_{\mathrm{e}}(t) = \hat{y}_{\mathrm{e}} \sin(\Omega t + \gamma_0) \tag{10.12b}$$

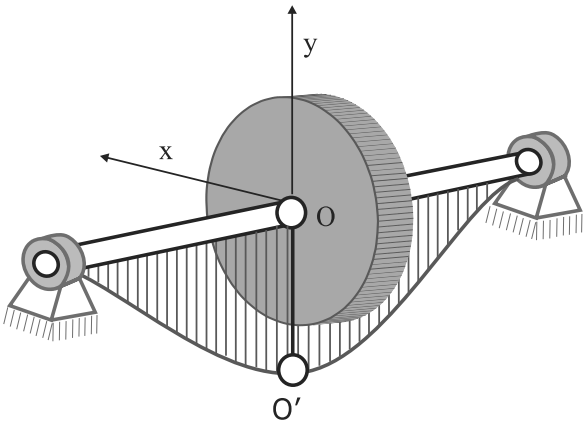


Fig. 10.5. Static deflection of the disk

This steady response occurs around the static solution $x_{\text{stat}} = 0$, $y_{\text{stat}} = -f_{\text{g}}/k$, which is equal to the static deflection of the disk center (distance $O - O'$ in Fig. 10.5)

The amplitudes of the unbalance vibrations $x_{\text{e}}(t)$ and $y_{\text{e}}(t)$ in the two directions are equal:

$$\hat{x}_e \;=\; \hat{y}_e \;=\; e\,\frac{(\Omega/\omega)^2}{1-(\Omega/\omega)^2} \;= e\,\frac{\overline{\omega}^2}{1-\overline{\omega}^2} \tag{10.13}$$

and depend on the mass eccentricity e and on the ratio of the frequencies $\overline{\omega} = \Omega/\omega$, expressing the angular velocity Ω of the shaft in relation to the natural frequency ω.

Circular Orbit of Disk Center

By superposition of the solution parts $x_{\text{e}}(t)$ and $y_{\text{e}}(t)$, it follows that the motion of the disk center C is a circular orbit around the static deflection point O'. The radius r_{c} of this circular orbit is

$$r_{\text{c}} \;=\; \hat{x}_{\text{e}} \;=\; \hat{y}_{\text{e}} \;=\; e\,\frac{\overline{\omega}^2}{1-\overline{\omega}^2} \tag{10.14}$$

Figure 10.6 demonstrates the superposition of the two part solutions $x_{\text{e}}(t)$ and $y_{\text{e}}(t)$ around the static deflection O' for the special case of $\gamma_0 = 0$. As can be seen in Fig. 10.6, the direction of the orbit motion is the same as the shaft rotation Ω. This case is called *forward motion*. If the two directions of orbit motion and shaft rotation are opposite, the motion is defined as a *backward motion*.

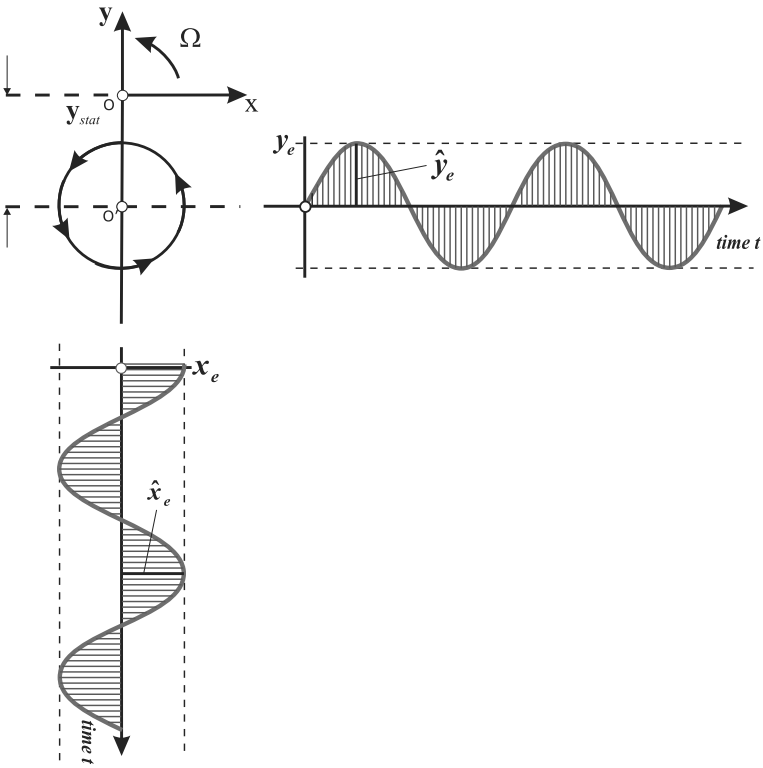


Fig. 10.6. Circular orbit of the disk center C

Amplitudes of Unbalance Vibrations vs Relative Speed $w = \Omega/\omega$

Equation (10.14) shows how the radius of the circular orbit of the disk center changes with the frequency ratio $\overline{\omega} = \Omega/\omega$. In Fig. 10.7, the ratio r_C/e – which is the orbit amplitude divided by mass eccentricity e – is presented as a function of the frequency ratio $\overline{\omega}$. The relative amplitudes are small for low rotational speeds and increase with increasing $\overline{\omega}$. Resonance appears at $\overline{\omega} = 1$ with amplitudes rising to infinity. In this critical case, the frequency of excitation Ω (rotational frequency) coincides with the natural frequency ω of the rotor. In practice, damping reduces the amplitude in this resonance area. For values $\overline{\omega} > 1$, the disk center amplitudes decrease again. They become equal to the mass eccentricity e for higher rotational frequencies. The range $0 < \overline{\omega} < 1$ is called undercritical, $\overline{\omega}$-values above 1 are overcritical and $\overline{\omega} = 1$ is the critical case (resonance).

Figure 10.7 also presents the amplitudes

$$r_S = \hat{x}_{se} = \hat{y}_{se} = e\frac{1}{1-\overline{\omega}^2} \tag{10.15}$$

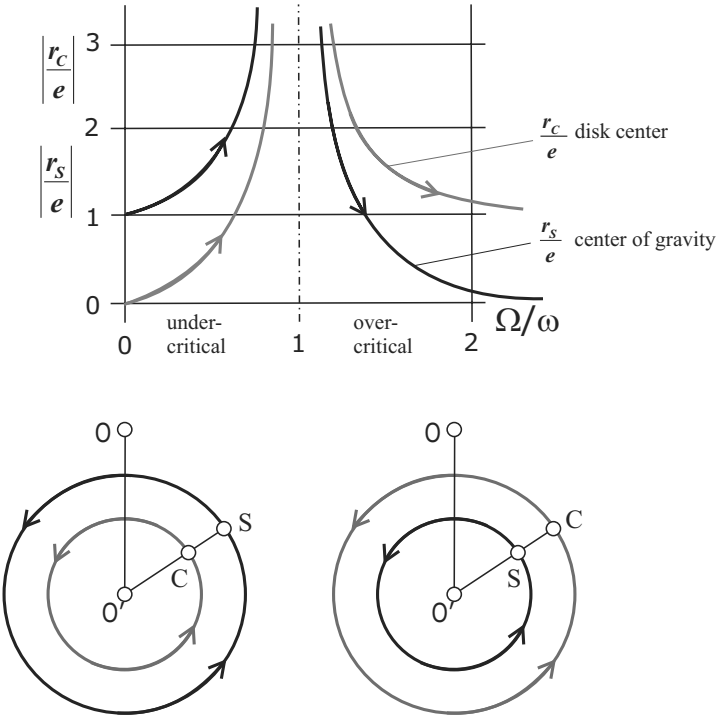


Fig. 10.7. Amplitudes of unbalance vibrations in dependence of rotational speed

of the center of gravity, related to the mass eccentricity, as a function of $\overline{\omega}$. There is always the difference of e between the two amplitudes of r_{C} and r_{S}. Of particular interest is the self-centering effect for the center of gravity S for very high speeds $\overline{\omega}$. This effect was observed long ago by Laval. Figure 10.7 shows clearly that the orbit configuration for the center of gravity r_{S} and the center of disk r_{C} is different for the two cases of undercritical and overcritical operation.

10.2.5 Influence of External Damping

For simplicity, we consider two linear damper elements, as shown in Fig. 10.8. The equations of motion (10.7a), (10.7b) are modified to

$$m\ddot{x} + d\dot{x} + kx = me\,\Omega^2 \cos(\Omega t + \gamma_0) \tag{10.16a}$$

$$m\ddot{y} + d\dot{y} + ky = me\,\Omega^2 \sin(\Omega t + \gamma_0) - f_{\mathrm{g}} \tag{10.16b}$$

The external damping has the following effects: First, the natural vibrations decrease with time. In addition, depending on the damping value d, the natural frequency also decreases.

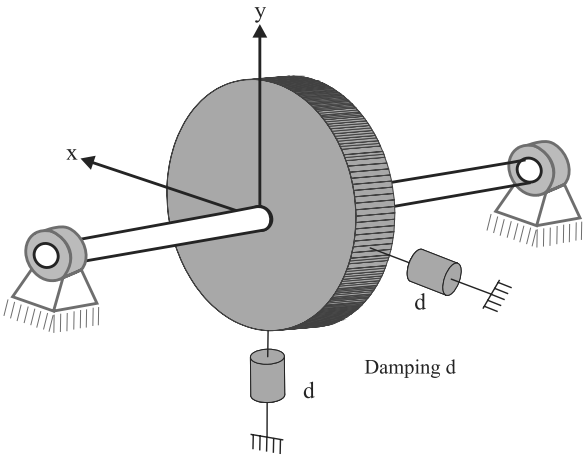


Fig. 10.8. Linear damper element acting at the disk

$$\omega_{\mathrm{d}} \;=\; \omega\,\sqrt{1-D^2} \tag{10.17}$$

in which ω_{d} is the natural frequency of the damped system with the damping factor

$$D \;=\; \frac{d}{2\sqrt{k\;m}} \tag{10.18}$$

The amplitudes of the disk center, but also of the center of gravity, are reduced by the effect of damping. This is especially true for the resonance range. As an example, Fig. 10.9 shows the amplitudes r_{C}/e versus $\overline{\omega}$ for different damping factors D.

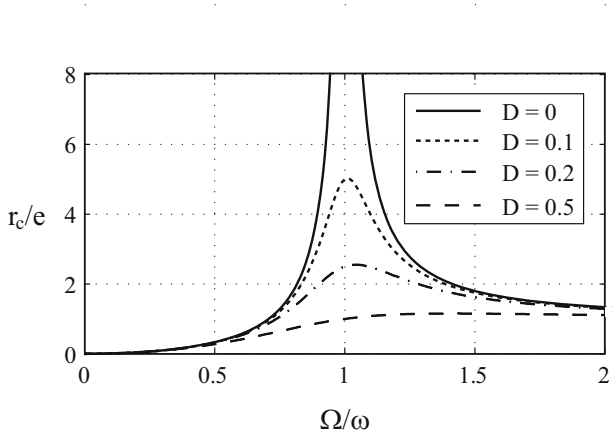


Fig. 10.9. Influence of damping to the vibration amplitudes of the disk center

10.2.6 Influence of Bearing Elasticity

In the previous sections, the bearings of the Jeffcott rotor were considered to be rigid. This assumption is not always satisfied in practical applications. In such cases, finite bearing stiffnesses should be introduced in order to take this effect into account.

Depending on the type of bearing (roller- and ball bearings, fluid bearings, magnetic bearings) and the bearing support, the size of the bearing stiffnesses may be quite different. They should always be evaluated in relation to the shaft stiffness. This is particularly important in applications of rotating systems with active magnetic bearings

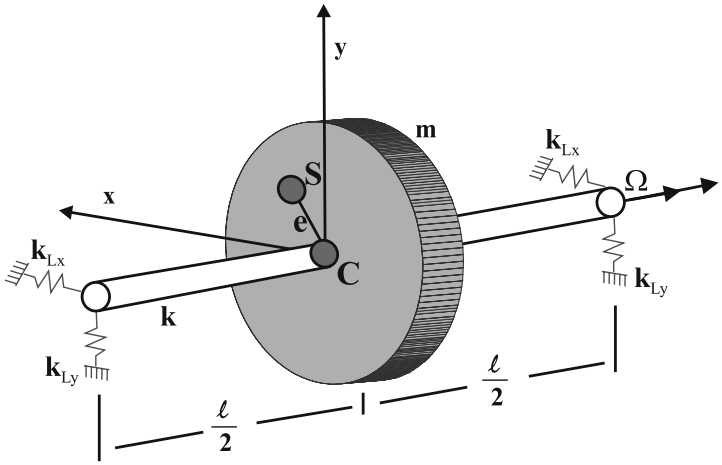


Fig. 10.10. Jeffcott rotor with elastic bearings

When elastic bearings are introduced into a rotor system, it has to be clarified whether they are equal in perpendicular directions. Very often, the stiffnesses are different in the horizontal and vertical directions, depending on the bearing type and the support system. In the following, the influence of bearing stiffnesses is investigated for the Jeffcott rotor as introduced in Fig. 10.10.

We assume that the bearing stiffnesses are different in two directions: k_{Lx} for the x-direction and k_{Ly} for the y-direction. The two bearings have the same bearing stiffnesses (symmetric configuration of the rotor system).

As shown for the y-direction in Fig. 10.11, the shaft stiffness k and the bearing stiffness are arranged in series. The resultant stiffnesses (defined for the location of the disk) of this arrangement are

$$k_{\mathrm{y}} = \frac{2k\, k_{\mathrm{Ly}}}{k + 2\, k_{\mathrm{Ly}}} \tag{10.19a}$$

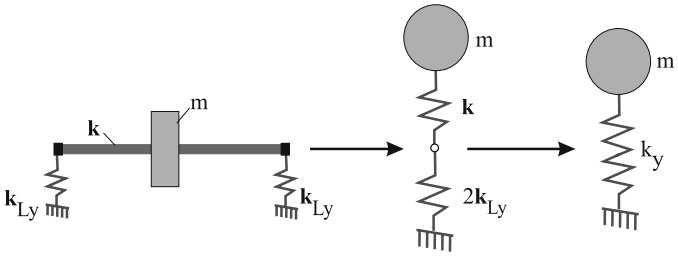


Fig. 10.11. Series arrangement of stiffnesses

$$k_{\mathrm{x}} \;=\; \frac{2k\, k_{\mathrm{Lx}}}{k \;+\; 2\, k_{\mathrm{Lx}}} \tag{10.19b}$$

Figure 10.11 demonstrates this arrangement for the y-direction only. The two equations of motion (10.7a) and (10.7b) can now easily be modified for the case of flexible bearing behaviour. The new equations are

$$m\ddot{x} \;+\; k_{\mathrm{x}}x \;=\; me\,\Omega^2\,\cos\,(\Omega t \;+\; \gamma_0) \tag{10.20a}$$

$$m\ddot{y} \;+\; k_{\mathrm{y}}y \;=\; me\,\Omega^2\,\sin\,(\Omega t \;+\; \gamma_0) - f_{\mathrm{g}} \tag{10.20b}$$

Natural Vibrations and Natural Frequencies

With the different stiffness values k_{x} and k_{y} for the two directions we obtain two different natural frequencies ω_{x} and ω_{x} for the two different directions. They can be expressed in terms of the natural frequency of the rigidly supported rotor ω and a stiffness parameter.

$$\omega_{\mathrm{x}} = \sqrt{\frac{k_{\mathrm{x}}}{m}} = \sqrt{\frac{k}{m}}\,\sqrt{\frac{2k_{\mathrm{Lx}}}{2k_{\mathrm{Lx}}+k}} = \omega\sqrt{\frac{1}{1+k/2k_{\mathrm{Lx}}}} \tag{10.21a}$$

$$\omega_{\mathrm{y}} = \sqrt{\frac{k_{\mathrm{y}}}{m}} = \sqrt{\frac{k}{m}}\,\sqrt{\frac{2k_{\mathrm{Ly}}}{2k_{\mathrm{Ly}}+k}} = \omega\sqrt{\frac{1}{1+k/2k_{\mathrm{Ly}}}} \tag{10.21b}$$

Figure 10.12 represents as an example, how the natural frequency ω_{x} depends on the bearing parameter k/k_{Lx}. We recognize that the natural frequency of the flexibly supported rotor is reduced by the bearing stiffness. If the staft stiffness is equal to the bearing stiffness, the natural frequency ω_{x} is already reduced to a value of 80 per cent of the natural frequency $\omega = \sqrt{k/m}$, of the rigidly supported rotor. For the y-direction the behaviour is similiar

Forced Unbalance Response

The two equations of motion (10.20a) and (10.20b) are independent of one another and lead to forced unbalance response solutions similar to (10.11a)

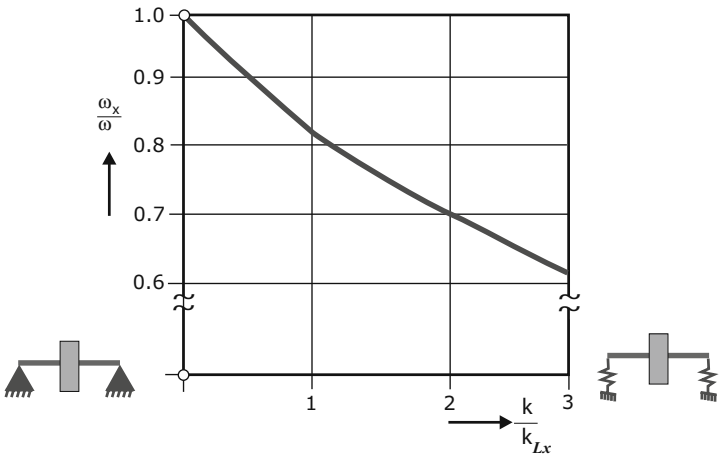


Fig. 10.12. Natural frequencies of a flexibly supported Jeffcott rotor

and (10.11b). The basic character of these amplitude curves is similar to the behaviour shown in Fig. 10.7. However, due to the fact that the two natural frequencies ω_{x}, ω_{y} are different because of the anisotropic bearings, there will be two critical rotational frequencies lower than 1:

$$\Omega_{\mathrm{crit1}}/\omega = \omega_{\mathrm{x}}/\omega \ < 1 \tag{10.22a}$$

$$\Omega_{\mathrm{crit2}}/\omega = \omega_{\mathrm{y}}/\omega \ < 1 \tag{10.22b}$$

where the amplitudes reach high resonance values.

The first critical rotational frequency will appear in the direction with the lower bearing stiffness. Figure 10.13 shows the forced unbalance response of the Jeffcott Rotor with anisotropic elastic bearings. It can be seen that, in this case, the x-direction has lower stiffness values k_{Lx} with reference to k_{Ly}

Due to the fact that the amplitudes for one rotational speed are different in the two directions, the resultant orbital motions are no longer circular, but show an elliptical character. Furthermore, in the range between the two natural frequencies, the orbital motion is a backward motion. Outside of this area, the orbits are in a forward motion mode.

10.3 Flexible Rotors with Continuous Mass and Stiffness Distribution

We now consider general flexible rotors, which usually have varying mass per unit length μ and elastic bending stiffness EJ along the shaft axis z. We assume that the shaft is running with constant angular velocity Ω, which implies that acceleration in circumferential direction is not considered. The rotating

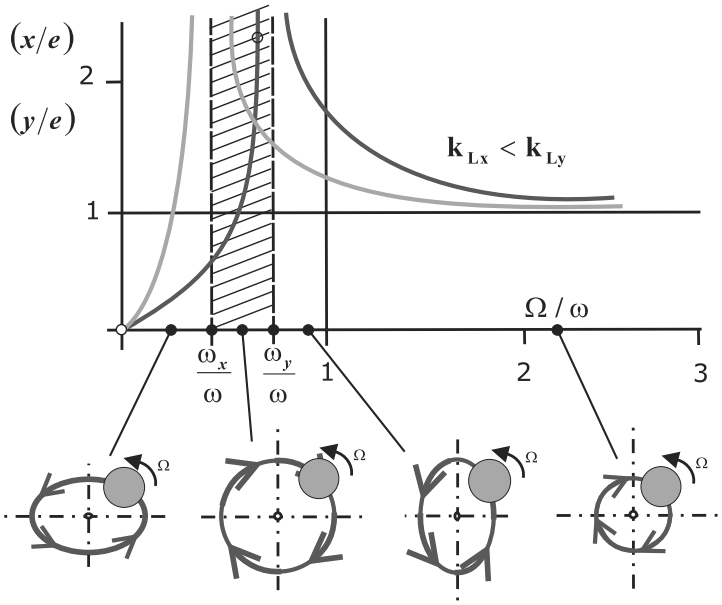


Fig. 10.13. Forced unbalance response of Jeffcott rotor with elastic bearings

shaft is supported in several bearings with linear stiffness and damping coefficients: see Fig. 10.14.

At a time t, the radial displacements of the shaft – relative to a static deflection line – are considered to be $x(z,t)$ and $y(z,t)$.

Besides the usual mass and stiffness characteristics, additional parameters have to be introduced, if further physical effects like gyroscopic moments, unbalance forces and forces of self excitation, e.g. in labyrinth seals or internal damping forces etc. are of importance for the rotordynamic behavior [6] [9] - [8] ,[11]- [10], [13, 14].

10.3.1 Modelling for the Flexible Rotor

The dynamic behavior of a flexible rotor system (Fig. 10.14) is dependent on forces (moments) acting on the shaft when it is vibrating around the static deflection line. Equations of motion express the dynamic equilibrium, including all important forces and moments. Some of these forces (moments) depend on the shaft motion (displacements, velocities, accelerations) while other forces and moments are independent of them. For initial discussion, we consider only the most important forces (moments). These are the translatory inertia forces, the restoring forces of the flexible shaft and the bearing forces. Additional forces and moments will be considered later.

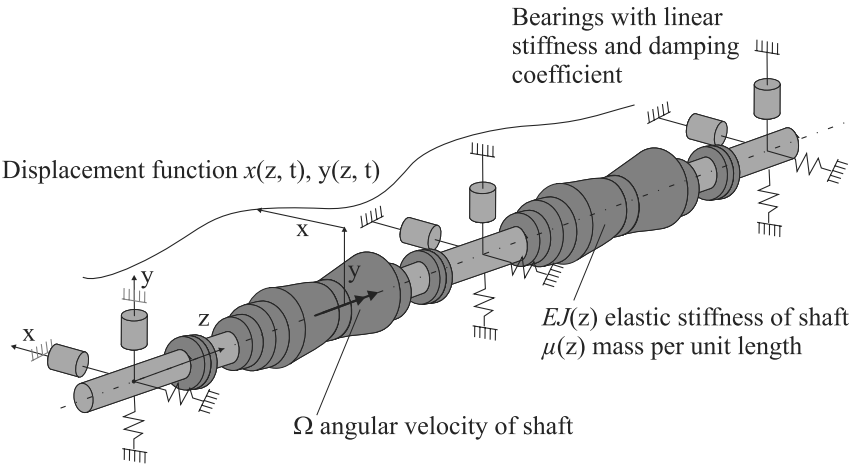


Fig. 10.14. Mechanical model of a general flexible rotor

Inertia Forces

For the case of a translatory acceleration of a general rotor element with length dz, the d'Alembert inertia forces for the mass element $dm = \mu dz$ are $dm\ddot{x}, dm\ddot{y}$ (Fig. 10.15), acting in opposite direction to the accelerations $\ddot{x}, \ddot{y}$. If the shaft rotates with angular velocity Ω, similar to (10.7a) and (10.7b), additional unbalance forces have to be added, due to the mass eccentricity e. This mass eccentricity may change its amplitude e and its phase γ along the axis z.

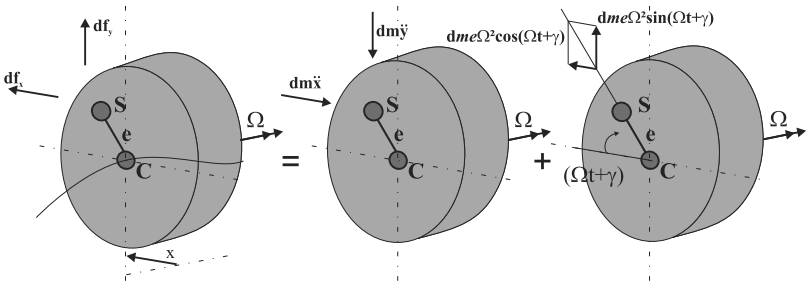


Fig. 10.15. Inertia forces of mass element dm

The translatory inertia forces of the rotor element dm consist of two parts as shown in formulas (10.23a), (10.23b):

$$df_{\mathrm{x}} = (e\Omega^2 \cos(\Omega t + \gamma) - \ddot{x})\, dm \tag{10.23a}$$

$$df_{\mathrm{y}} = (e\Omega^2 \sin(\Omega t + \gamma) - \ddot{y})\, dm \tag{10.23b}$$

As shown before, speed dependent harmonic vibrations can be excited by means of the unbalance distribution along the shaft. Besides the inertia forces, inertia moments must also be introduced, if their size is important. This depends on the moments of inertia of the rotor system.

Restoring Moments of the Flexible Shaft

The effect of restoring moments of the flexible shaft can be described in dependence of the shaft bow, expressed by the second derivative of the displacements with respect to the coordinate z. For a rotor element with bending stiffness EJ, the restoring moments are (Fig. 10.16)

$$M_{\mathrm{x}} = EJ\,\partial x^2/\partial z^2 = EJx"(z) \tag{10.24a}$$

$$M_{\mathrm{y}} = -EJ\,\partial y^2/\partial z^2 = -EJy"(z) \tag{10.24b}$$

These expressions are valid for the Bernoulli beam theory, which neglects shear deformation. If shear deformation becomes important, moments and shear forces have to be defined corresponding to the Timoshenko beam theory.

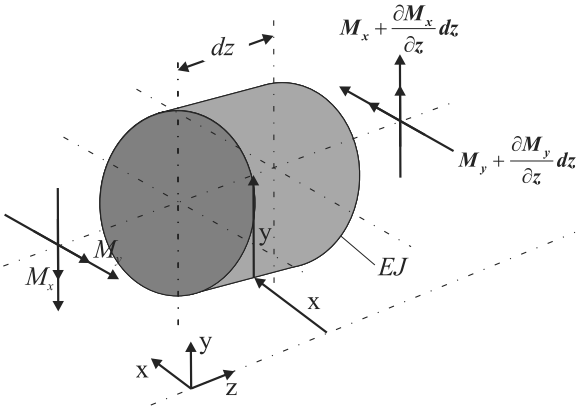


Fig. 10.16. Restoring forces of the flexible shaft

Bearing Forces

Regardless of the bearing type (roller bearing, fluid film bearing, magnetic bearing) we express the restoring forces $f_{\mathrm{bx}}, f_{\mathrm{by}}$ of the bearing number b ($b = 1, 2, 3, ...B$) in dependence of the shaft displacements $x_{\mathrm{b}}, y_{\mathrm{b}}$ and relative shaft velocities $\dot{x}_{\mathrm{b}}, \dot{y}_{\mathrm{b}}$ by the following linear expression (Fig. 10.17):

$$f_{\mathrm{bx}} = -c_{\mathrm{xx}} x_{\mathrm{b}} - d_{\mathrm{xx}} \dot{x}_{\mathrm{b}} \tag{10.25a}$$

$$f_{\mathrm{by}} = -c_{\mathrm{yy}} y_{\mathrm{b}} - d_{\mathrm{yy}} \dot{y}_{\mathrm{b}} \tag{10.25b}$$

In addition, restoring forces corresponding to any static deflection may have to be considered.

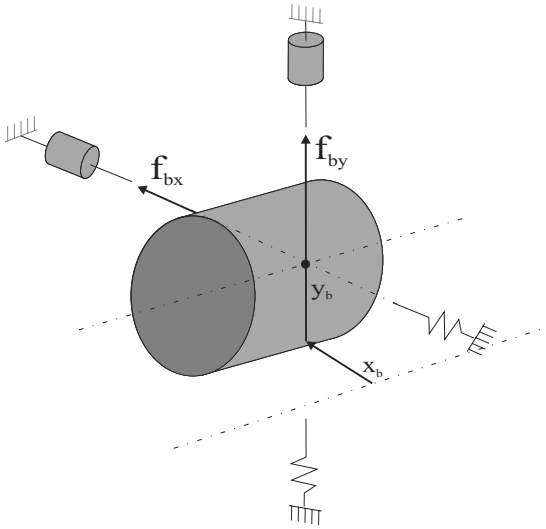


Fig. 10.17. Restoring forces $f_{\mathrm{bx}}, f_{\mathrm{by}}$ of bearing number b

10.4 Equations of Motion Based on the Finite Element Method

Complex rotor systems may be modeled by discretizing them into small elements of finite dimension, as described by the well established Finite Element Method - (FEM) [9] - [8], [11] - [10].

10.4.1 Elements of the Rotor System

The flexible rotor system, as shown in Fig. 10.14, can be subdivided into several beam elements, characterized by numbers n (n=1, 2, 3, ..., N). Each beam element n is described by length l_n, the bending stiffness EJ_n, the mass per unit length μ_n, the mass eccentricity e_n, the angle of eccentricity γ_n and, if necessary, by further parameters describing external and internal damping, additional inertia effects like rotatory inertia and gyroscopic effects and self excitation mechanisms (Fig. 10.18). For simplicity, we assume that the element parameters are constant for each element n.

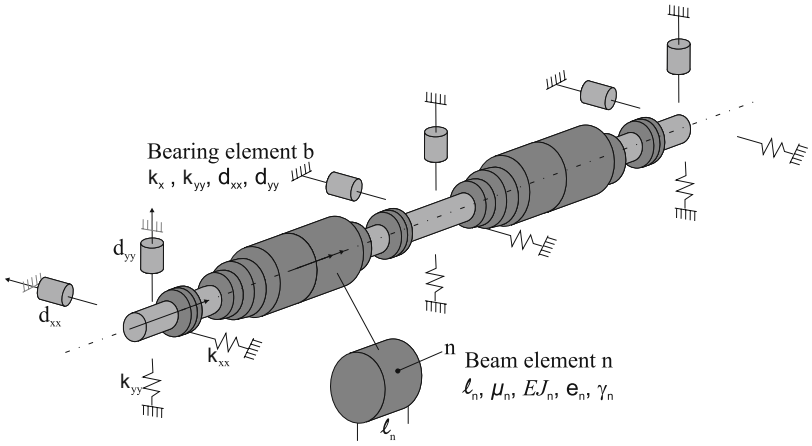


Fig. 10.18. Finite Element Model of the flexible rotor system with beam elements and bearings

10.4.2 Principle of Virtual Work

The dynamic behavior of the flexible rotor is described by its equations of motion. In these equations, the above forces and moments contribute to the dynamic equilibrium. For the finite element method, the starting point for constructing the equations of motion is the principle of virtual work:

> In case of a virtual displacement shape with components $\delta x(z)$ and $\delta y(z)$ along the shaft, the corresponding virtual work of the inner forces and moments (stresses) is equal to the virtual work of the external forces and moments, including the inertia forces.

$$\delta W_i \;=\; \delta W_e \tag{10.26}$$

> For the simplified case of the rotor system in Fig. 10.14 with only a few but very important forces and moments, the virtual work can be expressed for the complete system.

However, for a finite element model, the virtual work is formulated as a sum of the virtual work of all beam elements and bearing elements in the system (Fig. 10.18). Possible disk elements with mass and moments of inertia can, of course, be added. For each single element, the mechanical behavior can be described by force (moment-) motion relationships using basic element matrices for inertia, stiffness and damping, if relevant. Below, we briefly describe how such element matrices can be determined.

As an example, the virtual work of a beam element with number n includes the unknown displacement functions $x_n(z_n, t)$ and $y_n(z_n, t)$. It is a usual practice in the finite element method to express these unknown functions in terms of approximate functions, which have to fulfill special compatibility conditions

within an element and at the boundaries. The approximations consist of the boundary displacements (angles) and selected deformation functions for the inner area of the elements.

$$x_n(z_n,t) = \mathbf{H}_n^T \mathbf{x}_n \tag{10.27a}$$
$$y_n(z_n,t) = \mathbf{H}_n^T \mathbf{y}_n \tag{10.27b}$$

$$\mathbf{x}_n^T = \left\{x_n^l, \beta_n^l, x_n^r, \beta_n^r\right\}$$
$$\mathbf{y}_n^T = \left\{y_n^l, \alpha_n^l, y_n^r, \alpha_n^r\right\}$$
$$\mathbf{H}_n^T = \{H_1, H_2, H_3, H_4\}$$

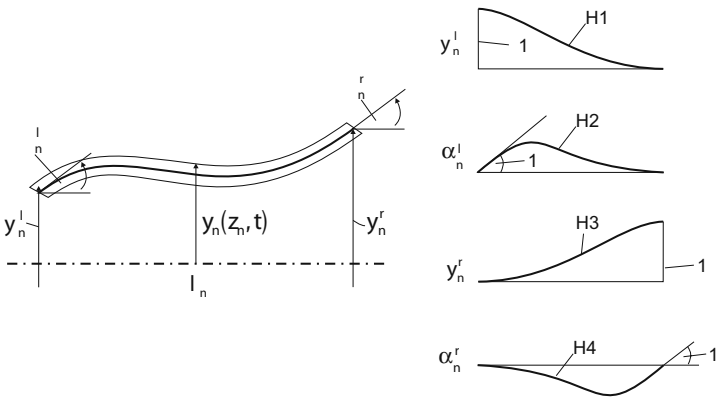


Fig. 10.19. Approximate functions for element n

Figure 10.19 shows, for example, the four approximate deformation functions H_1, H_2, H_3, H_4 with the corresponding boundary displacements and angles for the y-direction. With the expressions (10.27a) and (10.27b) the principle of virtual work for the overall system can be described by (10.28).

$$\begin{aligned}\delta W = & \sum_{n=1}^{N} \delta \mathbf{x}_n^T E J_n \int_0^{l_n} \mathbf{H}_n{}'' \mathbf{H}_n{}''^T dz_n \mathbf{x}_n \\ & + \sum_{n=1}^{N} \delta \mathbf{x}_n^T \mu_n \int_0^{l_n} \mathbf{H}_n \mathbf{H}_n^T dz_n \ddot{\mathbf{x}}_n \\ & + \sum_{b=1}^{B} \delta x_b (c_{\mathrm{xx}} x_b + d_{\mathrm{xx}} \dot{x}_b)\end{aligned}$$

$$
\begin{aligned}
&+ \sum_{n=1}^{N} \delta \mathbf{x}_n^T \mu_n \Omega^2 \int_0^{l_n} \mathbf{H}_n^T e_n \cos(\Omega t + \gamma_n) dz_n \\
&+ \sum_{n=1}^{N} \delta \mathbf{y}_n^T E J_n \int_0^{l_n} \mathbf{H}_n" \mathbf{H}_n"^T dz_n \mathbf{y}_n \\
&+ \sum_{n=1}^{N} \delta \mathbf{y}_n^T \mu_n \int_0^{l_n} \mathbf{H}_n \mathbf{H}_n^T dz_n \ddot{\mathbf{y}}_n \\
&+ \sum_{b=1}^{B} \delta y_b (c_{\mathrm{yy}} y_b + d_{\mathrm{yy}} \dot{y}_b) \\
&+ \sum_{n=1}^{N} \delta \mathbf{y}_n^T \mu_n \Omega^2 \int_0^{l\ n} \mathbf{H}_n^T e_n \sin(\Omega t + \gamma_n) dz_n \\
&= 0
\end{aligned} \tag{10.28}
$$

including all beam elements ($n = 1, ...N$) and all bearing elements ($b = 1, 2...B$) and defining $\mathbf{H}_n'' \equiv \partial^2 \mathbf{H}_n / \partial z^2$. Equation (10.28) has four terms for each of the two planes in the $x-$ and $y-$ directions. Due to the fact that, in this special case, no coupling exists between the two planes, each of the two planes can also be considered separately:

$$\delta W_x = 0, \delta W_y = 0 \tag{10.29}$$

Later on, coupling terms like gyroscopic moments or others will be considered: in this case, all terms of (10.28) have to be handled together.

10.4.3 *Element Matrices and Global Matrices*

At this stage, we concentrate on one plane, only, e.g. the x-plane. The terms of (10.28) can be interpreted as follows. The expressions of the two first terms:

$$
\begin{aligned}
\mathbf{K}_n &= E J_n \int_0^{l_n} \mathbf{H}_n" \mathbf{H}_n"^T dz_n \\
&= \frac{E J_n}{l_n^3} \begin{bmatrix} 12 & 6l_n & -12 & 6l_n \\ & 4l_n^2 & -6l_n & 2l_n^2 \\ & & 12 & -6l_n \\ & & & 4l_n^2 \end{bmatrix}
\end{aligned} \tag{10.30a}
$$

$$
\begin{aligned}
\mathbf{M}_n &= \mu_n \int_0^{l_n} \mathbf{H}_n \mathbf{H}_n^T dz_n \\
&= \frac{\mu_n l_n}{420} \begin{bmatrix} 156 & 22l_n & 54 & -13l_n \\ & 4l_n^2 & 13l_n & -3l_n \\ & & 156 & -22l_n \\ & & & 4l_n^2 \end{bmatrix}
\end{aligned} \tag{10.30b}
$$

are the symmetric stiffness matrix $\mathbf{K}_n$ and the symmetric mass matrix $\mathbf{M}_n$ of element n. Their 4×4 dimension corresponds to the four boundary displacements and angles. The matrices are related to the boundary forces (moments) and displacements (angles) for the element n. The last term of (10.28) corresponds to an external excitation due to mass unbalance of element n:

$$\mathbf{f}_{\mathrm{n\,e}} = \mu_n \Omega^2 \int_0^{l_n} \mathbf{H}_n^T e_n \sin(\Omega t + \gamma_n) dz_n \tag{10.31}$$

With these definitions for $\mathbf{M}_{\mathrm{n}}, \mathbf{K}_{\mathrm{n}}$ and $\mathbf{f}_{\mathrm{n\,e}}$ we obtain

$$\begin{aligned} \delta W_x = &\sum_{n=1}^{N} \delta \mathbf{x}_n^T \mathbf{K}_n \mathbf{x}_n + \sum_{n=1}^{N} \delta \mathbf{x}_n^T \mathbf{M}_n \ddot{\mathbf{x}}_n \\ &+ \sum_{b=1}^{B} \delta x_b (c_{\mathrm{xx}} x_b + d_{\mathrm{xx}} \dot{x}_b) + \sum_{n=1}^{N} \delta \mathbf{x}_n^T \mathbf{f}_{\mathrm{n\,e}} \end{aligned} \tag{10.32}$$

We now return to the overall system. Figure (10.20) is a representation of the system with all elements. For each nodal point, four global coordinates are shown: two displacements and two angles. Global coordinates are counted versus the overall system. We concentrate all coordinates in one global vector $\mathbf{x}$ (x-plane only). Now we can express the local element coordinates $\mathbf{x}_b$ as functions of the global coordinates:

$$\text{beam elements: } \mathbf{x}_n = \mathbf{T}_n \mathbf{x} \tag{10.33}$$

$$\text{bearing elements: } \mathbf{x}_b = \mathbf{T}_b \mathbf{x} \tag{10.34}$$

where the matrices $\mathbf{T}_n, \mathbf{T}_b$ show how the different elements are arranged in the overall coordinate system. By introducing these relations into δW_x from (10.32) it is possible to obtain

$$\delta W_x = \delta \mathbf{x}^T \left\{ \mathbf{M}_x \ddot{\mathbf{x}} + \mathbf{D}_x \dot{\mathbf{x}} + \mathbf{K}_x \mathbf{x} - \mathbf{f}_x \right\} = 0 \tag{10.35}$$

$$\mathbf{M}_x = \sum_{\mathrm{n}=1}^{N} \mathbf{T}_n^T \mathbf{M}_n \mathbf{T}_n \tag{10.36a}$$

$$\mathbf{D}_x = \sum_{\mathrm{b}=1}^{B} \mathbf{T}_b^T \mathbf{T}_b d_{\mathrm{bxx}} \tag{10.36b}$$

$$\mathbf{K}_x = \sum_{\mathrm{n}=1}^{N} \mathbf{T}_n^T \mathbf{K}_n \mathbf{T}_n + \sum_{\mathrm{b}=1}^{B} \mathbf{T}_b^T \mathbf{T}_b c_{\mathrm{bxx}} \tag{10.36c}$$

$$\mathbf{f}_x = \sum_{\mathrm{n}=1}^{N} \mathbf{T}_n^T \mathbf{f}_{\mathrm{ne}} \tag{10.36d}$$

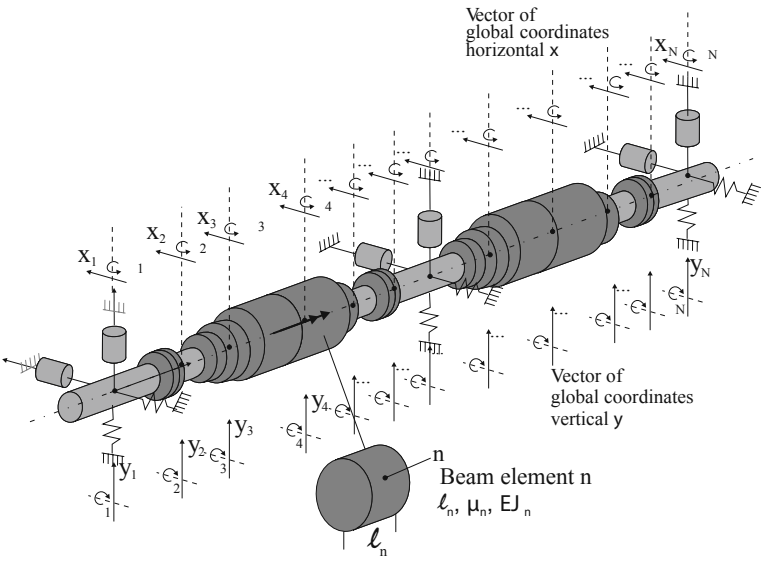


Fig. 10.20. Global coordinates of rotor system

The principle of virtual work states that the virtual displacements $\delta\mathbf{x}^T$ can be chosen arbitrarily as long as they are compatible. Therefore, to fulfill (10.35), the expression in parentheses has to be zero, which finally leads to the equations of motion of the considered rotor system in x-direction:

$$\mathbf{M}_x\ddot{\mathbf{x}} + \mathbf{D}_x\dot{\mathbf{x}} + \mathbf{K}_x\mathbf{x} = \mathbf{f}_x \tag{10.37}$$

The matrices $\mathbf{M}_x, \mathbf{D}_x, \mathbf{K}_x$ and the vector $\mathbf{f}_x$ are assembled from the previously defined element matrices and vectors. The order of the system matrices depends on the number of elements or the number of global coordinates. In the special case of a rotor system with a chain of elements, the matrix and vector structures are very clear, as it is shown in Fig. 10.21.

The matrices have a band structure resulting from the element chain and the overlapping of the element matrices. The bearing data c_{xx} and d_{xx} are inserted in the matrices on the main diagonal at positions corresponding to the global coordinates of the bearings.

The equations of motion for the y-direction can be built up in the same way as for the x-direction. If all elements (beams and bearings) have the same characteristics in perpendicular directions, then we will produce the same equations as 10.37. Should the stiffness and bearing coefficients $c_{\mathrm{yy}}, d_{\mathrm{yy}}$ be different from the values $c_{\mathrm{xx}}, d_{\mathrm{xx}}$, then the matrices $\mathbf{D}_y$ and $\mathbf{K}_y$ will be different in the main diagonal elements. Independently from this, we can introduce equations for the y-direction

$$\mathbf{M}_y\ddot{\mathbf{y}} + \mathbf{D}_y\dot{\mathbf{y}} + \mathbf{K}_y\mathbf{y} = \mathbf{f}_y \tag{10.38}$$

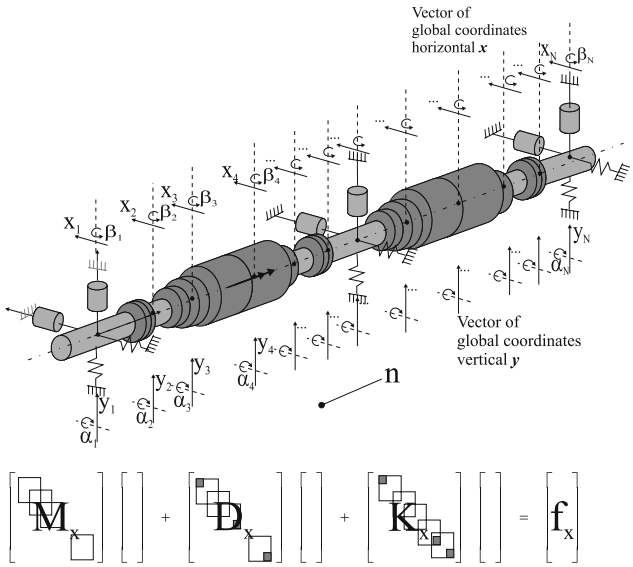


Fig. 10.21. Structure of the system matrices

By superposition of the two sets of equations (10.37) and (10.38) we obtain:

$$\begin{bmatrix} \mathbf{M}_x & 0 \\ 0 & \mathbf{M}_y \end{bmatrix} \begin{bmatrix} \ddot{\mathbf{x}} \\ \ddot{\mathbf{y}} \end{bmatrix} + \begin{bmatrix} \mathbf{D}_x & 0 \\ 0 & \mathbf{D}_y \end{bmatrix} \begin{bmatrix} \dot{\mathbf{x}} \\ \dot{\mathbf{y}} \end{bmatrix} + \begin{bmatrix} \mathbf{K}_x & 0 \\ 0 & \mathbf{K}_y \end{bmatrix} \begin{bmatrix} \mathbf{x} \\ \mathbf{y} \end{bmatrix} = \begin{bmatrix} \mathbf{f}_x \\ \mathbf{f}_y \end{bmatrix} \tag{10.39}$$

which can also be formulated in short form with the global matrices $\mathbf{M}, \mathbf{D}, \mathbf{K}$ and the vector $\mathbf{z}^T = (\mathbf{x}^T, \mathbf{y}^T)$ for both planes:

$$\mathbf{M}\ddot{\mathbf{z}} + \mathbf{D}\dot{\mathbf{z}} + \mathbf{K}\mathbf{z} = \mathbf{f} \tag{10.40}$$

Equation (10.39) or (10.40) describe the dynamic behavior of the rotor system (Fig.10.18) for both planes $x-$ and $y-$. In this special case the two equations are not coupled, due to the fact that physical coupling effects are not present. However, when effects like gyroscopic moments, coupling in oil film bearings, steam excitation, internal damping and others are present the coupling of the two planes has to be considered, as shown in the following section.

10.4.4 General Structure of the Rotor System Matrices

Regardless of the different physical effects, the equations of motion of a linear rotor system can be described with the general structure (see Sect. 7.3.2 on *Stability of Motion* as well):

$$\begin{bmatrix} \mathbf{M}_{\mathrm{x}} & \mathbf{M}_{\mathrm{xy}} \\ \mathbf{M}_{\mathrm{yx}} & \mathbf{M}_{\mathrm{y}} \end{bmatrix} \begin{bmatrix} \ddot{\mathbf{x}} \\ \ddot{\mathbf{y}} \end{bmatrix} + \begin{bmatrix} \mathbf{D}_{\mathrm{x}} & \mathbf{D}_{\mathrm{xy}} \\ \mathbf{D}_{\mathrm{yx}} & \mathbf{D}_{\mathrm{y}} \end{bmatrix} \begin{bmatrix} \dot{\mathbf{x}} \\ \dot{\mathbf{y}} \end{bmatrix} + \begin{bmatrix} \mathbf{K}_{\mathrm{x}} & \mathbf{K}_{\mathrm{xy}} \\ \mathbf{K}_{\mathrm{yx}} & \mathbf{K}_{\mathrm{y}} \end{bmatrix} \begin{bmatrix} \mathbf{x} \\ \mathbf{y} \end{bmatrix} = \begin{bmatrix} \mathbf{f}_x \\ \mathbf{f}_y \end{bmatrix} \tag{10.41}$$

In addition to the main diagonal matrices as presented in (10.39), the coupling matrices $\mathbf{M}_{xy}, \mathbf{M}_{yx}, \mathbf{D}_{xy}, \mathbf{D}_{yx}, \mathbf{K}_{xy}, \mathbf{K}_{yx}$ have been introduced. These coupling terms may lead to total matrices $\mathbf{M}, \mathbf{D}, \mathbf{K}$ which are unsymmetric and can be split into symmetric and skew symmetric parts.

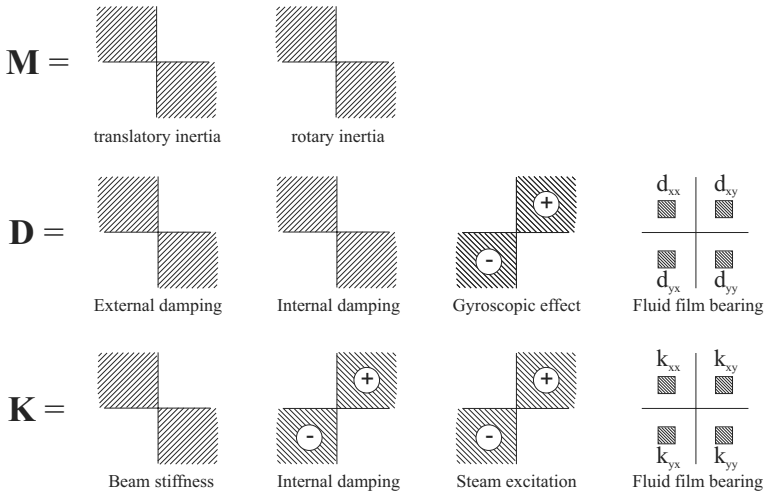


Fig. 10.22. General structure of the rotor system matrices

A more detailed analysis of the system matrices $\mathbf{M}, \mathbf{D}, \mathbf{K}$ shows that the mass matrix is usually symmetric ($\mathbf{M}_{xy} = \mathbf{M}_{yx} = 0$) and consists of the translatory and rotatory inertia terms from beam and disk elements. The damping matrix $\mathbf{D}$ has symmetric components from external and internal damping. A typical skew symmetric matrix results from gyroscopic moments of beam elements but more importantly from disks with high moments of inertia. From fluid film bearings, damping elements are introduced with main diagonal damping d_{xx}, d_{yy} and non-symmetric coupling terms d_{xy}, d_{yx} between the two planes.

The stiffness matrix $\mathbf{K}$ consists mainly of the symmetric matrix part of the beam elements. Additional skew symmetric components have their origin from internal damping and possibly steam excitation. Besides the main stiffnesses (k_{xx}) and (k_{yy}), fluid film bearings may also lead to non-symmetric stiffness coefficients k_{xy}, k_{yx}. Terms with non-symmetric stiffnesses may cause self-excited vibrations with the possibility of unstable rotor systems. Detailed discussion of the different physical effects can be found in rotordynamics textbooks [6].

As an example of a skew symmetric matrix, the effect of gyroscopic moments is considered. In Fig. 10.23, a rigid disk element is shown, characterized by its mass m, polar moment of inertia Θ_p and equatorial moment of inertia Θ_{eq}. Such disk elements may represent impellers or disks with blades in turbo-

machinery, axial bearing disks or other rotating elements. The rotary inertia effects caused by such elements may be of importance, particularly for high moments of inertia $\Theta_p, \Theta_{\text{eq}}$, high running speeds Ω and large tilting angles α_d, β_d of the shaft (Fig. 10.23 and 10.24). Under such circumstances, besides the translatory inertia terms due to mass m, the inertia terms due to tilting motions have to be taken into account. The disk element in Fig. 10.23 is running with constant angular velocity Ω. Its angular motion is described by α_d and β_d and the corresponding velocities are $\dot{\alpha}_d, \dot{\beta}_d$. The angular momentum of the disk consists of three components in the directions of $x-$, $y-$ and $z-$:

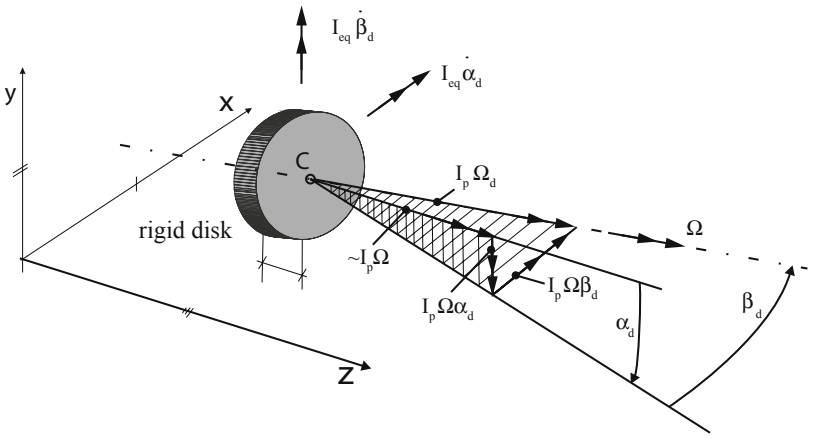


Fig. 10.23. Angular momentum of disk

$$\text{x-direction: } \Theta_{\text{eq}}\dot{\alpha}_d + \Theta_p \Omega \beta_d \tag{10.42a}$$

$$\text{y-direction: } \Theta_{\text{eq}}\dot{\beta}_d - \Theta_p \Omega \alpha_d \tag{10.42b}$$

$$\text{z-direction: } \approx \Theta_p \Omega \tag{10.42c}$$

The time derivatives lead to the corresponding inertia moments in $x-$ and $y-$ directions (Fig. 10.24).

$$\text{x-direction: } \Theta_{\text{eq}}\ddot{\alpha}_d + \Theta_p \Omega \dot{\beta}_d \tag{10.43a}$$

$$\text{y-direction: } \Theta_{\text{eq}}\ddot{\beta}_d - \Theta_p \Omega \dot{\alpha}_d \tag{10.43b}$$

The component in the $z-$ direction is equal to zero. The first terms in (10.43a) and (10.43b) are the usual rotatory inertia terms. They are part of the symmetric mass matrix in Fig. 10.22. The second terms are often referred to as the *gyroscopic moments*. Their size depends on the polar moment of inertia Θ_p, the angular velocity Ω and the tilting velocities $\dot{\alpha}_d, \dot{\beta}_d$. Due to the dependence on $\dot{\alpha}_d, \dot{\beta}_d$, the gyroscopic effects are part of the damping matrix

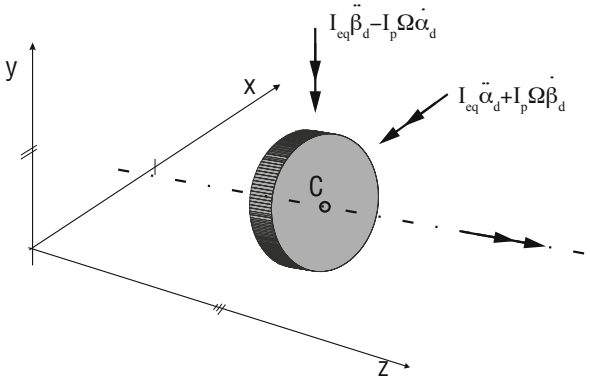


Fig. 10.24. Inertia terms of disk due to tilting

D. They belong to the skew symmetric matrix in Fig. 10.22. In general, all rotating elements – also the beam elements – show these gyroscopic effects. However, in most cases the influence is small due to the small moments of inertia.

Gyroscopic moments have an effect on the natural frequencies of the rotor. With increasing rotational speed Ω, the natural frequencies are split (see Sec. 7.4 on *Influence of Rotor Speed and Gyroscopic Effects*).

The solutions of the equations of motion $\mathbf{M}\ddot{\mathbf{z}} + \mathbf{D}\dot{\mathbf{z}} + \mathbf{K}\mathbf{z} = \mathbf{f}$ describe the vibrations of the rotor system. They can be represented in the time domain or in the frequency domain. In general, the vibrations depend on the system characteristics (inertia, damping, stiffness), the initial conditions and on the time dependent forces acting on the rotor system. It is common practice to subdivide the rotor vibrations into natural and forced vibrations. Natural vibrations are understood as those oscillations that can be observed after application of an initial force, when the right hand side forces $\mathbf{f}(t)$ are equal to zero.

Self-excited vibrations can be considered as natural vibrations of a special type. In this case, the external forces $\mathbf{f}(t)$ are still zero as before. The physical reason for such vibrations is an energy source that transfers energy into the vibration system depending on the frequency of the free vibrations. Typical self-excited vibrations are caused by fluid film bearings and seals in turbines and compressors, by internal damping and by steam excitation.

Forced vibrations are induced by means of external forces $\mathbf{f}(t)$. Of particular interest are unbalance forced vibrations with an excitation, depending on the unbalance and the rotational speed.

In the following discussion, natural and forced vibrations are treated in a separate way. In reality, both motions occur as a superposition of the two parts. However, there may be special operating conditions in which one or the other of the vibration states is dominant.

10.4.5 Natural Vibrations: Natural Frequencies and Mode Shapes

Natural vibrations – including self-excited vibrations – are the solutions of the homogeneous equations of motion:

$$\mathbf{M}\ddot{\mathbf{z}} + \mathbf{D}\dot{\mathbf{z}} + \mathbf{K}\mathbf{z} = 0 \tag{10.44}$$

In this case, the time history $\mathbf{z}(t)$ depends on the system characteristics $\mathbf{M}, \mathbf{D}, \mathbf{K}$ and on the initial conditions (displacements and velocities). Equation 10.44 has a solution of the form

$$\mathbf{z}(t) = \hat{\mathbf{z}} e^{\lambda \mathrm{t}} \tag{10.45}$$

If (10.45) is introduced into (10.44), then the resulting eigenvalue problem

$$\left(\lambda^2 \mathbf{M} + \lambda \mathbf{D} + \mathbf{K}\right) \hat{\mathbf{z}} = 0 \tag{10.46}$$

can be solved by well developed algorithms. As results, we obtain the eigenvalues λ_n and corresponding eigenvectors $\hat{\mathbf{z}}_n$. The number of eigenvalues and eigenvectors is the double of the number of degrees of freedom of the system. Usually, the eigenvalues are complex due to damping effects and self-excitation mechanisms. For each complex eigenvalue, a conjugate complex eigenvalue exists. The corresponding complex eigenvectors are conjugate complex as well:

$$\text{eigenvalues: } \lambda_n = \alpha_n + j\omega_n \quad \bar{\lambda}_n = \alpha_n - j\omega_n \tag{10.47a}$$

$$\text{eigenvectors: } \hat{\mathbf{z}}_n = \mathbf{s}_n + j\mathbf{t}_n \quad \hat{\bar{\mathbf{z}}}_n = \mathbf{s}_n - j\mathbf{t}_n \tag{10.47b}$$

Introducing the conjugate complex solution pairs into (10.45) the superposition leads to a real time dependent solution:

$$\mathbf{z}_n(t) = \hat{\mathbf{z}}_n e^{\mathrm{j}\lambda_n \mathrm{t}} + \hat{\bar{\mathbf{z}}}_n e^{\mathrm{j}\bar{\lambda}_n \mathrm{t}} \tag{10.48}$$

which can also be written

$$\mathbf{z}_n(t) = B_n e^{\alpha_n \mathrm{t}} \left\{\mathbf{s}_n \sin(\omega_n t + \gamma_n) + \mathbf{t}_n \cos(\omega_n t + \gamma_n)\right\} \tag{10.49}$$

This time solution is a part of the overall natural vibrations. It corresponds to the conjugate complex eigenvalue pair. The sign of α_n determines whether this part solution is stable or unstable (Fig. 10.25).

The imaginary part ω_n is the circular natural frequency of the natural vibration $\mathbf{z}_n(t)$. The two constants B_n and γ_n can be determined from the initial conditions. Without the factor $B_n e^{\alpha_n \mathrm{t}}$, the solution $\mathbf{z}_n(t)$ can be considered to be the natural mode shape $\tilde{\mathbf{z}}_n(t)$ of the rotor system described by (10.44):

$$\tilde{\mathbf{z}}_n(t) = \mathbf{s}_n \sin(\omega_n t + \gamma_n) + \mathbf{t}_n \cos(\omega_n t + \gamma_n) \tag{10.50}$$

$\tilde{\mathbf{z}}_n(t)$ contains all displacements and angles along the rotor axis. In general they are time dependent. Finally, the superposition of all natural vibrations

a) stable $\alpha_n < 0$ b) stability limit $\alpha_n = 0$ c) unstable $\alpha_n > 0$

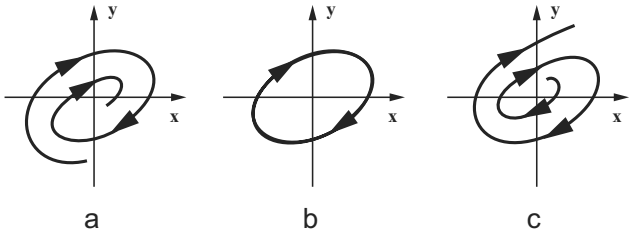


Fig. 10.25. Plane orbit of a rotor point for the natural vibration $\mathbf{z}_n(t)$

$\mathbf{z}_n(t)$ leads to the complete set of natural vibrations (n=1, 2,... N; N is number of degrees of freedom):

$$\mathbf{z}(t) = \sum_{n=1}^{N} \mathbf{z}_n(t) = \sum_{n=1}^{N} B_n e^{\alpha_n t} \left\{ \mathbf{s}_n \sin(\omega_n t + \gamma_n) + \mathbf{t}_n \cos(\omega_n t + \gamma_n) \right\} \tag{10.51}$$

For realistically damped systems, the natural vibrations always decrease (all $\alpha_n < 0$). There are several significant self-excitation mechanisms in rotating machinery that may lead to unstable or self-excited natural vibrations. Such mechanisms as internal damping, fluid film and seal excitations and steam excitation may lead to eigenvalues with positive real parts α_n. If only one real part α_n is positive, this leads to a corresponding increasing natural vibration $\mathbf{z}_n(t)$. With this unstable part solution $\mathbf{z}_n(t)$ the overall natural vibration $\mathbf{z}(t)$ is unstable.

If no damping or self-excitation effects are considered, the equations of motion (10.44) can be described in a simplified form:

$$\mathbf{M}\ddot{\mathbf{z}} + \mathbf{K}\mathbf{z} = 0 \tag{10.52}$$

In this special case, the mass matrix $\mathbf{M}$ contains all inertia terms as before and has a symmetric structure (see Fig. 10.22). The stiffness matrix $\mathbf{K}$ is symmetric as well and describes only the stiffness behavior of the beam elements and the bearing stiffnesses c_{xx}, c_{yy}. All other terms are neglected.

This special simplified rotor system is often investigated as a first step of a rotor design in order to have some initial information about the expected natural frequencies and the corresponding mode shapes. It is often the case that the neglected terms do not strongly influence the natural frequencies and mode shapes. However, nothing can be predicted in this way for the system stability. If rotor systems do not have dominant damping and also have no strong self-excitation mechanisms, then it is quite correct to use (10.52) for the investigation of the natural vibration behavior. Starting from (10.52), the solution form (10.45) leads to the eigenvalue problem

$$(\lambda^2 \mathbf{M} + \mathbf{K})\, \hat{\mathbf{z}} = 0 \tag{10.53}$$

with

$$\text{eigenvalues: } \lambda_n = +j\omega_n \quad \bar{\lambda}_n = -j\omega_n \tag{10.54a}$$

$$\text{eigenvectors: } \hat{\mathbf{z}}_n = j\mathbf{t}_n \quad \hat{\bar{\mathbf{z}}}_n = -j\mathbf{t}_n \tag{10.54b}$$

which finally leads to a time solution for the conjugate complex eigenvalue pair

$$\mathbf{z}_n(t) = B_n \mathbf{t}_n \cos(\omega_n t + \gamma_n) \tag{10.55}$$

The eigenvectors $\mathbf{t}_n$ of (10.53) consist of constant numbers. The eigenvalue problem (10.53) is often expressed in terms of ω_n so that

$$(\mathbf{K} - \omega_n^2 \mathbf{M})\, \hat{\mathbf{z}}_n = 0 \tag{10.56}$$

10.4.6 An Example: Flexible Test Rig Rotor of an Aeroengine

In Fig. 10.26, a flexible test rig rotor of an aeroengine is shown [1, 4]. It is a low pressure turbine of a helicopter, where the blades of the two turbine stages are cut off. This very flexible rotor with a maximum rotational speed of 20000 rpm is supported in two active magnetic bearings, AMB A and AMB B. The total length of the shaft is 1100 mm. Two additional imbalance rings A and B are mounted on the shaft. They allow active balancing during operation, by tangential movements of two rings which both carry unbalance weights [12, 15].

When operating this flexible rotor system up to its maximum rotational speed of 20000 rpm, three critical speeds have to be passed before reaching the normal operating speed range. A suitable rotor model has to be built up in order to simulate the vibrations. In the first stages of analysis, the active control of the magnetic bearings is not considered. However, the stiffnesses of the magnetic bearings are assumed and introduced into the model.

When the shaft is modeled by finite elements, the natural frequencies and the mode shapes of the rotor system at speed $\Omega = 0$ can be calculated. After this, the influence of the rotational speed Ω can be investigated. The rotational speed Ω influences the natural frequencies and mode shapes due to the gyroscopic moments of elements with high moments of inertia.

Forced vibrations due to unbalance forces can then be determined at different shaft positions. They depend on the size of the unbalance and its distribution along the shaft axis. In a later, more detailed analysis, it can be shown how the natural and forced vibrations are influenced by active control.

Finite Element Model

The rotor model consists of beam elements, body elements (masses, disks), stiffnesses and dampers. Figure 10.27 represents a sketch of the finite element model with 106 nodal points and 424 degrees of freedom (displacements and angles). Some additional data are presented in Table 10.1.

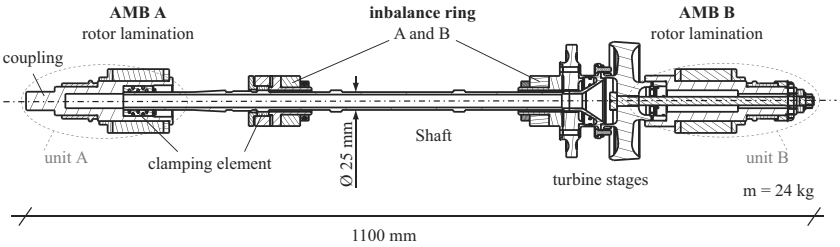


Fig. 10.26. Flexible test rig rotor of an aeroengine

length	(m)	1.100
weight	(kg)	24.165
position of center of gravity (CG)	(m)	0.632
mass moment of inertia (polar)	(kgm)	0.036

Table 10.1. Data of the rotor from the finite element calculation

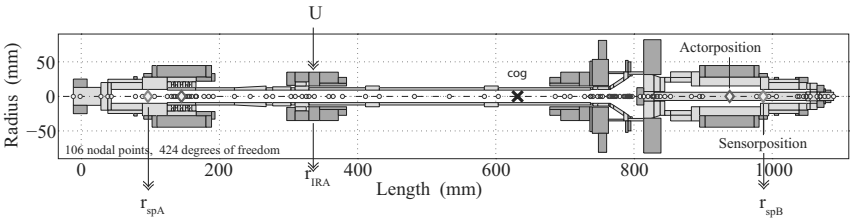


Fig. 10.27. Finite element model with 106 nodal points and 424 degrees of freedom

Using the detailed design drawings, the rotor system matrices can be built up. Calculations for natural frequencies and mode shapes can then be performed at first for zero speed.

Natural Frequencies and Mode Shapes

The calculation of the natural frequencies and mode shapes is a very important step for the prediction of the dynamic behavior. We start with the case of the free-free system (without bearings) and rotational speed $\Omega = 0$. The three first natural frequencies (without rigid body modes) are 50 Hz, 130 Hz and 355 Hz. They are shown with corresponding mode shapes in Fig. 10.28. The figure also indicates the positions of the sensors and actuators. This information is needed for the evaluation of the controllability and observability of the rotor system.

The calculated natural frequencies and mode shapes are often used as reference values for measurements. Experimental modal analysis (see Chap. 11) is usually performed for the free-free boundary condition (very weak support

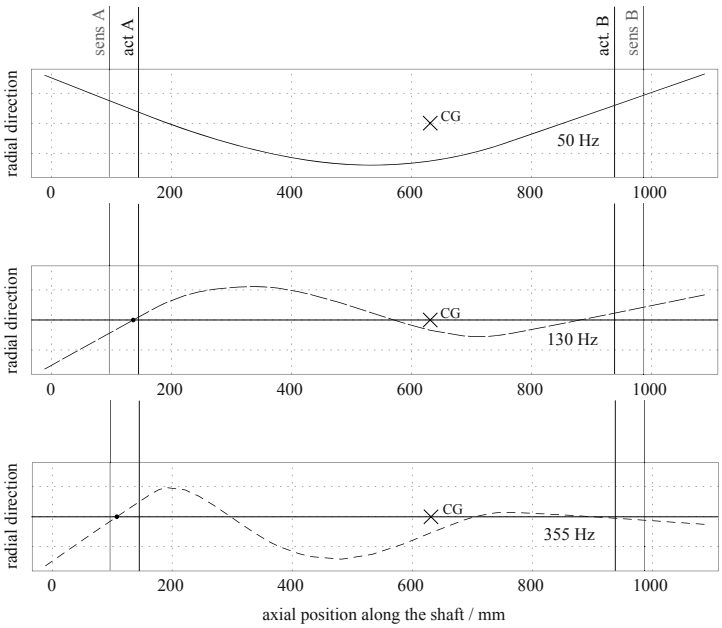


Fig. 10.28. The three first natural frequencies of the free-free rotor system

of shaft) and rotor speed equal zero. If calculated and measured natural frequencies are in good correlation, the model can be considered as good and used for further purposes. In reality, the boundary conditions of a rotor in magnetic bearings are not free. The active magnetic bearing supports the shaft by electromagnetic forces which depend on the control current in the windings and on the air gap. This support condition can also be expressed by a bearing stiffness k_L, which depends on the control parameters. For a specific operational point of the rotor system, the stiffness k_L can be calculated and can then be used for the calculation of natural frequencies and shapes of the elastically supported shaft.

For the active rotor bearing system considered in this model, a stiffness value of $k_L = 1000$ N/mm appears to be relevant for a controller with low amplification. The rotational speed is still assumed $\Omega = 0$. The natural frequencies for this case – including the new modes – are 33 Hz, 57 Hz, 66 Hz, 131 Hz and 357 Hz and the corresponding mode shapes are presented in Fig. 10.29. We have 5 natural frequencies now, compared to 3 in the former case. This apparent increase in number of model modes occurs because, in the first case, we did not consider the two zero frequencies for the rigid body modes.

Due to the fact that the bearing stiffness may change due to the control current, we vary the stiffness parameter k_L in a wide range. Figure 10.30 shows a diagram with the natural frequencies versus the bearing stiffness k_L. This calculation is also for $\Omega = 0$. For the free-free boundary conditions, the bearing

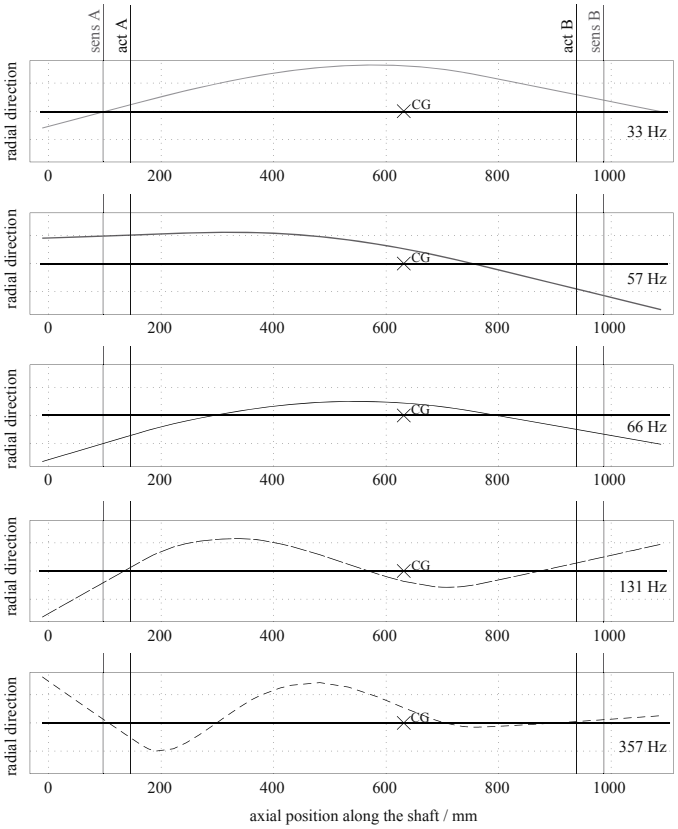


Fig. 10.29. The five natural frequencies of the rotor system with bearing stiffness $k_L = 1000\text{N/mm}$

stiffnesses k_L are equal to zero. Two rigid body mode shapes (translation and tilting) have the natural frequencies zero. The natural frequencies of the bending mode shapes are 50 Hz, 130 Hz and 355 Hz (see also Fig. 10.28).

By increasing the bearing stiffnesses to k_L= 1000 N/mm, the natural frequencies increase too. The originally 0-frequencies of the rigid body mode shapes become 33 Hz and 57 Hz, with the mode shapes shown in Fig. 10.29. These new mode shapes are characterized by the rigid body motion, superimposed by additional bending. The following natural frequencies are 66 Hz (50Hz), 131 Hz (130 Hz) and 357 Hz (355 Hz). The frequencies in parentheses are the natural frequencies for $k_L = 0$. It can be observed that the higher modes do not change very much with increasing bearing stiffness k_L.

If we further increase the bearing stiffness k_L, the natural frequencies will also become higher with changing mode shapes. Finally, if the bearing stiffnesses are very high, the mode shapes will be characterized by zero displacements at the bearing locations, corresponding to clamped/clamped boundary

conditions. The mode shapes for this limit case are shown on the right side of Fig. 10.30. The corresponding natural frequencies for this limit case are: 40 Hz, 125 Hz, 289 Hz and 526 Hz.

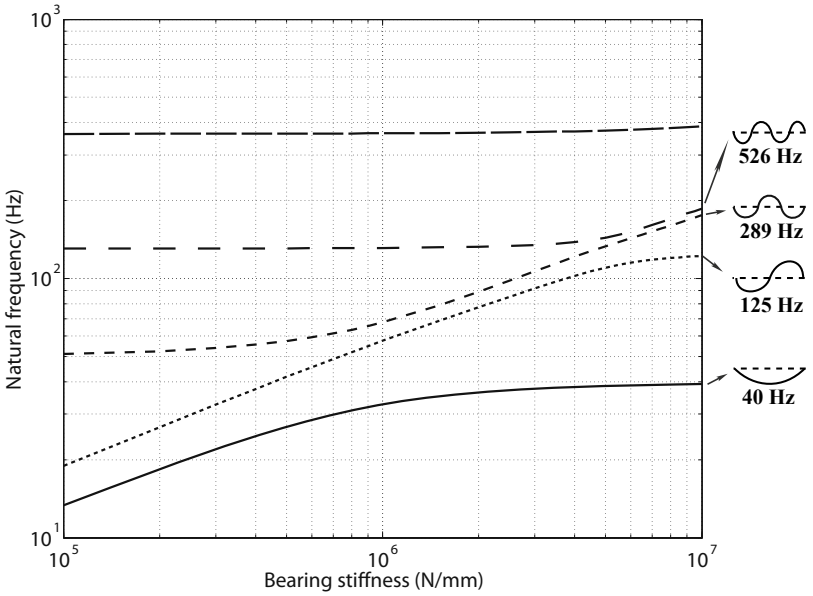


Fig. 10.30. Natural frequencies of the rotor system in dependence of the bearing stiffness k_L

Up to now, the influence of the rotational speed Ω has not been considered. As shown before in Sec. 10.4.4, gyroscopic moments may be of importance if high moments of inertia Θ_p are combined with high rotational speeds Ω and high tilting angles α_d, β_d. Figure 10.31 illustrates how the natural frequencies of the considered rotor system with bearing stiffness $k_L = 0$ change with increasing rotational speed Ω of the rotor. Starting with the well known natural frequencies 50 Hz, 130 Hz and 355 Hz at $\Omega = 0$, the frequencies are split into forward and backward frequencies.

In a diagram of natural frequency *versus* rotational frequency – often called a *Campbell diagram* – it is customary to also present the rotational frequency line, $\omega = \Omega$. The points where this line crosses the natural frequency curves show where resonances are expected. Of particular importance are the intersections with the forward frequency curves, due to the fact that the unbalance excitation forces are able to excite these forward natural frequencies. We will return to this point later when we consider forced vibrations.

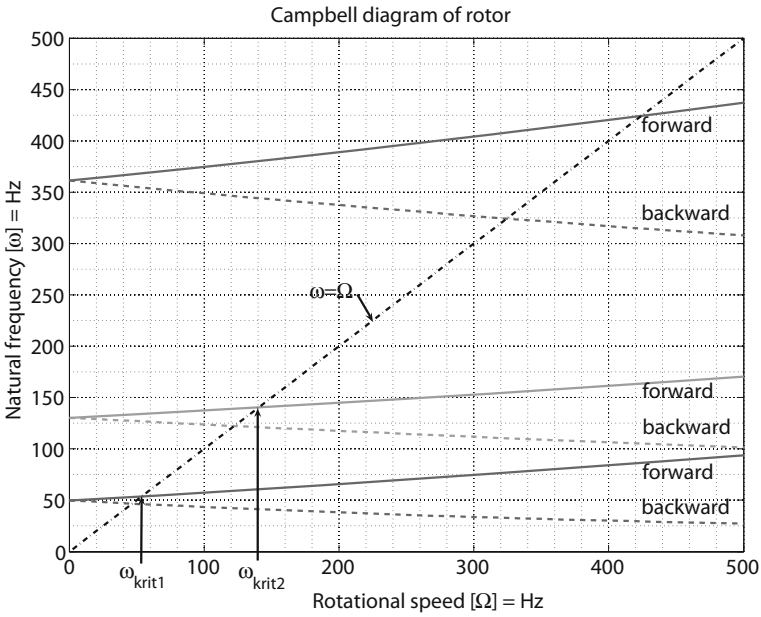


Fig. 10.31. Campbell diagram of the rotor

10.4.7 Forced Unbalance Vibrations

Forced vibrations are caused by forces $\mathbf{f}(t)$ of the right hand side terms in the equations of motion:

$$\mathbf{M}\ddot{\mathbf{z}} + \mathbf{D}\dot{\mathbf{z}} + \mathbf{K}\mathbf{z} = \mathbf{f}(t) \tag{10.57}$$

Such forces are either generated by unbalance, by the working process (e.g. turbo-machinery, milling spindle), or by actuators in case of active systems (e.g. by active magnetic bearings). In this chapter, we mainly consider unbalance forces as a source of excitation. The important case of actuator forces will be treated in a later chapter, when the complete control loop has to be included. Unbalance forces are described as force functions with the rotational frequency Ω of the shaft.

$$\mathbf{f}(t) = \mathbf{f}_c \cos(\Omega t) + \mathbf{f}_s \sin(\Omega t) \tag{10.58}$$

The vectors $\mathbf{f}_c$ and $\mathbf{f}_s$ depend on the unbalance distribution along the shaft and on the rotational frequency Ω. For the case of a constant speed rotor (Ω = constant) the natural vibrations decrease if the rotor system is stable and damped. The system response is then determined only by the stationary unbalance response, if no other disturbances are present. The unbalance response is a function of all system parameters $\mathbf{M}, \mathbf{D}, \mathbf{K}$, but also depends on the exciter forces $\mathbf{f}_c, \mathbf{f}_s$. If we describe the equations of motion in the following way

$$\begin{aligned}\mathbf{M}\ddot{\mathbf{z}} + \mathbf{D}\dot{\mathbf{z}} + \mathbf{K}\mathbf{z} &= \mathbf{f}_c \cos(\Omega t) + \mathbf{f}_s \sin(\Omega t) \\ &= Re[\mathbf{f}_c - j\mathbf{f}_s](\cos(\Omega t) + j\sin(\Omega t)) \\ &= Re[\bar{\mathbf{f}} e^{\mathrm{j}\Omega \mathrm{t}}]\end{aligned} \tag{10.59}$$

then the solution of this linear equation system has the form

$$\begin{aligned}\mathbf{z}(t) &= \mathbf{z}_c \cos \Omega(t) + \mathbf{z}_s \sin \Omega(t) \\ &= Re[\mathbf{z}_c - j\mathbf{z}_s](\cos(\Omega t) + j\sin(\Omega t)) \\ &= Re[\bar{\mathbf{z}} e^{\mathrm{j}\Omega \mathrm{t}}]\end{aligned} \tag{10.60}$$

After twice differentiating $\mathbf{z}(t)$ with respect to time t and introducing the expressions into (10.57) we obtain the complex equation system

$$(\mathbf{K} - \Omega^2 \mathbf{M} + j\Omega \mathbf{D})\bar{\mathbf{z}} = \bar{\mathbf{f}} \tag{10.61}$$

which can be solved by means of a complex Gaussian-elimination algorithm for each of the selected rotational speeds Ω. In this manner, the unknowns $\mathbf{z}_c, \mathbf{z}_s, \bar{\mathbf{z}}$ can be found. With the complex solution $\bar{\mathbf{z}}$ from (10.61), the time dependent solution of each component of $\mathbf{z}(t)$ has the form

$$z_j(t) = z_{\mathrm{cj}} \cos \Omega t + z_{\mathrm{sj}} \sin \Omega t = \hat{z}_j \sin(\Omega t + \gamma_j) \tag{10.62}$$

with

$$\hat{z}_j = \sqrt{z_{\mathrm{cj}}^2 + z_{\mathrm{sj}}^2} \tag{10.63}$$

and

$$\gamma_j = \tan^{-1} \frac{z_{\mathrm{sj}}}{z_{\mathrm{cj}}} \tag{10.64}$$

$z_j(t)$ may belong to a motion in x-direction (horizontal) or to a motion in y-direction (vertical).

Unbalance Response for the Flexible Test Rig Rotor of an Aeroengine

For the example of the flexible test rig rotor of Fig. 10.26, we assume unbalance forces at the two locations of the balancing devices A and B. The unbalance response is considered at the sensor locations of the two bearings AMB A and AMB B and of the shaft center. Figure 10.32 shows amplitudes and phases as functions of the rotational speed for the three response locations due to unbalance excitation at the above-mentioned balancing unit A. The assumed values for the bearing stiffnesses and bearing damping values are $k_L = 8.2 \times 10^5$ N/m and $d_L = 100$ Ns/m. These values correspond approximately to the stiffness and damping characteristics of the active magnetic bearing.

During run-up, the frequency of excitation is equal to the frequency of rotation. When this frequency coincides with one of the natural frequencies,

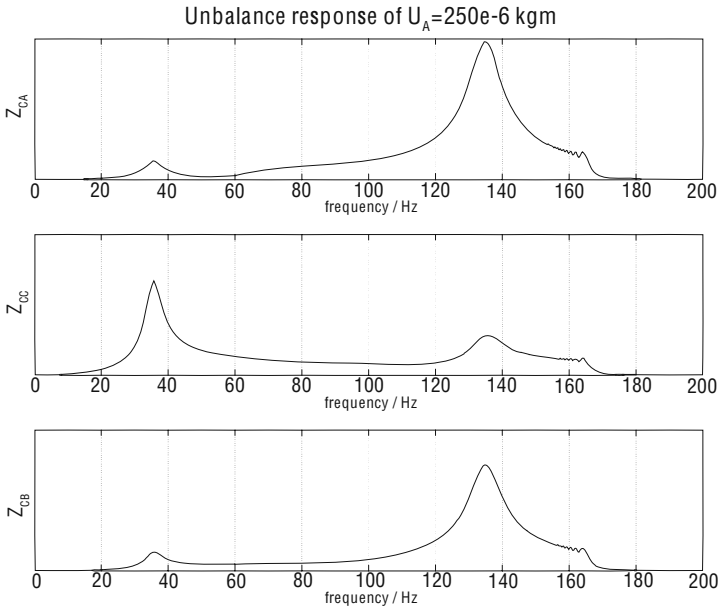


Fig. 10.32. Run up curve due to unbalance excitation at balancing unit A

the rotor is running in a resonance condition or in a critical speed with an amplification of the rotor amplitudes. Figure 10.32 shows such resonances at 37 Hz and 135 Hz. The other resonances are well damped. Figure 10.33 presents a very similar response behavior when the unbalance excitation is at balancing unit B.

The run-up can also be presented by plotting the rotor amplitudes *versus* time. In Fig. 10.34, the amplitudes for the three locations AMB A, AMB B and center of the shaft are shown versus time. When the rotor frequency is passing one of the natural frequencies, the rotor amplitudes increase and then subsequently decrease. The lower diagram in Fig. 10.34 illustrates that the rotor is accelerated in such a manner that the rotational speed increases linearly with time.

If the solution elements of $\mathbf{z}_c, \mathbf{z}_s$ for one location of the rotor system – but in two perpendicular directions – are superimposed for a constant rotational speed Ω the resulting plane motion is, in general, an elliptical orbit characterized by the two main axes and an angle relative to the coordinate axis x. Figure 10.35 shows such an elliptical orbit in a forward motion mode.

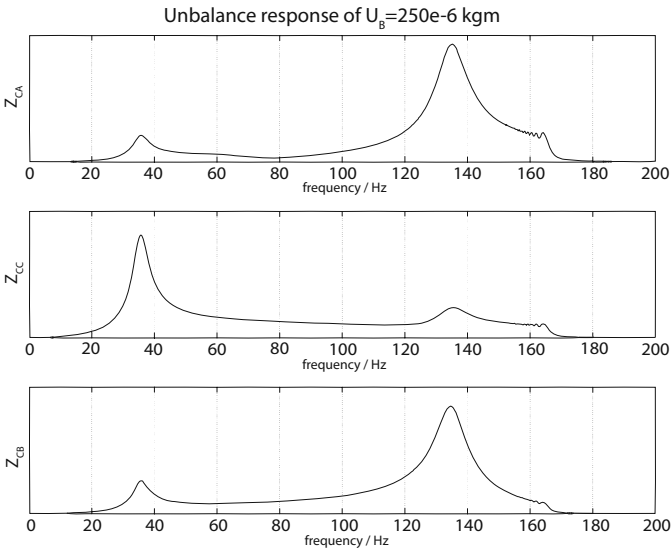


Fig. 10.33. Run up curve due to unbalance excitation at balancing unit B

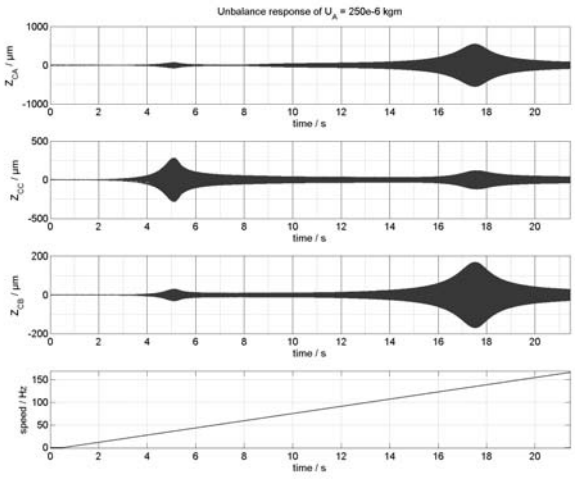
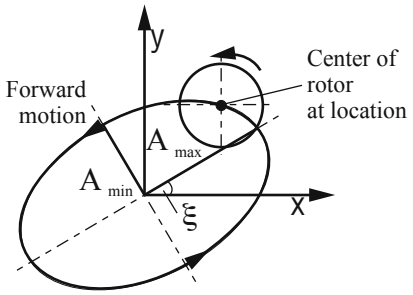


Fig. 10.34. Run up due to unbalance excitation in time domain



$A_{\max}$ major main axis of ellipse
$A_{\min}$ minor main axis of ellipse
ξ angle of major main axis against x-axis

Fig. 10.35. Plane elliptical orbit of a shaft location due to forced unbalance excitation

10.5 Flexible Rotor with Active Magnetic Bearings

10.5.1 Forces and Displacements

We now assume that a general flexible rotor is running in two active magnetic bearings AMB A and AMB B (Fig. 10.36). In order to build up the equations of motion for this rotor-bearing system, we introduce the forces of the two actuators $\mathbf{f}_a$:

$$\mathbf{f}_a = \begin{bmatrix} \mathbf{f}_A \\ \mathbf{f}_B \end{bmatrix}_a = \begin{bmatrix} f_{\mathrm{Ax}} \\ f_{\mathrm{Ay}} \\ f_{\mathrm{Bx}} \\ f_{\mathrm{By}} \end{bmatrix}_a \tag{10.65}$$

and the corresponding displacements $\mathbf{z}_a$:

$$\mathbf{z}_a = \begin{bmatrix} \mathbf{z}_A \\ \mathbf{z}_B \end{bmatrix}_a = \begin{bmatrix} z_{\mathrm{Ax}} \\ z_{\mathrm{Ay}} \\ z_{\mathrm{Bx}} \\ z_{\mathrm{By}} \end{bmatrix}_a \tag{10.66}$$

which are presented in Fig. 10.37

Measurements of such bearing displacements are needed for the feedback in the control loop of the active system. Due to the fact that the displacements of the bearing centers usually cannot be measured, we introduce the displacements of the sensor locations (see Fig. 10.37, lower figure):

$$\mathbf{z}_S = \begin{bmatrix} \mathbf{z}_{\mathrm{SA}} \\ \mathbf{z}_{\mathrm{SB}} \end{bmatrix} = \begin{bmatrix} z_{\mathrm{SAx}} \\ z_{\mathrm{SAy}} \\ z_{\mathrm{SBx}} \\ z_{\mathrm{SBy}} \end{bmatrix} \tag{10.67}$$

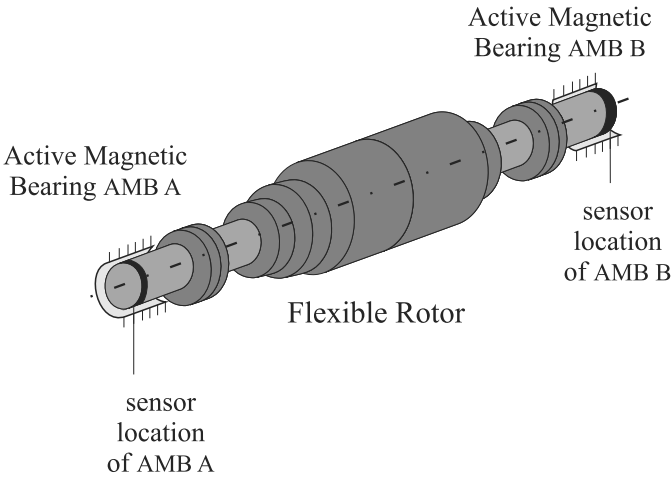


Fig. 10.36. Flexible Rotor with Active Magnetic Bearings

10.5.2 Equations of motion

Following the finite element derivation for a flexible rotor system of Sec. 10.4, we obtain the following equations of motion with two force vectors on the right hand side:

$$\mathbf{M}\ddot{\mathbf{z}} + \mathbf{D}\dot{\mathbf{z}} + \mathbf{K}\mathbf{z} = \mathbf{f}_u + \mathbf{f}_{\text{AMB}} \tag{10.68}$$

The vector $\mathbf{f}_u$ expresses the unbalance forces along the flexible rotor system. The force vector $\mathbf{f}_{\text{AMB}}$ contains the bearing forces $\mathbf{f}_a$ from (10.65) applied at the correct degrees of freedom for the overall rotor system. The relation between the force vector $\mathbf{f}_{\text{AMB}}$ and the force vector $\mathbf{f}_a$ can be described by a transformation matrix $\mathbf{T}_A^T$:

$$\mathbf{f}_{\text{AMB}} = \mathbf{T}_A^T \mathbf{f}_a \tag{10.69}$$

With the same matrix, we can also describe the local displacement vector $\mathbf{z}_a$ from (10.66) in terms of the overall displacement vector $\mathbf{z}$:

$$\mathbf{z}_a = \mathbf{T}_A \cdot \mathbf{z} \tag{10.70}$$

and, in a similar way, the vector $\mathbf{z}_s$ of the sensor locations:

$$\mathbf{z}_s = \mathbf{T}_S \cdot \mathbf{z} \tag{10.71}$$

It is well known that the bearing force vector $\mathbf{f}_a$ is a nonlinear function of the control currents in the bearings and on the air gaps. For small derivations around a static equilibrium point, it is possible to describe this relation in a linearized form:

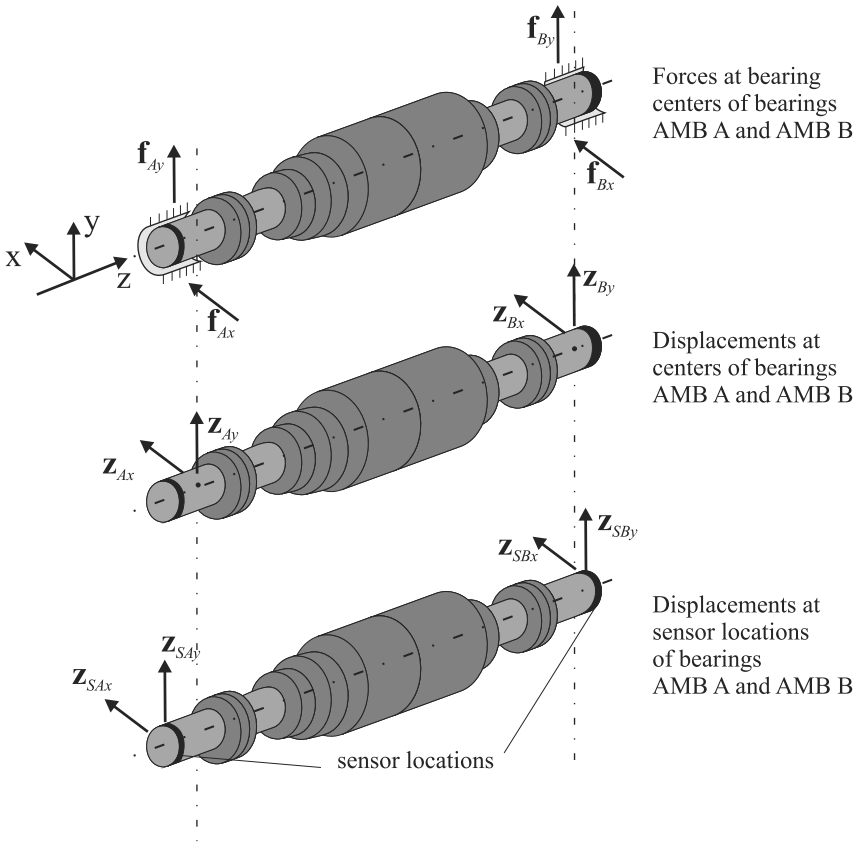


Fig. 10.37. Forces and Displacements of the two Active Magnetic Bearings AMB A and AMB B

$$\mathbf{f}_a = \begin{bmatrix} \mathbf{f}_A \\ \mathbf{f}_B \end{bmatrix}_a = k_s \begin{bmatrix} \mathbf{z}_A \\ \mathbf{z}_B \end{bmatrix} + k_i \begin{bmatrix} \mathbf{i}_A \\ \mathbf{i}_B \end{bmatrix} \tag{10.72a}$$

$$\mathbf{f}_a = k_s \mathbf{z}_a + k_i \mathbf{i}_a \tag{10.72b}$$

where the vector of the coil currents is related to the coordinates of $\mathbf{z}_a$:

$$\mathbf{i}_a = \begin{bmatrix} \mathbf{i}_A \\ \mathbf{i}_B \end{bmatrix}_a = \begin{bmatrix} i_{\mathrm{Ax}} \\ i_{\mathrm{Ay}} \\ i_{\mathrm{Bx}} \\ i_{\mathrm{By}} \end{bmatrix} \tag{10.73}$$

Combining (10.69) with (10.72), we obtain

$$\mathbf{f}_{\mathrm{AMB}} = \mathbf{T}_A^T \mathbf{f}_a = \mathbf{T}_A^T \cdot [k_s \mathbf{z}_a + k_i \mathbf{i}_a] \tag{10.74}$$

In (10.74), it is assumed that the bearing parameters k_s and k_i are the same for all four bearing forces. If they are different, two parameter matrices have to be introduced.

If we introduce (10.70) into (10.74) and the force vector $\mathbf{f}_{\mathrm{AMB}}$ into (10.68), it follows that

$$\mathbf{M}\ddot{\mathbf{z}} + \mathbf{D}\dot{\mathbf{z}} + \left[\mathbf{K} - k_s \mathbf{T}_A^T \mathbf{T}_A\right] \mathbf{z} = \mathbf{f}_u + k_i \mathbf{T}_A^T \mathbf{i}_a \tag{10.75}$$

An additional stiffness matrix

$$\mathbf{K}_a = -k_s \mathbf{T}_A^T \mathbf{T}_A \tag{10.76}$$

is caused due to the active magnetic bearings. It has a negative sign, signifying a destabilizing effect from the electromagnetic forces.

On the right hand side of (10.75), we find the second part of the electrodynamic force which is dependant on the coil current $\mathbf{i}_a$ of the bearings. This part can be used to control the bearing forces and to stabilize the rotor bearing system (see Chap. 12 on *Control of Flexible Rotors*).

10.5.3 State Space Representation of the Flexible Rotor with Active Magnetic Bearings

Modern control strategies are often based on a state space presentation. Therefore, we show how the equations of motion can be transfered into this form. We start with (10.68) and define the state space vector

$$\mathbf{x}_s = \begin{bmatrix} \mathbf{z} \\ \dot{\mathbf{z}} \end{bmatrix} \text{ and } \dot{\mathbf{x}}_s = \begin{bmatrix} \dot{\mathbf{z}} \\ \ddot{\mathbf{z}} \end{bmatrix} \tag{10.77}$$

By expressing $\ddot{\mathbf{z}}$ from (10.68)

$$\ddot{\mathbf{z}} = \mathbf{M}^{-1}\mathbf{f}_u + \mathbf{M}^{-1}\mathbf{f}_{\mathrm{AMB}} - \mathbf{M}^{-1}\mathbf{D}\dot{\mathbf{z}} - \mathbf{M}^{-1}\mathbf{K}\mathbf{z} \tag{10.78}$$

and introducing $\mathbf{f}_{\mathrm{AMB}}$ from (10.74), it is possible to transfer (10.68) into the first order form

$$\begin{bmatrix} \dot{\mathbf{z}} \\ \ddot{\mathbf{z}} \end{bmatrix} = \begin{bmatrix} 0 & I \\ -\mathbf{M}^{-1}\left(\mathbf{K} - \mathbf{K}_A\right) & -\mathbf{M}^{-1}\mathbf{D} \end{bmatrix} \begin{bmatrix} \mathbf{z} \\ \dot{\mathbf{z}} \end{bmatrix} + \begin{bmatrix} 0 \\ \mathbf{M}^{-1} \end{bmatrix} k_i \mathbf{T}_A^T \mathbf{i}_a + \begin{bmatrix} 0 \\ \mathbf{M}^{-1} \end{bmatrix} \mathbf{f}_u$$

$$\dot{\mathbf{x}}_s = \mathbf{A}_s \mathbf{x}_s \; + \; \mathbf{B}_{\mathrm{SA}} \mathbf{i}_a \; + \; \mathbf{B}_{\mathrm{SU}} \mathbf{f}_u \tag{10.79}$$

$\mathbf{A}_s$ is the system matrix and consists of $\mathbf{M}, \mathbf{D}, \mathbf{K}$ and the AMB-stiffness matrix $\mathbf{K}_a$. $\mathbf{B}_{\mathrm{SA}}$ and $\mathbf{B}_{\mathrm{SU}}$ are input matrices for the bearing currents $\mathbf{i}_a$ and the unbalance forces $\mathbf{f}_u$. As a second state space equation, we define the output relations. $\mathbf{y}_s$ is the vector with the measured displacements at the sensor locations $\mathbf{z}_s$.

$$\mathbf{y}_s = \mathbf{z}_s = [\mathbf{T}_s \; 0] \begin{bmatrix} \mathbf{z} \\ \dot{\mathbf{z}} \end{bmatrix} \tag{10.80}$$

$$\mathbf{y}_s = \mathbf{z}_s = \mathbf{C}_s \mathbf{x}_s \tag{10.81}$$

With $\mathbf{z}_s$ and $\mathbf{i}_a$, we have the connecting signals to the controller (input $\mathbf{z}_s$, output$\mathbf{i}_a$). Figure 10.38 shows the state space idea in a block diagram. Different controller strategies can now be applied (see Chap. 12 on *Control of Flexible Rotors*).

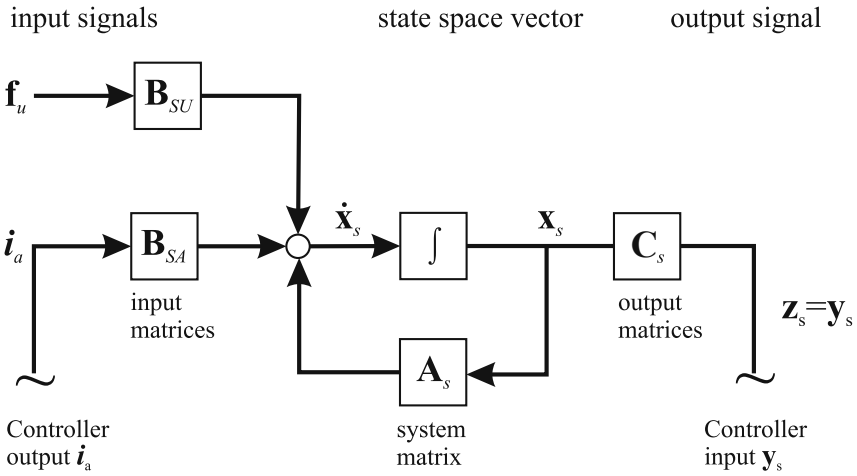


Fig. 10.38. State Space Presentation of Rotor Bearing System

10.6 Reduction of Finite Element Models

To take advantage of the precise description of the structural dynamics of a FE model it has to be transferred to the controller design software. Since the FE model can have many DOFs for complex structures, its order should be reduced significantly. Reduction techniques have been developed in two disciplines, namely structural dynamics and control.

The techniques developed in structural dynamics are denoted substructure techniques or component mode synthesis. Well-known are methods by Guyan, Hurty and Craig-Bampton. They aim at a good approximation of the global static and dynamic response. Criteria used in this field are the accuracy of the natural modes and the frequencies of the reduced order equations of motion [5]. Furthermore, exact static response is a usual requirement. The advantage of these techniques is their reliable numerical implementation with existing FE software.

Control theory provides reduction techniques for state-space systems. In contrast to the substructure methods, state-space methods focus on the approximation of the input-output response of the system. Since only a few interface DOFs are of interest, many modes may turn out to be weakly observable and controllable and a high degree of reduction may be obtained. Balanced reduction in particular aims at the minimization of the maximum deviation of the frequency response of the reduced system from the original system. It has become the standard technique for reduction of state-space systems because it is almost optimal in this sense. In opposition to substructure techniques, reduction methods in state-space are still lacking implementations capable of handling large scaled systems.

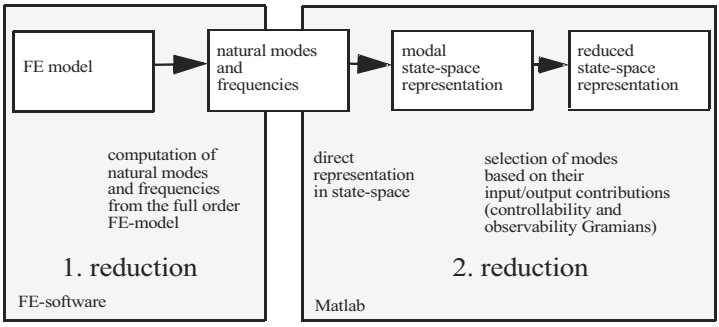


Fig. 10.39. Reduction

The numerical inadequacy of state-space techniques and the demand to export the data at suitable file size make it indispensable to perform a first reduction with component mode synthesis methods within the FE software. A second reduction is usually performed by state-space techniques within the controller design software (Fig. 10.39).

10.6.1 Substructure Techniques

The techniques for the first step, the reduction of equations of motion are denoted *substructure techniques* or *component mode synthesis*. Several methods, suitable for different applications, coexist.

Component mode synthesis is a generalized framework for the notation of substructure techniques. It covers the methods like Gyan condensation, modal truncation and Hurty reduction. A detailed description is given by Craig [2]. We assume a large scaled equation of motion of the mechanism

$$\mathbf{M}\ddot{\mathbf{z}} + \mathbf{D}\dot{\mathbf{z}} + \mathbf{K}\mathbf{z} = \mathbf{f} \tag{10.82}$$

given from FE modelling.

The basic idea for the system synthesis is the representation of the physical DOFs $\mathbf{z}$ in terms of generalized DOFs $\mathbf{z}$ by the transformation

$$\mathbf{z} = \psi \mathbf{p} \tag{10.83}$$

$$\psi^T \mathbf{M} \psi \ddot{\mathbf{p}} + \psi^T \mathbf{D} \psi \dot{\mathbf{p}} \psi^T \mathbf{K} \psi \mathbf{p} = \psi^T \mathbf{f} \tag{10.84}$$

which is of the order of the number of selected component modes. Different types of modes can be considered. Normal modes are eigenvectors from the eigenproblem. Fixed-interface modes are required for the Hurty and Craig-Bampton methods.

A constrained mode is the static deformation of the structure, when a unit displacement is applied to one DOF of the interface set while the remaining DOFs are restrained and the interior DOFs are force free. A more detailed description of the reduction can be found in [2].

10.6.2 Balanced Reduction

Assume a high order system given in state-space representation

$$\dot{\mathbf{x}} = \mathbf{A}\mathbf{x} + \mathbf{B}\mathbf{f}$$
$$\mathbf{y} = \mathbf{C}\mathbf{x} + \mathbf{D}\mathbf{f}$$

where $\mathbf{f}$ is the vector of inputs, in this case forces and $\mathbf{y}$ is the vector of outputs, in this case displacements, velocities and accelerations. The observability and controllability of the states is quantified by the controllability and observability Gramians

$$\mathbf{P} = \int_0^\infty e^{\mathrm{At}} \mathbf{B}\mathbf{B}^T e^{A^T t} \mathbf{d}t \tag{10.85}$$

and

$$\mathbf{Q} = \int_0^\infty e^{A^T t} \mathbf{C}^T \mathbf{C} e^{\mathrm{At}} \mathbf{d}t \tag{10.86}$$

Simply stated, the diagonal elements of P are the energy that reaches the states when all inputs are excited independently and with equal energy. The diagonal elements of Q are the minimum energy to obtain a certain equal level of energy at any output. The off-diagonal elements reflect the coupling of the states. The Gramians can be computed by solving the Lyapunov equations

$$\mathbf{A}\mathbf{P} + \mathbf{P}\mathbf{A}^T = -\mathbf{B}\mathbf{B}^T \tag{10.87}$$

and

$$\mathbf{A}^T\mathbf{Q} + \mathbf{Q}\mathbf{A} = -\mathbf{C}^T\mathbf{C} \tag{10.88}$$

It can be taken from (10.85) and (10.86) that Gramians only exist for stable systems. The reduction of unstable systems can be approached in three

ways: the decomposition in a stable and an unstable part, the stabilization in closed loop interconnection [16] and the generalization of Gramians to unstable systems [17]. A system is denoted *balanced* if the Gramians are diagonal and equal $\mathbf{P} = \mathbf{Q} = \text{diag}\,(\sigma_l)$. Any representation can be balanced by a state transformation $\mathbf{x} = \mathbf{T}\mathbf{x}'$, if no uncontrollable or unobservable states exist. The transformation matrix $\mathbf{T}$ can be computed from the Gramians e.g. by singular value decomposition.

The diagonal elements σ_l of the balanced Gramians are denoted *Hankel singular values*. They are a consistent measure of the controllability and observability of a state, whereas an isolated analysis of controllability and observability is not unique. For the purpose of reduction, the state pairs are divided into two sets based on the Hankel singular values, where the set k contains the states to be kept, showing large Hankel singular values and D is the set of the states to be deleted, showing small Hankel singular values:

$$\begin{bmatrix}\dot{\mathbf{x}}_k\\ \dot{\mathbf{x}}_d\end{bmatrix} = \begin{bmatrix}\mathbf{A}_{\mathrm{kk}}\mathbf{A}_{\mathrm{kd}}\\ \mathbf{A}_{\mathrm{dk}}\mathbf{A}_{\mathrm{dd}}\end{bmatrix}\begin{bmatrix}\mathbf{x}_k\\ \mathbf{x}_d\end{bmatrix} + \begin{bmatrix}\mathbf{B}_k\\ \mathbf{B}_d\end{bmatrix}\mathbf{f}, \mathbf{y} = [\mathbf{C}_k\mathbf{C}_d]\begin{bmatrix}\mathbf{x}_k\\ \mathbf{x}_d\end{bmatrix} + \mathbf{D}\mathbf{f} \tag{10.89}$$

Two methods exist to obtain a reduced order model - truncation and singular perturbation. Truncation assumes that the states $\mathbf{x}_d = 0$. The reduced order system is simply

$$\dot{\mathbf{x}} = \mathbf{A}_{\mathrm{kk}}\mathbf{x}_k + \mathbf{B}_k\mathbf{f} \text{ and } \mathbf{y} = \mathbf{C}_k\mathbf{x}_k + \mathbf{D}\mathbf{F}$$

Singular perturbation takes the static contribution of $\mathbf{x}_d$ into account by assuming $\dot{\mathbf{x}}_d = 0$ instead of $\mathbf{x}_d = 0$. This leads to an approximation with exact static gain

$$\dot{\mathbf{x}}_k = \left(\mathbf{A}_{\mathrm{kk}} - \mathbf{A}_{\mathrm{kd}}\mathbf{A}_{\mathrm{dd}}^{-1}\mathbf{A}_{\mathrm{dk}}\right)\mathbf{x}_k + \left(\mathbf{B}_k - \mathbf{A}_{\mathrm{kd}}\mathbf{A}_{\mathrm{dd}}^{-1}\mathbf{B}_d\right)\mathbf{f} \tag{10.90}$$

$$\mathbf{y} = \left(\mathbf{C}_k - \mathbf{C}_d\mathbf{A}_{\mathrm{dd}}^{-1}\mathbf{A}_{\mathrm{dk}}\right)\mathbf{x}_k + \left(\mathbf{D} - \mathbf{C}_d\mathbf{A}_{\mathrm{dd}}^{-1}\mathbf{B}_d\right)\mathbf{f} \tag{10.91}$$

A very important property of balanced reduction is the fact that *error bounds* can be given prior to reduction. A detailed description of the balanced reduction is given in [7, 16, 17].

10.7 Closing Remarks

The history of rotordynamics covers several interesting stages. At the beginning (1920 to 1950), the vibration related to the rotor's structural dynamics was mainly studied without detailed concern for the bearings. The calculation of critical speeds for flexible rotors was the most important task at this time.

In the early 1960s, attention was focused on hydrodynamic bearings and, related to this, to stability problems. Besides the routines for the calculation of forced vibrations, computer routines were developed in order to predict the rotor bearing stability behavior [3].

Instability problems were experienced with various high performance rotating machines in the 1970s due to the influence of other fluid structure interaction forces, e. g. forces due to liquid and gas seals and forces in impellers and turbines.

Today, well developed rotordynamic models and the corresponding computational tools are available. They take into account all of the important phenomena including the structure (rotor and housing), the bearings, fluid structure interactions and other important phenomena like gyroscopic forces, shear deformation, and so forth. As shown in this chapter, simplified models and more detailed finite element models are well suited to the prediction of vibration of flexible rotors and more general vibrations of rotating machinery.

Considering all previous investigations of different complex rotordynamic phenomena and the development of rotordynamic models and calculation procedures, it may appear that the research field of rotordynamics can be closed. However the two main international conferences concerning rotordynamics: the IFToMM Conferences *Rotordynamics* [8] [9] and the IMECHE conferences *Vibrations in Rotating Machinery* [10] [11] as well as several national conferences, demonstrate clearly that rotordynamics is still an interesting field of research and an important area for engineers in practice. The main program topics of the international and national conferences show, besides the traditional areas, particularly new areas in rotordynamics, including:

- Smart machines with active components for vibration control and active damping. Besides active magnetic bearings new actuator types like Piezoactuators and active Fluid actuators are under investigation.
- Electromechanical interactions, e. g. in rotating electrical machines.
- Condition monitoring and model based machine diagnostics.
- Modal testing and new identification procedures for the determination of better rotordynamic coefficients, e. g. for fluid structure interactions.
- Micromachines

The latest trends in research and practice will be presented and discussed between machine manufactures, operators and scientists at the rotordynamics conferences and will stimulate further research and development in a theoretically and technically challenging area.

References

1. K. Adler, Ch. Schalk, R. Nordmann, and B. Aeschlimann. Active balancing of a supercritical rotor on active magnetic bearings. In H. Bleuler and G. Genta, editors, *Proc. 10th Internat. Symp. on Magnetic Bearings*, pages 49–54, Aug. 2006.
2. R. Craig. Substructure methods in vibration. In *J. Vib. Acoust.* Vol 117, Iss. B, pages 207-213, June 1995.
3. D. Childs. *Turbomachinery Rotordynamics: Phenomena, Modeling, and Analysis.* John Wiley and Sons, 1993.

4. F. Fomi-Wamba. Active balancing of a flexible rotor in active magnetic bearings. In *ISMB11*, Japan, Aug. 2008.
5. P. De Fonseca, D. Vandepitte, H. Van Brussel, and P. Sas. Dynamic model reduction of a flexible three-axis milling machine. In *Int. Conf. on Noise and Vibration Engineering, ISMA23*, pages 185–194, Leuven, Belgium, 1998.
6. R. Gasch, R. Nordmann, and H. Pfützner. *Rotordynamik*. Springer-Verlag, 2001.
7. M. Green and D.J.N. Limebeer. Linear robust control. In *Prentice Hall, Englewood Cliffs*, 1995.
8. IFToMM. Rotordynamics. Darmstadt, 1998.
9. IFToMM. Rotordynamics. Sydney, 2002.
10. IMECHE. Vibrations in rotating machinery. 1996.
11. IMECHE. Vibrations in rotating machinery. 2004.
12. W. Kellenberger. *Elastisches Wuchten*. Springer-Verlag, 1987.
13. E. Krämer. *Maschinendynamik*. Springer-Verlag, 1984.
14. E. Krämer. *Dynamics of Rotors and Foundations*. Springer-Verlag, 1993.
15. H. Schneider. *Auswuchttechnik, mit DIN ISO 1940-1 und DIN ISO 11342*. VDI-Verlag, Düsseldorf, 2003.
16. P. Wortelboer. *Frequency-weighted Balanced Reduction of Closed-loop Mechanical Servo-Systems: Theory and Tools*. PhD thesis, Delft University of Technology, 1994.
17. K. Zhou, J.C. Doyle, and K. Glover. Robust and optimal control. In *Prentice Hall, Upper Saddle River, NJ*, 1996.

11

Identification

Rainer Nordmann

11.1 Introduction

Rotordynamics tools for computer simulations are available nowadays, usually based on the Finite Element method. These routines allow inclusion of all important components like shafts, impellers, bearings, seals etc. and take into consideration corresponding effects such as inertia, damping, stiffness, gyroscopics, unbalance and fluid structure interaction forces [7]. They predict modal parameters like natural frequencies, damping values, mode shapes and unbalance and transient vibrations as well. While these powerful tools themselves usually work without difficulties, problems more often occur in finding the correct input data. In particular, not all of the physical parameters are available from theoretical derivations. This is especially true for rotor designs with complicated geometry, shrink fits, additional masses etc. and for the various fluid structure interactions in fluid bearings, squeeze film dampers, seals, impellers etc. described by rotordynamic coefficients. In such cases, the required data have to be taken from former experience or have to be determined experimentally via identification procedures.

Identification techniques have already been used in various applications in order to find modal parameters of rotor systems (with and without rotation) and rotordynamic coefficients (stiffness, damping, inertia) e.g. in bearings and seals. A main identification technique is to excite the system under consideration with known forces (input) and to measure the response (output), and to use the measured input/output relations to identify unknown system properties [2]. One of the main obstacles to work with identification techniques in rotordynamics is the excitation of a rotating structure during operation. On the one side it is not easy to have access to the rotor and on the other side the force measurement is difficult, especially when a machine is running with full power and speed and the signal to noise ratio is bad. In some recent investigations active magnetic bearings (AMB's) have been used in order to solve this difficult task [1, 3, 4, 5, 6, 10]. These new techniques appear to be very promising, because AMB's do not only support the rotor, but may act

G. Schweitzer, E.H. Maslen (eds.), *Magnetic Bearings*,
DOI 10.1007/978-3-642-00497-1_11, © Springer-Verlag Berlin Heidelberg 2009

as excitation and force measurement equipment as well [4, 5, 8, 9]. In cases where AMB's are designed as bearing elements for turbomachinery systems, it appears helpful to use them also as excitation and force measurement tool. In such applications, identification of the dynamic behavior of the rotating machinery system would be possible during normal operation. With the information obtained from identification, rotordynamic models can be checked. This can be used to validate assumptions about the models, to determine unknown or uncertain parameters, to support design of the controller, or a model based diagnosis can follow, in order to find possible system failures during operation. This chapter describes briefly the dynamic characteristics of rotating systems which have to be identified and explains procedures for the identification process.

11.2 Dynamic Characteristics of Rotating Systems

For many machines with rotating shafts, the dynamic behavior can be described by linear models with time invariant system parameters (see Chap. 10 or [7]). In these models, the relation between input- and output quantities is given in terms of differential equations expressing the dynamic equilibrium of inertia-, damping-, stiffness- and external forces, see also (10.40) in Chap. 10.

$$\mathbf{M}\ddot{\mathbf{z}} + \mathbf{D}\dot{\mathbf{z}} + \mathbf{K}\mathbf{z} = \mathbf{f}(t) \tag{11.1}$$

Usually the vector of external forces $\mathbf{f}(t)$ is considered as system input and the vector of displacements $\mathbf{z}(t)$ as system output (Fig. 11.1). However, in general the input can also be given by defined displacements. In this case the necessary forces for the defined motion may be output quantities and can be determined analytically with (11.1). The physical mass, damping and stiffness parameters, assembled in the system matrices $\mathbf{M}, \mathbf{D}, \mathbf{K}$, characterize the stiffness, damping and inertia distribution of the rotating parts, and the dynamic behavior of the system. In general these matrices depend on the rotational speed due to gyroscopic effects and due to speed dependent stiffness and damping coefficients in case of fluid bearings and seals. Furthermore, the structure of the matrices $\mathbf{M}, \mathbf{D}, \mathbf{K}$, can be symmetric, skew symmetric or non-symmetric depending on the character of the above mentioned effects (gyroscopics, fluid structure interactions, etc.). The mass matrix can always be made symmetric.

Besides the physical parameters $\mathbf{M}, \mathbf{D}, \mathbf{K}$ another equivalent set of parameters, the so called modal parameters can also be used to completely describe the system dynamics [2]. These parameters consist of a set of natural frequencies ω_n, damping values α_n and corresponding eigenvectors $\mathbf{z}_n$, which are the so called mode shapes (Fig. 11.1).

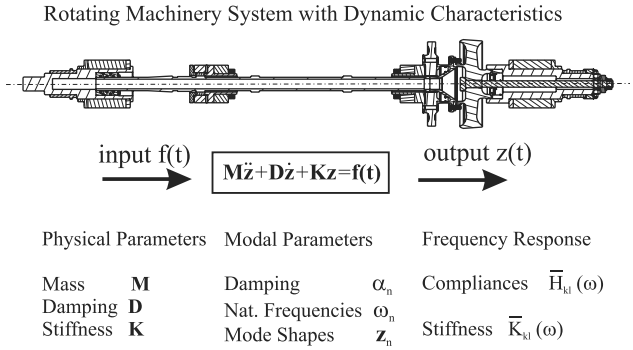


Fig. 11.1. Dynamic characteristics of rotating systems

When input-output relations are considered in the frequency domain (see also Sec. 10.2.4), the following complex frequency response functions have to be introduced with ω as the frequency of excitation

$$\hat{\bar{\mathbf{f}}}(\omega) = (\mathbf{K} - \omega^2\mathbf{M} + j\omega\mathbf{D})\hat{\bar{\mathbf{z}}}(\omega) = \bar{\mathbf{K}}(\omega) \cdot \hat{\bar{\mathbf{z}}}(\omega) \tag{11.2}$$

$$\hat{\bar{\mathbf{z}}}(\omega) = (\mathbf{K} - \omega^2\mathbf{M} + j\omega\mathbf{D})^{-1}\hat{\bar{\mathbf{f}}}(\omega) = \bar{\mathbf{H}}(\omega) \cdot \hat{\bar{\mathbf{f}}}(\omega) \tag{11.3}$$

They can be subdivided into the compliance functions $\bar{H}_{kl}(\omega)$ and the stiffness functions $\bar{K}_{kl}(\omega)$ which are elements of the matrices $\bar{\mathbf{H}}$ and $\bar{\mathbf{K}}$. $\bar{H}_{kl}(\omega)$ is the system response (amplitude and phase) of displacement $\hat{\bar{z}}_k$ due to a force excitation $\hat{\bar{f}}_l(\omega)$. In analogy $\bar{K}_{kl}(\omega)$ is the necessary force $\hat{\bar{f}}_k(\omega)$ divided by the displacement $\hat{\bar{z}}_l$, when an isolated motion $\hat{\bar{z}}_l(\omega)$ is excited without any other excitation at any other location. The frequency response functions $\bar{H}_{kl}(\omega)$ and $\bar{K}_{kl}(\omega)$, respectively are assembled in the global complex matrices $\bar{\mathbf{H}}(\omega)$ and $\bar{\mathbf{K}}(\omega)$, as presented in equations (11.2) and (11.3).

If electromagnetic actuators are used in order to excite and to identify the dynamics of a rotor system, then the applied forces of the magnetic field are considered to be external forces at the boundary. In this case, the AMB-dynamics including controllers, amplifiers, sensors etc. is not part of the system matrices (11.1) under investigation. If, on the other hand, a rotor running in active magnetic bearings shall be modeled as an overall "Mechatronic system", (11.1) has to be extended and all of the mechatronic components (actuator, amplifier, sensor, controller) have to be included.

11.3 Identification of Physical and/or Modal Parameters

The determination of the physical parameters $\mathbf{M}, \mathbf{D}, \mathbf{K}$ is possible by means of calculations or by measurements. The measurement procedure is known as identification. More precisely, if the structure of the rotordynamic model is

already known, e.g. by (11.1), and only the parameters are not known and have to be identified, this is called parameter identification [2]. Identification in this sense means to excite a rotating system artificially during operation and to measure the system excitation and the corresponding response (Fig. 11.2).

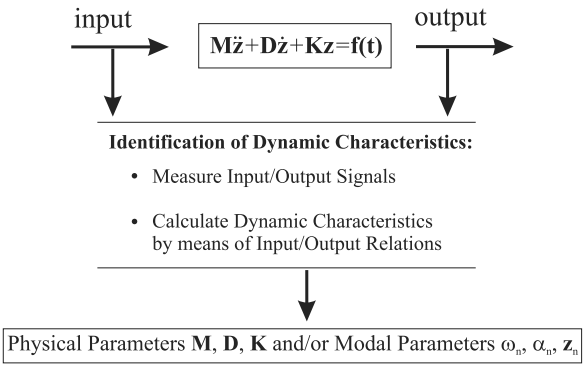


Fig. 11.2. Identification of dynamic characteristics

From the measured input and output signals, the dynamic characteristics can be calculated by means of well known input/output relationships in the time or in the frequency domain. Identification procedures to determine physical or modal parameters of a rotordynamic system consist of several steps (Fig. 11.3).

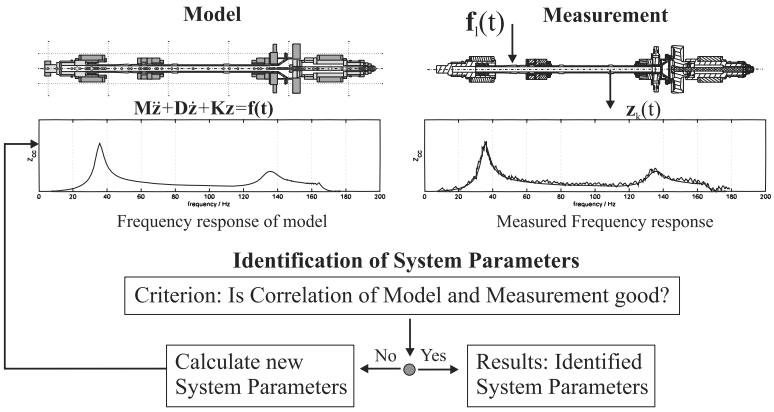


Fig. 11.3. Procedure for the identification of system parameters

At first, a model structure for the system under investigation has to be established, e.g. a linear model described by differential equations with con-

stant parameters as presented in (11.1). Based on this model, input-output functions, impulse response functions (time domain) or frequency response functions (frequency domain) can be calculated, if the system parameters are assumed. Such functions can also be determined from the measured input/output signals with signal processing.

Finally in the task of parameter estimation the functions of the model are fitted to the corresponding measured functions by variation of the physical or modal parameters in the model. This iterative procedure of improving the system parameters is interrupted if the correlation of model and measurement results is acceptable (Fig. 11.3).

11.3.1 Rotordynamic Model

An important assumption for a successful identification of system parameters is the selection of a suitable model. As mentioned before, in many cases of rotating systems, the model structure of (11.1) can be applied, which represents a time invariant linear model with symmetric or non symmetric matrices $\mathbf{M}, \mathbf{D}, \mathbf{K}$ depending on the rotational speed. From the different possible input/output relations in the time and frequency domain, in this chapter only frequency domain relations will be treated, particularly the before-mentioned complex compliance and stiffness frequency response functions as presented in (11.2) and (11.3). From a practical point of view, in most rotating systems it is easier to measure compliance functions instead of stiffness functions. On the other hand, concerning the parameter estimation, there is a very simple linear relation between the physical parameters and the stiffness frequency function.

11.3.2 Measurement of Frequency Response Functions

The objectives of the measurement task are to excite a rotordynamic system artificially by force or kinematic excitation, to measure input and output signals and to process functions that are used later for the parameter estimation. In case of linear systems, frequency domain functions are often used

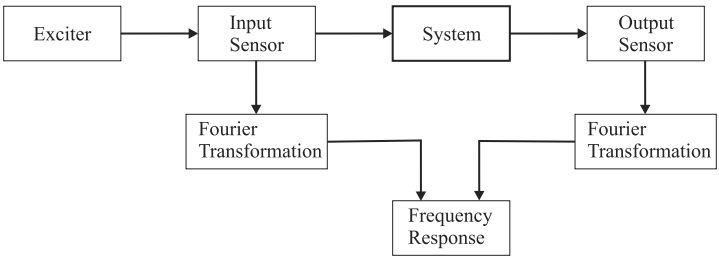


Fig. 11.4. Test Configuration to measure frequency response functions

(Fig. 11.4). The following expressions (11.4) and (11.5) point out the main differences between measuring compliance functions (force excitation) or stiffness functions (kinematic excitation). The compliance $\bar{H}_{kl}(\omega)$ is defined as output $\hat{\bar{z}}_k(\omega)$ divided by the force of excitation $\hat{\bar{f}}_l(\omega)$, where all other forces are considered to be zero. On the other hand the relation $\bar{K}_{kl}(\omega)$ is found from the forces $\hat{\bar{f}}_k$ that have to be applied to the system, when only the displacement $\hat{\bar{z}}_l(\omega)$ is present. This explains why it is easier to measure compliance than stiffness - it is easy to apply only a single force and practically impossible to constrain all but one degree of freedom. $\bar{\mathbf{H}}(\omega)$ and $\bar{\mathbf{K}}(\omega)$ are usually nonsymmetric matrices, due to the possible nonsymmetry in $\mathbf{K}$ and $\mathbf{D}$.

$$\hat{\bar{\mathbf{z}}}(\omega) = \begin{bmatrix} \hat{\bar{z}}_1 \\ \cdot \\ \cdot \\ \cdot \\ \hat{\bar{z}}_k \\ \hat{\bar{z}}_N \end{bmatrix} = \begin{bmatrix} \bar{H}_{11} & \cdots & \cdot & \cdot \\ \cdot & \cdots & \cdot & \cdot \\ \cdot & \cdots & \cdot & \cdot \\ \cdot & \cdots & \cdot & \cdot \\ \cdot & \cdots & \bar{H}_{kl} & \cdot \\ \bar{H}_{N_1} & \cdots & \cdot & \cdot \end{bmatrix} \begin{bmatrix} 0 \\ 0 \\ 0 \\ 0 \\ \hat{\bar{f}}_l \\ 0 \end{bmatrix} \rightarrow \boxed{\bar{H}_{kl}(\omega) = \hat{\bar{z}}_k(\omega)/\hat{\bar{f}}_l(\omega)} \quad (11.4)$$

To calculate the amplitude of the compliance function $\bar{H}_{kl}(\omega)$, the system is excited by a force amplitude $\hat{\bar{f}}_l$ only and the response $\hat{\bar{z}}_k$ is meassured. $\bar{H}_{kl}$ can than be determind from the ratio $\hat{\bar{z}}_k/\hat{\bar{f}}_l$.

$$\hat{\bar{\mathbf{f}}}(\omega) = \begin{bmatrix} \hat{\bar{f}}_1 \\ \cdot \\ \cdot \\ \cdot \\ \hat{\bar{f}}_k \\ \hat{\bar{f}}_N \end{bmatrix} = \begin{bmatrix} \bar{K}_{11} & \cdots & \cdot & \cdot \\ \cdot & \cdots & \cdot & \cdot \\ \cdot & \cdots & \cdot & \cdot \\ \cdot & \cdots & \cdot & \cdot \\ \cdot & \cdots & \bar{K}_{kl} & \cdot \\ \bar{K}_{N_1} & \cdots & \cdot & \cdot \end{bmatrix} \begin{bmatrix} 0 \\ 0 \\ 0 \\ 0 \\ \hat{\bar{z}}_l \\ 0 \end{bmatrix} \rightarrow \boxed{\bar{K}_{kl}(\omega) = \hat{\bar{f}}_k(\omega)/\hat{\bar{z}}_l(\omega)} \quad (11.5)$$

In a similar way $\bar{K}_{kl}(\omega)$ is found by the ratio $\hat{\bar{f}}_k/\hat{\bar{z}}_l$, when the system is excited only by $\hat{\bar{z}}_l$, and the force $\hat{\bar{f}}_k$ is measured.

One of the main problems to apply identification techniques in rotordynamics is the excitation of a rotating structure during operation. Various devices for excitation have been developed and used for identification, either of real machines or of small test rigs. They include the preload of a shaft with a following snap back, the hammer impact method, unbalance excitation via a second shaft with different running speeds, shaking the shaft via a rider and the use of active magnetic bearings. The last excitation possibility will be considered in Sec. 11.4.

11.3.3 Parameter Estimation

When input/output functions of the system have been measured in the frequency or time domain, corresponding model functions are fitted to the mea-

sured ones in order to estimate the unknown physical or modal parameters. In general parameter estimation procedures like the least squares method, instrumental variables or maximum likelihood method can be used for this task. When applying one of these methods, it is necessary to consider the different possibilities with respect to the measured data (time or frequency domain), the signal processing (online or offline), the available numerical algorithms (direct, linear, iterative, nonlinear) and the type of error (input, output or equation error).

11.4 Excitation of a Rotor by means of Magnetic Bearings

11.4.1 Excitation and Control for Forces and Motions

Figure 11.5 shows a schematic diagram of the AMB exciter system. Position control is needed to levitate the rotor with the magnetic bearings. A digital signal processor (DSP) runs the control program at a sampling time of 220 μs. It also computes the force from the measured flux and position signals. Force and position signals can be acquired on the DSP. A fast digital link interfaces the DSP to the general mathematics program MATLAB which runs on a personal computer. Force and displacement signals are also available in analog form, to be processed together with signals from additional sensors.

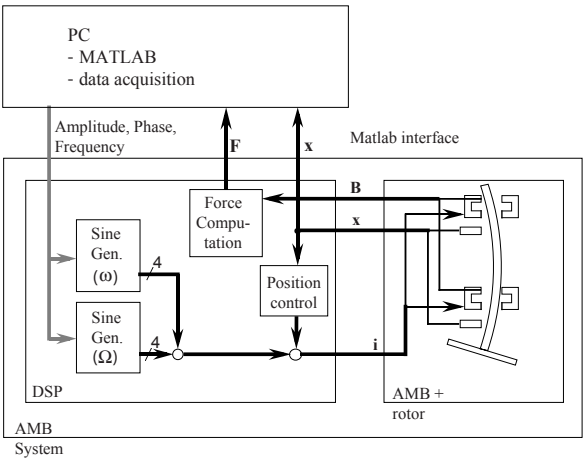


Fig. 11.5. Scheme of the AMB exciter system

For excitation, two sinewave generators are implemented on the DSP. One is synchronised to the rotor's revolution speed, while the frequency of the other one is user-defined. Each sinewave generator has four outputs, which are

connected to the four control currents (x and y direction of the two bearings). Amplitude and relative phase of each output can be defined via MATLAB. The described set-up gives the experimenter a number of possibilities which are new for rotordynamic experiments:

- Measurement of all bearing forces allows estimation of the Frequency Response Function (FRF) of the free rotor
- Contact free excitation allows experiments with the rotating rotor
- Stepped-sine excitation yields FRF data with high signal-to-noise ratio
- Arbitary choice of excitation amplitudes, phases and frequency allow selective excitation of forward and backward eigenmodes of the rotating rotor
- Synchronization of the excitation with the rotor's revolution speed allows simulation of unbalances. Alternatively, it allows compensation of unbalance forces stemming from the rotor's unbalance.
- The exciter in the specific example of [4] provides a dynamic force amplitude of 800 N up to a frequency of 200 Hz, 400 N up to 400 Hz. This high power allowed high quality measurements also close to the resonances.

11.4.2 Force Measurement Techniques

In principle, there exist two methods to measure the forces in an AMB [4, 5, 6]. In order to obtain good measurement results, the force measurement has to be very accurate in the whole range of possible AMB-forces, particularly in case of amplifier saturation and for small force amplitudes. Furthermore the measurements must be valid for a wide range of rotor positions. The first method is based on the direct measurement of the magnetic flux density B which is a more accurate method. In this flux measurement method, the force of the pole can be calculated by:

$$\mathbf{F} = \frac{B^2 A}{\mu_0} \tag{11.6}$$

with the pole surface A and the permeability coefficient μ_0.

The draw-back of the method is that Hall sensors have to be inserted in the magnetic circuit to measure the flux. They can be fixed either at the north poles only or at all poles. In the first case a network computing is necessary in order to determine the unmeasured fluxes in the south poles. Figure 11.6 is a view into the bearing and shows the poles with the Hall sensors. As summary, the direct force measurement via Hall Sensors at all poles needs no further assumptions or approximations and is a very accurate method. The measurement is not influenced by nonlinear effects like amplifier saturation etc.. The higher effort (hardware, more ampere windings) is more

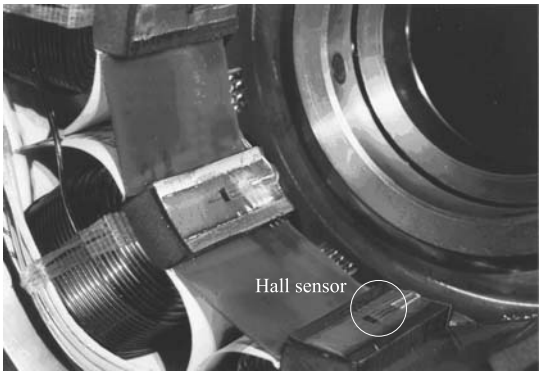


Fig. 11.6. Magnetic Bearing with Hall Sensors

than justified by the good quality of measurement results. However, a larger air gap is necessary, leading to a reduction of the electromagnetic forces.

The second method needs the coil current and the rotor displacements and is usually called the 'i-s-method'. This method has the advantage that it can be realized very easily: no additional hardware is needed. It has the disadvantage that the relation gets significantly nonlinear in the range of maximum magnetic forces. Furthermore, saturation, hysteresis and eddy current effects cannot be taken into account with this method.

11.5 Applications for Identification

11.5.1 Modal Analysis for Rotating Structures with AMB's

Modal testing methods for non-rotating structures are well developed. However, for a turbomachinery user, it is very important to get information also about the dynamic behavior of the machinery in the rotating state. In practice it is usual, mainly for monitoring purposes, to measure the output frequency spectrum of a rotating structure. Vibrational amplitudes can be measured in this way, but only limited information about vibrational properties can be obtained because the excitation forces are not known.

Vibrational properties can be assessed if frequency response functions are measured. They can be described in terms of modal parameters (natural frequencies, modal damping coefficients and mode shapes), which together form a modal description of the rotating structure. These parameters can then be compared with the modal parameters obtained from a finite element model of the structure. They can also be used to update the finite element model.

A Test Rig for Modal Analysis with AMB's

To verify the capability of the AMB as an exciter for modal analysis, a test rig was built which allows investigation of several rotordynamic effects. In Fig. 11.7, a schematic plot of the experimental setup is shown [3, 4, 5, 6]. In the center there is the flexible rotor structure with the shaft (S) including the AMB-bushes (BS) and the disk (D). The rotor is driven by an 1 kW AC-Servo-Motor (M) via the coupling (C). The physical parameters and specifications of the rotor bearing system are given in Tab. 11.1. The membrane coupling works like a cardanic joint and allows the shaft end to have radial and tilting displacement with a defined, low stiffness. The AMBs (AMB1, AMB2) are schematically shown with the position sensors (PS) and the Hall effect sensors (HS). All the components are linked to a PC and can be controlled with the mathematic program MATLAB. The movable additional displacement sensors along the shaft allow detection of the mode shapes of the structure.

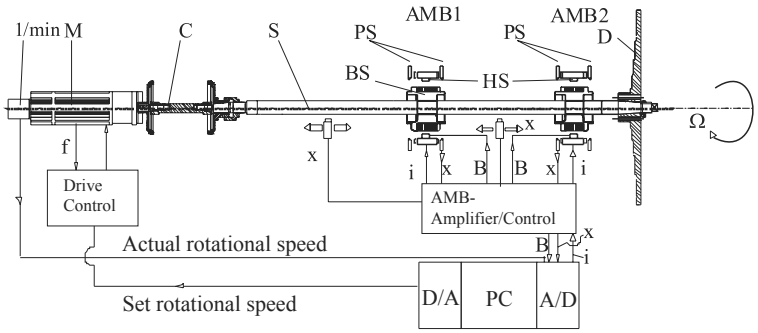


Fig. 11.7. Experimental setup

Shaft			
Length		1120 mm	
Diameter		37 mm	
Young's modulus		$1.96 * 10^{11}$ N/m^2	
Density		7850 kg/m^3	
Disk	mass (kg)	polar inertia (kg m^2)	diametrical inertia (kg m^2)
Rigid Disk	20.94	0.49	0.242
Flexible Disk	20.64	0.47	0.2415

Table 11.1. Rotor specifications

Furthermore, it is possible to configure the test rig in different ways. For each test rig configuration, either a "rigid" or a "flexible" disk can be mounted

on the shaft end. *Rigid* in this context means that the disk does not show any deformation at the first two bending modes of the rotor. In contrast to this, the flexible disk has deformations in this frequency range. Both disks have the same masses and moments of inertia. Hence the different dynamics of the rotor configurations depend only on the different disk stiffnesses. This creates the opportunity to investigate the influence of a rotating elastic element on the dynamic behavior of the whole structure.

Test Rig Configuration

Figure 11.8 shows the test rig configuration with the rigid disk mounted on a heavy concrete foundation, decoupled from the environment with viscous dampers. The rigid body modes of the foundation with test rig are all below 7 Hz and thus far away from the first bending eigenfrequency of the rotor.

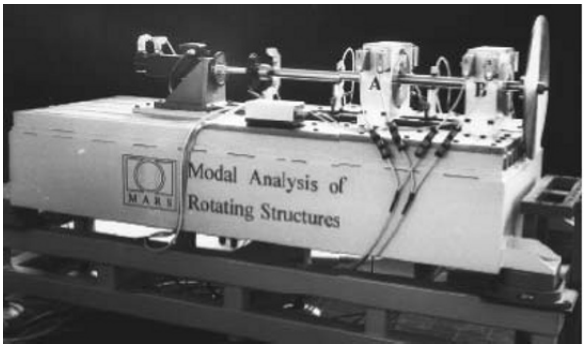


Fig. 11.8. Photograph of test rig configuration

Figure 11.9 shows the technical drawing of this test rig with rigid disk. In front of the rigid disk the flexible disk is shown, which can be used alternatively. In this configuration, the AMB has the function to support and excite the rotor at the same time.

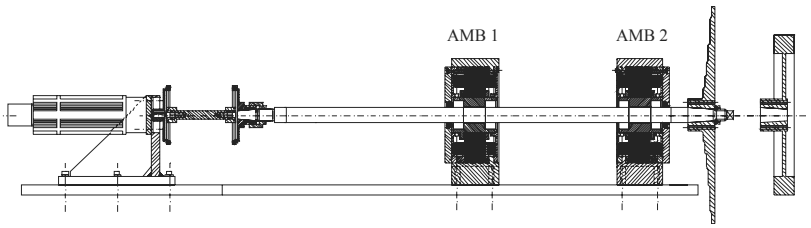


Fig. 11.9. Test rig

Some Experimental Results

In this section, some experimental results for the free-free rotor are presented. Fig. 11.10 shows the first three elastic mode shapes of the test rig rotor. It is obvious that each shape has a node near the disk position because of the large disk mass. The first two modes show a good observability (AMB sensor position not at a node) and controllability (actuator not at a node). The third mode is not controllable by AMB 2, because of the node in the middle of the AMB 2. This has to be taken into account when exciting the rotor structure. There will be no possibility to excite this mode via AMB 2.

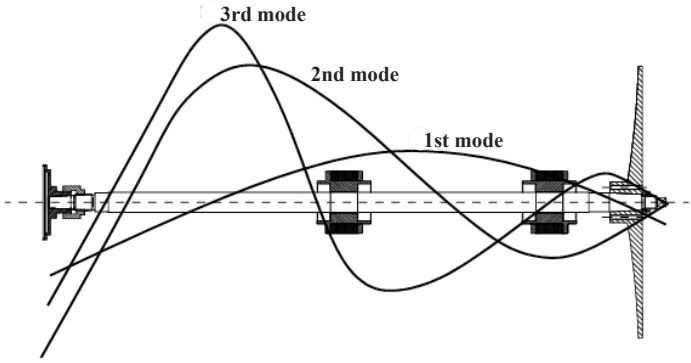


Fig. 11.10. First 3 elastic eigenmodes of test rig

The calculated results for the rotordynamic behavior were obtained using a Finite Element program especially adapted for rotordynamics. According to the usual modeling procedure, the shaft is divided into several beam elements with additional disk elements. The additional stiffness effects of the shrink-fitted AMB-bushes and the disk and coupling hub connection were considered in the simulation and adjusted with respect to experimental results obtained from a non-rotating modal analysis using the hammer test procedure.

To measure the frequency response functions such as defined above, the rotor is excited with stepped sine excitation from 10 to 400 Hz. The sinusoidal excitation excites the rotor at each bearing one after another in horizontal and vertical direction. At each individual test, all forces acting on the rotor are measured. If the structure is rotating, the frequency response functions include also the frequency component synchronous to rotational speed caused by unbalance. This component can be isolated before the frequency response function is computed.

In Fig. 11.11 the frequency response function H_{11} at AMB 1 in vertical direction is shown. To demonstrate the growth of the gyroscopic effects, the frequency response function is measured at four different speeds (0, 1000, 2000, 3000 1/min).

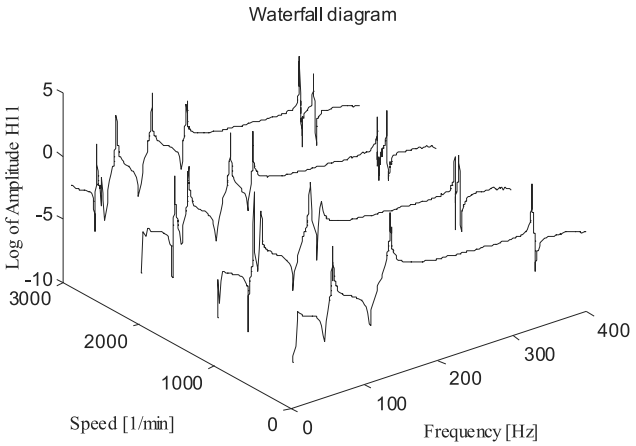


Fig. 11.11. Three-dimensional plot of Frequency Response for test rig

Figure 11.12 shows the natural frequencies versus the speed. The gyroscopic split is obvious at higher speeds. It is 26.6 Hz for the first eigenfrequency at 3000 1/min.

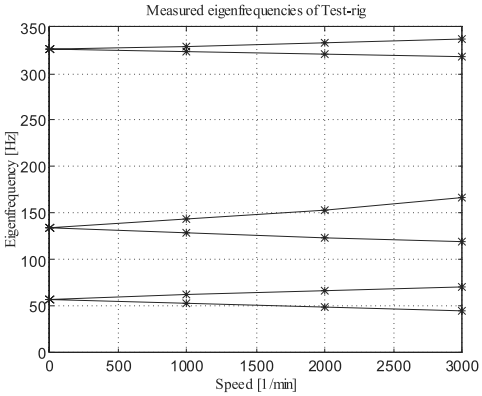


Fig. 11.12. Campbell diagram for test rig

The quality of the calculation is confirmed with a comparison of measured and calculated eigenfrequencies shown in Tab. 11.2. There is only a small difference between measured and calculated eigenfrequencies and this confirms the suitability of the AMB as an exciter and force measurement system.

	0 [1/min]		3000 [1/min]	
	Measured	Calculated	Measured	Calculated
1F (Hz)	57.6	57.3	71.0	70.9
1B (Hz)	57.6	57.3	44.4	44.4
2F (Hz)	135.2	134.9	166.0	166.3
2B (Hz)	135.2	134.9	118.8	118.6
3F (Hz)	326.6	328.4	338.0	339.5
3B (Hz)	326.6	328.4	319.0	320.5

Table 11.2. Comparison of measured and calculated eigenfrequencies

11.5.2 Identification of Rotordynamic Coefficients of Fluid Film Bearings and Seals

Fluid Structure Interaction Forces

Fluid-structure interaction forces in fluid film bearings and seals depend on the radial motions z_1, z_2 of the shaft [8, 9], on the bearing or seal geometry, on the fluid properties and the boundary conditions of bearings and seals. If the shaft motions are small compared to the radial clearances, the fluid forces can be expressed in a linearized form with stiffness-, damping- and inertia coefficients.

$$\begin{bmatrix} f_1 \\ f_2 \end{bmatrix} = \begin{bmatrix} m_{11}\ m_{12} \\ m_{21}\ m_{22} \end{bmatrix} \begin{bmatrix} \ddot{z}_1 \\ \ddot{z}_2 \end{bmatrix} + \begin{bmatrix} d_{11}\ d_{12} \\ d_{21}\ d_{22} \end{bmatrix} \begin{bmatrix} \dot{z}_1 \\ \dot{z}_2 \end{bmatrix} + \begin{bmatrix} k_{11}\ k_{12} \\ k_{21}\ k_{22} \end{bmatrix} \begin{bmatrix} z_1 \\ z_2 \end{bmatrix} \tag{11.7}$$

Test Rig for Identification

The designer of turbomachines needs to know these rotordynamic coefficients because they can have a strong influence on the overall rotordynamic behavior either by damping or destabilizing the vibrations of the rotating machinery. The coefficients can be determined by calculations via fluid film models or by experimental procedures. A very straightforward way to identify seal or bearing coefficients is to measure the complex stiffness frequency response functions, as shown in (11.8).

$$\begin{bmatrix} \hat{\bar{f}}_1 \\ \hat{\bar{f}}_2 \end{bmatrix} = \begin{bmatrix} \bar{K}_{11}\ \bar{K}_{12} \\ \bar{K}_{21}\ \bar{K}_{22} \end{bmatrix} \begin{bmatrix} \hat{\bar{z}}_1 \\ \hat{\bar{z}}_2 \end{bmatrix} = \bar{\mathbf{K}} \cdot \hat{\bar{\mathbf{z}}} \tag{11.8}$$

$$\bar{\mathbf{K}} = \begin{bmatrix} k_{11} - \omega^2 m_{11} + j\omega d_{11} & k_{12} - \omega^2 m_{12} + j\omega d_{12} \\ k_{21} - \omega^2 m_{21} + j\omega d_{21} & k_{22} - \omega^2 m_{22} + j\omega d_{22} \end{bmatrix} \tag{11.9}$$

Each of the four functions $\bar{K}_{kl}$ has a simple linear relation with the coefficients k_{kl}, d_{kl}, m_{kl}, that have to be identified. As shown in (11.4) and (11.5) the stiffness frequency response functions $\bar{K}_{kl}(\omega)$ can be found by a displacement excitation $\hat{\bar{z}}_l$ and measuring the force $\hat{\bar{f}}_k$. The test rig that allows such a

procedure is shown in Fig. 11.13. The test bearing or seal is located between two radial AMB's. The rotor is levitated by the magnetic bearings, its static position can be centered or offset in the journal bearing or seal. Subsequently, a defined dynamic excitation can be enforced (e.g. small movements in one or two planes, forward or backward whirl, synchronous or non synchronous to rotational speed).

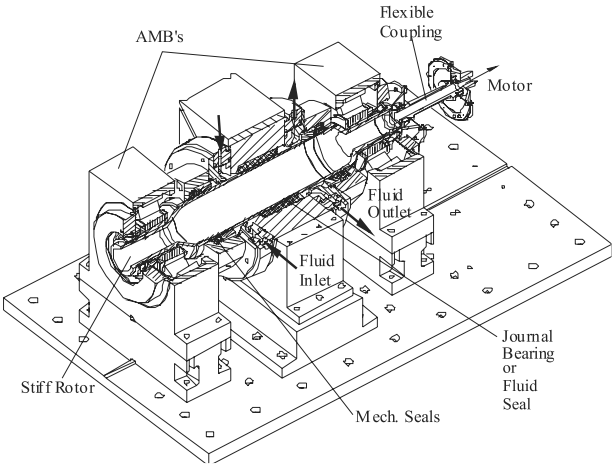


Fig. 11.13. Designed test rig for the identification of fluid film forces

This motion causes the above mentioned fluid-structure interaction-forces. The rotor behaves dynamically stiff within the working range so that the displacements and the resulting forces inside the bearing can easily be computed from the displacements and forces measured by the AMB's. The rotor is controlled by a DSP. The actual data analysis and signal processing is performed on an external PC that is connected to the DSP via a serial link. The hydraulic part of the test rig is sealed up by two mechanical seals. The rotor is connected via a flexible membrane coupling to a servomotor. Both of these measures ensure that no additional stiffness or damping is added to the system which would affect the identification in a negative way.

Identification of Rotordynamic Coefficients of a Fluid Bearing

The dynamic characteristics of journal bearings depend strongly on the static equilibrium point. For example, this operating point is determined by the static preload, which is normally caused by the weight and by process forces of the turbomachine. Figure 11.14 shows a measured static force-displacement relation for an increasing vertical force. Due to the hydrodynamic pressure distribution, the static deviation of the shaft is crosscoupled. This means that

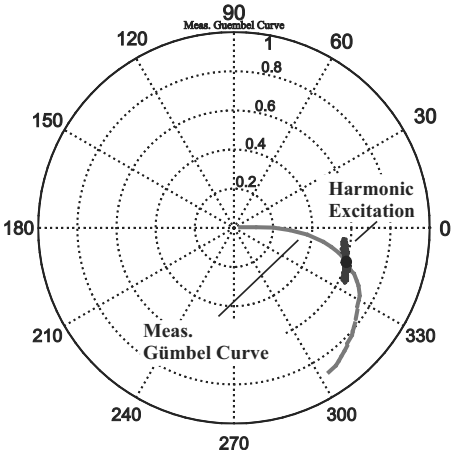


Fig. 11.14. Measured Guembel curve and dynamic excitation

the shaft reacts with displacements in horizontal and vertical direction to a purely vertical load. In the presented test rig, the static preload is generated by the AMB's. But with the AMB's, it is much easier to set the rotor to defined positions rather than to generate defined forces. Consequently, the measurement of the journal center loci (Guembel curve) should be done in an adaptive way (see Fig. 11.15).

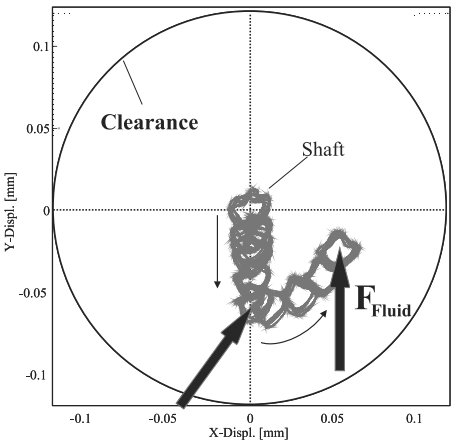


Fig. 11.15. Adaption of Guembel curve for a fluid bearing

First the rotor is moved in vertical direction to the desired eccentricity. The journal bearing reacts with fluid forces which are composed of a horizontal and vertical part. These forces are measured with the AMB's and subsequently the

rotor is moved on a circular orbit until the fluid force is purely vertical. The procedure can be repeated to reach a better accuracy. This method is very fast and easy for circular bearings but can be more time consuming for other types of bearings. By performing this adaption on different eccentricities, the complete Guembel curve can be measured (see Fig. 11.14).

Once the desired position on the Guembel curve is reached, the actual identification process can be started. The goal is now to determine the parameters of (11.7). During rotation, the rotor is oscillated in a defined direction (see Fig. 11.14) and with defined displacement amplitudes at discrete frequencies. This is also performed contactless with the AMB's. The resulting dynamic fluid reaction forces are measured with the AMB's and an identification of the force and displacement signals is performed. This results in complex force and displacement amplitudes, from which stiffness frequency response functions can be computed (see Fig. 11.16) and the rotordynamic parameters can be extracted.

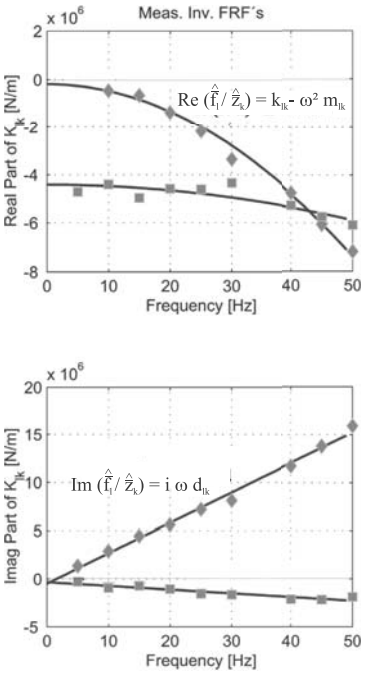


Fig. 11.16. Measured Frequency Response Functions $\mathbf{K}_{lk}$

Based on this method, a large number of measurements under different boundary conditions were made. The tested bearing was a cylindrical type with a diameter D= 120 mm, L/D (length versus diameter)= 0.6, and clearance C=0.12 mm. It was operated under turbulent conditions.

11.5.3 Use of the Identification for Diagnosis in a Pump

Another application for the use of identification is to improve existing diagnostic techniques to satisfy the demands for higher efficiency and longer life durations of turbo machines. Nowadays, the diagnosis of turbo machines is usually based on measured output data (displacements) from which indicators like orbits, frequency spectra, etc. are derived. The indicators of the diagnosis tools developed with identification methods are based on input and output data, which are well known due to the application of the active magnetic bearings used as actuators and as bearings for force and motion control [1].

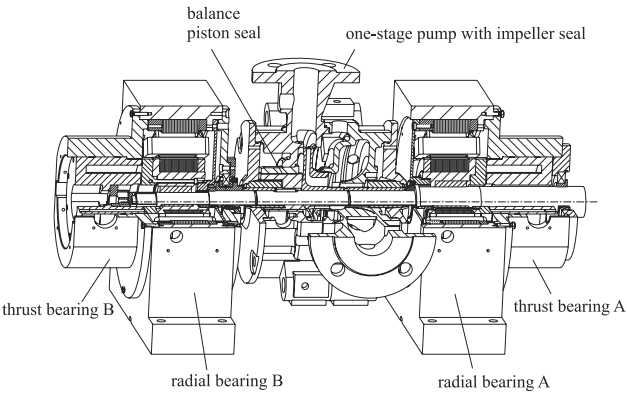


Fig. 11.17. Single stage pump with active magnetic bearings

A test rig of a single-stage pump (see Fig. 11.17) serves as a system where the method is demonstrated. The pump is located between two active magnetic bearings levitating the rotor. In addition to two mechanical seals sealing up the hydraulic part, the pump contains two more contactless seals. One is placed at the suction side and one at the pressure side of the impeller: this is the seal at the balance piston. The identification technique applied to the system for diagnosis purposes is able to detect faults like shaft cracks, wear of seals, loose shaft nut, etc.. In this application, the detection of the wear of the balance piston seal of the one-staged pump is explained exemplarily.

At first, the fault-free rotordynamic system including fluid-structure interactions in the seals (see Fig. 11.18) is being modeled inserting (11.7) as forces from the fluid-structure interactions at the seals. Now, using measured compliance frequency response functions, the above described method leads to the identification of the system parameters including the rotordynamic coefficients of the new piston seal (see Fig. 11.19).

After a period of full operation of the pump system, the compliance function will change due to the wear of the piston seal, as shown in Fig. 11.19. In this regard, the measured compliance function is a feature of the fault

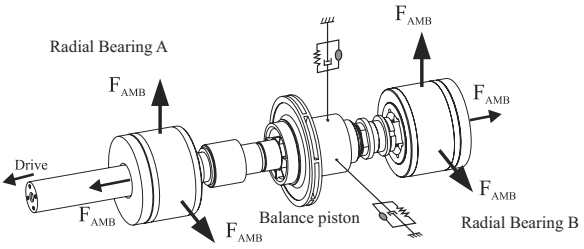


Fig. 11.18. Fault-free rotordynamic system

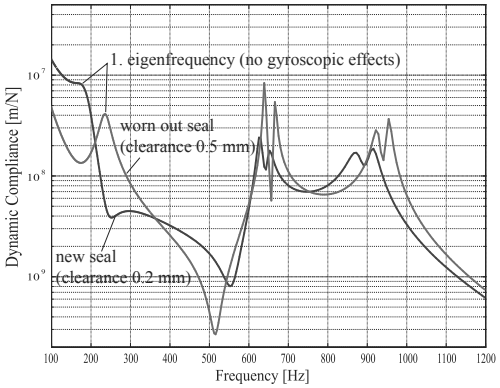


Fig. 11.19. Measured compliance functions of a single stage pump

diagnosis and the change of that feature is symptom of that fault in the system. Applying the identification procedure again, a set of changed rotordynamic coefficients of the seal can be identified which then can be related to the extent of the seal wear based on a model of the fluid-structure interaction. In our case (Fig. 11.19) the clearance of the seal changed from 0.2 mm (new) to 0.5 mm (worn out).

11.6 Closing Remarks

Modeling and simulation becomes more and more important in mechanical engineering, particularly also for rotating machinery. In this important application field, rotordynamic models are not only used for the prediction of the dynamic behavior, but are also needed for different model-based procedures like model-based control and model-based diagnosis.

It is well known that modeling cannot only be achieved theoretically based on physical laws. Quite often, modeling needs also experimental techniques like identification in order to determine the physical and/or modal parameters of rotating system. These identification techniques usually excite the system

under investigation artificially and measure the system response. By means of input/output relations, the model parameters can then be calculated.

In this chapter, mainly frequency response functions have been used as input/output relations, compliance as well as stiffness functions. They are often used in rotordynamic applications. Time domain procedures have not been treated here, they can be found in the special literature for identification. Also, the different parameter estimation procedures are well described there.

Concerning the difficult task of excitation of a rotating system, the very powerful technique with AMB's has been presented. The different applications with AMB-excitation show very good identified parameters with this procedure.

This chapter mainly described how to identify rotordynamic parameters. The identification techniques can of course be extended to determine also parameters of the mechatronic components.

References

1. M. Aenis and R. Nordmann. Active magnetic bearings for fault detection in a centrifugal pump. In *7th International Symposium on Magnetic Bearings, Zürich, Switzerland*, 2000.
2. D.J. Ewins. *Modal testing theory and practice*. John Wiley ans Sons, 1995.
3. P. Förch. *Dynamische Untersuchungen an rotierenden Strukturen mittels Magnetlagern*. PhD thesis, Technische Universität Darmstadt, Fachgebiet Mechatronik im Maschinenbau und Universität Kaiserslautern, 1999.
4. P. Förch and C. Gähler. AMB systems for rotordynamic experiments, calibration results and control. In *5th International Symposium on Magnetic Bearings, Kanazawa, Japan*, 1996.
5. C. Gähler. *Rotor Dynamic Testing and Control with Active Magnetic Bearings*. PhD thesis, ETH Zürich, Switzerland, 1998.
6. C. Gähler and P. Förch. A precise magnetic bearing exciter for rotordynamic experiments. In *4th International Symposium on Magnetic Bearings, Zürich, Switzerland*, 1994.
7. R. Gasch, R. Nordmann, and H. Pfützner. *Rotordynamik*. Springer-Verlag, 2001.
8. E. Knopf and R. Nordmann. Active magnetic bearings for the identification of dynamic characteristics of fluid bearings. In *6th International Symposium on Magnetic Bearings, Cambridge, USA*, 1998.
9. E. Knopf and R. Nordmann. Identification of the dynamic characteristics of turbulent journal bearings using active magnetic bearings. In *7th International Conference on Vibrations in Rotating Machinery, Nottingham, GB*, 2000.
10. G. Schweitzer, H. Bleuler, and A. Traxler. *Magnetlager*. Springer Verlag, 1994.

12

Control of Flexible Rotors

Eric Maslen

The goal of this chapter is to discuss the problems that rotor flexibility and hardware limitations introduce in the design of AMB controllers and to present some solution strategies for these problems. Rotor flexibility means that the rotor can have relatively high gain at higher frequencies and this introduces complications in designing controllers with physically realizable bandwidths. Further, non-collocation of actuators and sensors along with finite bandwidth of actuation, sensing, and control mechanisms can mean that a passivity type of approach to controller design is not feasible.

These issues and others will be explored here through a series of examples. Control solutions are presented for a flexible rotor ranging from the simplest PID approach through to a fairly sophisticated $\mu-$synthesis solution. The performances of these controllers are compared in terms of complexity, forced response performance, and sensitivity to model parameters.

The literature relating to control of AMBs and, especially, those supporting flexible rotors is vast: certainly the largest segment of AMB literature is devoted to control. The bibliography for this chapter attempts to provide a survey of this literature but is by no means complete: a comprehensive survey would contain hundreds of references. Over 80 references are provided: a mix of background material on the general control problem and papers directed specifically at AMB control.

12.1 Flexibility Effects

There are two reasons why flexible systems present more of a challenge to the control system designer than does a rigid rotor. The first is the simple matter that a flexible rotor has a much wider mechanical bandwidth than does a rigid rotor. This means that the mechanical response to high frequency forcing is much larger for a flexible rotor than for a rigid rotor and, as a result, the dynamic behavior of the feedback controller at high frequencies is much more important for flexible rotors than for rigid rotors. The second reason is that,

G. Schweitzer, E.H. Maslen (eds.), *Magnetic Bearings*,
DOI 10.1007/978-3-642-00497-1_12, © Springer-Verlag Berlin Heidelberg 2009

when the sensors and actuators are not collocated axially along the rotor, there will always be flexible modes with a node between a sensor-actuator pair. If these modes have frequencies within the bandwidth of the controller, then they pose special dynamics problems for the system. Both of these issues must be attended to either explicitly or implicitly in the design of an AMB controller for a flexible rotor.

To illustrate these problems in a simple way, consider the control problem posed by a flexible beam that has a pinned support at one end so there is only one axis of control: this is illustrated in Fig. 12.1. This arrangement eliminates the complicating effects of interaction between control axes normally encountered in a fully levitated rotor while still exhibiting the bandwidth and non-collocation problems of a flexible rotor.



Fig. 12.1. A pinned beam controlled at the free end by an active magnetic bearing.

Denote the transfer function from actuator location input to sensor location output as $G_r(s)$. For a rigid rotor, this transfer function is

$$G_r(s) = \frac{y_s(s)}{f_a(s)} = \frac{\lambda}{s^2} \tag{12.1}$$

and has the frequency response plot indicated in Fig. 12.2. The value of λ depends both on the mass of the rotor and on the locations of the sensor and actuator. For a slender uniform cylinder with mass per unit length ρA, total length L, sensor located at x_s and actuator located at x_a,

$$\lambda \approx \frac{3x_a x_s}{\rho A L^3} \ , \ A \ll L^2$$

Moving the sensor or the actuator along the beam only changes the *gain* of the plant transfer function, not its dynamic character - in this case, its *poles* or *eigenvalues*.

A plant with such a simple transfer function can readily be stabilized using a phase lead controller:

$$C(s) = k\frac{s+z}{s+\beta z} \ : \ z > 0, \ \beta > 1 \tag{12.2}$$

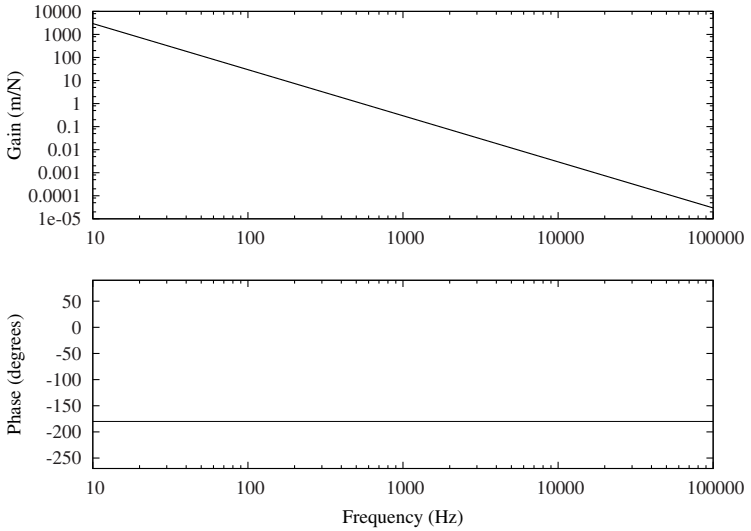


Fig. 12.2. Plant transfer function for a pinned *rigid* beam controlled at the free end by an active magnetic bearing.

PD control, as discussed in Chap. 8 is an example of a phase lead control and it is easily shown that any such transfer function with $z > 0$ and $\beta > 1$ will stabilize this plant.

12.1.1 Bandwidth

However, a *practical* controller must have more poles than zeroes so that its gain goes to zero as frequency goes to infinity: the controller must have a *finite bandwidth*. The requirement of finite bandwidth is partly imposed by practical sensor and actuator technology (see Chap. 3 and Chap. 4) and also by the physical implementation of the controller. In particular, if the controller is implemented digitally as discussed in Chap. 9, then the bandwidth is absolutely limited to half the controller sampling rate. Finally, sensor and other electronics noise sources typically become more significant as frequency increases so that very high bandwidth control loops tend to be very noisy, leading to poor performance.

Consequently, a more realistic controller has the form

$$C(s) = k\frac{s+z}{(s+\beta z)(s+\gamma\beta z)} \quad : \quad z > 0,\ \beta > 1,\ \gamma > 1 \tag{12.3}$$

In this case, it is no longer true that any such controller will stabilize the plant because of the second pole: the controller does not exhibit phase lead over the entire frequency range and has a terminal (high frequency) *lag* phase of $-90°$. However, if the conditions $z > 0$, $\beta > 1$, and $\gamma > 1$ are satisfied, there will

always be a value of $k > 0$ for which the closed loop system is stable. Practical solutions typically have $\beta \approx 10$ and $\gamma \approx 3$. With these choices, the range of stabilizing k for the rigid rotor transfer function (12.1) will be quite wide.

When flexibility of the rotor is introduced, as discussed in Chapter 10, the dynamics of the rotor become significantly more complicated. Figure 12.3 shows the frequency response plot of the transfer function from actuator input to sensor output using a model that retains eight modes (one rigid mode and seven flexible modes). First, note that the gain near the flexible modes

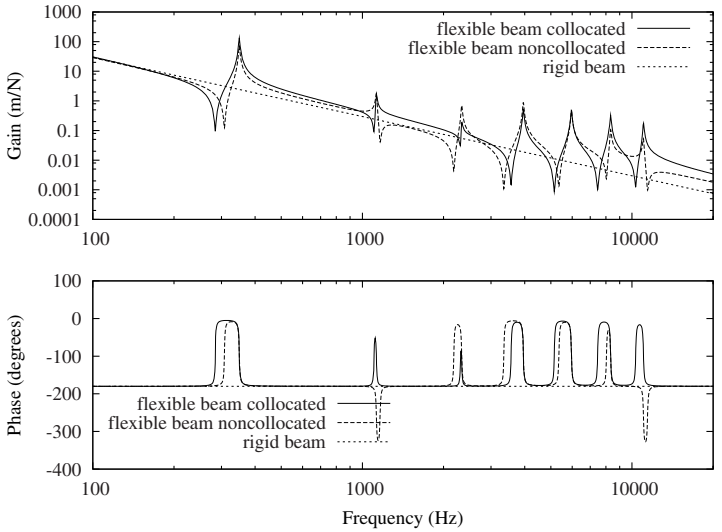


Fig. 12.3. Plant transfer functions for a pinned *flexible* beam controlled at the free end by an active magnetic bearing.

rises well above the corresponding rigid body model gain at corresponding frequencies: the relative gain may be in excess of 100. This means that the gain of the controller is now quite important at higher frequencies: in the example presented here, there is a mode near 350 Hz and the controller must ensure stability of this mode as well as the higher ones.

There are essentially two approaches available for stabilizing flexible modes:

phase compensation requires that the phase of the controller is positive at frequencies in the vicinity of the flexible mode while the product of the controller and plant gains is typically greater than 1.0 at the mode.

gain compensation permits the controller to have negative phase at frequencies near the flexible mode but requires that the product of the controller and plant gains is less than 1.0 at the mode.

For the plant depicted in Fig. 12.3, the controller would probably use phase compensation to manage the mode at 350 Hz and gain compensation for the rest of the flexible modes. This means that the controller gain must be less than about 0.5 N/m for frequencies above about 800 Hz while the phase of the controller must be positive at 350 Hz. As discussed in Chap. 8, it is likely that the controller gain at low frequencies will need to be much higher than 0.5 N/m both for reasons of system performance and to avoid sensitivity to the actuator's innate negative stiffness, k_s.

These requirements can probably be translated into a practical controller of the form of (12.3) because the two flexible modes at 350 Hz and 1000 Hz are *well separated* (by a factor of 3). If the two modes were closer together, then it might not be practical to use such a strategy and a different controller would be required.

In general, any practical AMB controller will employ some form of phase compensation to manage stability and performance for the lower frequency flexible modes of the system and gain compensation for the higher modes. This means that the controller will generally increase the damping of the lower modes and slightly decrease the damping of the higher modes. An important advantage of gain stabilizing the higher modes is that this approach does not require precise knowledge of the frequencies of these modes: only a bound on the plant gain at these higher frequencies is required.

12.1.2 Non-collocation

The effect of sensor-actuator non-collocation can be seen by comparing the transfer function assuming that the sensor is located at the actuator to that which assumes that the sensor is displaced along the rotor axis: for the present example, by just 2 cm on a 30 cm long rotor. Looking at Fig. 12.3, the locations of the poles and zeros of the transfer functions are easily identified by the peaks (poles) and valleys (zeros) of the frequency response magnitude.

In the collocated case, it is interesting to note that the transfer function exhibits a sequence of poles interlaced with zeros: the transfer function has a pair of poles at the origin corresponding to the rigid body motion and then a sequence of lightly damped poles corresponding to the flexible modes. Interspersed amongst the poles are the transfer function zeros (valleys in the frequency response magnitude plot) and the sequence along the frequency axis is: poles - zeroes - poles - zeroes - . . . , which is referred to as "interlaced." An important consequence of this interlacing is seen in the phase plot where it is seen that the phase alternates between -180 degrees and 0 degrees. Without the zeros, the phase would decrease by 180 degrees each time a flexible mode is passed so that the phase lag of the transfer function would become very large at high frequency.

When the sensor is not collocated with the actuator, this interlacing is disturbed. Looking at the frequency response magnitude plot for the non-collocated system (again, Fig. 12.3), things start at low frequency in the same

manner as for the collocated system but there is no transfer function zero between the second and third modes (first and second flexible modes). Subsequently, there are *two* zeros between the third and fourth modes. The same phenomenon can be noted between modes seven and eight. One important consequence of this is that the phase is no longer constrained between -180 and zero degrees: in intervals lacking a zero, the phase drops below -180, toward -360 degrees. A very thorough treatment of the zeros of non-collocated flexible rotors may be found in [46]

Considerable insight to this behavior can be obtained by examining the mode shapes of the pinned-free beam, shown in Fig. 12.4. It is easily observed that modes three and eight have nodes lying between the sensor and the actuator locations whereas none of the other modes exhibit this *defect*. These nodes imply that, when the beam vibrates with this mode shape at the corresponding modal frequency, the displacement at the sensor is 180 degrees out of phase with that at the actuator. This is the source of the distinctive phase behavior exhibited by the non-collocated model.

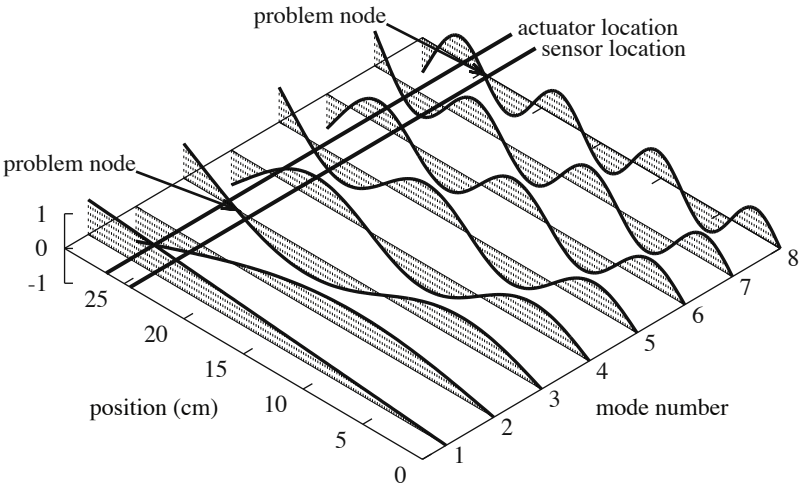


Fig. 12.4. Mode shapes of the pinned-free flexible beam.

Because problematic sensor-actuator non-collocation can easily be recognized by looking at the free-free mode shapes of the rotor, it is common to examine these mode shapes during an AMB design process. By contrast, designers of machines with fluid film or rolling element bearings essentially never look at the free-free mode shapes.

Although it may seem intuitive that this odd phase behavior associated with non-collocated sensor-actuator pairs could potentially be a problem, the best insight is obtained by examining the root locus behavior. In a root locus, it is assumed that negative feedback is introduced from the output of the

transfer function back to the input and the gain of this feedback is varied from zero (open loop) to infinity. As the gain is varied, the closed loop eigenvalues are computed and plotted as trajectories on the complex plane. Ideally, the eigenvalues stay to the left of the imaginary axis, implying that the closed loop system is stable.

Figure 12.5a shows a typical root locus for the collocated plant with lightly damped (0.5%) modes. All of the locii stay in the left-half plane, implying closed loop stability. Adding some phase lead to the feedback path (a PD controller) would move all of the locii to the left to some degree, increasing the relative stability of the closed loop system. In contrast, Fig. 12.5b shows the root locus for the non-collocated plant with the same lightly damped modes. In this case, four of the locii move strongly into the right half plane, corresponding to instability of the closed loop system. Adding phase lead to the feedback path will tend to move the locii to the left, but will not generally be able to stabilize the system.

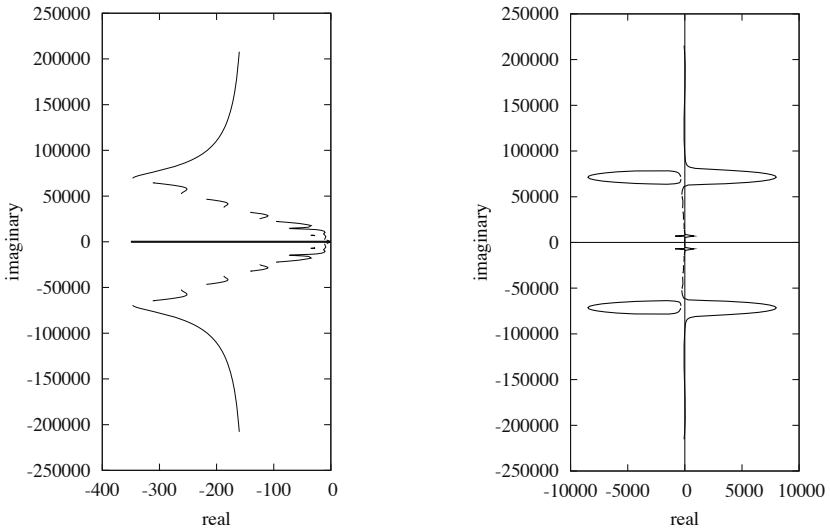


Fig. 12.5. Root locii of the pinned-free flexible beam. The non-collocated case has extensive unstable (positive real) locus.

The solution to this problem is fairly simple: because the problem is associated with interlacing defects, we simply add poles and zeros where they are needed: Table 12.1 lists the non-collocated transfer function's poles and zeros. The actual values of the added poles and zeros need only be selected to repair the interlacing defect: generally, they should be kept well away from the poles and zeros of the plant so as to avoid error due to model uncertainty. Choosing

a compensator transfer function with 0.5% damped poles at 10000 rad/sec and 75000 rad/sec and corresponding 0.5% damped zeros at 5000 rad/sec and 64000 rad/sec produces the root locus indicated in Fig. 12.6, showing that the *repaired* system is now nicely behaved and its closed loop performance can be enhanced using a conventional phase lead approach like PD or PID control.

Table 12.1. List of poles and zeros of the non-collocated transfer function for the pinned-free beam with 0.5% damping. "Missing" pole and zero locations are indicated.

pole	zero
$0 \pm 0j$	
	$-8.51 \pm 1933j$
$-10.0 \pm 2196j$	
	(missing zero)
$-35.4 \pm 7081j$	
	$-37.7 \pm 7307j$
(missing pole)	
	$-62.6 \pm 13721j$
$-73.3 \pm 14666j$	
	$-89.7 \pm 21032j$
$-124.2 \pm 24835j$	
	$-158.5 \pm 33656j$
$-187.2 \pm 37444j$	
	$-248.6 \pm 50538j$
$-261.6 \pm 52328j$	
	(missing zero)
$-346.5 \pm 69307j$	
	$-366.5 \pm 71763j$
(missing pole)	

Of course, most practical AMB systems are not single input - single output (SISO) for the radial bearing system. As a result, this *relatively* simple approach to compensation is not sufficient for these systems. The objective of the ensuing material is to present some fairly systematic strategies for constructing controllers for practical AMB systems.

In outline, Sect. 12.2 describes the general structure of a model of the rotor, sensors, actuators, and associated electronics that is suitable for design and evaluation of controllers for AMB support of flexible rotors. Section 12.3 then elaborates the specific methods by which the various elements of this model are constructed and illustrates their assembly into a single comprehensive model of the system without controller. Section 12.4 discusses collocated local PID control of this system, simplifying the model to neglect all but the rotor dynamics and assumes that the sensors and actuators are collocated. Section 12.5 develops some formal methods of performance assessment. In

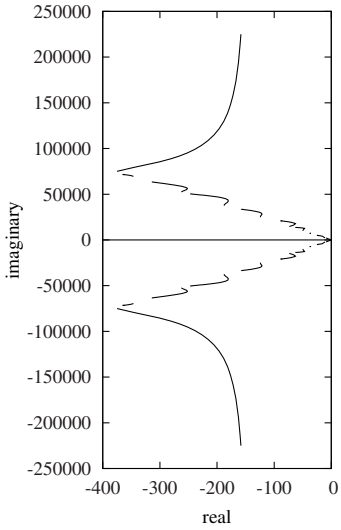


Fig. 12.6. Root locus of non-collocated beam transfer function with interlacing repair compensator. Locus now lies entirely in the stable (negative real) half of the complex plane.

Sect. 12.6, the full model of the plant is used (including the dynamics of the electrical components as well as sensor/actuator non-collocation) and a more realistic local feedback PID controller is developed. Section 12.7 introduces the concepts of model uncertainty and the methods by which the impact of this uncertainty on system stability are assessed. Section 12.8 demonstrates that end-to-end coupling of the plant can be reduced by a transformation of the input and output signal vectors, leading to the mixed axis PID control problem. Section 12.9 then generalizes the performance and sensitivity ideas developed in Sect. 12.5 and 12.7, producing the $\mathcal{H}_\infty$ norm. This performance measure is then used in Sect. 12.10 to automatically synthesize a fully MIMO controller. Section 12.11 explores the reasons for which $\mathcal{H}_\infty$ control is poor at balancing performance against robustness to model uncertainty and introduces the structured singular value. The section is completed with a discussion of control synthesis with the goal of minimizing the structure singular value: $\mu-$synthesis. The problems that sensor–actuator non-collocation can introduce are explored in Sect. 12.12 while Sect. 12.13 discusses the flexible rotor control issues introduced by gyroscopic effects and outlines some solution methods. Section 12.14 looks at specialized methods of compensating for mass unbalance in AMB systems with flexible rotors and the chapter concludes with summary remarks in Sect. 12.15.

12.2 Model Structure

In the most general view, every linear control problem has the structure indicated in Fig. 12.7. The model has five components:

G(s) is the *plant*, a mathematical description of how the physical inputs to the system affect its behavior.

w are the *loads and noise*. These are physical signals (forces, voltages,...) that act on the system but cannot be controlled by the engineer. The engineer does, however, have some description of these signals such as bounds on amplitude, typical time domain character, or expected spectrum.

u are the *controls*. These are also physical signals that act on the system but, unlike loads, they may be selected nearly arbitrarily by the engineer. They will be subject to some bounds which are known *a-priori* by the engineer.

z are the *performance measures*. These signals measure the physical response of the system and are used in assessing performance. They may or may not be physically measurable, but the engineer is interested in ensuring that they stay within specific constraints under *reasonable* conditions. These *reasonable* conditions will be described by the expected behavior and bounds of the loads.

y are available *sensor outputs*. These signals are always corrupted by noise (part of **w** and therefore bounded in some useful fashion) but are available for use by the controller in producing the signals **u**. The signals **y** along with a model of the plant are the only means by which the controller deduces the instantaneous behavior of the plant.

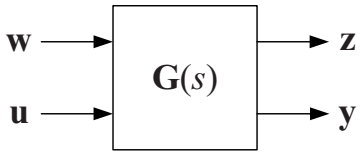


Fig. 12.7. Generic model of the plant for a control problem.

To better understand this structure as it applies to AMB problems, Fig. 12.8 sketches a generic AMB system and indicates which signals fall into which categories. Essentially, the controller accepts signals from position sensors and delivers signals to power amplifiers, so the outputs from the sensors are **y** while the inputs to the power amplifiers are **u**. Noise infiltrating the sensors and gravity, unbalance, or aerodynamic loads acting on the rotor are all examples of **w**. Lateral displacements of the rotor at points adjacent to close clearances are the most obvious performance signals, **z**.

The contents of the dynamic block **G** in Fig. 12.7 take the form

$$\mathbf{G}(s) = \begin{bmatrix} \mathbf{G}_{wz}(s) & \mathbf{G}_{uz}(s) \\ \mathbf{G}_{wy}(s) & \mathbf{G}_{uy}(s) \end{bmatrix} \tag{12.4}$$

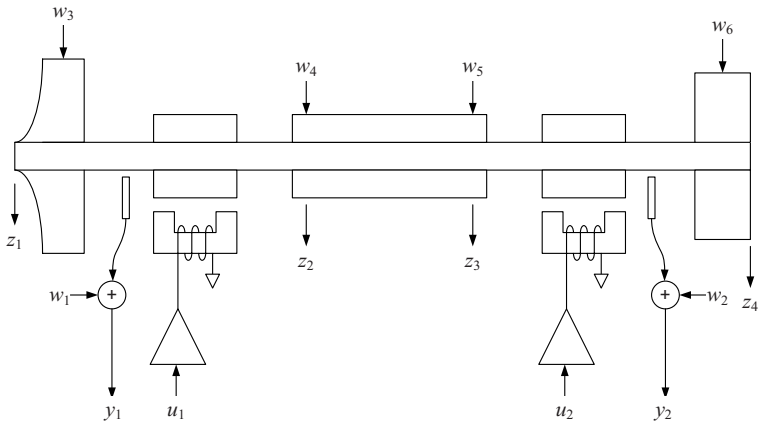


Fig. 12.8. Generic AMB supported rotor and peripheral hardware: u signals are controls, w are loads, y are outputs, and z are performance measures.

Generally, these transfer functions will be defined through a state-space description of the form

$$\begin{bmatrix} \frac{d}{dt}\mathbf{x} \\ \mathbf{z} \\ \mathbf{y} \end{bmatrix} = \left[\begin{array}{c|cc} \mathbf{A} & \mathbf{B}_1 & \mathbf{B}_2 \\ \hline \mathbf{C}_1 & & \mathbf{D}_{12} \\ \mathbf{C}_2 & \mathbf{D}_{21} & \end{array}\right] \begin{bmatrix} \mathbf{x} \\ \mathbf{w} \\ \mathbf{u} \end{bmatrix} \tag{12.5}$$

The missing elements $\mathbf{D}_{11}$ and $\mathbf{D}_{22}$ are normally zero in such a model. The poles of the transfer function elements of $\mathbf{G}(s)$ are the eigenvalues of the matrix $\mathbf{A}$ [83]. The vector x is the set of states used to construct the system dynamics. Converting (12.5) to the transfer functions of (12.4) is a matter of taking the Laplace transform and solving for the output variables in terms of the input variables:

$$Z(s) = C_1(sI - A)^{-1}B_1W(s) + D_{12}U(s) \tag{12.6a}$$

$$\Rightarrow G_{wz}(s) \equiv C_1(sI - A)^{-1}B_1,\ G_{uz}(s) \equiv D_{12} \tag{12.6b}$$

$$Y(s) = D_{21}W(s) + C_2(sI - A)^{-1}B_2U(s) \tag{12.6c}$$

$$\Rightarrow G_{wy} \equiv D_{21}W(s),\ G_{uy} \equiv C_2(sI - A)^{-1}B_2U(s) \tag{12.6d}$$

12.3 Model Elements and Assembly

In order to clearly distinguish between what is *plant* and what is *controller*, we will adopt here the convention that the plant comprises all of the physical hardware that is specified prior to design of the controller algorithm while the controller is entirely described by its algorithm. For a typical digital control implementation, this will mean that the plant includes:

1. power amplifiers which convert controller specified voltages into magnetic actuator fields
2. radial and axial electromagnets which convert amplifier driven fields into rotor forces
3. the rotor itself, which converts applied forces into physical displacements and velocities
4. sensors which convert physical displacements into voltages
5. anti-aliasing filters used to condition the sensor signals before they are sampled by a digital controller
6. sampling delays introduced by the digital controller hardware

In this convention, the inputs to the controller are voltages (generally between -10 volts and +10 volts) and the outputs from the controller are also voltages (also generally between -10 volts and +10 volts).

Technically, it might also make sense to include the analog-to-digital and digital-to-analog converters in this plant model structure since these devices are typically chosen prior to controller design. In this case, the inputs and outputs of the controller would simply be integers. But these converters are normally treated as fixed gains, so it is most common to neglect them. Such a model view has the merit that it can also describe the plant seen by an analog controller.

From a signal path point of view, this model structure can be described as in Fig. 12.9: the controller signals $\mathbf{u}$ act on the amplifier which interacts with the actuator. The actuator, in turn, interacts with the rotor applying forces and responding to changes in rotor position. The rotor reacts to actuator forces as well as loads $\mathbf{w}$ to produce displacements and performance measures, $\mathbf{z}$. These displacements are sensed by sensors and their electronics and the resulting signals are passed to the anti-aliasing filters. The resulting signals are delayed when sampled and the result, with noise $\mathbf{w}$ added, is provided to the controller as measured signals $\mathbf{y}$.

12.3.1 Actuation

In an AMB system, actuation is accomplished through the combined action of power amplifiers and an array of electromagnets. Chapter 4 develops a detailed linearized model of the actuator with this structure, resulting in (4.22):

$$\begin{aligned}\frac{d}{dt}\mathbf{x}_{\text{act}} &= \mathbf{A}_{\text{act}}\mathbf{x}_{\text{act}} + \mathbf{B}_{\text{act},1}\mathbf{u} + \mathbf{B}_{\text{act},2}\mathbf{y}_{\text{mag}}\\ \mathbf{z}_{\text{act}} &= \mathbf{C}_{\text{act},1}\mathbf{x}_{\text{act}} + \mathbf{D}_{\text{act},1}\mathbf{u} + \mathbf{D}_{\text{act},2}\mathbf{y}_{\text{mag}}\\ \mathbf{f}_{\text{mag}} &= \mathbf{C}_{\text{act},2}\mathbf{x}_{\text{act}}\end{aligned}$$

in which $\mathbf{x}_{\text{act}}$ are the internal states of the electromagnets (fluxes) and power amplifiers.

As expected, the inputs to this model include the rotor journal displacement, $\mathbf{y}_{\text{mag}}$ (from the rotor model) and the amplifier command signal, $\mathbf{u}$.

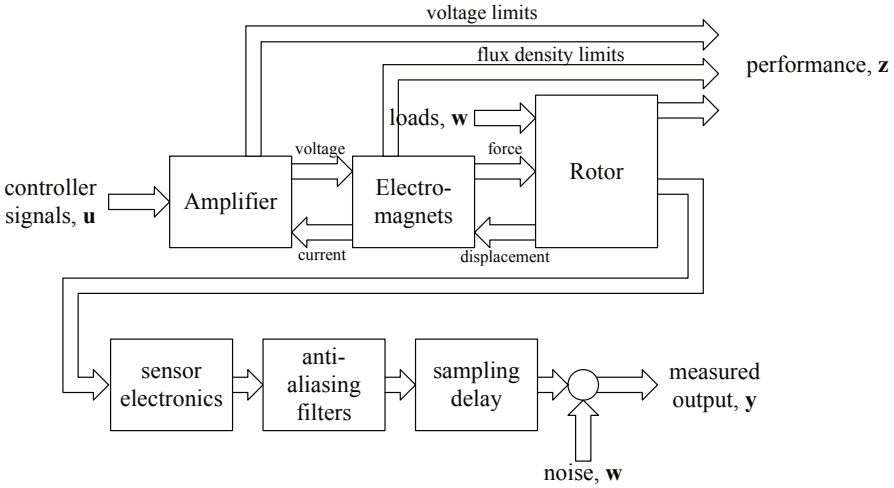


Fig. 12.9. Signal path through AMB plant.

The output of this model component to the rest of the model physics is the vector of actuator forces, $\mathbf{f}_{\text{mag}}$, while the performance output, $\mathbf{z}_{\text{act}}$, includes command signals, coil voltages, magnet flux densities, and coil currents.

12.3.2 Rotor

Following the development of Chap. 10, the rotor model should look like

$$\frac{d}{dt}\mathbf{x}_{\text{rot}} = [\mathbf{A}_{\text{rot}} + \Omega\mathbf{G}_{\text{rot}}]\,\mathbf{x}_{\text{rot}} + \mathbf{B}_{\text{rot},1}\mathbf{w}_{\text{rot}} + \mathbf{B}_{\text{rot},2}\mathbf{f}_{\text{mag}} \tag{12.7a}$$

$$\mathbf{z}_{\text{rot}} = \mathbf{C}_{\text{rot},1}\mathbf{x}_{\text{rot}} \tag{12.7b}$$

$$\mathbf{y}_{\text{mag}} = \mathbf{C}_{\text{rot},2}\mathbf{x}_{\text{rot}} \tag{12.7c}$$

$$\mathbf{y}_{\text{sense}} = \mathbf{C}_{\text{rot},3}\mathbf{x}_{\text{rot}} \tag{12.7d}$$

In this model, $\mathbf{x}_{\text{rot}}$ are the rotor states, Ω is the rotor spin speed, the elements of $\mathbf{w}_{\text{rot}}$ are exogenous forces acting on the rotor such as mass unbalance or aerodynamic loading, the elements of $\mathbf{f}_{\text{mag}}$ are the forces produced by the AMB actuators, and $\mathbf{z}_{\text{rot}}$ is the collection of physical rotor displacements associated with critical clearances in the machine: points where rub might occur in the event of excessive rotor motion.

A joint model of the actuators and rotor is easily assembled by combining (4.22) and (12.7). Thus,

$$\frac{d}{dt}\begin{bmatrix}\mathbf{x}_{\text{act}}\\ \mathbf{x}_{\text{rot}}\end{bmatrix} = \begin{bmatrix}\mathbf{A}_{\text{act}} & \mathbf{B}_{\text{act},2}\mathbf{C}_{\text{rot},2}\\ \mathbf{B}_{\text{rot},2}\mathbf{C}_{\text{act},2} & \mathbf{A}_{\text{rot}} + \Omega\mathbf{G}_{\text{rot}}\end{bmatrix}\begin{bmatrix}\mathbf{x}_{\text{act}}\\ \mathbf{x}_{\text{rot}}\end{bmatrix} + \begin{bmatrix}0\\ \mathbf{B}_{\text{rot},1}\end{bmatrix}\mathbf{w}_{\text{rot}} + \begin{bmatrix}\mathbf{B}_{\text{act},1}\\ 0\end{bmatrix}\mathbf{u} \tag{12.8a}$$

$$\begin{bmatrix} \mathbf{z}_{\text{act}} \\ \mathbf{z}_{\text{rot}} \end{bmatrix} = \begin{bmatrix} \mathbf{C}_{\text{act},1} & \mathbf{D}_{\text{act},2}\mathbf{C}_{\text{rot},2} \\ 0 & \mathbf{C}_{\text{rot},1} \end{bmatrix} \begin{bmatrix} \mathbf{x}_{\text{act}} \\ \mathbf{x}_{\text{rot}} \end{bmatrix} + \begin{bmatrix} \mathbf{D}_{\text{act},1} \\ 0 \end{bmatrix} \mathbf{u} \tag{12.8b}$$

$$\mathbf{y}_{\text{sense}} = \begin{bmatrix} 0 & \mathbf{C}_{\text{rot},3} \end{bmatrix} \begin{bmatrix} \mathbf{x}_{\text{act}} \\ \mathbf{x}_{\text{rot}} \end{bmatrix} \tag{12.8c}$$

12.3.3 Sensors, Anti-aliasing Filters, and Sampling Delay

Each sensor has associated with it an anti-aliasing filter and a sampling delay: all three elements are connected in series for each sensor. For notational convenience, we will group the three elements as a single dynamic component:

$$u_{\text{delay},i} = G_{\text{delay},i} G_{\text{aa},i} G_{\text{sense},i} y_{\text{sense},i} = G_{\text{out},i} y_{\text{sense},i}$$

Sensor

Typically, position sensors are assumed to have some fixed low frequency sensitivity (DC gain) and some bandwidth. Generally, the bandwidth of the sensors is high enough to have only a small effect on system stability and performance but, if a reasonable estimate of bandwidth is available, it makes sense to include this in the model.

On a sensor-by-sensor basis, the form of the model is:

$$u_{\text{sense},i}(s) = G_{\text{sense},i}(s) y_{\text{sense},i}(s)$$

in which $u_{\text{sense},i}(s)$ is the ith sensor output signal, in volts, while $y_{\text{sense},i}(s)$ is the measured rotor displacement, in meters. $G_{\text{sense},i}(s)$, at a minimum, has the form

$$G_{\text{sense},i}(s) = \frac{G_{DC}}{\tau s + 1}$$

which is a simple first order low pass filter. The bandwidth (in Hz) is $\frac{1}{2\pi\tau}$ while the sensitivity is G_{DC}. A state-space model of such a transfer function is:

$$\frac{d}{dt} x_{\text{sense},i} = -\frac{1}{\tau} x_{\text{sense},i} + \frac{G_{DC}}{\tau} y_{\text{sense},i} \tag{12.9a}$$

$$u_{\text{sense},i} = x_{\text{sense},i} \tag{12.9b}$$

or, generically,

$$\frac{d}{dt} \mathbf{x}_{\text{sense},i} = \mathbf{A}_{\text{sense},i} \mathbf{x}_{\text{sense},i} + \mathbf{B}_{\text{sense},i} y_{\text{sense},i} \tag{12.10a}$$

$$u_{\text{sense},i} = \mathbf{C}_{\text{sense},i} \mathbf{x}_{\text{sense},i} \tag{12.10b}$$

in which, for this example,

$$\mathbf{A}_{\text{sense},i} = -\frac{1}{\tau}\ , \quad \mathbf{B}_{\text{sense},i} = \frac{G_{DC}}{\tau}\ , \quad \mathbf{C}_{\text{sense},i} = 1$$

Anti-aliasing Filter

In most modern AMB systems, the controller is digital. As such, it samples its inputs and updates its outputs at a fixed rate: generally, this rate is between 5 kSa/sec and 20 kSa/sec. This sampling process requires filtering of the input signal in order to avoid aliasing of signals with frequency higher than half the sampling rate. Consequently, it is common to equip digital controllers with anti–aliasing filters that act on the input signal, as discussed in Sect. 9.5. Although these filters are technically a component of the controller, it is convenient to treat them as a component of the plant: in designing the controller, the filter dynamic behavior is probably fixed and operates as a constraint on what the controller can accomplish.

In general, the form of the anti-aliasing filter is:

$$u_{\mathrm{aa},i} = G_{\mathrm{aa},i}(s)u_{\mathrm{sense},i} = G_{\mathrm{aa},i}G_{\mathrm{sense},i}(s)y_{\mathrm{sense},i}$$

Anti-aliasing filters take many forms, ranging from very simple first order low-pass filters to relatively high order Bessel or Chebyshev filters. Typically, the objective in choosing the anti-aliasing filter is to drive the gain at the half-sampling frequency as low as possible while introducing as little phase lag as possible at frequencies where the compensator will need to generate phase lead.

There are many strategies for transforming a filter in this form to a state space model compatible with (12.8): the development surrounding (4.3) and (4.4) is one such method. The result is that such a filter may be represented generically in state-space form by

$$\frac{d}{dt}\mathbf{x}_{\mathrm{aa},i} = \mathbf{A}_{\mathrm{aa},i}\mathbf{x}_{\mathrm{aa},i} + \mathbf{B}_{\mathrm{aa},i}u_{\mathrm{sense},i} \tag{12.11a}$$

$$u_{\mathrm{aa},i} = \mathbf{C}_{\mathrm{aa},i}\mathbf{x}_{\mathrm{aa},i} \tag{12.11b}$$

Sampling Delay

In addition, digital controllers introduce delay between when a signal arrives to be sampled and when the corresponding action is taken. This delay is most typically between one and two sample intervals. For purposes of control synthesis modeling, this delay must be approximated by a finite ordered dynamic system: the most widely used model is the Padé approximation. Padé approximations are available with any order: as the order increases, the range of frequencies over which the approximation is valid also increases. Experience indicates that a third order Padé approximation is nearly always sufficient: this is illustrated in Fig. 12.10 where the phase responses of first, second, and third order Padé approximations to a 100 microsecond delay are compared.

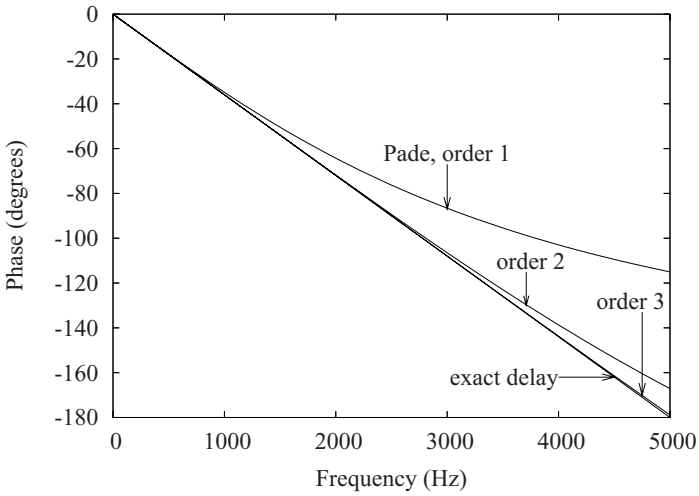


Fig. 12.10. Comparison of the phase for first, second, and third order Padé approximations to the exact phase for a 100 microsecond delay.

As an example, for a delay of τ seconds, a third order Padé approximation is provided by

$$G_{\text{delay}} \approx \frac{24\tau^2 s^2 + 240}{\tau^3 s^3 + 12\tau^2 s^2 + 60\tau s + 120} - 1 \tag{12.12}$$

Note that the delay dynamic is stable (all of the transfer function poles are in the left half plane) but not minimum phase: the transfer function has *all* of its zeros in the right half plane. In particular, if λ is a pole of G_{delay}, then $-\lambda$ is a zero of the transfer function. This pole-zero structure provides a constant gain magnitude of 1.0 while the pole arrangement provides a phase lag nearly proportional to frequency over a wide range of frequencies (see Fig. 12.10).

As with the anti-aliasing filter, the Padé approximation to a time delay is a finite ordered transfer function; the only structural difference is that the time delay has a constant term of -1. Hence, this transfer function may be represented by

$$\frac{d}{dt}\mathbf{x}_{\text{delay},i} = \mathbf{A}_{\text{delay},i}\mathbf{x}_{\text{delay},i} + \mathbf{B}_{\text{delay},i}u_{\text{aa},i} \tag{12.13a}$$

$$u_{\text{delay},i} = \mathbf{C}_{\text{delay},i}\mathbf{x}_{\text{delay},i} + \mathbf{D}_{\text{delay},i}u_{\text{aa},i} \tag{12.13b}$$

in which $\mathbf{A}_{\text{delay},i}$, $\mathbf{B}_{\text{delay},i}$, and $\mathbf{C}_{\text{delay},i}$ represent the rational polynomial part of (12.12) following the strategy of (4.3)-(4.4) while $\mathbf{D}_{\text{delay},i} = -1$.

Composite Sensing Dynamics

As previously discussed, these three elements (sensor dynamics, anti-aliasing filter, and delay) act in series and are repeated for each rotor displacement

that is measured. Consequently, it is convenient to treat them as a composite dynamic by interconnecting them:

$$\frac{d}{dt}\begin{bmatrix}\mathbf{x}_{\text{sense},i}\\ \mathbf{x}_{\text{aa},i}\\ \mathbf{x}_{\text{delay},i}\end{bmatrix} = \begin{bmatrix}\mathbf{A}_{\text{sense},i} & 0 & 0\\ \mathbf{B}_{\text{aa},i}\mathbf{C}_{\text{sense},i} & \mathbf{A}_{\text{aa},i} & 0\\ 0 & \mathbf{B}_{\text{delay},i}\mathbf{C}_{\text{aa},i} & \mathbf{A}_{\text{delay},i}\end{bmatrix}\begin{bmatrix}\mathbf{x}_{\text{sense},i}\\ \mathbf{x}_{\text{aa},i}\\ \mathbf{x}_{\text{delay},i}\end{bmatrix} + \begin{bmatrix}\mathbf{B}_{\text{sense},i}\\ 0\\ 0\end{bmatrix} y_{\text{sense},i} \tag{12.14a}$$

$$u_{\text{delay},i} = \begin{bmatrix}0 & \mathbf{D}_{\text{delay},i}\mathbf{C}_{\text{aa},i} & \mathbf{C}_{\text{delay},i}\end{bmatrix}\begin{bmatrix}\mathbf{x}_{\text{sense},i}\\ \mathbf{x}_{\text{aa},i}\\ \mathbf{x}_{\text{delay},i}\end{bmatrix} \tag{12.14b}$$

The signal actually delivered to the controller will *always* be corrupted by noise. Hence:

$$y_i = u_{\text{delay},i} + w_{\text{noise},i} \tag{12.15}$$

As a matter of compactness in ensuing notation, represent this single signal composite model:

$$\frac{d}{dt}\mathbf{x}_{\text{out},i} = \mathbf{A}_{\text{out},i}\mathbf{x}_{\text{out},i} + \mathbf{B}_{\text{out},i}y_{\text{sense},i} \tag{12.16a}$$

$$y_i = \mathbf{C}_{\text{out},i}\mathbf{x}_{\text{out},i} + \mathbf{D}_{\text{out},i}w_{\text{noise},i} \tag{12.16b}$$

in which $\mathbf{D}_{\text{out},i} = 1.0$. Finally, the entire system of sensors, anti-aliasing filters, and delays may be combined into a single system:

$$\frac{d}{dt}\mathbf{x}_{\text{out}} = \mathbf{A}_{\text{out}}\mathbf{x}_{\text{out}} + \mathbf{B}_{\text{out}}\mathbf{y}_{\text{sense}} \tag{12.17a}$$

$$\mathbf{y} = \mathbf{C}_{\text{out}}\mathbf{x}_{\text{out}} + \mathbf{D}_{\text{out}}\mathbf{w}_{\text{noise}} \tag{12.17b}$$

12.3.4 Complete Model

The complete plant can now be assembled by combining the rotor-actuator-amplifier dynamics (12.8) with the measurement dynamics (12.17):

$$\frac{d}{dt}\begin{bmatrix}\mathbf{x}_{\text{act}}\\ \mathbf{x}_{\text{rot}}\\ \mathbf{x}_{\text{out}}\end{bmatrix} = \begin{bmatrix}\mathbf{A}_{\text{act}} & \mathbf{B}_{\text{act},2}\mathbf{C}_{\text{rot},2} & 0\\ \mathbf{B}_{\text{rot},2}\mathbf{C}_{\text{act},2} & \mathbf{A}_{\text{rot}} + \Omega\mathbf{G}_{\text{rot}} & 0\\ 0 & \mathbf{B}_{\text{out}}\mathbf{C}_{\text{rot},3} & \mathbf{A}_{\text{out}}\end{bmatrix}\begin{bmatrix}\mathbf{x}_{\text{act}}\\ \mathbf{x}_{\text{rot}}\\ \mathbf{x}_{\text{out}}\end{bmatrix} + \begin{bmatrix}0 & 0\\ \mathbf{B}_{\text{rot},1} & 0\\ 0 & 0\end{bmatrix}\begin{bmatrix}\mathbf{w}_{\text{rot}}\\ \mathbf{w}_{\text{noise}}\end{bmatrix} + \begin{bmatrix}\mathbf{B}_{\text{act},1}\\ 0\\ 0\end{bmatrix}\mathbf{u} \tag{12.18a}$$

$$\begin{bmatrix}\mathbf{z}_{\text{act}}\\ \mathbf{z}_{\text{rot}}\end{bmatrix} = \begin{bmatrix}\mathbf{C}_{\text{act},1} & \mathbf{D}_{\text{act},2}\mathbf{C}_{\text{rot},2} & 0\\ 0 & \mathbf{C}_{\text{rot},1} & 0\end{bmatrix}\begin{bmatrix}\mathbf{x}_{\text{act}}\\ \mathbf{x}_{\text{rot}}\\ \mathbf{x}_{\text{out}}\end{bmatrix} + \begin{bmatrix}\mathbf{D}_{\text{act},1}\\ 0\end{bmatrix}\mathbf{u} \tag{12.18b}$$

$$\mathbf{y} = \begin{bmatrix}0\ 0\ \mathbf{C}_{\text{out}}\end{bmatrix}\begin{bmatrix}\mathbf{x}_{\text{act}}\\ \mathbf{x}_{\text{rot}}\\ \mathbf{x}_{\text{out}}\end{bmatrix} + \begin{bmatrix}0\ \mathbf{D}_{\text{out}}\end{bmatrix}\begin{bmatrix}\mathbf{w}_{\text{rot}}\\ \mathbf{w}_{\text{noise}}\end{bmatrix} \tag{12.18c}$$

which has the standard model form of (12.5).

12.3.5 Example Model

As an example of a rotor/AMB system, consider the rotor depicted in Fig. 12.11. The rotor has a motor mass mounted midspan and smaller disks (impellers) mounted at each end. The rotor is controlled by two AMB actuators and has sensors mounted outboard of these actuators.

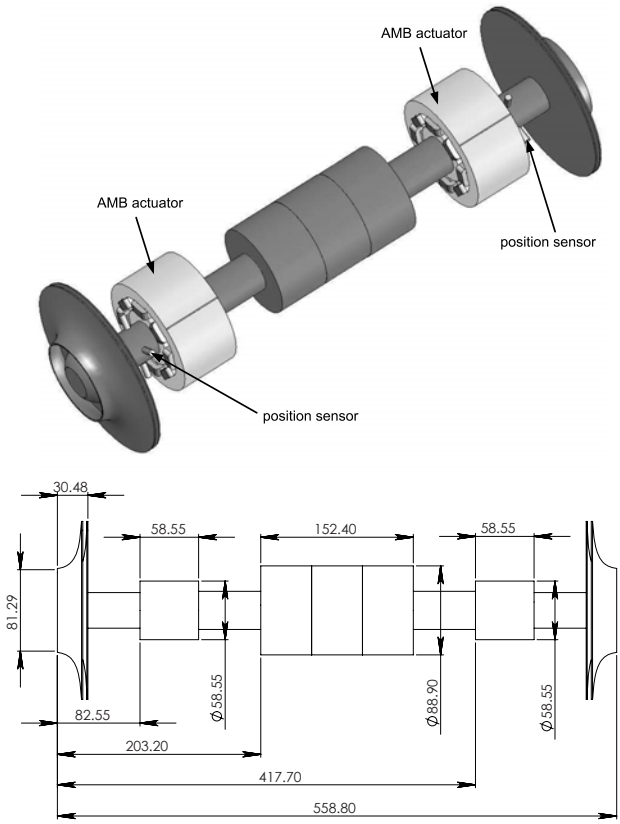


Fig. 12.11. A simple, symmetric flexible rotor with end mounted wheels and a distributed motor in the center. AMB journals are installed toward either end. All dimensions are in mm.

The Rotor

The rotor has a total length of 559 mm and a total mass of 14.7 kg. It is symmetric about its midpoint so the rotor center of mass is located 279.5 mm from either end. The first free-free bending mode of this rotor has a

frequency of 1752 rad/sec (279 Hz) and the second free–free bending mode has a frequency of 4873 rad/sec (776 Hz). The rotor was modeled using an Euler-Bernoulli beam element model with 56 mass stations, as described in Chap. 10. It was assumed that each of the flexible modes exhibits one percent modal damping[1]. The first four free–free modes of the rotor when not spinning are depicted in Fig. 12.12: the first two modes are rigid (zero frequency) modes while the third and fourth modes are the first two bending modes.

In order to keep the size of the model manageable, this large finite element model (224 states per rotor plane) was truncated in modal space to retain the first two rigid body modes and the first six flexible modes. This results in a fairly good representation of the rotor dynamics out to a frequency of 2.8 kHz but requires only 16 states per rotor plane.

Performance expectations for this rotor focus on unbalance response: The rotor is component balanced so that the mass unbalance at the disks, at the journals, and at each of the two ends of the motor is less than 10 g-mm in each plane (a total of six planes). The maximum expected operating speed of the rotor is 30000 RPM, which is above the first free–free bending mode, but below the second. Radial excursions at the journals must be less than 0.12 mm from geometric center in order to avoid contact with touch-down bearings (not indicated in Fig. 12.11) while motion at each of the motor ends must be less than 0.3 mm to avoid contact with the motor stator (also not indicated in Fig. 12.11.) Radial motion of each of the two impellers must be less than 0.25 mm to avoid contact at the eye seals.

AMB Electromagnets

The AMB journals have centerlines located 111.81 mm and 446.99 mm from the left end of the rotor. They have projected surface areas (diameter × length) of 3428 mm^2 and are assumed to achieve magnetic saturation at a flux density

[1] One must use significant caution in applying modal damping and appreciate the assumptions involved. In particular, most "modal" damping is provided either by friction between assembled components or by hysteretic damping of rotor materials: for steel rotors, the former is the primary mechanism while for composite rotors, the latter may dominate. This means that this "internal" damping is *body fixed* and, as such, not only dissipates energy from lateral rotor motion (whirl) but *also* couples spin energy into whirl. At low speeds, the rate of energy transfer into whirl is less than the rate of dissipation, but this relationship can reverse at high speeds, leading to instability. For a symmetric rotor, this reversal occurs at the first free–free bending mode frequency: for rotor spin rates higher than this frequency, the damping associated with the first bending mode is destabilizing. Consequently, and in a somewhat pragmatic way, the modeler may wish to model modes whose frequencies are below maximum operating speed either as undamped or even negatively damped. A correct modeling of the internal damping forces leads to non-conservative restoring forces increasing with the rotor speed (see Sect. 7.4.4)

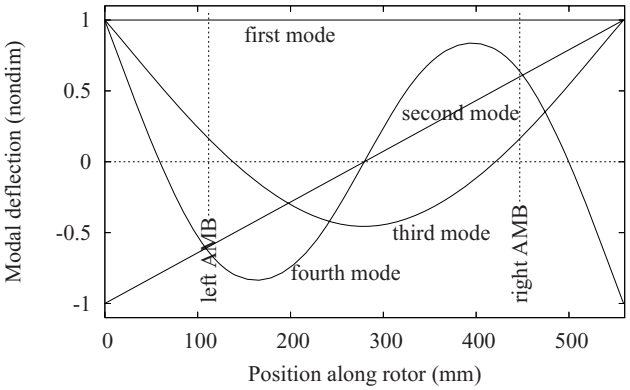


Fig. 12.12. Free–free modes of the rotor shown in Fig. 12.11.

of 2.2 Tesla. The useful projected surface area is $\eta = 50\%$ (ie: coil slot width is equal to pole width at the air gap): this provides an expected load capacity of 2400 N per actuator. The electromagnet is wound to saturate at a coil current of 10 A and has a radial air gap of 0.25 mm. The coils have a series resistance of 1.5Ω and are biased to 4 A. The resulting electromagnet properties are easily computed as:

$$A_{\text{pole}} = 2l_{\text{journal}}(0.5D_{\text{journal}} + s_0)\sin(22.5^\circ\eta) = 675 \text{ mm}^2 \quad (12.19a)$$

$$P_{\text{sat}} = \frac{B_{\text{sat}}^2}{2\mu_0} = 1.93 \text{ MPa} \quad (12.19b)$$

$$F_{\text{sat}} = 2\cos(22.5^\circ)P_{\max}A_{\text{pole}} = 2400 \text{ N} \quad (12.19c)$$

$$K_i = \frac{4F_{\text{sat}}I_{\text{bias}}}{I_{\text{sat}}^2} = 384 \text{ N/A} \quad (12.19d)$$

$$K_s = -\frac{4F_{\text{sat}}I_{\text{bias}}^2}{s_0 I_{\text{sat}}^2} = -K_i\frac{I_{\text{bias}}}{s_0} = -6144 \text{ N/mm} \quad (12.19e)$$

$$L = \frac{2s_0K_i}{\cos(22.5^\circ)I_{\text{bias}}} = \frac{8s_0F_{\text{sat}}}{\cos(22.5^\circ)I_{\text{sat}}^2} = 52 \text{ mH} \quad (12.19f)$$

$$R = 1.5\Omega \quad (12.19g)$$

Note that, if the journal motion can be as large as half the gap length (0.125 mm) and the electromagnet has a capacity of 2400 N, then the maximum stiffness that can be realized across this entire stroke is $2400/0.125 = 19200$ N/mm. Thus, we expect the nominal stiffness of the bearing to be somewhere close to this value. Further, this value is about three times $-K_s$, which means that expected variations in K_s of perhaps 40% will not have too adverse an effect on the net nominal stiffness of the bearing.

Power Amplifiers

The power amplifiers have a gain of 1 Amp/volt and a bandwidth of 1200 Hz when connected to this electromagnet. High frequency roll-off is second order with a damping ratio of 0.8. This means that, referring to (4.2) in Section 4.2,

$$T(s) = \frac{5.69 \times 10^7}{s^2 + 1.2 \times 10^4 s + 5.69 \times 10^7}$$

If we assume that $R_f = 1.0\Omega$ and that $G_{\text{amp},a} = G_{\text{amp},b}$, then the open loop amplifier gain from command voltage to amplifier output voltage may be computed using (4.2) with the actuator properties ($L = 52$mH and $R = 1.5\Omega$) as

$$G_{\text{amp},a}(s) = \frac{7069}{s} + \frac{244}{8.3 \times 10^{-5} s + 1}$$

Sensors

The sensors are eddy current type devices and measure shaft motion at positions 44.45 mm and 514.35 mm from the left end of the rotor. The sensors have a gain of 50 volts per millimeter and a bandwidth of 8.0 kHz with typical first order roll-off.

Digital Controller

The digital controller will be assumed to be capable of executing the control algorithm at a rate of 20 kSa/sec with a total delay through the controller of 100 microseconds. Anti-aliasing filters are provided at the input: simple first order low pass filters with bandwidth of 6 kHz.

Complete Model

The resulting model has a total of 30 states per rotor plane: coupling the two planes through the gyroscopic matrix $\mathbf{G}$ results in a 60 state model. The eigenvalues of the model without gyroscopic coupling are presented in Table 12.2.

12.3.6 Including Casings and Substructures

In some AMB applications, substructure or casing flexibility may be significant and need to be modeled. Assume that the casing or substructure model is available in the form

$$\frac{d}{dt}\mathbf{x}_{\text{sub}} = \mathbf{A}_{\text{sub}}\mathbf{x}_{\text{sub}} + \mathbf{B}_{\text{sub},1}\mathbf{w}_{\text{sub}} - \mathbf{B}_{\text{sub},2}\mathbf{f}_{\text{mag}} \tag{12.20a}$$

$$\mathbf{z}_{\text{rot,sub}} = \mathbf{C}_{\text{sub},1}\mathbf{x}_{\text{sub}} \tag{12.20b}$$

$$\mathbf{y}_{\text{mag,sub}} = \mathbf{C}_{\text{sub},2}\mathbf{x}_{\text{sub}} \tag{12.20c}$$

$$\mathbf{y}_{\text{sense,sub}} = \mathbf{C}_{\text{sub},3}\mathbf{x}_{\text{sub}} \tag{12.20d}$$

Table 12.2. Example plant eigenvalues with the rotor stationary (not spinning)

Eigenvalue	interpretation
-5862.1 $\pm$ j4393.6	power amplifier / actuator dynamics
-5832.6 $\pm$ j4401.7	power amplifier / actuator dynamics
854.92	unstable rigid body mode
935.55	unstable rigid body mode
-1057.7	stable rigid body mode
-1183.8	stable rigid body mode
-23.1 $\pm$ j1733	first flexible rotor mode
-113.04 $\pm$ j4835.3	second flexible rotor mode
-145.62 $\pm$ j8301.5	third flexible rotor mode
-131.1 $\pm$ j12166	fourth flexible rotor mode
-179.27 $\pm$ j17918	fifth flexible rotor mode
-221.92 $\pm$ j22062	sixth flexible rotor mode
-50265.	sensor bandwidth
-50265.	sensor bandwidth
-37699.	anti-aliasing filter
-37699.	anti-aliasing filter
-36778.$\pm j$35088	delay dynamics
-46444.	delay dynamics
-36778.$\pm j$35088	delay dynamics
-46444.	delay dynamics

Note that the AMB sensors will measure the *difference* between rotor motion and casing motion:

$$\mathbf{y}_{\text{sense}} = \mathbf{y}_{\text{sense,rot}} - \mathbf{y}_{\text{sense,sub}}$$

and, in the same manner, the actuator journal displacements (needed by the actuator models) are also relative:

$$\mathbf{y}_{\text{mag}} = \mathbf{y}_{\text{mag,rot}} - \mathbf{y}_{\text{mag,sub}}$$

Of course, if the rotor performance measures are based on rotor–casing clearance, then

$$\mathbf{z}_{\text{rot}} = \mathbf{z}_{\text{rot,rot}} - \mathbf{z}_{\text{rot,sub}}$$

Forces exerted on the casing by the AMB actuator will be equal and opposite to those applied to the rotor, hence the negative sign in (12.20).

It is simply a matter of bookkeeping to combine (12.20) with (12.18) to produce a model of the aggregate AMB-rotor-casing system:

$$\frac{d}{dt}\begin{bmatrix}\mathbf{x}_{\text{act}}\\ \mathbf{x}_{\text{rot}}\\ \mathbf{x}_{\text{sub}}\\ \mathbf{x}_{\text{out}}\end{bmatrix} = \begin{bmatrix}\mathbf{A}_{\text{act}} & \mathbf{B}_{\text{act},2}\mathbf{C}_{\text{rot},2} & -\mathbf{B}_{\text{act},2}\mathbf{C}_{\text{sub},2} & 0\\ \mathbf{B}_{\text{rot},2}\mathbf{C}_{\text{act},2} & \mathbf{A}_{\text{rot}} + \Omega\mathbf{G}_{\text{rot}} & 0 & 0\\ -\mathbf{B}_{\text{sub},2}\mathbf{C}_{\text{act},2} & 0 & \mathbf{A}_{\text{sub}} & 0\\ 0 & \mathbf{B}_{\text{out}}\mathbf{C}_{\text{rot},3} & -\mathbf{B}_{\text{out}}\mathbf{C}_{\text{sub},3} & \mathbf{A}_{\text{out}}\end{bmatrix}\begin{bmatrix}\mathbf{x}_{\text{act}}\\ \mathbf{x}_{\text{rot}}\\ \mathbf{x}_{\text{sub}}\\ \mathbf{x}_{\text{out}}\end{bmatrix}$$

$$+\begin{bmatrix} 0 & 0 & 0 \\ \mathbf{B}_{\text{rot},1} & 0 & 0 \\ 0 & \mathbf{B}_{\text{sub},1} & 0 \\ 0 & 0 & 0 \end{bmatrix} \begin{bmatrix} \mathbf{w}_{\text{rot}} \\ \mathbf{w}_{\text{sub}} \\ \mathbf{w}_{\text{noise}} \end{bmatrix} + \begin{bmatrix} \mathbf{B}_{\text{act},1} \\ 0 \\ 0 \\ 0 \end{bmatrix} \mathbf{u} \tag{12.21a}$$

$$\begin{bmatrix} \mathbf{z}_{\text{act}} \\ \mathbf{z}_{\text{rot,rot}} \end{bmatrix} = \begin{bmatrix} \mathbf{C}_{\text{act},1} & \mathbf{D}_{\text{act},2}\mathbf{C}_{\text{rot},2} & -\mathbf{D}_{\text{act}}\mathbf{C}_{\text{sub},2} & 0 \\ 0 & \mathbf{C}_{\text{rot},1} & -\mathbf{C}_{\text{sub},1} & 0 \end{bmatrix} \begin{bmatrix} \mathbf{x}_{\text{act}} \\ \mathbf{x}_{\text{rot}} \\ \mathbf{x}_{\text{sub}} \\ \mathbf{x}_{\text{out}} \end{bmatrix}$$

$$+\begin{bmatrix} \mathbf{D}_{\text{act},1} \\ 0 \end{bmatrix} \mathbf{u} \tag{12.21b}$$

$$\mathbf{y} = \begin{bmatrix} 0\ 0\ 0\ \mathbf{C}_{\text{out}} \end{bmatrix} \begin{bmatrix} \mathbf{x}_{\text{act}} \\ \mathbf{x}_{\text{rot}} \\ \mathbf{x}_{\text{sub}} \\ \mathbf{x}_{\text{out}} \end{bmatrix} + \begin{bmatrix} 0\ 0\ \mathbf{D}_{\text{out}} \end{bmatrix} \begin{bmatrix} \mathbf{w}_{\text{rot}} \\ \mathbf{w}_{\text{sub}} \\ \mathbf{w}_{\text{noise}} \end{bmatrix} \tag{12.21c}$$

As with (12.18), (12.21) satisfies the expectations for model format identified in (12.5).

12.3.7 Closing the Loop

No matter how the controller is constructed, if it is linear (or may be approximated as linear), it will be able to be represented as

$$\frac{d}{dt}\mathbf{x}_{\text{cont}} = \mathbf{A}_{\text{cont}}\mathbf{x}_{\text{cont}} + \mathbf{B}_{\text{cont}}\mathbf{y} \tag{12.22a}$$

$$\mathbf{u} = \mathbf{C}_{\text{cont}}\mathbf{x}_{\text{cont}} \tag{12.22b}$$

Note that this model has no $\mathbf{D}$ matrix: any realizable controller will be *strictly proper* which means that its gain will go to zero at infinite frequency. In a state space model, this implies that $\mathbf{D} = 0$.

Combining (12.22) with the plant as described either by (12.18) or by (12.21) is quite straightforward: simply equate the control and measurement signals to produce (for the model without casing):

$$\frac{d}{dt}\begin{bmatrix} \mathbf{x}_{\text{act}} \\ \mathbf{x}_{\text{rot}} \\ \mathbf{x}_{\text{out}} \\ \mathbf{x}_{\text{cont}} \end{bmatrix} = \begin{bmatrix} \mathbf{A}_{\text{act}} & \mathbf{B}_{\text{act},2}\mathbf{C}_{\text{rot},2} & 0 & \mathbf{B}_{\text{act},1}\mathbf{C}_{\text{cont}} \\ \mathbf{B}_{\text{rot},2}\mathbf{C}_{\text{act},2} & \mathbf{A}_{\text{rot}} + \Omega\mathbf{G}_{\text{rot}} & 0 & 0 \\ 0 & \mathbf{B}_{\text{out}}\mathbf{C}_{\text{rot},3} & \mathbf{A}_{\text{out}} & 0 \\ \mathbf{B}_{\text{cont}}\mathbf{C}_{\text{out}} & 0 & 0 & \mathbf{A}_{\text{cont}} \end{bmatrix} \begin{bmatrix} \mathbf{x}_{\text{act}} \\ \mathbf{x}_{\text{rot}} \\ \mathbf{x}_{\text{out}} \\ \mathbf{x}_{\text{cont}} \end{bmatrix}$$

$$+\begin{bmatrix} 0 & 0 \\ \mathbf{B}_{\text{rot},1} & 0 \\ 0 & \mathbf{B}_{\text{cont}}\mathbf{D}_{\text{out}} \\ 0 & 0 \end{bmatrix} \begin{bmatrix} \mathbf{w}_{\text{rot}} \\ \mathbf{w}_{\text{noise}} \end{bmatrix} \tag{12.23a}$$

$$\begin{bmatrix} \mathbf{z}_{\text{act}} \\ \mathbf{z}_{\text{rot}} \end{bmatrix} = \begin{bmatrix} \mathbf{C}_{\text{act},1} & \mathbf{D}_{\text{act},2}\mathbf{C}_{\text{rot},2} & 0 & \mathbf{D}_{\text{act},1}\mathbf{C}_{\text{cont}} \\ 0 & \mathbf{C}_{\text{rot},1} & 0 & 0 \end{bmatrix} \begin{bmatrix} \mathbf{x}_{\text{act}} \\ \mathbf{x}_{\text{rot}} \\ \mathbf{x}_{\text{out}} \\ \mathbf{x}_{\text{cont}} \end{bmatrix} \tag{12.23b}$$

12.3.8 Some Remarks on AMB System Models

One conclusion that should be clear is that the dynamics of AMBs when controlling flexible rotors can be quite complex in comparison to the models commonly employed for mechanical bearings (fluid film or rolling element) in doing stability or forced response analysis. In particular, it is generally not possible to simplify the bearing dynamics for the purpose of stability assessment in the manner of "synchronously reduced coefficients" widely used for analysis of systems with fluid film bearings. This means that AMB bearing models can not be easily introduced to standard finite element models if the modeling package assumes a second order formulation of mass, spring, and damper type properties. This point cannot be overstated as synchronous reduction of AMB properties at very low or very high frequencies will always produce a "synchronously reduced" model with negative stiffness which would imply system instability.

12.4 Simplest Control: Collocated Local PID

In most AMB configurations, each actuator has associated with it a pair of position sensors aligned with the actuator control axes. Thus, current applied to the $x-$ axis of the actuator produces motion measured by the $x-$ axis sensor and so forth. In such a system, the most obvious control approach is to attempt to make the AMB act like conventional mechanical bearings at the actuator locations [38], an approach often referred to as decentralized control [10]. Although, as will be seen, this approach over-simplifies the problem and must be adapted and extended for realistic rotor systems, examining the design process and resulting behavior is helpful in establishing a baseline performance position and in understanding the general objectives of the control design.

12.4.1 PID Control Concepts

Given this observation, a commonly discussed scheme is to use PID control on an axis-by-axis basis:

$$u_{\mathrm{amp},i}(s) = -G_{\mathrm{PID}}(s)u_{\mathrm{delay},i}(s) \tag{12.24}$$

in which, ideally,

$$G_{\mathrm{PID}} = K_P + K_D s + \frac{K_I}{s}$$

Avoiding the intricacies of the model, this control can be understood in simple terms. Assume for the moment that the sensor gain is K_{sense} and that there is no controller delay or other filtering. Further, neglect amplifier dynamics (the amplifier becomes a simple gain, K_{amp}) and noise as well as sensor noise so that

$$\begin{aligned} u_{\text{delay},i} &= K_{\text{sense}} y_{\text{sense},i} \\ i_{\text{amp},i} &= K_{\text{amp}} u_{\text{amp},i} \\ f_{\text{mag},i} &= -K_s\, y_{\text{mag},i} + K_i\, i_{\text{amp},i} \end{aligned}$$

which, combined with (12.24) produces

$$f_{\text{mag},i} = -K_s y_{\text{mag},i} - K_i K_{\text{amp}} \left(K_P + K_D s + \frac{K_I}{s} \right) K_{\text{sense}} y_{\text{sense},i}$$

If we make the further simplification that $y_{\text{mag},i} = y_{\text{sense},i}$ (this means that the sensor and actuator are *collocated*) then

$$f_{\text{mag},i} = -K_i K_{\text{amp}} \left(K_P + \frac{K_s}{K_i K_{\text{amp}} K_{\text{sense}}} + K_D s + \frac{K_I}{s} \right) K_{\text{sense}} y_{\text{mag},i}$$

Thus, the force at the actuator consists of three terms that depend on the motion:

$$f_{\text{prop}} = -K_i K_{\text{amp}} \left(K_P + \frac{K_s}{K_i K_{\text{amp}} K_{\text{sense}}} \right) K_{\text{sense}} y$$

which is proportional to displacement,

$$f_{\text{deriv}} = -K_i K_{\text{amp}} K_D K_{\text{sense}} s y$$

which is proportional to velocity, and

$$f_{\text{int}} = -K_i K_{\text{amp}} K_I K_{\text{sense}} \frac{1}{s} y$$

which is proportional to the integral of y.

As discussed in detail in Sect. 2.2.3, the first two terms are precisely what is expected of a spring/damper support:

$$f = -ky - c\dot{y} \Leftrightarrow f_{\text{prop}} + f_{\text{deriv}}$$

so they are easy to interpret. The last term (f_{int}) grows without bound as long as the average value of y is non-zero. Hence, if the closed loop system is stable, then the average value of y must be zero. This is very useful in rejecting static loads (like that due to gravity).

Thus, the *effective stiffness* of this PID based AMB is

$$k_{\text{effective}} = K_i K_{\text{amp}} \left(K_P + \frac{K_s}{K_i K_{\text{amp}} K_{\text{sense}}} \right) K_{\text{sense}}$$

Note that $K_s < 0$ so, to have a net positive stiffness, we require that

$$K_P > -\frac{K_s}{K_i K_{\text{amp}} K_{\text{sense}}}$$

In a similar manner, the *damping* of this PID based AMB is

$$c_{\text{effective}} = K_i K_{\text{amp}} K_D K_{\text{sense}}$$

12.4.2 PID Control Example

To illustrate this control in a simple manner, consider the flexible rotor described in Section 12.3.5.

For this rotor, the variation in eigenvalues as a function of bearing stiffness can easily be computed:

$$\mathrm{eig}(\mathbf{A}_{\mathrm{rot}} - \mathbf{B}_{\mathrm{mag}} k\, \mathbf{C}_{\mathrm{mag}}) \quad : \quad k_{\min} \leq k \leq k_{\max}$$

and is plotted in Fig. 12.13. Note that this is not the same as a critical speed map because gyroscopic effects have been ignored.

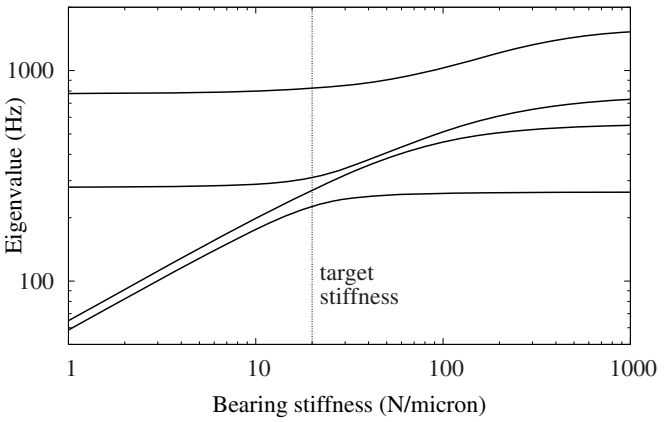


Fig. 12.13. Variation of rotor eigenvalues with changes in AMB effective stiffness.

It can be noticed that the first three modes all show significant slope when the bearing stiffness is about

$$K_{\mathrm{target}} = 20 \text{ N}/\mu\text{m}. \tag{12.25}$$

This implies that there is a reasonable balance of strain energy between the bearings and the rotor when the bearing has this stiffness, so this may be a sensible choice of bearing stiffness in order to be able to introduce significant damping to the rotor. Further, referring to section 12.3.5 which describes the actuators, this target stiffness is consistent with the actuator capacity and clearance, which yielded a characteristic stiffness of 19.2 N/μm. This confirms that the actuators are sized suitably for this rotor.

With this observation, choose K_P so that

$$K_i K_{\mathrm{amp}} K_P K_{\mathrm{sense}} + K_s = K_{\mathrm{target}} \quad \Rightarrow K_P = \frac{K_{\mathrm{target}} - K_s}{K_i K_{\mathrm{amp}} K_{\mathrm{sense}}} = 1.362$$

Next, choose K_D to give good damping for the three modes it must control. Reviewing Fig. 12.13, this means that the AMB should provide significant damping between about 150 Hz and 300 Hz. With an ideal PID controller, damping is large at most frequencies. However, a real PID controller must have finite bandwidth which implies that the damping is only effective over a finite range of frequencies. This bandwidth limiting is accomplished by adding a pair of poles to the PD component:

$$G(s) = K_i K_{\text{amp}} K_{\text{sense}} \left(\frac{K_D s + K_P}{(\tau_1 s + 1)(\tau_2 s + 1)} + \frac{K_I}{s} \right) + K_s \quad (12.26a)$$

$$= K_i K_{\text{amp}} K_{\text{sense}} \left(\frac{K_P \left(\frac{K_D}{K_P} s + 1 \right)}{(\tau_1 s + 1)(\tau_2 s + 1)} + \frac{K_I}{s} \right) + K_s \quad (12.26b)$$

$$= K_i K_{\text{amp}} K_{\text{sense}} \left(\frac{K_P (\tau_0 s + 1)}{(\tau_1 s + 1)(\tau_2 s + 1)} + \frac{K_I}{s} \right) + K_s \quad (12.26c)$$

A common choice in order to manage sensitivity to sensor noise is to set the ratio of maximum to minimum frequency to about 10:1 or, equivalently, let

$$\tau_0 = 10\tau_1$$

The high frequency roll–off is controlled by τ_2 which should be about one third τ_1:

$$\tau_1 = 3\tau_2$$

which produces

$$G(s) = K_i K_{\text{amp}} K_{\text{sense}} \left(\frac{K_P (30\tau_2 s + 1)}{(3\tau_2 s + 1)(\tau_2 s + 1)} + \frac{K_I}{s} \right) + K_s \quad (12.27)$$

Since we hope to provide good damping from about 150 to 300 Hz, we set the peak phase for this filter to a frequency of about

$$\omega_{\text{peak phase}} \approx 2\pi\sqrt{150 \times 300} = 1333 \text{ rad/sec}$$

For a filter with the structure of (12.27), the peak phase occurs at approximately

$$\omega_{\text{peak phase}} \approx \frac{1}{\sqrt{\tau_0 \tau_1}} = \frac{1}{9.4868\tau_2}$$

Thus, a first choice for τ_2 is:

$$\tau_2 = \frac{1}{9.4868 \times 1333} = 79 \ \mu\text{sec}$$

Choice of τ_2 will determine all of the controller parameters except for K_I. However, this choice is based on a rather simple treatment of the problem, so it should only be viewed as a starting point for some iteration. To accomplish

this, set $K_I = 0$ and examine the effect of choice of τ_2 on the closed loop system eigenvalues. The objective in optimizing choice of τ_2 will be to maximize the minimum damping ratio of the first three oscillatory modes of the closed loop system. In this manner, an "optimal" value of τ_2 is found, producing

$$K_D = 449.4\ \mu\text{sec} \tag{12.28a}$$

$$\tau_1 = 33\ \mu\text{sec} \tag{12.28b}$$

$$\tau_2 = 11\ \mu\text{sec} \tag{12.28c}$$

The integrator gain should be as large as possible while not significantly degrading system stability: too high a value of K_I will make the system unstable while too low a value will render the integrator too slow to be effective. Thus, increase the integrator gain, K_I until the closed loop system becomes unstable to find the threshold value of K_I. For the present system, this value is about 826 sec^{-1}. A reasonable value to use is about one tenth of this threshold:

$$K_I = 82.6\ \text{sec}^{-1} \tag{12.29}$$

A Bode plot of the resulting controller transfer function is shown in Fig. 12.14. Each individual controller has a total of three states and the system requires four such controllers (excluding control of the rotor's axial motion) so the complete controller system has twelve states: the complexity of this controller is very low.

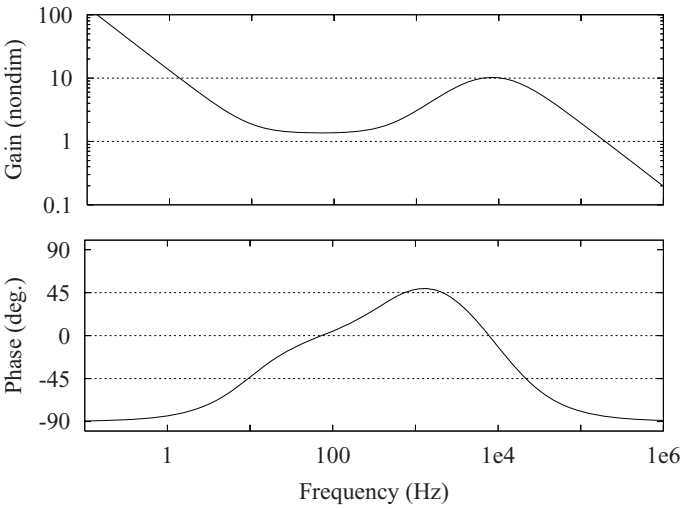


Fig. 12.14. Bode plot of PID controller.

The eigenvalues of the resulting closed loop system are listed in Table 12.3. Only the highest three flexible modes (2 kHz and beyond) remain lightly damped and all of the closed loop eigenvalues are stable, as required.

Table 12.3. Eigenvalues of rotor with collocated PID AMB control.

real part	imaginary part	frequency (Hertz)	damping ratio
-92692.	–	–	–
-93228.	–	–	–
-24934.	–	–	–
-23836.	–	–	–
-81.606	–	–	–
-81.644	–	–	–
-184.2	1515.8	241.3	0.121
-463.22	1706.4	271.6	0.262
-296.99	1838.2	292.6	0.160
-723.27	5204.0	828.2	0.138
-1356.0	8968.9	1427.4	0.149
-628.43	12490.	1987.9	0.050
-193.81	17930.	2853.6	0.011
-608.54	22551.	3589.1	0.027

12.5 Performance Assessment

The most basic requirement of the feedback control in an AMB system is stability and the results presented in Table 12.3 establish that this closed loop system is stable: all of the closed loop eigenvalues have negative real parts.

In operation, however, the rotor will be subject to various forces and the control system will be subject to noise. The response of the system will be assessed through various performance measures such as rotor displacement, amplifier voltage, and so forth. This connection is established by the closed loop system model (12.23) which may be represented in transfer function form as[2]:

$$\mathbf{z} = \mathbf{G}_{cl}(s;\Omega)\mathbf{w} \tag{12.30}$$

Acceptable performance of the system means that the *exogenous* signals $\mathbf{w}$ (forces and noise) will not lead to excessive response: that the rotor displacements will not be so large as to lead to contact with the casing, that the amplifier voltages will not need to be so large as to lead to saturation, and so forth. As formulated, (12.18) or (12.30) includes as its performance outputs

[2] To construct (12.30) from (12.23), take the Laplace transform of (12.23) and solve for $\mathbf{z}$ in terms of $\mathbf{w}$.

numerous rotor displacements, the amplifier output voltages, the amplifier currents, electromagnet flux densities, and amplifier input signals.

12.5.1 Signal Weighting

Each of these signals has some threshold value beyond which the system performance may be said to be unacceptable. If the performance measures are collected into a vector $\mathbf{z}$ as in (12.18) then performance assessment seeks to establish that

$$|z_i| < z_{\max,i}$$

simultaneously for all elements of $\mathbf{z}$ in response to any foreseeable combination of exogenous inputs, $\mathbf{w}$.

Of course, this stipulation *any foreseeable combination of exogenous inputs* is crucial: this is a linear system model so, if the exogenous signals can be arbitrarily large, then so too will the performance measures. This stipulation implies that some measure of the input signals is bounded. Here, a convenient measure will be signal amplitude:

$$|w_i| < w_{\max,i}$$

Strict definition of the amplitude of a signal x can take many forms. The most mathematically tractable choice of signal measures is the 2-norm:

$$|x|^2 \equiv \lim_{T\to\infty} \frac{1}{T} \int_0^T x^2 dt$$

Of course, using this measure can have important implications for engineering interpretation. In particular, if z_i is measured in this way, then the very largest instantaneous value of z_i could be quite a bit larger than its norm if z_i is a transient response. Hence, selection of this norm means that we are focusing on *steady state performance*. This approach is very commonly followed in engineering practice, where the frequency response of a system is evaluated - in the present context, unbalance response is an example of frequency response assessment. This frequency response view leads to the relatively convenient notion that $|w_i|$ or $|z_i|$ means the *amplitude* of each signal at some particular frequency.

So, with this caveat in mind, performance analysis seeks to establish that $|z_i| < z_{\max,i}$ for any, including some worst case, $|w_i| < w_{\max,i}$. To exactly establish that each element of a vector $\mathbf{z}$ is less than some limit value, construct the normalized vector

$$\overline{z}_i = \frac{1}{z_{\max,i}} z_i \quad \Rightarrow \quad \overline{\mathbf{z}} = \mathbf{W}_z \mathbf{z} \ : \quad \mathbf{W}_z = \mathrm{diag}(1/z_{\max,i})$$

In a similar fashion, the exogenous signal vector $\mathbf{w}$ can also be normalized

$$\overline{w}_i = \frac{1}{w_{\max,i}} w_i \quad \Rightarrow \quad \mathbf{W}_w \overline{\mathbf{w}} = \mathbf{w} \ : \quad \mathbf{W}_w = \mathrm{diag}(w_{\max,i})$$

Note that, since this assessment will be carried out on a frequency-by-frequency basis, it is possible that the normalization will be frequency dependent. In the case of rotor displacements, it is most likely that the bound is not frequency dependent but, in the case of unbalance loading, the bound is obviously frequency dependent. In particular, unbalance loading increases with the square of frequency out to the maximum expected rotor operating speed so the weighting *function* for an unbalance force might be

$$W_i = me_u \Omega^2 \ : \ 0 < \Omega < \overline{\Omega}$$

in which me_u is an estimate of the maximum mass eccentricity producing the unbalance force while $\overline{\Omega}$ is the maximum anticipated spin rate of the rotor.

In a similar manner, bounds on sensor noise are also likely to depend on frequency: there might be significant noise near the frequency of power distribution (50 Hz, 60 Hz, or 400 Hz). Perhaps more importantly, we can approximate the effect of digital sampling by saying that signals at frequencies above half the sampling rate are *entirely noise*, so that the noise bound will rise abruptly to the entire sensor signal range at frequencies above half of the sampling rate, f_s:

$$W_i = \begin{cases} w_0 & : \ 0 < \omega < \pi f_s \\ y_{\max} & : \ \omega > \pi f_s \end{cases}$$

12.5.2 Vector Norms

With this weighting introduced, performance assessment checks to see that

$$|\overline{z}_i| < 1$$

for any possible combination of $\mathbf{w}$ subject to

$$|\overline{w}_i| < 1$$

Such norm limits as these are called *infinity*-norms. The infinity-norm of a vector is just the magnitude of its largest element. To illustrate, some examples of a vector infinity norms are:

$$\left\| \begin{bmatrix} 0.8 \\ 0.3 \\ -0.9 \\ 0.1 \end{bmatrix} \right\|_\infty = 0.9 \qquad \left\| \begin{bmatrix} 0.3 \\ 0.3 \\ -0.3 \\ 0.3 \end{bmatrix} \right\|_\infty = 0.3 \qquad \left\| \begin{bmatrix} 0.5e^{0.3j} \\ 0.0 \\ 0.0 \\ 0.0 \end{bmatrix} \right\|_\infty = 0.5$$

This permits the notationally convenient statement of the performance requirement:

$$|\overline{\mathbf{z}}|_\infty < 1 \; \forall \; |\overline{\mathbf{w}}|_\infty < 1 \; : \; \overline{\mathbf{z}} = \mathbf{W}_z \mathbf{G}_{cl} \mathbf{W}_w \overline{\mathbf{w}} \tag{12.31}$$

To *exactly* test the condition (12.31) requires an exhaustive search of all feasible $\overline{\mathbf{w}}$. For systems with only a very few inputs, this might be possible, but it becomes very difficult as the dimension of $\overline{\mathbf{w}}$ becomes large.

Fortunately, a slight reformulation of (12.31) permits a much simpler assessment – one which will prove immensely useful in subsequent discussions of control development. If, instead of using the vector infinity norm, bounding of $\overline{w}$ and $\overline{z}$ is accomplished using the vector 2-norm, then analysis becomes much simpler.

The vector 2-norm is defined by

$$|\mathbf{x}|_2 \equiv \sqrt{\sum_{i=1}^{n} |x_i|^2}$$

Some examples, which may be compared to those given above for the infinity norm are:

$$\left| \begin{bmatrix} 0.8 \\ 0.3 \\ -0.9 \\ 0.1 \end{bmatrix} \right|_2 = 1.245 \qquad \left| \begin{bmatrix} 0.3 \\ 0.3 \\ -0.3 \\ 0.3 \end{bmatrix} \right|_2 = 0.6 \qquad \left| \begin{bmatrix} 0.5e^{0.3j} \\ 0.0 \\ 0.0 \\ 0.0 \end{bmatrix} \right|_2 = 0.5$$

The connection between the 2-norm and the infinity norm may be understood by the inequality

$$|\mathbf{x}|_\infty \leq |\mathbf{x}|_2 \leq \sqrt{\dim(\mathbf{x})} |\mathbf{x}|_\infty$$

where $\dim(\mathbf{x})$ denotes the number of scalar elements in the column array $\mathbf{x}$. In particular, this relationship guarantees that

$$|\mathbf{x}|_2 < 1 \quad \Rightarrow \quad |\mathbf{x}|_\infty < 1 \tag{12.32}$$

12.5.3 The Singular Value

The connection between the infinity norm and the 2 norm provided in (12.32) prompts reformulation of (12.31) as

$$|\overline{\mathbf{z}}|_2 < 1 \; \forall \; |\overline{\mathbf{w}}|_2 < 1 \; : \; \overline{\mathbf{z}} = \mathbf{W}_z \mathbf{G}_{cl} \mathbf{W}_w \overline{\mathbf{w}} \tag{12.33}$$

Establishing (12.33) may be accomplished by computing the *maximum singular value* of $\mathbf{W}_z \mathbf{G}_{cl} \mathbf{W}_w$:

$$\overline{\sigma}(\mathbf{W}_z \mathbf{G}_{cl} \mathbf{W}_w) < 1 \quad \Leftrightarrow \quad |\overline{\mathbf{z}}|_2 < 1 \; \forall \; |\overline{\mathbf{w}}|_2 < 1 \; : \; \overline{\mathbf{z}} = \mathbf{W}_z \mathbf{G}_{cl} \mathbf{W}_w \overline{\mathbf{w}} \tag{12.34}$$

Use of the maximum singular value in analysis of rotordynamics problems is treated in detail in [17].

The reason that (12.33) represents an improvement over (12.31) is that computing the maximum singular value of the weighted closed loop transfer function $\mathbf{W}_z\mathbf{G}_{cl}\mathbf{W}_w$ is direct and does not involve an exhaustive search. Thus, the performance requirement implied by (12.33) is mathematically tractable and, consequently, quick to compute.

12.5.4 Example

Returning to the example developed in Section 12.4.2, consider the mechanical response of the closed loop system to unbalance excitation. As described in Section 12.3.5, the clearance limits for the 6 evaluated displacements are [0.25 0.12 0.3 0.3 0.12 0.25] mm while the unbalance bounds for the 6 planes of potential unbalance are all assumed to be 10 g-mm, which is the same as 10^{-5}N-sec^2.

This leads to the output performance weighting function

$$\mathbf{W}_z = \begin{bmatrix} \frac{1}{0.00025} & & & & & \\ & \frac{1}{0.00012} & & & & \\ & & \frac{1}{0.00030} & & & \\ & & & \frac{1}{0.00030} & & \\ & & & & \frac{1}{0.00012} & \\ & & & & & \frac{1}{0.00025} \end{bmatrix}$$

and the input load weighting function

$$\mathbf{W}_w = \begin{bmatrix} 10^{-5}\omega^2 & & & & & \\ & 10^{-5}\omega^2 & & & & \\ & & 10^{-5}\omega^2 & & & \\ & & & 10^{-5}\omega^2 & & \\ & & & & 10^{-5}\omega^2 & \\ & & & & & 10^{-5}\omega^2 \end{bmatrix} \quad : \quad 0 < \omega < 30000\frac{2\pi}{60}$$

The weighted closed loop unbalance response transfer function has 36 elements. A necessary, but not sufficient condition for satisfying either (12.31) or (12.33) is that none of these elements, individually, ever exceeds 1.0 in the frequency range of interest. Fig. 12.15 shows all 36 weighted gains, establishing this *necessary* condition, but leaving the analyst to wonder: "What if all of the individual unbalances are large and phased in the worst possible manner? How large might the mechanical response be? Will it still be less than 1.0?"

The answer to this question is provided by the dashed line in Fig. 12.15. Since the maximum singular value of the weighted closed loop unbalance response transfer function is less than 1.0 over the entire operating speed range, the system meets the unbalance response specification. The singular value plot provides a very useful and powerful summary of a tremendous amount of information, providing a quick and reliable assessment of worst case system behavior.

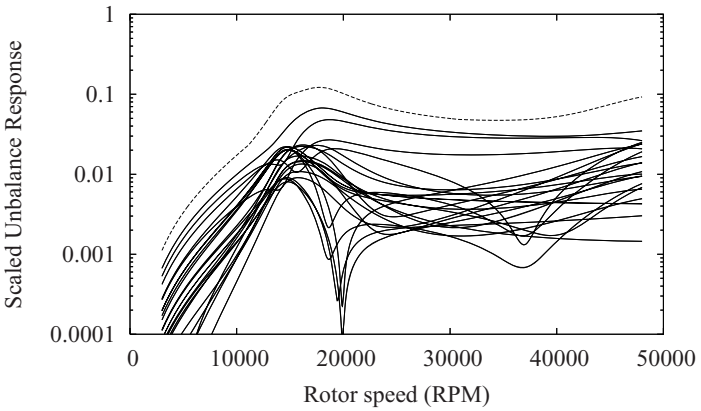


Fig. 12.15. Unbalance response of example rotor with collocated PID control. Solid lines are each component of the 6×6 weighted transfer function. Dashed line is the maximum singular value of the transfer function, whose maximum value is 0.122.

Note that, for this example, the peak value is 0.122 at a speed of roughly 18000 RPM, so the unbalance could be increased by a factor of more than 8 without jeopardy of contacting any of the close clearances.

12.6 Non-collocated Local PID Control

It is tempting to conclude from the preceding examples that this PID control result is good: the controller is simple and the resulting performance is quite promising. Indeed, there are no apparent resonances near or below the target operating speed so this rotor would seem to satisfy most reasonable industrial acceptance standards. However, a number of very important dynamic features have been neglected in predicting this performance. These include:

- The sensors are not collocated with the actuators, as assumed above.
- The power amplifiers have finite bandwidth and this bandwidth is considerably lower than the controller bandwidth as designed (about 100 kHz!).
- The controller will be implemented digitally and the digital controller samples at a rate of 20 kSa/sec so the highest frequency signal that can be faithfully rendered is 10 kHz. Further, the controller will introduce a time delay of 100 microseconds, substantially degrading the phase lead of the compensator.

In order to better reflect the physical limitations of this design problem, the model was revised to use actual sensor location output and the first order sensor dynamics were modeled. Further, the second order power amplifier dynamics were modeled and a third order Padé approximation of the controller delay was added. Finally, a first order anti-aliasing filter was added to the

Table 12.4. Eigenvalues of rotor with PID control designed for collocated control without delay or bandwidth limits: the simple PID controller is not stabilizing.

real part	imaginary part	frequency (Hertz)	damping ratio
-90825.	–	–	–
-90857.	–	–	–
-58889.	–	–	–
-57561.	–	–	–
-4709.2	–	–	–
-4440.8	–	–	–
-81.287	–	–	–
-74.561	–	–	–
17.80	**1239.5**	**197.3**	**-0.014**
564.04	**2469.4**	**393.0**	**-0.223**
298.98	**2480.8**	**394.8**	**-0.120**
-400.63	4822.	767.4	0.083
-14341.	4883.4	777.2	0.947
-13733.	5788.7	921.3	0.921
-34.85	8240.8	1311.6	0.004
-122.54	12057.	1919.	0.010
-43546.	13979.	2224.9	0.952
-43663.	15738.	2504.8	0.941
-168.04	17922.	2852.3	0.009
-182.6	22042.	3508.2	0.008
-36365.	34941.	5561.1	0.721
-36515.	35027.	5574.8	0.722

model. Of course, all of these added dynamics tend to reduce the system phase, making stabilization harder.

As a starting point for the design revision, the controller designed in the previous section was connected to this model and the closed loop system eigenvalues were computed as indicated in Table 12.4: many of the resulting eigenvalues have positive real parts, indicating that the closed loop system is unstable.

The first redesign measure taken was to set the integrator gain to zero ($K_I = 0$) as the integrator generally degrades stability. Once a stabilizing controller is found, the value of K_I can be increased until it begins to degrade system stability.

From here, the parameters manipulated included: K_P, the pole/zero ratio τ_0/τ_1, and the overall controller bandwidth, $1/\tau_2$. Increasing the pole/zero ratio increases phase lead near the flexible modes, generally increasing stability but at the cost of unrealistically high controller gain at high frequency. Increasing τ_2 reduces controller bandwidth, but at the cost of phase lead near the flexible modes. Reducing K_P permits the controller to roll–off at lower frequency, but increases sensitivity to the uncertain K_s. After a number of

iterations, it was found that a pole/zero ratio of 15 coupled with a bandwidth reduced to 2.2 kHz was stabilizing for *most* of the system modes when K_P was reduced to 0.477. Phase margin was generally increased by moving the two primary controller poles together: instead of $(3\tau_2 s + 1)(\tau_2 s + 1)$, bandwidth limiting is now accomplished by $\tau_2^2 s^2 + 2\xi\tau_2 s + 1$ in which $\xi = 0.4$. This further enabled addition of a fourth order Butterworth low pass filter with bandwidth of 5 kHz without a significant effect on system stability.

With this accomplished, the third bending mode remained unstable, with a frequency of $f = 1239$ Hz. To solve this, a mild notch filter was added to the controller:

$$G_{\text{notch}} = \frac{\frac{\alpha^2}{4\pi^2 f^2} s^2 + \frac{2\alpha\xi}{2\pi f} s + 1}{\frac{1}{4\pi^2 f^2} s^2 + \frac{2\times 0.05}{2\pi f} s + 1}$$

The parameters of this notch filter are the notch frequency, f (simply set equal to the problematic mode), the notch width α (set to 0.95 here: 1.0 gives no notch), and the notch depth ξ (set to 0.05 here: a moderately deep notch, smaller ξ makes a deeper notch). With $f = 1293$, $\xi = 0.05$ and $\alpha = 0.95$ the third bending mode was no longer destabilized by the controller.

At this point, the unbalance response was examined and found to be reasonable but with a peak gain in excess of 1.0, indicating that the unbalance limits specified for the rotor would be too high and the rotor might contact the auxiliary bearings or other critical clearances during run up (the largest response occurred at 22,600 RPM: below the target operating speed.) After trying a number of approaches, a solution was found: by reducing the damping ratio of the primary bandwidth limiting poles from 0.4 down to 0.05 the bearing damping near this speed was significantly increased.

Finally, an integrator was added to the controller with a small gain. The gain was increased until the system stability was noticeably degraded, then reduced until the effect on system stability was small. The resulting integrator gain was 50 sec^{-1}.

A Bode plot of the resulting controller is shown in Fig. 12.16. The performance of the rotor with this controller is indicated in Fig. 12.17 which shows that the peak unbalance gain is 0.424: more than three times higher than the previous, idealized solution. However, this is still below the threshold of 1.0, indicating that the level of unbalance could increase by a factor of 2.5 before clearance contact problems arise. The reduction of K_P did lead to an increase in sensitivity to K_s: the final system can tolerate an increase in magnitude of K_s of only about 28% before the system becomes unstable. By contrast, the idealized system could tolerate a 300% increase in K_s.

In summary to this point, it can be seen that solid classical control engineering will provide a path to reasonably successful controller design. However, as will be seen in the subsequent development, this approach may not provide a well structured and clear strategy for contending with parametric variability in the system at the same time as managing forced response.

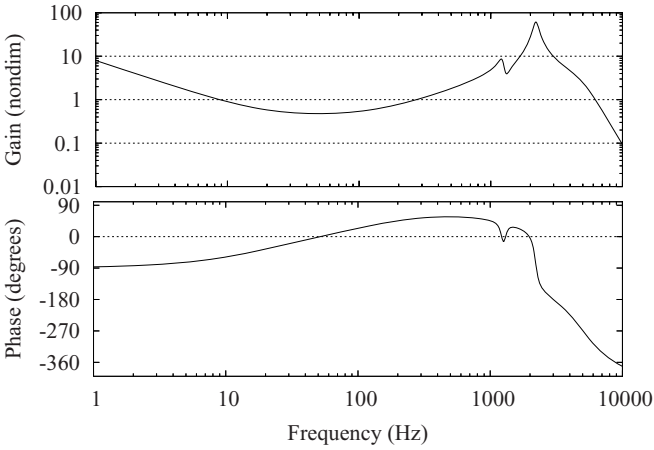


Fig. 12.16. Bode plot of controller for local non-collocated control.

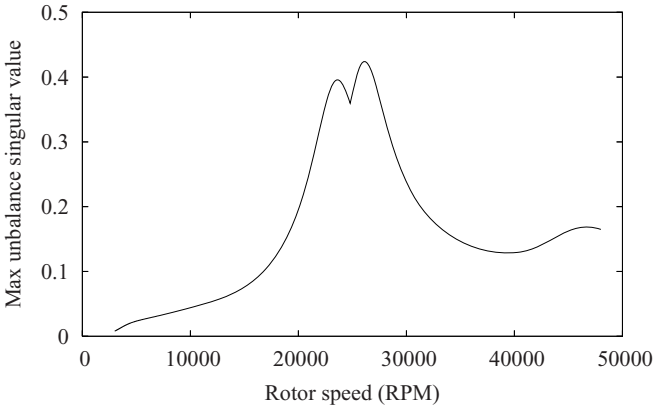


Fig. 12.17. Unbalance response of example rotor with non-collocated PID control: maximum singular value. Maximum value is 0.424.

12.7 Sensitivity

Although the forced response performance of the closed loop AMB system is important, recall that an absolute requirement is that the system is stable. In the preceding examples, each ultimate controller was stabilizing for the system model assumed in the example. However, a real controller must not only be stabilizing for the system model assumed in the design process, but must also stabilize the *actual* system. Of course, the competent system designer will make every effort to ensure that the design model represents the actual system as closely as possible, but it is never possible to do so exactly. Further, the dynamic character of the rotor and associated components may change over

time and the controller must be able to accommodate these changes without the system becoming unstable or the performance degrading excessively. A controller which exhibits this desirable attribute is referred to as *robust*.

The importance of this consideration is well known: most control engineers will pay close attention to protecting gain and phase margin in the design of a controller, which means that they ensure that unexpected or unmodeled changes in loop gain will not destabilize the closed loop system. Of course, this attention to gain and phase margin also acknowledges a connection between these margins and closed loop performance.

12.7.1 The Small Gain Theorem

The ISO standards for magnetic bearings [39, 47] explicitly establish expectations for the robustness of commercial AMB systems in terms of the *output sensitivity function*. To understand this output sensitivity function and other measures of robustness, we appeal to a relatively simple concept called the *small gain theorem* [83]. This theorem considers the system described by Fig. 12.18 in which a stable linear system $\mathbf{G}$ is connected in feedback to an uncertain gain $\mathbf{\Delta}$.

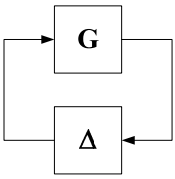


Fig. 12.18. Small gain problem: a known plant $\mathbf{G}$ is connected in feedback to an unknown gain $\mathbf{\Delta}$.

The small gain theorem establishes that the closed loop system is stable if

$$\overline{\sigma}(\mathbf{G}(j\omega)\mathbf{\Delta}(j\omega)) < 1 \; \forall \; \omega \in \mathbb{R}$$

In simplest terms, this condition ensures that the signal gain around the loop is less than 1.0 so that perturbations introduced to the system get smaller as they circulate around the loop.

Of course, the block gain $\mathbf{\Delta}$ is unknown so it is not possible to assess this product. However, it is easily established that

$$\overline{\sigma}(\mathbf{G}(j\omega)\mathbf{\Delta}(j\omega)) \; \leq \; \overline{\sigma}(\mathbf{G}(j\omega)) \; \overline{\sigma}(\mathbf{\Delta}(j\omega))$$

so that a *sufficient* condition for stability of the loop is that

$$\overline{\sigma}(\mathbf{G}(j\omega)) < \frac{1}{\overline{\sigma}(\mathbf{\Delta}(j\omega))} \; \forall \; \omega \in \mathbb{R} \tag{12.35}$$

This problem is obviously tractable if it is possible to establish a bound on the maximum singular value of $\mathbf{\Delta}$. Of course, this is generally possible because

it is only reasonable to assume that uncertainties in a system are *bounded*. A good way to describe the bounding of $\overline{\sigma}(\mathbf{\Delta})$ (which may be a function of frequency) is to choose two reasonably simple matrix functions $\mathbf{W}_{sl}$ and $\mathbf{W}_{sr}$ such that

$$\overline{\sigma}\left(\mathbf{W}_{sl}^{-1}(j\omega)\mathbf{\Delta}(j\omega)\mathbf{W}_{sr}^{-1}(j\omega)\right) < 1 \; \forall \; \omega \in \mathbb{R}$$

With these two functions in hand, (12.35) becomes

$$\overline{\sigma}\left(\mathbf{W}_{sr}(j\omega)\mathbf{G}(j\omega)\mathbf{W}_{sl}(j\omega)\right) < 1 \; \forall \; \omega \in \mathbb{R} \tag{12.36}$$

The similarity between (12.36) and (12.34) is obviously not accidental and points out that both performance and sensitivity are, in the end, well represented by the maximum singular value of some weighted plant transfer function. This leads to a slight generalization of the plant model presented in Fig.12.7, suggesting that a more complete model of a system, suitable for both performance and sensitivity assessment, includes three sets of inputs: control $\mathbf{u}$, load $\mathbf{w}_p$, and sensitivity input $\mathbf{w}_s$ and three corresponding sets of outputs: measurement $\mathbf{y}$, performance $\mathbf{z}_p$, and sensitivity output $\mathbf{z}_s$. Figure 12.19 indicates the relationship amongst these signals and their connection to the plant $\mathbf{G}$, the controller $\mathbf{H}$, and the sources of uncertainty $\mathbf{\Delta}$.

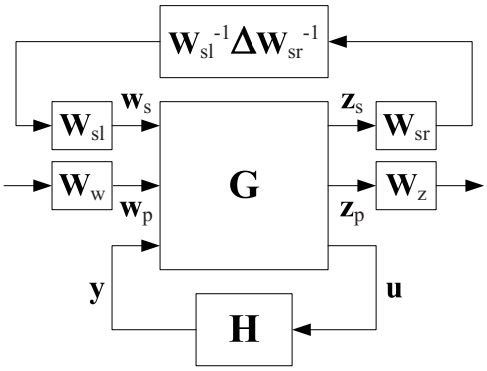


Fig. 12.19. Generalized plant $\mathbf{G}$ connected to uncertainty $\mathbf{\Delta}$ and a controller $\mathbf{H}$.

12.7.2 Example

As a very simple example of a sensitivity problem, consider the stability problem posed by a mass m supported by a spring k and a damper c. Assume that the damper has some nominal value c_0 and some uncertainty Δ_c. In this case, a state space description of the plant might be

$$\frac{d}{dt}\mathbf{x} = \begin{bmatrix} 0 & 1 \\ -\frac{k}{m} & -\frac{c_0+\Delta_c}{m} \end{bmatrix}\mathbf{x} + \begin{bmatrix} 0 \\ \frac{1}{m} \end{bmatrix} w_p \tag{12.37a}$$

$$z_p = \begin{bmatrix} 1 & 0 \end{bmatrix}\mathbf{x} \tag{12.37b}$$

Apparently, the uncertain gain Δ_c is internal to the plant, but it can be brought outside the plant by introducing the signals w_s and z_s:

$$\frac{d}{dt}\mathbf{x} = \begin{bmatrix} 0 & 1 \\ -\frac{k}{m} & -\frac{c_0}{m} \end{bmatrix}\mathbf{x} + \begin{bmatrix} 0 \\ \frac{1}{m} \end{bmatrix} w_p + \begin{bmatrix} 0 \\ \frac{1}{m} \end{bmatrix} w_s \tag{12.38a}$$

$$z_s = \begin{bmatrix} 0 & -1 \end{bmatrix}\mathbf{x} \tag{12.38b}$$

$$z_p = \begin{bmatrix} 1 & 0 \end{bmatrix}\mathbf{x} \tag{12.38c}$$

$$w_s = \Delta_c z_s \tag{12.38d}$$

Clearly, (12.38b) and (12.38d) can be combined to solve for w_s in (12.38a) so that (12.38a) becomes (12.37a). Hence, the two models are identical.

Now, suppose that

$$\overline{\sigma}(\Delta_c) < \gamma c_0 \quad \Leftrightarrow \quad \overline{\sigma}\left(\frac{1}{c_0}\Delta_c\frac{1}{\gamma}\right) < 1.0$$

In this case, (12.38) may be rewritten as

$$\frac{d}{dt}\mathbf{x} = \begin{bmatrix} 0 & 1 \\ -\frac{k}{m} & -\frac{c_0}{m} \end{bmatrix}\mathbf{x} + \begin{bmatrix} 0 \\ \frac{1}{m} \end{bmatrix} w_p + \begin{bmatrix} 0 \\ \frac{c_0}{m} \end{bmatrix} \overline{w}_s \tag{12.39a}$$

$$\overline{z}_s = \begin{bmatrix} 0 & -\gamma \end{bmatrix}\mathbf{x} \tag{12.39b}$$

$$z_p = \begin{bmatrix} 1 & 0 \end{bmatrix}\mathbf{x} \tag{12.39c}$$

$$\overline{w}_s = \frac{1}{c_0}\Delta_c\frac{1}{\gamma}\overline{z}_s \tag{12.39d}$$

and the system described by (12.39) will be stable as long as the gain from $\overline{w}_s$ to $\overline{z}_s$ is less than 1.0:

$$\overline{\sigma}\left(\begin{bmatrix} 0 & -\gamma \end{bmatrix}\begin{bmatrix} j\omega & -1 \\ \frac{k}{m} & j\omega + \frac{c_0}{m} \end{bmatrix}^{-1}\begin{bmatrix} 0 \\ \frac{c_0}{m} \end{bmatrix}\right) < 1 \;\forall\; \omega \in \mathbb{R}$$

Figure 12.20 plots this singular value as a function of frequency ω for $m = 1$ kg, $c_0 = 10$ N-sec/m, $k = 1000$ N/m and $\gamma = 0.8$. Not surprisingly, the maximum singular value reaches a peak of 0.8 indicating that this level of uncertainty can be tolerated without fear of system instability.

12.7.3 ISO Sensitivity

The ISO standards for magnetic bearings [39] set limits for peak gain of the output sensitivity function for AMB systems. The output sensitivity function $\mathbf{S}_o$ is defined as indicated in Fig. 12.21:

$$\mathbf{z}_s = \mathbf{S}_o\mathbf{w}_s$$

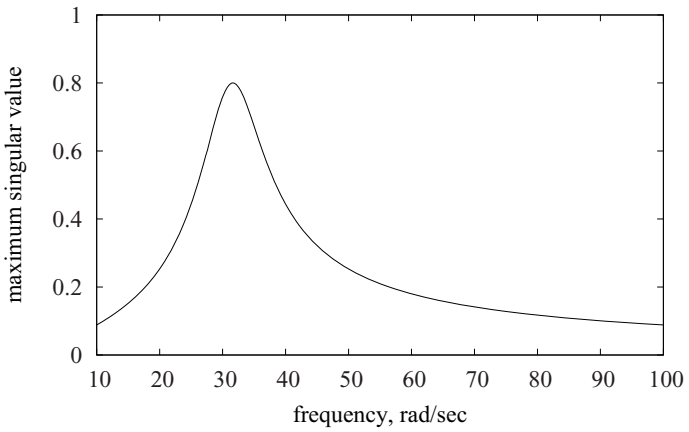


Fig. 12.20. Maximum singular value of damping sensitivity for the simple mass-spring-damper example.

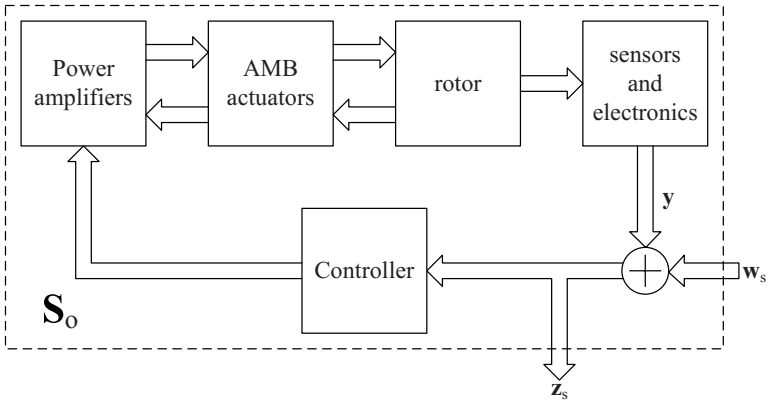


Fig. 12.21. Output sensitivity of an AMB system, as assessed in the ISO AMB standard.

The ISO standard sets limits for the peak values of the diagonal elements of the transfer function $\mathbf{S}_o$. To interpret this in terms of tolerable model uncertainty, connect an uncertainty between $\mathbf{z}_s$ and $\mathbf{w}_s$:

$$\mathbf{w}_s = \boldsymbol{\Delta}_o \mathbf{z}_s$$

so that the system is stable as long as

$$\overline{\sigma}\left(\mathbf{S}_o(j\omega)\right) < \frac{1}{\overline{\sigma}(\boldsymbol{\Delta}_o)} \; \forall\, \omega \in \mathbb{R}$$

This is equivalent to assessing the maximum permissible uncertainty in the gain between the sensors and the controller:

$$\mathbf{z}_s = (\mathbf{I} - \mathbf{\Delta}_o)^{-1}\mathbf{y}$$

If the peak of the maximum singular value of $\mathbf{S}_0$ is, for instance, 3.0, then the system can tolerate a complex gain uncertainty acting in series with the sensors with a maximum singular value peak of less than 0.33: the lower the peak value of $\overline{\sigma}(\mathbf{S}_0)$ is, the larger $\mathbf{\Delta}_0$ can be without causing the AMB system to be unstable.

12.7.4 Example: Output Sensitivity of the Flexible Rotor

The output sensitivity of the AMB system developed in Sect. 12.6 can easily be evaluated by introducing input signals $\mathbf{w}_s$ that are added to the outputs of the sensor system and measuring the gain from this set of signals to the set of signals supplied to the controller, consistent with Fig. 12.21. Figure 12.22 plots the maximum singular value of this transfer function for the closed loop system as a function of frequency.

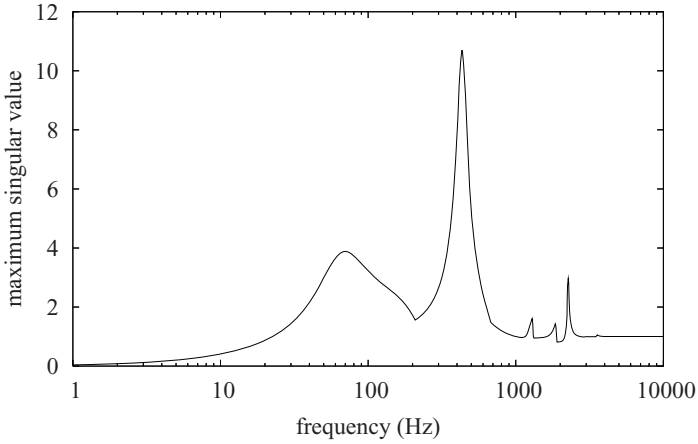


Fig. 12.22. Output sensitivity of the non-collocated PID control solution.

The peak value of sensitivity in Fig. 12.22 is 10.69, occurring at a frequency of 431 Hz. This means that the closed loop AMB system can tolerate a maximum gain uncertainty acting in series with the sensors of only 9.4%[3]. This sensitivity is about 3 times higher than the ISO standard permits: the solution would be considered too sensitive for commercial implementation.

[3] The reciprocal of 10.69 is 0.094.

12.7.5 General Comments on Sensitivity in AMB Systems

AMB systems are subject to a number of sources of uncertainty [47]. Perhaps the most significant source is uncertainty in the actuator stiffness, $\mathbf{K}_s$. This parameter is very sensitive to static load acting on the rotor and also to anything that modifies the nominal air gap in the actuator including: manufacturing tolerances, thermal growth, and centrifugal growth. It is common to assume that uncertainty in $\mathbf{K}_s$ is on the order of 25%. Another important uncertainty in flexible systems is the bending mode eigenvalues. In particular, the damping associated with the flexible modes is usually very uncertain and sensitive to operating conditions, rotor temperature, and aging. Importantly, these sources of uncertainty are usually not well approximated by output gain uncertainty so a well-formulated controller design process will evaluate these sources of uncertainty as well as the output sensitivity mandated by the ISO standards.

12.8 Non-collocated Mixed PID Control

Two significant factors complicate the design of control for this problem. The first factor is that the transfer function from one end of the rotor to the other (eg: left end actuator to right end sensor) is comparable in gain to the "direct" transfer function (eg: left end actuator to left end sensor): see Fig. 12.23 in which the gains of four transfer functions (two direct, two end-to-end) are plotted. Thus, it is a very rough approximation to assume that the control problem is single input-single output (SISO).

The second factor is that the flexible modes of the rotor are fairly closely spaced: it is difficult to phase stabilize any of the modes without also phase stabilizing the adjacent modes because of this close spacing. The largest separation is between the first and second flexible modes: a ratio of 2.78:1.

These two observations lead to a simple trick. If the inputs and outputs of the plant are recombined into sum and difference coordinates, then it may be possible to reduce the coupling between ends and reduce the modal density in the resulting "direct" transfer functions. This can happen because the system is symmetric and its modes are alternately *even* and *odd*. This means that the first mode, third mode, fifth mode, and so forth are symmetric about the rotor mass center while the other modes are anti-symmetric. Hence, the simple transformation

$$H(s) = \begin{bmatrix} 1 & -1 \\ 1 & 1 \end{bmatrix} G(s) \begin{bmatrix} 1 & -1 \\ 1 & 1 \end{bmatrix}^{-1} = \frac{1}{2} \begin{bmatrix} 1 & -1 \\ 1 & 1 \end{bmatrix} G(s) \begin{bmatrix} 1 & 1 \\ -1 & 1 \end{bmatrix}$$

may lead to an improved form. This transformation is discussed in detail in Sect. 8.2.3 where it is identified as separation into "conical" and "parallel" modes. It is also sometimes referred to as a "tilt and translate" or "center of gravity" transformation.

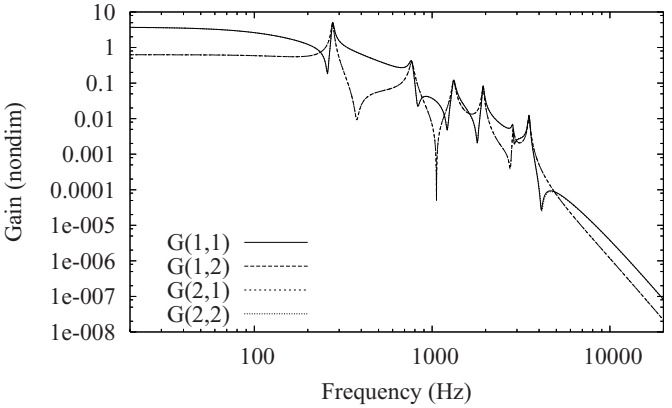


Fig. 12.23. Transfer functions of rotor and connected sensing and actuation hardware. Six flexible modes of the rotor have been retained in the model.

The utility of this concept is clearly revealed by Fig. 12.24, which plots the gains of the component transfer functions of $H(s)$. The "direct" transfer function components, $H_{1,1}$ and $H_{2,2}$ have much higher gains than the "coupling" functions (this is a terrible abuse of terminology since the transfer functions have been intermingled by the transformation). Further, $H_{2,2}$ now has very strong separation of modes: it contains only the first and third bending modes which are separated by a ratio of 7.3:1. Finally, $H_{1,1}$ has a number of modes, but the first is the second rotor bending mode at 769 Hz: it may be possible to simply roll the controller for this "axis" off early enough to not interact with any of the modes in $H_{1,1}$.

12.8.1 Stabilizing $H_{1,1}$ (the "Conical Mode")

Rather than viewing the control problem in rotordynamic terms, we may now view this as a pair of decoupled SISO control problems of fairly common character. The only complicating factor is that both $H_{1,1}$ and $H_{2,2}$ are non-minimum phase so the usual Bode type methods will not work [48]. However, the character of the problem can be understood by looking at a root locus of the dominant system dynamics: a zero at 44530, a pole at 936, and another pole at -1182. The transfer function has a number of other complex poles and zeros, but they are reasonably well separated and of very high frequency. Hence, the goal is to design a simple compensator that will attract the pole at 936 into the left half plane, away from the zero at 44530. To do this, introduce a zero at $-\omega$ and a complex pair of poles at a larger radius, $\alpha\omega$ with a damping ratio of ξ:

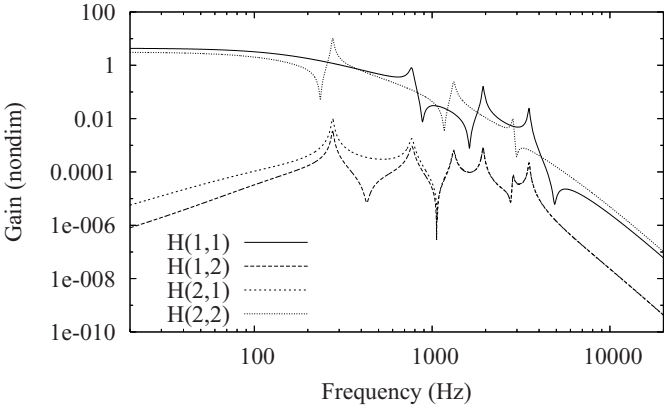


Fig. 12.24. Transfer functions of rotor/sensing/actuation hardware after mixing.

$$C_{11,a} = k\frac{\alpha^2\omega(s+\omega)}{s^2 + 2\alpha\xi\omega s + \alpha^2\omega^2}$$

The parameters of this controller are its DC gain k, its zero location ω, its pole/zero ratio α, and its damping ratio ξ. To get started, pick $\omega = 1000$, $\alpha = 10$, $\xi = 0.7$, and $k = 1$. Do a root locus on the resulting system $H_{11}g_{11}$ to determine a suitable value for k: see Fig. 12.25. In this case, a value of 0.6

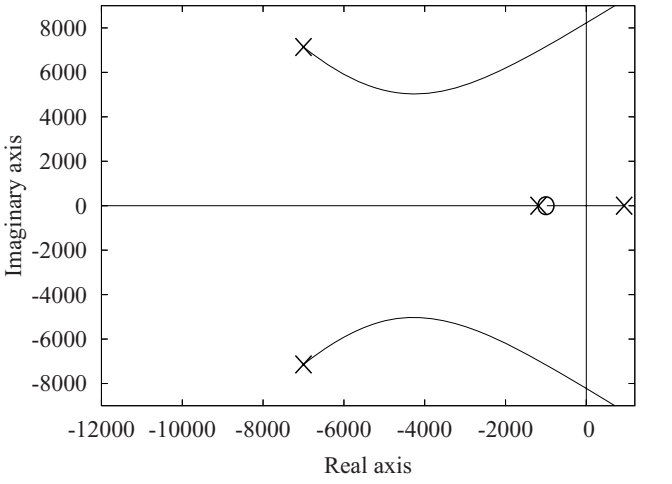


Fig. 12.25. Root locus of initial design: mixed PID control for H_{11}.

was found to be stabilizing. Now, iterate on k, ω, α, and ξ with the goal of maximizing the stability margin while keeping ω as low as possible to limit high frequency gain. A favorable solution is:

$$C_{11,a} = k\frac{\alpha^2\omega(s+\omega)}{s^2+2\alpha\xi\omega s+\alpha^2\omega^2} \;:\; \omega = 1000,\ \xi = 0.06,\ \alpha = 10,\ k = 0.36$$

which results in a gain margin of 37%, a phase margin of 30°, a peak sensitivity gain of 2.6, and a 10 kHz control gain of 0.59.

Next, add an integrator term with as high a gain as is possible without substantially affecting the closed loop gain margin:

$$C_{11,b} = \alpha^2\omega k\frac{s+\omega}{s^2+2\alpha\xi\omega s+\alpha^2\omega^2} + \frac{K_I}{s} \;:\; K_I = 10$$

which maintains a gain margin of 35%, a phase margin of 30°, a peak sensitivity gain of 2.6, and a 10 kHz control gain of 0.59.

Finally, add a low pass Butterworth filter with a bandwidth of $\gamma\alpha\omega_1$ of order n, adjusting γ and n to drive the controller gain at 10 kHz as low as possible while maintaining a peak sensitivity of 3.0:

$$C_{11} = C_{11,b}C_{\mathrm{LP},\gamma,n} \;:\; \gamma = 2.5,\ n = 2$$

to give a final gain margin of 35%, a phase margin of 25°, a peak sensitivity gain of 3.0, and a 10 kHz control gain of 0.09. A Bode plot of the resulting controller is provided in Fig. 12.26.

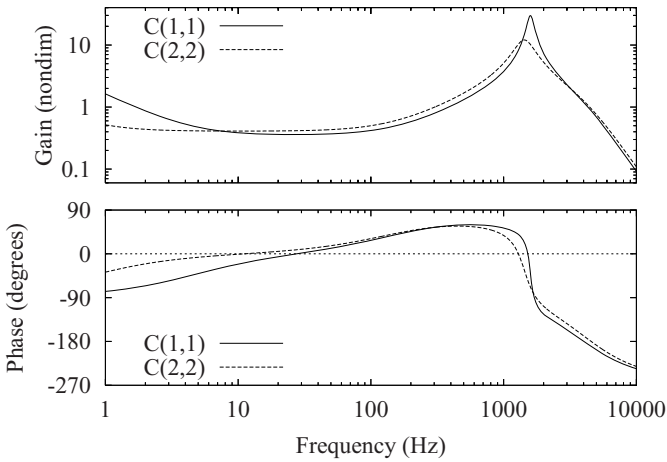


Fig. 12.26. Bode plot of controllers: mixed PID problem.

12.8.2 Stabilizing $H_{2,2}$ (the "Parallel Mode")

The process of developing a controller for $H_{2,2}$ was essentially the same as for $H_{1,1}$. The resulting controller parameters and performance are summarized in Table 12.5 while Fig. 12.26 provides a Bode plot of this controller.

Table 12.5. Controller parameters and performance: mixed PID design.

	control axis	
parameter	$C_{1,1}$	$C_{2,2}$
nominal gain, k	0.36	0.41
integrator gain, K_I (1/sec)	10	2
zero, ω (rad/sec)	1000	900
pole/zero ratio, α	10	10
damping ratio, ξ	0.06	0.17
bandlimit ratio, γ	2.5	3.0
bandlimit order, n	2	2
gain margin	35%	21%
phase margin	25°	15°
peak sensitivity	3.0	4.5
gain at 10 kHz	0.09	0.11

These two controllers can be transformed back the sensor/actuator natural coordinates of the physical plant:

$$C(s) = T^{-1} \begin{bmatrix} C_{1,1} & 0 \\ 0 & C_{2,2} \end{bmatrix} T$$

and connected to the plant to assess the resulting system performance. Figure 12.27 plots the maximum singular value of the output sensitivity function for this system, showing a peak value of 4.588.

Figure 12.28 plots the maximum weighted unbalance response singular value, showing a peak of 0.24: the rotor can sustain an unbalance level four times higher than that specified before the rotor contacts critical clearances. For comparison, Fig. 12.28 plots the same information for the previous non-collocated local PID control result: the present solution shows significantly better performance.

Keep in mind, of course, that mass unbalance rejection was not considered in iterating on the controller design: that process only considered sensitivity or gain/phase margin. Thus, neither result (local PID or mixed PID) can be expected to be optimal in the sense of minimizing unbalance response.

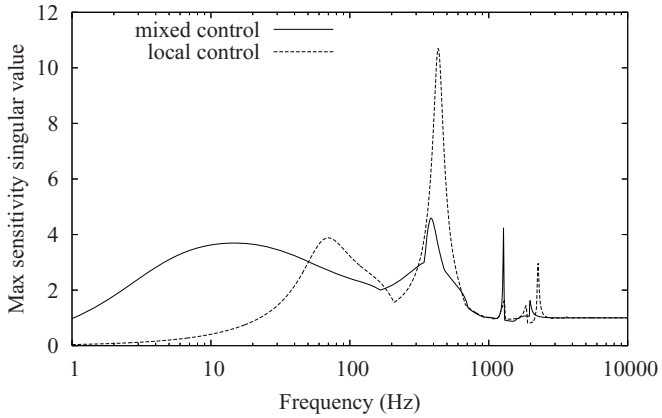


Fig. 12.27. Maximum singular value of the output sensitivity function for the mixed PID control solution.

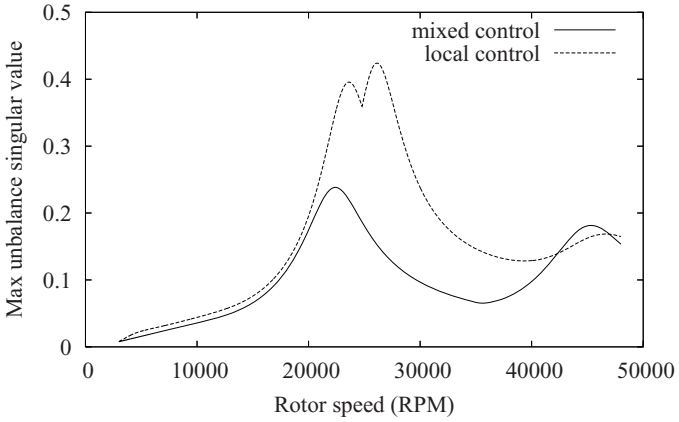


Fig. 12.28. Maximum singular value of the weighted unbalance function for the mixed PID control solution.

12.9 $\mathcal{H}_\infty$ Norm

The discussions of performance (Sect. 12.5) and sensitivity (Sect. 12.7) both lead to requirements of the form

$$\overline{\sigma}(\mathbf{S}_o(j\omega)) < \frac{1}{\overline{\sigma}(\mathbf{\Delta}_o)} \; \forall \; \omega \in \mathbb{R}$$

or

$$\overline{\sigma}\left(\mathbf{W}_z\mathbf{G}_{cl}\mathbf{W}_w\right) < 1 \;:\quad 0 \le \omega \le \omega_{\max}$$

Each represents a stipulation on some *measure* of the gain of a system transfer function (sensitivity or weighted unbalance response).

The repeated emergence of this important measure as a specification for control leads to the idea of the $\mathcal{H}_\infty$ norm and the related control problem. For a transfer function $\mathbf{G}(s)$, the $\mathcal{H}_\infty$ norm is a measure of peak gain:

$$|\mathbf{G}(s)|_\infty = \sup_{\omega\in\mathbb{R}} \bar{\sigma}\left(\mathbf{G}(j\omega)\right)$$

Note that $\overline{\sigma}(\mathbf{G}(j\omega))$ is a scalar function of ω: at each possible value of ω, the function $\mathbf{G}(j\omega)$ is evaluated as a matrix of numbers and the maximum singular value of this matrix is found. Thus, the $\mathcal{H}_\infty$ norm of $\mathbf{G}$ finds that frequency ω at which this maximum singular value is largest (its *supremum*) and this largest value represents the numerical norm of the transfer function.

Comparing to the unbalance response specification given above, it is clear that the unbalance specification is *nearly* an $\mathcal{H}_\infty$ constraint on $\mathbf{W}_z\mathbf{G}_{cl}(s)\mathbf{W}_w(s)$. The only thing missing is that unbalance specification limits ω to the range $[0, \omega_{\max}]$. We can adapt the definition of $\mathbf{W}_w(s)$ to permit this range to be extended by simply adding a low–pass filter to $\mathbf{W}_w$ as, for instance:

$$\hat{\mathbf{W}}_w(s) = \frac{\omega_{\max}^3 s^2}{(s+\omega_{\max})(s^2+\sqrt{3}\omega_{\max}s+\omega_{\max}^2)} \begin{bmatrix} w_{1,\max} & & \\ & \ddots & \\ & & w_{m,\max} \end{bmatrix}$$

Essentially, this maintains a scaling of ω^2 at frequencies up to $\omega_{\max}$ and then quickly brings the scaling back toward zero. With this, the unbalance specification becomes

$$|\mathbf{W}_z\mathbf{G}_{cl}(s)\hat{\mathbf{W}}_w(s)|_\infty < 1.0 \tag{12.40}$$

This means that we can determine whether or not the unbalance response of the system is acceptable simply by determining whether or not the $\mathcal{H}_\infty$ norm of the weighted unbalance response function is less than 1. The plots provided in Figures 12.15, 12.17, and 12.28 plot the maximum singular values of the weighted unbalance response functions for the three respective control schemes versus frequency. While the plots themselves are interesting, the important assessment is to determine how close these curves come to 1.0: if they are always well below 1.0, then the system unbalance response is acceptable.

12.10 $\mathcal{H}_\infty$ Control

Given that the performance of a system is often nicely stated in terms of an $\mathcal{H}_\infty$ norm of the system response, it should come as no great surprise to discover that it is possible to *synthesize* controllers with the objective of satisfying an $\mathcal{H}_\infty$ norm. The normal statement of the problem takes the form

indicated in Fig. 12.29. Consistent with Fig. 12.29, the *plant* $\mathbf{G}(s)$ is defined by:

$$\frac{d}{dt}\mathbf{x} = \mathbf{A}\mathbf{x} + \mathbf{B}_1\mathbf{w} + \mathbf{B}_2\mathbf{u} \tag{12.41a}$$

$$\mathbf{z} = \mathbf{C}_1\mathbf{x} + \mathbf{D}_{12}\mathbf{u} \tag{12.41b}$$

$$\mathbf{y} = \mathbf{C}_2\mathbf{x} + \mathbf{D}_{21}\mathbf{w} \tag{12.41c}$$

or, equivalently,

$$\mathbf{G}(s) = \begin{bmatrix} \mathbf{G}_{wz} & \mathbf{G}_{uz} \\ \mathbf{G}_{wy} & \mathbf{G}_{uy} \end{bmatrix}$$

in which

$$\mathbf{G}_{wz} = \mathbf{C}_1(s\mathbf{I} - \mathbf{A})^{-1}\mathbf{B}_1 \tag{12.42a}$$

$$\mathbf{G}_{uz} = \mathbf{C}_1(s\mathbf{I} - \mathbf{A})^{-1}\mathbf{B}_2 + \mathbf{D}_{12} \tag{12.42b}$$

$$\mathbf{G}_{wy} = \mathbf{C}_2(s\mathbf{I} - \mathbf{A})^{-1}\mathbf{B}_1 + \mathbf{D}_{21} \tag{12.42c}$$

$$\mathbf{G}_{uy} = \mathbf{C}_2(s\mathbf{I} - \mathbf{A})^{-1}\mathbf{B}_2 + \mathbf{D}_{22} \tag{12.42d}$$

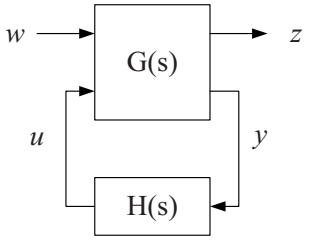


Fig. 12.29. Control problem schematic with an $\mathcal{H}_\infty$ performance specification.

With this definition, the $\mathcal{H}_\infty$ problem is: Given a plant $\mathbf{G}(s)$, find a controller $\mathbf{H}(s)$ so that the closed transfer function

$$\mathbf{G}_{cl} = \mathbf{G}_{wz} + \mathbf{G}_{wz}(\mathbf{I} - \mathbf{H}\mathbf{G}_{uy})^{-1}\mathbf{G}_{wy}$$

is *stable* and satisfies

$$|\mathbf{G}_{cl}|_\infty < \gamma$$

in which γ is some fixed target maximum gain. In the present discussion, $\gamma \leq 1.0$. Thus, if we can assemble the AMB control problem so that $\mathbf{G}_{wz}$ is the weighted unbalance response function described in (12.40), then any controller satisfying the $\mathcal{H}_\infty$ control problem with $\gamma < 1$ will result in acceptable unbalance response.

12.10.1 Problem Formulation

The $\mathcal{H}_\infty$ synthesis problem is formulated by specifying the target performance: γ and the matrix elements of (12.41). Thus, formulation is essentially trivial in that construction of the model and statement of the performance specification provide the primary elements of the problem formulation and need only the addition of the target gain γ to be complete.

12.10.2 Solution Mechanics

Once the problem is formulated: the model and associated weighting functions are assembled to produce the component matrices in (12.41), then the controller component matrices are computed using a standard tool such as the MatLab® function `hinfsyn` [25]. That is, the design of the controller is entirely controlled by the plant model in conjunction with the input and output weighting matrices, which together constitute a performance specification. For the present problem, the resulting controller is symmetric and 2×2, with the Bode plots indicated in Fig. 12.30. The main diagonal term ($C(1,1)$) is similar to the main diagonal term controllers in the previous solutions except for the local peak near 210 Hz.

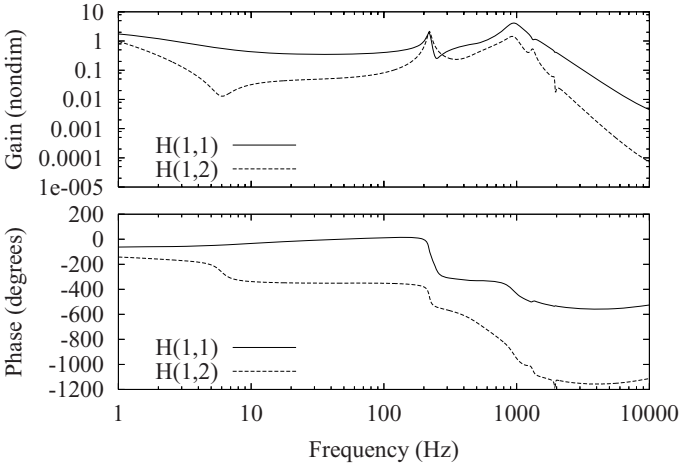


Fig. 12.30. Controller Bode plot: $\mathcal{H}_\infty$ control. Symmetry of the problem dictates that $H(2,2) = H(1,1)$ and that $H(2,1) = H(1,2)$ so only $H(1,1)$ and $H(1,2)$ are plotted here.

12.10.3 Solution Performance

The performance of this solution can be summarized, as before, with a singular value plot of the weighted unbalance response function, as shown in Fig. 12.31. The peak of this curve is 0.1918. If the frequency range had been limited to 30000 RPM, the peak would be less than 0.16. Thus, the unbalance response performance achieved by this controller is substantially better than that achieved by either the local PID approach or the mixed PID approach.

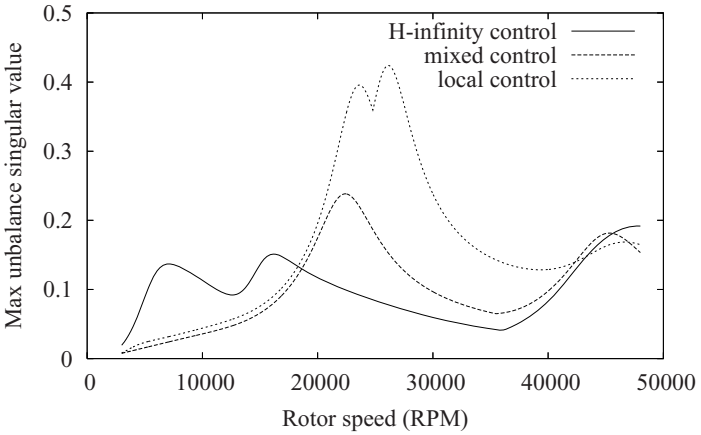


Fig. 12.31. Maximum singular value of the weighted unbalance function for the $\mathcal{H}_\infty$ control solution.

However, this improved performance comes at a cost. When the output sensitivity function is examined (see Fig. 12.32), the peak of the sensitivity function is found to be 15.5 as opposed to 10.7 for the local PID design and just 4.58 for the mixed PID design. The reasons for both the improved unbalance response and degraded sensitivity performance both lie in the method: hand synthesis of the two PID designs referred extensively to metrics of sensitivity (gain and phase margins or the actual sensitivity gain) but not to unbalance response. By contrast, the $\mathcal{H}_\infty$ design specifications make no mention of sensitivity and, instead, focus entirely on unbalance response performance.

12.11 $\mu-$Control

The essential objective of μ control is to find a compromise control design that achieves a balance between input/output performance and other objectives like sensitivity. In point of fact, since sensitivity can be defined in terms

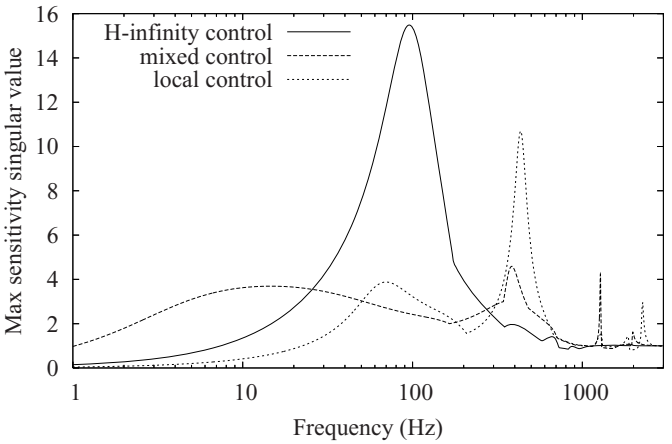


Fig. 12.32. Maximum singular value of the output sensitivity function for the $\mathcal{H}_\infty$ control solution.

of system gain from a mathematically defined input to the system to a mathematically defined output of the system, it is possible to construct an $\mathcal{H}_\infty$ control design specification that can optimize the sensitivity of the closed loop system (minimize the peak of the sensitivity function). However, in general, optimizing sensitivity will degrade performance while optimizing performance will lead to high sensitivity. Hence the need for a compromise. Very detailed discussions of μ control may be found in numerous textbooks: [83] is a good example. In addition, there are several careful studies of application of μ control to the AMB problem in the literature, including [27, 49, 61, 73].

In the end, μ control synthesis attempts to simultaneously make the $\mathcal{H}_\infty$ norm of several different plant transfer functions meet independent target values. Figure 12.33 illustrates the components of the problem. In this block diagram, denote the closed loop transfer function from $\mathbf{w}_p$ to $\mathbf{z}_p$ as $\mathbf{G}_{pp}(s)$:

$$\mathbf{z}_p = \mathbf{G}_{pp}\mathbf{w}_p$$

and the closed loop transfer function from $\mathbf{w}_r$ to $\mathbf{z}_r$ as $\mathbf{G}_{rr}$:

$$\mathbf{z}_r = \mathbf{G}_{rr}\mathbf{w}_r$$

Acceptable controller performance means that the $\mathcal{H}_\infty$ gain from $\mathbf{w}_p$ to $\mathbf{z}_p$ is less than 1.0 and, at the same time, the gain from $\mathbf{w}_r$ to $\mathbf{z}_r$ to also less than 1.0. There is no particular requirement for the gain from $\mathbf{w}_r$ to $\mathbf{z}_p$ or from $\mathbf{w}_p$ to $\mathbf{z}_r$:

$$\mathbf{H} : |\mathbf{G}_{pp}|_\infty \leq 1.0 \ , \quad |\mathbf{G}_{rr}|_\infty \leq 1.0$$

Either of these specifications, individually, constitutes a standard $\mathcal{H}_\infty$ problem, but the two together are not. One approach is to simply concatenate

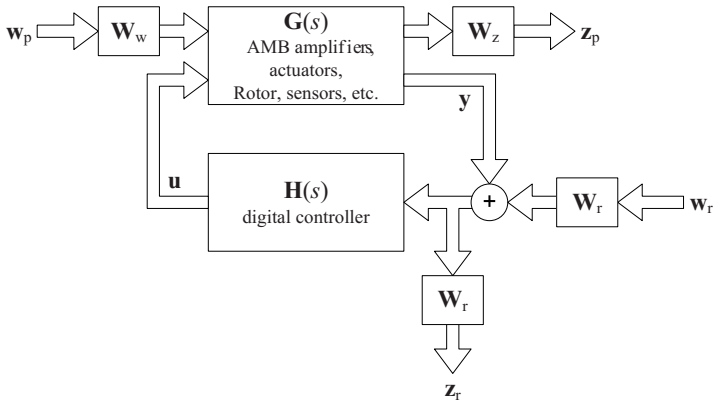


Fig. 12.33. Block diagram of $\mu-$ control problem balancing system forced response against output sensitivity.

the vectors $[\mathbf{w}_p'\mathbf{w}_r']'$ and $[\mathbf{z}_p'\mathbf{z}_r']$:

$$\begin{bmatrix}\mathbf{z}_p\\ \mathbf{z}_r\end{bmatrix} = \begin{bmatrix}\mathbf{G}_{pp}\ \mathbf{G}_{pr}\\ \mathbf{G}_{rp}\ \mathbf{G}_{rr}\end{bmatrix}\begin{bmatrix}\mathbf{w}_p\\ \mathbf{w}_r\end{bmatrix}$$

and require that

$$\mathbf{H}: \left\|\begin{bmatrix}\mathbf{G}_{pp}\ \mathbf{G}_{pr}\\ \mathbf{G}_{rp}\ \mathbf{G}_{rr}\end{bmatrix}\right\|_\infty \leq 1 \tag{12.43}$$

In this case, the problem becomes an $\mathcal{H}_\infty$ control problem: ensuring that the gain from the resulting extended input $\mathbf{w}$ to the extended $\mathbf{z}$ is less than 1.0 ensures that the two component transfer functions *also* have gains less than 1.0. However, this approach is conservative in that the "cross" transfer functions must also be minimized in some sense. In order to achieve this, the norms of the target components, $\mathbf{G}_{pp}$ and $\mathbf{G}_{rr}$ will most likely have to be significantly less than 1. Thus, such an approach may be regarded as conservative, but is usually excessively so, achieving a relatively poor tradeoff between the two specifications.

The goal of $\mu-$control design is specifically to ensure that the $\mathcal{H}_\infty$ norms of $\mathbf{G}_{pp}$ and $\mathbf{G}_{rr}$ are less than 1.0 while ignoring, to the greatest possible extent, the gains $\mathbf{G}_{pr}$ and $\mathbf{G}_{rp}$. As it turns out, it is not tractable to precisely accomplish this objective and actual $\mu-$synthesis results will generally represent a compromise between this ideal and the solution described by (12.43).

12.11.1 Solving the $\mu-$Synthesis Problem

The essential difference between the $\mu-$ and $\mathcal{H}_\infty-$synthesis problems is the block structure. Thus, to formulate the $\mu-$synthesis problem, augment the $\mathbf{w}$ and $\mathbf{z}$ vectors as described above to form a standard $\mathcal{H}_\infty$ synthesis problem

but with both performance and robustness partitions (or any other partitions, for that matter). The added component that completes the formulation is specification of the *block structure*.[4] In the present example, the problem has two blocks: an unstructured performance block and an unstructured robustness block corresponding to $\mathbf{G}_{pp}$ and $\mathbf{G}_{rr}$. This model and structure are then provided to a $\mu-$synthesis engine, such as the MatLab® function `DKSYN` [4, 51]. The product of such an engine is generally the controller (if one is found) and an estimate of μ for the resulting system, which is an indication of whether or not the specifications have been met: if $\mu < 1$ then they have been met while if $\mu > 1$ then they have not.

In most cases, it will be necessary to iterate a bit on the specifications: if they are overly stringent, then it will not be possible to meet them and μ will be substantially larger than 1.0 or no controller at all will be found. On the other hand, if the specifications are overly lax, then the problem will be poorly conditioned and may also not produce a solution.

Once an acceptable controller is synthesized, there still remains work to be done. The order of the controller produced by $\mu-$synthesis can be very large: the *minimum* order is equal to the sum of the orders of the plant (rotor, amplifiers, actuators, sensors, delays, filters) plus those of the input and output weighting functions. The iterative process by which the solver approximates the μ objective adds additional orders to the controller. For the example developed here, the final controller order is 108: compare this to the mixed PID controller, which had order 6! However, much of this high complexity is not really required and it is generally possible to reduce the controller order with negligible impact on system performance.[5] For the present example, the order was reduced to a more manageable 28 using internally balanced truncation.

12.11.2 Performance of the $\mu-$Controller

The resulting controller is depicted in Fig. 12.34. Only two of the four terms are shown because the symmetry of the problem dictates that the other two terms are the same. The controller shares many of the features of the $\mathcal{H}_\infty$ controller developed in Section 12.10. In particular, there is a sharp anti-notch at about 220 Hz.

The output sensitivity performance is indicated in Fig. 12.35, where it is compared to the controllers derived previously using other strategies. Importantly, it is clear that the sensitivity performance, which is specifically

[4] Specifying structure in the uncertainty block leads to the generalized structured singular value problem [56].

[5] Apparently, this reduction in controller order should be part of the $\mu-$synthesis process. However, it is not always required or desired so such reductions are left to the user. Indeed, it is usually not possible to determine *a priori* how much reduction can be introduced without losing the robustness and performance goals of the synthesis process. Consequently, order reduction is a bit of a trial-and-error process.

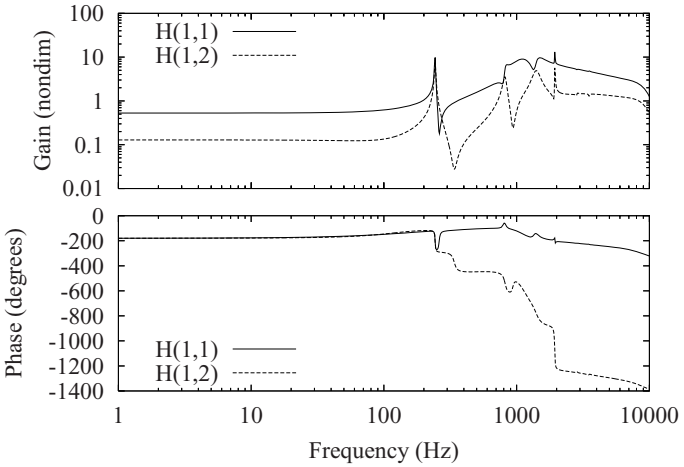


Fig. 12.34. Controller transfer function components H_{11} and H_{12}. The controller is symmetric so $H_{22} = H_{11}$ and $H_{21} = H_{12}$.

targeted by this synthesis approach is significantly better than for any of the previous controllers, especially the $\mathcal{H}_\infty$ controller.

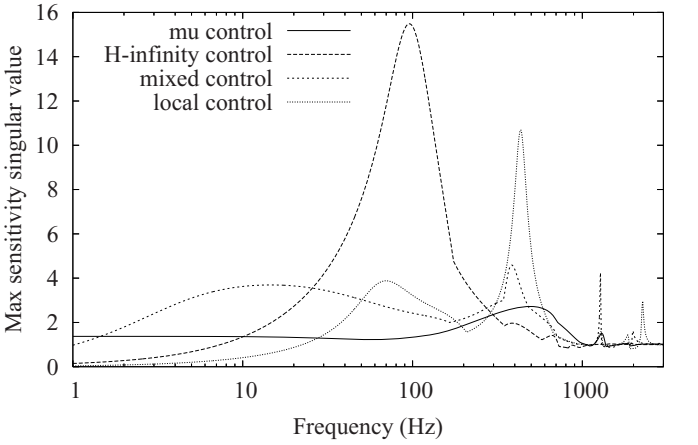


Fig. 12.35. Output sensitivity with $\mu-$controller. Peak value is 2.72

The unbalance performance obtained with this $\mu-$controller is shown in Fig. 12.36. Clearly, unbalance accommodation has been sacrificed in order to achieve excellent output sensitivity: the peak unbalance response gain is 2.5

times higher than for the $\mathcal{H}_\infty$ controller. However, it still certainly meets the nominal specification for unbalance: it can accommodate unbalance levels 80% higher than are expected before the rotor begins to contact critical clearances.

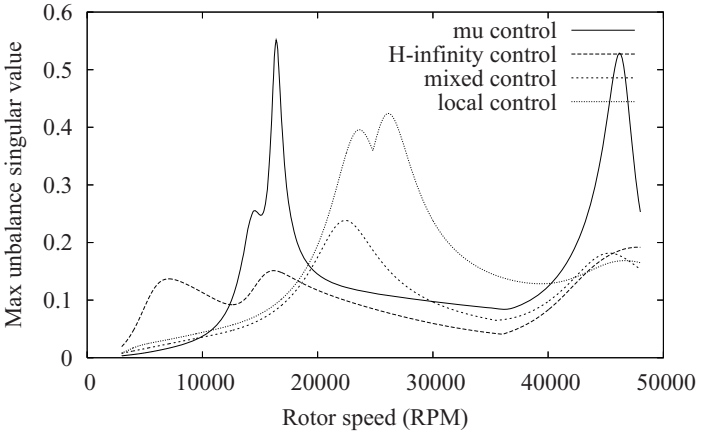


Fig. 12.36. Unbalance response with $\mu-$controller. Peak value is 0.55

12.12 Asymmetric Example

To emphasize the consequences of flexible rotor dynamics complexity, the size of the wheel on the right end of the rotor was increased, the size of the AMB on the left end of the rotor was slightly decreased, and the size of the AMB on the right end of the rotor was slightly increased. This eliminated the symmetry of the rotor and, at the same time, introduced some serious sensor–actuator collocation issues that must be addressed by the controller.

Figure 12.37 shows the free–free mode shapes of the resulting rotor with actuator and sensor locations indicated. Notice, in particular, that the third mode (first bending mode) has a node between the right sensor and right actuator while the fourth mode (second bending mode) has a node between the left sensor and left actuator. The frequencies associated with these two modes are 250.5 Hz and 691.8 Hz, respectively.

As discussed in Sect. 12.1.2, the issue that this interposed mode creates is that the phase of the modal response from actuator to sensor is reversed relative to what it would be were there no node interposed. Consequently, "passive" control applied to these two modes will actually destabilize them.

Using the same control weighting scheme as in the previous example, a controller was generated using $\mu-$synthesis. The resulting performance was

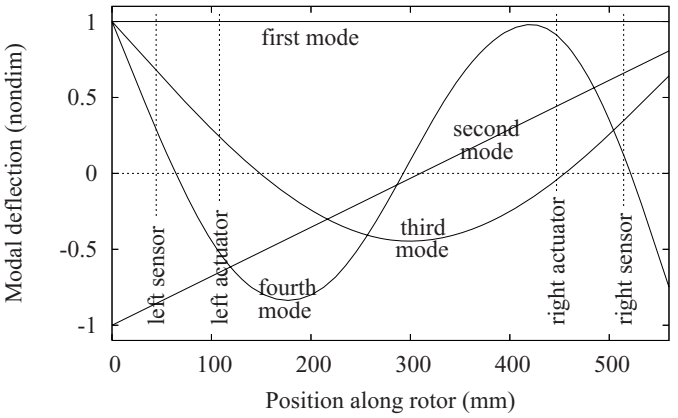


Fig. 12.37. Free–free mode shapes of the asymmetric rotor, indicating sensor and actuator locations.

similar to that for the symmetric rotor: maximum sensitivity of 4.0 and maximum normalized unbalance gain of 0.5. Bode plots of the two "direct" transfer functions, H_{11} and H_{22} are shown in Fig. 12.38.

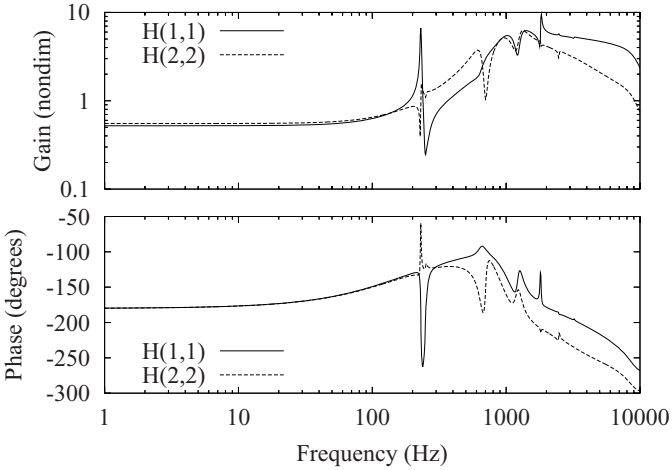


Fig. 12.38. Bode plots of H_{11} and H_{22}

It is interesting in these Bode plots that the two direct controllers must take special action near the first two bending modes: both introduce notch filters and the filters are of completely different character between the two controllers. Figure 12.39 shows the Bode plots for the other two (off-diagonal) controller transfer functions, again indicating substantial asymmetry.

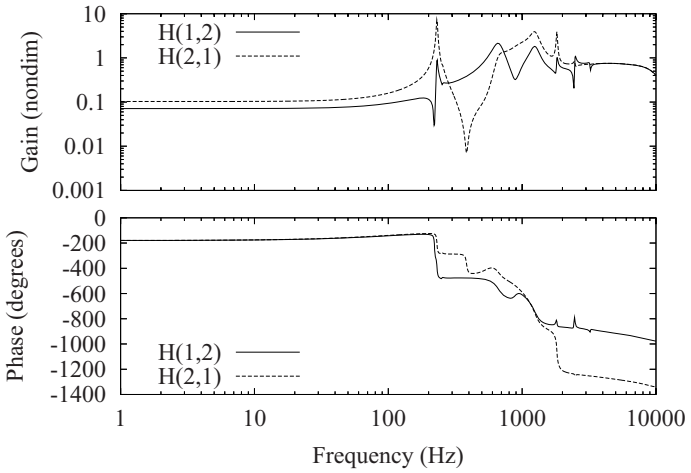


Fig. 12.39. Bode plots of H_{12} and H_{21}

12.13 Gyroscopics

In the discussion and examples presented so far, the issue of rotor gyroscopic behavior has been ignored. However, this can be a very significant issue in control of flexible rotors. The reason is that, as has been seen, it is common that controllers must be tightly tailored to the flexible dynamics of the rotor: notch filters carefully aligned with characteristic frequencies of the rotor. This presents a problem because these characteristic frequencies may be relatively strong functions of rotor speed, due to gyroscopic behavior in the large diameter elements of the rotor. This fact is reflected in the rotor model (12.7) where the A matrix is affine in rotor speed:

$$\frac{d}{dt}\mathbf{x}_{\text{rot}} = [\mathbf{A}_{\text{rot}} + \Omega\mathbf{G}_{\text{rot}}]\,\mathbf{x}_{\text{rot}} + \dots$$

If this problem is not addressed, then a very flexible rotor / AMB system which is stable at rotor stand-still may not maintain stability in the whole speed range.[6]

There are several general categories of approach for solving this problem. The most obvious approach is called *gain scheduling* [35, 45, 68]: controllers are developed for rotor plants at numerous values of Ω and, since Ω is generally known quite accurately, the digital control hardware can switch from one controller to the next as the rotor speed increases. If the variation in rotordynamics is slow enough, then this may be a sufficient solution. Another

[6] Note that, for the rotor by itself, gyroscopic forces tend to stabilize the rotor motion (see Sect. 7.3.2). However, in an AMB system, instability may occur due to control forces because the AMB system is not *passive*.

emerging approach is to solve what is known as the *linear parameter varying* or *LPV* [78] control problem which explicitly considers the function dependence $\mathbf{A}+\Omega\mathbf{G}$. The product of LPV control synthesis is a controller whose $\mathbf{A}$, $\mathbf{B}$, and $\mathbf{C}$ matrices are all functionally dependent on Ω, i.e.: $\mathbf{A}(\Omega) = \sum \mathbf{A}_i \Omega^i$. Implementation of LPV control in AMB systems has not been reported in the literature yet, but may emerge as a powerful approach.

Presently, perhaps the most promising approach to formally ensuring that a fixed gain controller will stabilize a flexible rotor over a wide range of rotor speeds is $\mu-$synthesis. The reason for this is that it is possible to represent this wide range of rotor speeds explicitly as an uncertainty in the rotor model when the problem is formulated. If the $\mu-$synthesis process is successful, then the resulting controller is guaranteed to stabilize the rotor over the specified speed range. In some cases, it is not possible to synthesize a $\mu-$controller for the entire running speed range of a rotor. In this case, the speed range is broken into a sequence of shorter intervals (generally, overlapping intervals), and $\mu-$controllers are computed for each interval. Gain scheduling is then used to switch from controller to controller as the rotor speed moves through this sequence of intervals. In this manner, gain scheduling becomes a formal synthesis process with guaranteed stability throughout the entire rotor speed range without having to introduce an excessive number of distinct controllers.

12.14 Unbalance Control

A thorough treatment of unbalance control for rigid rotors is provided in Sect. 8.3. The purpose of the present discussion is to extend that material to consider the implications of rotor flexibility and how the control strategy can be altered to account for this model feature. The architecture of most commonly used unbalance control strategies is indicated in Fig. 8.12: the unbalance controller acts in parallel with the feedback controller and has access both to the total control effort requested (signal sent to the power amplifiers) and measured rotor response (signals from the position sensors).

Viewed abstractly, the purpose of unbalance control is to attempt to minimize some aspect of the AMB/Rotor system's *synchronous* response to mass unbalance. This could mean minimizing the rotor synchronous component of the control signals going to the amplifier (Group A in Table 8.5), minimizing the measured rotor motion (Group B), or some mixture of the two.

Assume a rotor/AMB plant with transfer function $\mathbf{G}$:

$$\begin{bmatrix} \mathbf{z} \\ \mathbf{y}_s \end{bmatrix} = \begin{bmatrix} \mathbf{G}_{11} & \mathbf{G}_{12} \\ \mathbf{G}_{21} & \mathbf{G}_{22} \end{bmatrix} (j\Omega) \begin{bmatrix} \mathbf{f}_u \\ \mathbf{u}_c \end{bmatrix} \tag{12.44}$$

Outputs from this model are $\mathbf{y}_s$, the measured rotor displacements and $\mathbf{z}$, the displacement measures that are to be regulated: $\mathbf{y}_s$ could be the same as $\mathbf{z}$ or they could be different. Inputs include the unbalance forces, $\mathbf{f}_u$ and the

control signals $\mathbf{u}_c$. The rotor is regulated by feedback controller with transfer function $\mathbf{H}$ from the sensor signals and also by the unbalance signal $\mathbf{u}_u$:

$$\mathbf{u}_c = \mathbf{H}(j\Omega)\mathbf{y}_s + \mathbf{u}_u \tag{12.45}$$

For the moment, ignore this feedback law with the assumption that the gain of $\mathbf{H}$ is finite at any frequency of interest and compute a *best* synchronous $\mathbf{u}_c$ which can then be used in conjunction with the resulting solution for $\mathbf{y}_s$ to find $\mathbf{u}_u$. This sidesteps a lot of messy algebra.

A strategy for choosing the *total synchronous* control force $\mathbf{u}_c$ is to minimize the quadratic cost

$$J = \frac{1}{2}\left(\mathbf{z}^{\mathrm{T}}\mathbf{W}_z\mathbf{z} + \mathbf{u}_c^{\mathrm{T}}\mathbf{W}_u\mathbf{u}_c\right) \tag{12.46}$$

The weighting matrices $\mathbf{W}_z$ and $\mathbf{W}_u$ (which could be functions of frequency) accomplish the tradeoff between minimization of rotor response (large $\mathbf{W}_z$) and minimization of control effort (large $\mathbf{W}_u$).

To minimize J, simply differentiate (12.46) with respect to $\mathbf{u}_c$, set the result equal to zero to find the stationary point, and solve for $\mathbf{u}_c$:

$$\mathbf{u}_c = -\left(\mathbf{G}_{12}^{\mathrm{T}}\mathbf{W}_z\mathbf{G}_{12} + \mathbf{W}_u\right)^{-1}\mathbf{G}_{12}^{\mathrm{T}}\mathbf{W}_z\mathbf{G}_{11}\mathbf{f}_u \tag{12.47a}$$

$$\mathbf{z} = \left(\mathbf{G}_{11} - \mathbf{G}_{12}\left(\mathbf{G}_{12}^{\mathrm{T}}\mathbf{W}_z\mathbf{G}_{12} + \mathbf{W}_u\right)^{-1}\mathbf{G}_{12}^{\mathrm{T}}\mathbf{W}_z\mathbf{G}_{11}\right)\mathbf{f}_u \tag{12.47b}$$

$$\mathbf{y}_s = \left(\mathbf{G}_{21} - \mathbf{G}_{22}\left(\mathbf{G}_{12}^{\mathrm{T}}\mathbf{W}_z\mathbf{G}_{12} + \mathbf{W}_u\right)^{-1}\mathbf{G}_{12}^{\mathrm{T}}\mathbf{W}_z\mathbf{G}_{11}\right)\mathbf{f}_u \tag{12.47c}$$

$$\mathbf{u}_u = -\left(\mathbf{H}\mathbf{G}_{21} + (\mathbf{I} - \mathbf{H}\mathbf{G}_{22})\left(\mathbf{G}_{12}^{\mathrm{T}}\mathbf{W}_z\mathbf{G}_{12} + \mathbf{W}_u\right)^{-1}\mathbf{G}_{12}^{\mathrm{T}}\mathbf{W}_z\mathbf{G}_{11}\right)\mathbf{f}_u \tag{12.47d}$$

Of course, in practice, none of the quantities in (12.47) except $\mathbf{H}$, $\mathbf{W}_z$, and $\mathbf{W}_u$ are actually known: they will have to be estimated. But for the moment, assume that they are perfectly known so that we can examine the influence of the design parameters $\mathbf{W}_z$ and $\mathbf{W}_u$.

12.14.1 Minimum Control Effort

If the goal of the unbalance control is to minimize loss of AMB dynamic capacity by driving the synchronous control component small, then the cost of rotor motion is zero: $\mathbf{W}_z = 0$. In this case, (12.47) becomes

$$\mathbf{u}_c = 0 \tag{12.48a}$$

$$\mathbf{z} = \mathbf{G}_{11}\mathbf{f}_u \tag{12.48b}$$

$$\mathbf{y}_s = \mathbf{G}_{21}\mathbf{f}_u \tag{12.48c}$$

$$\mathbf{u}_u = -\mathbf{H}\mathbf{G}_{21}\mathbf{f}_u \tag{12.48d}$$

That is, the synchronous response of the rotor is just what it would be without any control: the free–free response. Not surprisingly, this is a problem when

the rotor attempts to pass a bending flexible mode, as illustrated by the forced response plot shown in Fig. 12.40. This leads to the conclusion that this type of unbalance compensation will work fine at rotor speeds well separated from the free–free critical speeds but will not permit the rotor to run through critical speeds: in the example, the system gets into trouble when it reaches the first free–free mode at 16551 RPM. Note that, while the feedback control will modify the system eigenvalues and may move the rotor resonances around, the unbalance control problem frequencies are unaffected by this feedback.

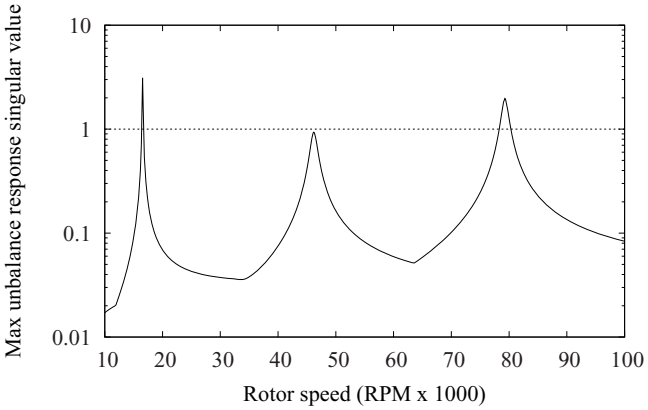


Fig. 12.40. Unbalance response of the example rotor with $\mathbf{W}_z = 0$.

12.14.2 Minimum Response

The opposite extreme is where the optimization targets only the rotor response, without consideration of control effort, so that $\mathbf{W}_u = 0$. Now,

$$\mathbf{u}_c = -\left(\mathbf{G}_{12}^{\mathrm{T}}\mathbf{W}_z\mathbf{G}_{12}\right)^{-1}\mathbf{G}_{12}^{\mathrm{T}}\mathbf{W}_z\mathbf{G}_{11}\mathbf{f}_u \tag{12.49a}$$

$$\mathbf{z} = \left(\mathbf{G}_{11} - \mathbf{G}_{12}\left(\mathbf{G}_{12}^{\mathrm{T}}\mathbf{W}_z\mathbf{G}_{12}\right)^{-1}\mathbf{G}_{12}^{\mathrm{T}}\mathbf{W}_z\mathbf{G}_{11}\right)\mathbf{f}_u \tag{12.49b}$$

$$\mathbf{y}_s = \left(\mathbf{G}_{21} - \mathbf{G}_{22}\left(\mathbf{G}_{12}^{\mathrm{T}}\mathbf{W}_z\mathbf{G}_{12}\right)^{-1}\mathbf{G}_{12}^{\mathrm{T}}\mathbf{W}_z\mathbf{G}_{11}\right)\mathbf{f}_u \tag{12.49c}$$

$$\mathbf{u}_u = -\left(\mathbf{H}\mathbf{G}_{21} + (\mathbf{I} - \mathbf{H}\mathbf{G}_{22})\left(\mathbf{G}_{12}^{\mathrm{T}}\mathbf{W}_z\mathbf{G}_{12}\right)^{-1}\mathbf{G}_{12}^{\mathrm{T}}\mathbf{W}_z\mathbf{G}_{11}\right)\mathbf{f}_u \tag{12.49d}$$

In the special case that the number of responses to be minimized equals the number of control signals – the *square* problem – then $\mathbf{G}_{12}^{-1}$ exists at most frequencies and this expression simplifies to

$$\mathbf{u}_c = -\mathbf{G}_{12}^{-1}\mathbf{G}_{11}\mathbf{f}_u \tag{12.50a}$$

$$\mathbf{z} = 0 \tag{12.50b}$$

$$\mathbf{y}_s = \left(\mathbf{G}_{21} - \mathbf{G}_{22}\mathbf{G}_{12}^{-1}\mathbf{G}_{11}\right)\mathbf{f}_u \tag{12.50c}$$

$$\mathbf{u}_u = -\left(\mathbf{H}\mathbf{G}_{21} + (\mathbf{I} - \mathbf{H}\mathbf{G}_{22})\,\mathbf{G}_{12}^{-1}\mathbf{G}_{11}\right)\mathbf{f}_u \tag{12.50d}$$

Thus, for the *square* problem, the rotor response is driven precisely to zero and the control effort matches the unbalance. This condition is indicated in Fig. 12.41. It is interesting to note that the control force becomes unbounded at certain frequencies and that these frequencies are not rotor critical speeds. Rather, they represent special *transmission zeros* of the transfer function $\mathbf{G}_{12}$ and are frequencies at which the control authority vanishes. At these frequencies, the only possible response of the rotor with finite control effort is the free–free response. For the example here, the system gets into trouble at the first transmission zero frequency: 15864 RPM.

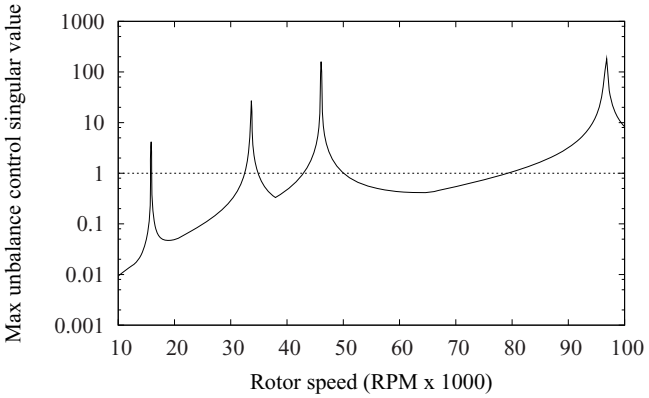


Fig. 12.41. Unbalance control signal for the example rotor with $\mathbf{W}_u = 0$.

12.14.3 Mixed Optimization

Obviously, if the rotor must run through speeds corresponding to both of these singularities, then neither of these two approaches will be satisfactory. In this case, it makes sense to seek a balance between rotor response and use of control effort. Following the arguments presented in Sect. 12.5, it seems to make sense to use the natural scalings of the problem to construct the cost function. In particular, perhaps it is permissible for the synchronous rotor response to consume 25% of the available clearance and, at the same time, for the synchronous control effort to be 20% of the available bearing capacity. In this case,

$$\mathbf{W}_z = \text{diag}\left(\frac{1}{(0.25c_i)^2}\right) \quad \text{and} \quad \mathbf{W}_u = \text{diag}\left(\frac{1}{(0.20f_i)^2}\right)$$

The resulting behavior is indicated in Fig. 12.42 which shows both rotor response and control effort. Here, the sharp peaks associated with free–free resonances or transmission zeros are eliminated and the system meets the more exacting specification (25% of clearance, 20% of control capacity) at speeds up to 76519 RPM.

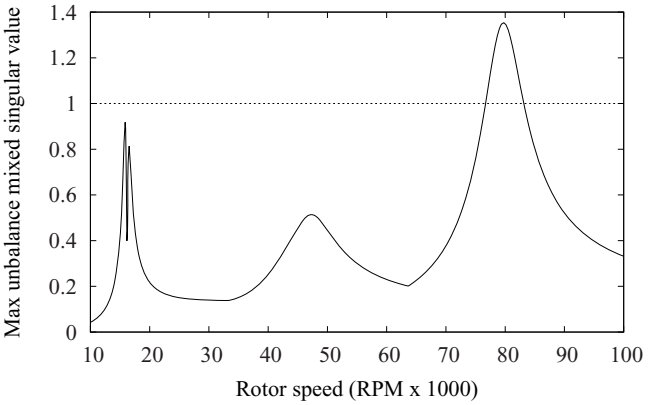


Fig. 12.42. Unbalance gain for the example rotor with mixed optimization. Note that, in this case, the gain is a maximum singular value and summarizes gain to response *and* gain to control effort simultaneously.

12.14.4 Implementation

When $\mathbf{W}_z = 0$ and the objective is solely to minimize the synchronous control effort, implementation is simplified because the solution

$$\mathbf{u}_u = -\mathbf{H}\mathbf{y}_s$$

requires no knowledge of the plant. Indeed, if the point of unbalance control injection is moved from the *output* of the feedback controller to its *input*, then

$$\mathbf{u}_u = -\mathbf{y}_s$$

and the only requirement is knowledge of the synchronous component of the sensor signals. For this reason and because of the advantage of conserving precious actuator capacity, this solution is most commonly implemented on commercial AMB systems as some form of generalized notch filter [36].

However, when the unbalance control must be used when running near or through free–free critical speeds, such a solution is no longer acceptable and it is necessary to resort to the more generalized solution of (12.49). In this case, the unbalance control must have some way to estimate both the unbalance force and the plant transfer functions $\mathbf{G}_{11}$, $\mathbf{G}_{12}$, $\mathbf{G}_{21}$, and $\mathbf{G}_{22}$. There are several discussions of this class of problems in the literature: [43], for instance, develops recursion relations based on estimates of these matrices and establishes the level of model error that the recursion method can tolerate before it becomes unstable (fails to converge). Such methods have not been implemented commercially, but are likely to see commercial application as the operating speed of AMB supported turbomachinery increases.

12.15 Closing Remarks

Reviewing the various control design methods explored in this chapter, some obvious observations arise. First, the hand synthesis strategies (collocated PID, non-collocated PID, mixed PID) produced a sequence of steadily improving performance and reasonably good robustness (in terms of output sensitivity). Further, the resulting controllers were of low order: only order 5 for each axis for the mixed PID result which means a total of order 20 for the entire radial AMB system. Finally, these methods will seem accessible to engineers with experience in designing simple controllers.

By contrast, the last two methods ($\mathcal{H}_\infty$ and $\mu-$synthesis) will seem much less accessible: they rely on heavy mathematical machinery. Further, the performance improvements realized by these controllers over the best hand-synthesized result are not spectacular. The $\mathcal{H}_\infty$ controller realized somewhat better unbalance performance but at the cost of unacceptably high sensitivity. The μ controller managed to realize the best sensitivity result, but compromised the unbalance response significantly to do so. Finally, these equivocal results are achieved at significant expense in terms of controller complexity: the μ controller had order 28 for a single plane of control: the full 2-plane solution would have order 56. It would probably be possible to reduce this order below 28 without substantially degrading system performance, but it is unlikely that it can be brought all of the way down to 10 without substantial degradation.

Thus, one cannot say without hesitation that the $\mu-$synthesis approach, with all of its heavy machinery, produces controllers which are obviously superior to those that can be hand designed by a skilled engineer.

However, there are several of considerations which militate in favor of the $\mu-$ approach or other similar methods. First, writing the specifications for $\mu-$synthesis is reasonably straightforward and follows intuitively accessible reasoning. Once a viable specification is developed, generation of the actual controller is essentially automatic and does not rely on the control engineer finding clever tricks - special filters - to stabilize the system even if the plant is *difficult*. By contrast, hand synthesis can require many tricks and special insights.

The second observation pushing toward $\mu-$synthesis is the simple fact that the formulation allows the engineer to *explicitly* address specialized sensitivity issues that admit really no direct strategy in hand synthesis. Generally, experienced control engineers will realize that aligning very sharp notch filters with plant eigenvalues is poor practice if the exact location of these eigenvalues is uncertain. But quantifying how such notch filters should be adapted in the face of specific levels of uncertainty is only possible for very specific scenarios and will generally be handled in an ad-hoc fashion. This sort of problem is handled with aplomb by $\mu-$synthesis.

The final observation is that, because $\mu-$synthesis is driven by clear engineering specifications, the engineering investment in a design process centered

on a tool like this is primarily in these specifications and the underlying strategies that guide their development. Such an investment is easy to document and easy to transmit to successive generations of engineers: much more so than the arcane bag of tricks that enables hand design of controllers (see, for instance, the discussion in Sec. 9.4). Indeed, automated synthesis methods, in conjunction with emerging tools for automated system identification promise the emergence of practical and effective *self tuning* systems, pointing the way to faster system commissioning and drastically reduced engineering effort.

References

1. J. Ackermann. *Sampled Data Control*. Springer-Verlag, Berlin, 1985.
2. Markus Ahrens and Ladislav Kucera. Cross feedback control of a magnetic bearing system: Controller design considering gyroscopic effects. In *Proceedings of the Third International Symposium on Magnetic Bearings*, pages 177–191, Alexandria, Virginia, USA, 1996.
3. E. Anton and H. Ulbrich. Active control of vibrations in the case of asymmetrical high-speed rotors by using magnetic bearings. *ASME, Transactions, Journal of Vibration, Acoustics, Stress, and Reliability in Design*, 107:410–415, 1985.
4. G.J. Balas, J.C. Doyle, K. Glover, A.K. Packard, and R. Smith. *μ Analysis and Synthesis Toolbox User's Guide*. The MathWorks, Natick, MA, 1995.
5. M. J. Balas. Active control of flexible systems. *Journal of Optimization Theory and Applications*, 25(3):415–436, July 1978.
6. John S. Bay. *Fundamentals of Linear State Space Systems*. McGraw-Hill, 1999.
7. H. Bleuler, C. Gähler, R. Herzog, R. Larsonneur, T. Mizuno, R. Siegwart, and S. Woo. Application of digital signal processors for industrial magnetic bearings. *IEEE Transactions on Control Systems Technology*, 2(4):280–289, Dec. 1994.
8. H. Bleuler, D. Vischer, G. Schweitzer, A. Traxler, and D. Zlatnik. New concepts for cost-effective magnetic bearing control. *Automatica*, 30(5):871–876, 1994.
9. H. Bleuler and D. Vischer. Magnetic bearing systems with minimal hardware requirement. In *ROMAG '91: Magnetic Bearings and Dry Gas Seals International Conference and Exhibition*, March 1991.
10. Hannes Bleuler. *Decentralized Control of Magnetic Rotor Bearing Systems*. PhD thesis, Federal Institute of Technology (ETH), Zürich, 1984.
11. Hendrick W. Bode. *Network Analysis and Feedback Amplifier Design*. D. Von Nostrand Company, Inc., 1945.
12. T. S. Brinsmead and G. C. Goodwin. Fundamental limits in sensitivity minimization: Multiple–input–multiple–output (MIMO) plants. *IEEE Transactions on Automatic Control*, 46(9):1486–1490, September 2001.
13. C. R. Burrows and M. N. Sahinkaya. Vibration control of multi-mode rotor-bearing systems. *Proceedings of the Royal Society of London. Series A, Mathematical and Physical Sciences*, 386(1790):77–94, March 1983.
14. S. Carabelli, C. Delprete, and G. Genta. Rotor on active magnetic suspension, part I : Theoretical considerations. *European Journal of Mechanical and Environmental Engineering*, 43(3):123–128, 1998.
15. V. H. L. Cheng and C. A. Desoer. Limitations on the closed–loop transfer function due to right–half plane transmission zeros of the plant. *IEEE Transactions on Automatic Control*, 25(6):1218–1220, December 1980.

16. Dara Childs *Turbomachinery Rotordynamics*. Hoboken, NJ: John Wiley and Sons,Inc.,1993.
17. C.H. Cloud, W.C. Foiles, G. Li, E.H. Maslen, and L.E. Barrett. Practical applications of singular value decomposition in rotordynamics. In *Proceedings of* 6th *international conference on rotor dynamics*, pages 429–438, Sydney, Australia, Oct. 2002. IFToMM.
18. J. B. Cruz Jr. James S. Freudenberg, and Douglas P. Looze. A relationship between sensitivity and stability of multivariable feedback systems. *IEEE Transactions on Automatic Control*, 26(1):66–74, 1981.
19. J. B. Cruz Jr. and W. R. Perkins. A new approach to the sensitivity problem in multivariable feedback system design. *IEEE Transactions on Automatic Control*, 9:216–223, 1964.
20. Jose B. Cruz Jr., editor. *System Senstivity Analysis*. Dowden, Hutchinson & Ross, Inc., 1973.
21. R. Lane Dailey. Lecture notes for the workshop on H_∞ and μ methods for robust control. In *American Control Conference*, May 1990.
22. J. P. Den Hartog. *Mechanical Vibrations*. McGraw Hill, New York, 1947.
23. J.C. Doyle. Guaranteed margins for LQG regulators. *IEEE Transactions on Automatic Control*, AC-23(4):756–757, August 1978.
24. J.C. Doyle. Analysis of feedback systems with structured uncertainties. *IEE Proceedings*, 129, Part D(6):242–250, 1982.
25. J.C. Doyle, K. Glover, K. Khargonekar, and B. Francis. State–space solutions to standard h_2 and h_∞ control problems. *IEEE Trans. Auto. Control*, AC-34(8):831–847, 1989.
26. John C. Doyle and Gunter Stein. Multivariable feedback design: Concepts for a classical/modern synthesis. *IEEE Trans. Auto. Control*, 26(1):4–16, 1981.
27. Roger Fittro and Carl Knospe. The μ approach to control of active magnetic bearings. *ASME J. Engineering for Gas Turbines and Power*, 124(3), July 2002.
28. Bruce A. Francis and George Zames. On H_∞-Optimal sensitivity theory for SISO feedback systems. *IEEE Trans. Auto. Control*, 29(1):9–16, Jan. 1984.
29. R. Gasch, R. Nordmann, and H. Pfützner. *Rotordynamik*. Berlin, Heidelberg: Springer-Verlag, 2001.
30. G. Genta, C. Delprete, and S. Carabelli. Active magnetic bearing control loop modeling for a finite element rotordynamics code. In *Proc. of the 3rd Intl. Symp. on Magnetic Suspension Technology*, pages 319–333, May 1994.
31. Giancarlo Genta. *Dynamics of Rotating Systems*. Springer, 2005.
32. M. Green and D. Limebeer. *Linear Robust Control*. Prentice-Hall, Inc., 1995.
33. H. Habermann and M. Brunet. The active magnetic bearing enables optimum damping of flexible rotor. In *Proceedings of the 29th International Gas Turbine Conference and Exhibition*, Amsterdam, Netherlands, June 1984.
34. H. Habermann and G. Liard. An active magnetic bearing system. *Tribology International*, pages 85–89, April 1980.
35. L. Hawkins, B. T. Murphy, and J. Kajs. Analysis and testing of a magnetic bearing energy storage flywheel with gain-scheduled, MIMO control. In *Proceedings of the 45th ASME International Gas Turbine and Aeroengine Technical Congress, Exposition, and Users Symposium*, Munich, Germany, May 2000.
36. H. Herzog, Ph. Bühler, C. Gähler, and R. Larsonneur. Unbalance compensation using generalized notch filters in the multivariable feedback of magnetic bearings. *IEEE Trans. Control Systems Technology*, 4(5):580–586, Sep. 1996.

37. Sung-Kyung Hong and R. Langari. Robust fuzzy control of a magnetic bearing system subject to harmonic disturbances. *IEEE Transactions on Control Systems Technology*, 8(2):366–371, March 2000.
38. R. R. Humphris, R. D. Kelm, D. W. Lewis, and P. E. Allaire. Effect of control algorithms on magnetic journal bearings. *Trans. ASME Journal of Engineering for Gas Turbines and Power*, 108:624–632, October 1986.
39. ISO TC108/SC2 Working Group 7. Active magnetic bearings - evaluation of stability margin. ISO-14839-3, September 2006.
40. Marty E. Johnson, Luiz P. Nascimento, Mary Kasarda, and Chris R. Fuller. The effect of actuator and sensor placement on the active control of rotor unbalance. *J. Vibration and Acoustics – Trans. ASME*, 125(3):365–373, July 2003.
41. Y. Kanemitsu, M. Ohsawa, and E. Marui. Comparison of control laws for magnetic levitation. In *Proceedings of the Fourth International Symposium on Magnetic Bearings*, 1994.
42. C. R. Knospe, R. W. Hope, S. J. Fedigan, and R. D. Williams. Experiments in the control of unbalance response using magnetic bearings. *Mechatronics*, 1995.
43. C. R. Knospe, R. W. Hope, S. M. Tamer, and S. J. Fedigan. Robustness of adaptive unbalance control of rotors with magnetic bearings. *Journal of Vibration and Control*, 2(1):33–52, 1996.
44. C. R. Knospe, S. M. Tamer, and S. J. Fedigan. Robustness of adaptive rotor vibration control to structured uncertainty. *ASME Journal of Dynamic Systems, Measurement, and Control*, 119(2):243–250, 1997.
45. C. R. Knospe and C. Yang. Gain-scheduled control of a magnetic bearing with low bias flux. In *Proceedings of the 36th IEEE Conference on Decision and Control*, San Diego, CA, USA, pages 418–423, December 1997.
46. V. S. Lefante. Noncollocation in magnetic bearings for flexible rotors. Master's thesis, University of Virginia, 1992.
47. Guoxin Li, Eric Maslen, and Paul Allaire. A note on ISO AMB-rotor system stability margin. In *Proceedings of the Tenth International Symposium on Magnetic Bearings*, Martigny, Switzerland, August 2006.
48. D. P. Looze and J. S. Freudenberg. Limitations of feedback properties imposed by open–loop right half plane poles. *IEEE Transactions on Automatic Control*, 36(6), June 1991.
49. Florian Lösch. *Identification and Automated Controller Design for Active Magnetic Bearing Systems*. PhD thesis, ETH Zürich, 2002.
50. E. H. Maslen and J. R. Bielk. A stability model for flexible rotors with magnetic bearings. *ASME Journal of Dynamic Systems, Measurement, and Control*, 114(1):172–175, March 1992.
51. The Mathworks, Inc. *μ-Analysis and Synthesis Toolbox User's Guide, Version 3*, 1998.
52. F. Matsumura and T. Yoshimoto. System modeling and control design of a horizontal–shaft magnetic bearing system. *IEEE Transactions on Magnetics*, 22(3):196–203, May 1986.
53. Abdelfatah M. Mohamed, Fumio Matsumura, Toru Namerikawa, and Jun-Ho Lee. Modeling and robust control of self-sensing magnetic bearings with unbalance compensation. *IEEE Conference on Control Applications - Proceedings*, pages 586 – 594, 1997.
54. K. Nonami, H. E. Weidong, and H. Nishimura. Robust control of magnetic levitation systems by means of H^∞ control/μ–synthesis. *JSME International Journal*, 37(3):513–520, 1994.

55. Y. Okada, T. Nagata, J.Tani, and H. B. Zhang. Vibration analysis and active control of flexible–shell– structured rotor supported by magnetic bearings. *JSME International Journal Series C*, 37(3):488–493, 1994.
56. A. Packard and J.C. Doyle. The complex structured singular value. *Automatica*, 29:71–109, 1993.
57. N. K. Rutland, P. S. Keogh, and C. R. Burrows. Comparison of controller designs for attenuation of vibration in a rotor-bearing system under synchronous and transient conditions. In *Proceedings of the Fourth International Symposium on Magnetic Bearings*, 1994.
58. J. R. Salm. Active electromagnetic suspension of an elastic rotor : Modelling, control, and experimental results. *Journal of Vibration, Acoustics, Stress, and Reliability in Design*, 110:493–500, October 1988.
59. Jerzy Sawicki and Eric Maslen. AMB controller design for a machining spindle using $\mu-$synthesis. In *Proceedings of the Tenth International Symposium on Magnetic Bearings*, Martigny, Switzerland, August 2006.
60. J. Schmied and J. C. Pradetto. Rotor dynamic behaviour of a high-speed oil-free motor compressor with a rigid coupling supported on four radial magnetic bearings. In *Proceedings of the Third International Symposium on Magnetic Suspension Technology*, pages 557–572, May 1994.
61. U. Schonhoff, J. Luo, G. Li, E. Hilton, R. Nordmann, and P. Allaire. Implementation results of μ-synthesis control for an energy storage flywheel test rig. In *Proceedings of the Seventh International Symposium on Magnetic Bearings*, Zürich, Switzerland, 2000.
62. G. Schweitzer, H. Bleuler, and A. Traxler. *Active Magnetic Bearings*. Hochschulverlag AG an der ETH Zurich, 1994.
63. M. B. Scudiere, R. A. Willems, and G. T. Gillies. Digital controller for a magnetic suspension system. *Rev. Sci. Instrum.*, 57(8):1616–1626, August 1986.
64. J. D. Setiawan, R. Mukherjee, and E. H. Maslen. Synchronous sensor runout and unbalance compensation in active magnetic bearings using bias current excitation. *ASME Journal of Dynamic Systems, Measurement, and Control*, 124:14–24, March 2002.
65. B. Shafai, S. Beale, P. Larocca, and E. Cusson. Magnetic bearing control systems and adaptive forced balancing. *IEEE Control Systems Magazine*, 14(2):4–13, April 1994.
66. T. N. Shiau, G. J. Sheu, and C. D. Yang. Vibration and control of a flexible rotor in magnetic bearings using hybrid method and H_∞ control theory. *ASME J. Engineering for Gas Turbines and Power*, 119(1):178–185, January 1997.
67. R. Siegwart, D. Vischer, R. Herzog, A. Traxler, H. Bleuler, and G. Schweitzer. Control concepts for active magnetic bearings. In *Proc, of the First International Symposium on Magnetic Suspension Technology*, pages 401–422, May 1992.
68. S. Sivrioglu and K. Nonami. LMI approach to gain scheduled H_∞ control beyond PID control for gyroscopic rotor-magnetic bearing system. In *Proceedings of the 35th IEEE Conference on Decision and Control*, pages 3694–3699, Dec. 1996.
69. S. Skogestad and I. Postlethwaite. *Multivariable Feedback Control: Analysis and Design*. John Wiley & Sons Ltd, West Sussex, England, 1996.
70. V. A. Spector and H. Flashner. Modeling and design implications of nocollocated control in flexible systems. *Journal of Dynamic Systems, Measurement, and Control*, 112:186–193, June 1990.

71. M. Spirig, J. Schmied, P. Jenckel, and U. Kanne. Three practical examples of magnetic bearing control design using a modern tool. *ASME Journal of Engineering for Gas Turbines and Power*, pages 1025–1031, October 2002.
72. S. Srinivasan, E. Maslen, and L. Barrett. Optimization of bearing locations for rotor systems with magnetic bearings. *ASME Journal of Engineering for Gas Turbines and Power*, 119:464–468, April 1997.
73. L. Scott Stephens. *Design and Control of Active Magnetic Bearings for a High Speed Machining Spindle*. PhD thesis, University of Virginia, 1995.
74. A. F. Storace, D. Sood, J. P. Lyons, and M. A. Preston. Integration of magnetic bearings in the design of advanced gas turbine engines. In *NASA Second International Symposium on Magnetic Suspension Technology*, Seattle, 1989.
75. H. Q. Tian and K. Nonami. Robust-control of flexible rotor magnetic bearing systems using discrete-time sliding mode control. *JSME International Journal Series C*, 37(3):504–512, 1994.
76. D. L. Trumper, S. M. Olson, and P. K. Subrahmanyan. Linearizing control of magnetic suspension systems. *IEEE Transactions on Control Systems Technology*, 5(4):427–438, July 1997.
77. S. R. Weller. *Structural Issues in Control Design for Linear Multivariable Systems*. PhD thesis, University of Newcastle, Australia, 1993.
78. F. Wu. A generalized LPV system analysis and control synthesis framework *International Journal of Control*, 74(7): 745–759, May 2001.
79. K. Youcef-Toumi. Modeling, design, and control integration: a necessary step in mechatronics. *IEEE/ASME Trans. Mechatronics*, 1(1):29–38, March 1996.
80. K. Youcef-Toumi and S. Reddy. Dynamic analysis and control of high speed and high precision active magnetic bearings. *Journal of Dynamical Systems, Measurement, and Control*, 114:623–633, December 1992.
81. George Zames. Feedback and optimal sensitivity: Model reference transformations, multiplicative seminorms, and approximate inverses. *IEEE Transactions on Automatic Control*, 26(2):301–320, April 1981.
82. George Zames and Bruce A. Francis. Feedback, minimax sensitivity, and optimal robustness. *IEEE Transactions on Automatic Control*, 28(5):585–601, May 1983.
83. K. Zhou, J. C. Doyle, and K. Glover. *Robust and Optimal Control*. Prentice-Hall, Inc., 1996.
84. Shiyu Zhou. Active balancing and vibration control of rotating machinery: A survey. *The Shock and Vibration Digest*, 33(5):361–371, 2001.

13

Touch-down Bearings

Gerhard Schweitzer and Rainer Nordmann

Magnetic bearings have a load capacity which is defined by design and limited in size. If the actual load surpasses this load capacity, or if the magnetic suspension fails to work for any reason, the rotor will not hover freely any more but will touch its mechanical boundaries. In order to avoid damage to the rotor laminations and the AMB stator during such a touch-down the rotor is equipped with "touch-down bearings." These are an additional set of passive bearings, and the rotor will only come into touch with them in extraordinary situations. In literature they are also known as retainer bearings, or in a more general way as back-up or auxiliary bearings. For such touch-down bearings, usually simple retainer rings or special ball bearings are used. They should be able to support the rotor for a limited time period until the normal operating mode can be recovered or until the rotor can run down safely. In addition to that, at zero power to the AMB, the rotor rests on the touch-down bearings, which allows the rotor to be rolled over easily, for inspection and maintenance. Back-up or auxiliary bearings can even be actively controlled: an example is given in [11].

In this chapter, the phenomenology of touch-down behavior, basic contact modeling for *journal retainer bearings*, experiments and design aspects are discussed. Finally, *ball bearings*, which are the most common industrial solution for touch-down bearings, and guidelines for the design of touch-down bearings, are discussed in Sect. 13.4 and 13.5. Further issues related to touch-down bearings are detailed in other places: in Chap. 14 on Dynamics and Control Issues for Fault Tolerance, the complicated nonlinear dynamics of a touch-down are introduced and modeled. There, a theoretical model of the contact dynamics is used to derive control laws for recovering the rotor and restoring normal operation. In Chap. 18 on Safety and Reliability Aspects, the role of touch-down bearings in the context of fail/safe behavior is briefly addressed.

G. Schweitzer, E.H. Maslen (eds.), *Magnetic Bearings*,
DOI 10.1007/978-3-642-00497-1_13, © Springer-Verlag Berlin Heidelberg 2009

13.1 A Rotor Contacting its Housing - Survey

Contact between a high speed rotor and a stationary second body can arise in different types of machines. Research is being carried out because the thermodynamic efficiency of many high performance rotating machines is strongly dependent upon the very small running clearances between the rotor and its casing. However, reduction of the clearance may lead to contact, rubbing or impacts, with severe implications for mechanical integrity. Instabilities may occur, either of the whole rotor casing system or the dynamically flexible components.

Contact occurs also in systems where rotors are supported by active magnetic bearings, when the magnetic bearing fails or is exposed to an overload. The rotor then makes contact with a mechanical touch-down bearing, which, obviously, has to be designed in such a way that it can withstand the dynamical loads.

The rotor dynamics literature on rotor/stator contact interaction shows a wealth of models and rotor behaviors as a result of the complex, nonlinear dynamics. As early as 1934, J.P. Den Hartog described in his book on "Mechanical Vibrations" the friction induced rotor backward whirl [13]. Another milestone was the work of Black [3].

The result of such a rub contact can be a reverse or *backward whirl* of the rotor, as well as synchronous, subsynchronous and chaotic motions, or spirally increasing bending vibrations caused by rub induced hot spots on the rotor. An extensive literature survey is given, for example, in the review paper of Muszynska [22] or in the thesis of Isakson [18]. Results on modelling the rotor dynamics caused by contact with the touch-down bearings or the housing and resulting phenomena are dealt with as well in [2, 6, 8, 10, 15, 23, 26, 28].

In general, three typical states of motion and mixed forms of these are found after a failure of the magnetic bearings and a subsequent touch-down. These are oscillations of the rotor in the base of the retainer bearing, chaotic jumping of the rotor, and the backward whirl motion. In case of an unbalanced rotor a fourth state of motion, the forward whirl, is possible. The schemes and the measured orbits are depicted in Figs. 13.1 and 13.2. The orbits of the rotor axis are represented typically in a circle where the radius equals the air gap, which in this case was 0.3 mm. The test rig for the experiments is described in Sect. 13.2.1.

The testing of touch-down bearings for AMB has been described in [5, 8, 15, 20, 29], and suggestions for touch-down bearing design for various applications are given in [19, 24, 25, 27]. For standard applications - touch-down bearings are being industrially implemented - guidelines will be summarized in Sect. 13.5.

In order to investigate the consequences of potential contacts, one of the key aspects is the realistic modelling of the contact itself. Most of the investigations are based on simplified assumptions about the geometry of the contact or even about the resulting rotor motion to explain certain dynamics

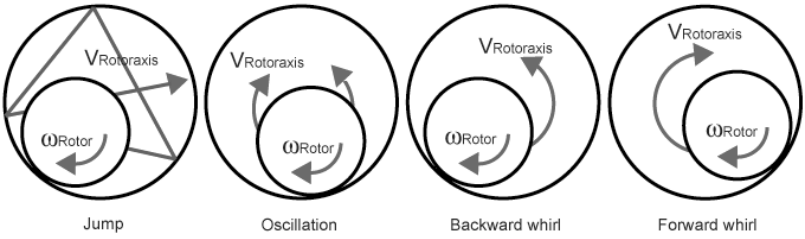


Fig. 13.1. Typical states of motion - schemes

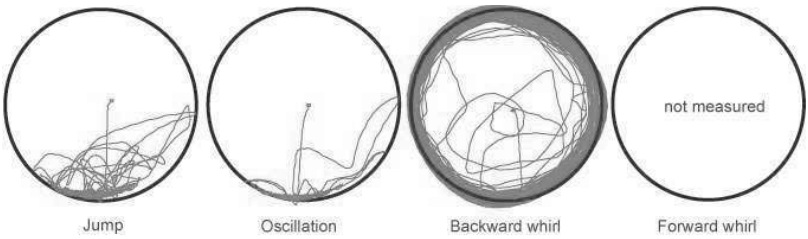


Fig. 13.2. Typical states of motion - measured orbits at 150 Hz rotor spin rate.

phenomena. Existing literature on experimentally verified rotor contacts concentrate on the description of resulting vibration phenomena, and give little data on the contact itself. The inherent difficulties of contact measurements become very distinctive when the contact body is rotating.

Nevertheless, a qualitative classification of phenomena is possible and might be sufficient in practical applications for touch-down bearings in AMB.

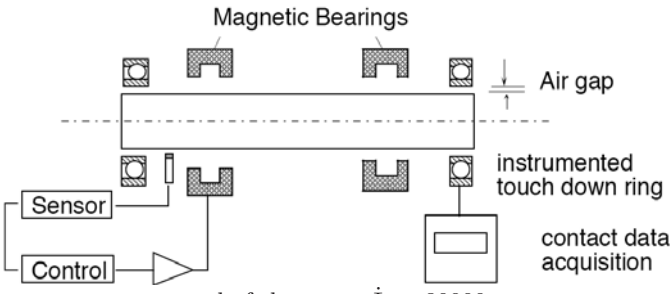
13.2 Modeling of Contacts

13.2.1 Test Rig

The modeling of contacts in a purely theoretical way, by deriving impact and contact parameters just from kinematical and material parameters, such as impact velocities and elasticities, may be rather questionable unless a sufficiently sophisticated model is used. Such models are usually not available and they can hardly be verified in practical applications. Therefore it appears to be more reasonable to rely from the very beginning on data which have been measured or which can, at least, be related to observations.

The test rig in Fig. 13.3 allows measurement of contact dynamics, primarily the first contact and the onset of the contact induced vibrations. The main specifications of the test rig are shown in Fig. 13.3: details about the test rig are given in [9]. The rotor is suspended in contact free magnetic bearings. By suitably actuating these magnetic bearings, any initial conditions for a contact at the specially instrumented, elastically suspended touch down ring

can be generated. The ring can be made of different materials such as bronze, steel, nylon, or ceramic, or ball bearings with various designs can be used.



max. speed of the rotor	$\dot{\Phi}$	= 30000 rpm
touch down ring radius	r	= 10 mm
mass	m	= 3.36 kg
air gap	ρ	= 0.3 mm
length	L	= 326 mm
polar moment of inertia	J	= 6.72 10^4kgm^2

Fig. 13.3. Test rig for measuring rotor/bearing contacts

The *lateral motions of the rotor* within the air gap are measured with the four inductive sensors, which are used for the control of the magnetic bearings. To measure the *contact forces*, an instrumented touch down ring is excited by the impacting rotor; the resulting accelerations of the ring are measured by accelerometers, and their measurement signals, after suitable calibration and signal processing, represent the contact forces. The contact ring is rather stiff, with an eigenfrequency of about 14 kHz. The essential part of the frequency spectrum of the impact is much below that eigenfrequency and the ring can be regarded as quasi-rigid. The contact ring is supended by four special springs, and it carries two accelerometers for measuring its motions in the lateral directions. The spring suspension reduces all undesired vibrations transmitted from the housing and the supporting foundation. This suspension has a translational eigenfrequency of about 300 Hz and a rotational one of 900 Hz. By calibrating the accelerometers with a reference impact, a technique known from modal analysis, the contact forces can be determined in the normal and tangential directions. The transfer function of the force measuring device relates, in the frequency domain, the impact force to the measured acceleration.

The *contact time* is an important parameter for the analysis of an impact. Its measurement is quite simple due to the contact-free magnetic suspension of the rotor. A voltage is applied to the rotor which is electrically separated from the housing and when the rotor contacts the grounded housing the resulting change in voltage is registered. The *rotor spin velocity* is measured by optically reading a black and white mark on the rotor, giving one pulse per revolution.

When one of the magnetic bearings is shut down, the other one keeps the rotor in a hovering position, so that the rotor falls like a pivoting hammer onto the contact ring. The impact coefficient of restitution, ε, can be derived by comparing the velocities of ring and rotor before and after impact, yielding values between $\varepsilon = 0.3$ and 0.8, depending on the material of the contact ring.

13.2.2 Contact Force Model

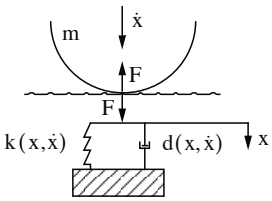


Fig. 13.4. Free-body model of the spring/damper arrangement for the impacting rotor with the relevant coordinates and parameters

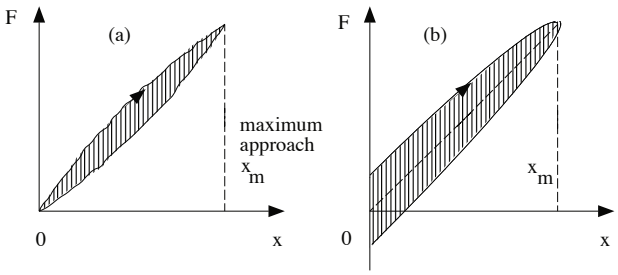


Fig. 13.5. Force/displacement diagram for nonlinear (a) and linear spring/damper model (b)

Normal Force

Modelling impacts by simple models is a questionable endeavour, as impact physics is quite complex [12]. The simplest model, which, at least, does not contradict basic physical behavior and which allows a pragmatic approach in modelling the impact, is a contact model formulated by Hunt and Crossley [17]. It describes the elastic and the damping characteristics of a contact by a nonlinear impact vibration model, as indicated by Fig 13.4, which can be suitably integrated into a rotor dynamics simulation model.

During the impact, the contact builds up from an initial point or line contact to an areal impression. The force increases with the depth of intrusion in a proportional or over-proportional manner. The impact is characterized by unilateral constraints, i.e., there will only be forces of compression: no tensile forces between the rotor and stator. Some indication of the force will be given by the Hertz theory for static contact forces. In general, such an analysis will lead to a nonlinear spring characteristic. A realistic force/displacement diagram has to look similar to that of Fig.13.5(a), where the path for loading and unloading is indicated. This means that, for the unloaded initial position x=0 the spring/damper force F has to be zero, independent of the impact velocity $\dot{x}(0)$. This excludes a linear spring/damper characteristic, such as that represented in Fig. 13.5(b). The loss of energy ΔE during an impact is proportional to the hatched areas in Fig. 13.5.

The vibrational motion of the rotor impinging on the nonlinear spring-damper can be modelled by

$$\begin{gathered} m\ddot{x} = -F, \qquad \text{with} \qquad x(0) = 0, \qquad \dot{x}(0) = v_i \\ F = F_D + F_E = d(x, \dot{x})\dot{x} + k(x, \dot{x})x \end{gathered} \tag{13.1}$$

The elastic force F_E is approximated by the Hertzian force for localized normal and frictionless contact between linearly elastic bodies. For two spheres, it is of the form

$$F_E = kx^n \tag{13.2}$$

with k depending on elasticity and geometry, as derived, for example, by Timoshenko [31]. For a contact between perfectly flat surfaces, or for parallel cylinders in longitudinal contact along a line, an index n somewhere between 1 and 3/2 should be expected to match the conditions fairly well.

A general expression for the damping force such as

$$F_D = \lambda x^p \dot{x}^q \tag{13.3}$$

satisfies the physical boundary conditions. The damping will be related somehow to the impact restitution coefficient ε. This restitution coefficient is, in the case of a simple one-dimensional impact between two reasonably shaped rigid bodies in pure translation, the ratio of their relative speed after impact v_{i+1} to the speed v_i before, so that $v_{i+1} = \epsilon v_i$. This ϵ is a very illustrative parameter, and it can be determined by relatively simple experiments with reasonable efforts. It is known from experiments [4, 12] that, for an impact between two given bodies, the coefficient ε decreases when the speed v_i increases. For a limited range of low v_i, below 50 cm/s, and for most materials with a linear elastic range, such as metals, it appears that one can write with tolerable accuracy

$$\varepsilon = 1 - \alpha v_i \tag{13.4}$$

For very elastic contacts, for example between steel or bronze, α will have a value somewhere between 0.08 and 0.32 s/m: in general it may even be

higher. The relation between the parameters ϵ and α and the loss of energy ΔE over a total single-impact sequence for one body (the other is assumed to be stationary) is illustrated by

$$\Delta E = m(v_i^2 - v_{i+1}^2)/2 = mv_i^2(1 - \epsilon^2)/2$$

Using (13.4), this can be approximated for small α and v_i by

$$\Delta E = \alpha m v_i^3$$

By simplifying the general expression for the damping force (13.3) into

$$F_D = \lambda x^n \dot{x} \tag{13.5}$$

with $n = 3/2$, Hunt and Crossley [17] show that the constant λ can be derived as

$$\lambda = (3/2)\alpha k$$

and thus the vibroimpact of (13.1) can be described by

$$m\ddot{x} + (3/2)\alpha k x^n \dot{x} + kx^n = 0 \tag{13.6}$$

Eventually, in this equation, a restoring force, resulting from the deflection of the elastic rotor shaft may have to be considered, too. The contact time is determined by a half cycle of the damped free vibration.

Tangential Force

The situation for modelling the tangential contact is even more complex than that for the normal direction. For example, a tangential impact with a corresponding restitution coefficient may occur, in particular, if a blade brushes along the housing. This effect will not be considered here, as well as rolling of the rotor along the surface of the housing. Sliding is seen as the predominant motion phase. The tangential sliding force F_R, acting on the rotor at the point of contact, has a distinct direction, opposite to the relative velocity v_{rel}. Friction or viscosity will determine the character of the tangential force. Friction will be modelled by the coefficient μ for dry friction. Values for dry friction run from $\mu = 0.1$ for smooth surfaces (steel, bronze,...) to $\mu = 0.6$ or higher for run-out and rough surfaces. The frictional force depends on the normal force F (13.1), and it obviously only exists as long as $F > 0$, a condition which is consistent with the normal force model of Fig. 13.5(a). The tangential frictional force is

$$F_R = \mu F \text{sign}(v_{Rel}) \tag{13.7}$$

A viscous tangential force may be relevant if the contact surface is lubricated, and remains lubricated during impact, or if the contact material becomes so hot that it melts (tip blades, nylon bearings, ...). Experimental data on the physics of high speed tangential contact appear not yet to be available.

13.3 Whirl Motion

13.3.1 Modeling the Whirl Motion

From the results of simulations on contact induced vibrations and from preliminary measurements, it appears that the reverse or *backward whirl* is the most violent motion among a rich pattern of possible motions [9]. Measurements have been performed on a slender rotor, horizontally supported in two bearings, Fig. 13.3, undergoing cylindrical motion, showing the typical whirl motion of Fig 13.6. For such a rotor, conical motions have not been observed. In other investigations, however, conical motions have been observed, as well, but they do not appear to occur in a stable motion [9].

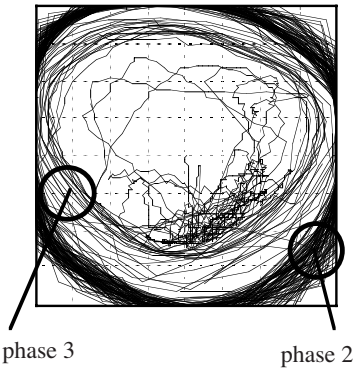


Fig. 13.6. Typical whirl motion of the rotor center. The test rig is shown in Fig. 13.3, the radius of the "circle" equals the air gap of 0.3 mm.

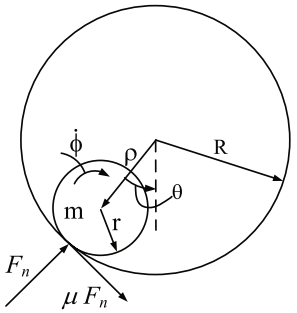


Fig. 13.7. Variables for describing the whirl motion. The normal force F_N corresponds to the force F of (13.1)

A planar model for a rigid rotor in rigid bearings has been used to explain the motion. Fig. 13.7 defines the geometry and the variables. The rotor is in

permanent contact and the sliding motion is governed by Coulomb friction μ. The rotation Φ is the clockwise motion of the shaft; the spin velocity is $\dot{\Phi}$. Revolution or whirl motion refers to the motion of the rotor center inside the touchdown bearing clearance and is labeled θ. If the rotor is rolling along the housing surface, the contact point is its instantaneous centre of rotation and the kinematic rolling condition

$$\dot{\theta} = \dot{\Phi} r/\rho \tag{13.8}$$

holds. In general, the air gap ρ is very small and the spin velocity is very high. If the rotor goes into a revolutional motion and is constrained to roll, theory leads to practically unrealistic high values for the whirl velocity $\dot{\theta}$. Equations of motion for the spin and the whirl motion in the polar coordinates of Fig. 13.7 have been derived in [7] and are given by

$$\begin{aligned} m\rho\ddot{\theta} + mg\sin\theta - \mu m(g\cos\theta + \rho\dot{\theta}^2)\text{sign}(\dot{\Phi}r - \dot{\theta}\rho) = 0 \\ J\ddot{\Phi} + \mu mr(g\cos\theta + \rho\dot{\theta}^2)\text{sign}(\dot{\Phi}r - \dot{\theta}\rho) = 0 \end{aligned} \tag{13.9}$$

Neglecting the gravitational force, the spin deceleration is approximated by

$$\ddot{\Phi} \simeq -\mu m\rho\dot{\theta}^2 r/J \tag{13.10}$$

and the acceleration of the whirl motion is given by

$$\ddot{\theta} \simeq \mu\dot{\theta}^2 \tag{13.11}$$

The normal force, on each of the two bearings, during the cylindrical rigid body motion is

$$F_{\text{cyl}} = m\rho\dot{\theta}^2/2 \tag{13.12}$$

The total kinetic energy for the cylindrical motion is

$$E_{\text{cyl}} = E_{\text{spin}} + E_{\text{whirl}} = J\dot{\Phi}^2/2 + m\rho^2\dot{\theta}^2/2 \tag{13.13}$$

and the power dissipation due to the deceleration of the spin motion follows from differentiating E_{spin} with respect to time, and substituting $\ddot{\Phi}$ from (13.10)

$$P_{\text{spin}} = \mu m\rho\dot{\theta}^2\dot{\Phi} r \tag{13.14}$$

This power loss, arising between the rotor and stator during interaction, can reach rather high values. Subsequently, measurements on whirl motions will demonstrate the whirl phases, and indicate some values for the above derived velocities, forces, energies, and power losses.

13.3.2 Experiments on Whirl Motion

At one side of the magnetically suspended rotor of Fig. 13.3, a rigidly mounted touch-down ring is used and at the other side a touch-down ring, instrumented

for force sensing, has been placed. The experiment was started by shutting down both magnetic bearings and the motor drive, while the rotor speed was 24000 rpm. The initial position of the rotor was out of centre in such a way, that, after a free fall phase, the impact velocity had a sufficiently large component tangential to the housing and in the direction of the reverse whirl. Fig. 13.8 shows a pre-whirling stage between 0.2 and 0.3 s, which finally turns into whirling motion. At 0.23 s the rotor makes permanent contact with the touch-down bearing. After the first revolution, the whirling velocity of the rotor is already sufficiently large ($\dot{\theta} = 95$ Hz) to start a permanent whirl. After five revolutions, the rotor accelerates in about 0.03 s to the final whirl velocity $\dot{\theta} = 190$ Hz. In [15] it has been shown experimentally that even several whirl frequencies may occur. This phenomenon of a limited whirl velocity will be discussed in connection with Fig 13.9.

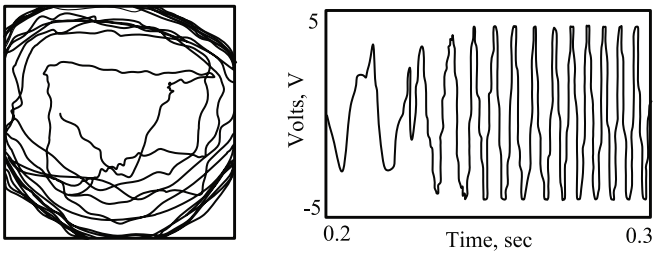


Fig. 13.8. Pre-whirl motion, trajectory of the rotor center within the air gap of 0.3 mm for a time period of 0.1 sec, and time history of the displacement in lateral direction

Further experiments have been performed on the whirl motion itself without the initial phase, using different materials for the contact surface. For example, a rigid graphite ring was placed at each side of the assembly, with an inherent elasticity for the suspension of the instrumented touch-down ring of about 300 Hz. The test procedure consisted of shutting down both magnetic bearings and motor drive at a rotor speed of 21000 rpm, of generating an initial condition capable of exciting a whirl as described above and of measuring rotor displacements and spin velocity during run down. The time behavior of various variables is shown in Fig. 13.9. To explain the measurements for the whirl motion, they can be considered to be divided into *three phases*.

Phase 1 can be described by the equations of motion (13.9) for the planar model. It begins when the rotor makes permanent contact with the stator and ends when the whirl frequency reaches the first elastic eigenfrequency ω_1 of the instrumented touch down ring of about 270 to 300 Hz. This phenomenon is not included in our simple rigid rotor model; its existence, however, has been predicted by Black [3] and experimentally shown by Lingener [21]. The spin velocity $\dot{\Phi}$ is reduced by frictional forces from initially 350 Hz to 320 Hz,

the friction parameter $\mu = 0.14$ follows from (13.10) together with the measurements on the kinematics. The spin energy has reduced to 1.4 kJ by the end of phase 1 and during this run-down, the power loss P_{spin} reaches a maximum value of 8 kW. The normal force F_{cyl} can be estimated from (13.12) to achieve a maximal value of about 1.4 kN, which is more than 40 times higher than the rotor weight. The energy transferred into the whirl motion is very small, $E_{\text{whirl}} = 0.2$ J, but quite sufficient to overcome the potential energy for lifting the rotor to its highest position within the small air gap.

Phase 2 represents the whirl motion itself. During this phase, the whirl velocity tends to the eigenfrequency ω_1, it increases only slightly and linearly. Experiments show that the whirl acceleration depends on the contact material and the energy transfer between the rotor and the vibrating stator. It appears to be similar to the effect where a rotor tries to pass a resonance and gets locked to that resonance. It is a balance of energy which, on one hand, is supplied by the rotor through the frictional mechanism and which, on the other hand, is used to maintain and further build up the whirl[1]. Some open questions are yet to be answered: the damping mechanism is not yet fully clear, in some experiments the friction seems to change during that phase, possibly due to excessive wear, and the contact forces will still have to be measured, as in this phase they cannot be derived from the rigid body motion, i.e. by (13.12), any more. Other experiments are detailed in [7] for various material combinations (steel/beryllium bronze, steel/elastic bronze ring, steel/Nylube).

Phase 3 begins when the rotor reaches the kinematic rolling condition (13.8). At this point the whirl velocity is $\omega_1 \simeq 300$ Hz, and the spin velocity $\dot{\Phi} \simeq 9$ Hz. The subsequent, dramatic break-down of the motion is clearly seen in Fig. 13.9.

The total time for the rotor to come to a complete standstill is 0.9 s. The experiments should not be carried out without some caution. The very sharp braking of the the rotor speed, caused by the friction at the site of the contact, and a high inertia J of the rotor can generate a high torsional torque and eventually shear the rotor axis.

13.3.3 Influence of Initial Conditions on the Development of a Whirl

Initial conditions, i.e. the position and velocity of the rotor when it is contacting the touch-down bearing, are important influence variables deciding whether a whirl will develop. The sensitivity to initial conditions is characteristic of the nonlinear touch-down dynamics, resulting eventually in whirl motions with varying attractor domains and chaotic motions. Detailed experiments have been performed [15]. Analysis with different whirl speeds show

[1] This might imply that a soft support with damping will limit the whirl frequency and limit the whirl amplitude and loads. This is an approach used by many manufacturers [14]

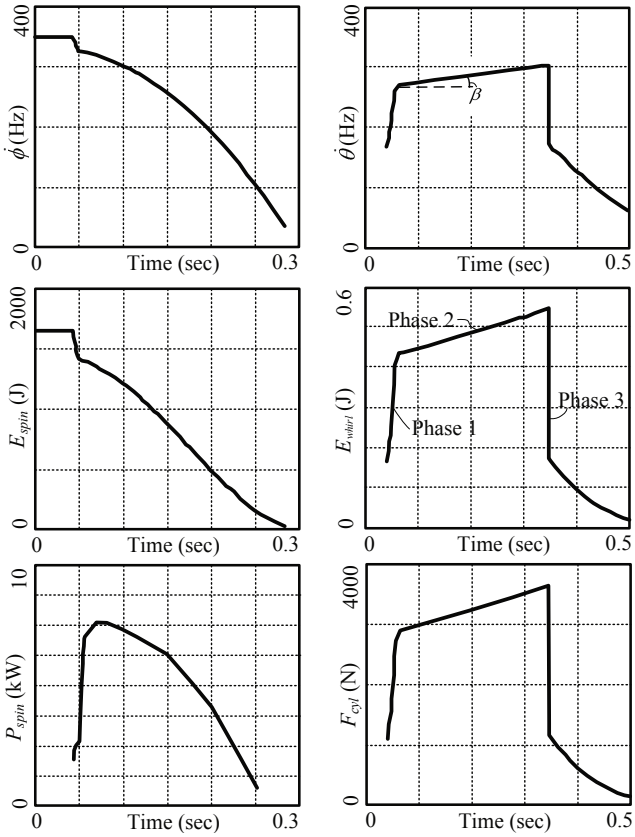


Fig. 13.9. Time history for the whirling motion of a rotor contacting its housing (steel/graphite) for various variables: spin velocity $\dot{\Phi}$, whirl velocity $\dot{\theta}$, spin energy E_{spin}, whirl energy E_{whirl}, spinning rotor power loss P_{spin}, and normal force, F_{cyl}

that the whirl is independent of the rotation speed of the rotor. The only dependency on the rotation speed that could be determined is that there exists an energy limit represented by the inertia and rotation speed of the rotor that must be exceeded to develop a whirl motion. This limit depends on the contact friction which is controlled primarily by the kind of touch-down bearing and its life-history.

13.4 Ball Bearings

For industrial applications, it is most common to use ball bearings for touch-down bearings. Their low friction reduces the potential of exciting the critical backward whirl. Research to model the dynamics of ball bearings under high speed rotational acceleration in the case of a rotor touch-down is underway,

even making use of statistical approaches to accommodate the variations in ball sizes. Results on experimental research are already available [7, 16, 32]. Figure 13.10 shows the acceleration of ball bearing elements (type Koyo 6904) after a touch down, using the test rig of Fig. 13.3. The data have been taken with a high speed camera and processed subsequently. After 0.09 sec, the inner ring has been accelerated to the speed of the rotor of 150 Hz.

Drop tests on industrial rotors are being defined now as performance standards [1]. Actual results and guidelines for the design are published for example in [5, 20, 24, 25, 27, 29], and summarized subsequently.

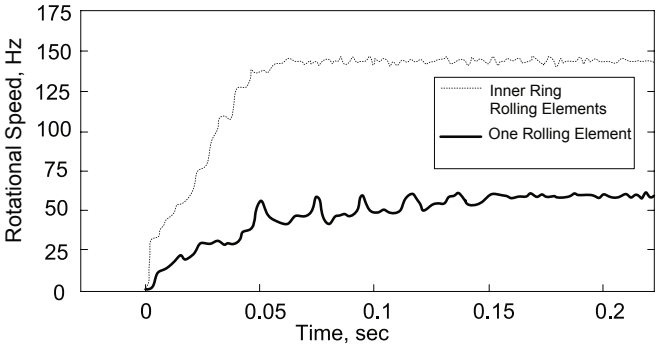


Fig. 13.10. Speed of inner ring and of one rotating element that had been highlighted, after a rotor touch-down [16]

13.5 Design Considerations

Up to now, results show that the touch-down dynamics cannot be predicted exactly - the system is too sensitive to parameter variations and often close to chaotic behaviour. However, the general types of behaviour and their physical background have been explained, and some conclusions for the design can be drawn. While the individual design of touch-down bearings is still an art and depends much on the requirements for specific applications, some general guidelines will be summarized subsequently:

- Low friction is essential.
- The surface of the landing sleeve should be made of high strength material with low friction and great hardness to avoid early wear.
- The touch-down bearing should be kept clean from contamination.
- For damping the impacts of a touch-down, special components, such as damping ribbons between the outer ring and the housing have been designed. An example is given below.

- An elastically soft support, with damping, may limit the whirl frequency and limit the whirl amplitude and loads. This is an approach used by many manufacturers. However, the support-structure in itself should be sufficiently rigid to maintain alignment.
- For industrial applications ball bearings are the most common kind of touch-down bearing. Where the spin down time has to be long, the DN[2] should be relatively low (1.0 - 1.5e6 mm-rpm). Caged bearings, in many cases, have shown to be a good solution. A higher internal clearance may be necessary to allow for thermal expansion. Under heavy loads, the life-time of the bearings may be limited to only a few touch-downs.
- For very high acceleration rates and short spin down times, cage-less designs to reduce the inertia may be necessary. Good results have been obtained with ball bearings with coated balls or balls made of ceramics.
- The time for permanent contact has to be kept short to avoid overheating of the touch-down bearings, and therefore the rotor should be actively slowed down or recovered by control actions (see Chap. 18 on Safety and Reliability Aspects and Chap. 14 on Fault Tolerant Control).
- Care has to be taken to avoid driving the unloaded ball bearing by air drag, causing run-out of the bearing.

A case study [15] for the design and choice of damping elements is summarized subsequently: It is known from simulations mainly that damping elements with high damping and low stiffness between the touch-down bearing and the housing are a constructive measure to avoid critical behavior [30]. Experiments have been performed with elastomer 'O'-rings made from Fluor-Kautschuk (Typ DT-11 4007 1500 by Angst and Pfister) and with tolerance rings made of flat spring steel (Typ AN 42-512 by Tretter). The design of the elements is shown in Figs. 13.11 and 13.12.

For the touch-down experiments, the rotor was initially displaced horizontally, parallel to its reference (centered) position. The touch-down bearings were ball bearings of the type SKF 6004, already with traces of wear. With no damping elements, whirl was observed for 28% of the various initial conditions, as indicated in the "stability charts" of Fig. 13.13. The stability chart indicates a number of distinct initial positions of the rotor center, which after a drop-down of the rotor, lead to a critical whirl, or not. However, when using the damping elements, experiments with rotational frequencies of 150 Hz, 300 Hz, and 400 Hz never led to whirl. Therefore, the use of such damping elements can be recommended. In addition, Fig. 13.13 shows typical, non-critical orbits for the touch-down.

It can be seen that an intensive jumping of the rotor only occurs with the undamped touch-down bearing. With the damped systems, the initial contact is followed only by some benign oscillation at the bottom of the retainer bearing clearance. In the case of the elastomer-rings with little stiffness, a vertical

[2] The speed value (DN) for inner ring rotation is the product of the ball bearing's bore in mm and shaft speed in rpm.

oscillation is superimposed on the horizontal rolling, resulting from the motion of the retainer bearing itself. Using the tolerance rings, this vertical motion remains relatively small.

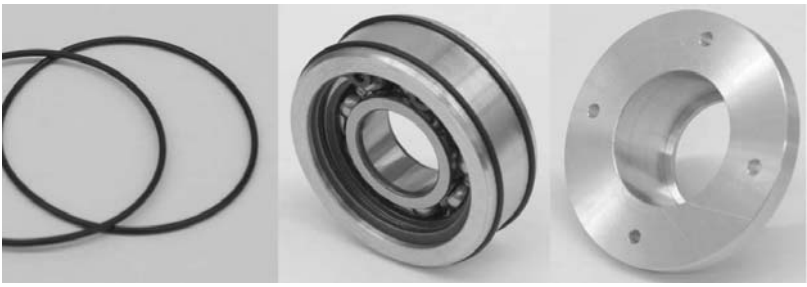


Fig. 13.11. Damping elements, elastomer O-rings



Fig. 13.12. Damping element, elastic tolerance rings

Up to now, it has been tacitly assumed that the direction of the rotor axis is horizontal as is the case in many stationary rotating machines. However, designing a stationary machine in such a way that the rotor axis is vertical might have a major influence on the touch-down dynamics and on the choice of suitable touch-down bearings. The radial retainer bearings at the upper and the lower end of the rotor could be of a conical type, with the consequence that, in case of a touch-down, the rotor would fall into the conical receptors and the air gap could be reduced to zero. In addition to that, the active magnetic bearings would be smaller and fully symmetric as they would not have to carry the rotor weight. It is the active axial bearing that would have to carry most of the rotor weight. This could be alleviated to some extent by making use of permanent magnets or, in the case of turbo-machinery, by directing the axial turbo-forces against gravity. As yet, there are only a few examples available for the design and testing of a deliberately vertical configuration, such as in [5], Figs. 1.18 and 1.21 in Chap. 1.

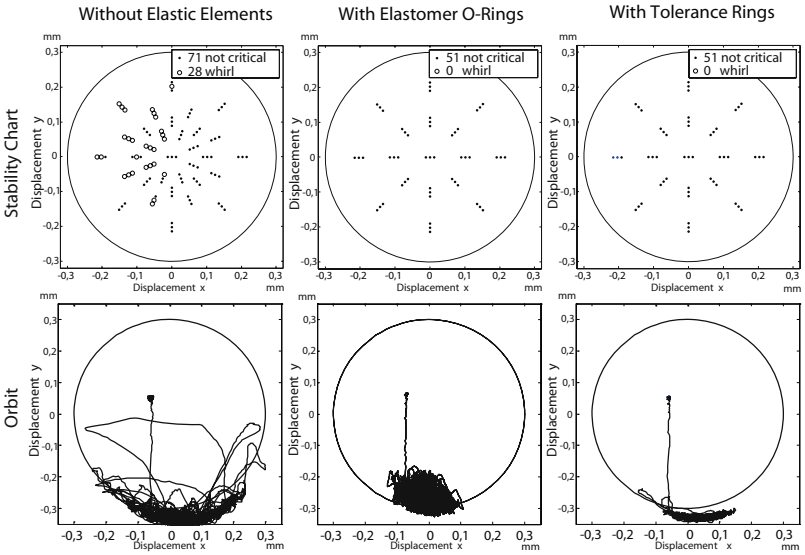


Fig. 13.13. Stability of touch-down from various initial positions, with and without damping elements; typical orbits; rotational frequency 150 Hz, parallel rotor displacement

13.6 Conclusions

Contact between a rotor and a stator can lead to violent vibrations. As a back-up, in order to avoid potential damage, AMB supported rotors are equipped with *touch-down bearings (retainer bearings)*. These are an additional set of conventional bearings, and the rotor will only come into touch with them in extraordinary situations. A survey is given on various contact phenomena in rotating machinery, and for touch-down bearings they are demonstrated by experiments on a test rig. Basic modeling is derived, the onset of whirl, leading to the most critical *backward whirl* is shown. Contact forces, the sudden breaking of the rotor spin velocity, and the power dissipated by the friction forces are discussed. Experimental results on ball bearings, which are the kind of touch-down bearings most commonly used industrially, are shown.

Guidelines on the design of touch-down bearings summarize the general state of the art. References show that there are various approaches and reliable design solutions for industrial applications of touch-down bearings.

However, the optimal design of touch-down bearings still relies mostly on experience, and a systematic, generally accepted design procedure has yet to be developed. Open research questions include the choice of material, the damping properties, the physical insight into high-speed contacts, i.e. for contact speeds above 200 m/s, the running down through critical speeds in touch-down bearings, and control aspects in critical contact situations.

References

1. ISO Standard 14839-4. Mechanical vibration - Vibrations of rotating machinery equipped with active magnetic bearings - Part 4: Technical guidelines, system design (Draft), 09 2006.
2. A.R. Bartha. Dry friction induced backward whirl: theory and experiment. In *Proc. 5th Internat. IFToMM Conf. on Rotor Dynamics, Darmstadt*, pages 756–767, Sept. 1998.
3. H.F. Black. Interaction of a whirling rotor with a vibrating stator across a clearance annulus. *J. Mech. Eng. Sci., Trans. IFToMM*, 10:1–12, 1968.
4. R.M. Brach. *Mechanical impact dynamics.* John Wiley and Sons, 1991.
5. H. Dell, J. Engel, R. Faber, and D. Glass. Developments and tests on retainer bearings for a large active magnetic bearing. In *Magnetic Bearings, Proc. First Internat. Symp. on Magnetic Bearings*, Springer-Verlag, 1988. ETH Zurich.
6. D. Ewins and R. Nordmann et al. Modelling of rotor/stator interaction dynamics (ROSTADYN). Technical Report Research Project BRITE/EURAM 5463, European Community, 1997.
7. M. Fumagalli. *Modelling and measurement analysis of the contact interaction between a high speed rotor and its stator.* PhD thesis, ETH Zurich No 12509, 1997.
8. M. Fumagalli and Schweitzer G. Measurements on a rotor contacting its housing. In *Proc. 6th Internat. Conf. on Vibrations in Rotating Machinery, Oxford*, Sept. 1996.
9. M. Fumagalli, P. Varadi, and G. Schweitzer. Impact dynamics of high-speed rotors in retainer bearings and measurement concept. In G. Schweitzer, R. Siegwart, and R. Herzog, editors, *Proc. 4th Internat. Symp. on Magnetic Bearings*, pages 239–244. ETH Zurich, Aug. 1994.
10. R. Gasch, R. Nordmann, and H. Pfützner. *Rotordynamik.* Springer-Verlag, 2001.
11. L. Ginzinger and H. Ulbrich. Simulation-based controller design for an active auxiliary bearing. In *Proc. 11th Internat. Sympos. on Magnetic Bearings, Nara, Japan*, pages 412–419, Aug. 2008.
12. W. Goldsmith. *Impact.* Edward Arnold Ltd, London, 1960.
13. J.P. Den Hartog. *Mechanical vibrations.* Dover Publications, 1985.
14. Hawkins, L.A., McMullen, P.M., Vuong, V. Development and Testing of the Backup Bearing System for an AMB Energy Storage Flywheel. ASME GT2007-28290, Presented at ASME IGTI Conference, Montreal, Canada, May 14-17, 2007.
15. M. Helfert. *Rotorabstürze in Wälzlager - Experimentelle Untersuchungen des Rotor-Fanglager-Kontakts.* PhD thesis, TU Darmstadt, Fachgebiet Mechatronik im Maschinenbau, 2008.
16. M. Helfert, M. Ernst, R. Nordmann, and B. Aeschlimann. High speed video analysis of rotor-retainer-bearing-contacts due to failure of active magnetic bearings. In H. Bleuler and G. Genta, editors, *Proc. 10th Internat. Symp. on Magnetic Bearings*, pages 206–207, 2006.
17. K.H. Hunt and F.R.E. Crossley. Coefficient of restitution interpreted as damping in vibroimpact. *Trans ASME, J. Applied Mechanics*, pages 440–445, June 1975.
18. J.L. Isaksson. *On the Dynamics of a Rotor Interacting with Non-Rotating Parts.* PhD thesis, Linkoping University, Thesis No 426, 1994.

19. R.G. Kaur and H. Heshmet. 100 mm diameter self-contained solid/powder lubricated auxiliary bearing operated at 30'000 rpm. *Tribology Transactions*, 45:76–84, 2002.
20. R.G. Kirk. Evaluation of AMB turbomachinery auxiliary bearings. *J. Vibrations and Acoustic, Trans. ASME*, 121:156–161, 1999.
21. A. Lingener. Experimental investigation of reverse whirl of a flexible rotor. In *Proc. 3rd Internat. Conf. on Rotordynamics (IFToMM), Lyon*, pages 13–18, 1990.
22. A. Muszynska. Rotor-to-stationary element rub-related vibration phenomena in rotating machinery - literature survey. *The Shock and Vibration Digest*, pages 3–11, March 1989.
23. A. Muszynska. Rotor-to-stationary part full annular contact modelling. In *Proc. 9th Internat. Symp. on Transport Phenomena and Dynamics of Rotating Machinery (ISROMAC), Honolulu, Hawaii*, 2002.
24. Y. Ohura, K. Ueda, and S. Sugita. Performance of touchdown bearings for turbo molecular pumps. In Y. Okada, editor, *Proc. 8th Internat. Symp. on Magnetic Bearings, Mito, Japan. on Magnetic Bearings, Mito, Japan*, pages 515–520, Aug. 2002.
25. S.R. Penfield and E. Rodwell. Auxiliary bearing design for gas cooled reactors. In *Proc. IAEA Technical Committee Mtg. Gas Turbine Power Conversion Systems for Modular HTGRs, Palo Alto*, Nov. 2000.
26. P.S.Keogh and M.O.T. Cole. Rotor vibration with auxiliary bearing contact in magnetic bearing systems, Part 1: Synchronous dynamics. *Proc. IMechE, part C, J. of Mechanical Engineering Science*, 217:377–392, 2003.
27. T.W. Reitsma. Development of long-life auxiliary bearings for critical service turbomachinery and high-speed motors. In Y. Okada, editor, *Proc. 8th Internat. Symp. on Magnetic Bearings, Mito, Japan*, Aug. 2002.
28. M.N. Sahinkaya, A.G. Abulrub, and P.S. Keogh. On the modelling of flexible rotor/magnetic bearing systems when in contact with retainer bearings. In *Proc. 9th Internat. Symp. on Magnetic Bearings, Kentucky, USA*, Aug. 2004.
29. M. Schmied and B. Pradetto. Drop of rigid rotor in retainer bearings. In P. Allaire, editor, *Proc. Third Internat. Symp. on Magnetic Bearings, Washington*, pages 145–156, July 1992.
30. Smalley, A. J.; Darlow, M. S.; Mehta, R. K.. The Dynamic Characteristics of Oö-Rings. ASME Paper No. 77-DET-27, Journal of Mechanical Design, 1978.
31. S.P. Timoshenko and J.N. Goodier. *Theory of elasticity.* McGraw-Hill, 3 edition, 1970.
32. S. Zeng. Modelling and experimental study of the transient response of an active magnetic bearing rotor during rotor drop on back-up bearings. *Proc. IMechE, part I, J. of Systems and Control Engineering*, 217:505–517, 2003.

14

Dynamics and Control Issues for Fault Tolerance

Patrick S. Keogh and Matthew O.T. Cole

Introduction

This chapter will consider some key issues in the fault tolerant design of magnetic bearing systems. The chapter deals primarily with control considerations, while more general aspects are covered in Chap. 18 on *Safety and Reliability Aspects*. The first section surveys typical faults that may need to be accommodated and provides some suggestions for mitigation. The second section considers the dynamics of an AMB controlled rotor during touch-down bearing interaction. A methodology to predict vibration phenomena and contact force levels is presented. The final section examines control strategies for recovery of contact-free operation of a rotor from a state involving persistent rub with touch-down bearings. Further issues relating to touch-down bearings and touch-down are described in Chap. 13 on *Touch-down Bearings*.

14.1 Avoiding Touchdown

Although magnetic bearings are generally reliable, an important concern for both current and future machine applications is fault tolerance. Fault tolerance in AMB equipped machinery should enable the continued safe running of the rotor during the occurrence of a fault so that the machine can be shut down in a safe manner.

If touch-down cannot be avoided, the key issue is whether rotor motion and the mechanical stresses that result from rotor–stator interaction are likely to cause further damage. Without fault tolerance, a defective AMB component could give rise to destructive rotordynamic behavior and premature failure, particularly if the rotor motion is not constrained effectively by touch-down bearings. The issue of actively controlling the non-linear dynamic response of a rotor during interaction with touch-down bearings is also an important aspect of fault tolerance. However, the focus of this first section will be the design of control systems aimed at maintaining rotor levitation following occurrence

G. Schweitzer, E.H. Maslen (eds.), *Magnetic Bearings*,
DOI 10.1007/978-3-642-00497-1_14, © Springer-Verlag Berlin Heidelberg 2009

of a fault. One requirement for achieving this is that system stability can be conserved. However, certain operational requirements such as safe rundown through critical speeds may also be important.

14.1.1 Typical Faults

Within a magnetic bearing system, faults may arise from a variety of events. A fault may be termed *external* if its dynamic effect can be considered as an external disturbance applied to the system. When such a fault occurs, the resulting response of the system will introduce abnormal components in measured signals, giving scope for compensation through suitable control action. The remaining faults may be classified as *internal*. Internal faults are those that cannot be considered as external disturbances as they affect the actuation, measurement or control processes and thereby the system dynamics. There are also some faults, such as rotor impacts and rubs, that could be considered as either external or internal depending on the exact nature and severity. The following sections provide an indication of possible faults and their consequences, with options for mitigating or reducing the associated risks.

Internal faults

1. *Power electronics or amplifier faults*. Although solid state technology is reliable, dynamic performance of amplifier units will depend on variables such as ambient temperature and power demand. Under voltage control, amplifiers could experience current overload. When an intermittent fault occurs the consequences will depend on the fault duration. If this is short, tolerance could be incorporated into the magnetic bearing control system to prevent excessive rotor motions.
2. *Power electronics or amplifier failures*. In these cases, loss of rotor levitation or rotor instability will occur. Component redundancy with reconfigurable amplifiers would allow risk to be mitigated.
3. *Position sensor faults*. A position sensor fault may cause a signal used for closed loop feedback to be erroneous. Physical damage to the circumference of the shaft in the measurement plane or debris on the surface will tend to produce glitches in the measurement signals. Without fault tolerance the control algorithm will attempt to compensate for these glitches and possibly cause touchdown. Run-out compensation or appropriate filtering can prevent this problem from occurring.
4. *Position sensor failure*. A circuit failure in the position sensor electronics will often result in a fixed signal, independent of rotor position. Since the measurement signal will be permanently in error, rotor instability will occur. Sensor redundancy is required to mitigate the risk.
5. *Loss of I/O board channel*. This will typically produce a constant value control input or output signal, resulting in closed loop instability. Component redundancy is required to mitigate the risk.

6. *Magnetic bearing coil failure.* This is most commonly caused by a short circuit arising from a breakdown in the wire insulation. This will change the characteristics of the coil and hence the control forces will deviate and probably result in touchdown. With appropriate redundancy, a reconfiguration of the coil driving will enable this problem to be overcome.
7. *Computer hardware failure.* Although the failure of microprocessors is uncommon, the consequences would be a complete loss of control. The only possibility to avoid the risk is to use back-up hardware operating in a parallel mode.
8. *Software errors.* Real-time control software is susceptible to programming errors that may not have been detected during trials. Even without errors problems may still occur. For example, if the characteristics of the rotor change under a particular operating condition the control algorithm may no longer be appropriate and cause closed loop instability. Notably, the use of notch filters to suppress excitation of higher frequency rotor vibration modes will be problematic if the modes of vibration exhibit significant shifts in frequency. The use of robust control algorithms can make the system tolerant to such changes.

External faults

1. *Dynamic rotor loading.* Changes in loading conditions may occur during operation. Blade loss events cause almost step-like variations in unbalance. Some environments may cause more gradual changes in unbalance due to deposition or erosion of rotor material. Direct rotor forcing is also possible through aerodynamic or fluid dynamic effects caused, for example, by sudden changes in pressure. The effect of these external events will be to induce transient rotor motion. In principle it is possible to use controller design to limit rotor displacements, however, the control forces required may exceed magnetic bearing capacity and contact with a touch-down bearing must then be expected.
2. *Abnormal base motion.* This may be caused by other vibration sources, accidents or seismic events, and is a normal occurrence in mobile applications. Base motion is analogous to an inertia force applied to the rotor, which influences relative rotor–to–base motion. Such motions can be particularly significant when the rotor is strongly gyroscopic. If a control system has been configured for soft bearings to reduce transmitted forces then high acceleration base motion could cause large rotor–to–base displacements and hence contact with a touch-down bearing. High stiffness bearings can alleviate the effects of base motion but it must be ensured that modal damping levels are not compromised, particularly when supercritical operation of flexible rotors is required. It is possible to use multiobjective controller design to obtain an acceptable compromise in bearing characteristics. The use of measured base accelerations as additional controller inputs would also be beneficial.

Internal/external faults

1. *Rotor rub.* Steady rubbing between the rotor and a stator component can cause vibration at sub-synchronous and higher harmonic frequencies. The resulting change in the system dynamics could be significant enough to produce closed loop instability. It is also well known that relatively light rubs on seals may cause thermal bending of the rotor. This causes a slow scale change in near synchronous vibration, which may become unstable. Compensation through controller design is feasible in this case.
2. *Cracked rotor* A cracked rotor will cause vibration not only at the synchronous frequency, but also at higher harmonics due to the nonlinear effects caused by crack opening and closing. A magnetic bearing system is ideal for monitoring and controlling the vibration and even preventing further crack growth.
3. *Rotor contact.* A touch-down or back-up bearing is a typical component in a magnetic bearing system, which is expected to make contact with the rotor when faults occur. Cases of rotor drop and rundown are normal design considerations. However, there may be instances of temporary faults that induce sufficiently large displacements to cause contact. Recovery of contact free levitation may not be possible if the control system has not been designed appropriately. In some systems, it may be expected that the magnetic bearings will be unable to fully support the rotor during certain operating conditions and so load sharing with touch-down bearings must be considered. Again, the success of load sharing operation will be dependent on appropriate configuration of the bearings and control system.
4. Power failure. In terms of control operation, loss of power must be considered as the most severe form of internal fault, resulting in a complete loss of AMB forces. A backup power supply can be provided in various forms including battery, generator, or UPS technologies. Effects of switching power source on AMB operation may still need to be considered.

14.1.2 Component Redundancy

AMB fault tolerance requirements must be considered during machine design as they will influence selection of bearing, coil and sensor configurations as well as levels of component redundancy. Redundancy in a set of components or subsystems can be either *parallel*, when two or more components perform exactly the same operation so that each could take over the function of the other, or *analytical*, when the functions of different subsystems overlap so that not all are required for satisfactory operation. However, incorporating redundancy may be detrimental to machine maintainability as system complexity and the probability of component failure are both increased. There is therefore a strong classical argument for achieving fault tolerance with the minimum

system complexity. In contrast, there are also developments of a *smart machine* concept, where a suitable integration of sensors, actuators and software with high complexity is able to increase reliability, in analogy to the survival capabilities of living beings. An outlook is given in Sect 18.5 on *Smart Machine Technologies*.

There are various components in a magnetic bearing system for which redundancy can be introduced. Magnetic bearings with a surplus number of stator poles or with two multiple coils on the same pole can be reconfigured following the functional loss of one or more coils so that the correct control forces can be maintained. Maslen and Meeker developed a method to derive suitable laws by which required coil currents can be calculated to provide desired x and y axis forces for a generalized and possibly asymmetric coil configuration [17]. In this way, control laws can be chosen from a precalculated set that accommodates a maximal range of coil failure modes, although bearing load capacity is reduced as a result. In the case of a heteropolar bearing with eight independently powered coils (Fig. 14.1a), up to five individual coil failures can be accommodated. Similar schemes have been developed for homopolar magnetic bearings with permanent magnet bias flux [12].

Subject to an increase in complexity and cost, additional electronic hardware can be incorporated within the AMB system to provide back-up for failed power amplifiers, microprocessors, etc. [15, 16]. Successful fault tolerance then requires automatic identification of faulty subsystems and a rapid switching of duties. In any system with redundant components it is necessary to have some form of self-monitoring so that faults can be automatically identified and the necessary reconfigurations undertaken. Sensing of coil current or flux is integral to the feedback operation of power amplifiers, and can be used as a basis for detecting coil faults. Detecting an open circuit caused, for example, by a broken wire or bad connection is straightforward. Reliable detection of more subtle faults, such as insulation breakdown, may require an algorithm based on reference models of current-voltage or flux-voltage relationships for the coil under operation. Faults in rotor position sensors can be more difficult to detect and algorithms that do so can range from simple voting schemes to sophisticated observer-based fault detectors (see Chap. 11 on *Identification*).

Another difficulty with position sensors is that collocation of redundant sensors is sometimes difficult due to space limitations. Although theoretically a minimum of two axial planes with orthogonal sensor pairs is required to achieve stable levitation with radial AMBs, rotor flexibility needs to be considered when sensors are not sufficiently close to bearing locations as simple PID feedback algorithms may destabilize rotor flexural modes. One simple solution to incorporating sensor redundancy is the configuration shown in Fig. 14.1b, for which any two healthy sensors can provide complete x and y axis positional information.

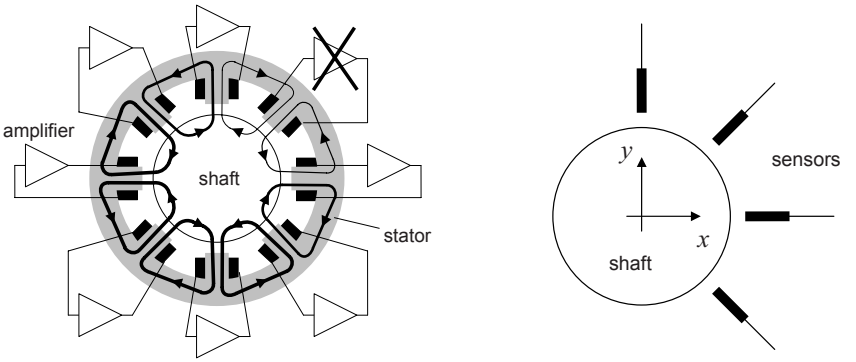


Fig. 14.1. Fault tolerance through redundancy (a) heteropolar magnetic bearing with independently powered coils (b) position sensors configuration

14.2 Touch-down Dynamics

There are two circumstances that should be distinguished under which machines operating with magnetic bearings experience rotor touch-down. One circumstance is when a fault in the magnetic bearing system causes erroneous forces to be applied to the rotor such that the possibility of maintaining effective control and levitation of the rotor has been lost. Such cases are often referred to as *rotor drop* [9]. A quite different circumstance is when the magnetic bearings are still fully functioning and so there is the possibility of maintaining effective control and even recovering contact-free levitation of the rotor. The latter type of situation may result from a temporary fault in the magnetic bearing system, excessive load changes or external disturbances such as motion of the machine base. It should be remarked that in most machines the stator components that prevent excessive rotor motion are the touch-down bearings. However, in some machines the rotor could also make contact with seals, bushes, shrouds or other components.

The following sections will focus on the second circumstance and will examine two important issues that result. The first issue is whether stability of the closed loop system will be preserved, or instead will a loss of stability increase the severity of the rotor–stator contact interaction? In any application it is important to ensure that excessive levels of rotor vibration and rotor–stator interaction forces are avoided. The second issue is whether, in a situation involving persistent contact, it is possible to use the magnetic bearings to apply a control action that restores the rotor to contact-free conditions. There are often operational advantages if this can be achieved without the rotor being run down under touch-down bearing support, not least because it is difficult to ensure that vibration levels during rundown will be tolerable.

14.2.1 Rigid Disk Model

The dynamic behavior of an unbalanced disk interacting with a stator component has been investigated by a number of researchers. The papers and dissertations associated with Schweitzer and co-workers, Fumagalli and Bartha, provide a useful insight into the issues relating to nonlinear dynamics, contact force and backward whirl of rotors [1, 2, 6, 7]. In Chap. 13 on *Touch-down Bearings* the phenomenology of touch-down behavior, design aspects and experiments have been discussed. Subsequently, control strategies for avoiding touch-down and for recovery after a touch-down will be developed. For a basic understanding of the problem and its control aspects, the touch-down of a simple disk rotor is first considered, for which steady orbits involving bouncing and full rub will be determined and simulated.

Consider a disk of mass m that is able to move within the clearance space of a fixed touch-down bearing under PID control from the magnetic bearing. The proportional and derivative gains may be set so that the magnetic bearing has linearized radial spring (k) and damper (b) characteristics. The integral gain provides a centralizing action to overcome static loads and if it is sufficiently small, the rotor dynamics will be little changed. Let (x, y) be the position of the disk center of rotation in an inertial frame of reference. The equations of motion for the unbalanced disk are then written as

$$\begin{aligned} m\ddot{x} + b\dot{x} + kx &= D\cos\Omega t - f_n\cos\theta + \mu f_n\sin\theta \\ m\ddot{y} + b\dot{y} + ky &= D\sin\Omega t - f_n\sin\theta - \mu f_n\cos\theta \end{aligned} \tag{14.1}$$

where D is the unbalance force magnitude, Ω is the angular speed, f_n is the normal contact force component at a polar angle θ and μ is the friction coefficient. These two equations can be combined by defining the disk position in complex form as $z = x + jy = re^{j\theta}$:

$$\ddot{z} + 2\zeta\omega_n\dot{z} + \omega_n^2 z = \frac{D}{m}\,\mathrm{e}^{j\Omega t} - (1 + j\mu)\frac{f_n z}{m|z|} \tag{14.2}$$

where $\omega_n = \sqrt{k/m}$ and $\zeta = b/2\sqrt{mk}$. Within a synchronously rotating reference frame, the unbalance force will be a static vector while the disk position (u, v) can be written $w = u + jv = z\mathrm{e}^{-j\Omega t}$. It is then possible to rewrite (14.2) in terms of rotating frame motion as

$$\begin{aligned} \ddot{w} + 2(\zeta\omega_n + j\Omega)\dot{w} + (\omega_n^2 - \Omega^2 + 2j\zeta\omega_n\Omega)w \\ = \frac{D}{m}\mathrm{e}^{j\Omega t} - (1 + j\mu)\frac{f_n w}{m|w|} \end{aligned} \tag{14.3}$$

Specification of the normal contact force f_n in (14.3) depends on the mechanics of contact between the disk and the touch-down bearing. However, certain vibrational states (*contact modes*) induced by contact forces can be investigated by considering two idealized cases of continuous and very short duration contacts.

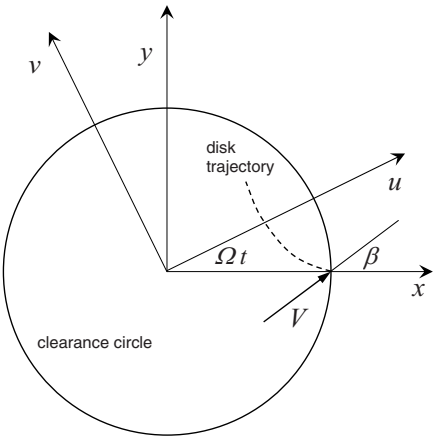


Fig. 14.2. Disk trajectory following impact at inclination β

Continuous contacts

Continuous rub behavior is well documented in the open literature, e.g. [3, 18]. For the case in hand, the unbalance force can be written as $D = me\Omega^2 e^{j\phi}$, where e is the eccentricity and the phase angle is ϕ. For a forward circular rub at $w = c$, where c is the radial clearance, (14.3) yields the steady equilibrium equation

$$f_n\sqrt{1+\mu^2} = me\Omega^2 e^{j(\phi-\lambda)} + m(\Omega^2 - \omega_n^2 - 2j\zeta\omega_n\Omega)ce^{-j\lambda} \tag{14.4}$$

where $\lambda = \tan^{-1}\mu$. It follows that a forward whirl rub will exist only if a value of the unbalance phase angle ϕ can be found to make the right hand side of (14.4) positive and real.

Another well known form of continuous contact is that of backward whirl, which corresponds to the disk moving in rolling contact on the inside of the auxiliary bearing. A fully developed backward whirl involves a rolling contact without slip. The backward whirl frequency is then $\omega = \Omega R/c$ (where R is the rotor radius and c is the radial clearance) and the contact force is $f_n = mc\omega^2 = mR^2\Omega^2/c$. This is usually a large value that is significantly greater than any unbalance or control force capacity from the magnetic bearing. Hence if backward whirl has become firmly established there is little that can be done to recover contact free levitation and the system must be shut down. For the rigid disk model presented, a self-sustaining backward whirl is possible only if

$$\frac{\mu}{\zeta} > \frac{2k}{k_b}\sqrt{\frac{k_b}{k}+1} \tag{14.5}$$

where k_b is a linear stiffness for the rotor-auxiliary bearing contact [18]. Therefore, in addition to low friction auxiliary bearings, avoiding backward whirl

would require a high level of modal damping and magnetic bearings that are sufficiently stiff compared with the auxiliary bearings.

Short duration contacts

In this case, infinitesimally short duration contacts are assumed to occur at regular time intervals, starting at $t = 0$ and $(x(0), y(0)) = (c, 0)$ as shown in Fig. 14.2. The impulsive contact force is modelled as

$$f_n = (1 + \epsilon) m \dot{x}(0-) \delta(t) \tag{14.6}$$

where ϵ is the coefficient of restitution and $\delta(t)$ is the Dirac delta function. Since the contact force specified by (14.6) is impulsive, it is zero for $t > 0$. The solution of (14.3) for the disk motion is then

$$w(t) = \frac{D}{m s_1 s_2} + A \mathrm{e}^{s_1 t} + B \mathrm{e}^{s_2 t} \tag{14.7}$$

where $s_1, s_2 = -\zeta\omega_n - j(\Omega \pm \omega_d)$ are characteristic roots with $\omega_d = \omega_n \sqrt{1 - \zeta^2}$.

The impulsive contact force given in (14.6) may be used with (14.3) to evaluate the change in velocity before and after contact. Conditions at contact may be stated as

$$w(0) = c, \qquad \dot{w}(0+) - \dot{w}(0-) = -\alpha V \cos\beta \tag{14.8}$$

where $\alpha = (1 + \epsilon)(1 + j\mu)$.

Following the contact event at $t = 0$, the disk will move within the clearance circle until at some time $t = T$ another contact event occurs. The trajectory between contact events will be repeating if

$$w(T) = w(0), \qquad \dot{w}(T-) = \dot{w}(0-) \tag{14.9}$$

It is now possible to determine expressions for the boundary conditions $w(0)$, $\dot{w}(0+)$, $w(T)$ and $\dot{w}(T-)$ using (14.7–14.9) to yield the system of equations

$$\begin{bmatrix} 1 & 1 & 0 & 0 \\ s_1 & s_2 & -1 & 0 \\ \mathrm{e}^{s_1 T} & \mathrm{e}^{s_2 T} & 0 & 0 \\ s_1 \mathrm{e}^{s_1 T} & s_2 \mathrm{e}^{s_2 T} & -1 & -\alpha \end{bmatrix} \begin{bmatrix} A \\ B \\ \dot{w}(0+) \\ v_c \end{bmatrix} = \begin{bmatrix} c_e \\ 0 \\ c_e \\ 0 \end{bmatrix} \tag{14.10}$$

where $v_c = V \cos\beta$ and $c_e = c - e\Omega^2 \mathrm{e}^{j\phi} / s_1 s_2$ is a modified clearance parameter. Furthermore, $\dot{w}(0-) = V \mathrm{e}^{j\beta} - j\Omega c$ and hence (14.9) dictates that $v_s = j\dot{w}(0+) + \Omega c + j(1 - \alpha) v_c$ where $v_s = V \sin\beta$.

Equation (14.10) may be solved and a root finding procedure used to vary T and ϕ until v_c and v_s are both real-valued for physically plausible solutions. If such solutions do not exist then repeatable trajectories are not feasible. However, non-periodic motions may still be possible. Non-periodic and chaotic motions have been studied as an educational example in [23].

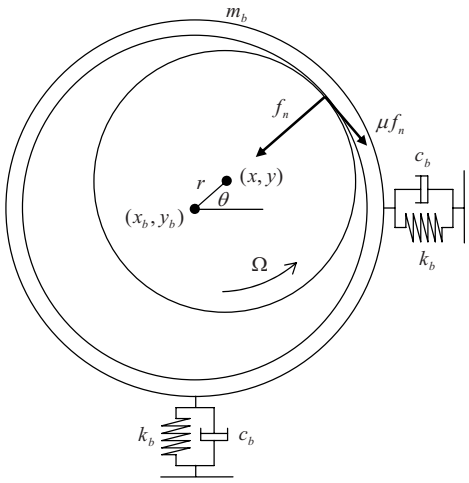


Fig. 14.3. Auxiliary bearing model

Finite duration contacts

The study of finite duration contacts requires a realistic model of the contact mechanics to be specified. Since this may be nonlinear, numerical solution of the equations of motion may then be necessary in which case it is also beneficial to include more representative touch-down bearing and magnetic bearing dynamic models, as in [9, 10].

As an illustrative case, an touch-down bearing ring with mass m_b is now considered, resiliently mounted within a rigid housing using radial stiffness k_b and radial damping c_b as shown in Fig. 14.3. The bearing translation (x_b, y_b) relative to the housing occurs due to loading from the contact forces:

$$\begin{aligned} m_b\ddot{x}_b + c_b\dot{x}_b + k_b x_b &= f_n \cos\theta - \mu f_n \sin\theta \\ m_b\ddot{y}_b + c_b\dot{y}_b + k_b y_b &= f_n \sin\theta + \mu f_n \cos\theta \end{aligned} \tag{14.11}$$

The contact force is now a function of the relative displacement between the disk and bearing, $(x - x_b, y - y_b)$. The contact force will be non-zero only if the distance between the centers is greater than the radial clearance i.e. if $r = \sqrt{(x - x_b)^2 + (y - y_b)^2} \geq c$. In this case, the normal force arising due to contact will be a nonlinear function of the penetration where, for simplicity, a Hertzian contact model can be considered appropriate for well aligned contact along a contact strip of circumferential arc-length l_c. If the rotor and bearing materials are assumed similar then the penetration depth may be expressed in terms of the contact force according to [21]

$$r - c = \frac{2f_n(1-\nu^2)}{\pi E l}\left(2/3 + \ln\frac{16RR_b}{l_c^2}\right) \tag{14.12}$$

where $l_c = 2.15\sqrt{2RR_b f_n/Elc}$, E is the Young's modulus, ν is the Poisson ratio, R is the disk radius, R_b is the bearing radius, and l is the axial bearing length. The contact force/penetration depth relation may be determined numerically in the form of a look-up table.

A magnetic bearing model may also be introduced to replace the linearized stiffness and damping terms in (14.1). For opposing pole pairs in a differential driving mode, together with a simplified sigmoid function representation of saturation effects, the x-axis component of the magnetic bearing force can be expressed using an empirically-based formula

$$f_x = -\frac{k_m}{k_f} \tanh\left(\frac{k_f(V_0 + V_c)^2}{(c_m + x)^2} - \frac{k_f(V_0 - V_c)^2}{(c_m - x)^2}\right) \tag{14.13}$$

The parameter k_m is the voltage gain for the bearing and amplifiers, while c_m is the effective air gap and k_f is a parameter that can be chosen to set the saturation limit. The control voltage V_c is the output from a PID position feedback controller. For the y-axis the force f_y may be specified in a similar manner.

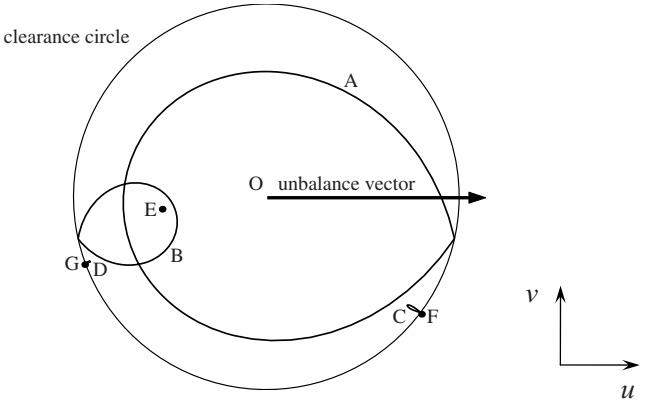


Fig. 14.4. Idealized contact mode solutions in the rotating frame: Bouncing modes (A-D), non-contact response (E) and full circular rub (F, G) . The loci for A-D are traversed in a clockwise sense

Example calculations

The data given in Table 14.1 was used to calculate rotor vibration solutions for idealized contacts. Solutions were obtained by solving (14.10) and are shown in Fig. 14.4 in terms of (u, v) for the rotating reference frame and Fig. 14.5 in terms of (x, y) for the fixed frame. Bouncing solutions overlayed in

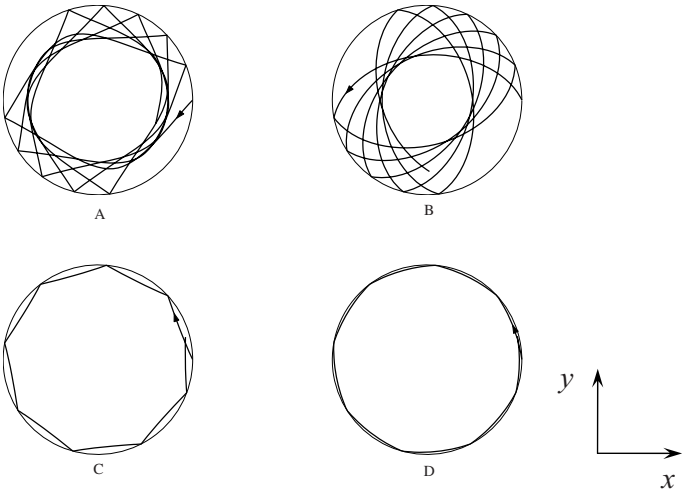


Fig. 14.5. Idealized contact mode orbits in fixed frame

the rotating frame appear as distinct repeated loops, however, these become dispersed orbits when transformed to the stationary frame. The durations between contacts are $T \approx 0.011$ s for solutions A and B, and $T \approx 0.0025$ s for solutions C and D. These times compare with the synchronous period of 0.021 s. Figure 14.4 also shows non-contacting synchronous orbit solution E, which has a phase lag relative to the unbalance of around 170°, since the running speed is above the rotor natural frequency $\omega_n = 140$ rad/s. The synchronous circular rub solutions F and G from (14.4) are single points on the clearance circle, while the short duration contact modes C and D are very similar.

Table 14.1. Model data

parameter	value	unit	parameter	value	unit
m	50	kg	b	1400	N s/m
k	9.8×10^5	N/m	μ	0.15	
ϵ	0.95		Ω	300	rad/s
c	0.7	mm	e	0.3	mm

Numerical solutions of (14.1) and (14.11), together with nonlinear contact force and magnetic bearing models, have also been calculated for comparison. The magnetic bearing PD gains were chosen to give the same linearized stiffness and damping characteristics as in the idealized cases. The effective gap length in (14.13) was set at $c_m = 1.3$ mm and the parameter k_f set to

give a magnetic bearing saturation limit of ±1500 N. The auxiliary bearing parameters were:

$$m_b = 0.1\,\text{kg}, \quad c_b = 10000\,\text{N s/m}, \quad k_b = 2 \times 10^8\,\text{N/m}$$

Figure 14.6 shows different numerical solutions obtained by varying the initial conditions for the disk position and velocity. In case 1, initial conditions for a forward synchronous rub were adopted, as for mode G. In case 2, initial conditions appropriate for mode D of Fig. 14.5 were used. However, this mode is not sustainable and so the rotor returns to the contact-free orbit after four contacts. In case 3, with initial conditions appropriate for mode C, a full backward whirl develops. The rotor response is also sensitive to the magnetic bearing control, as illustrated by case 4, which shows the solution obtained with the same initial conditions as case 3 but with the linearized damping increased from 1400 N s/m to 1800 N s/m. In this case, the increase in the magnetic bearing damping force inhibits the onset of full backward whirl. Instead, the rotor response settles to a mode A type solution.

In conclusion, it can be stated that, even for simple systems, though certain steady-state rotor vibrations can be predicted by analytical methods, a full evaluation of rotordynamic behavior and particularly the potential for transitions from forward rub/whirl to more destructive backward whirl type motion generally requires extensive numerical simulation. However, the uncertainty in assessing the contact model and its parameters, as well as the sensitivity to initial conditions, can prevent detailed prediction of the exact rotor motions in real cases. Prediction capabilities are generally restricted to a classification of potential response types and, ideally, some evaluation of their likelihood.

14.2.2 Complete Rotor-AMB System

In real magnetic bearing applications, rotor levitation and vibration control are usually achieved by means of dynamic feedback of rotor displacements, measured at or close to the magnetic bearing locations. As a consequence, one issue of concern during touchdown is that the closed loop system will remain stable under all possible conditions of rotor–stator contact interaction. Theoretical investigations in the previous section have shown that, even for a simple system, a broad range of possibly degenerate transient and steady state rotor motions involving rubbing and bouncing can occur. Moreover, the system dynamics relating the measured rotor displacements to the forces applied to the rotor are non-linear and sensitive to the characteristics of the stator contact.

Let us assume that the AMB controller has been designed so that prolonged rotor–stator interaction results in steady *forward whirl* with *full circular rub* occurring at one or more auxiliary bearings. This is the likely case providing controller stability is maintained and friction and disturbance forces are low enough to avoid backward whirl. In such cases, model–based prediction of contact forces and rotor motions are quite straightforward to obtain

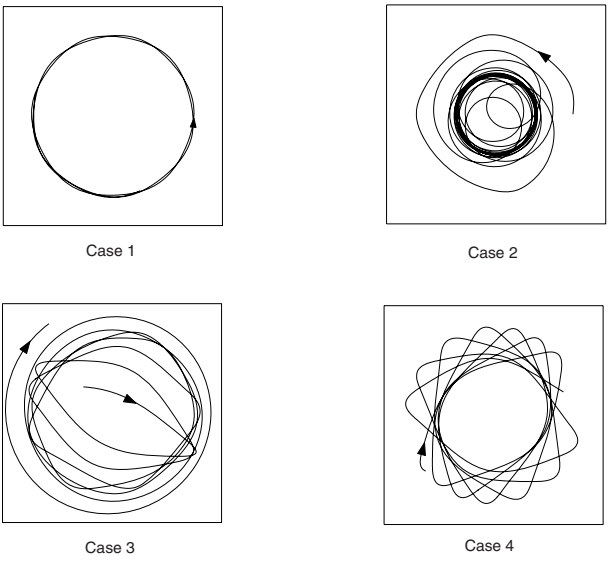


Fig. 14.6. Simulated disk motions with various initial conditions

[3, 18]. We will consider a typical system model for which magnetic bearings and touch-down bearings have radially isotropic force characteristics i.e. there are no misalignments or other directional biases in the system. Forces due to unbalance can again be expressed using complex representation to distinguish x and y axis components as $\mathbf{d}_x(t) + j\mathbf{d}_y(t) = \mathbf{D}\mathrm{e}^{j\Omega t}$. The dimensions of this vector are $m \times 1$, with m being the number of unbalance planes. Consequently, the orbits in the plane of the touch-down bearings, numbering n, will be circular $\mathbf{x}(t) + j\mathbf{y}(t) = \mathbf{Z}\mathrm{e}^{j\Omega t}$, as will the corresponding contact forces at the touch-down bearings $\mathbf{f}_x(t) + j\mathbf{f}_y(t) = \mathbf{F}\mathrm{e}^{j\Omega t}$. The $n \times 1$ complex amplitude vector $\mathbf{Z}$ can be related to the forces acting on the rotor according to

$$\mathbf{Z} = \mathbf{R}_d\mathbf{D} + \mathbf{R}_f\mathbf{F} \tag{14.14}$$

The speed-dependent complex matrices $\mathbf{R}_f$ and $\mathbf{R}_d$, having dimensions $n \times n$ and $n \times m$ respectively, are sometimes referred to as *influence coefficient matrices*, appropriate values for which can be derived from theoretical modelling or identified by online testing [20]. Note that, as the system we are considering is the levitated rotor, these matrices will also be dependent on the AMB controller dynamics. This type of *harmonic balance* equation can in fact be applied to any steady rotor vibration having periodicity $2\pi/\Omega$, for which the complex vectors will comprise the fundamental Fourier coefficients for each signal.

To analyze the effects of a circular rub we can consider the contact geometry in a frame rotating with the rotor, as shown in Fig. 14.7. In this frame,

the displacements and forces are given by the static vectors **Z**, **D** and **F**. Assuming there are no misalignments, we can write the shaft displacement at the kth bearing as $Z_k = R_k + c_k e^{j\phi_k}$ where R_k is the deflection of the auxiliary bearing and c_k is the radial clearance. Friction at the rub location, which has a contact normal inclined at the angle ϕ, can be simply modelled by a Coulomb friction law. This means that the angle δ between F_k and the contact normal is determined by the coefficient of friction $\mu = \tan\delta$, although for touch-down bearings in good condition δ can generally be taken as zero. If we now write the contact force vector in polar form $F_k = |F_k|e^{j\theta_k}$, it can be seen from Fig. 14.7 that the direction of F_k is

$$\theta_k = \pi + \phi_k + \delta \tag{14.15}$$

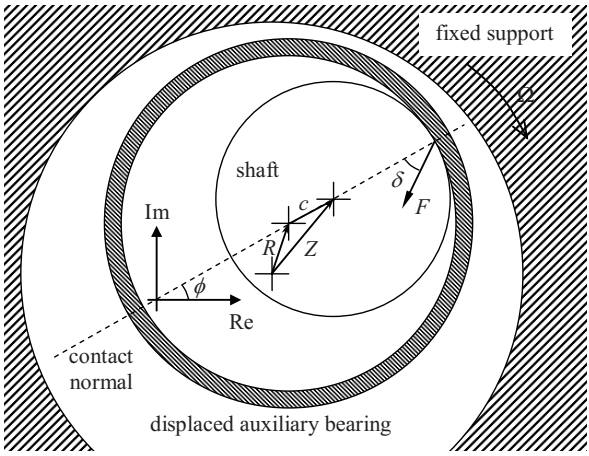


Fig. 14.7. Rotating frame geometry for rub at an auxiliary (touch-down) bearing or bush

How the contact force relates to the rotor orbit depends on the dynamic characteristics of the touch-down bearing supports, which can be selected to some degree through the use of resilient mounts. However, there are various factors that will determine the best choice of stiffness and damping. Let us assume that, at the frequency Ω, the bearing support has a (complex) dynamic stiffness K_k so we may write

$$F_k = -K_k R_k = -K_k(Z_k - c_k e^{j\phi_k}) \tag{14.16}$$

Equations 14.15 and 14.16 can be combined to give

$$\mathbf{F} = \mathbf{P}(\mathbf{f})\mathbf{Z} \tag{14.17}$$

where $\mathbf{P}(\mathbf{f})$ is a diagonal matrix that varies depending on the severity of the contacts:

$$\mathbf{P}(\mathbf{f}) = \begin{bmatrix} P_1 & 0 & \dots & 0 \\ 0 & P_2 & & \vdots \\ \vdots & & \ddots & 0 \\ 0 & \dots & 0 & P_n \end{bmatrix}, \quad P_k = -\frac{K_k|F_k|}{|F_k| + K_k c_k \mathrm{e}^{-j\delta}} \tag{14.18}$$

Here, $\mathbf{f} = [|F_1|, ..., |F_n|]^{\mathrm{T}}$ is the vector formed from the magnitudes of each contact force. According to (14.14) we now define the response without contact as

$$\mathbf{Q} = \mathbf{R}_d\mathbf{D} \tag{14.19}$$
$$= \mathbf{Z} - \mathbf{R}_f\mathbf{F} \tag{14.20}$$
$$= (\mathbf{P}(\mathbf{f})^{-1} - \mathbf{R}_f)\mathbf{F} \tag{14.21}$$

It is possible to assign the contact forces $\mathbf{F}$ arbitrarily and use (14.18) and (14.21) to obtain corresponding non-contact orbits $\mathbf{Q}$. This seemingly backward calculation method is far simpler than trying to find a solution $\mathbf{F}$ corresponding to a given non-contact orbit $\mathbf{Q}$. Note that, depending on K_k and thus Ω, a stable rotor motion involving persistent contact can occur even when the orbits without contact do not exceed the touch-down bearing clearance i.e. $|Q_k| < c_k$. This implies that transient disturbances acting on the system could cause a transition from a contact-free state to a persistent rub condition. Note also that, for a given non-contact orbit $\mathbf{Q}$, a corresponding $\mathbf{D}$ may be non-unique or may not exist, depending on the dimension and rank of the matrix $\mathbf{R}_d$ i.e. the number and axial location of unbalance planes. In the case of a single contact, (14.21) simplifies to a scalar equation. Such cases have been considered extensively by Black [3], who also gives a method to identify running speed ranges for which sustained rotor-stator contact interaction is possible.

Example

Consider a rigid rotor and magnetic bearing model, as covered in Sect. 8.1 of Chap. 8, with the details given in tables 14.2 and 14.3. If the touch-down bearing support stiffness is $k_b = 10$ MN/m and the damping is $c_b = 10$ N s/m then at a nominal running speed of $\Omega = 700$ rad/s the following model parameters can be derived:

$$\mathbf{R}_f = \begin{bmatrix} -0.653 - 0.229j & -0.109 - 0.298j \\ -0.109 - 0.298j & -1.119 - 0.739j \end{bmatrix} \times 10^{-6} \text{ m/N},$$
$$\mathbf{R}_d = \begin{bmatrix} -0.5548 - 0.2417j & -0.2002 - 0.2862j \\ -0.2917 - 0.3773j & -0.9501 - 0.6648j \end{bmatrix} \times 10^{-6} \text{ m/N},$$
$$K_k = k_b + \Omega c_b j = 10^7 + 7 \times 10^3 j \text{ N/m}, \ \ k = 1, 2$$
$$c_k = 0.0005 \text{ m} \ \ k = 1, 2$$

The rotor has two touch-down bearings at which rub could occur. However, we will consider unbalance in the plane of magnetic bearing A that results in continuous rub at touch-down bearing A only:

$$\mathbf{D} = \begin{bmatrix} me\Omega^2 \\ 0 \end{bmatrix} \tag{14.22}$$

The magnitude of the rotor orbit at touch-down bearing A is shown in Fig. 14.8 for various levels of unbalance (mass-eccentricity me), calculated according to (14.21). These predicted synchronous responses indicate that non-contact orbits would be within seemingly acceptable levels, at less than 60% of the bearing clearance. However, over the upper portion of the running speed range, vibrational modes with contact can also occur for the same unbalance conditions. Under certain conditions the rotor motion could switch from a non-contact orbit to a contacting orbit, for example following a temporary bearing overload or loss of control. The contact orbit magnitudes are significantly greater than the bearing clearance and it must be checked that, as a result, rotor–stator contact would not occur at more damaging locations such as rotor and stator laminations.

Table 14.2. Rigid rotor-AMB model parameters

parameter	value	unit
rotor mass	4.49	kg
axial moment of inertia	0.01054	$\mathrm{kg\,m^2}$
moment of inertia	0.02132	$\mathrm{kg\,m^2}$
magnetic bearing A position (distance from mass center)	0.022893	m
magnetic bearing B position (distance from mass center)	0.074907	m
auxiliary bearing A position (distance from mass center)	0.05	m
auxiliary bearing B position (distance from mass center)	0.1	m
auxiliary bearing radial clearance	0.0005	m
maximum speed	1000	rad/s

Table 14.3. Controller parameters

parameter	value	unit
proportional gain (equivalent bearing stiffness)	50 000	N/m
derivative gain (equivalent bearing damping)	1 000	Ns/m
break frequency	1 000	rad/s
net AMB stiffness	40 000	N/m

It is possible to reduce the contact orbit sizes by increasing the support stiffness of the touch-down bearing (Fig. 14.9). However, corresponding rotor-

bearing interaction forces (Fig. 14.9b) are not significantly reduced and may be increased in situations where the rotor is undergoing bouncing impacts, resulting in accelerated damage to the touch-down bearing. High stiffness bearing supports can also lead to controller instability during rub. Currently, analytical methods to predict these two types of behavior and, in particular, determine peak contact forces are not well developed and investigations would probably require time-step simulations or experimental testing.

The results presented here also indicate that if this rotor has entered into a contact mode orbit then a rundown will be required before a non-contact orbit is reestablished. The speed to which the rotor must be run down will depend on the unbalance condition. An alternative approach to recover contact free orbits without rundown is to apply appropriate control forces at the magnetic bearings. This will be covered in Sect. 14.3 on *Control Before and During Touchdown*.

14.2.3 Contact Mode Stability

In general, contact modes can be found for all positive values of $|F_k|$. However, not all predicted contact modes are stable i.e. will give rise to continuous rub. To predict whether a certain contact mode solution (value of F) could occur in practice, a stability analysis can be undertaken by considering small perturbations about the circular rub orbit [18]. It can be shown that, of the two solutions corresponding to a given non-contact orbit magnitude $|Q|$ for which $Q_{min} < |Q| < c$, only the one corresponding to the larger contact force magnitude will be sustainable. The other contact orbit will be unsustainable and a rotor initially in this orbit would fall away from the touch-down bearing and resume a contact-free orbit. This can be explained in simplistic terms by the fact that, for the solutions with the smaller contact force levels $d|F|/d|Q| < 0$, and so the contact mode has an unstable negative stiffness property i.e. increasing the applied unbalance force decreases the contact force and therefore the size of orbit at the touch-down bearing.

Even when rotor unbalance conditions are such that predicted contact modes are sustainable, a vibratory instability may still occur, preventing steady rub and leading to a bouncing whirl motion similar to that predicted with the rigid disk model. This type of motion may progress to destructive levels or settle into a less severe limit cycle behavior. In general, a severe bouncing response is most likely when the touch-down bearing has a stiff, lightly damped support. Rubs with significant friction levels, not normally associated with touch-down bearings, also contribute to such *asynchronous contact modes* and full backward whirl [4].

This type of instability can also be induced by an inappropriate feedback controller for the magnetic bearings. Feedback control algorithms designed so that the magnetic bearings possess the characteristics of passive elements are less prone to instability during contact interactions. A standard PD controller, which emulates stiffness and viscous damping forces at the bearing

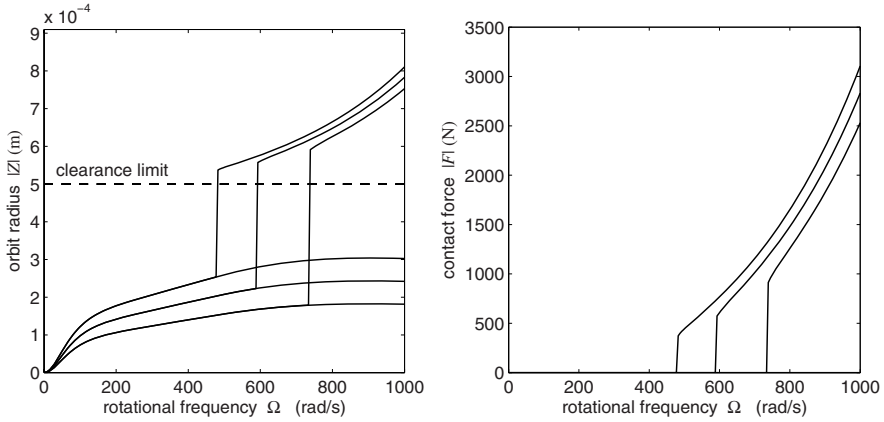


Fig. 14.8. Rotor vibration response at touch-down bearing A for different unbalance levels me = 0.6, 0.8, 1.0 g-m. Touch-down bearing support stiffness is 10 MN/m

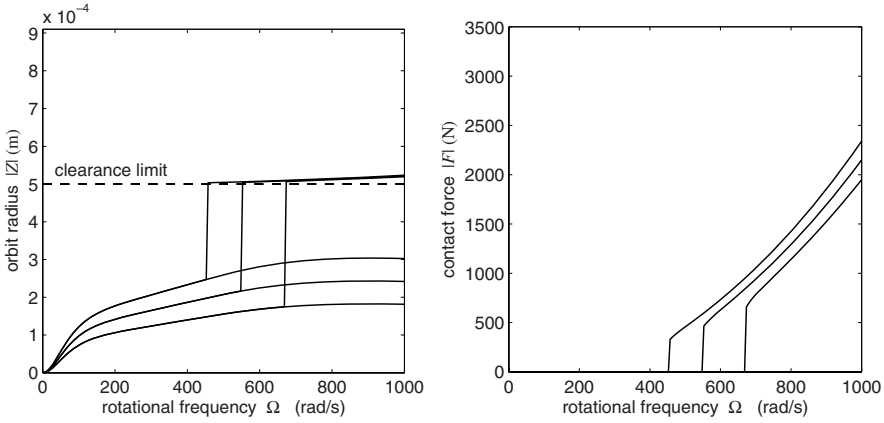


Fig. 14.9. Rotor vibration response at touch-down bearing A for different unbalance levels me = 0.6, 0.8, 1.0 g-m. Touch-down bearing support stiffness is 100 MN/m

locations is one such controller. However, factors such as non-collocation of bearings and sensors, flexural dynamics of the rotor or stator and also the effects of additional filter or sensor/actuator dynamics in the feedback loop can be detrimental to stability. Undertaking experimental tests with a particular machine design to evaluate controller stability is one option but this would need to be done for a range of touch-down conditions and could result in machine damage. If this is unacceptable, it is better to use model-based techniques similar to the numerical simulations presented earlier in this chapter to investigate behavior and thereby assist in system design.

14.3 Control Before and During Touch-down

When circumstances have resulted in a quasi-steady rotor motion involving rub at one or more touch-down bearings it may be possible to restore the rotor to a non-contacting orbit by applying, through the magnetic bearings, sinusoidal control forces of appropriate amplitude and phase. This can be possible even in cases when the rotor motion does not closely approximate the idealized contact modes considered previously.

Synchronous or *harmonic control* algorithms have been used extensively with magnetic bearings to achieve attenuation of synchronous signal components during machine operation [5, 8, 11, 13, 14, 22]. Further details are given in Sect. 8.3 on *Unbalance Control*. However, the issue of stability of such control algorithms during touch-down bearing contact is often overlooked. A common case is when the control forces are chosen to minimize amplitudes of measured rotor orbits, often referred to as *auto-centering* or *automatic balancing*. Generally, however, the signals selected to be attenuated may be any measurable or calculable signal, such as rotor displacements, magnetic bearing control currents, bearing forces or linear combinations thereof.

14.3.1 Rigid Disk Model

The basic synchronous control problem can be easily visualized for the rigid disk system previously described in Sect. 14.2.1. Although the inertial frame solutions shown in Fig. 14.5 show the actual vibration, the rotating frame representations of Fig. 14.4 are perhaps more relevant here as it is easier to see the phase changes in synchronous components that occur between the orbit without contact E and the contact mode solutions A - G. The problem to be anticipated for any controller designed for recovering contact-free levitation is that a control force can be applied to compensate the unbalance force, but only if the correct phase can be determined. Unless the rotor's actual contact mode is known, measurement of the rotor orbits does not allow easy determination of the correct phase (i.e. direction) of the unbalance force, and thus the synchronous force required to compensate it will be uncertain.

14.3.2 Avoiding Contact

In practice, the magnetic bearing control forces can be constructed from a linear combination of a stabilizing dynamic feedback $\mathbf{u}_c$ and additional synchronous rotating forces with suitably chosen amplitude and phase:

$$\mathbf{u}(t) = \mathbf{u}_c(t) + \mathbf{U}\mathrm{e}^{j\Omega t} \tag{14.23}$$

Suppose we wish to minimize the orbit magnitudes at the touch-down bearings, which is a natural objective if the aim is to avoid touch-down. Accounting for the synchronous control forces, (14.14) is modified to

$$\mathbf{Z} = \mathbf{R}_d\mathbf{D} + \mathbf{R}_u\mathbf{U} + \mathbf{R}_f\mathbf{F} \tag{14.24}$$

$$= \mathbf{Q} + \mathbf{R}_u\mathbf{U} + \mathbf{R}_f\mathbf{F} \tag{14.25}$$

The effect of the feedback control signal $\mathbf{u}_c$ on the rotor response is accounted for in the matrices $\mathbf{R}_{d,f,u}$. If we wish to minimize the rotor orbits during machine operation, an unbalance compensation scheme of the type explained in Sect. 8.3 on *Unbalance Control* may be used. In one such scheme, the rotor displacements at the touch-down bearing locations are measured, or inferred from measurements at other locations, and stored over a number of rotor revolutions N. This data is then used to calculate the fundamental Fourier coefficients for rotor motion in the plane of each touch-down bearing:

$$Z_k = \frac{\Omega}{2\pi N} \int_0^{2\pi N/\Omega} (x_k(t) + jy_k(t))\mathrm{e}^{-j\Omega t}\, dt \tag{14.26}$$

where x_k and y_k are the displacement signals at the kth sensor plane. Suppose that the rotor is contact-free ($\mathbf{F} = 0,\ \mathbf{U} = 0$) and we have determined the complex amplitudes $\mathbf{Q} = \mathbf{Z}$ through the calculation (14.26). The rotor orbits can be reduced by applying the synchronous control forces calculated from $\mathbf{Z}$ according to

$$\mathbf{U} = -\mathbf{K}\mathbf{Z} \tag{14.27}$$

When $\mathbf{R}_u$ is a square matrix then we can choose $\mathbf{K} = \mathbf{R}_u^{-1}$ and according to (14.24) then after application of the control forces the rotor motion will become perfectly centered in the auxiliary bearings:

$$\mathbf{Z}' = (\mathbf{I} - \mathbf{R}_u\mathbf{R}_u^{-1})\mathbf{Q} = 0 \tag{14.28}$$

If, alternatively, the number of sensor planes is greater than the number of magnetic bearings, a least-squares minimization of $\mathbf{Z}$ can be achieved by using the pseudo-inverse $\mathbf{K} = (\mathbf{R}_u^{\mathrm{T}}\mathbf{R}_u)^{-1}\mathbf{R}_u^{\mathrm{T}}$ so the minimized orbits are then

$$\mathbf{Z}' = (\mathbf{I} - \mathbf{R}_u(\mathbf{R}_u^{\mathrm{T}}\mathbf{R}_u)^{-1}\mathbf{R}_u^{\mathrm{T}})\mathbf{Q} \tag{14.29}$$

A merit of this particular control approach is that the influence coefficient matrix $\mathbf{R}_u$ can be identified by on-line testing prior to application. Typically, this would involve applying a small test signal through each bearing axis in turn and measuring the corresponding change in $\mathbf{Z}$ from which the value of each element of $\mathbf{R}_u$ can be inferred.

14.3.3 Recovery from Contact

The aim here will be to derive a control method that will reduce the rotor orbits at touch-down bearings whether or not the rotor is contacting with them. Such a controller could operate continuously, or be activated following occurrence of a touch-down in order to eliminate contact. In the latter case,

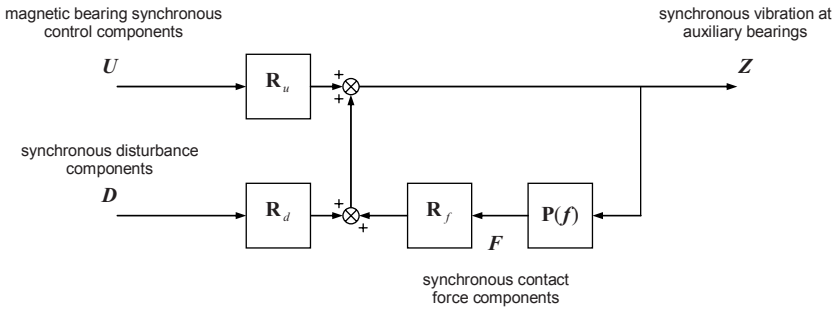


Fig. 14.10. System structure for synchronous dynamics with time-varying feedback interconnection arising due to touch-down bearing contact

rotor positions sensors could be used to deduce whether touch-down has occurred, providing precise clearances are known. However, additional contact or motion sensors at the touch-down bearings would greatly facilitate timely activation of the controller.

Suppose that a steady rub has occurred between the rotor and one or more touch-down bearings. Using the matrix $\mathbf{P}$, previously defined by (14.18), which relates $\mathbf{F}$ and $\mathbf{Z}$ but also varies with the contact force magnitudes $\mathbf{f}$, we can write

$$\mathbf{F} = \mathbf{P}(\mathbf{f})\mathbf{Z} = \mathbf{P}(\mathbf{f})(\mathbf{Q} + \mathbf{R}_u\mathbf{U} + \mathbf{R}_f\mathbf{F}) \tag{14.30}$$

giving

$$\mathbf{F} = (\mathbf{I} - \mathbf{P}(\mathbf{f})\mathbf{R}_f)^{-1}\mathbf{P}(\mathbf{f})\,(\mathbf{Q} + \mathbf{R}_u\mathbf{U}) \tag{14.31}$$

This leads to the feedback structure of Fig. 14.10 and gives modified time-varying dynamics such that the orbits at touch-down bearing locations can be written

$$\mathbf{Z} = (\mathbf{I} + \boldsymbol{\Delta}(\mathbf{f}))(\mathbf{Q} + \mathbf{R}_u\mathbf{U}) \tag{14.32}$$

In control terminology, the matrix $\boldsymbol{\Delta} = \mathbf{R}_f(\mathbf{I} - \mathbf{P}\mathbf{R}_f)^{-1}\mathbf{P}$ is called a multiplicative perturbation. Without contact, $\mathbf{P} = \mathbf{0}$ and these equations reduce to the linear case (14.14). However, during contact, the response $\mathbf{Z}$ will undergo a shift in orbit amplitudes and phases depending on the contact force magnitudes $\mathbf{f}$. The nature of this behavior can be seen in Fig. 14.11 for the rigid rotor model. The rotor response for increasing/decreasing unbalance magnitude shows *amplitude jump hysteresis* typical of non-linear contact phenomena. If unaccounted for, the contact-induced changes will lead to incorrect conclusions about the level and phasing of rotor unbalance.

If the control forces required to reduce orbit sizes were to be calculated from (14.27) assuming the non-contact relation (14.14), i.e. by choosing $\mathbf{K} = \mathbf{R}_u^{-1}$, then according to (14.32) the control action could result in more severe rotor vibration and increased contact forces:

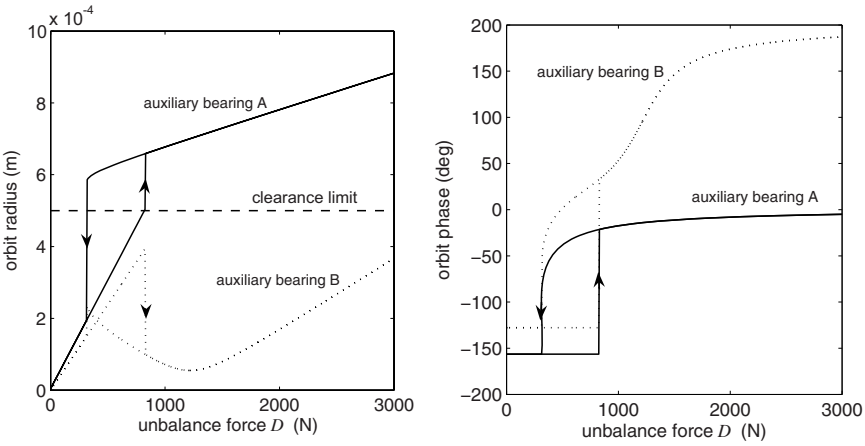


Fig. 14.11. Variation of rotor orbit magnitudes and phases with unbalance force level. Contact occurs with touch-down bearing A

$$\mathbf{Q} + \mathbf{R}_u\mathbf{U} = (\mathbf{I} - (\mathbf{I} + \boldsymbol{\Delta}(\mathbf{f}))\mathbf{R}_u\mathbf{K})\mathbf{Q} = \boldsymbol{\Delta}(\mathbf{f})\mathbf{Q} \tag{14.33}$$

This implies that $|\mathbf{Q} + \mathbf{R}_u\mathbf{U}|$ can become larger than $|\mathbf{Q}|$ if the induced norm (maximum singular value) of the matrix $|\boldsymbol{\Delta}(\mathbf{f})|$ is greater than 1. Note that this condition involves the initial value of $\boldsymbol{\Delta}(\mathbf{f})$ before the control action is applied. In such situations, rather than cancelling the effect of the unbalance forces, the control action could compound it and cause an increase in contact severity.

If the rotor unbalance condition can be estimated from the rotor vibration measured during normal operation then, following the onset of a rub, it is possible to apply the correct forces to compensate for this known unbalance and bring the rotor out of contact with the touch-down bearing. In cases where the unbalance condition has not been determined, or there is a possibility it may have changed, then it may still be possible to return to non-contacting conditions by employing a robust control algorithm. The difficulty with this approach is that usually no information regarding the severity of contact is available to the controller, which therefore must be designed to reduce orbit magnitudes over a range of expected contact conditions.

There is no unique strategy for achieving this but one approach is to calculate a value for $\mathbf{K}$ based on a rewritten version of (14.32) with a different choice of unperturbed system and a new perturbation matrix $\boldsymbol{\Delta}_X(\mathbf{f})$:

$$\mathbf{Z} = (\mathbf{I} + \boldsymbol{\Delta}_X(\mathbf{f}))(\mathbf{X}\mathbf{Q} + \mathbf{X}\mathbf{R}_u\mathbf{U}) \tag{14.34}$$

The control action (14.27) would then be calculated with

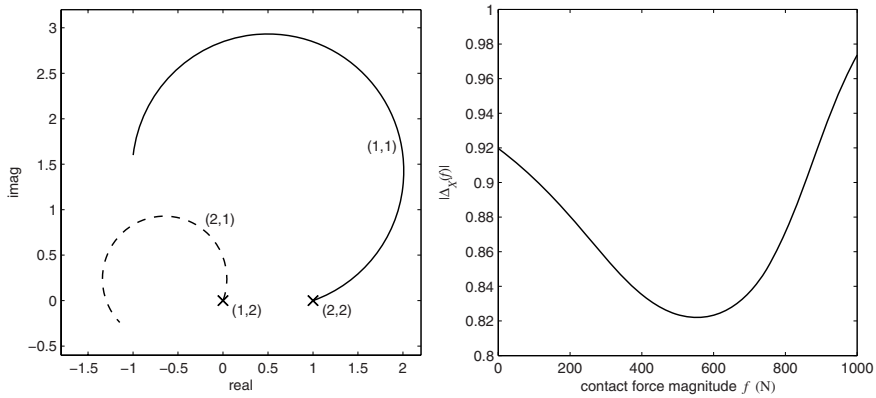
$$\mathbf{K} = (\mathbf{X}\mathbf{R}_u)^{-1} \tag{14.35}$$

Comparison of (14.32) and (14.34) shows that $\boldsymbol{\Delta}_X(\mathbf{f})$ must satisfy

$$\boldsymbol{\Delta}_X(\mathbf{f}) = (\mathbf{I} + \boldsymbol{\Delta}(\mathbf{f}))\mathbf{X}^{-1} - \mathbf{I} \tag{14.36}$$

Despite this different choice of perturbation matrix, the criterion for reducing orbit sizes is essentially unchanged and therefore we should select $\mathbf{X}$ so that $|\boldsymbol{\Delta}_X(\mathbf{f})| < 1$ for a given range of $\mathbf{f}$. Although the control action calculated from (14.27) may be unable to eliminate rub after one application, repeated updates can be used to restore the rotor to a non-contact condition, after which the non-contact 'optimal' control action can be applied.

Regarding the issue of how the expected range of values for $\boldsymbol{\Delta}$ should be derived: if an accurate system model is available, then it is possible to directly calculate using $\boldsymbol{\Delta} = \mathbf{R}_f(\mathbf{I} - \mathbf{P}\mathbf{R}_f)^{-1}\mathbf{P}$ and $\mathbf{P}$ given by (14.18) with a range of contact forces. However, it may also be possible to estimate a range of values from online identification procedures. This may be achieved by applying test forces to the rotor by attaching unbalance masses or by applying simulated unbalance through the bearings sufficient to induce contact [5]. The changes in the measured response during contact can then be used to estimate $\boldsymbol{\Delta}$, as in the flexible rotor example to follow. Such a procedure may be appropriate for a prototype rotor under test conditions.



(a) (b)

Fig. 14.12. Variation with contact force magnitude of (**a**) elements of perturbation matrix $\mathbf{I} + \boldsymbol{\Delta}$ (**b**) value of $|\boldsymbol{\Delta}(\mathbf{f})|$ with suitably chosen $\mathbf{X}$

Rigid rotor example

To apply the described contact-robust control method to the rigid rotor system (table 14.2) we first calculate the variation in the matrix $\mathbf{I} + \boldsymbol{\Delta}(\mathbf{f})$ for a range of contact force magnitudes $f_1 = (0, 1000)$ N. This variation is shown in Fig. 14.12a for each matrix element. A subset of discrete values of f_1 is then selected and a suitable optimization routine used to find a value for $\mathbf{X}$

such that $|\mathbf{\Delta}_X(\mathbf{f})| < 1$ for all the selected values. The resulting variation in $|\mathbf{\Delta}_X(\mathbf{f})|$ is shown in Fig. 14.12b. Contact-free orbits can then be re-established following a full rub condition by repeated application of the control action $\mathbf{U} = (\mathbf{X}\mathbf{R}_u)^{-1}\mathbf{Z}$ as shown in Fig. 14.13.

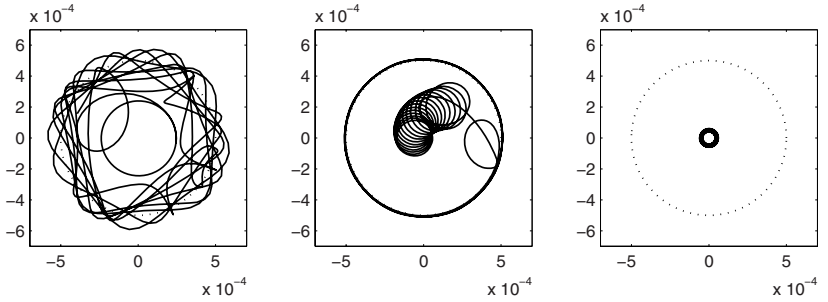


Fig. 14.13. Rotor motion at touch-down bearing (**a**) during temporary AMB loss (**b**) rotor recovery from full rub (**c**) final controlled orbit

Flexible rotor example

In tests on an experimental flexible rotor system, it was found that, for low levels of contact with the auxiliary bearings, the changes in the rotor response could be approximated by

$$\mathbf{I} + \mathbf{\Delta}(\mathbf{f}) \approx \gamma \mathrm{e}^{j\theta}\mathbf{I} \tag{14.37}$$

where θ varied between 0 and -1.15 rad and γ between 1 and 1.75. If we base our choice of $\mathbf{X}$ on the median expected phase-shift and maximum γ ($\mathbf{X} = 1.75\mathrm{e}^{-0.575j}\mathbf{I}$) then

$$\mathbf{\Delta}_X(\mathbf{f}) = (\mathbf{I} + \mathbf{\Delta}(\mathbf{f}))\mathbf{X}^{-1} - \mathbf{I} = (0.57\gamma \mathrm{e}^{(\theta+0.575)j} - 1)\mathbf{I} \tag{14.38}$$

With this choice of $\mathbf{X}$ it is easy to verify that $|\mathbf{\Delta}_X(\mathbf{f})| < 1$ for all possible values of γ and θ.

If a robust approach to contact recovery cannot achieve required stability and performance for a particular machine then it will be necessary to use additional sensors to provide indication of contact locations or force levels. This additional information can then be used for adjusting the control algorithm and ensuring stable operation over a wider range of contact conditions. The success of such strategies has, as yet, not been openly reported and this is an area of ongoing research.

References

1. A. R. Bartha (1998) Dry Friction Induced Backward Whirl: Theory and Experiment. In *Proceedings, 5th IFToMM Conf. Rotor Dynamics*, Darmstadt, 756–767.
2. A. R. Bartha (2000) Dry Friction Backward Whirl of Rotors. Doctoral Dissertation, ETH, Zürich, No. 13817.
3. H. F. Black (1968) Interaction of a whirling rotor with a vibrating stator across a clearance annulus. *ASME Journal of Mechanical Engineering Science,* 10(1):1–12.
4. M. O. T. Cole and P. S. Keogh (2003) Asynchronous periodic contact modes for rotor vibration within an annular clearance. *Proc. Instn. Mech. Engrs Part C, Journal of Mechanical Engineering Science,* 217(10): 1101–1115.
5. M. O. T. Cole, P. S. Keogh, and C. R. Burrows (2003) Robust control of multiple discrete frequency vibration components in rotor - magnetic bearing systems. *JSME International Journal, Series C,* 46(3):891–899.
6. M. A. Fumagalli (1997) Modelling and Measurement Analysis of the Contact Interaction between a High Speed Rotor and its Stator. Doctoral Dissertation, ETH No. 12509.
7. M. Fumagalli and G. Schweitzer (1996) Measurements on a Rotor Contacting its Housing. Paper C500/085/96, In *Proceedings, 6th Int. Conf. Vibrations in Rotating Machinery,* University of Oxford, UK, 779–788.
8. R. Herzog, P. Bühler, and C. Gahler (1996) Unbalance compensation using generalized notch filters in the multivariable feedback of magnetic bearings. *IEEE Transactions on Control Systems Technology,* 4(5): 580–586.
9. T. Ishii and R. G. Kirk (1996) Transient response technique applied to active magnetic bearing machinery during rotor drop. *ASME Journal of Vibration and Acoustics,* 118(2):154–163.
10. P. S. Keogh and M. O. T. Cole (2003) Rotor vibration with auxiliary bearing contact in magnetic bearing systems, *Parts 1 & 2. Proc. Instn. Mech. Engrs Part C, Journal of Mechanical Engineering Science,* 217(4):393–409.
11. C. R. Knospe, R. W. Hope, S. J. Fedigan, and R. D. Williams (1995) Experiments in the Control of Unbalanced Response Using Magnetic Bearings. *Mechatronics,* 5:385–400.
12. M-H. Li, A. B. Palazzolo, A. J. Provenza, R. F. Beach, and A. F. Kascak (2004) Fault tolerant homopolar magnetic bearings. *IEEE Transactions on Magnetics,* 40(5): 3308–3318.
13. Z. Liu, K. Nonami, and Y. Ariga (2002) Adaptive Unbalance Vibration Control of Magnetic Bearing Systems with Rotational Synchronizing and Asynchronizing Harmonic Disturbance. *JSME Int. J. Ser. C.* 45(1):142–149.
14. K-W. Lum, V. T. Coppola, and D. S. Bernstein (1996) Adaptive autocentering control for an active magnetic bearing supporting a rotor with unknown mass imbalance. *IEEE Transactions on Control Systems Technology,* 4(5):587–597.
15. J. P. Lyons, M. A. Preston, R. Gurumoorthy, and P. M. Szczesny (1994) Design and control of a fault-tolerant active magnetic bearing system for aircraft engines. In *Proceedings of the 4th International Symposium on Magnetic Bearings,* Zurich, Switzerland 449–454.
16. E. H. Maslen, C. K. Sortore, G. T. Gillies, R. D. Williams, S. J. Fedigan, and R. J. Aimone (1999) Fault tolerant magnetic bearings. *ASME Journal of Engineering for Gas Turbines and Power,* 121:504–508.

17. E. H. Maslen and D. C. Meeker (1995) Fault tolerance of magnetic bearings by generalized bias current linearisation. *IEEE Transactions on Magnetics,* 31(3): 2304–2314.
18. A. Muszynska (2002) Rotor-to-stationary part full annular contact modeling. In *Proceedings of the 9th International Symposium on Transport Phenomena and Dynamics of Rotating Machinery,* Honolulu, Hawaii.
19. U. J. Na, A. B. Palazzolo, and A. Provenza (2002) Test and theory correlation study for a flexible rotor on fault-tolerant magnetic bearings. *ASME Journal of Vibration and Acoustics,* 124:359–366.
20. J. S. Rao (1992) *Rotor Dynamics,* 2nd revised edition, Wiley.
21. R. J. Roark and W. C. Young (1975) *Formulas for Stress and Strain,* 5th edition, McGraw-Hill.
22. B. Shafai, S. Beale, P. La Rocca, and E. Cusson (1994) Magnetic bearing control systems and adaptive force balancing. *IEEE Control Systems Magazine,* 1994, 14(2):4–13
23. W. M. Szczygielski (1986) Dynamisches Verhalten eines schnell drehenden Rotors bei Anstreifvorgängen. Doctoral Dissertation, ETH, Zürich, No. 8094.

15

Self–Sensing Magnetic Bearings

Eric Maslen

Self–sensing approaches permit active magnetic bearings to dispense with the usual position sensor and, instead, extract rotor position information from the voltage and current histories for the electromagnet coils. Mirroring the development of back–emf sensing of angular position in brushless DC motors, this technology has begun to be applied to commercial products.

After many years of promoting the notion of self–sensing as a route to a simpler hardware realization for magnetic bearings, it is now possible to simply quote the December 2005 newsletter of the prominent AMB vendor, S2M:

> One of the key issues here, and a major challenge in terms of innovation, is the selfsensing bearing technique, where the position sensor and the bearing actuator form a single component. This leads to a far more simple design, with no sensor at all, and fewer connections and related cabling. The cost reduction for a typical bearing is substantial, representing a very strong product differentiation compared to a standard magnetic bearing.[4]

Self-sensing magnetic bearing technology is no longer primarily a research problem but now finds commercial application to turbo–molecular pumps [4] and elevator guideways [25].

Application of self-sensing technology to a broader range of applications will require solving a number of remaining technical challenges. Perhaps the most significant issue is that existing self-sensing techniques must avoid magnetic saturation, thereby substantially reducing the available bearing load capacity. An outline of some of these challenges is provided in Section 15.4.

15.1 Concepts

The essential purpose of any self–sensing AMB technology is to eliminate the position sensing device normally associated with active magnetic bearings as

G. Schweitzer, E.H. Maslen (eds.), *Magnetic Bearings*,
DOI 10.1007/978-3-642-00497-1_15, © Springer-Verlag Berlin Heidelberg 2009

discussed in Chap. 2 and depicted in Fig. 15.1. The function of this sensor is then replaced by some form of signal processing which extracts information about the rotor position from available electromagnet current and voltage waveforms, as suggested in Fig. 15.1. This is possible because the electro-

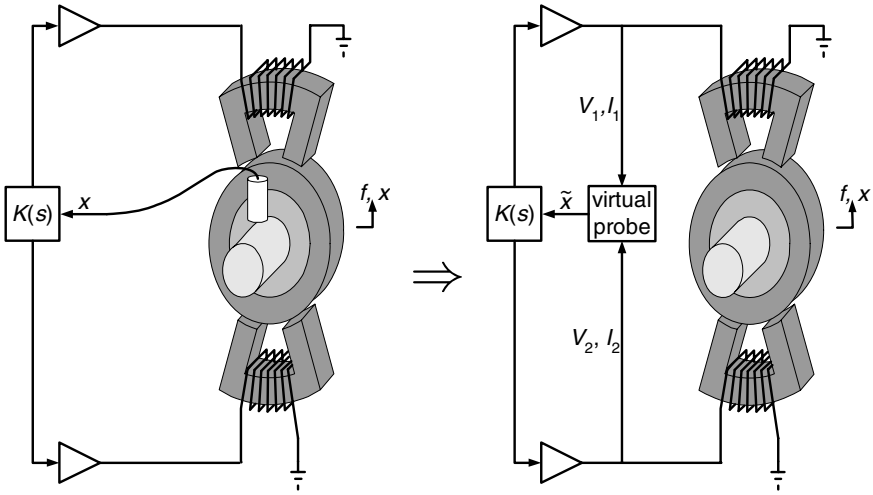


Fig. 15.1. Changing from a conventionally sensed AMB configuration to a self–sensing configuration.

magnet inductance is a function of rotor position. Referring to Fig. 15.2 (see also Chap. 3), voltage u applied to the magnet induces magnetic flux Φ according to

$$u = N\frac{d\Phi}{dt} + iR \tag{15.1}$$

in which i is the coil current, R is the coil resistance, and N is the number of turns of wire in the coil. The first term on the right side of (15.1) is due to Faraday's law while the second is due to Ohm's law.

Neglecting eddy currents, leakage/fringing effects, and assuming that the flux density is distributed uniformly throughout the magnet core and air gap, the flux in the magnet is related to the coil current by

$$\Phi = A\frac{\mu_0 N i}{2s + \frac{\ell}{\mu_r}} \tag{15.2}$$

in which A is the magnet cross sectional area, s is the length of the air gap, ℓ is the iron length, and μ_r is the relative permeability of the magnet iron.

Combining (15.1) and (15.2) produces the relationship

$$u = \frac{\mu_0 N^2 A}{2s + \frac{\ell}{\mu_r}}\frac{di}{dt} - 2\frac{\mu_0 N^2 A i}{\left(2s + \frac{\ell}{\mu_r}\right)^2}\frac{ds}{dt} + iR \tag{15.3}$$

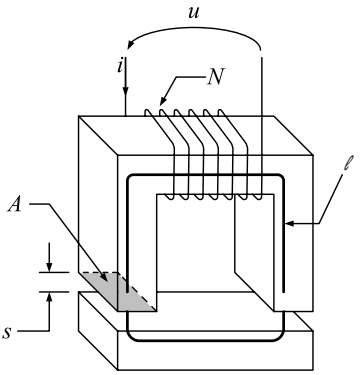


Fig. 15.2. A gapped electromagnet: the simplest actuator magnet for an AMB.

Clearly, the electrical relationship between the coil voltage and resulting current is strongly dependent on the length of the air gap and its rate of change. With perfect knowledge of the voltage and current, one might reasonably expect to be able to reconstruct the gap and, hence, determine the rotor position.

The implication is that it should be possible to construct an AMB which uses no explicit position sensor. Such an AMB, which extracts position information from measurements of coil voltage and current, is referred to as *self–sensing.*

15.2 Motivation

There are numerous reasons for wishing to build self–sensing AMBs, rather than conventional sensor based devices. The most obvious motives relate to the hardware itself: it is common to monitor coil currents in AMB systems so converting to self–sensing will eliminate the cabling, physical sensing device, drive electronics, and signal processing hardware associated with each discrete rotor position sensor while replacing them only with signal processing hardware or software to interpret the coil current and voltage signals. Potentially, this realizes some cost savings but, perhaps more importantly, it reduces the amount of hardware in the machine environment (hot, cold, wet, vacuum, etc.) and the amount of cabling between the machine and the drive cabinet. This has substantial potential to increase reliability of these systems if the dynamics of the resulting system are not compromised in the process.

In addition, as discussed in Chap. 12, when the flexibility of the supported rotor is significant[1], then axial displacement of the sensor relative to the actuator electromagnet (sensor/actuator noncollocation) can produce substantial

[1] Here, "significant" means that the first bending mode of the flexible rotor is within or at least near to the small signal bandwidth of the sensor / amplifier / controller ensemble.

difficulties in stabilizing the system. In particular, if the node of a flexible mode lies between an actuator and its associated sensor, then the modal phase from actuator to sensor is reversed. Of course, the controller can be designed to take this phase reversal into account, but small changes in system parameters can easily displace this modal node so that it is no longer between the sensor and actuator. In this case, a system which has been stabilized by carefully accounting for the modal node location becomes abruptly unstable: the system robustness is poor. Self–sensing AMBs avoid this problem because the sensor and actuator devices are identical: self–sensing AMBs are *always collocated*.

15.3 Control Approaches

Although (15.3) suggests a structure for interpreting coil current and voltage to determine rotor position, a mathematically simpler approach was developed in [63, 64] which first introduced the notion of the self–sensing AMB. This work examined the problem of control of a single axis AMB with an opposed pair of magnets, as indicated in Fig. 15.3.

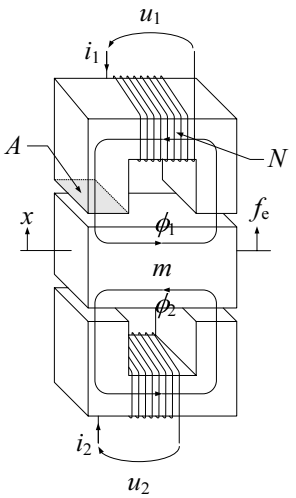


Fig. 15.3. Opposed electromagnets: a single axis AMB supporting a mass M.

Following the developments of Chap. 2 and Chap. 4, one can readily derive the governing equations for the dynamics of this system:

$$\frac{d^2}{dt^2}x = \frac{1}{\mu_0 mA}\left(\phi_1^2 - \phi_2^2\right) + \frac{1}{m}f_e \tag{15.4a}$$

$$\frac{d}{dt}\phi_1 = \frac{1}{N}u_1 - \frac{R}{N}i_1 \tag{15.4b}$$

$$\frac{d}{dt}\phi_2 = \frac{1}{N}u_2 - \frac{R}{N}i_2 \tag{15.4c}$$

$$i_1 = \frac{2(s_0 - x)}{\mu_0 NA}\phi_1 \tag{15.4d}$$

$$i_2 = \frac{2(s_0 + x)}{\mu_0 NA}\phi_2 \tag{15.4e}$$

For purposes of self–sensing, it is important to recognize that this nonlinear model has the two voltages u_1 and u_2 as its inputs and the two currents i_1 and i_2 as its outputs. That is, in contrast to the common control view in which the inputs are currents and the output is position, this model acknowledges the fact that only the coil *voltages* can actually be directly manipulated (hence, the inputs are voltages) and it further assumes that the position states x and dx/dt cannot be directly measured but that the currents can.

In the sequel, it will prove convenient to make the change of coordinates:

$$\phi_b \equiv \phi_1 + \phi_2\ , \quad \phi_c \equiv \phi_1 - \phi_2\ , \quad i_b \equiv i_1 + i_2\ ,$$
$$i_c \equiv i_1 - i_2\ , \quad u_b \equiv u_1 + u_2\ , \quad u_c \equiv u_1 - u_2$$

so that

$$\frac{d^2}{dt^2}x = \frac{1}{\mu_0 mA}\phi_b\phi_c + \frac{1}{m}f_e \tag{15.5a}$$

$$\frac{d}{dt}\phi_b = \frac{1}{N}\left(u_b - Ri_b\right) \tag{15.5b}$$

$$\frac{d}{dt}\phi_c = \frac{1}{N}\left(u_c - Ri_c\right) \tag{15.5c}$$

$$i_b = \frac{2s_0}{\mu_0 NA}\phi_b - \frac{2}{\mu_0 NA}x\phi_c \tag{15.5d}$$

$$i_c = \frac{2s_0}{\mu_0 NA}\phi_c - \frac{2}{\mu_0 NA}\phi_b x \tag{15.5e}$$

15.3.1 Linear time invariant estimation

The approach developed in [63] and numerous subsequent papers imposes the assumption that ϕ_b in (15.5) is controlled through u_b to be constant:

$$\phi_b(t) = \Phi_b \tag{15.6}$$

(where Φ_b is called the *bias flux*) and explores the opportunities presented by the resulting linear, time invariant (LTI) system model:

$$\frac{d^2}{dt^2}x = \frac{\Phi_b}{\mu_0 mA}\phi_c + \frac{1}{m}f_e \tag{15.7a}$$

$$\frac{d}{dt}\phi_c = -\frac{R}{N}i_c + \frac{1}{N}u_c \tag{15.7b}$$

$$i_c = \frac{2s_0}{\mu_0 NA}\phi_c - \frac{2\Phi_b}{\mu_0 NA}x \tag{15.7c}$$

The self-sensing literature based on (15.7) capitalizes on the fundamental controllability and observability of this *constant bias linearized* model as well as its useful linearity and time invariance. These properties permit the implied control problem to be attacked using the broad array of analysis and synthesis tools available for such systems.

Any controller derived for such a model may be separated into a state estimator acting to generate estimates of rotor position and velocity followed by a state feedback controller (a static gain matrix, K) – the standard LQG controller[2] structure, for instance, as diagrammed in Fig. 15.4. Thus, the state estimator functions as a virtual probe, extracting estimates of position, velocity, and control flux states from available measurements of coil voltage and current.

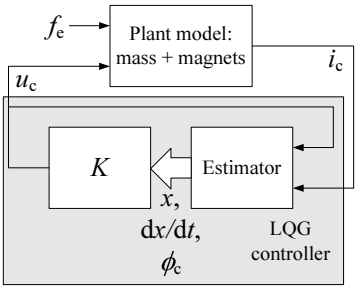


Fig. 15.4. Structure of an LTI controller, broken into estimator (virtual probe) and state feedback components.

A quick examination of the equilibrium of (15.7) for a static load f_e reveals some important properties of this system. First, assume the generic LTI self-sensing feedback rule

$$u_c(s) = G_c(s) i_c(s)$$

Further, assume that this feedback stabilizes (15.7), in which case it is possible to consider the equilibrium condition in which the time derivatives in (15.7) go to zero. If the static gain of G_c is defined, then $\lim_{s\to 0} G_c(s) = k_c$:

$$0 \leftarrow \frac{\Phi_b}{\mu_0 m A}\phi_c + \frac{1}{m} f_e \tag{15.8a}$$

$$0 \leftarrow -\frac{R}{N} i_c + \frac{1}{N} k_c i_c \tag{15.8b}$$

$$i_c = \frac{2 s_0}{\mu_0 N A}\phi_c - \frac{2\Phi_b}{\mu_0 N A} x \tag{15.8c}$$

[2] **L**inear **Q**uadratic **G**aussian control is the most basic MIMO synthesis procedure where specification of a performance index (a set of performance and noise weighting matrices) leads through direct computation to an output feedback controller. See, for instance, [68].

But k_c finite and (15.8b) imply that $i_c \to 0$ unless[3] $k_c = R$. Hence, (15.8c) and (15.8a) imply that

$$x \to \frac{s_0}{\Phi_b}\phi_c \to -\frac{\mu_0 A s_0}{\Phi_b^2} f_e \tag{15.9}$$

That is, the self-sensing suspension will exhibit a negative static stiffness with a value determined by the geometry of the actuator and by the bias flux, Φ_b, but entirely independent of the static gain of the controller. Indeed, if we relax the assumption that the static gain of G_c is defined and permit it to be unbounded, we reach the same conclusion: in either case, $\lim_{t\to\infty} i_c = 0$ and this always implies, by (15.8c) and (15.8a), this negative stiffness behavior.

This behavior may be deemed desirable in that it implies (in some sense) a minimum energy dissipation condition in the steady state, but a more important implication is that the estimator is unable to detect the static value of x: if it were able to do so, then it would be possible to design a controller that would drive the static value of x to zero.

Other problems endemic to this approach are explored in numerous publications, especially [12, 29, 42, 58]. The central problem is that the transfer function from input voltage to output current has a pole–zero pair in the right half plane and this makes the feedback stabilization problem very difficult. While such systems can be levitated and can provide some useful performance, they can quickly become unstable with slight drifts in system parameters.

To understand this, consider a specific example. Let the parameters of the system be those in Table 15.1. For this system, the transfer function from voltage in to current out is:

$$G_{iu} = \frac{272(s-297)(s+297)}{(s-249.5)(s^2+847.4s+2.11\times 10^5)}$$

This transfer function has a right half-plane pole at $s = 249.5$ and a right half-plane zero at $s = 297$: the open-loop system is unstable and the RHP zero will tend to attract the closed-loop root locus into the right half-plane, making stabilization difficult.

However, a stabilizing feedback controller may readily be derived using an LQG approach and an example is:

$$G_c = \frac{-34444.2553(s^2+847.4s+2.114\times 10^5)}{(s+297.1)(s^2+1697s+1.06\times 10^7)}$$

The root locus of the plant/controller combination is illustrated in Fig. 15.5. This locus enters the left half-plane (becomes stable) at a scale gain of 0.951 and leaves the left half-plane (becomes again unstable) at a scale gain of 1.06. The gain margin is extremely low as is the phase margin.

[3] It can be shown that the special case $k_c = R$ does not stabilize (15.7) so this case may be ignored.

Table 15.1. Parameters of LTI self-sensing example.

symbol	definition	value	units
A	pole gap area	4.84×10^{-5}	m^2
Φ_B	bias flux	1.68×10^{-5}	V s
s_0	nominal air gap length	0.0004	m
μ_0	permeability of free space	$4\pi \times 10^{-7}$	V s/A m
R	coil resistance	2.2	Ohms
N	coil turns	220	–
m	mass	0.1315	kg

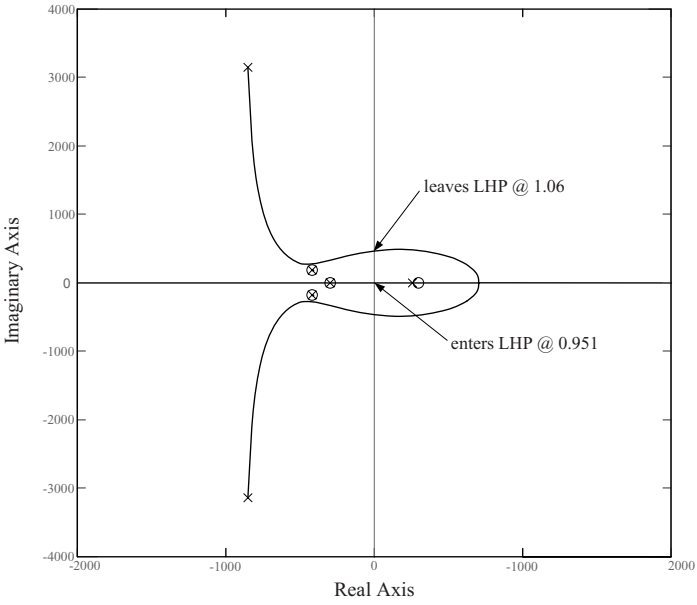


Fig. 15.5. Root locus of LTI self-sensing plant/controller combination.

The static gain of the closed loop system from f_e to x can be computed directly as -8.62×10^{-5}, which is easily established as equal to $-\mu_0 A s_0 / \Phi_b^2$, as expected from (15.9). As predicted, this static compliance is independent of the controller (as long as the controller is stabilizing) and is determined only by the physical parameters of the plant and choice of biasing flux level.

Despite these problems, [25] describes a successful commercial application to an elevator car guideway bearing. Some of the poor robustness issues are mitigated in this work by doing real-time estimation of a number of system parameters which are expected to vary (such as coil resistance) and to be a primary source of system variability or drift. Physical experience with this clever approach clearly indicates that this is a useful direction to pursue, particu-

larly where the fundamental negative stiffness of the suspension is acceptable or desirable.

15.3.2 A Linear Periodic Perspective

The combination of inability to properly estimate a static offset of the rotor position and general difficulty in obtaining adequate gain and phase margin is fundamental to the structure of the LTI plant model. The primary underlying structural defect is that the output signal i_c is a linear combination of the rotor position x and the magnetic force $\Phi_b\phi_c/\mu_0 A$ and these two signals tend to cancel one another in an inconvenient manner.

To sidestep these limitations, the very simplest approach is to challenge the decision to render the original nonlinear plant LTI by using a constant flux biasing. If, instead, the bias flux is made to be *periodic*, then the resulting plant will be linear periodic (LP) and may have better properties. This notion is explored extensively in [20, 39, 50]: the central ideas are reproduced here.

The LTI model (15.7) was produced from the base nonlinear model (15.5) by introducing constant bias (15.6). Instead, consider the periodic biasing rule

$$\phi_b(t) = \Phi_b(1 + \gamma \sin \omega t) \tag{15.10}$$

With this assumption, (15.5) becomes

$$\frac{d^2}{dt^2}x = \frac{\Phi_b(1 + \gamma \sin \omega t)}{\mu_0 m A}\phi_c + \frac{1}{m}f_e \tag{15.11a}$$

$$\frac{d}{dt}\phi_c = \frac{1}{N}\left(u_c - Ri_c\right) \tag{15.11b}$$

$$i_c = \frac{2s_0}{\mu_0 N A}\phi_c - \frac{2\Phi_b(1 + \gamma \sin \omega t)}{\mu_0 N A}x \tag{15.11c}$$

As with (15.7), (15.11) is linear, but unlike (15.7), its coefficients are now periodic in time. Such a linear periodic plant has significant differences from the more familiar linear time invariant plant and its analysis is substantially more involved. If the frequency of the perturbation, ω, is very large relative to the dynamics that the plant would exhibit if γ were zero, then some simplifications arise that render the analysis easier: such an approach is called *asymptotic* analysis [3] and the associated control theory is referred to as *vibrational control* [10] or *generalized dither* [16].

With ω large, the main result of an asymptotic analysis is that we may neglect the periodic term in (15.11a) and focus, instead, on the output periodicity in (15.11c). In this case, one might construct the very simple synchronous demodulator depicted in Figure 15.6.

The key to such a demodulator, and the key to why periodic biasing is useful in this problem, is that multiplying the signal $a \sin \omega t$ by $\sin \omega t$ shifts the signal both up and down in frequency: the product $\sin^2 \omega t$ has a constant component and a high frequency component:

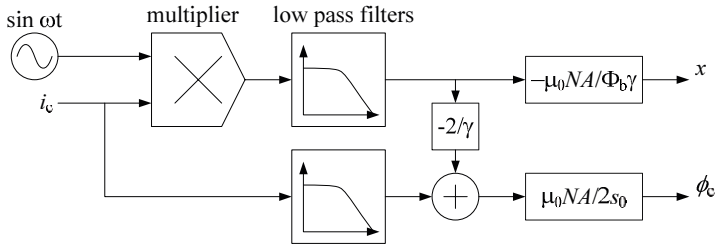


Fig. 15.6. Synchronous demodulator to separate ϕ_c (force) from x (displacement) in the current output signal i_c.

$$\sin\omega t \times a \sin\omega t = \frac{1}{2} a \left(1 - \cos 2\omega t\right)$$

So the signal process in the upper path of Fig. 15.6 is to first scale i_c by $\sin\omega t$:

$$\begin{aligned} i_c \sin\omega t &= \sin\omega t \left(\frac{2s_0}{\mu_0 NA}\phi_c - \frac{2\Phi_b}{\mu_0 NA}x\right) - \sin^2\omega t \left(\frac{2\Phi_b\gamma}{\mu_0 NA}x\right) \\ &= \sin\omega t \left(\frac{2s_0}{\mu_0 NA}\phi_c - \frac{2\Phi_b}{\mu_0 NA}x\right) + \frac{\cos(2\omega t)\Phi_b\gamma}{\mu_0 NA}x \\ &\quad - \frac{\Phi_b\gamma}{\mu_0 NA}x \end{aligned} \tag{15.12}$$

and then filter out signals at high frequency (ω and higher) under the assumption that the signals x and ϕ_c have no components at this high frequency (the *asymptotic* assumption). This filtering process (approximately) discards all but the last term in (15.12) so that the resulting signal may be scaled as in Fig. 15.6 to yield x.

The lower path of the demodulator in Fig. 15.6 uses a similar low pass filter to remove the $\sin\omega t$–modulated image of x and then removes the remaining unmodulated image by simply subtracting the version extracted by the upper path. This then produces a measure of the control flux (or of the control force) which may also be useful for control of the system.

This approach is nearly identical to that explored in [12] and employed by S2M, depicted schematically in Fig. 15.7. In [4], the performance of this system is reported as completely satisfactory for turbo–molecular pump application and plans to apply a similar scheme to "light" turbo–machinery are reported.

The only difference between the scheme of Fig. 15.7 and the discussion above is that Fig. 15.7 uses a different demodulation technique which is not precisely synchronous: instead, they insert a narrow bandpass filter (marked "42" in the figure) and then multiply by a synchronous square wave, which has the same effect as rectification. Subsequent low pass filtering would be accomplished by the PID controller (marked "32" in the figure).

Of course, the simple synchronous demodulation analysis presented here relies heavily on the asymptotic assumption[3] which essentially means, in this

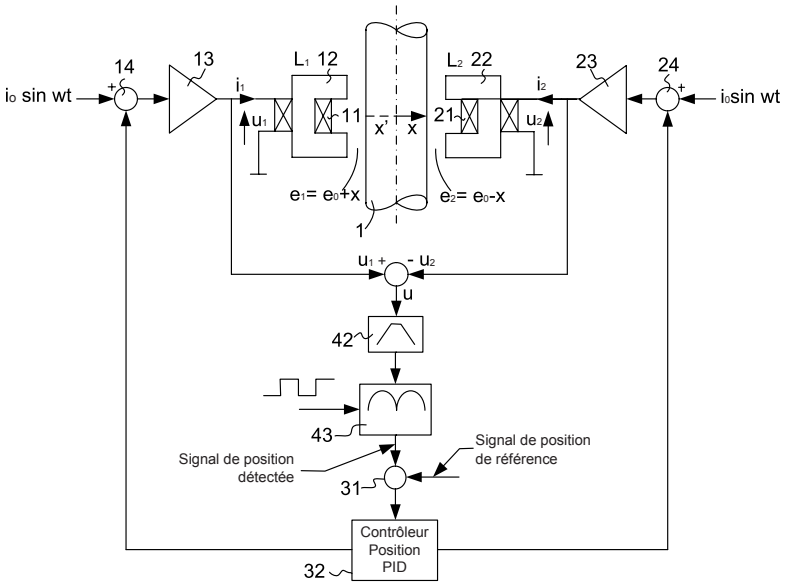


Fig. 15.7. Schematic of the S2M self–sensing scheme, from [59].

case, that the spectra of the signals x and ϕ_c do not overlap the spectrum of the parametric perturbation $\sin \omega t$. In real systems, the spectra of x and ϕ_c extend to very high frequency and practical considerations (specifically, limitations on amplifier voltage as well as eddy current production in the magnet iron) encourage keeping ω as low as possible. Hence the asymptotic assumption may represent a substantial approximation. This issue is explored in [20, 50] where a more exact analysis permits quantification of the effects of modest ω and also the effect of γ (the preceding analysis makes no assumption about γ except that it is non-zero.)

The performance metric examined in [20, 50] is the peak of the sensitivity function[68], which varies essentially inversely with attainable gain and phase margin (high peak sensitivity tends to imply low gain and phase margins.) The main finding is summarized in Fig. 15.8 which shows that, for the example studied in [20, 50], the best LTI ($\gamma = 0$) sensitivity is about 11.7 while large ω and γ can achieve, asymptotically, the theoretical limit of 1.0. This means that a typical system with perturbed bias flux can tolerate nearly 12 times as much uncertainty or variation in plant gain as the LTI approach can tolerate. For reference, the ISO 14839-3 standard for active magnetic bearings recommends a peak sensitivity function of less than 3. Reviewing Fig. 15.8, this implies that the amplitude (γ) of the perturbation should be at least 15% of the nominal bias flux: $\gamma > 0.15$.

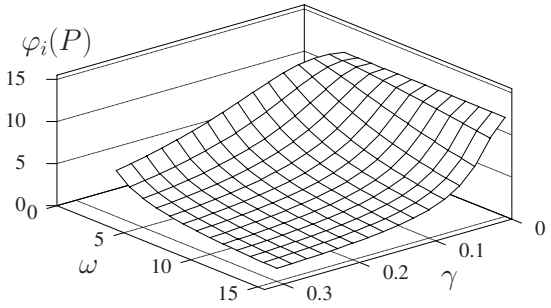


Fig. 15.8. Achievable peak input sensitivity (φ_i) as a function of perturbation amplitude (γ) and nondimensionalized perturbation frequency (ω). From [20]

The key conclusions to be drawn from this linear periodic approach are:

1. if the bias is perturbed periodically then it is possible to estimate the static position of the mass (because position and magnetic force can be separated)
2. periodic biasing permits design of feedback controllers that achieve much higher robustness than without periodic biasing
3. the required amplitude and frequency of bias perturbation can be assessed for a given target level of performance

One valuable perspective on this approach is to understand the signal that produces this periodic perturbation – $\gamma \sin \omega t$ in (15.10) – as an *interrogation* signal. That is, this signal is added to the system in order to improve the estimate of rotor position obtained from the measured output of the plant. Without this interrogation signal, the system becomes LTI and the limitations discussed in Section 15.3.1 again apply.

15.3.3 Switching Ripple

An important feature of most practical AMB systems is that the amplifiers driving the coils are switching amplifiers, as discussed in Chap. 3. From a self-sensing point of view, the significance of this feature is that switching amplifiers induce high frequency perturbations to the coil currents: they tend to produce periodically perturbed bias flux. Hence, one might expect that this switching ripple could serve as the periodic perturbation (interrogation signal) that was intentionally introduced in (15.10).

This observation is appealing because it might provide a mechanism for estimating rotor position using existing hardware. That is, one might be able to design an estimation device that uses measurements of voltage and current in existing AMB systems to produce a position signal that is comparable to that produced by the discrete position sensor in the system. If so, then

AMB vendors would have a safe technology transition strategy from a conventionally position sensed AMB to self-sensing with minimal disruption of the existing technology: adding this "piggy-back" estimator produces a plug-in replacement for the existing sensor signal with no other changes to the system hardware.

Numerous researchers have worked on strategies to exploit this ripple. Perhaps the most obvious approach is suggested in [17]. This strategy looks directly at the electrodynamics driving either of the pair of electromagnets, extracted from (15.4):

$$\frac{d}{dt}\phi_1 = \frac{1}{N}u_1 - \frac{R}{N}i_1 \tag{15.13a}$$

$$i_1 = \frac{2(s_0 - x)}{\mu_0 NA}\phi_1 \tag{15.13b}$$

Differentiate (15.13b) by time to obtain:

$$\frac{d}{dt}i_1 = \frac{2(s_0 - x)}{\mu_0 NA}\left(\frac{1}{N}u_1 - \frac{R}{N}i_1\right) - \frac{2\phi_1}{\mu_0 NA}\frac{d}{dt}x \tag{15.14}$$

Now, similar to the asymptotic assumption made in the preceding section, assume that

$$\left|\frac{d}{dt}x\right| \ll \left|\frac{s_0 - x}{N\phi_1}(u_1 - Ri_1)\right| \tag{15.15}$$

With this assumption, it is possible to compute $s_0 - x$ from (15.14):

$$s_0 - x \approx \frac{\mu_0 N^2 A}{2(u_1 - Ri_1)}\frac{d}{dt}i_1 \tag{15.16}$$

That is, if it is possible to measure the instantaneous slope of i_1 at a time when $|u_1|$ is large so that (15.15) is satisfied, then this slope can be used to estimate the gap length, $s_0 - x$. (Note, of course, that the same analysis can be applied to i_2 and u_2 to obtain $s_0 + x$.) With very fast A/D conversion and careful synchronization of sampling with the logic driving the switching amplifier, this measurement of instantaneous current slope is possible, as illustrated in Fig. 15.9, and has been demonstrated [17].

Importantly, notice that this analysis relies on the notion that u_1 is regularly not equal to Ri_1. In particular, that there is no "equilibrium" condition in which $u_1 = Ri_1$ for more than an instant. This need for regular perturbation of u_1 is, in every way, equivalent to the observation in the preceding section that the bias flux requires regular perturbation of significant amplitude in order to estimate position well in the LP framework. Such a requirement is sometimes referred to as *persistency of excitation* [57].

Much of the literature on self-sensing is devoted to what are essentially *ad-hoc* approaches to estimating x from features of the switching ripple. Generally, the approaches either exploit a direct filtering of the ripple waveform

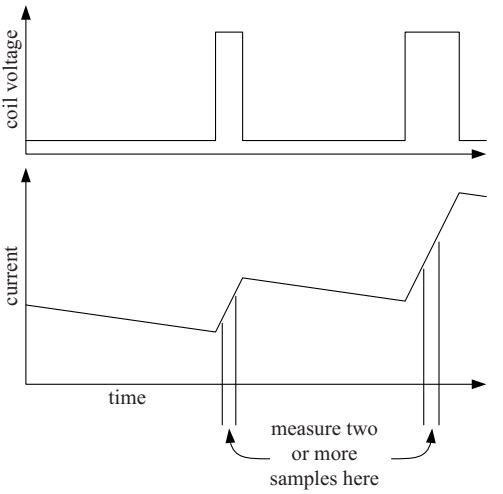


Fig. 15.9. Slope based estimation: multiple current samples are obtained during intervals of large, fixed coil drive voltage.

or some form of parameter estimator. The direct filtering approaches process the switching waveform in order to recover the switching ripple amplitude and then, under assumptions about the switching frequency and duty cycle as well as nominal air gap length (s_0), this amplitude is interpreted as rotor position.

An example of a parameter estimator is discussed in [39, 44, 46] and is diagrammed in Fig. 15.10. Here, a simulation of the electrodynamics (15.13) is driven by the actual coil voltage and by an *estimated* gap length. The resulting current waveform is then compared to the actual current waveform: if the estimated gap length is correct, then the two waveforms should agree. The purpose of the envelope filter is to make this comparison be monotonic in gap estimate error: if the two waveforms are compared directly, then the error will switch between positive and negative throughout the switching cycle. Discrepancies are then used to adjust the gap length estimate. This correction is performed very quickly and is able to produce a useful estimator bandwidth of about 1.0 kHz.

Parameter estimators for this problem may be developed formally by using a Lyapunov approach [57]. Here, a Lyapunov function is constructed that is strictly positive in the errors between actual and estimated dynamic states and parameters. The estimator dynamic behavior is then *designed* so that the time derivative of this Lyapunov function is strictly negative.

For the problem defined by (15.13), choose the estimator states $\hat{\phi}_1$ and $\hat{x}$ as estimates of ϕ_1 and x. The nondimensionalized error between estimated currents is

$$\epsilon \equiv (\hat{i}_1 - i_1)/I_0 = \frac{2}{\mu_0 N A I_0} \left((s_0 - \hat{x})\hat{\phi}_1 - (s_0 - x)\phi_1 \right)$$

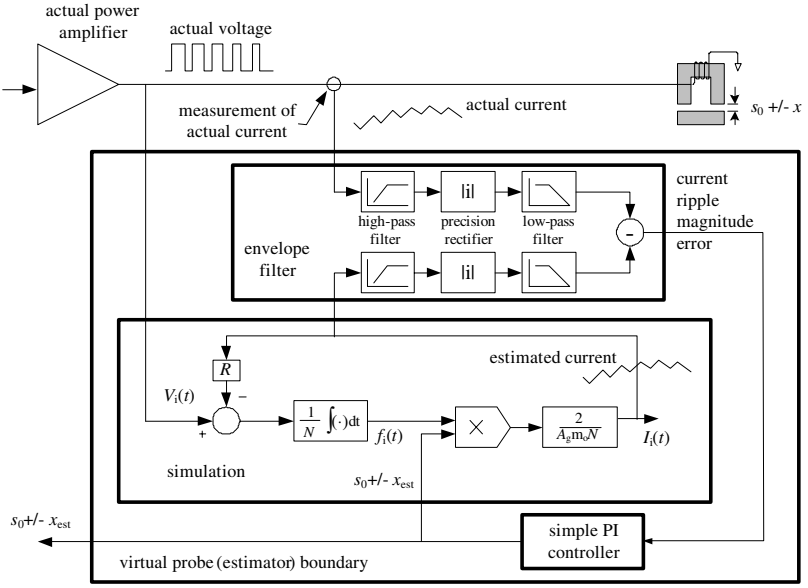


Fig. 15.10. A simple parameter estimator for self-sensing. From [39].

while the nondimensionalized error between estimated parameters is

$$\sigma \equiv (\hat{x} - x)/s_0$$

The scaling current, I_0, is chosen for convenience as $I_0 \equiv 2s_0 B_{\text{sat}}/\mu_0 N$ in which B_{sat} is the saturation flux density of the actuator iron. To derive the required dynamics for $\hat{\phi}_1$ and $\hat{x}$, choose the Lyapunov function[4]

$$V = \frac{1}{2}\left(\epsilon^2 + \gamma^2\sigma^2\right) \tag{15.17}$$

Obviously, $\sigma = 0 \;\Rightarrow\; \hat{x} = x$ and it is readily established that $\epsilon, \sigma = 0 \;\Rightarrow\; \hat{\phi}_1 = \phi_1$. To design the required dynamics of the estimator, differentiate (15.17) with respect to time and choose a rule for the evolution of $\hat{x}$ and $\hat{\phi}_1$ so that this derivative is strictly negative.

After extensive algebra [21], a solution to this problem is

$$\dot{\hat{\phi}} = \frac{\hat{\lambda}\gamma^2 + \epsilon\hat{\phi}}{\hat{\lambda}\gamma^2}(v - i) - \left(\frac{\hat{\lambda}\gamma^2 + \epsilon\hat{\phi}}{\hat{\lambda}\gamma^2}\psi^2 + \frac{\varphi^2}{\hat{\lambda}}\right)\epsilon \tag{15.18a}$$

$$\dot{\hat{\lambda}} = -\frac{1}{\gamma^2}\left(v - i - \psi^2\epsilon\right)\epsilon \tag{15.18b}$$

[4] The choice is not unique: other choices may yield a different estimator or may not yield any estimator. An unfortunate aspect of Lyapunov methods is that there is no guarantee that a given choice of function is useful.

$$\epsilon = \hat{\lambda}\hat{\phi} - i \tag{15.18c}$$

$$\hat{x} = s_0(1 - \hat{\lambda}) \tag{15.18d}$$

The input signals to this estimator are measured coil voltage $v = v_1/RI_0$ and current $i = i_1/I_0$. The dynamic performance of this estimator is tuned by adjusting the parameters γ, ψ, and φ.

An assumption in proving convergence of (15.18) is that $v_1 - i_1 R$ is persistently time varying, meaning that $v_1 = i_1 R$ only "occasionally". More formally, the signal v_1 must be persistently exciting: the persistent switching character of v_1 that is a natural consequence of using a switching power amplifier is crucial to the performance of the estimator. In [21], this issue is explored by assuming that v_1 is the sum of a constant term and a sinusoidal term: $v = v_0 + v_s \sin \omega t$. For constant v_0 and ω, it is demonstrated that the rate of convergence of (15.18) to a constant $\hat{\lambda} = \lambda$ varies nearly exactly in proportion to v_s^2.

Some important conclusions that may be drawn from this work on use of switching ripple are:

1. The method of actuator linearization is not actually critical to self-sensing: none of the methods explored in this section make any assumptions about linearization.
2. What *is* critical is the presence of a persistent perturbation which may be a sinusoidal interrogation signal (as in Section 15.3.2, where it lead to a linear periodic model) or natural switching ripple induced by amplifier switching (as in Section 15.3.3.)
3. The performance of the estimator is quite sensitive to the strength of this persistent perturbation (amplitude of the switching ripple or interrogation signal.)
4. From Section 15.3.2, we also expect the performance of the estimator to be sensitive to the regularity (essentially, frequency) of this persistent perturbation: it must be frequent enough to provide numerous signal reversals within the smallest time constant of the AMB + suspended rotor system.

15.4 Remaining Technical Challenges

Despite the emergence of real commercial applications of self-sensing AMB technology, several technical challenges persist that should continue to stimulate academic and industrial research.

15.4.1 Ripple Amplitude

A key result presented in [20, 50] is that the robustness of self–sensed AMB systems, regardless of the signal processing method employed, hinges on the amplitude of the switching ripple. The robustness does not go to zero in the

event that the switching ripple is eliminated (as in [63]) but is very substantially diminished. As a result, self-sensing systems will tend to work better when the coil currents exhibit a lot of high frequency ripple.

This observation is significant because switching amplifier technology for AMB systems has moved from early approaches that used only two output states ($+V_{ps}$ or $-V_{ps}$) to use of three output states ($+V_{ps}$, 0, $-V_{ps}$). The reason for this is that the amplifier becomes more efficient and eddy current losses and acoustic emissions from the AMB are reduced.

However, with three state drive, the amplitude of the switching ripple is substantially reduced (sometimes by a factor of 10 or so) so that self–sensing with three state amplifiers is difficult. Of course, solutions such as that proposed originally by [12] and implemented in [59] sidestep this problem by injecting a special signal into the power amplifier intended to achieve sufficient ripple amplitude to obtain adequate system robustness. However, this is only accomplished at the expense of much of the efficiency targeted by the three state switching operation.

The approach examined in [17] is apparently perfectly suited to three-state switching in that it only measures the gap during high voltage pulses and, even with three-state switching, these pulses are guaranteed to occur at a very regular interval (the amplifier's switching rate). In this case, the only issue is how well the slope can be measured, particularly when the width of the high voltage pulse is very short, as may arise in three-state switching. In practical application of this method, it seems likely that the signal-to-noise ratio of the estimate will depend on pulse width so, in the end, there may be a similar correlation between ripple amplitude and performance as that seen with the other schemes. This question remains to be investigated.

This limitation may prove to be fundamental which would mean that robust self-sensing AMB systems will typically be somewhat less efficient (in terms of electrical power) than the equivalent discretely sensed AMB. Approaches are likely to be a combination of accepting higher losses combined with methods such as presented in [25] to mitigate the modest robustness achieved at lower ripple levels.

A corollary issue is that of acoustic emissions: as the perturbation amplitude is increased, it will tend to produce acoustic emission or other symptoms of mechanical response that, in many applications, may be unacceptable. In this case, such applications may simply be incompatible with self-sensing. The underlying reason for this is the simple physical size of the device being used for sensing (the actuator). By using a much smaller device to sense (the position sensor) than to actuate, the forces produced as a byproduct of sensing are minimized while maintaining high actuation capacity: this is the tradeoff that is best achieved by discretely sensed AMB systems.

15.4.2 Eddy Currents

Eddy currents pose a special problem, particularly in unlaminated actuators such as thrust bearings. The primary consequence of eddy currents is an effective reduction in iron permeability at high frequencies (see [24] for instance). This means that the variation in actuator impedance with changes in gap – the sensitivity of the device as a position sensor – is poor at high excitation frequencies. It further means that the shape of the current ripple waveform may not be the clean triangle anticipated by [17].

Figure 15.11 illustrates a typical eddy current waveform in response to 2–state switching. The cusps in the current waveform that appear at each

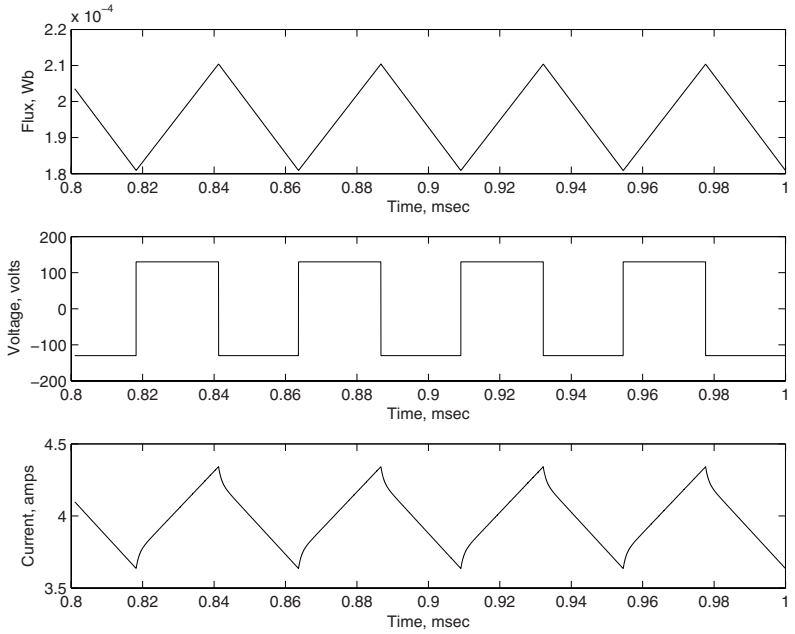


Fig. 15.11. AMB waveforms for 2-state switching with eddy current production.

switching instant are controlled almost entirely by eddy currents in the actuator iron. The size of these cusps can be quite large: for an unlaminated thrust actuator, they can be 20 or 30 percent of the bias current level, depending on the amplifier switching voltage. The problem with these cusps is that they are not affected by changes in air gap length so they represent a substantial loss in sensitivity of the waveform to air gap.

The primary solution to this problem is to reduce the frequency of the excitation signal – go to lower switching rates (and also lower switching voltages) or use a special, relatively low frequency sinusoidal *interrogation* signal.

In [59], this issue is addressed by recommending use of a special interrogation signal whose frequency is selected to be just a bit above the effective bandwidth of the actuator. This bandwidth is determined, in part, by the eddy current production. Therefore, linking the interrogation frequency to the actuator bandwidth attempts to preserve sensitivity to gap by minimizing production of eddy currents by the sensing process.

In methods such as [17] which rely on the instantaneous slope of the waveform to determine gap length, a sampling delay needs to be inserted between the switching instant and the sampling interval. This delay should be proportional to the eddy current time constant: the decay time of the cusps in Fig. 15.11. Of course, this delay implies that the minimum voltage pulse width that can be employed for sensing is significantly longer than the eddy current time constant. This may introduce problems when applied to three-state switching amplifiers.

Parameter estimation methods, such as [46], should add an eddy current model to the embedded electrodynamic simulation in order to account for this effect. This notion is explored in [19] where it is demonstrated that eddy current effects are readily incorporated into parameter estimators and that the benefit is a significant reduction in harmonic distortion of the estimated position signal: effectively, a higher signal-to-noise ratio. The reason for this is that, absent an eddy current model in the internal simulation of the parameter estimator, the estimator must manipulate the position estimate very rapidly in order to produce the current cusps characteristic of eddy currents. Consequently, the resulting position estimate contains substantial components at harmonics of the switching frequency.

15.4.3 Saturation

Perhaps the most vexing problem facing researchers in self-sensing is that of magnetic saturation. This problem has been acknowledged since some of the earliest work in self-sensing [18] while a more general discussion is provided in [55]. The issue is that saturation reduces the permeability of the actuator iron at high flux densities and this dramatically alters the sensitivity of the actuator to air gap.

In particular, if the mean electromagnet coil current is held constant and the air gap is changed, then the slope of the switching ripple will diminish with decreasing gap until the iron begins to saturate. At this point, further reduction in air gap produces two results: a reduction in circuit reluctance due to the narrowing gap and an *increase* in circuit reluctance due to iron saturation. The result is summarized in Fig. 15.12 which shows that the sensitivity (slope of the curve) actually reverses at some point and a simple demodulation scheme will actually produce an ambiguous signal: the same output can arise at two different rotor positions.

Several solutions to this problem have been posited. In [18], the actuator has an excess of poles (six horseshoe pole pairs rather than the usual four).

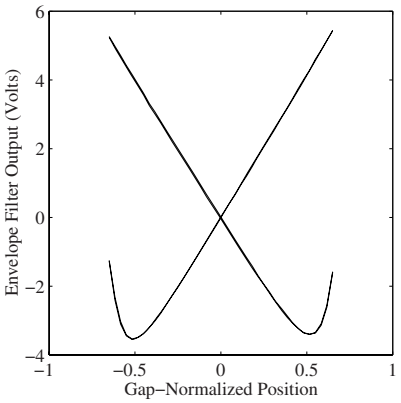


Fig. 15.12. Switching waveform amplitude *vs* rotor position for two opposing AMB sectors. From [39].

In this case, it is possible to momentarily reduce the flux density in selected pole pairs to ensure a fixed level well away from saturation. The current in this pair is then perturbed to estimate the gap length. The principal drawback to such an approach is that the amplifier voltage required to rapidly de-saturate the pole pair, interrogate the gap, and bring the pole pair back into saturation can be substantial: well in excess of the nominal requirement of the system. Another solution is proposed in [45] in which all of the pole gaps are simultaneously estimated in a MIMO parameter estimation scheme. In this case, it is shown that such a scheme can be robust to short periods of actuator saturation and still yield a reliable position estimate. The literature on self–sensing since [45] has generally stayed away from the saturation problem so this appears to be a relatively ripe area for continued research.

15.5 Conclusions

Self–sensing AMB technology now presents a commercially viable alternative to using discrete position sensors in AMB systems. This alternative offers significant cost savings and the potential for dynamics advantages due to its fundamental sensor-actuator collocation. Several technical approaches are available: linear system based, linear system with parameter identification, switching ripple based, and interrogation signal based. Of these, the linear system with parameter estimation and interrogation signal based approaches have been developed as commercial products. Generally, the existing commercial products make modest demands on the system sensing performance: in order to realize products with more aggressive requirements, a number of lingering technical hurdles remain to be crossed.

References

1. H. Bleuler and D. Vischer. Magnetic bearing systems with minimal hardware requirement. In *ROMAG '91: Magnetic Bearings and Dry Gas Seals International Conference and Exhibition*, March 1991.
2. Hannes Bleuler. Survey of magnetic levitation and magnetic bearing types. *JSME International Journal, Series 3: Vibration, Control Engineering, Engineering for Industry*, 35(3):335 – 342, 1992.
3. N. N. Bogoliubov and Y. A. Mitropolsky. *Asymptotic Methods in the Theory of Non-Linear Oscillations*. Hindustan Publishing Corporation (India), 1961.
4. Maurice Brunet and Bruno Wagner. Innovation: Self-sensing technology, simplified mechanical design. In *S2M News*, 5, December 2005.
5. Guang-Ren Duan, Zhan-Yuan Wu, and D. Howe. Explicit parametric solution to observer-based control of self-sensing magnetic bearings. *Proceedings of the 14th World Congress. International Federation of Automatic Control*, vol.16:379 – 84, 1999.
6. Z. Gosiewski. Control design of sensorless magnetic bearings for rigid rotor. In *Proceedings of the Sixth International Symposium on Magnetic Bearings*, pages 548–557, 1998.
7. R. Gurumoorthy, W. L. Soong, J. P. Lyons, and A. F. Storace. Implementation of sensorless control of radial magnetic bearings. In *Proceedings of MAG '95 Magnetic Bearings, Magnetic Drives and Dry Gas Seals*, Washington, D.C., August 1995.
8. V. Iannello. Sensorless position detector for an active magnetic bearing. U.S. Patent No. 5,696,412.
9. Hiroaki Ito, Mimpei Morishita, Yoshiaki Fujita, Akira Yamamoto, and Kazuo Shimane. Development of elevator car non-contact guide system. In *Proceedings of ELEVCON2006*, 2006.
10. P. T. Kabamba, S. M. Meerkov, and E K. Poh. Pole placement capabilities of vibrational control. *IEEE Transactions on Automatic Control*, 43(9):1256–1261, September 1998.
11. Mochimitsu Komori and Chaki Shiraishi. A levitated motor with superconducting magnetic bearings assisted by self-sensing ambs. *IEEE Transactions on Applied Superconductivity*, 13(2):2189–2192, June 2003.
12. L. Kucera. Robustness of self-sensing magnetic bearing. In *Proceedings of MAG'97 Industrial Conference and Exhibition on Magnetic Bearings*, pages 261–270, Alexandria, Virginia, August 1997.
13. Ladislav Kucera. Method and device for regulating a sensor-free magnetic bearing, January 1998. International Patent Application No. PCT/CH1998/000014, Designee: Eidgenössische Technische Hochshule ETH-Zentrum.
14. T. Kurosu, K-I. Matsuda, and Y. Okada. Self-sensing control technique of self-bearing motor. In *Proceedings of the Eighth International Symposium on Magnetic Bearings*, pages 293–297, August 2002.
15. Tomonori Kuwajima, Tetsuya Nobe, Kenji Ebara, Akira Chiba, and Tadashi Fukao. An estimation of the rotor displacements of bearingless motors based on a high frequency equivalent circuit. In *Proceedings of the International Conference on Power Electronics and Drive Systems*, volume 2, pages 725–731, 2001.
16. S. Lee and S. M. Meerkov. Generalized dither. *International Journal of Control*, 53(3):741–747, 1991.

17. Lichuan Li, Tadahiko Shinshi, and Akira Shimokohbe. State feedback control for active magnetic bearings based on current change rate alone. *IEEE Transactions on Magnetics*, 40(6):3512–3517, November 2004.
18. J. P. Lyons, S. R. MacMinn, and M. A. Preston. Flux/current methods for SRM rotor position estimation. In *Proc. 1991 IEEE Industry Application Society Annual Meeting*, 1991.
19. Roza Mahmoodian. Formal parameter estimation for self-sensing magnetic bearings. Master of Science Thesis, University of Virginia, January 2007.
20. E.H. Maslen, D.T. Montie, and T. Iwasaki. Robustness limitations in self–sensing magnetic bearings. *ASME Journal of Dynamic Systems, Measurement, and Control*, 128(2):197–203, 2006.
21. Eric Maslen, Tetsuya Iwasaki, and Roza Mahmoodian. Self-sensing magnetic bearings: development of a virtual probe. In *Proceedings of the 2006 NSF Design, Service, and Manufacturing Grantees and Research Conference*, St. Louis, Missouri, July 2006.
22. Ken-ichi Matsuda, Yohji Okada, and Junji Tani. Self-sensing magnetic bearing using the differential transformer principle. *Nippon Kikai Gakkai Ronbunshu, C Hen/Transactions of the Japan Society of Mechanical Engineers, Part C*, 63(609):1441 – 1447, 1997.
23. F. Matsumura, Y. Okada, M. Fujita, and T. Namerikawa. State of the art of magnetic bearings. *JSME International Journal*, 40(4):553–560, 1997.
24. David C. Meeker, Eric H. Maslen, and Myounggyu D. Noh. Augmented circuit model for magnetic bearings including eddy currents, fringing, and leakage. *IEEE Transactions on Magnetics*, 32(4 pt 2):3219 – 3227, 1996.
25. Mimpei Morishita and Hiroaki Ito. The self-gap-detecting electromagnetic suspension system with robust stability against variation of levitation mass. In *Proceedings of the International Symposium on Power Electronics, Electrical Drives, Automation and Motion*, Taorima, Italy, May 2006.
26. T. Mizuno. Phase–locked loops for the stabilization of active magnetic suspensions. *JSME International Journal Series C*, 37(3):499–503, 1994.
27. T. Mizuno, K. Araki, and H. Bleuler. Stability analysis of self–sensing magnetic bearing controllers. *IEEE Transactions on Control Systems Technology*, 4(5):572–579, September 1996.
28. T. Mizuno and H. Bleuler. A geometric approach to control system design of self-sensing magnetic bearings. *Automatic Control. World Congress 1993. Proceedings of the 12th Triennial World Congress of the International Federation of Automatic Control. Vol.3. Applications I*, pages 465 – 70, 1994.
29. T. Mizuno and H. Bleuler. Self–sensing magnetic bearing control system design using the geometric approach. *Control Engineering Practice*, 3(7):925–932, July 1995.
30. T. Mizuno, H. Bleuler, C. Gähler, and D. Vischer. Towards practical applications of self-sensing magnetic bearings. In *Proceedings of the Third International Symposium on Magnetic Bearings*, 1992.
31. T. Mizuno, H. Bleuler, H. Tanaka, K. Komatsu, H. Ueyama, H. Hashimoto, and L. Kucera. An industrial application of sensorless magnetic bearings. In *Proceedings of the Fourth International Symposium on Magnetic Bearings*, ETH Zurich, August 1994.
32. T. Mizuno and Y. Hirasawa. Self-sensing magnetic suspension using a hysteresis amplifier with a two-quadrant drive. In *Proceedings of the Sixth International Symposium on Magnetic Suspension Technology*, pages 76–80, October 2001.

33. T. Mizuno, T. Ishii, and K. Araki. Realization of phase–locked and frequency–feedback magnetic bearings. In *Proceedings of the Fourth International Symposium on Magnetic Bearings*, ETH Zurich, August 1994.
34. T. Mizuno, H. Namiki, and K. Araki. Self–sensing operations of frequency-feedback magnetic bearings. In *Proceedings of the Fifth International Symposium on Magnetic Bearings*, pages 119–123, August 1996.
35. T. Mizuno, H. Nimiki, and K. Araki. Counter-interfaced digital control of self-sensing magnetic suspension systems with hysteresis amplifiers. *JSME International Journal Series C - Mechanical Systems, Machine Elements and Manufacturing*, 42(1):71–78, March 1999.
36. Takeshi Mizuno, Kenji Araki, and Hannes Bleuler. On the stability of controllers for self-sensing magnetic bearings. *Proceedings of the SICE Annual Conference*, pages 1599 – 1604, 1995.
37. Takeshi Mizuno, Hannes Bleuler, Hiroaki Tanaka, Hideki Hashimoto, Fumio Harashima, and Hirochika Ueyama. An industrial application of position sensorless active magnetic bearings. *Transactions of the Institute of Electrical Engineering of Japan*, 117(5):124–133, November 1996.
38. Abdelfatah M. Mohamed, Fumio Matsumura, Toru Namerikawa, and Jun-Ho Lee. Modeling and robust control of self-sensing magnetic bearings with unbalance compensation. *IEEE Conference on Control Applications - Proceedings*, pages 586 – 594, 1997.
39. D. T. Montie. *Performance Limitations and Self–Sensing Magnetic Bearings*. PhD thesis, University of Virginia, 2003.
40. D. T. Montie and E. H. Maslen. Experimental self–sensing results for a magnetic bearing. In *Proceedings of the ASME International Gas Turbine Institute Turbo Expo*, June 2001.
41. D. T. Montie and E. H. Maslen. Self–sensing in fault tolerant magnetic bearings. *ASME Journal of Engineering for Gas Turbines and Power*, 123:864–870, October 2001.
42. N. Morse, R. Smith, B. Paden, and J. Antaki. Position sensed and self–sensing magnetic bearing configurations and associated robustness limitations. In *Proceedings of the IEEE Conference on Decision and Control Including the Symposium on Adaptive Processes*, volume 3, pages 2599–2604, 1998.
43. R. Mueller et al. Position sensorless AMB in four degrees of freedom. In *Proceedings of the Fifth International Symposium on Magnetic Bearings*, pages 101–106, August 1996.
44. M. D. Noh. *Self–Sensing Magnetic Bearings Driven by a Switching Power Amplifier*. PhD thesis, University of Virgina, 1996.
45. M. D. Noh and E. H. Maslen. Self–sensing magnetic bearings (Part II). In *Proceedings of the Fifth International Symposium on Magnetic Bearings*, pages 113–118, August 1996.
46. M. D. Noh and E. H. Maslen. Self–sensing magnetic bearings using parameter estimation. *IEEE Transactions on Instrumentation and Measurement*, 46(1):45–50, February 1997.
47. K. Ohnishi, N. Matsui, and Y. Hori. Estimation, identification, and sensorless control in motion control-system. *Proceedings of the IEEE*, 82(8):1253–1256, 1994.
48. Y. Okada, K. Matsuda, and B. Nagai. Sensorless magnetic levitation control by measuring the PWM carrier frequency component. In *Proceedings of the Third International Symposium on Magnetic Bearings*, 1992.

49. Yohji Okada and Kenzou Nonami. Research trends on magnetic bearings (overview of the 8th international symposium on magnetic bearings, ismb8). *JSME International Journal*, 46(2):341–342, 2003.
50. K. S. Peterson, R. H. Middleton, and J. S. Freudenberg. Fundamental limitations in self-sensing magnetic bearings when modeled as linear periodic systems. In *Proceedings of the American Controls Conference*, 2006.
51. A. Schammass and H. Bleuler. Experimental results on self–sensing AMB using a three-state PWM amplifier. In *Proceedings of the Eighth International Symposium on Magnetic Bearings*, pages 289–292, August 2002.
52. Alexandre Schammass. *A Self–sensing Active Magnetic Bearing: Modulation Approach*. PhD thesis, Swiss Federal Institute of Technology Lausanne - EPFL, 2003.
53. Alexandre Schammass, Raoul Herzog, Philipp Bühler, and Hannes Bleuler. New results for self-sensing active magnetic bearings using modulation approach. *IEEE Transactions on Control Systems Technology*, 13(4):509–516, July 2005.
54. K. K. Sivadasan. Analysis of self–sensing active magnetic bearings working on inductance measurement principle. *IEEE Transactions on Magnetics*, 32(2), March 1996.
55. N. Skricka and R. Markert. Compensation of disturbances on self–sensing magnetic bearings caused by saturation and coordinate coupling. In *Proceedings of the Seventh International Symposium on Magnetic Bearings*, pages 165–170, August 2000.
56. N. Skricka and R. Markert. Influence of cross-axis sensitivity and coordinate coupling on self–sensing. In *Proceedings of the Sixth International Symposium on Magnetic Suspension Technology*, pages 179–184, October 2001.
57. Gang Tao. *Adaptive Control Design and Analysis*. Wiley-IEEE Press, 2003.
58. N. M. Thibeault and R. Smith. Robustness comparison of a magnetic bearing system in various measurement configurations. In *Proceedings of the American Control Conference*, volume 5, pages 3002–3003, IEEE, Piscataway, NJ, USA, 2000.
59. Yann Tremaudant, Maurice Brunet, and Ulrich Schroeder. Active magnetic bearing with automatic detection of the position thereof, March 2005. International Patent, Application No: PCT/FR2005/000626, Designee: Societe de Mecanique Magnetique.
60. Perry Tsao, Seth R. Sanders, and Gabriel Risk. Self-sensing homopolar magnetic bearing: Analysis and experimental results. In *Proceedings of the 1999 IEEE Industry Applications Conference - 34th IAS Annual Meeting*, pages 2560–2565, 1999.
61. S. Ueno et al. Position self–sensing control of an axial self-bearing motor. In *Proceedings of the Eighth International Symposium on Magnetic Bearings*, pages 299–304, August 2002.
62. V. M. G. van Acht, A. A. H. Damen, and P. P. J. van den Bosch. On self–sensing magnetic levitated systems. In *Proceedings of the Sixth International Symposium on Magnetic Bearings*, pages 538–547, August 1998.
63. D. Vischer and H. Bleuler. A new approach to sensorless and voltage controlled AMBs based on network theory concepts. In *Proceedings of the Second International Symposium on Magnetic Bearings*, pages 301–306, Tokyo, Japan, July 1990.
64. D. Vischer and H. Bleuler. Self–sensing active magnetic levitation. *IEEE Transactions on Magnetics*, 29(2):1276–1281, March 1993.

65. Jing Yang, Qinxiang He, and Huarong Zhang. Self-sensing position sensor of magnetic bearings. *Zhendong Ceshi Yu Zhenduan/Journal of Vibration, Measurement and Diagnosis*, 23(2):114 –, 2003.
66. T. Yoshida, Y. Kuroba, K. Ohniwa, and O. Miyashita. Self-sensing active magnetic bearings using a new PWM equipped with a bias voltage source. *European Power Electronics and Drives Journal*, 15(2):19 – 24, April 2005.
67. T. Yoshida and K. Ohniwa. A PWM amplifier for self-sensing active magnetic bearings with low-sensitivity to cable length. *Transactions of the Institute of Electrical Engineers of Japan, Part D*, 123-D(10):1206 – 12, October 2003.
68. K. Zhou, J. C. Doyle, and K. Glover. *Robust and Optimal Control*. Prentice-Hall, Inc., 1996.

16

Self–Bearing Motors

Yohji Okada

16.1 Introduction

Magnetic bearings can support rotors without physical contact [1]-[3]. This requires a separate driving motor in addition to the magnetic bearings, as shown schematically in Fig. 16.1. As a consequence, the rotor can become

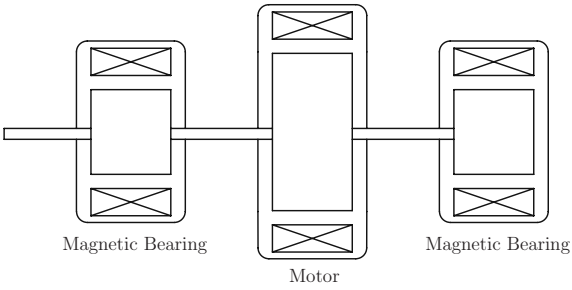


Fig. 16.1. Schematic of Motor with Magnetic Bearings

long and is apt to undergo bending vibration. The constructions of radial magnetic bearings and AC motors are similar. Hence, several types of self-bearing motors have been introduced which are a functional combination of a rotary motor and an active magnetic bearing [3]-[19]. A typical construction of a self-bearing motor and a conventional magnetic bearing is shown in Fig. 16.2. This means that the size of the system can be reduced, but the control becomes complex to realize due to the combined functions.

This type of research has started in the end of 1980 in Europe [4], [5], especially by Prof. Hugel's group in ETH, and was followed by Japanese researchers [6]-[11]. Such a system was first called a *bearingless motor* or *combined motor bearing*. In this book, we use the term *self-bearing motor*, because the motor itself has the function of bearing support capability. Recently, this

G. Schweitzer, E.H. Maslen (eds.), *Magnetic Bearings*,
DOI 10.1007/978-3-642-00497-1_16, © Springer-Verlag Berlin Heidelberg 2009

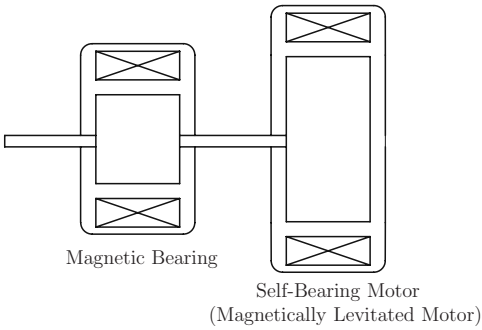


Fig. 16.2. Schematic of Magnetically Levitated Self-Bearing Motor

research has become very popular and is reported widely [12]-[19]. Recently, a similar introduction book of this type of motor was published and described in details [3].

The most common self-bearing motor uses two kinds of rotating magnetic flux: rotational control is achieved with the same pole number (P) of the rotor, while a pure drag force is produced by the plus two or minus two pole ($P \pm 2$) of the motor magnetic pole. The biggest problem with this type is the complicated control by using the two different rotating magnetic fluxes [4]-[8].

A simpler self-bearing motor is introduced which uses DC flux to control the radial force [9],[10]. The construction is a combination of a hybrid type active magnetic bearing (AMB) and a permanent magnet (PM) type AC motor.

The self-bearing motors described above use reluctance force to produce the bearing force which requires relatively thin permanent magnets. Hence the approach has the defects of low efficiency and poor reliability. Subsequently, the Lorentz type of self-bearing motor was developed. Both rotary torque and levitation force are produced by the Lorentz principle. The permanent magnets can be thick and the design has the merits of good dynamic response, good linearity and high reliability [11]-[13].

A simplest self-bearing motor is introduced which controls only the axial displacement and gives rotary torque. The construction is similar to a bi-directional disc motor except that this motor uses changes in the magnitude of the rotating flux to control the axial attractive force [14].

In this section, the construction and the simplified principles of all of the self-bearing motors described above are introduced. Their experimental results and characteristics are mentioned. One of the most important applications might be artificial heart pumps [15]-[24]. A centrifugal type blood pump is introduced and discussed. Recently, other applications of self-bearing motor to blowers and canned pumps have become commercially available [26], [27].

16.2 Self-Bearing Motor of the Type $P \pm 2$

The most common self-bearing motor uses a $P \pm 2$ design where P is the pole number of the motor. In addition to the motoring control of P pole flux, the $P + 2$ or $P - 2$ flux is used for levitation control which will increase the motoring flux on one side and decrease the flux on the other side to control the radial force [4]-[8].

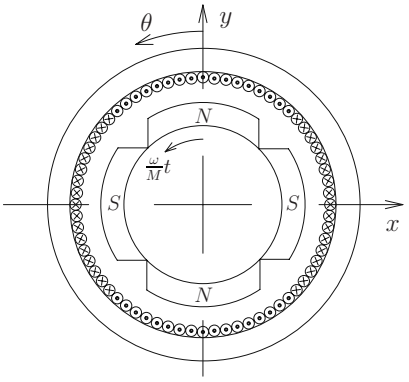


Fig. 16.3. 4 pole PM Motor and Coordinate System

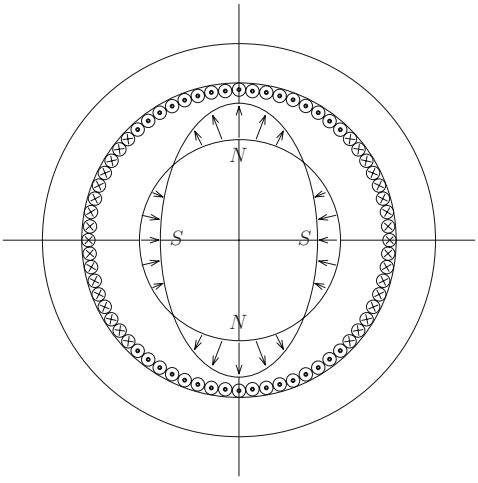


Fig. 16.4. Flux Distribution of 4 pole PM Motor

16.2.1 Structure and Principle

Consider a rotor with M pole pair number (pole number $P = 2M$) produced by permanent magnets (PM). The stator is assumed to have a current sheet which produces an arbitrary distributed magnetic flux. The case of $M = 2$ ($P = 4$) is shown schematically in Fig. 16.3.

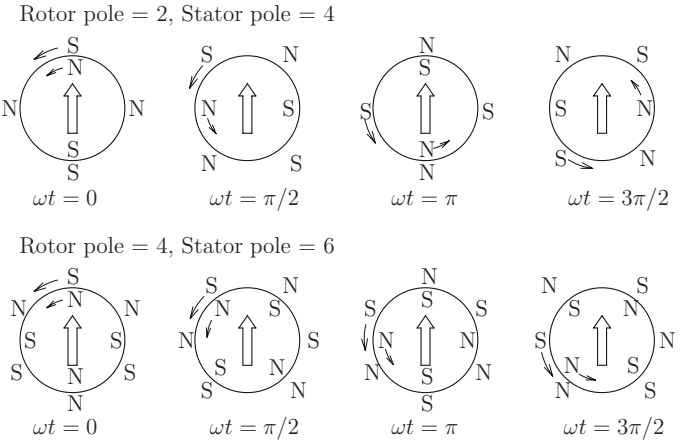


Fig. 16.5. Levitation Force with +2 Pole Algorithm

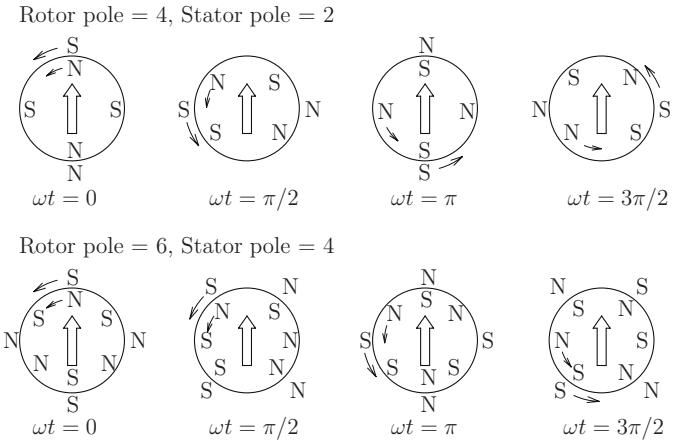


Fig. 16.6. Levitation Force with −2 Pole Algorithm

The PMs of the rotor are assumed to produce the following flux density:

$$B_r(\theta, t) = B_R \cos(\omega t - M\theta) \tag{16.1}$$

where B_R is the peak value of flux distribution which is schematically shown in Fig. 16.4. When the rotor is in the center of stator, the flux distribution and

the stator current is symmetric. Hence the radial force should be balanced. The stator is assumed to have the following current distribution to produce the rotating torque:

$$I_m(\theta, t) = -I_M \cos(\omega t - M\theta - \psi) \tag{16.2}$$

The rotating torque is controlled by changing the magnitude I_M or the angle ψ. In this chapter, the subscripts R or r mean the rotor, those of M or m indicate motor and those of F or f are radial force.

In addition to the torque control current of (16.2), a levitation control current is required. Let us consider the N pole pair current in the stator which gives the following magnetic flux:

$$B_f(\theta, t) = -B_{F1} \cos(\omega t - N\theta) - B_{F2} \sin(\omega t - N\theta) \tag{16.3}$$

where B_{F1} and B_{F2} are the peak densities of two components of flux distribution. Hence, the gap flux is the summation of (16.1) and (16.3) as

$$\begin{aligned} B &= B_r(\theta, t) - B_f(\theta, t) \\ &= B_R \cos(\omega t - M\theta) + B_{F1} \cos(\omega t - N\theta) \\ &\quad + B_{F2} \sin(\omega t - N\theta) \end{aligned} \tag{16.4}$$

This flux produces the radial attractive force ΔF over the infinitesimal area ΔS in the θ direction:

$$\Delta F(\theta) = \frac{B^2}{2\mu_0} \Delta S \tag{16.5}$$

By inserting $B = B_r - B_f$, the total levitation force in the $\theta = 0$ direction is given by

$$\begin{aligned} F_y &= \int_0^{2\pi} \int_0^L \Delta F(\theta) \cos\theta \\ &= \frac{B_R B_{F1} r L}{4\mu_0} \int_0^{2\pi} \Big[\cos\Big\{ (M - N - 1)\theta \Big\} \\ &\qquad + \cos\Big\{ (M - N + 1)\theta \Big\} \Big] d\theta \end{aligned} \tag{16.6}$$

Equation (16.6) becomes a constant force

$$F_y = \frac{\pi B_R r L}{2\mu_0} B_{F1} \tag{16.7}$$

when $M - N = \pm 1$. This solution is schematically shown in Fig. 16.5 ($P + 2$ pole algorithm) and Fig. 16.6 ($P - 2$ pole algorithm).

The x-directional force is calculated by integrating the x component of (16.5):

$$F_x = \frac{\pi B_R r L}{2\mu_0} B_{F2} \tag{16.8}$$

Hence, the two dimensional radial position of the rotor can be controlled by changing the magnitudes of B_{F1} and B_{F2}.

This theory can also be applied to induction type motors [6]. But the two different rotating fluxes cause poor efficiency and coupling between the $x-$ and $y-$ directional forces.

The merit of the self-bearing motor is to reduce the rotor size. But the theory uses a linear assumption for both flux and current. Usual magnetic materials have nonlinear characteristics for flux and current which causes some trouble or instability of the levitation control. Further, the sinusoidal flux distribution can only be approximated by the concentrated coils. Hence, one must use care in the design of self-bearing motors.

16.2.2 Experimental Results and Considerations

To test the capability of the self-bearing motor, a horizontal type experimental apparatus was constructed, as shown schematically in Fig. 16.7. The rotor was

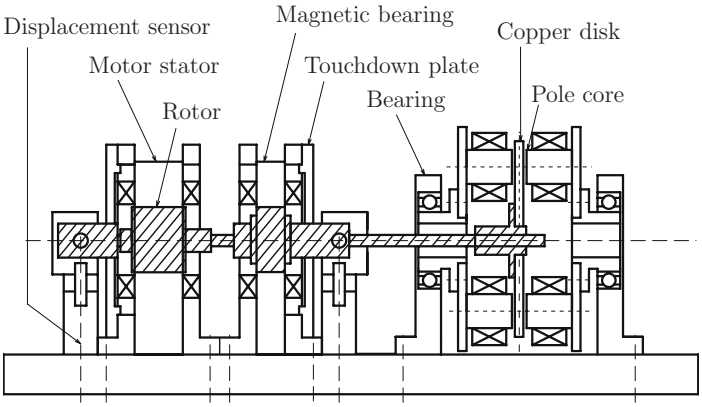


Fig. 16.7. Schematic of Experimental Setup

oriented horizontally. External torque is applied by an eddy current type brake system, while the gravity of the rotor is the radial load to the motor. The load side of the rotor shaft is supported by a standard magnetic bearing while the free end is housed with the proposed self-bearing motor.

The current sheet stator is approximated by an 8 salient pole stator with coil, the current of which is controlled by the power amplifiers individually. The rotor of the motor has a diameter of 40.3 mm and a width of 35 mm, while

the size of magnetic bearing differs only in the width of 25 mm. The average airgap is 0.8 mm.

The proposed motor is similar to the traditional PM synchronous motor. But the width of surface permanent magnet changes to approximate the sinusoidal flux assumption of (16.1). The stator current is the summation of two different frequency rotating fluxes; one is for motoring and the other is for levitation control, according to the previous theory.

The levitation and rotation is controlled by a digital signal processor (DSP: TMS320C40). The control system is shown in Fig. 16.8. Four gap sensors

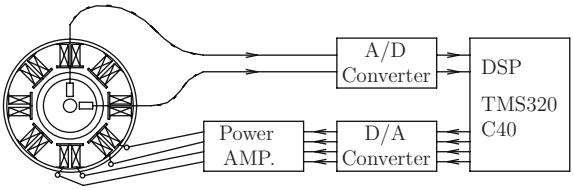


Fig. 16.8. Digital Control System

are installed to measure the $x-$ and $y-$ displacements of the rotor. Based on the measured gap displacements, the DSP calculates each coil current from the summation of the motoring current and the levitation control current. The stator levitation currents are approximated at the salient pole position according to the levitation theory of (16.7) and (16.8). The motoring current is approximated at the pole position and then the target leviation and motor currents are added and sent to the power amplifiers.

The levitation control algorithm is the standard PD controller:

$$G(z) = K_P + \frac{K_D(z-1)}{T_D\left(z - e^{-\tau/T_D}\right)} \tag{16.9}$$

where K_P, K_D and T_D are determined experimentally as $K_P = 2.0\,\mathrm{A/mm}$, $K_D = 0.007\,\mathrm{As/mm}$ and $T_D = 0.1\,\mathrm{ms}$. The sampling interval τ used is 0.1 ms.

Two PM rotors were built and tested: 2-pole and 4-pole ones. The stator can produce two rotating magnetic fields; 2-pole and 4-pole ones. Hence two types of experiments can be performed using 2-pole and 4-pole ones with the proposed $P \pm 2$ algorithm.

The combined control of levitation and rotation shows promising results. The levitated unbalance responses and the load torques are shown in Figs. 16.9 and 16.10. These experiments were performed by increasing the motoring field speed in increments of 50 r/min. After the rotor reached the steady-state speed, the vibration amplitude at the fundamental frequency and the load torque were recorded. The load torque increased with the rotating speed because it was added with the eddy current brake system. We could not identify any coupling between the torque control and levitation control. But

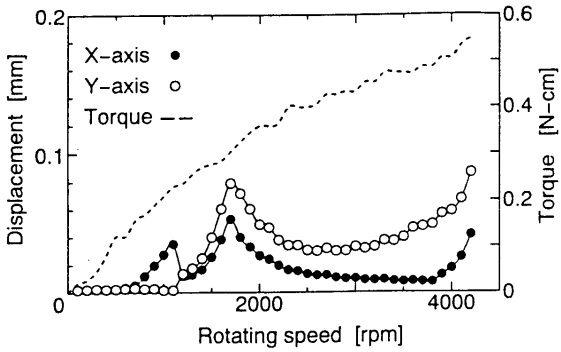


Fig. 16.9. Unbalance response and load torque (PM 2-pole motor, +2 algorithm)

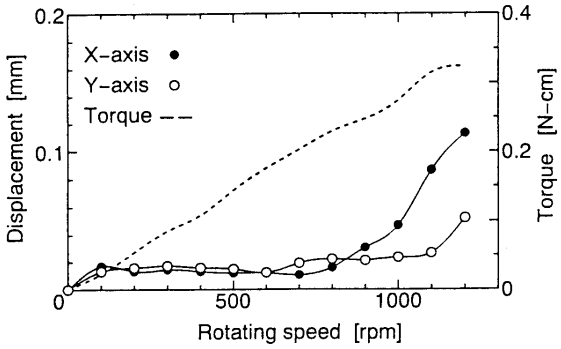


Fig. 16.10. Unbalance response and load torque (PM 4-pole motor, −2 algorithm)

the $x-$ and $y-$ directional levitation controls are coupled slightly. This seems to be due to the use of salient pole current which can only approximate the current sheet assumption in the theory.

In the case of $P + 2$ algorithm, the rotation and levitation control are stable. The maximum rotating speed reaches 4,200 r/min (Fig. 16.9).

In the case of $P - 2$ algorithm, the rotating torque is weaker. The resulting unbalance response is shown in Fig. 16.10, which indicates a relatively low maximum speed of 1,200 r/min compared to the previous cases of $P + 2$ algorithm. This is mainly due to the flux distortion of the stator which significantly degrades the results. If one can reduce the flux distortion, a higher torque and a higher top speed might be obtained.

16.3 Hybrid Type Self-Bearing Motor

Here, a simpler self-bearing motor is developed which uses DC flux to control the radial force [9],[10]. This is fundamentally a combination of the hybrid

type magnetic bearing and an AC motor. The standard hybrid type AMB has the bias permanent magnet between the two radial magnetic bearings.

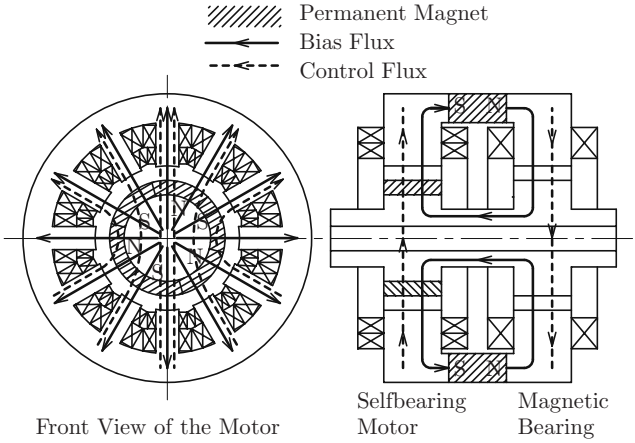


Fig. 16.11. Schematic of hybrid AMB type self-bearing motor

16.3.1 Structure and Principle

A schematic drawing of the hybrid type self-bearing motor is provided in Fig. 16.11. The side view indicates two components: the left side is the proposed motor, while the right side is the hybrid type magnetic bearing. A bias PM is installed between them which gives the bias flux, as shown by the solid arrow lines. The radial force is produced by controlling the coil current which produces the control flux, as shown by the dotted arrow lines. The flux on one side is increased while the flux on the other side is decreased by the control current to produce the radial force.

The front view indicates the construction of the proposed motor. The stator has two windings on each pole: one is the thick coils (bigger winding turns) and installed near the outer yoke, the inner one has thinner coils (smaller winding turns). This construction is used to increase the coil space efficiency. The pole coil pairs are connected in series and each pair is controlled by a digital signal processor through an individual power amplifier. The coil array is then controlled to approximate a sinusoidal distribution, producing the control flux indicated by the dotted arrow lines in the front view of Fig. 16.11.

Thin permanent magnets are glued on the surface of the rotor which gives a polarity of M pole pair number to the rotor. Motor coils are wound in the stator which produce the same pole pair number as the rotor. The electric angle difference between the stator current and the rotor position controls the rotating torque.

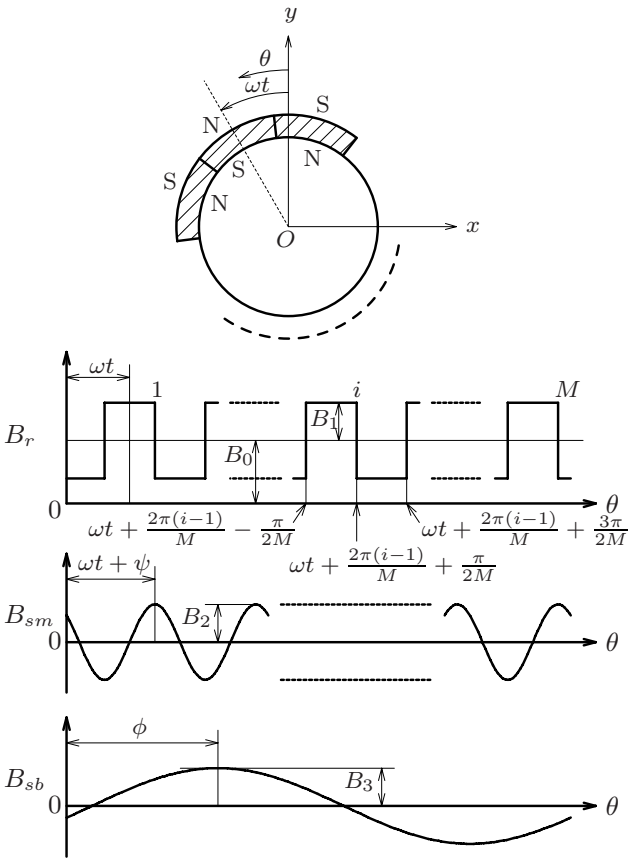


Fig. 16.12. Coordinates and Flux Distributions

The motor coordinate system and flux distributions are shown in Fig. 16.12. The stator is assumed to have a current sheet which produces arbitrarily distributed magnetic flux. The total flux distribution produced by PMs is indicated by the following equation and is shown schematically in Fig. 16.12:

$$B_r = \begin{cases} B_0 + B_1 \cdots \text{from } \left(\omega t + \frac{2\pi(i-1)}{M} - \frac{\pi}{2M}\right) \text{ to } \left(\omega t + \frac{2\pi(i-1)}{M} + \frac{\pi}{2M}\right) \\ B_0 - B_1 \cdots \text{from } \left(\omega t + \frac{2\pi(i-1)}{M} + \frac{\pi}{2M}\right) \text{ to } \left(\omega t + \frac{2\pi(i-1)}{M} + \frac{3\pi}{2M}\right) \end{cases} \tag{16.10}$$

The motor coil current produces the following flux distribution:

$$B_{sm} = B_2 \cos M(\theta - \omega t - \psi) \tag{16.11}$$

The radial force control flux B_{sb} is produced by the levitation coil current as:

$$B_{sb} = B_3 \cos(\theta - \varphi) \tag{16.12}$$

Then the total flux distribution B_g in the air gap is given by

$$B_g = B_r + B_{sm} + B_{sb} \tag{16.13}$$

The radial force dF is calculated as

$$dF = \frac{1}{2\mu_0} B_g^2 rld\theta$$

Hence, the $x-$ and $y-$ directional forces F_x, F_y are calculated by integrating the $x-$ and $y-$ components of dF over the entire gap in the θ direction [7].

The minimum pole number which guarantees the control independent condition for rotation and radial force is developed as $M \geq 3$, so that

$$F_x = \frac{B_0 B_3 lr\pi}{\mu_0} \cos\varphi \tag{16.14}$$

$$F_y = \frac{B_0 B_3 lr\pi}{\mu_0} \sin\varphi \tag{16.15}$$

That is, F_x and F_y are controlled by B_3 and φ, and is independent of both the rotor angle θ and the motor control.

In addition, the rotating torque T is controlled independently of the levitation control when $M \geq 2$:

$$T = -\frac{rlgMB_1 B_2 \pi}{\mu_0} \sin M\psi \tag{16.16}$$

That is, T is controlled only by B_2 and ψ.

16.3.2 Experimental Results and Considerations

Figure 16.13 shows the experimental setup. The left side is the proposed self-bearing motor, while the middle is the hybrid type magnetic bearing. For experimental simplicity, the magnetic bearing was not operated but was used as a bias flux source. The rotor was supported by a ball bearing at the right end. Hence the rotor had three degrees of control freedom; two in radial coordinates and one in rotation. All three degrees can be controlled by the proposed motor.

A ferrite permanent magnet was installed on the base plate to give the bias flux. On the surface of the rotor, thin permanent magnets (Neodymium magnets, thickness 0.8 mm) were glued to give polarity to the rotor. In the present example, a six pole configuration was selected. The diameter of the motor rotor part was 38 mm and the length was 35 mm.

The control system was similar to the previous case. The levitation control used was the standard digital PID controller.

$$G(z) = K_P + \frac{K_D(z-1)}{T_D\left(z - e^{-\tau/T_D}\right)} + \frac{K_I \tau z}{z-1} \tag{16.17}$$

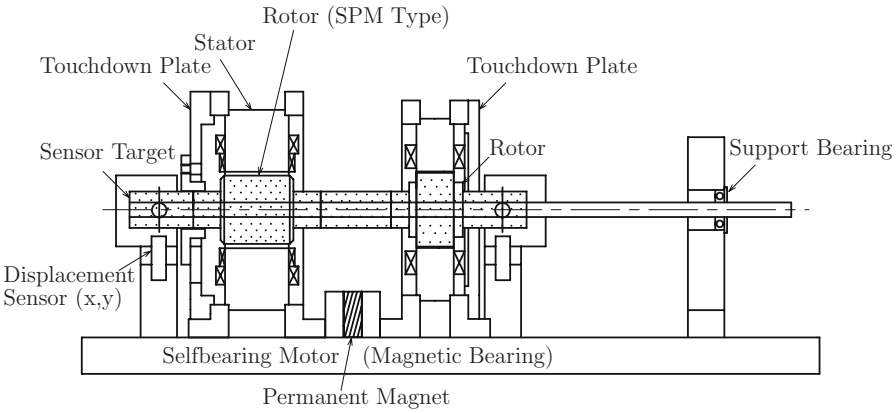


Fig. 16.13. Schematic of Experimental Setup

The values were determined experimentally as $K_P = 25$ A/mm, $K_D = 5$ A s/mm, $K_I = 0.2$ A/s mm and $T_D = 30$ ms. The sampling interval τ was 0.1 ms in this case.

The stator had 12 concentrated windings: each of them was controlled individually by a single digital signal processor (DSP: TMS320C40). Two gap sensors were used to measure the $x-$ and $y-$ displacements of the rotor. Based on the measured gap displacement, the DSP calculated each coil current from the summation of the motoring current and the levitation control current. Then they are fed to each power amplifier through a D/A converter. Hence, the target coil current distribution was approximated by the concentrated windings at that position.

The unbalance response was tested and the results are shown in Fig. 16.14. The rotor could run up to 4,400 r/min. By grasping the shaft, a strong ro-

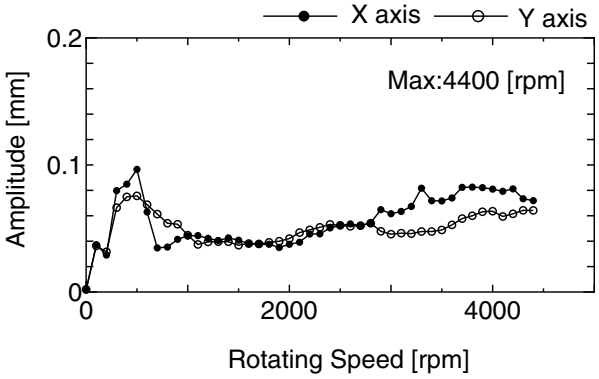


Fig. 16.14. Unbalance Response when the Motoring Current is 0.5 A

tating torque was felt. However, the top speed was limited due to the higher harmonics of the flux distribution produced by the surface permanent magnets.

16.4 Lorentz Type Self-Bearing Motor

A Lorentz type self-bearing motor is proposed which uses Lorentz force to produce motor torque and bearing forces [11]-[13]. This type can use thick permanent magnet to produce strong motor torque and levitation forces.

16.4.1 Structure and Principle

Figure 16.15 depicts the cross section of a cylindrical motor with eight strong permanent magnets mounted on the rotor and twelve coil windings: six for motoring and six for levitation. Now, consider a pair of facing motor coils.

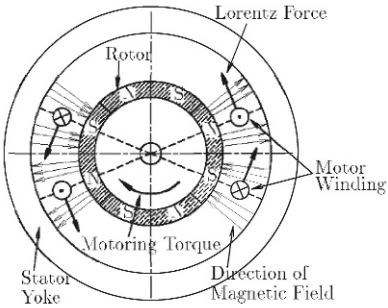


Fig. 16.15. Principle of Torque Generation

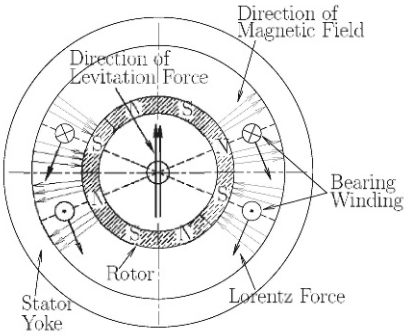


Fig. 16.16. Principle of Bearing Force Generation

The Lorentz forces exerted on the stator coils are aligned along the counterclockwise direction for the given current flow directions. The reaction torque for motoring the rotor is then produced in the clockwise direction.

The levitation coils are wound at the same circumferential location but the current flow direction of the right side is reversed, resulting in the Lorentz force vectors as shown in Fig. 16.16. The resultant force becomes a pure radial force. Six equi-angular spaced levitation coils can generate a radial force in any direction.

The expanded schematics with the slotted and the slotless stators are shown in Fig. 16.17. These figures show the radial motors unwrapped along

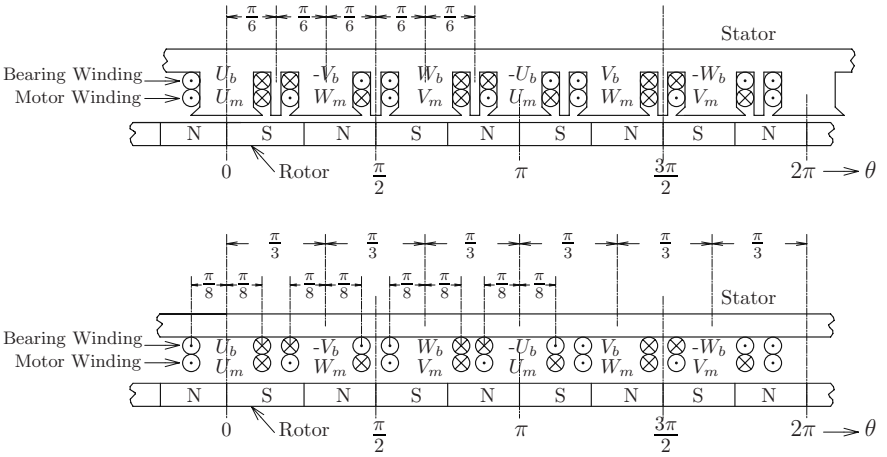


Fig. 16.17. Arrangement of Motor and Bearing Windings

their circumference. The entry and return paths of each of the coil windings are set to be $\pi/4$ apart. The U, V and W coils are placed $\pi/3$ apart.

Suppose that the air gap flux produced by the rotor PMs can be adequately approximated as

$$B_g = -B\sin(\omega t + 4\theta) \tag{16.18}$$

The motoring coils are driven by the three phase currents, i.e.

$$\begin{aligned} I_{U_m} &= A\cos(\omega t + \psi) \\ I_{V_m} &= A\cos(\omega t + \frac{2}{3}\pi + \psi) \\ I_{W_m} &= A\cos(\omega t + \frac{4}{3}\pi + \psi) \end{aligned} \tag{16.19}$$

From Fig. 16.17, the current distribution along the semi-circular stator part from $-\pi/8$ to $7\pi/8$ is written as

$$i_m = I_{U_m}\left[\delta(\theta + \frac{\pi}{8}) - \delta(\theta - \frac{\pi}{8})\right]$$

$$+ I_{W_m}\left[\delta(\theta - \frac{5}{24}\pi) - \delta(\theta - \frac{11}{24}\pi)\right] \tag{16.20}$$
$$+ I_{V_m}\left[\delta(\theta - \frac{13}{24}\pi) - \delta(\theta - \frac{19}{24}\pi)\right]$$

The torque produced can then be calculated as [11].

$$T = 2rl\int_{-\frac{\pi}{8}}^{\frac{7}{8}\pi} B_g i_m d\theta = 6rlAB\cos\psi \tag{16.21}$$

Note that the torque, independent of the rotor position and time, can be controlled by the motoring current magnitude A and phase ψ.

The levitation coils are driven by the three phase currents, i.e.:

$$\begin{aligned} I_{U_b} &= C\cos(\omega t + \varphi) \\ I_{V_b} &= C\cos(\omega t + \frac{2}{3}\pi + \varphi) \\ I_{W_b} &= C\cos(\omega t + \frac{4}{3}\pi + \varphi) \end{aligned} \tag{16.22}$$

From Fig. 16.17 and the current distribution expressed similar to (16.21), the levitation force can be calculated as [9]

y directional force

$$F_y = l\int_{-\frac{1}{8}\pi}^{\frac{15}{8}\pi} B_g i_b \cos\theta d\theta = \frac{3\sqrt{2+\sqrt{2}}}{2} BlC\cos\varphi \tag{16.23}$$

x directional force

$$F_x = l\int_{-\frac{1}{8}\pi}^{\frac{15}{8}\pi} B_g i_b \sin\theta d\theta = -\frac{3\sqrt{2+\sqrt{2}}}{2} BlC\sin\varphi \tag{16.24}$$

Equations (16.23) and (16.24) indicate that levitation of the rotor is achieved solely by the levitation coil control, independent of the rotation control. Note that the levitation force can be controlled by the levitation current magnitude C and phase angle φ.

16.4.2 Experimental Results and Considerations

Experiments were carried out in order to verify the theoretical development. The schematic of the experimental setup is shown in Fig. 16.18. The cylindrical inner rotor was vertically hung by a ball bearing, allowing the planar motion of the rotor in the $x-$ and $y-$ directions.

Rotating the levitated motor and recording the steady state vibration measured the unbalance responses. The results are shown in Fig. 16.19. The

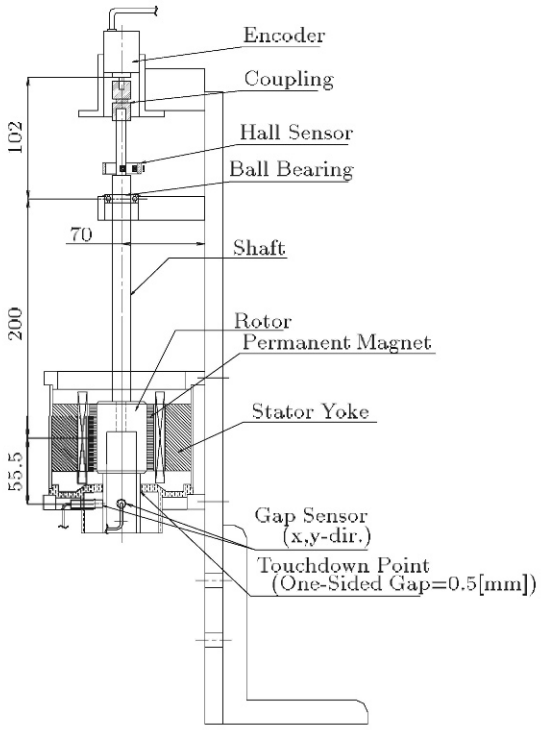


Fig. 16.18. Schematic of Experimental Setup

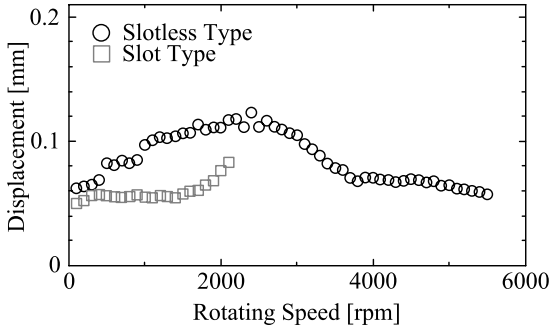


Fig. 16.19. Unbalance Response

highest vibration of the slotless type is recorded at 2400 r/min, which is considered to be the influence of the rigid mode. The top speed is restricted to 5500 r/min to avoid the centrifugal tear off of the permanent magnets, and can thus be improved by redesign.

The slot type motor can run up to 2100 r/min. Near this top speed, however, the levitation voltage approaches the supply voltage and the levitation becomes unstable. This is considered to be the result of the high inductance of the slotted coil leading to high Back-Electromotive-Voltage.

16.5 Axial Self-Bearing Motor

The axial type self-bearing motor has the merit of simple construction and control mechanisms [14].

16.5.1 Structure and Principle

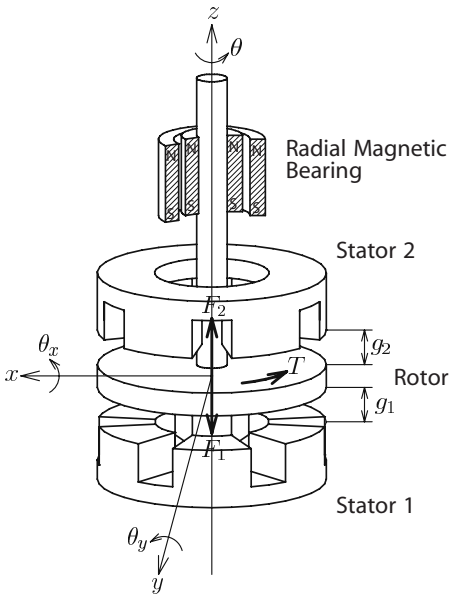


Fig. 16.20. Schematic of Bidirectional Axial Self-Bearing Motor

Figure 16.20 shows the schematic structure. It consists of two opposed stators and a rotor, which is similar to a bi-directional disc motor commonly used in disc drives. But here, the magnitude of the driving current for each

stator is controlled according to the rotor position. The radial direction should be stabilized by other methods (PM repulsion magnetic bearings are shown in the figure). On the upper and lower surfaces of the rotor, there are four PMs that are two N poles and two S poles by turns. Each stator has six cores with three-phase windings. The fluxes from the stator windings and the PMs produce the magnetic attractive force as well as motor torque.

Assuming that the magnetic flux density generated by PMs of the rotor is sinusoidal,

$$B_r(\theta, t) = B_R \cos(\omega t - 2\theta) \tag{16.25}$$

Similarly, the magnetic flux density generated by the stator windings is written as

$$B_s(\theta, t) = B_S \cos(\omega t - 2\theta - \psi) \tag{16.26}$$

With this, the single stator case leads to simple expressions of the axial force F and the motoring torque T as [12]:

$$F = \frac{A_r}{4\mu_0}(B_R^2 + 2B_R B_S \cos\psi + B_S^2) \tag{16.27}$$

$$T = \frac{A_r g_0}{2\mu_0} B_R B_S \sin\psi \tag{16.28}$$

Now, expand the axial force of (16.27) and the motoring torque of (16.28) to the bi-directional case. The peak value B_S of (16.26) can be written about the upper and lower stators as

$$B_{S,\text{upper}} = B_M + B_C \tag{16.29}$$

$$B_{S,\text{lower}} = B_M - B_C \tag{16.30}$$

With this, (16.27) and (16.28) produce

$$F_{total} = \frac{A_r}{\mu_0}(B_R \cos\psi + B_M)B_C \tag{16.31}$$

$$T_{total} = \frac{A_r}{\mu_0} B_R B_M \sin\psi \tag{16.32}$$

Note that, in this case, one can control the axial motion of the rotor without affecting the motoring torque.

16.5.2 Experimental Results and Considerations

To confirm the capability of the proposed theory, experimental apparatus was constructed and tested. The control system is shown in Fig. 16.21. For levitation, the axial displacement of the rotor measured by a proximity probe is

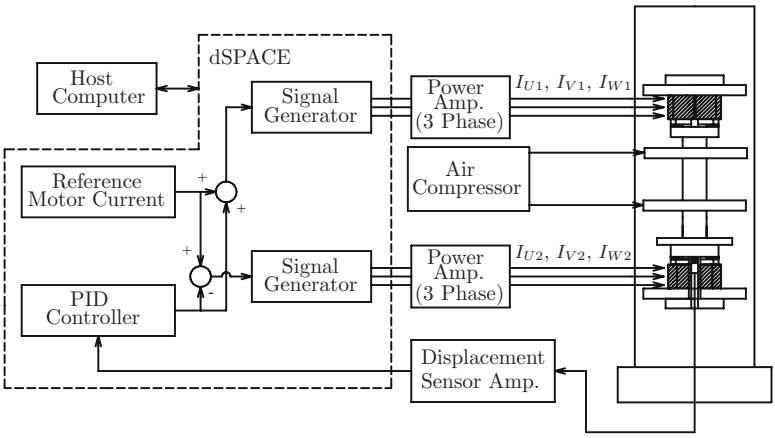


Fig. 16.21. Control System

provided to a DSP (dSPACE DS1103) via an A/D converter and the calculated controller output is added to or subtracted from the amplitude of the target motor current. Then, two sets of three-phase currents are generated and fed to the stators through a six-channel power amplifier. The levitation control uses a standard PD controller.

The dynamic torque was also measured for the single stator and rotor as shown in Fig. 16.22. The torque is maximum at the non-rotational condition and decreases with increasing rotational speed.

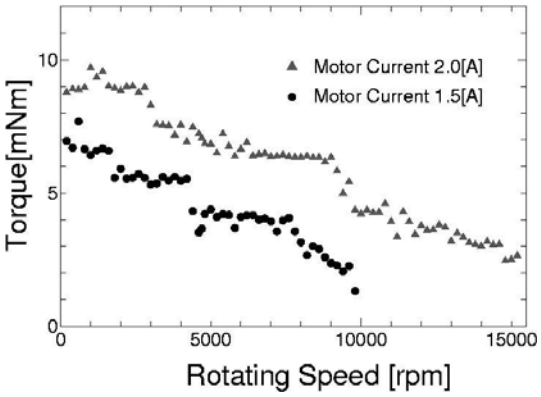


Fig. 16.22. Dynamic Torque

The levitated rotating test was carried out for this self-bearing motor in air. The unbalance response is shown in Fig. 16.23. Here, one can see that the levitation is very stable up to the top speed of 6,000 r/min. In this case, radial

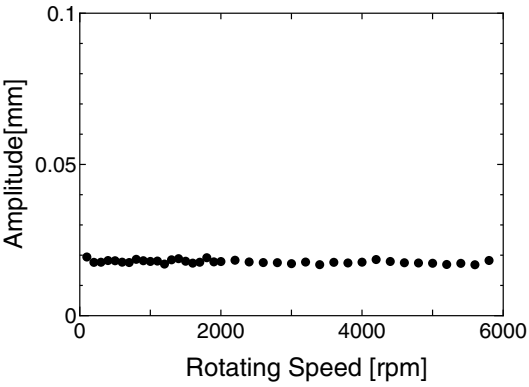


Fig. 16.23. Maximum Amplitude of Axial Displacement

air bearings were used to improve the lateral support capability. If a small radial bearing is necessary, these air bearings are replaced by other radial bearings, for example PM repulsion bearings as shown in Fig. 16.20.

16.6 Application to Artificial Heart Pump

The most important application of self-bearing motors is the implantable artificial heart pump [20]-[24].

16.6.1 Motivation

Heart transplant has become a popular medical treatment, but there are still significant problems. In particular, the number of donors is always far lower than the number of people with chronic heart disease in need of transplants. As a result, an implantable artificial heart is highly requested. Figure 16.24 indicates the schematic concept of this project. Already, the artificial blood pump is available in the hospital. With an implantable heart pump, the heart patient could return to normal social activities. A rotary blood pump is small and adequate for this purpose [25]. Experience using conventional (blood lubricated) bearings for such a pump suggests that the rate of hemolysis is excessive. Consequently, contact-less bearings may be more successful. A miniature magnetically levitated rotor is highly requested which can be implanted in the human body, which might be smaller than 80 mm in diameter and 60 mm in width.

The first magnetically suspended rotary pump was developed by Professor Akamatsu and Terumo, Co.[23]. It used a magnetic bearing and the rotary torque was provided by an AC motor with a ball bearing through a magnetic coupling. The canned rotor was levitated, but it used contact bearings outside the canned pump to support the motor. The first application of a self-bearing

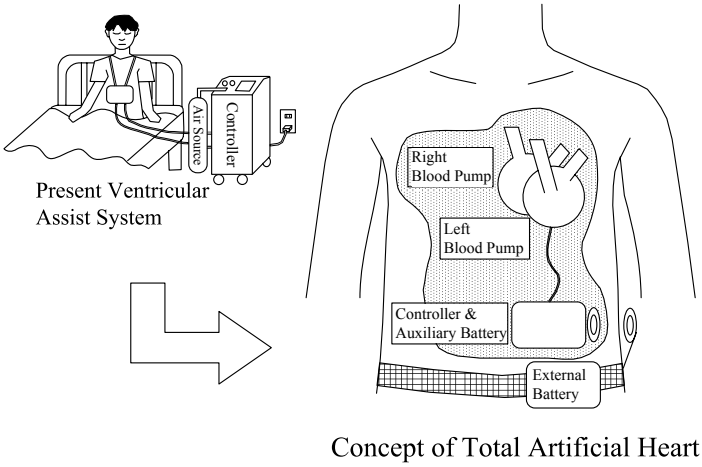


Fig. 16.24. Concept of Implantable Artificial Heart

motor to artificial heart was made by Schöb, et. al, [24]. Currently, the author's group is developing several types of maglev pumps.

16.6.2 Centrifugal Pump with Radial Motor

Figure 16.25 shows a magnetically levitated centrifugal pump with an outer rotor type self-bearing motor [20]-[22]. An impeller of the centrifugal pump with six open-type vanes (without back-shroud) was set on the rotor. The centrifugal pump has a double volute in order to minimize the fluid dynamic imbalance inside the centrifugal pump.

Figure 16.26 shows the radially suspended self-bearing motor. The outer rotor structure, in which the rotor surrounds the stator, was adopted to miniaturize the self-bearing motor. The rotor, which is a yoke itself, has four thin permanent magnets on its inner circumferential surface. The thickness of the permanent magnets is 0.7 mm. The outer diameter, the inner diameter and the thickness of the rotor are 63.4 mm, 53.4 mm, and 8 mm respectively. The stator has twelve radial poles. Each pole has a bulge at the end facing the rotor to distribute the magnetic field effectively and a narrow radial spoke to wind the coil wire. The diameter and the thickness of the prototype stator are 50 mm and 8 mm respectively. Rotation coils to produce a 3-phase 4-pole magnetic field and levitation coils to produce a 2-phase 6-pole magnetic field were constructed separately in the stator. The $P \pm 2$ algorithm was adopted to levitate and rotate the rotor. The radial gap between the rotor and the stator was set at 1 mm. A closed magnetic circuit was formed through the stator pole and the rotor yoke.

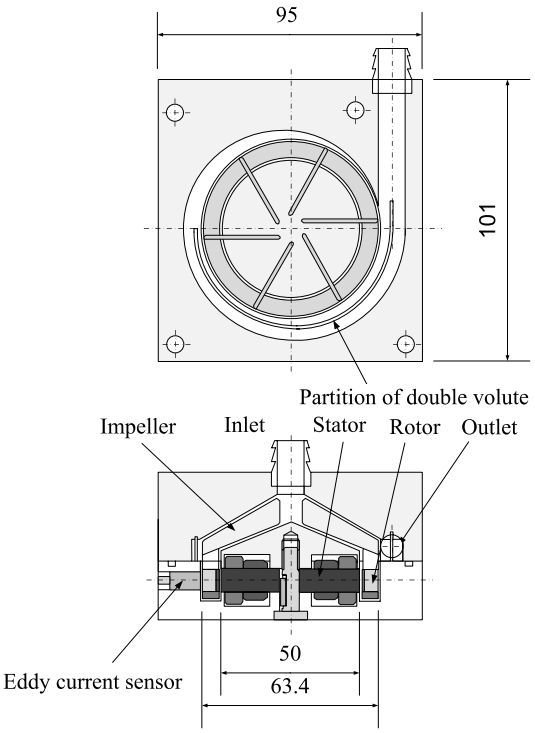


Fig. 16.25. Centrifugal Blood Pump



Fig. 16.26. Outer Rotor Self-Bearing Motor

Figure 16.27 shows a schematic view of the control system. Levitation and rotation of the rotor were controlled by a DSP. Two eddy current sensors were used to measure rotor radial position.

The pump performance and the total power consumption of the maglev pump are shown in Fig. 16.28 and Fig. 16.29, respectively. The levitated rotor could be rotated up to a rotational speed of 2400 r/min with pumping as in Fig. 16.28. The maximum flow rate and the maximum head pressure were 9.7 l/min and 313 mm Hg, respectively. The maximum total efficiency

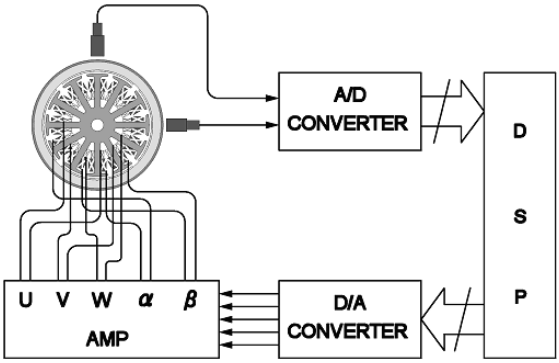


Fig. 16.27. Control System of Self-Bearing Motor

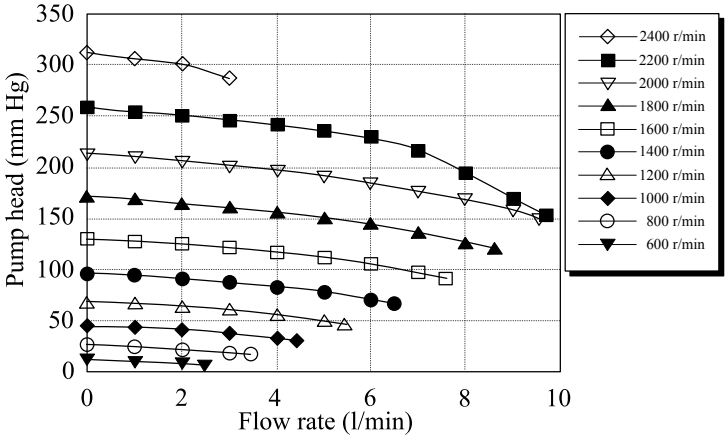


Fig. 16.28. Head and Flow Rate of Centrifugal Pump

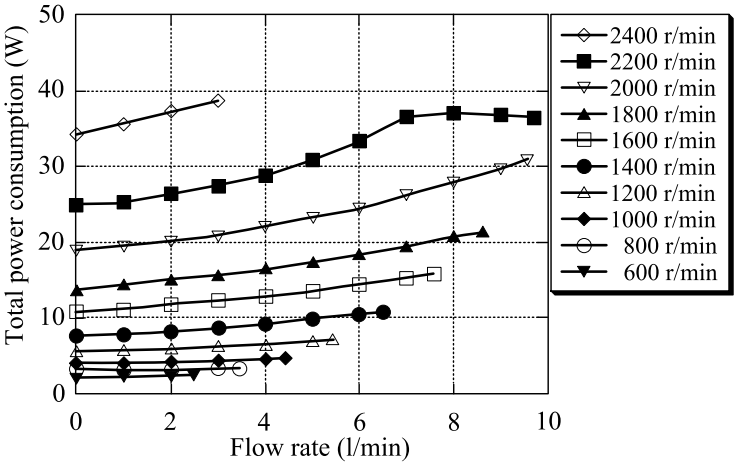


Fig. 16.29. Total Power Consumption

was 11 %. The input electric power and pump efficiency with a pressure head of 100 mm Hg and a flow rate of 5 l/min were 12 W and 9 %.

This system has been improved and the hemolysis test has been started. The results show low hemolysis formation.

16.7 Concluding remarks

Four types of self-bearing motors were introduced and their test results were explored. The data reported here are from the old experiments. The systems have already been improved. New types of self-bearing motor are also reported, for example [15]. The implantable artificial heart pump is one of the most important applications. A centrifugal flow pump is reported which is under development.

References

1. Y. Okada, et. al., JSME Publication on New Technology Series, No. 1, Magnetic Bearings - Fundamental Characteristics, Design and Applications, Yokendo Ltd., Tokyo, 1995, in Japanese (translated into Korean).
2. Schweitzer, G., et al., "Active Magnetic Bearings", Hochschulverlag AG an der ETH Zurich, 1994.
3. A. Chiba, et. al., "Magnetic Bearings and Bearingless Drives", Elsevier, 2005.
4. Bichsel, J., "Beiträge zum lagerlosen Elektromotor", Dissertation ETH Zürich, 1990.
5. Bichsel, J., "The Bearingless Electric Machines," *NASA Conf. on Magnetic Suspension Technology*, 1992, pp. 563-570.
6. Chiba, A., et. al., "Radial Force in a Bearingless Reluctance Motor," *IEEE Trans. Magnetics*, 27(2), 1991, pp. 786-791.
7. Okada, Y., et al., "Levitation Control of Permanent Magnet (PM) Type Rotating Motor", *Proc. of Magnetic Bearings, Magnetic Drives and Dry Gas Seals Conf. Exhibitions*, Alexandria, VA, USA, 1992, pp. 157-165.
8. Okada, Y., et. al., "Analysis and Comparison of PM Synchronous Motor and Induction Motor Type Magnetic Bearings", *IEEE Trans. on Industry Applications*, 31(5), 1995, pp. 1047-1052.
9. Okada, Y., et. al., "Hybrid AMB type Selfbearing Motor", *Proc. of 6th Int. Symp. on Magnetic Bearings*, MIT, Cambridge, 1998, pp. 497-506.
10. Kanebako, H, and Okada, Y., "New Design of Hybrid-Type Self-Bearing Motor for Small, High Speed Spindle", *IEEE/ASME Trans. on Mechatronics*, Vol. 8, No. 1 March 2003.
11. Okada, Y., et. al., "Lorentz Force type Self-Bearing Motor", *Proc. of 7th Int. Symp. on Magnetic Bearings*, ETH Zurich, 2000, pp. 353-358.
12. Stephens, L. S., and Kim, D.-G., "Force and Torque Characteristics for a Slotless Lorentz Self-Bearing Servomotor", *IEEE Trans. on Magnetics*, Vol. 38, No. 4, 2002, pp. 1764-1773.

13. Han, W.-S., Lee, C.-W., and Okada, Y., "Design and Control of a Disk-Type Integrated Motor-Bearing System", *IEEE/ASME Trans. on Mechatronics*, Vol. 7, No. 1, March 2002, pp. 15-22.
14. Ueno, S., and Okada, Y., "Characteristics and Control of a Bidirectional Axial Gap Combined Motor-Bearing", *IEEE/ASME Trans. on Mechatronics*, Vol. 5, No. 3, September 2000, pp. 310-318.
15. Takemoto, T., et. al., "A Principle and a Design of a Consequent-Pole Bearingless Motor", *Proc. of 8th Int. Symp. on Magnetic Bearings*, Mito, Japan, August 26-28, 2002, pp. 259-264.
16. Amrhein, W., Silber, S., Nenninger, K., Trauner, G., Reisinger, M., and Schöb, R., "Developments on bearingless drive technology", *Proc. of 8th Int. Symp. on Magnetic Bearings*, Mito, Japan, August 2002, pp. 229-234.
17. Cai, J., and Henneberger, G., "Radial force of bearingless wound rotor induction motor", *Proc. of 8th Int. Symp. on Magnetic Bearings*, Mito, Japan, August 2002, pp. 41-46.
18. Ming Chen, H., and Walter, T., "A rotor controlled magnetic bearing", *Proc. of 8th Int. Symp. on Magnetic Bearings*, Mito, Japan, August 2002, pp. 21-26.
19. Zhiquan Deng, Xiaolin Wang, Xiaoli Meng, and Yangguang Yan, "An independent controller of radial force subsystem for super-high-speed bearingless induction motors", *Proc. of 9th Int. Symp. on Magnetic Bearings*, Lexington, Kentucky, USA, August 2004, CD-ROM.
20. Masuzawa, T., et. al., "Magnetically Suspended Rotary Blood Pump with Radail Type Combined Motor-Bearing", *Artificial Organs*, Vol. 24, 2000, pp. 469-474.
21. Masuzawa, T., et. al., "Magnetically Suspended Centrifugal Blood Pump with an Axially Levitated Motor", *Artificial Organs*, Vol. 27, 2003, pp. 631-638.
22. Onuma, H., et. al., "Magnetically Levitated Centrifugal Blood Pump with Radially Suspended Self-Bearing Motor", *Proc. of 8th Int. Symp. on Magnetic Bearings*, Mito, Japan, August 26-28, 2002, pp. 3-8.
23. Nojir, C., Kijima, T., Maekawa,J., et. al., "Recent Progress in the Development of Termo Implantable Left Ventricular Assist System", ASAIO Journal, 45-3, (1999), pp. 199-203.
24. Schöb, R., Barletta, N., Fleischli, A., Foriera, G., Gempp, T., Reiter, H-G., Poirier V., L., Gernes, D., B., Bourque, K., Loree, H., M., and Richardson, J., S., "A Bearingless Motor for a Left Venticular Assist Device (LVAD)", *Proc. of 7th Int. Symp. on Magnetic Bearings*, ETH Zurich, 2000, pp. 383-388.
25. Allaire, P. E., Maslen, E. H., Kim, H. C., Bearnson, G. B., and Olsen, D. B., "Design of a Magnetic Bearing Supported Protopype Centrifugal Artificial Heart Pump", STLE Tribology Journal, 39-3, (1996), pp. 663-672.
26. Baumschlager, R., Schöb, R., and Schmied, J., "Bearingless hydrogen blower", *Proc. of 8th Int. Symp. on Magnetic Bearings*, Mito, Japan, August 2002, pp. 277-282.
27. Bösch, P. N., and Barletta, N., "High power bearingless slice motor (3-4kw) for bearingless canned pumps", *Proc. of 9th Int. Symp. on Magnetic Bearings*, Lexington, Kentucky, USA, August 2004. CD-ROM.

17

Micro Magnetic Bearings

Hannes Bleuler

17.1 Introduction to micro magnetic actuators and their down-scaling

A micro magnetic actuator is any device based on magnetic effects to achieve mechanical actuation. The meaning of the word "micro" depends very much on context. Let us call such an actuator "micro" when the magnetic part of the actuator proper, i.e. without electronics, is confined to sizes typically measured in micrometers and up to a maximum of about one or two centimeter in overall size. This includes mm and sub-mm actuators and MEMs devices (definition see below) based on magnetic effects. Larger actuators are treated in other chapters. After an introduction to downscaling of magnetic actuators, this chapter will concentrate on micro magnetic bearings. There are, up to now, only very few examples of realizations: all are purely experimental systems, but there is a number of potential applications to be explored once the basic issues will have been resolved.

17.1.1 MEMS

"MEMs" stands for "Micro Electro Mechanical Systems" and designates essentially devices fabricated by technologies developed for microelectronics, and ICs. Technologies such as photolithography, chemical or ionic etching, sputtering, vapor deposition, screen printing, LIGA etc. all typically are MEMS technologies. Materials include silicon, other metals and semiconductors, oxides and nitrides, polymers, glasses, ceramics etc. A MEMS device combines some electronics with a mechanical component, i.e. certain parts should be in mechanical motion, as opposed to purely electronic devices. Examples are integrated miniaturized accelerometers (as used e.g. for the deployment of airbags in cars), integrated pressure transducers or micro pumps used in microfluidic devices for chemical analysis of very small quantities of reactants or for localized drug delivery.

G. Schweitzer, E.H. Maslen (eds.), *Magnetic Bearings*,
DOI 10.1007/978-3-642-00497-1_17, © Springer-Verlag Berlin Heidelberg 2009

17.1.2 Some potential application fields of micro magnetic bearings

- gyroscopes
- rotating mirrors
- beam choppers
- spinning vacuum gauges
- micromachining
- micro turbines

17.1.3 Often underestimated: The potential of micro magnetic actuators vs. electrostatic actuators

It is commonplace to state that electrostatic actuators are greatly favored over magnetic actuators when it comes to microsystems. The argument essentially states that electrostatic forces scale down with the square of length because they are proportional to surface. Magnetic forces are assumed to scale down with the third power of length as they are, so it is claimed, proportional to volume. Therefore, there is a crossover to be expected. This crossover is generally situated in the mm order of magnitude. It is not evident to define the models and the hypotheses involved in a computation of this supposed "crossover point". The argument is supported by the fact that there are no large mechanical actuators based on electrostatic forces. MEMS devices on the other hand, rely to a great majority on electrostatic effects, a few on piezo effects and indeed very few only on magnetic effects. Does this alone support the argument against micro magnetic actuators? A careful analysis reveals that the commonplace argument banning magnetic actuators from the micro world does not stand so strongly. It will be shown in the following sections that magnetic actuators in general, and in many cases even electromagnetic actuators promise superior performance as compared to electrostatic actuators. There are several reasons why this is not yet generally recognized:

1. The fabrication of electrostatic actuators is relatively straightforward in the context of production technologies for microcircuits and, by extension, for MEMS. A large workforce of engineers and scientists is familiar with these technologies and their expensive equipment. Ferromagnetic materials do not fit into this production technology and are exotic to many processes. Microelectronics production equipment is very sensitive to unusual materials, it is easily "polluted" and this reinforces the tendency to favor processes with the usual material. This point has strongly played in favor of electrostatic actuators for MEMS, which can be easily produced in silicon.
2. The comparison is often carried out for the interaction of capacitor plates versus current carrying leads. As we will see, this is the least favorable configuration for magnetic actuators, the use of ferromagnetic material or permanent magnets greatly improves the efficiency of magnetic actuators.

3. Constant current density is usually assumed when scaling down electromechanical systems. However, in accordance with physical considerations and as proven by realizations of magnetic microsystems, current densities may significantly increase with downscaling.

The following estimate of what is achievable is freely translated from "Micro-actionneurs électromagnétiques" [4]:

> Let us compare the energy density in the respective fields for macroscopic arrangements. An electrostatic field of 3 MVm^{-1} is about what is achievable in usual configurations and ambient conditions, as is a magnetic flux density of 1 T. This gives an energy density respectively 40 Jm^{-3} for electrostatic actuation and an energy density of 400000 Jm^{-3} for magnetic actuation. This difference of four orders of magnitude is the reason why electrostatic actuation is not present on macroscopic scale. This advantage remains effective down to sizes of about 10 μ. Below this size, the breakdown field strength increases, so that effectively electrostatic actuation starts to look more advantageous. Jack W. Judy from UCLA [6] locates the crossover at 50 nm.

When the crossover actually takes place depends so strongly on the practical example at hand and on available fabrication technologies that the answer will, at any rate, vary widely from case to case.

One of the reasons why magnetic actuators have such a strong potential is the use of *ferromagnetic material*. If such material is used, the magnetic energy will essentially be present in the air gap. This principle is fundamental for macroscopic magnetic actuators and it remains so for micro actuators. Therefore, we may expect further development in magnetic micro actuators as we will learn microstructuring technologies to work with ferromagnetic materials.

Specifically, it can be shown that force per mass increases in inverse proportion to the down-scaling factor. This opens up fields of applications not possible for macro magnetic bearings.

Under the same assumptions, eigenfrequencies can be shown to behave in the same way, i.e. to increase in linear proportion with the downscaling factor.

17.1.4 Down scaling of electromagnets

For practical reasons such as manufacturing accuracy, the copper wire in a downscaled electromagnet will become relatively thicker and the air-gap will become relatively larger. For similar reasons, the number of poles will also be diminished. This means that leakage flux will increase and the specific force (expressed as a pressure) will go down from the roughly 40 $\mathrm{N/mm}^2$ of macroscopic systems. Specific power in terms of effective power per volume will decrease, the coils, isolation and other unutilized space will all take up proportionally more space. This decrease in efficiency is initially not noticeable. But below an order one or two cm, the effect becomes gradually more

pronounced, i.e. a milimeter size bearing will have an air-gap not much smaller than a cm-size one. However this loss of efficiency at small size is outweighted by the reduction of volume-specific forces (inertias, mass) with the third power of linear scale. Therefore an electromagnet will rapidly increase in effectiveness for the task of interest, levitating a body, when scaled down.

17.1.5 Downscaling of contact-free bearings

After this general introduction to micro magnetic actuators, let us look more specifically at some effects of downscaling bearings. The word "bearing" means guidance for rotational motion, (in some cases also linear motion), the guidance force being "contact free" (avoiding solid-solid contact).

Scaling laws imply that rotational speeds increase with smaller dimensions, whether it be for constant power density, for constant surface velocity or for constant centrifugal stress. At the same time, surface related effects such as friction and wear also increase with smaller scale. *These two facts taken together make a very strong point for contact free bearings at small dimensions.*

The potential of AMBs in this domain has by far not yet been realized. This chapter will analyze the basics of miniaturized AMBs, "micro magnetic bearings". We will cover in this chapter a range of devices from a few watts of power down to microsystems (MEMS), i.e. down to sub–mm dimensions.

Higher rotational speed means increased performance for many industrial products, be they machine tools, gyroscopes or hard disk drives. Classical products are spindles, turbines for compact devices like scanners, gyroscopes, centrifuge units and so on. Often the bearings are the one component limiting rotational speed. The key to achieving high rotating speeds is therefore to achieve contactless operation. Active magnetic bearings (AMBs), gas bearings or passive magnetic bearings are possible choices. Gas bearings are not vacuum compatible. Rotational speed is limited through viscous friction for small high-speed devices. Passive magnetic bearings on the other hand have the drawback of very low damping for radial motion. We will therefore in a first step concentrate on AMBs, but also include some sections on other contact-free micro bearing types.

High rotational speed

The maximum rotating speed achieved ever reported was obtained in 1946 by J. Beams [2]. A 0.795 mm diameter steel rotor of spherical shape reached the speed of 23.16×10^6 rpm in high vacuum conditions (10^{-5} Torr, 1.333×10^{-8} bar) and exploded under centrifugal stresses. This corresponds to a circumferential speed far higher than what could be expected from available material properties. This effect is due to a different stress limit for very small samples as compared to "bulk" materials. This setup is shown later in the section 17.5.

Some of the key points to be considered for a high speed motor are:

1. During high speed rotation, high centrifugal loads arise in the rotor. The yield strength of the rotor material limits the maximum achievable speed without rotor plastic deformation. An optimized geometry and a minimum size of the rotor can reduce the stresses inside the rotor and therefore a higher speed can be reached. This is described in more detail in [3].
2. As to the induction motor, the iron losses are increased with the operational speed, hence a high resistivity magnetic circuit is needed and magnetic cores should have low hysteresis.
3. Windage losses increase with the square of the speed. Therefore, the system will have to be operated in vacuum.
4. Mechanical losses are the result of vibrations induced by the interactions between the rotor and the stator. An effective suppression of vibrations when the rotor passes critical speeds reduces mechanical losses and therefore higher rotational speeds can be reached.

Rotor Stress under Centrifugal Load

The absolute limit to high rotational speed is the centrifugal load on the rotating solid. We will limit ourselves to the analysis of isotropic materials. For 2-D and 3-D stresses, the Tresca criterion and the von Mises criterion can are used respectively to predict ductile material failure. For the following calculations (3-D) the von Mises criterion is applied. The main results for spherical and cylindrical rotors are as follows

- spherical rotors
  In this case, the maximum stress is at the center of the sphere
- cylindrical rotors
  The points of maximum stress in this case are at the center of the flat faces of the cylinder

The stress is always proportional to the square of the highest surface velocity and to the rotor density and to a constant K depending on rotor shape and Poisson's ratio [3]. The higher the shape factor, the higher rotor stress. Calculation of stress for different shapes gives the following results: Sphere 0.427, Disk (L/r=0.1) 0.413, (L/r=1) 0.431 (L/2=2) 0.395, (L/r=10) 0.391. It can be seen that the rotor shape has a comparatively modest influence; material properties (crystalline structure) dominate.

Using the classical elastic yield strength limit for bulk material gives the following top circumferential speeds for spherical rotors: 480 m/s for steel and 1160 m/s for carbon fiber composite. It is seen that, in theory, composite material is much better (by a factor of the order of two) than bulk material, for any rotor shape. For microrotors, i.e. roughly below the 1mm diameter order, the theory does not apply anymore because the micro crystalline structure of the material (grain size) violates the assumption of homogenous bulk material;

the text-book value for maximum yield stress is no more valid. The maximum permissible stress increases by a factor of about two and comes into the range of composite materials. A "thin-film" value is available from literature [1], bringing a steel rotor into the carbon fiber composite range of over 1000 m/ circumferential speed.

Jesse Beams reported a circumferential speed of this order of magnitude in his famous 1946 paper, where he reached 23 Million rpm for a rotor below the mm diameter, i.e. well above the yield stress limit of 'macro'-sized bulk steel.

Potential applications of very high speed rotation are various and range from micro-machining and milling to gyroscopes, beam choppers and micro turbines to information storage, optical (high–speed cameras), vacuum and high precision equipment. Flywheels or momentum wheels are another potential application area of these considerations on stress under high rotational speed, although in these cases dimensions would rather be in the cm order than in the mm order.

The large range of new issues to be addressed in this context is highlighted through a reassessment of the basic working principles of contact-free bearings in view of down scaling. The first observation concerns the relation of aerodynamic and aerostatic bearings on one hand and "true" contact-free bearings on the other hand ("true contact–free" meaning essentially magnetic and electrostatic bearings).

17.1.6 Aerodynamic effects for micro rotors

Down–scaling implies a massive change of the Reynolds number. The viscosity of air, which has been (almost) always neglected for large scale magnetic bearings, becomes an essential parameter for micro bearings. Unless in high or very high vacuum, aerodynamic effects will not be neglectable. The application of spinning rotor vacuum gauges illustrates well how dominant the viscous forces of gases become, even at high vacuums, as soon as the rotor size gets down to the cm or mm order. For smaller rotors, these effects will be even more dominant and a spinning rotor gauge for UHV in MEMS technology seems a very realistic application.

Friction losses due to rotation

Aerodynamic effects on the rotor will thus increase dramatically with down–scaling. Viscous friction losses due to the rotation and damping of rotor motion in the other five degrees of freedom are most affected. (Another aerodynamic effect which could become important is non–conservative stiffness). As the scale goes down, viscous friction will limit the rotational speed of microrotors well before centrifugal stress becomes critical. Because the driving torque generated by a micro induction motor is limited, very high rotational speed is obtainable only in high vacuum. The design of such a system for a 3 million

RPM motor will be described in Sec. 17.5, which also gives indications on achievable performance.

Aerodynamic damping

The other effect of air viscosity, the damping of oscillatory motion, is rather helpful for micro rotors as it helps to stabilize rotor position. The damping could be so strong that small micro bearings could eventually be designed with stiffness only, the damping being left to the residual viscous effects of the medium. At ambient atmospheric pressure, aerodynamic damping manifests itself noticeably already for a rotor size of a few mm; the effect grows fast as size decreases. It depends on the ratio of inertia vs. air gap geometry; therefore it is not possible to give a general value of the strength of the effect. To our knowledge, no systematic attempt to utilize and optimize this damping effect has yet been published. This topic could be of interest for research.

For the remainder of this chapter, attention now shifts to "true" non–contact forces, i.e. ferromagnetic, diamagnetic and electrostatic forces. As a conclusion to what has just been treated, one should however keep in mind that down scaling implies increasing aerodynamic effects, essentially losses of rotational energy and damping of vibrational (radial and thrust) motion. These effects can therefore become significant, even at low or very low pressures (rotational vacuum gauges!). The motion of small levitated objects is essentially subject to all three effects simultaneously, aerodynamic, electrostatic and magnetic and can usually not be reduced to one dominant effect alone, as in the macroscopic case.

Thus the down-scaling implies that electrostatic and diamagnetic forces, completely negligible for macroscopic bearings, become important. The classification of magnetic bearings of Chap. 1 needs to be revisited here under this new aspect. The classification presented in the introduction describes the eight technological types of magnetic bearings. In that context, diamagnetic levitation seemed uninteresting because of the weak forces.

17.2 Classification of magnetic bearing types

All magnetic bearings fall into one of six categories according to the physical principle of levitation, as outlined in Fig. 17.1. The origin of magnetic phenomena are moving charges. The effects of special relativity on moving charges are described as magnetic effects. The prime source of magnetic force is therefore the Lorentz force which can be considered as a relativistic correction of electrostatic effects due to the motion of charges. For many applications, such as voice coil actuators, the Lorentz force law can be applied directly. If the structure of electron shells is involved, engineers have found a simplified way of describing the resulting forces through diamagnetism, ferromagnetism and paramagnetism. A given material is characterized by a scalar constant, the

permeability μ . In this case, forces are not computed directly with the Lorentz force law, but indirectly over the energy stored in the magnetic field. These two ways of obtaining magnetic forces differ fundamentally and are therefore the basis of the classifications in this book.

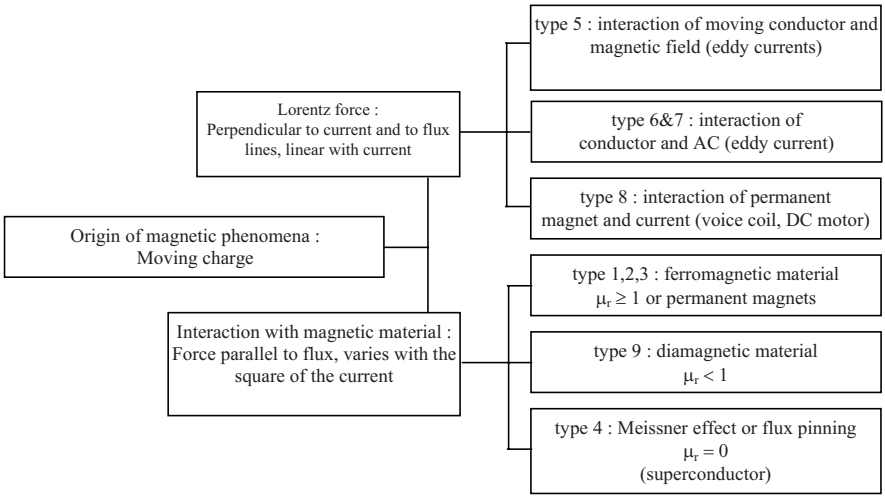


Fig. 17.1. Magnetic force taxonomy with the same bearing types as in Chap. 1

Magnetic force can be computed in two basically different ways: as Lorentz force, it is a cross product perpendicular to magnetic flux, linear with the current. It acts on the current carrier: no ferro-magnetic materials are involved in this case. If ferromagnetic materials are present in the field, the force is computed through derivation of the field energy. In this case, it is parallel to the flux line and perpendicular to the surface of the ferromagnetic material. These two situations form a first distinction into two groups of magnetic actuators in the classification chart.

Each of these two groups is subdivided into different magnetic bearing types. In the Introduction (Chap. 1), these bearing types have been defined according to technical criteria. Here, these types are regrouped according to more basic physical considerations. This highlights a new bearing type, which has been dismissed as uninteresting from a purely technical viewpoint. The grouping of the magnetic bearing types is illustrated in the chart above and results in the following six categories:

Type 5 Interaction of a moving conductor in a magnetic field. The eddy current induced when the conductor experiences a change of magnetic flux will be subject to the Lorentz force. This type of levitation is applied e.g.

for the Yamanashi Shinkansen test vehicle of the superconducting Maglev train (having surpassed 500 km/h). The permanent magnetic field is on the vehicle generated by superconducting magnets, the eddy current is in the track (nullflux system). This vehicle levitates at speeds above ca. 100 km/h; it needs a "landing gear" for low speeds and standstill.

Type 6 & 7 Interaction of a conductor and a changing current. An example is the famous "jumping ring" experiment or the levitation of a molten metal droplet. The heating is the result of the induced eddy currents, which illustrates that this type of bearing is not energy efficient.

Type 8 Interaction of the field of a permanent magnet and a conductor. This is the classical voice coil actuator, it can be used for an active magnetic bearing, e.g. in self bearing motors (sometimes called "bearingless").

Basically different are the next three types of magnetic bearings where force is parallel to the flux lines. They are:

Type 1, 2, 3 This class contains all bearings with ferromagnetic materials, i.e. both those where the material is attracted by an electromagnet or by a permanent magnet. In this category, we have over 90 percent of all magnetic bearings. They are based on attractive force and are usually actively controlled for stabilization, although there are a few exceptions.

Type 9 Diamagnetic bearings are based on the diamagnetic effect of materials such as bismuth or graphite. This bearing type is newly introduced here: it was not classified in the Introduction chapter. The effect is weak, therefore applications will be limited to small masses or to the stabilisation of passive type 3 bearings where the weight is compensated by attractive permanent magnets. An example will be presented below. This type of inherently passively stable magnetic bearing is well suited for microsystems as the small mass of sub-mm size rotors can easily be supported by such bearings. The structure of the bearing is extremely simple: essentially diamagnetic material will be pushed out of a magnetic field. Configurations of permanent magnets to obtain stable levitation are given below.

Type 4 Bearings are based on superconducting materials. The levitation effect is either (more commonly) flux pinning (with bulk high temperature superconductors) or also the Meissner-Ochsenfeld effect (low temperature superconductors of high purity). This effect is essentially due to the relative permeability of zero of superconductors. It is a kind of strongly amplified diamagnetic effect. A magnetic bearing system based on high temperature superconductors has been presented by Siemens in 2005 and 2006, this system is already close to industrial application. [8]

17.3 Diamagnetic rotor bearings

The "vanishing" of gravity with down-scaling opens up the diamagnetic bearings as fully equivalent in potential to the other five principles of levitation.

We have realized several prototypes of such bearings which will be described in Sec. 17.3.2 and we believe that the potential of this bearing type for technical application is wide and as yet absolutely untapped.

Realization of six electromagnetic coils with iron cores all acting on a small (let's say sub-cm size) rotor is difficult, at mm size or below it becomes practically impossible, simply for geometric reasons. This fact poses a basic limitation on the down-scaling of "macro" magnetic bearings, even more fundamental than the scaling laws of physical forces, i.e. the cross-over of surface effects over gravity. Because the air gap is relatively large compared to the rotor and because the coils have to be placed relatively far from the rotor, simply to have enough room for them, leakage flux will become huge for micro magnetic bearings. Only a small fraction of total flux will be efficient if we simply try to downscale "conventional" active electromagnetic bearings.

For similar reasons, many arrangements of passive or semi-passive bearings, which seem rather exotic at macro-size, become interesting for micro bearings.

17.3.1 Basics

The two most interesting materials suited for diamagnetic levitation are bismuth and graphite. Bismuth is familiar because it has long been used for demonstrations of the diamagnetic effect in physics classes. Less familiar is that graphite has a diamagnetic effect just as strong as bismuth, provided it is oriented. The graphite of your pencil is not oriented and will therefore not float above a strong permanent magnet. A chip of pyrolithic graphite will do the trick, because the layers are then oriented. Although it works very well, we will not need the high purity and homogeneity of Highly Oriented Pyrolithic Graphite (HOPG) as it is widely used in surface physics experimentation (e.g. as test sample for STMs). Simple pyrolithic graphite is therefore a relatively cost-efficient way, together with a set of Nd-Fe-B magnets, to demonstrate diamagnetic levitation.

17.3.2 PM arrangements for optimal diamagnetic bearings

With a simple permanent magnet, it will not be possible to obtain stable levitation as the potential surfaces of the magnetic field are convex. A diamagnetic object will be pushed out in direction of the field gradient towards weaker field, i.e. away from the magnet. In order to avoid radial escape, a kind of a potential trough has to be formed. This can be achieved e.g. with an axially magnetized ring-shaped permanent magnet. If the inner ring diameter is sufficiently large in ratio to the outer diameter, a potential well will appear in the ring axis. A piece of pyrolithic graphite up to half a millimeter thickness will easily float over such a magnet, provided it is a rare earth magnet (ferrite magnets are usually too weak except for very small pieces of diamagnetic material)

The effect can be amplified for a given volume of magnetic material by arranging the magnets in arrays. The arrays can have a 1-dimensional periodicity (in bands) or a 2-dimensional one, see Fig. 17.2

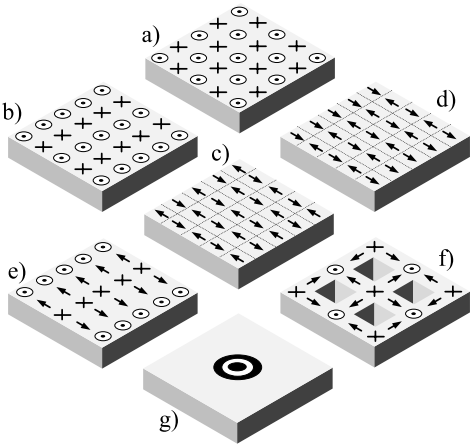


Fig. 17.2. Possible magnet arrays for diamagnetic levitation. a) Opposite 2D, b) Opposite 1D, c) Repulsive 2D, d) Repulsive 1D, e) Halbach 1D, f) Halbach 2D, g) Reference

For each of these, the repetition pattern can simply be N-S-N-S or Hallbach. The 2-D Halbach arrangement will not cover the plane: it will have 'holes'. Nevertheless, this last arrangement seems the most efficient one, i.e. the one providing the strongest levitation force for a given stator size. There is just one drawback of Halbach arrays: They need strong bonding or other fixation for the individual magnets as they repel each other forcefully and thus tend to jump apart. (Assembly needs skill and patience!)

In the N-S-N-S arrangement, the magnets will stick together without any bonding. In case of the 2-D arrangement, this gives simply a checkerboard pattern for the magnetizations. This arrangement, although slightly suboptimal, still produces a good lifting force. For all these arrangements, radial stabilization is achieved by choosing a graphite pellet smaller than the stator (otherwise the graphite will slide off sideways).

17.3.3 Combination with permanent magnetic bearings

Pure diamagnetic levitation is limited to low weights. But it can easily be combined with permanent magnet weight compensation, the diamagnetic effect then serving only to stabilize the unstable point of equilibrium of a permanent magnet bearing. In this manner, any weight can be supported in a stable

manner and with absolutely no energy supply. The only drawback remains then the low stiffness of such bearings, but further developments might find a solution to this as well. The next section presents a simple demonstration system for such a bearing

17.3.4 A passively levitated 80g rotor with permanent magnet bearings and diamagnetic stabilization

A very simple system along this idea has been realized [7]. The rotor consists of a graphite disc of ca 10 cm diameter at the bottom and an aluminum cylinder of ca 3 cm length with a small cylindrical ferrite permanent magnet at the top. This magnet is attracted by a ferromagnetic stator on the top, which centers the rotor radially. The graphite disc at the bottom is repelled by the PM array on the bottom (in this case NdFeB magnets). This arrangement stabilizes the otherwise unstable attractive arrangement at the top, the 3 cm aluminum cylinder on the rotor axis ensures that the two bearings are not interfering.

17.4 Active Magnetic Micro Bearings

By definition, these bearings will mainly be activated by electromagnets. Micro size electromagnets fall into two main categories:

1. 'Conventional' coils consisting of copper wire wrapped around a ferromagnetic core
2. MEMS coils

The first type, 'conventional' coils, are fabricated at over 600 million pieces per year in the Lavet motor for electronic watches. Such coils typically can have up to several thousand windings (!) within a few cubic mm, are very cheap in mass production, have inductances up to a few hundreds of micro-henry and relatively high electrical resistance (Q-factors of a few tens only. The Q-factor is the quality factor of a resonator, a high Q-factor means low damping, definition see any textbook on vibrations). Typical copper wire diameters are in the range of 20 microns. Such coils may be used up to several MHz, but are limited to low current densities. The size of such actuators cannot go much below the cubic mm range, but technology might rapidly progress in this domain.

For the second type, MEMS coils, there is a wide range of fabrication procedures. They are most widely used for the read/write heads of hard disks and, in this case, include electrochemical deposition, screen printing, LIGA or other "non-standard" MEMS technologies in their fabrication process. "LIGA" stands for "Lithographie und Galvanische Abformung", i.e. lithography and galvanic deposition, a well published, but expensive technology as it needs synchrotron radiation). Most often, MEMS coils are essentially flat

and thus have far less windings than the first type of coils. The topography is either one-plane (spiraling), i.e. single layer except for the connection at the center, or true "winding" around a core, which requires complex multilayer microfabrication. Even then, the winding itself will still be single layer around a core. This is why all these "true" MEMS coils have many fewer windings than "conventional" windings of thin copper wire.

Finally, active magnetic bearings are conceivable with permanent magnet actuators and additional control of the flux in some "non conventional" way, e.g. by positioning the permanent magnet with a piezo electric element or otherwise influencing the magnetic circuit, such as including magnetostrictive material. [5]

17.5 A microbearing for 3 million rpm

17.5.1 System Setup

The absolute record of rotational speed ever reported seems to be the 23 million rpm of an AMB setup realized by Jesse Beams in 1946. The experimental setup is shown in the following Fig. 17.3

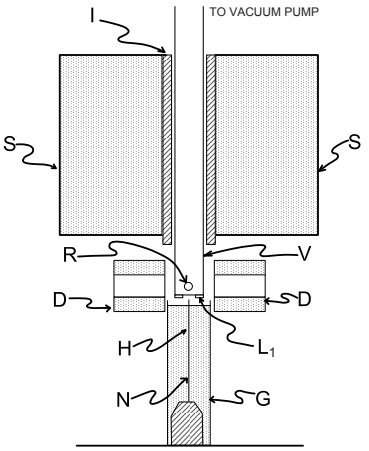


Fig. 17.3. Jesse Beam's Setup for High Centrifugal Fields. The rotor R is suspended by solenoid S and core I, driven by two coreless pairs of coils D. Horizontal damping is provided by the wire H inserted in liquid.

An active magnetic bearing system has recently been realized for a mm-size rotor and a speed of 2.88 million rpm has been reported. The coils of this system are conventional electromagnets with hand-wound copper wire, overall stator size fits roughly into a 5 cm cube. The main difference to the

system of Jesse Beams from 1946 is that the size of the stator should be small as well. The setup of 1946 featured a very small spinning sphere within a large evacuated glass tube and large coils outside the vacuum. Active bearing control was in the single vertical degree of freedom.

In the new system, the coils are small and must therefore be much closer to the rotor, inside the vacuum. This implies that the radial degrees of freedom need stabilization as well. With only a single actively controlled degree of freedom, the radial stiffness of passive centering was too weak to cope with the disturbance caused by the induction motor. The result was a loss of energy in radial vibration. This problem is solved by adding active radial stabilization. A total of three degrees of freedom of the spherical rotor are actively stabilized, the x, y and $z-$position are measured with two radial laser beams and four–segment photosensitive diodes. The rotor consists of a steel ball from a small ball bearing. Rotor diameters range from 1 mm down to 0.4 mm. Fig. 17.4 shows the setup of the system (seen from above, with the top magnet removed) and Fig. 17.5 shows the floating rotor.

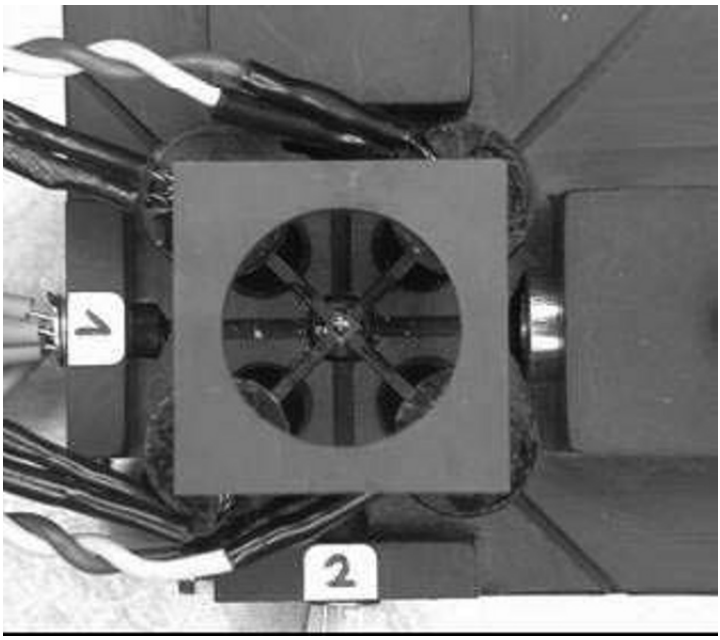


Fig. 17.4. System setup.

17.5.2 Induction Motor

As these rotors are completely unstructured, the most obvious driving principle is by eddy currents, i.e. operated as an induction motor. The leakage flux

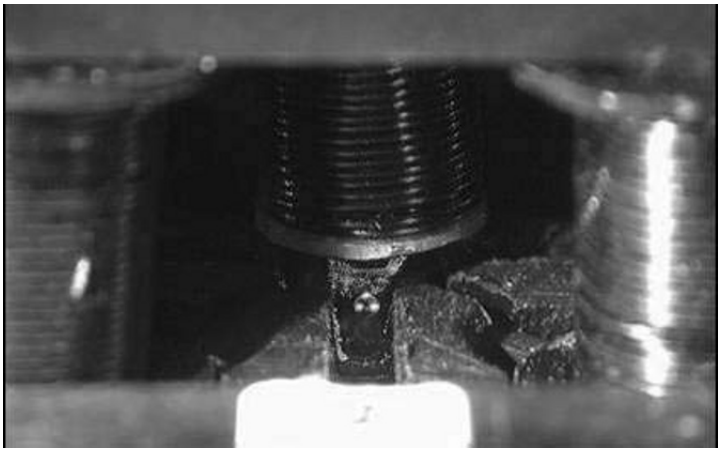


Fig. 17.5. The floating rotor.

ratio is very large, essentially due to geometric constraints (relatively large air gaps). Therefore, the drive is of low efficiency and the torque relatively weak. High rotational speeds need partial evacuation as the friction losses prevent any acceleration above about 30,000 rpm. Furthermore, the stator current will need to be modulated up to the 60 kHz range or more in order to reach the desired high rotation speed. This in turn calls for relatively powerful amplifiers, which seem far out of size for such a small rotor. Furthermore, at these frequencies, the skin effect and iron losses become significant. Small diameter wire or litz wire is therefore preferred and the core material should be of low hysteresis and high electrical resistance. For very high frequencies, ironless coils might become necessary, of course at the cost of further reduction of the effective flux density. Many of these choices are typical for a first prototype: careful analysis of the trade-offs and optimization could lead to significant improvement in efficiency.

17.5.3 Windage losses at different pressures

Windage losses are the limiting factor to high speed rotation of very small rotors, as shown by these experiments [3]. There are two basically different ranges of vacuum: The viscous range and the ballistic range. In the first case, the assumptions of fluid dynamics hold, it ranges from atmospheric pressure (or higher) down to about 1 mbar or slightly less. In the second case, the mean free path of gas particles gets into the range of a hundreds of micrometers, i.e. the range of typical geometric dimensions of the air gap and rotor.

In the viscous regime, windage torque is proportional to the square of rotational speed, power dissipation to the third power of rotational speed and thus to the fourth power of rotor diameter. Gas density can be influenced not only through the degree of vacuum, but also through the choice of gas.

At equal pressure, a rotor in helium will be roughly seven times faster than in air, this is why the rotating mirrors of high speed cameras run in helium. (over a million rpm for an octagonal mirror of a few cm in diameter).

In the ballistic range, i.e. at pressures below about 1 mbar, losses increase linearly with rotational speed and decrease with the fourth power of the radius. This means that below 1 mbar, rotational speed will vary as the inverse of the pressure, i.e.: a pressure ten times lower will allow a rotational speed ten times higher. In order to reach high rotational speeds, it is therefore essential to achieve vacuums significantly better than this 1 mbar limit.

17.5.4 Measurement of Rotational Speed

The obvious method would be to have one half face of the spherical rotor in black and another half in white and to detect rotational speed optically. This works well down to about mm-sized rotors, below that limit, there are some problems. First, it is not possible to define a rotational axis in a spherical rotor, it will align itself differently on each startup, depending on rotor imperfections, remanent magnetization and initial conditions. Secondly, patterning of the rotor becomes difficult and the thickness and weight of paint are not negligible. There is a much easier way. As every rotor has some imperfections, the radial displacement sensor signal has a clearly detectable peak at rotational frequency, to be seen on any oscilloscope in spectral analysis mode. This peak is therefore used as measurement of rotational speed.

The experimental setup described here achieved a vacuum of 0.05 mbar. At this pressure for the 1 mm rotor, the equilibrium of torques was reached at 2,880,000 rpm. At this low pressure, the laser diodes of the sensors are not cooled effectively anymore. This and imperfections in the vacuum containment prevented reaching higher rotational speeds. Fig. 17.6 shows the measurement of rotational speed as a function of pressure for two different rotors.

17.6 Conclusions

Micro contact-free bearings based on magnetic actuation, i.e. active and passive magnetic micro bearings, are an essential component for small very high speed rotation. It has been argued in this chapter that there is a strong technical potential for such bearings, although up to now only some preliminary experimental systems have been reported. Nevertheless, such systems hold, by a large margin, world records for rotational speed.

It is therefore established that the fundamental physical limits do allow very high rotational speeds (up to millions of rpm) and that contact-free bearings can be designed for such systems. But there are many technological obstacles to be overcome before practical applications will emerge. These obstacles are linked to fabrication technologies, to design of efficient micro magnetic actuators and to integration such of actuators into MEMS. Novel

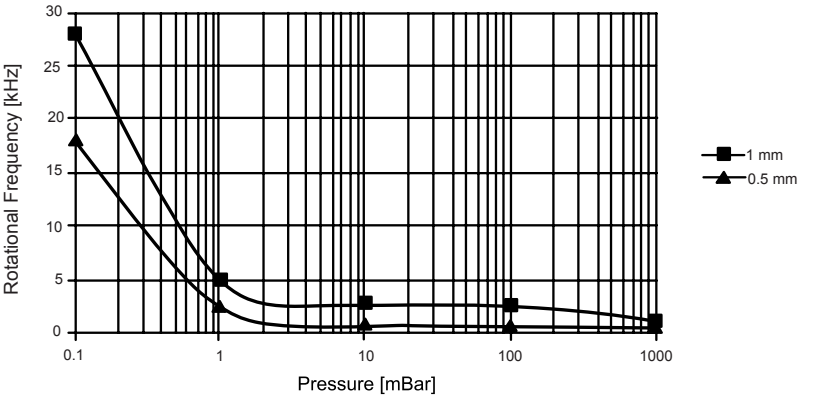


Fig. 17.6. Measured rotational speed as a function of pressure for two different rotors.

passive (or active) bearing types such as PM bearings, diamagnetic bearings or electrostatic bearings seem well suited for micro levitation systems. Viscous damping of gas (ambient or at vacuum pressure) can provide significant damping, but also significant rotational losses. Last but not least, reaching high vacuum and therefore achieving vacuum compatibility of all components will also be needed for very high rotational speeds.

References

1. J. Beams, J. Breazeale, and W. Bart. Mechanical strength of thin film of metals. *Physical Review*, 100(6):1675–1661, 1955.
2. J. Beams, J. Young, and J. Moore. The production of high centrifugal fields. *Journal of Applied Physics*, 12(7):886–890, 1946.
3. A. Boletis. *High Speed Micromotor on a Three Axis Active Magnetic Bearing*. PhD thesis, EPFL, 2005.
4. Orphée Cugat, editor. *Micro-actionneurs électromagnétiques MAGMAS*. Hermes Science Publications, 2002. ISBN 2-7462-0449-5.
5. Toshiro Higuchi and Masahiro Wanatabe. Apparatus for effecting fine movement by impact force produced by piezoelectric or electrostrictive element. United States Patent Number 4894579, January 1990. Assignee: Research Development Corporation of Japan.
6. J. W. Judy. Microelectromechanical systems (mems): Fabrication, design and applications. *Smart Materials and Structures*, 10:1115–1134, 2001.
7. J. Sandtner and H. Bleuler. Electrodynamic passive magnetic bearing with planar halbach arrays. In *Proceedings of the 9th International Symposium on Magnetic Bearings, ISMB9*, Lexington, KY, USA, August 2004.
8. F. N. Werfel, U. Floegel-Delor, T. Riedel, R. Rothfeld, D. Wippich, B. Goebel, P. Kummeth, H.-W. Neumueller, and W. Nick. Progress toward 500 kg HTS bearings. *IEEE Trans. Applied Superconductivity*, 13(2):2173–2178, June 2003.

18

Safety and Reliability Aspects

Gerhard Schweitzer

The application of active magnetic bearings for rotating machinery has become state of the art and ranges from research prototypes to industrial applications, from small turbo-molecular pumps to powerful pipeline compressors in the megawatt range. Users are aware that, beyond function, the safety and reliability of this equipment is critical to its continued commercial development. Safety is more than a mere technical issue. It contains a strong component of psychological interpretation, and societal demands for safety in machinery are ever increasing. Reliability, on the other side, has a definitely technical touch, and it appears to be more amenable to engineering calculations and to economic considerations. Mathematical tools for assessing reliability of classical technical systems, and performance numbers for comparing them, such as mean time between failures, are readily available. The reliability analysis of given technical structures and systems, consisting of a more or less large number of classical components, is rather well developed [33]. However, the active magnetic bearing is not a classical technical system. It is a typical mechatronic product, and as such it contains information processing components, software and feedback loops. For such components, in particular for software, reliability analysis is still under development. In addition, the synthesis of a safe mechatronic system, the method of designing it, is not structured in a systematic way. There is a strong opportunity, however, to make mechatronic systems, despite their obvious complexity, more reliable than classical ones. It is the potential of internal information processing, somehow resembling the ability of living beings to use information to increase their chances of 'survival', which could make mechatronic systems more reliable.

This chapter will, firstly, address conceptual questions of safety and reliability, in particular, stating that it is theoretically not possible to build a fully safe system. Philosophical reasoning on the logic of science shows that safety can only be improved, step by step: it cannot be guaranteed. Subsequently, the main emphasis is put on the technical side of safety and reliability for AMB/rotor systems. Section 18.3 will give a survey on failure examples in mechatronic systems and AMBs. In Sect. 18.4, means for reducing the

G. Schweitzer, E.H. Maslen (eds.), *Magnetic Bearings*,
DOI 10.1007/978-3-642-00497-1_18, © Springer-Verlag Berlin Heidelberg 2009

risks of failure will be discussed. First, safety and reliability are put into the framework of quality management and design, and then more specific ways of dealing with AMB are considered. Redundancy schemes, exception handling and robust control are proven tools, and examples are given. The fail/safe operation with AMB systems requires additional touch-down bearings. The state of the art in modeling the nonlinear rotor dynamics in contacting the touch-down bearings, drop tests, and design for specific applications are referenced. Guidelines for the design of touch-down bearings are summarized. The design of touch-down bearings still needs further research.

The potential of AMB/rotor systems to become fault-tolerant is seen as a general feature of smart machinery. "Smart" means that such a machine knows its state – as it already has sensors and internal control loops for its functionality – and makes best use of the internal information processing capabilities within the machine to optimize its state. Examples of the design of fault-tolerant AMB, using diagnostics, identification methods and reconfigurable control will be discussed and referenced. It is expected that future research will support these trends and make them available for further applications, contributing to the already very impressive, but still growing, safety and reliability features of AMB's.

18.1 Psychological and Philosophical Background of Safety

Safety is an ambiguous term, and it is important to see the non-technical side of it as well. Danger has always been an immanent part of human life, and safety, the absence of danger, is precious. Dangers may come from environmental catastrophes, wild animals, unknown enemies, or unexpected illness. It is a permanent effort of our society to convert danger into risk, to make it calculable and controllable, to tame fate. Dams have been built to avoid flooding, wild animals have vanished to the zoo, and against illness and death we have, at least, insurance to mitigate the consequences. Technical means to increase safety in advanced products, nowadays, are mainly based on mechatronic methods. Driving a car has been made safer by mechatronic driver assist systems, which control dangerous situations, such as braking or skidding.

The acceptance level of danger and risk has a strong *psychological background* and varies with emotional attitude, habits, and individual exposure. Let some examples speak for themselves, without dwelling on arguments or further explanations: car accidents versus train accidents, smoking and drinking habits even against medical advice, danger in hobby sports versus danger in work conditions. In hobby sports, people even enjoy the thrills of risks, be it bungee jumping, or car racing. A nice headline-making example is shown in Fig. 18.1, which could initiate lively discussions on various safety aspects.

On the *philosophical side*, safety might spur some discussion as well. The philosopher Karl Popper [34], in his famous treatise "Logic of Science", 1934,



Fig. 18.1. Raymond Mays, participant of a car race near Cardiff in 1924, looses one of his wheels while driving with a speed of more than 90 km/h (photo Dukas/Keystone, Paris)

asserted that any progress in science probably is coming from falsifying existing theories and modifying them or stating new ones that correspond better to experience than the previous ones. This means that you cannot prove that a theory is right, you can only try to falsify it or parts of it, and improve the situation. As a consequence, the statement that a system is safe, describes an ideal state that cannot be verified, but only, to some extent, be falsified. It is an uncomfortable insight to many people, that risk is something that, principally, cannot be avoided. However, there are various techniques to reduce risk, in stepwise approaches. These will be discussed in the subsequent chapters.

18.2 Definitions and Technical Aspects of Safety, Reliability and Dependability

Safety is one of the four aspects of *dependability*, a term which has been coined by Laprie in 1992 [25]. Dependability encompasses safety, reliability, availability and security. Here, availability means the readiness for usage; security addresses the access to the system, the authority to operate it, to give commands, and to alter software. In brief, security concerns regulations for the communication to the world outside of the technical system under consideration [24].

The areas characterized by the two terms safety and reliability [10] are somewhat overlapping, as illustrated by Fig. 18.2. Customers, of course, are

interested in this overlap; they want a safe and reliable product. The product, the active magnetic bearing system, and its safety aspects will be introduced in the next sections.

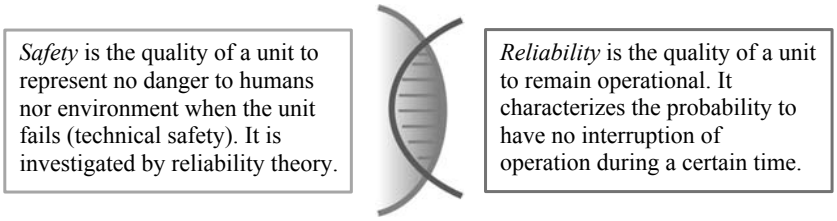


Fig. 18.2. Definitions of safety and reliability

18.3 The AMB as a Mechatronic Product and Failure Examples

The active magnetic bearing is a typical mechatronic device consisting of mechanical, electrical and information processing elements. An application area already well established and developing rapidly further is turbo-machinery. Products range from small turbo-molecular pumps to large compressors for pipeline gas, and to turbo-generators for power plants. A recent research project of international interest is the turbo-generator in AMB's for the High Temperature Helium Reactor technology [39]. Even though the underlying nuclear technology is inherently fail/safe, safety requirements are obvious.

Due to the specific structure of mechatronic systems we may have failures in the mechanical elements, the electronics, or in the software. A few examples from the AMB experience will be given to illustrate the scope of potential failures.

Examples of *software failures* are a system breakdown, run-time exceptions, i.e. address errors and bus time-out, or incompatible program versions. The software area is least covered by systematic approaches to improve its reliability.

The *electronics* may fail or the signals may be disturbed, most often by excessive noise from electromagnetic sources, which are mistaken as sensor signals. The area of EMC (electro-magnetic compatibility) is to be taken most seriously, considering the high-powered switched amplifiers in the AMB loop, but the means for dealing with these problems are more or less standard and will not be addressed further. Defects in the microprocessor hardware, or disturbances in the power supply are to be taken into account and will be discussed in some detail in Sects. 18.4.4 to 18.4.7.

For *mechanical failures*, there is a wealth of experience and established procedures to avoid them. The break down of mechanical parts, i.e. a blade

loss or a rotor crack, or a leakage in a cooling system are failure modes well known from classical rotor design. Two major sources of excessive mechanical loads, however, shall be mentioned in particular. Centrifugal forces at high rotor speeds will lead to limitations, given by the strength of materials for the rotor, be it the lamination under the magnetic bearing area, be it the design of the motor part. Some details are given in Chap. 6 on *Design Criteria and Limiting Characteristics*, Sect. *Speed*. A circumferential speed of 200 m/s is considered state of the art. Higher speeds of 380 m/s for the critical motor drive have been realized but they require special design efforts such as carbon fiber bindings around the rotor. Flywheel designs, with an inner stator and an outer rotor may allow even higher speeds. The other excessive load can be caused by contacts of the high-speed rotor with its housing, which can cause serious safety problems. Such a contact has to be avoided by using touch-down bearings, (Sect. 18.4.7), which have to be designed carefully.

Subsequently, methods and means for reducing the risk of failures will be summarized.

18.4 Measures for Reducing Risks of Failure

The different measures range from systematic design procedures, software development tools, redundancies, individual measures, and quality control to the smart machine concept, which includes various control strategies, active fault diagnostics and corrections. These measures will be described briefly in this chapter. More details on the state-of-the-art in reliability engineering are given in [33].

18.4.1 Quality Control, Standards

An overall approach for systematically introducing quality aspects into the design, production and operation of products and systems, is *standardized procedures* as described in the ISO 9000 series [6]. A company or an establishment following the procedures of ISO 9000 can be recognized as a certified institution with a defined quality level.

In addition, there is the ISO 14839 on AMB [1, 2, 3, 4]. Part 1, concerning vocabulary, and part 2, on the evaluation of vibrations in AMB, have been published; further editions are under development by the ISO Technical Committee 108, Working Group 7, under the direction of O. Matsushita. Standards try to avoid misunderstandings and contribute to quality management.

The field of AMB's is still very young, and therefore company and application specific guidelines are important elements of quality control. The American Petroleum Institute, for example, has added an informative section on "Application Considerations for Active Magnetic Bearings" to its API Standard [5]. For specific applications, drop tests into touch-down bearings, temperature and vacuum tests are commonly performed as part of a customer-required acceptance process.

18.4.2 Systematic Check of the Design

A classical method to ensure best practice of the state of the art is to use the FMECA approach for checking the design, i.e., to do a *Failure Modes, Effects, and Criticality Analysis*. In this approach, a group of experts with different backgrounds – from design, production, test, repair, and potential users – evaluate the design or the product. The experts point to potential failure modes, determine the effects and consequences of such failures and their criticality, and suggest modifications of the design to improve it. There are various standards and specifications on how to proceed in detail, depending on application areas (see, for example, the military standard procedures MIL-STD-1629A). FMECA is an integral part of any ISO 9000 compliant quality system.

18.4.3 Software Development

In a mechatronic product, software is an integral part of the product: it is a component of the machine. In particular, the software must be developed and implemented. Of course, the software must be logically correct, and the operating system should take care of the syntax. But, in addition, the correct time sequence of the computational tasks is most essential in real time applications.

For *industrial AMB applications*, proprietary software is most often run on single chip digital signal processors (DSP) giving an efficient and economic solution. The software is streamlined and dedicated to specific tasks with well-defined constraints.

For an *experimental set-up*, the tasks are usually much more diverse and sometimes complex, and require a versatile solution. For complex tasks it may not be sufficient to just use a high-speed computer with high sampling frequency and to hope that this is adequate for real time operation. It might be better to use a real time operating system (RTOS) from the onset in order to develop and finally operate the software. Such RTOS are available in various versions, such as RT Linux, dSPACE, and VxWorks, differing in complexity, overhead size, speed, price, and availability.

The *design of software* is still an 'art', like any design process. Nevertheless, there are a number of accepted ways for designing complex software, and for validating it. One way of reducing the probability of errors in the software design is a *development system* as shown in Fig.18.3, [15]. The designer preferably makes use of software packages from libraries, configuring them interactively with graphical tools. The RTOS being used is the same for the design and the process application, allowing for meaningful simulations and emulations, fast modifications and realistic tests. Such software packages for rapid control prototyping are very versatile and useful for the design of embedded systems. They include signal processing tools and actuator drivers and allow hardware-in-the-loop tests. An example is described in [32].

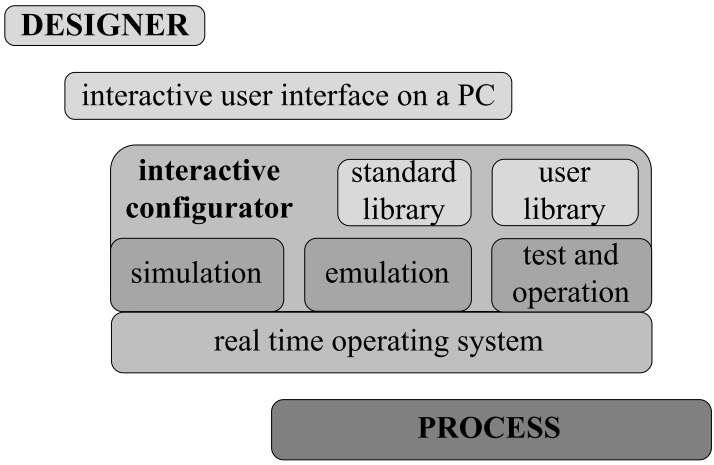


Fig. 18.3. Basic concept for a software development system for embedded microprocessor

In addition, a development system with extensive modeling of the rotor in AMB facilitates the *simulation of design variations*, which aim at an optimization of safety features. As there are many ideas and suggestions on how to avoid or monitor faults and improve safety, these potential solutions, before implementing them in hardware, should be investigated for their usefulness. This includes control variations to accommodate disturbances and faults, control packages for recovering the rotor after a touch down in its touch-down bearings, exception monitoring and handling devices such as watchdogs, the optimizing of sensor and actuator locations, or the arrangement of redundant components.

18.4.4 Redundancy

One way of improving reliability is to use *redundant components* and *redundant information*. Thus, there are two different kinds of redundancies, hardware redundancy and analytical redundancy. If the failure of a single component cannot be corrected and is critical for the system's safety, the function of this component should be guaranteed by redundant hardware. Two or more of these same components have to be arranged in parallel, in order to replace any failed component. An example is shown in (Fig. 18.4(i)). In this case, appropriate failure detection and switchover schemes are crucial, and the increase in the number of components actually counteracts the overall reliability to some extent. On the other side, if the function of a component is at least partially performed by another component as well, then the functional relation between these components can be used as an analytical redundancy to

replace the failed component partially, or to reduce the extent and cost of a hardware redundancy (Fig. 18.4(ii)).

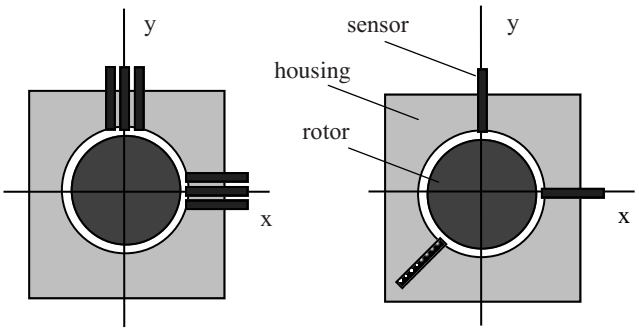


Fig. 18.4. Cross-section of the rotor/bearing with redundant sensors, [15]: (i) hardware redundancy with triplex sensor configuration, (ii) analytical redundancy, simplex sensor configuration with one redundant sensor

In magnetic bearing technology both redundancy schemes have been investigated, and some examples will be cited. For future *aircraft engine applications* a redundant magnetic bearing structure has been suggested in [29]: Each radial bearing has three independently controlled axes. The controller consists of two hierarchical levels, a supervisory level and an actuation level. The supervisory controllers are configured in a duplex fault tolerant configuration, one controller is active, the other in standby mode. For *industrial applications*, central controllers with duplex hardware redundancy have been developed. The switchover time between the active and the standby controller is about 500 ms, considered to be short enough to avoid overheating of the touch-down bearings during a possible, brief touch down of the rotor caused by a failure of the active controller. The second controller, then, has the task to recover the rotor and bring it back to normal operation. *Further investigations* deal with multiple sensors, with redundant flux paths in the case where an electromagnetic coil fails [18, 20, 19, 38]. In [30], controller fault tolerance is achieved through a high speed voting mechanism which implements triple modular redundancy with a powered spare CPU, thereby permitting failure of up to three CPU modules without system failure. Using a separate power amplifier for each bearing coil and permitting amplifier reconfiguration by the controller upon detection of faults leads to fault tolerance against amplifier/cabling/coil failures. This allows "hot" replacement of failed amplifiers – no intermediate shut down of amplifiers is required and the switch over can occur under load – without any system degradation. A recent suggestion of using hot-swap controller-amplifier modules, however, for decentralized control only, is described in [37].

With growing experience in AMB technology and many advances in control techniques, the emphasis of reliability design has been shifting from hardware redundancy to software based robust and fault tolerant systems, making the AMB a key component in smart rotating machinery (Sects. 18.4.6 and 18.5).

18.4.5 Exception Handling, Watchdog

The occurrence of single, exceptional events and failures of safety-critical components has to be detected in order to introduce countermeasures. In a classical approach, a "watchdog" monitors the actual behavior and compares it to the expected normal operation, giving an alarm when deviations occur and initiating a switch-over to a safe operating mode. As an example, a *failure of the power supply* has to be considered as a serious exceptional event, and it can be compensated by various means. One way is the switchover to a second power supply such as a set of batteries or capacitors, being part of a classical UPS (*uninterruptible power supply*). Another way is to make use of the rotational energy stored in the rotating rotor. If the rotor is driven by a motor drive, switching the motor from its drive mode to generator mode can supply sufficient electrical power to the system, keeping the rotor levitated until it can coast down safely in its touch-down bearings [26]. There may be other special subsystems in an AMB/rotor system for exception handling, deserving a separate investigation, but in general these tasks will be integrated into a smart system concept.

18.4.6 Robust Control

The design for robust control of the AMB should allow for uncertainties in the system parameters and for a variety of disturbances acting as additional inputs to the sensors that classical control can no longer handle. The uncertainties may arise in the bearing characteristics changing with temperature, the rotor mass being modified by the inertia of gas being transported in a turbo-machine, or the damping characteristics of a flexible rotor. The disturbances acting as strong additional inputs are most often from external sources. They may arise from motions of the machine base caused by earthquake or from using an AMB/rotor system in a moving vehicle, or from tool-generated forces in a milling process. Robust control often requires a higher order controller; methods for the design of robust H_∞-control are given for example in [40], a robust μ-synthesis AMB application is detailed in [35]. Further examples are cited in Chap. 12 on *Flexible Rotor Control*.

18.4.7 Fail-safe System, Auxiliary Bearings

The best way to build a safe system is to make it fail/safe. This means that, if anything goes wrong, eventually and as a last resort, the system will degenerate to a safe system. An airplane, for example, is not a fail/safe system.

This is the main reason why AMB systems are equipped with auxiliary bearings. Auxiliary bearings are an additional set of active or passive bearings, and the rotor will only come into contact with them when the contact-free suspension in AMB is not working, or fails, or operates under heavy overload. An example of active auxiliary bearings is described in [22]. For passive bearings, usually simple retainer bearings or special ball bearings are used for an eventual touch-down. The dynamics of a high-speed rotor dropping into such touch-down bearings is strongly nonlinear. If the friction between the spinning rotor and the touch-down bearing is too high, a violent and destructive backward whirl can develop. During whirl, the contact forces can become quite high: for example, more than 300 times the rotor weight. The touch-down of a rotor can be a serious safety hazard and the understanding of touch-down dynamics and the design of bearings are important issues in AMB. Therefore these questions are dealt with separately in Chap. 13 on *Touch-down Bearings*.

Heavy overload can even occur as part of the "regular" operation in so-called "load sharing bearings". In aero-engines, for example, heavy loads are expected during high acceleration flight maneuvers, and during landing shocks.

A question closely related to the touch down behavior of the rotor is the associated *control of the rotor dynamics*. It is of interest to detect when a contact is going to happen and, if possible, to modify the control in order to avoid the contact, or after contact has occurred to recover the rotor, i.e. to bring it back to its operating position - or to enable a stable load sharing by suitable control action. Results have been obtained and will be discussed in Chap. 14 on *Dynamics and Control Issues for Fault Tolerance*.

18.5 Smart Machine Technologies

The basic idea of mechatronics, of combining mechanics, electronics and information processing within a product in a synergetic way, has developed into the concept of smart machines, where the capability of internal information processing is used in an extensive way. The use of this concept in AMB applications has been shown in [36], and a definition might run as

> Smart machines know their internal state and optimize it by internal information processing. This leads to better functionality with features such as self-calibration, self-diagnostics, self-tuning, self-corrections, and eventually, it leads to less maintenance and higher safety.

In classical machinery, the growing number of components and ever increasing complexity is considered to be detrimental to reliability. For machines with sufficiently high potential for information processing, this tendency may no longer be valid, leading to a change of paradigm. In *analogy to biological systems*, which are tremendously complex compared to classical machines, the complexity allows for survival in unforeseen and unstructured environments

and makes the biological system extremely reliable. It is conceivable that intelligent or smart machinery can make use of such strategies.

A block diagram illustrating the structure of such a machine is shown in Fig. 18.5. The diagram has been developed by R. Nordmann for a European Research Project [17], demonstrating improved machinery performance by the use of active control technology.

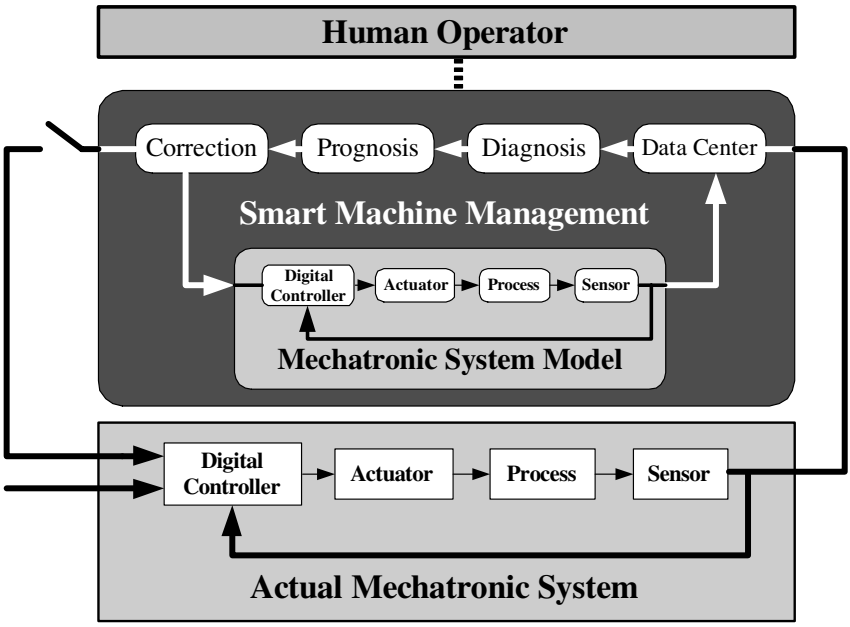


Fig. 18.5. Structure of a smart machine

The smart machine in Fig. 18.5 consists of three main parts. One is the "Actual Mechatronic System", the real machine with its process, sensors, actuators and the controller. As an example, this could be the rotor of a machine tool or a turbo-rotor in magnetic bearings.

The second part is the "Mechatronic System Model", a software representation of the real machine. Of course, setting up such a model may not be simple, and that is why identification techniques are an important tool in this technology. The model, or a part of it, will be used for designing, modifying or reconfiguring the control of the real machine.

The third part describes the "Smart Machine Management". It indicates the additional functions that can be incorporated into the system by making "smart" use of the available information. At first, data has to be collected from the real machine and its sensors, and in addition, data has to be collected from the model, which runs in parallel to the real machine, if necessary even at a faster time scale for predictions of future behavior. Based on this information,

a diagnosis of the present state will be possible . The diagnosis, for example, can be model-based, a method that has been investigated for rotating machinery in a BRITE/EURAM project [9]. Furthermore, due to the built-in control loop, self-diagnosis and even *active diagnosis* will be possible, i.e., the system itself will be able to derive hypotheses about parameters or faults and to check them by creating suitable test signals for the model and for the real system. This approach could further improve identification procedures, and it will be of interest for reliability management. For example, the system itself could identify failures in mechanical components such as cracks in the rotor or the location of excessive unbalance, or failures in electrical components, for example in sensors. Based on the results of diagnosis, indicating details on deviations from normal operation, a prognosis about the future behavior of the machine can be derived. The system can even make suggestions for *corrective measures* and predict their consequences. Such corrections might include, for example, unbalance compensation, special procedures for passing critical speeds, changing the feed of a machine tool during the manufacturing of delicate parts by taking into account cutting forces or tool wear, or it may even lead to a self-tuning of the parameters of the actual control loop. Some examples will demonstrate the state of the art and actual research topics.

Identification procedures have been developed for multivariable AMB systems [21], at first, to identify the structure of the unstable open loop system during closed loop operation. The results have been extended and used to derive in an automated, iterative way a robust controller for a flexible rotor [27]. The experimental set-up is shown in Figs. 18.6 and 18.7. The set-up represents a realization of the structural block diagram of Fig. 18.5. In addition to the control loop for supporting the rotor, a diagnosis and a correction module have been implemented.

Diagnostics and identification tools are being used as well for fault detection of various kinds and for the development of fault-tolerant control. A general introduction is given in [11, 12]. A variety of examples, using AMB, are cited below:

An already well-established correction procedure is *balancing*. It uses learning procedures and estimation techniques as diagnostic tools. For the compensation of the unbalance signal in the sensors, a feed forward control signal is generated (Chap. 8 on *Control of the Rigid Rotor in AMB*). For larger unbalances, an active online balancing with commercially available balancing rings [7, 16] is being used.

In magnetic bearings, *faults in sensors and actuators and other machine components* have been detected and corrected [8, 13, 14, 28, 31]. The techniques involved span from processing just the bearing sensor signals appropriately to the use of sophisticated identification software, from monitoring the deviations of normal operating behavior to actively switching to an alternative control strategy in case of need. Two examples are indicated subsequently.

The malfunction and the wear of tools in a milling process has been diagnosed from sensor signals of the AMB-supported milling spindle [31]. Thus,

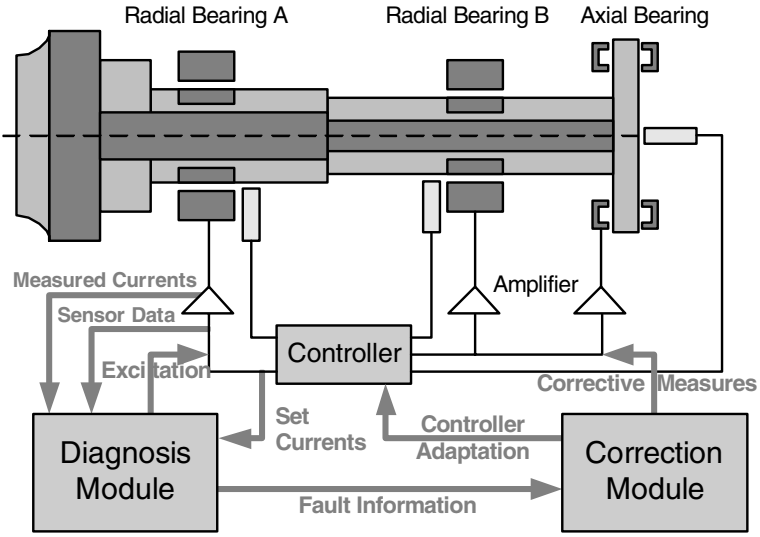


Fig. 18.6. Rotor in AMB with additional smart machine modules for diagnosis and correction [27, 28]

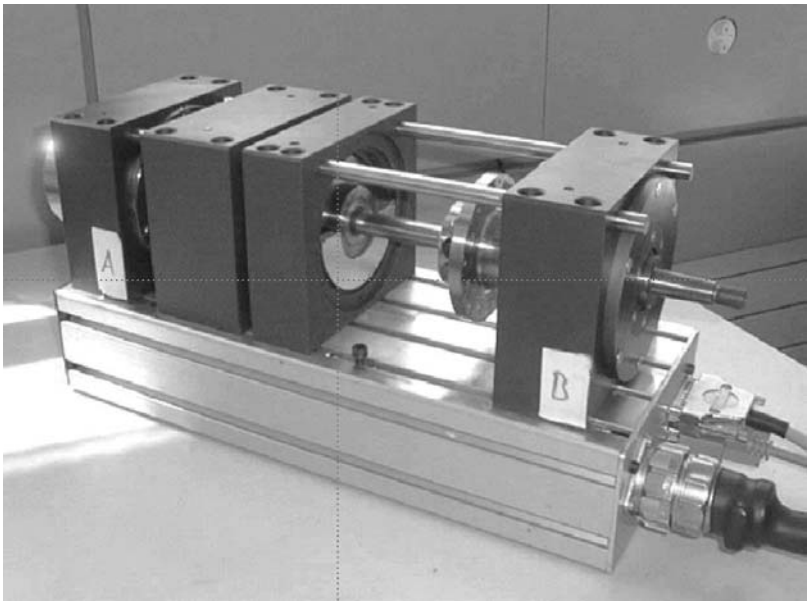


Fig. 18.7. Test rig for smart machine technology [27, 28]

the AMB can even be used to detect faulty process parameters which are not directly related to the functioning of the AMB itself, and the AMB can contribute to the reliability of the whole machine and its working process.

The dynamics of a rotor touching upon a touch-down bearing have been described [23], and based upon this model, as a correction measure, the control is reconfigured in order to recover the rotor [13]. A different correction procedure would be to avoid the potentially critical touch down, i.e., to detect the impending contact and to reconfigure the control in time to prevent the rotor from touching the touch-down bearing [14]. It can be expected that these approaches will be extended in theory and application and will strongly contribute to the overall safety performance of the AMB technology. Two separate chapters are devoted to the development in these areas, Chap. 11 on *Identification* and Chap. 14 on *Fault Tolerant Control*.

18.6 Conclusions

Safety of a product is an ambiguous term that requires considerations from a user's point of view. Some of these aspects have been addressed. Philosophical reasoning on the logic of science shows that safety can only be improved, step after step; it cannot be guaranteed.

Main emphasis is put on the technical side of safety and reliability for AMB/rotor systems. Section 18.2 gives a survey on failure examples in mechatronic systems and AMB's. In Sect. 18.4, means for reducing the risks of failure are discussed. First, safety and reliability are put into the framework of quality management and design, and then more specific ways of dealing with AMB are considered. Redundancy schemes, exception handling and robust control are proven tools, and examples are given.

The potential of AMB/rotor systems to become fault-tolerant is seen as a general feature of smart machinery. "Smart" means that such a machine knows its state – as it already has sensors and internal control loops for its functionality – and makes best use of the internal information processing capabilities within the machine to optimize its state. Examples on the design of fault-tolerant AMB, using diagnostics, identification methods and reconfigurable control are discussed and referenced. It is expected that future research will support these trends and make them available for further applications, contributing to the already very impressive, but still growing, safety and reliability features of AMB's.

References

1. ISO Standard 14839-1. Mechanical vibration - Vibrations of rotating machinery equipped with active magnetic bearings - Part 1: Vocabulary, 05 2002.

2. ISO Standard 14839-2. Mechanical vibration - Vibrations of rotating machinery equipped with active magnetic bearings - Part 2: Evaluation of vibration, 05 2004.
3. ISO Standard 14839-3. Mechanical vibration - Vibrations of rotating machinery equipped with active magnetic bearings - Part 3: Evaluation of stability margin, 01 2005.
4. ISO Standard 14839-4. Mechanical vibration - Vibrations of rotating machinery equipped with active magnetic bearings - Part 4: Technical guidelines, system design (Draft), 09 2006.
5. API Standard 617. Axial and centrifugal compressors and expander-compressors for petroleum, chemical and gas industry services, July 2002.
6. ISO Standard 9000. Quality management and quality assurance.
7. K. Adler, Ch. Schalk, R. Nordmann, and B. Aeschlimann. Active balancing of a supercritical rotor on active magnetic bearings. In H. Bleuler and G. Genta, editors, *Proc. 10th Internat. Symp. on Magnetic Bearings*, pages 49–54, Martigny, Aug. 2006.
8. M. Aenis and R. Nordmann. Fault diagnosis in rotating machinery using active magnetic bearings. In Y. Okada, editor, *Proc. 8th Internat. Sympos. on Magnetic Bearings, Mito, Japan*, pages 125–132, 2002.
9. N. Bachschmidt et al. Model based diagnosis of rotor systems in power plants. BRITE/EURAM Research Project BRPR950022, European Community, June 1999.
10. A. Birolini. *Quality and reliability of technical systems. Theory – practice – management.* Springer-Verlag Berlin, 1998.
11. M. Blanke, M. Kinnaert, J. Lunze, and M Staroswiecki. *Diagnosis and Fault-Tolerant Control.* Springer-Verlag, 2003.
12. F. Caccavale and L. Villani, editors. *Fault Diagnosis and Fault Tolerance for Mechatronic Systems. Proc. Workshop at the 2002 IEEE Internat. Symp. on Intelligent Control, Vancouver.* Springer-Verlag, 2003.
13. M.O.T. Cole and P.S. Keogh. Rotor vibration with auxiliary bearing contact in magnetic bearing systems, Part 2: Robust synchronous control to restore rotor position. *Proc. IMechE, part C, J. of Mechanical Engineering Science*, 217:393–409, 2003.
14. M.O.T. Cole, P.S. Keogh, M.N. Sahinkaya, and C.R. Burrows. Towards fault-tolerant control of rotor-magnetic bearing systems. *IFAC J. Control Engineering Practice*, 12(4):491–501, 2004.
15. D. Diez and G. Schweitzer. Simulation, test and diagnostics integrated for the safety design of magnetic bearing prototypes. In G. Schweitzer and M. Mansour, editors, *Proc. IUTAM-Symp. on Dynamics of Controlled Mechanical Systems*, pages 51–62. ETH Zurich, Springer-Verlag, 1989.
16. D. Ewins and R. Nordmann et al. Magnetic bearings for smart aero-engines (MAGFLY). Final Report, EC GROWTH Research Project G4RD-CT-2001-00625, European Community, Oct. 2006.
17. D. Ewins, R. Nordmann, G. Schweitzer, and A. Traxler et al. Improved Machinery Performance Using Active Control Technoloy (IMPACT). Final Report, BRITE/EURAM Research Project BRPR-CT97-0544, European Community, April 2001.
18. M. Fairbert. Design considerations for an active magnetic bearing used in aerospace environmental control systems. In *Proc. 7th Internat. Symp. on Magnetic Bearings*, pages 519–524. ETH Zurich, Aug. 2000.

19. S.J. Fedigan, R.D. Williams, Feng Shen, and R.A.Ross. Design and implementation of a fault tolerant magnetic bearing controller. In *Proc. 5th Internat. Symp. on Magnetic Bearings*, pages 307–312. Univ of Kanazawa, Aug. 1996.
20. R.J. Field and V. Ianello. Reliable magnetic bearing system for turbo-machinery. In *Proc. 6th Internat. Symp. on Magnetic Bearings*, pages 42–51. MIT Cambridge, Aug. 1998.
21. C. Gähler and R. Herzog. Multivariable identification of active magnetic bearing systems. In *Proc. IUTAM. Symp. on Interaction between Dynamics and Control in Advanced Mechanical Systems, Eindhoven*, April 1996.
22. L. Ginzinger and H. Ulbrich. Simulation-based controller design for an active auxiliary bearing. In *Proc. 11th Internat. Sympos. on Magnetic Bearings*, Nara, Japan, pages 412-419, Aug. 2008.
23. P.S.Keogh and M.O.T. Cole. Rotor vibration with auxiliary bearing contact in magnetic bearing systems, Part 1: Synchronous dynamics. *Proc. IMechE, part C, J. of Mechanical Engineering Science*, 217:377–392, 2003.
24. P. Koopman and H. Madeira. Dependability benchmarking and prediction: a gradn challenge technology problem. In *Proc. 1st Internat. Workshop on Real-Time Mission-Critical Systems: Grand Challenge Problems*, Nov. 30, 1999.
25. J.C. Laprie et al. Dependability: basic concepts and terminology. In *Proc. IFIP, WG 10.4 on Dependable Computing and Fault Tolerances*, 1992.
26. R. Larsonneur, P. Buehler, and P. Richard. Active magnetic bearings and motor drive towards integration. In *Proc. 8th Internat. Symp. on Magnetic Bearings, Mito, Japan*, pages 187–192, Aug. 2002.
27. F. Loesch. *Identification and automated controller design for active magnetic bearing systems*. PhD thesis, ETH Zurich No 14474, 2002.
28. F. Loesch. Detection and correction of actuator and sensor faults in active magnetic bearing systems. In *Proc. 8th Internat. Sympos. on Magnetic Bearings, Mito, Japan*, pages 113–118, Aug. 2002.
29. J.P. Lyons, M.A. Preston, R.Gurumorthy, and P.M. Szczesny. Design and control of a fault tolerant active magnetic bearing system for aircraft engines. In *Proc. 4th Internat. Symp. on Magnetic Bearings*, pages 449–454. ETH Zurich, Aug. 1994.
30. E.H. Maslen, C.K. Sortore, G.T. Gillies, R.D. Williams, S.J. Fedigan, and R.J. Aimone. Fault tolerant magnetic bearings. *J. Engineering for Gas-Turbines and Power, Trans ASME*, 121(3):504–508, 1999.
31. M.K. Mueller. *On-line-Process Monitoring in High Speed Milling with an Active Magnetic Bearing Spindle*. PhD thesis, ETH Zurich No 14626, 2002.
32. R. Otterbach, M. Eckmann, and F. Mertens. Rapid Control Prototyping - neue Möglichkeiten und Werkzeuge. *Automatisierungstechnische Praxis atp*, (6):78–83, 2004.
33. H. Pham, editor. *Handbook of reliability engineering*. Springer-Verlag, 2003.
34. K.R. Popper. *Logik der Forschung*. Springer-Verlag, Wien, 1934.
35. U. Schoenhoff, G. Luo. J., Li, Hilton E., R. Nordmann, and P. Allaire. Implementation results of μ-synthesis control for an energy storage flywheel test rig. In *Proc. 7th Internat. Sympos. on Magnetic Bearings*, pages 317–322. ETH Zurich, 2000.
36. G. Schweitzer. Magnetic bearings as a component of smart rotating machinery. In *Proc. 5th Internat. IFToMM Conf. on Rotor Dynamics, Darmstadt*, pages 3–15, Sept. 1998.

37. A. Schulz, B. Gross, N, Neumann, and J. Wassermann. A sophisticated active magnetic bearing system with supreme reliability. In *Proc. 11th Internat. Sympos. on Magnetic Bearings,* Nara, Japan, pages 267-273, Aug. 2008.
38. J. Na Uhn and A. Palazzolo. Optimized realization of fault-tolerant heteropolar magnetic bearings. *J. Vibration and Acoustics, Trans ASME*, 122(3):209–221, 2000.
39. Suyuan YU, Guojun YANG, Lei SHI, and Yang XU. Application and research of the active magnetic bearing in the nuclear power plant of high temperature reactor. In H. Bleuler and G. Genta, editors, *Proc. 10th Internat. Symp. on Magnetic Bearings*, keynote, Martigny, Switzerland, Aug. 2006.
40. K. Zhou and J.C. Doyle. *Essentials of robust control.* Prentice Hall, 1997.

Index

AC motor, 461
active magnetic bearings, 1, 10
actuator, 111, 152
  electrostatic, 488
  gain, 117
  measuring, 131
  micro magnetic, 487
  model, 330
  model assembly, 117
  response limitations, 127
  stiffness, 117
  voice coil, 495
actuator offset, mechanical, 187
aerodynamic losses, 136, 140
aeroengine, 279
aerospace, 7
air drag losses, 159
algorithm
  levitation control, 467
  P+2, 467
  P-2, 467
aliasing, 236, 245
alloys
  cobalt, 93
AMB system model, 328
Ampére's loop law, 115
Ampére's law, 72
amplifier, 112
  analog, 97
  losses, 148
  operating modes, 126
  power, 69, 77, 97
  switching, 97, 450
  transconductance, 121
  transpermance, 122
analog
  control, 229, 231, 233
  electronics, 229
  filter, 245
  hardware, 236
analog-to-digital A/D
  conversion channel, 230
  conversion resolution, 231, 233, 245
  conversion time, 231, 238
  converter, 229, 230, 233, 234, 246
anti-aliasing filter, 231, 236, 333
applications of AMB, 17
arithmetics
  fixed-point, 220
  floating point, 245
  integer, 220, 245, 246
artificial heart
  implantable, 480
  pump, 462, 480
artificial heart pump, 17
automatic balancing, 426
auxiliary bearing, 389, 407, 412, 513
  contact, 407, 410, 412–421, 423, 424
  contact modes, 413–421, 423, 424
  friction, 413, 415, 419, 424
  touchdown recovery, 410, 427, 431
axial
  self-bearing motor, 477
axis of geometry, 215

back-up bearing, 389

backward difference, 239, 242
backward whirl, 390, 396, 413, 414, 424
balancing
  active, 516
  automatic, 426
bandwidth, 320, 321
  power bandwidth, 153
base motion, 409
Beams, Jesse, 499
bearing
  auxiliary, 407, 412
  ball, 475
  combined, motor, 461
  elastic suspension, 260
  forces, 171, 173
  homopolar, 140, 148
  load capacity, 81
  PM repulsion, 477
  stiffness, 153, 173
  thrust, magnetic, 93
bearingless motor, 461
bi-quad representation, 246
bias
  current, 31–33, 35, 41, 79, 224
  flux, 28
  linearization, 79, 95, 440, 443
  permanent magnet, 95, 468
bismuth, 496
blade loss, 409
braking torque, 135, 144
  cylinder, 141
  disc, 141
  measurement, 146

cable losses, 138, 148
Campbell diagram, 207, 212
capacitive displacement sensor, 103
casing model, 339
center of gravity control, 361
central difference, 243
chaotic motion, 390
characteristic polynomial, 35, 61
characteristics of AMB, 15
circuit
  magnetic, 74
classification of AMB, 10
closed loop model, 341
cobalt alloys, 93
coefficient
  drag, 141, 144
  influence, 420
coercive field intensity, 74
coil
  configuration, 411
  design, 82, 88
  temperature, 88
  winding scheme, 90
collocated, 199, 203, 204
  non-, 194, 199, 200, 203, 208
collocation, 437
combined motor bearing, 461
compliance
  dynamic, 66
compressors
  losses in, 149
conductor, 71
conical
  mode, 198, 199, 206, 208, 210–212, 214
  motion, 198
continuous-time, 233
  control, 237, 240, 243–245
  differential equation, 233
  eigenvalue, 235, 240
  equivalent, 243
  frequency variable, 236
  plant, 233, 234, 238
  signal, 239
  system, 234–238, 240, 243
control, 29, 33, 152
  $\mathcal{H}_\infty$, 37, 52, 57, 61, 214, 242, 367
  μ, 370
  axial, 220
  bandwidth, 41, 205, 211, 321
  center of gravity, 361
  COG coordinate, 210–212
  complexity, 383
  conical mode, 211, 212, 214, 224
  current, 49–52, 193–195, 224
  decentralized, 342
  decentralized/local, 194–197, 199, 203–208, 210, 212
  decoupled, 208, 211, 212, 224
  design, 33, 34, 37, 52, 54, 193, 208, 215
  digital, 29, 38, 50, 57, 65, 220
  digital PID, 471
  fault tolerant, 514

flexible rotor, 194, 215
force, 34, 37, 207, 209
gain, 65
gain compensation, 322
gain scheduled, 377
harmonic, 426
levitation, 467
linear, 31, 34, 53, 54
LPV, 377
LQ, 243
LQ/LQG, 54, 56, 214
LQG, 441
MIMO (multi-channel), 30, 52, 65, 204, 208, 219
minimal energy, 160
Mixed PID, 361
modal, 209, 210
moment of force, 209
non-collocated PID, 352
order, 57
parallel mode, 211, 212, 214, 224
passive, 28, 57, 375
PD, 418, 425, 467, 479
PD/PID, 39, 42, 44–46, 57, 194, 196, 199, 205–208, 213, 237, 239–245
phase, 65
phase compensation, 322
phase lag, 47
phase lead, 321
PID, 47, 342, 411, 413, 417
pole-placement, 54, 56, 214, 243
rigid body, 194, 199, 214
robust, 42, 57, 61, 513
roll off, 205
SISO (single-channel), 30, 51, 65, 208, 219
state estimator/observer, 214
state space, 52, 53, 60
synchronous, 378, 426, 427
synchronous current, 220, 223
synchronous displacement, 220
synchronous force, 221, 222, 224
system, 69
$\mu-$synthesis, 37, 52, 57, 61, 214, 242
tilt and translate, 361
unbalance, 215–217, 219, 220, 224, 378, 426
underlying current, 49, 50
underlying force, 51
  voltage, 49, 50, 53, 54, 224
controller
  design, 319
cooling, 81, 151, 158
coordinates
  bearing, 193
  center of gravity/mass (COG), 193, 194, 196, 211, 212
  sensor, 193, 209
copper losses, 137
copper resistance, 87
corrective procedures, 516
coupling
  A-B, 208, 211
  cross-, 208, 211, 214
  de-, 211
coupling effects, 174
cracked rotor, 410
critical speed, 167, 182, 183
  bending, 215, 217, 218
  rigid body, 216, 220, 221
current
  measurement, 105
  phase, 475
  sheet, 466, 468, 470

damping, 28, 29, 34, 36, 39, 61, 65, 66, 153, 199, 206, 212, 337
  critical, 36, 43
  cross-, 203
  external, 204, 259
  inner, 203
  matrix, 196, 201, 203, 210, 213
  “natural”, 196, 208
  nutation, 207
  overcritical, 36
  synchronous, 216
  undercritical, 36
dead time, 238
decentralized control, 342
decomposition, 199, 210
degree of freedom (DOF), 28, 30, 51, 52, 59, 65, 191, 196, 208, 213
delay, 333
  computation, 231, 245, 246
  sampling, 238–241, 243–246
  time, 230, 231, 245
density
  gas, 141

dependability, 507
design, 147
  coil, 88
  limitations, 151
  magnets, 81
  quality, 510
  software, 510
  systematic checks, 510
  thrust magnetic bearings, 93
  touch-down bearing, 401
destabilization, 199, 201, 203, 208, 214
diagnosis, 316, 515
  active, 515
diamagnetic materials, 6, 495
difference equation, 233
differential
  driving mode, linearization, 80
  sensing, 101
differential equation, 59, 195, 210
  closed-loop, 35, 212
  first-order, 52, 53
  homogeneous, 36, 55
  inhomogeneous, 58
  matrix, 193, 194, 196, 201, 210, 213
  second-order, 53
  state space, 213
  vector, 52
differential winding, 124
digital
  control, 229, 231, 233, 237, 245
  control design, 243
  control, PID, 471
  filter, 231, 245
  hardware, 230, 231
  signal processor, 467, 472, 478, 482
digital signal processor (DSP), 229, 230, 232, 245, 247, 248
digital-to-analog D/A
  conversion resolution, 231
  conversion time, 231
  converter, 229–231, 233, 234, 236, 245
discrete-time, 233
  control, 233, 236–241, 244, 245
  eigenvalue, 235, 240
  equivalent, 243
  filter, 241
  frequency response, 236
  frequency variable, 236
  plant, 237, 244
  system, 231, 233, 235, 236, 240
  transfer function, 236, 241
disk
  rigid model, 413
displacement
  virtual, 78
dither, generalized, 443
drag
  viscous, 140
drag coefficient, 141, 144
  shrouded cylindrical rotor, 142
drop
  rotor, 412
dynamic
  compliance, 66
  stiffness, 28, 34, 46, 63, 66
dynamics
  rigid rotor, 167
dynamic stiffness, 153

Earnshaw's theorem, 5
eccentricity, 169
eddy current losses, 135, 137, 139, 159
eddy currents, 14, 84, 130, 452
  sensor, 101, 482
eigendamping, 37, 41
eigenfrequencies, 30, 37, 41, 59, 171
  closed-loop, 205, 208
  gyroscopic effects, 176
  nutation, 207, 212
  rigid body, 205, 207, 208, 212
eigenmode, 55
  backward, 198
  bending, 205
  closed-loop, 205
  conical, 198, 204, 206, 207
  coupling, 200
  decomposition, 198
  forward, 204, 206
  nutation, 207, 212
  parallel, 198, 204
  precession, 198
  rigid body, 205, 206, 209
eigenvalues, 36, 50, 53, 55, 58, 61, 196, 198, 206, 235–237, 240, 246, 320
  closed-loop, 34, 36, 40, 41, 196, 198, 199
  conjugate complex, 35
  open-loop, 33, 35, 49, 205, 208

real, 36, 201
trajectory, 196, 197, 199, 212
electro-dynamic levitation, 14
electromagnet, 27–30, 32, 35, 44, 69, 115
inductance, 436
elevator guideways, 435, 442
energy
magnetic, 489
equations of motion
flexible rotor, 272
estimation
parameter, 447
Euler angles, 191
Euler-Bernoulli beam model, 337
example
$\mathcal{H}_\infty$ control, 369
actuator model, 120
asymmetric rotor, 375
center of gravity control, 362
mixed PID control, 362
non-collocated PID control, 352
PID control, 344
PID performance analysis, 351
rotor sensitivity, 360
sensitivity analysis, 357
system model, 336
tilt and translate control, 362
excitation, 182
backward whirl, 187
external, 58
force, 28, 58, 59
forward whirl, 185
frequency, 58, 59
harmonic, 55
mechanical sources, 187
node, 62
non-periodic, 188
parametric, 188
periodic, 55
sensor and actuator offset, 187
unsymmetries of the rotor, 188

factor
force-current, k_i, 79
force-displacement, k_s, 79
fail-safe, 513
failure modes, 411
failures of AMB, 508, 513
Faraday's law, 115, 436
fault detector, 411
fault tolerance, 407
faults, 516
AMB system, 408
rotor, 409, 410
feedback, 34
gain, 41, 42
integrating, 45, 47
output, 54, 56, 57
state, 54, 56, 214
velocity, 43, 47
ferromagnetic, 28, 35
ferromagnetic materials, 6, 73, 495
field
magnetic, 71
filter
anti-aliasing, 333
Finite Element Method, 251, 267
model reduction, 292
finite element modeling, 82
flexibility
rotor, 319
flexible
mode shapes, rotor, 324
flexible rotor, 155, 191, 193, 194, 203, 205, 208, 215, 251, 263
equations of motion, 272
with AMB, 288
fluid bearing
identification, 312, 313
fluid structure interaction, 312
flux
distribution, 465
leakage, 88
measurement, 105
flywheels, 17
losses in, 149
force
levitation, 465
Lorentz, 70, 473, 494
magnetic, 77, 152
magnetomotive, 75
maximum, 152
specific, 489
force-free, 223, 224
force/current
factor, 33, 45, 48, 192
matrix, 210

relationship, 31, 45
force/displacement
factor, 33, 192
matrix, 193
relationship, 31, 33
forced vibrations, 256
aeroengine, 285
response, 262
unbalance, 284
forces
bearing, 171
nonconservative, 167, 174, 179
forward whirl, 414, 419
Fourier/frequency analyzer, 247
FPGA, 231
free rotor, 175
free-free mode shapes, 324
frequency domain, 57, 59, 61
frequency response, 34, 52, 55, 60–63, 223, 236, 237, 241, 243, 244
amplification, 58–60
amplitude, 59–61
identification, 302
matrix, 61
measurement, 247, 249
phase, 60, 61
unbalance, 185
friction, 413, 415, 419, 424

gain compensation, 322
gain margin, 356
gain scheduled control, 377
gap sensor, 467
gas density, 141
gas friction losses, 136, 140
graphite
pyrolithic, 496
gyrodynamics, 176
gyroscopic effects, 173, 176
elastic rotor, 274
gyroscopics, 28, 65, 231, 242, 247, 248, 377
effect, 191, 198, 200, 204, 208, 211
matrix, 194, 196, 198, 199, 201, 213
rotor, 202

H-bridge, 98
Hall effect, 105
current measurement, 107
hallbach array, 497
harmonic balance, 420
harmonic control, 426
heart
artificial, pump, 462, 480
implantable, artificial, 480
transplant, 480
heat loss, 84
heteropolar, 159
heteropolar magnetics, 82
high speed, 7
high speed rotor, 154
high temperature, 158
homopolar, 159
homopolar bearing, 140, 148
homopolar magnetics, 83, 97
hybrid
magnetic bearing, 468
hysteresis, 74, 151, 491
losses, 159
hysteresis losses, 137, 138

identification, 229, 247, 252, 299, 516
for diagnosis, 316
excitation by AMB, 305
fluid structure interaction, 312
parameter estimation, 304
response functions, 302
implantable artificial heart, 480
impulse response
identification, 302
inductance, 72, 76
electromagnet, 436
inertia properties, 167
influence coefficient, 420
information processing, 152
initial condition, 36, 52
instrumentation, 39
built-in, 230, 246, 247
external, 247, 248
integrator
gain, PID controller, 346
inter-sample skew, 230, 231
interlacing
defect repairing, 326
pole-zero, 323
interrogation signal, 446, 450, 454
iron resistivity, 139
ISO standards

for AMB, 509
quality, 509
sensitivity, 358
unbalance, 181

Jeffcott rotor, 252

kinematic viscosity, 141

lamination, 139
Laval rotor, 252
leakage flux, 88
levitation
coil current, 470
control, 467
control algorithm, 467
force, 465
Levitron, 5
lifetime at high temperature, 158
LIGA, 487
linear
periodic, 443
time invariant, 439
linearity/nonlinearity, 31, 33, 41, 43, 48, 50, 51, 57
linearization, 28, 33, 44, 46, 48, 49, 124
bias, 95
current bias, 79
square root, 126
load capacity, 39, 44, 47, 67, 81, 151
radial bearings, 92
specific, 92
thrust bearing, 94
loads
centrifugal, 491
torque, 467
Lorentz
force, 473
self-bearing motor, 462, 473
Lorentz force, 10, 13, 70, 494
loss mechanisms, 135
losses, 135, 159
aerodynamic, 140, 147
amplifier, 148
cable, 138, 148
copper, 84, 137
eddy current, 135, 137, 139
electrical power, 95
gas friction, 140
hysteresis, 137, 138
iron, 84, 147
magnetic, 136
mitigation, 147
power amplifier, 138
rotational, 492
stator, 148
windage, 135, 140, 501
low pass filter, 205, 215, 239, 241, 242, 245
LPV control, 377
LQG control, 440, 441
Lyapunov
function, 448

machine
smart, 411
MAGLEV, 6, 14
magnet
permanent, 496
rare earth, 496
magnetic
circuit, 74
field, 71
field energy, 77
flux, 71
flux density, 71
force, 77
permeability, 72
polarization, 73
saturation, 81, 92, 435, 453
magnetic actuator, 111
magnetic bearing
active, 27–29, 37, 47
active micro, 498
hybrid, 29, 468
Lorentz force, 27
passive, 27–29, 37
reluctance force, 27
superconducting, 27
types, 493
magnetic displacement sensor, 103
magnetic flux
load capacity, 151
magnetic force, 10
magnetic loss, 136
magnetism, 70
magnetization curve, 76
magnetomotive force, 75

maintainability, 410
margin, gain and phase, 356
mass
  matrix, 194, 201, 203, 213
  rotor, 205
materials
  carbon fiber, 155
  cobalt, 152
  diamagnetic, 6, 495
  ferromagnetic, 6, 10, 151, 495
  for high temperature, 158
  strength, 94
  superconducting, 12, 495
maximum singular value, 350
measurement
  force, 306
mechanical energy
  conversion, 48
  kinetic, 52
  potential, 52
mechatronics, 39, 135
  definition, 4
MEMS, 487
micro magnetic actuator, 487
microprocessor, 229–231, 245, 247, 248
  fixed-point, 220
MIMO
  control, 230, 231, 246
  control design, 241–243, 245, 247
  measurement, 247
  transfer function, 247, 248
modal analysis, 252
  for rotating structures, 307
modal parameters, 300
modal truncation, 337
mode shapes
  flexible rotor, 324
  free-free, 324
model
  actuator, 330
  AMB system, 328
  assembly, 335
  casings and substructures, 339
  closed loop, 341
  Euler-Bernoulli beam, 337
  rotor, 331
  sensor, 332
  state space, 113, 329
  structure, 330
  synchronously reduced, 342
modeling
  finite element, 82
modes, 337
modulation
  pulse-width, 97
moment of inertia
  polar, 206
  transverse, 205, 206
monitoring, 229, 230, 247, 248
motor
  AC, 461, 468
  axial self-bearing, 477
  bearingless, 461
  combined, bearing, 461
  induction, 466, 500
  Lorentz self-bearing, 462, 473
  self-bearing, 461, 479
  self-bearing or bearingless, 27
motor control, 230
multi-processor, 230
multiplexer, 230, 246
multiply-accumulate (MAC), 246

natural vibrations, 256, 262
  aeroengine, 279
  flexible rotor, 277
network
  thermal, 85
non-collocation, 320, 323
non-conservative forces, 167, 179, 203, 214
  matrix, 213, 214
nonlinear
  magnetic analysis, 76
nonlinear dynamics
  amplitude jump, 428
  aperiodic response, 415
  contact modes, 413–421, 423, 424
  rotordynamics, 413–421, 423, 424
norm
  vector, 349
  $\mathcal{H}_\infty$, 366
notch filter
  generalized, 216, 219, 220
nutation, 167, 178
Nyquist frequency, 236–238

Ohm's law, 436

operating point, 31, 34, 35, 45, 48
optical displacement sensor, 104
optimization
  bearing geometry, 88
order reduction, 246, 373
oscillation
  amplitude, 37, 58
  damped, 36, 37, 43
  harmonic, 37, 58
  periodic, 37
  phase, 58
  pseudo-periodic, 37
oscilloscope, 247, 248
over-sampling, 231

Padé approximation, 333
Padé approximation, 245
parallel
  mode, 198, 199, 204, 206, 208, 210–212, 214
paramagnetic material, 73
parameter estimation, 304
parameter estimator, 447
parametric excitation, 188
PD control, 321, 418, 425, 467, 479
performance
  assessment, 347
peripheral, 229–231
permanent magnets, 5, 12, 28, 29, 31, 95
  bias, 468
permeability, 10
persistency of excitation, 447, 450
phase
  currents, 475
phase compensation, 322
phase lag
  anti-aliasing filter, 236
  sampling delay, 237–239, 244
phase lead controller, 321
phase margin, 238, 356
PID
  control,digital, 471
PID control, 342, 411, 413, 417
  non-collocated, 352
pinned beam, 320
plant
  MIMO, 208
  rigid body, 208
polarity sequence, 140
polarization
  magnetic, 73
poles, 320
  angle, 78
  number, 463
  pair number, 464
  plus two or minus two, 462
  salient, 466–468
  shoes, 88
  transfer function, 323
position
  sensor, 99
position reference command, 44–46
position sensor, 69, 435
power
  specific, 489
power amplifier, 27, 29, 41, 42, 44, 50, 69, 77, 97, 153
  bandwidth, 50, 56
  current, 29, 44, 48, 49
  dynamics, 30, 34, 44, 57
  voltage, 29, 48
power amplifier losses, 138
power bandwidth, 153
power failure, 410
power supply, 513
precession, 167, 178
precision bearings, 161
preventive maintenance, 229, 248
principal/inertial axis, 215, 223, 224
probe
  proximity, 478
processor
  digital signal, 467, 472, 478, 482
properties of AMB, 15
proximity
  probe, 478
pulse width modulation (PWM), 97, 224
  signal pattern, 230
  unit, 229, 231
pump
  artificial heart, 462, 480
  performance, 482
  rotary blood, 480

real time operating system, 510
recomposition, 209

redundancy, 408–411, 511
reliability, 505
reluctance force, 10
remanence, 74
resistance
  copper, 87
resistivity
  iron, 139
resonance, 182
  rigid body, 221
response
  unbalance, 351, 467, 468, 472, 475, 479
response functions
  identification, 302
  measurement, 303
retainer bearing, 389
Reynolds number, 140
rigid disk model, 413
rigid rotor, 320
  equations of motion, 171
rigid rotor/body, 191, 193, 194, 196, 200, 204, 208, 210, 212, 214
robust control, 513
robustness, 34, 50, 56, 57, 61, 63, 356
root locus, 325
rotary
  blood pump, 480
rotation
  force-free, 160
  high speed, 7
  high-speed, 154
  precision, 161
rotational losses, 492
rotor, 29
  -stator contact, 33, 62
  drop, 412
  excitation, 182
  flexibility, 319
  flexible, 155, 251, 263
  free, 175
  model, 331
  modes, 337
  non-rotating, 175
  position, 29, 30, 39, 46, 47
  rigid, 320
  rigid, dynamics, 167
  velocity, 52
rotor losses
  measurement, 146
rotor response
  backward whirl, 413, 419
  contact modes, 413, 418, 424
  forward whirl, 414
rotor speed
  gyroscopic effects, 176
  influence on eigenfrequencies, 178
rotor/stator contact, 390
rub, 410, 414, 419, 420, 423, 424, 431

safety, 505
  definitions, 507
  philos. background, 506
salient pole, 466–468
sample-and-hold, 230, 234
sampling period, 231, 233, 234, 239, 241
sampling rate/frequency, 231, 233, 236, 237, 244–246
saturation, 74, 151
  dynamic, 205
  magnetic, 81, 435, 453
  numerical, 220
  power amplifier, 223
scaling, 489, 490
secant algorithm, 239, 242, 244
self monitoring, 411
self–sensing, 435
self-bearing motor, 27, 461, 479
sensitivity, 355
  ISO standards, 358
  sources of, 361
sensitivity function, 62, 63
sensor, 27, 41, 42
  capacitive, displacement, 103
  displacement, position, 411
  dynamics, 30, 34, 44, 57
  eddy current, 29, 101, 482
  gap, 467
  inductive, 29
  inductive, displacement, 101
  magnetic displacement, 103
  model, 332
  noise, 56
  optical, 3
  optical displacement, 104
  position, 69, 99
  transverse flux, 102
sensor offset, mechanical, 187

Shannon theorem, 236, 245
signal
  interrogation, 446, 450, 454
signal generator, 247
signal injection, 247
singular value, 350
SISO
  control, 230, 241
  transfer function, 247
size of the bearing, 158
skew-symmetric, 194, 201, 203, 211
small gain theorem, 356
smart
  definition, 514
  examples, 514
  machines, 514
smart machine, 411
smart machine technology, 161
software, 510
  as a machine element, 4
  development system, 510
specific force, 489
specific load capacity, 152
specific power, 489
speed
  supercritical, 155
spring
  -damper, 28, 34, 37, 49
  mechanical, 30, 31, 34, 44
square root linearization, 126
stability margins, gain and phase, 356
stability of motion, 171, 174
stability/instability, 28, 31, 33, 35
  asymptotic, 58, 61
  closed-loop, 41, 57
  limit-stable, 36
  open-loop, 30, 35, 49, 50
  stabilization, 29, 33
standards, 509
  for magnetic bearings, 9
  ISO, sensitivity, 358
state space
  description, 196, 214
  matrix, 199
state space model, 113, 329
stator
  slotless, 474
  slotted, 474
stiffness, 30, 34, 36, 39, 42, 44, 61, 65, 66, 199
  closed-loop, 39, 42
  compensation matrix, 211, 212, 224
  coupling, 214
  cross-, 201, 203
  dynamic, 28, 34, 46, 63, 66, 153
  external, 222
  high, 41, 42
  low, 40, 50
  matrix, 196, 201, 203, 210, 213
  mechanical, 31
  "natural", 42, 196, 208
  negative bearing, 31, 33, 40, 42, 45, 193, 194, 211, 223, 224
  static, 28, 34, 42, 47, 63, 67
strength
  material, 94
stresses, centrifugal forces, 154
substructure model, 339
superconducting materials, 495
superconductivity, 12, 14, 18
superconductor, 495
suspension
  active, 29
  five axes, 29
  passive, 28
  permanent magnet, 29
  rigid body, 30
switching
  amplifier, 97, 446, 450
  noise, 97
  ripple, 446, 450
  three state, 451
symmetric, 194, 198, 201, 203–205, 208, 211, 212
  non-, 199, 212
synchronous control, 378, 426, 427
synchronously reduced model, 342
synthesis
  μ, 370
system model, 328

technology of AMB, 9
temperature
  coil, 88
test rig
  aeroengine, 279
  for identification, 312

for modal analysis, 308
for touch-down, 391
thrust magnetic bearings, 93
tilt and translate control, 361
tilting motion, 198
time domain, 36, 55, 59–61
timer interrupt, 232
torque
braking, 135, 144
dynamic, 479
load, 467
reaction, 473
rotating, 468, 471
touch-down bearing, 389
ball bearings, 400
contact dynamics, 391
contact force, 399
control reconfig., 518
design guidelines, 401
friction force, 395
test rig, 391
time history of touch-down, 399, 400
vertical axis arrangement, 403
whirl motion, 396
touchdown, 407, 413
avoiding, 407, 426
dynamics, 412
recovery, 410, 427, 431
transconductance amplifier, 112, 121
transfer function, 60–64, 211, 219, 235, 236, 241, 247, 248
matrix, 60, 219
poles and zeros, 323
transform
FFT, 61
Fourier, 55, 61
Laplace, 59, 60
transformation
$\mathcal{Z}$, 236
bilinear, 243
Fast Fourier (FFT), 247
Laplace, 235
matrix, 193, 209–211
natural coordinates, 365
Tustin, 243
transition
matrix, 235
sampling instant, 234, 235
state, 233
translational motion, 211
transpermeance amplifier, 122
transplant
heart, 480
transportation, 6
transverse flux sensor, 102
turbo–molecular pump, 435, 444
turbo-machinery, 17
turbomolecular pumps, 149

unbalance, 38, 256, 409, 413, 414, 420
adaptation, 216, 218
compensation, 516
definition, 180
excitation, 55
excitation of rotor vibr., 183
force attenuation, 28, 216
forced vibrations, 284
forward whirl, 185
quality grade, 181
residual, 215, 216
response, 215, 220, 222, 224, 262, 468, 472, 475, 479
technical example, 169
vibration attenuation, 216
unbalance control, 229, 378, 426
unbalance response, 351, 467
unit circle, 235, 236
unsymmetry of the rotor, 188

vacuum, 501
vacuum applications
losses in, 149
velocity, 34, 43, 48, 52, 53, 239
velocity measurement, 104
vertical axis, 403
vibrational control, 443
vibrations
bending, 461
forced, 256, 284, 285
natural, 167, 171, 175, 256, 262, 277, 279
steady state, 475
virgin magnetization curve, 84
virtual displacement, 78
viscosity
kinematic, 141
viscous drag, 140
voice coil actuator, 495

voltage control, 439

whirl
  backward, 413, 414
  forward, 414
whirl motion, 396
whirl, forward and backward, 167, 178
windage losses, 135, 136, 140, 501
winding
  differential, 124

zero power control, 160
zero-order hold (ZOH), 233, 234, 238, 239, 243
zeros
  transfer function, 323